

NIST Special Publication 1018-5

Fire Dynamics Simulator (Version 5)
Technical Reference Guide

Volume 3: Validation

Kevin McGrattan
Simo Hostikka
Jason Floyd
Randall McDermott



NIST Special Publication 1018-5

Fire Dynamics Simulator (Version 5) Technical Reference Guide

Volume 3: Validation

Kevin McGrattan
Randall McDermott
*Fire Research Division
Building and Fire Research Laboratory*

Simo Hostikka
*VTT Technical Research Centre of Finland
Espoo, Finland*

Jason Floyd
*Hughes Associates, Inc.
Baltimore, Maryland*

September 3, 2010
FDS Version 5.5
SVNRepository Revision : 6591



U.S. Department of Commerce
Gary Locke, Secretary

National Institute of Standards and Technology
Patrick Gallagher, Director

Preface

This is Volume 3 of the FDS Technical Reference Guide. Volume 1 describes the mathematical model and numerical method. Volume 2 documents past and present model verification work. Instructions for using FDS are contained in a separate User’s Guide [1].

The FDS Technical Reference Guide is based in part on the “Standard Guide for Evaluating the Predictive Capability of Deterministic Fire Models,” ASTM E 1355 [2]. ASTM E 1355 defines *model evaluation* as “the process of quantifying the accuracy of chosen results from a model when applied for a specific use.” The model evaluation process consists of two main components: verification and validation. *Verification* is a process to check the correctness of the solution of the governing equations. Verification does not imply that the governing equations are appropriate; only that the equations are being solved correctly. *Validation* is a process to determine the appropriateness of the governing equations as a mathematical model of the physical phenomena of interest. Typically, validation involves comparing model results with experimental measurement. Differences that cannot be explained in terms of numerical errors in the model or uncertainty in the measurements are attributed to the assumptions and simplifications of the physical model.

Evaluation is critical to establishing both the acceptable uses and limitations of a model. Throughout its development, FDS has undergone various forms of evaluation, both at NIST and beyond. This volume provides a survey of validation work conducted to date to evaluate FDS.

About the Authors

Kevin McGrattan is a mathematician in the Building and Fire Research Laboratory of NIST. He received a bachelors of science degree from the School of Engineering and Applied Science of Columbia University in 1987 and a doctorate at the Courant Institute of New York University in 1991. He joined the NIST staff in 1992 and has since worked on the development of fire models, most notably the Fire Dynamics Simulator.

Randall McDermott joined the research staff of the Building and Fire Research Lab in 2008. He received a bachelors of science from the University of Tulsa in Chemical Engineering in 1994 and a doctorate at the University of Utah in 2005. His research interests include subgrid-scale models and numerical methods for large-eddy simulation, adaptive mesh refinement, and Lagrangian particle methods.

Simo Hostikka is a Senior Research Scientist at VTT Technical Research Centre of Finland. He received a master of science (technology) degree in 1997 and a doctorate in 2008 from the Department of Engineering Physics and Mathematics of the Helsinki University of Technology. He is the principal developer of the radiation and solid phase sub-models within FDS.

Jason Floyd is a Senior Engineer at Hughes Associates, Inc., in Baltimore, Maryland. He received a bachelors of science degree and a doctorate from the Nuclear Engineering Program of the University of Maryland. After graduating, he won a National Research Council Post-Doctoral Fellowship at the Building and Fire Research Laboratory of NIST, where he developed the combustion algorithm within FDS. He is currently funded by NIST under grant 70NANB8H8161 from the Fire Research Grants Program (15 USC 278f). He is the principal developer of the multi-parameter mixture fraction combustion model and control logic within FDS.

Acknowledgments

FDS is supported financially via internal funding at both NIST and VTT, Finland. In addition, support is provided by other agencies of the US Federal Government:

- The US Nuclear Regulatory Commission Office of Research has funded key validation experiments, the preparation of the FDS manuals, and the development of various sub-models that are of importance in the area of nuclear power plant safety. Special thanks to Mark Salley and Jason Dreisbach for their efforts and support. The Office of Nuclear Material Safety and Safeguards, another branch of the US NRC, has supported modeling studies of tunnel fires under the direction of Chris Bajwa and Allen Hansen.
- The Micro-Gravity Combustion Program of the National Aeronautics and Space Administration (NASA) has supported several projects that directly or indirectly benefited FDS development.
- The US Forest Service has supported the development of sub-models in FDS designed to simulate the spread of fire in the Wildland Urban Interface (WUI). Special thanks to Mark Finney and Tony Bova for their support.
- The Minerals Management Service of the US Department of the Interior funded research at NIST aimed at characterizing the burning behavior of oil spilled on the open sea or ice. Part of this research led to the development of the ALOFT (A Large Outdoor Fire plume Trajectory) model, a forerunner of FDS. Special thanks to Joe Mullin for his encouragement of the modeling efforts.

The following individuals and organizations played a role in the validation process of FDS.

- Anthony Hamins directed the NIST/NRC and WTC experiments, conducted smaller methane burner measurements, and quantified the experimental uncertainty of these and other experiments used in this study. Alex Maranghides was the Director of the Large Fire Laboratory at NIST at the time these tests were conducted, and he helped to design the experiments. Therese McAllister oversaw the instrumentation of the structural steel during the WTC experiments.
- Anthony Hamins developed the technique of evaluating experimental uncertainty that is used throughout this Guide. Blaza Toman of the Statistical Engineering Division of NIST developed the method of quantifying the model error.
- Rick Peacock of NIST assisted in the interpretation of results from the “NBS Multi-Room Test Series,” a set of three room fire experiments conducted at the National Bureau of Standards (now NIST) in the mid-1980’s.
- Bryan Klein of NIST assisted in the development of techniques to automatically generate the plots that are found throughout this Guide.

- Bill Pitts, Nelson Bryner, and Erik Johnsson of NIST contributed and interpreted test data for the “NIST Reduced Scale Enclosure Experiments.”
- Thanks to VTT, Finland, for their contribution of experimental data, referred to in this document as the “VTT Large Hall Experiments.” Also, Jukka Hietaniemi, Jukka Vaari and Timo Korhonen have performed validation studies of various sub-models. The VTT Fire Research group continues to work on model development and validation of the model for various applications.
- David Sheppard, currently of the Bureau of Alcohol, Tobacco and Firearms (ATF), conducted the experiments referred to as the “UL/NFPRF Test Series” on behalf of the Fire Protection Research Foundation (then known as the National Fire Protection Research Foundation) while working at Underwriters Labs in Northbrook, Illinois. Sheppard, along with Bryan Klein of NIST, conducted the experiments referred to as the “ATF Corridors” series in 2008.
- Thanks to Jerry Back, Craig Beyler and Phil DiNenno of Hughes Associates and Pat Tatem of the Naval Research Laboratory for their contribution of experimental data for the “HAI/NRL Wall Fire” series. Thanks also to Craig Beyler for assistance with the data for the “Beyler Hood Experiments.”
- Thanks to Ken Steckler for providing details about the “Steckler Compartment Experiments” of 1979.
- Jianping Zhang at the University of Ulster contributed heat flux measurements from the SBI apparatus.
- At the University of Maryland, Professor Fred Mowrer and Phil Friday were the first to apply FDS to the NRC-sponsored experiments referred to in this document as the “FM/SNL Test Series” (Factory Mutual and Sandia National Laboratories conducted these experiments).
- Steve Nowlen of Sandia National Laboratory provided valuable information about the FM/SNL series, and he also conducted the CAROLFIRE experiments.
- Ulf Wickström of SP, Sweden, contributed experimental data from a series of experiments (SP 2009 AST) that were designed to evaluate the feasibility of using plate thermometer measurements as boundary conditions for a heat conduction calculation within several types of steel beams. The adiabatic surface temperature concept was tested in both the experiments and model.
- Thanks to Jeremy Thornock at the University of Utah for providing data on the Sandia helium plume.
- Taylor Meyers, a student at the University of Maryland and a Summer Undergraduate Research Fellow (SURF) at NIST, analyzed the Vettori Flat and Sloped Ceiling sprinkler experiments. Thanks also to Bob Vettori of the U.S. Nuclear Regulatory Commission and formerly of NIST for his help in locating the original test data and laboratory notebooks.
- Hans la Cour-Harbo, a masters degree student at the Technical University of Denmark, provided guidance and insight on the NRCC Facade experiments. Scott Bareham of NIST provided the technical drawing of the test enclosure.

Contents

Preface	i
About the Authors	iii
Acknowledgments	v
1 What is Model Validation?	1
1.1 Model Scenarios	1
1.2 Model Outputs	2
1.3 Model Accuracy	3
1.4 How to Use the Guide	3
2 Survey of Past Validation Work	5
2.1 Validation Work with Pre-Release Versions of FDS	5
2.2 Validation of FDS since 2000	6
2.2.1 Fire Plumes	6
2.2.2 Pool Fires	7
2.2.3 Air and Gas Movement in the Absence of Fire	7
2.2.4 Wind Engineering	8
2.2.5 Atmospheric Dispersion	8
2.2.6 Growing Fires	9
2.2.7 Flame Spread	10
2.2.8 Compartment Fires	11
2.2.9 Sprinklers, Mist System, and Suppression by Water	11
2.2.10 Airflows in Fire Compartments	12
2.2.11 Tunnel Fires	13
2.2.12 Smoke Detection	13
2.2.13 Combustion Model	14
2.3 Reconstructions of Actual Fires	14
3 Description of Experiments	17
3.1 VTT Large Hall Tests	17
3.2 UL/NFPRF Sprinkler, Vent, and Draft Curtain Study	20
3.3 NIST/NRC Test Series	23
3.4 WTC Spray Burner Test Series	25
3.5 FM/SNL Test Series	27
3.6 NBS Multi-Room Test Series	29
3.7 Steckler Compartment Experiments	31

3.8	Bryant Doorway Velocity Measurements	33
3.9	SP Adiabatic Surface Temperature Experiments	33
3.10	ATF Corridors Experiments	33
3.11	McCaffrey Plume Experiments	36
3.12	Sandia Plume Experiments	36
3.13	Smyth Slot Burner Experiment	36
3.14	Beyler Hood Experiments	36
3.15	NIST Reduced Scale Enclosure Experiments	36
3.16	Hamins Methane Burner Experiments	37
3.17	Restivo Compartment Air Flow Experiment	37
3.18	NRL/HAI Wall Heat Flux Measurements	37
3.19	Ulster SBI Corner Heat Flux Measurements	37
3.20	FM Parallel Panel Experiments	37
3.21	NRCC Facade Heat Flux Measurements	38
3.22	Cable Response to Live Fire – CAROLFIRE	38
3.23	BRE Spray Test for Radiation Attenuation	40
3.24	Vettori Flat Ceiling Experiments	40
3.25	Vettori Sloped Ceiling Experiments	42
3.26	Summary of Experiments	43
4	Quantifying Model Uncertainty	45
4.1	Introduction	45
4.2	Sources of Model Uncertainty	46
4.3	Quantifying the Experimental Uncertainty	47
4.4	Calculating Model Uncertainty	49
4.5	Verifying the Procedure	53
4.6	Making Use of the Model Uncertainty	55
4.7	Limitations	56
4.8	Conclusion	57
5	HGL Temperature and Depth	59
5.1	HGL Reduction Method	59
5.2	WTC Test Series	60
5.3	VTT Test Series	63
5.4	NIST/NRC Test Series	65
5.5	FM/SNL Test Series	70
5.6	NBS Multi-Room Test Series	72
5.7	Summary of Hot Gas Layer Temperature and Height	76
5.8	Steckler Compartment Experiments	78
6	Fire Plumes	87
6.1	McCaffrey’s Plume Correlation	87
6.2	Heskestad’s Flame Height Correlation	90
6.3	VTT Large Hall and FM/SNL Test Series	92
6.4	Sandia 1 m Helium Plume	95
6.5	Sandia 1 m Methane Pool Fire	98
6.6	Sandia 1 m Hydrogen Pool Fire	103

7	Ceiling Jets and Device Activation	105
7.1	WTC Test Series	105
7.2	NIST/NRC Test Series	107
7.3	FM/SNL Test Series	110
7.4	ATF Corridors Series	111
7.5	UL/NFPRF Sprinkler, Vent, and Draft Curtain Experiments	118
7.6	Vettori Flat Ceiling Experiments	123
7.7	Vettori Sloped Ceiling Experiments	131
8	Gas Velocity	143
8.1	Steckler Compartment Doorway Velocity Profiles	143
8.2	Bryant Doorway Experiments	152
8.3	Restivo Experiment	154
8.4	ATF Corridor	155
9	Gas Species and Smoke	161
9.1	WTC and NIST/NRC Test Series, Oxygen and CO ₂	161
9.2	NIST/NRC Test Series, Smoke	169
9.3	Smyth Slot Burner Experiment	173
9.4	Beyler Hood Experiments	177
9.5	NIST Reduced Scale Enclosure (RSE) Test Series, 1994	179
10	Compartment Pressure	181
10.1	NIST/NRC Test Series	181
11	Surface Temperature	185
11.1	WTC Test Series, Steel Structural Members and “Slug” Calorimeters	185
11.2	SP Adiabatic Surface Temperature Experiments	202
11.3	NIST/NRC Test Series, Cables	213
11.4	CAROLFIRE Cable Temperatures	223
11.5	WTC Ceiling and Wall Temperatures	229
11.6	NIST/NRC Test Series, Compartment Walls, Floor and Ceiling	239
12	Heat Flux	249
12.1	Hamins Methane Burner Heat Flux Measurements	249
12.2	NRL/HAI Wall Heat Flux Measurements	252
12.3	Ulster SBI Heat Flux Measurements	255
12.4	FM Parallel Panel Heat Flux Measurements	257
12.5	WTC Heat Flux Measurements	259
12.6	NIST/NRC Test Series, Heat Flux to Cables	268
12.7	NRCC Facade Heat Flux Measurements	278
12.8	BRE Spray Tests, Attenuation of Thermal Radiation in Water Spray	282
Bibliography		285
References		296

List of Figures

3.1	Geometry of the VTT Large Fire Test Hall	19
3.2	Plan view of the UL/NFPRF Experiments.	21
3.3	Geometry of the NIST/NRC Experiments.	24
3.4	Geometry of the WTC Experiments.	26
3.5	Geometry of the FM/SNL Experiments.	28
3.6	Geometry of the NBS Multi-Room Experiments.	30
3.7	Geometry of the ATF Corriodrs Experiments	35
3.8	Geometry of the NRCC Facade Experiments	39
3.9	Geometry of the Vettori Flat Ceiling.	41
4.1	Demonstration of model uncertainty.	46
4.2	Sample scatter plot.	48
4.3	Sample time history plots.	51
4.4	Verification of the model uncertainty calculation, Case 1.	54
4.5	Verification of the model uncertainty calculation, Case 2.	55
4.6	Testing the normality of validation data.	58
5.1	Summary of HGL temperature and height predictions, VTT, NIST/NRC, WTC, NBS and FM/SNL series	77
5.2	Summary of peak temperature predictions for the Steckler Compartment Experiments.	86
6.1	Summary of flame height predictions, Heskestad correlation.	91
6.2	Summary of plume temperature predictions, VTT and FM/SNL test series.	94
6.3	Sandia 1 m helium plume image.	95
6.4	Sandia 1 m helium plume mean velocity profiles.	96
6.5	Sandia 1 m helium plume mean mass fraction profiles.	97
6.6	Sandia 1 m methane pool fire instantaneous temperature contours.	98
6.7	Sandia 1 m methane pool fire (Test 14) mean velocity profiles.	99
6.8	Sandia 1 m methane pool fire (Test 24) mean velocity profiles.	100
6.9	Sandia 1 m methane pool fire (Test 17) mean velocity profiles.	101
6.10	Sandia 1 m methane pool fire velocity signal and power spectrum.	102
6.11	Sandia 1 m hydrogen pool fire instantaneous temperature contours.	103
6.12	Sandia 1 m hydrogen pool fire (Test 35) mean velocity profiles.	104
7.1	Summary of ceiling jet temperature predictions, WTC, NIST/NRC and FM/SNL test series.	117
7.2	Summary of sprinkler actuation predictions, UL/NFPRF test series.	122
7.3	Predicted vs. Measured Activation Times of all the Vettori Cases	130
7.4	Predicted vs. Measured Activation Times of all the Vettori Sloped Ceiling Cases	141

8.1	Summary of velocity predictions, Steckler compartment experiments.	151
9.1	Summary of gas species predictions, NIST/NRC and WTC test series.	168
9.2	Summary of smoke concentration predictions, NIST/NRC test series	172
9.3	Temperature and gas species predictions 7 mm above burner, Smyth experiment.	174
9.4	Temperature and gas species predictions 9 mm above burner, Smyth experiment.	175
9.5	Temperature and gas species predictions 11 mm above burner, Smyth experiment.	176
9.6	Summary of gas species predictions, Beyler hood experiments.	178
9.7	Summary of NIST Reduced Scale Enclosure (1994) experiments.	180
10.1	Summary of pressure predictions, NIST/NRC test series.	184
11.1	Summary of steel temperature predictions, WTC test series.	201
11.2	Summary of gas, plate thermometer, and steel temperatures, SP2009 AST Experiments.	212
11.3	Summary of cable surface temperature predictions, NIST/NRC test series.	222
11.4	Summary of wall and ceiling temperature predictions, WTC test series.	238
11.5	Summary of wall, floor and ceiling temperature predictions, NIST/NRC test series.	248
12.1	Radial heat flux predictions, Hamins methane burner experiments.	250
12.2	Vertical heat flux predictions, Hamins methane burner experiments.	251
12.3	Wall heat flux predictions, NRL/HAI experiments.	253
12.4	Wall heat flux predictions, NRL/HAI experiments.	254
12.5	Corner heat flux predictions, Ulster SBI experiments.	256
12.6	Side wall heat flux predictions, FM Parallel Panel experiments.	258
12.7	Summary of heat flux predictions, WTC test series.	267
12.8	Summary of heat flux predictions to cables, NIST/NRC test series.	277
12.9	Smokeview rendering of NRCC Facade experiment.	278
12.10	Comparison of experimental and predicted droplet speeds and mean diameters for the three nozzles and different pressures.	283
12.11	Summary radiation attenuations, BRE Spray test series.	283

List of Tables

3.1	Results of the UL/NFPRF Experiments.	22
3.2	Summary of Steckler compartment experiments.	32
3.3	Summary of the major experimental parameters.	43
4.1	Sensitivity of model outputs from Volume 2 of NUREG-1824 [3].	49
4.2	Summary of Hamins' uncertainty estimates [3].	50
4.3	Estimated bias and relative error from random trials used to verify the analysis.	56
6.1	Summary of parameters for the flame height predictions. The grid cell size, δx_{10} , refers to the case where $D^*/\delta x=10$	90
11.1	Locations of ceiling surface temperature measurements relative to the fire pan in the WTC series.	229
11.2	Wall thermocouple positions for the NIST/NRC series.	239
12.1	Summary of Hamins methane burner experiments.	249
12.2	Summary of the NRL/HAI Wall Heat Flux Measurements.	252
12.3	Heat flux gauge positions relative to the center of the fire pan in the WTC series.	259

Chapter 1

What is Model Validation?

Although there are various definitions of model validation, for example those contained in ASTM E 1355 [2], most define it as the process of determining how well the mathematical model predicts the actual physical phenomena of interest. Validation typically involves (1) comparing model predictions with experimental measurements, (2) quantifying the differences in light of uncertainties in both the measurements and the model inputs, and (3) deciding if the model is appropriate for the given application. This Guide only does (1) and (2). Number (3) is the responsibility of the model user.

A common question asked of any mathematical model is whether it is validated. To say that FDS is “validated” means that the model has been shown to be of a given level of accuracy for a given range of parameters for a given type of fire scenario. Although the FDS developers continuously perform validation studies, it is ultimately the end user of the model who decides if the model is adequate for the job at hand. Thus, this Guide provides the raw material for a validation study, but it does not and cannot be considered comprehensive.

The following sections discuss key issues that you must consider when deciding whether or not FDS has been validated. It depends on (a) the scenarios of interest, (b) the predicted quantities, and (c) the desired level of accuracy. Keep in mind that FDS can be used to model most any fire scenario and predict almost any quantity of interest, but the prediction may not be accurate because of limitations in the description of the fire physics, and also because of limited information about the fuels, geometry, and so on.

1.1 Model Scenarios

When doing a validation study, the first question to ask is, “What is the application?” There are countless fire scenarios to consider, but from the point of view of validation it is useful to divide them into two classes – those for which the fire is *specified* as an input to the model and those for which the fire is *predicted* by the model. The former is often the case for a design application, the latter for a forensic reconstruction. Consider each in turn.

Design applications typically involve an existing building or a building under design. A so-called “design fire” is specified either by a regulatory authority or by the engineers performing the analysis. Because the fire’s heat release rate is specified, the role of the model is to predict the transport of heat and combustion products throughout the room or rooms of interest. Ventilation equipment is often included in the simulation, like fans, blowers, exhaust hoods, HVAC ducts, smoke management systems, *etc.* Sprinkler and heat and smoke detector activation are also of interest. The effect of the sprinkler spray on the fire is usually less of interest since the heat release rate of the fire is specified rather than predicted. Detailed descriptions of the contents of the building are usually not necessary because these items are assumed to not contribute to the fire, and even if they are, the burning rate will be specified, not predicted. Sometimes, it is necessary to

predict the heat flux from the fire to a nearby “target,” and even though the target may heat up to some specified ignition temperature, the subsequent spread of the fire usually goes beyond the scope of the analysis because of the uncertainty inherent in object to object fire spread.

Forensic reconstructions require the model to simulate an actual fire based on information that is collected after the event, such as eye witness accounts, unburned materials, burn signatures, *etc.* The purpose of the simulation is to connect a sequence of discrete observations with a continuous description of the fire dynamics. Usually, reconstructions involve more gas/solid phase interaction because virtually all objects in a given room are potentially ignitable, especially when flashover occurs. Thus, there is much more emphasis on such phenomena as heat transfer to surfaces, pyrolysis, flame spread, and suppression. In general, forensic reconstructions are more challenging simulations to perform because they require more detailed information about the room contents, and there is much greater uncertainty in the total heat release rate as the fire spreads from object to object.

Validation studies of FDS to date have focussed more on design applications than reconstructions. The reason is that design applications usually involve specified fires and demand a minimum of thermophysical properties of real materials. Transport of smoke and heat is the primary focus, and measurements can be limited to well-placed thermocouples, a few heat flux gauges, gas samplers, *etc.* Phenomena of importance in forensic reconstructions, like second item ignition, flame spread, vitiation effects and extinction, are more difficult to model and more difficult to study with well-controlled experiments. Uncertainties in material properties and measurements, as well as simplifying assumptions in the model, often force the comparison between model and measurement to be qualitative at best. Nevertheless, current validation efforts are moving in the direction of these more difficult issues.

1.2 Model Outputs

For a given fire scenario, there are a number of different quantities that the model predicts, like gas temperature, heat flux, and so on. A typical fire experiment can produce hundreds of time histories of point measurements, each of which can be reproduced by the model to some level of accuracy. It is a challenge to sort out all the plots and graphs of all the different quantities and come to some general conclusion. For this reason, this Guide is organized by output quantity, not by individual experiment or fire scenario. In this way, it is possible to assess, over a range of different experiments and scenarios, the performance of the model in predicting a given quantity. Overall trends and biases become much more clear when the data is organized this way.

Keep in mind that for any fire experiment, FDS might predict a particular quantity accurately (within the experimental uncertainty bounds, for example), but another quantity less accurately. For example, in a series of 15 full-scale fire experiments conducted at NIST in 2003, sponsored by the U.S. Nuclear Regulatory Commission, the average hot gas layer (HGL) temperature predictions were within the accuracy of the experiments themselves, yet the smoke concentration predictions differed from the measurements by as much as a factor of 3. Why? Consider the following issues associated with various types of measurements:

- Is the measurement taken at a single point, or averaged over many points? In the example above, the HGL temperature is an average of many thermocouple measurements, whereas the smoke concentration is based on the extinction of laser light over a short length span. Model error tends to be reduced by the averaging process, plus most fire models, including FDS, are based on global mass and energy conservation laws that are expressed as spatial averages.
- Is the measured quantity time-averaged or instantaneous? For example, a surface temperature prediction is less prone to error in comparison to a heat flux prediction because the former is, in some sense, a time-integral of the latter.

- In the case of a point measurement, how close to the fire is it? The terms “near-field” and “far-field” are used throughout this Guide to describe the relative distance from the fire. In general, predictions of near-field phenomena are more prone to error than far-field. There are exceptions, however. For example, a prediction of the temperature directly within the flaming region may be more accurate than that made just a fire diameter away because of the fact that temperatures tend to stabilize at about 1000 °C within the fire itself, but then rapidly decrease away from the flames. Less accurate predictions typically occur in regions of steep gradients (rapid changes, both in space and time).

1.3 Model Accuracy

The desired accuracy for each predicted quantity depends on the technical issues associated with the analysis. You must ask the question: How accurate does the analysis have to be to answer the technical question posed? Returning to the earlier definitions of “design” and “reconstruction,” design applications typically are more accurate because the heat release rate is typically specified rather than predicted, and the initial and boundary conditions are better characterized – at least in the analysis. Mathematically, a design calculation is an example of a “well-posed” problem in which the solution of the governing equations is advanced in time starting from a known set of initial conditions and constrained by a known set of boundary conditions. The accuracy of the results is a function of the fidelity of the numerical solution, which is mainly dependent on the size of the computational grid.

A reconstruction is an example of an “ill-posed” problem because the outcome is known whereas the initial and boundary conditions are usually not. There is no single, unique solution to the problem, that is, it is possible to simulate numerous fires that produce the same general outcome. There is no right or wrong answer, but rather a small set of plausible fire scenarios that are consistent with the collected evidence. These simulations are then used to demonstrate to fire service personnel why the fire behaved as it did based on the current understanding of fire physics incorporated in the model. Most often, the result of the analysis is only qualitative. If there is any quantification at all, it could be in the time to reach critical events, like a roof collapse or room flashover.

1.4 How to Use the Guide

This Guide is merely a repository of calculation results. As FDS develops, it will expand to include new experimental measurements of newly modeled physical phenomena. With each minor release of FDS (version 5.2 to 5.3, for example), the plots and graphs will all be redone to ensure that changes to the model have not decreased the accuracy of a previous version. If you are embarking on a validation study, you might want to consider the following steps:

1. Survey Chapter 2 to learn about past efforts by others to validate the model for applications similar to yours
2. Identify in Chapter 3 experimental data sets appropriate for your application
3. Read the specific chapters for the quantities of interest

The experimental data sets and FDS input/output files are all managed via the on-line project archiving system. You might want to re-run examples of interest to better understand how the calculations were designed, and how changes in the various parameters might affect the results. This is known as a *sensitivity study*, and it is difficult to document all the parameter variations of the calculations described in this report. Thus, it is a good idea to determine which of the input parameters are particularly important.

Chapter 2

Survey of Past Validation Work

In this chapter, a survey of FDS validation work will be presented. Some of the work has been performed at NIST, some by its grantees and some by engineering firms using the model. Because each organization has its own reasons for validating the model, the referenced papers and reports do not follow any particular guidelines. Some of the works only provide a qualitative assessment of the model, concluding that the model agreement with a particular experiment is “good” or “reasonable.” Sometimes, the conclusion is that the model works well in certain cases, not as well in others. These studies are included in the survey because the references are useful to other model users who may have a similar application and are interested in even qualitative assessment. It is important to note that some of the papers point out flaws in early releases of FDS that have been corrected or improved in more recent releases. Some of the issues raised, however, are still subjects of active research. The research agenda for FDS is greatly influenced by the feedback provided by users, often through publication of validation efforts.

2.1 Validation Work with Pre-Release Versions of FDS

FDS was officially released in 2000. However, for two decades various CFD codes using the basic FDS hydrodynamic framework were developed at NIST for different applications and for research. In the mid 1990s, many of these different codes were consolidated into what eventually became FDS. Before FDS, the various models were referred to as LES, NIST-LES, LES3D, IFS (Industrial Fire Simulator), and ALOFT (A Large Outdoor Fire Plume Trajectory).

The NIST LES model describes the transport of smoke and hot gases during a fire in an enclosure using the Boussinesq approximation, where it is assumed that the density and temperature variations in the flow are relatively small [4, 5, 6, 7]. Such an approximation can be applied to a fire plume away from the fire itself. Much of the early work with this form of the model was devoted to the formulation of the low Mach number form of the Navier-Stokes equations and the development of the basic numerical algorithm. Early validation efforts compared the model with salt water experiments [8, 9, 10], and fire plumes [11, 12, 13, 14]. Clement validated the hydrodynamic model in FDS by measuring salt water flows using Laser Induced dye Fluorescence (LIF) [15]. An interesting finding of this work was that the transition from a laminar to a turbulent plume is very difficult to predict with any technique other than DNS.

Eventually, the Boussinesq approximation was dropped and simulations began to include more fire-specific phenomena. Simulations of enclosure fires were compared to experiments performed by Steckler [16]. Mell *et al.* [17] studied small helium plumes, with particular attention to the relative roles of baroclinic torque and buoyancy as sources of vorticity. Cleary *et al.* [18] used the LES model to simulate the environment seen by multi-sensor fire detectors and performed some simple validation work to check the model before using it. Large fire experiments were performed by NIST at the FRI test facility in Japan,

and at US Naval aircraft hangars in Hawaii and Iceland [19]. Room airflow applications were considered by Emmerich and McGrattan [20, 21].

These early validation efforts were encouraging, but still pointed out the need to improve the hydrodynamic model by introducing the Smagorinsky form of large eddy simulation. This addition improved the stability of the model because of the relatively simple relation between the local strain rate and the turbulent viscosity. There is both a physical and numerical benefit to the Smagorinsky model. Physically, the viscous term used in the model has the right functional form to describe sub-grid mixing processes. Numerically, local oscillations in the computed flow quantities are damped if they become large enough to threaten the stability of the entire calculation.

2.2 Validation of FDS since 2000

There is an on-going effort at NIST and elsewhere to validate FDS as new capabilities are added. To date, most of the validation work has evaluated the model's ability to predict the transport of heat and exhaust products from a fire through an enclosure. In these studies, the heat release rate is usually prescribed, along with the production rates of various products of combustion. More recently, validation efforts have moved beyond just transport issues to consider fire growth, flame spread, suppression, sprinkler/detector activation, and other fire-specific phenomena.

The validation work discussed below can be organized into several categories: Comparisons with full-scale tests conducted especially for the chosen evaluation, comparisons with previously published full-scale test data, comparisons with standard tests, comparisons with documented fire experience, and comparisons with engineering correlations. There is no single method by which the predictions and measurements are compared. Formal, rigorous validation exercises are time-consuming and expensive. Most validation exercises are done simply to assess if the model can be used for a very specific purpose. While not comprehensive on their own, these studies collectively constitute a valuable assessment of the model.

2.2.1 Fire Plumes

There are several examples of fire flows that have been extensively studied, so much so that a set of engineering correlations combining the results of many experiments have been developed. These correlations are useful to modelers because of their simplicity. The most studied phenomena include fire plumes, ceiling jets, and flame heights.

Although much of the early validation work before FDS was released involved fire plumes, it remains an active area of interest. One study by Chow and Yin [22] surveys the performance of various models in predicting plume temperatures and entrainment for a 470 kW fire with a diameter of 1 m and an unbounded ceiling. They compare the FDS results with various correlations and a RANS (Reynolds-Averaged Navier-Stokes) model.

Battaglia *et al.* [23] used FDS to simulate fire whirls. First, the model was shown to reproduce the McCaffrey correlation of a fire plume, then it was shown to reproduce qualitatively certain features of fire whirls. At the time, FDS used Lagrangian elements to introduce heat from the fire (no longer used), and this combustion model could not replicate the extreme stretching of the core of the flame zone.

Quintiere and Ma [24, 25] compared predicted flame heights and plume centerline temperatures to empirical correlations. For plume temperature, the Heskestad correlation [26] was chosen. Favorable agreement was found in the plume region, but the results near the flame region were found to be grid-dependent, especially for low Q^* fires. At this same time, researchers at NIST were reaching similar conclusions, and it was noticed by both teams that a critical parameter for the model is $D^*/\delta x$, where D^* is the characteristic fire diameter and δx is the grid cell size. If this parameter is sufficiently large, the fire can be considered

well-resolved and agreement with various flame height correlations was found. If the parameter is not large enough, the fire is not well-resolved and adjustments must be made to the combustion routine to account for it.

Gutiérrez-Montes *et al.* [27] simulated 1.3 MW and 2.3 MW fires in a 20 m cubic atrium using FDS version 4. The authors conclude that FDS “significantly over-predicts by 40 % to 80 % the plume temperature near the flame (below 9 m) but only slightly over-predicts by 10 % to 25 % the plume temperature above 9 m.” Similar results were found for experiments conducted at VTT, Finland, in a 19 m tall test hall with similar sized fires. These results are included in Section 6.3. Both of these studies point out the sensitivity of the centerline plume temperature close to the flame tip to the prediction of the flame height. FDS does not use a flame height correlation, but rather predicts the flame height based on the fuel stoichiometry and fluid dynamics of the turbulent plume.

Hurley and Munguia [28, 29] compared FDS (version 4) simulations with plume and ceiling jet measurements from a series of full-scale tests conducted by Underwriters Laboratories. The tests were conducted in a 36.6 m by 36.6 m compartment with ceiling heights ranging from 3 m to 12.2 m. Heat release rates followed a modified t-squared growth profile. Thermocouples attached to brass disks were used to simulate thermal detectors. The FDS simulations were conducted with a grid spacing of 10 cm. A convergence study found that grid-size convergence was achieved outside of the plume region. However, grid convergence was not achieved in the plume region at this grid spacing. Outside of the plume region, FDS predictions were within a factor of 1.9 of the test data.

2.2.2 Pool Fires

Xin *et al.* [30] used FDS to model a 1 m diameter methane pool fire. The computational domain was 2 m by 2 m by 4 m with a uniform grid size of 2.5 cm. The predicted results were compared to experimental data and found to qualitatively and quantitatively reproduce the velocity field. The same authors performed a similar study of a 7.1 cm methane burner [31] and a helium plume [32].

Hostikka *et al.* [33] modeled small pool fires of methane, natural gas and methanol to test the FDS radiation solver for low-sooting fires. They conclude that the predicted radiative fluxes are higher than measured values, especially at small heat release rates, due to an over-prediction of the gas temperature. These tests are also included in the Heat Flux section of this report.

Hietaniemi, Hostikka and Vaari [34] consider heptane pool fires of various diameters. Predictions of the burning rate as a function of diameter follow the trend observed in a number of experimental studies. Their results show an improvement in the model over the earlier work with methanol fires, due to improvements in the radiation routine and the fact that heptane is more sooty than methanol, simplifying the treatment of radiation. The authors point out that reliable predictions of the burning rate of liquid fuels require roughly twice as fine a grid spanning the burner than would be necessary to predict plume velocities and temperatures. The reason for this is the prediction of the heat feedback to the burning surface necessary to *predict* rather than to *specify* the burning rate.

2.2.3 Air and Gas Movement in the Absence of Fire

The low Mach number assumption in FDS is appropriate not only to fire, but to most building ventilation scenarios. An example of how the model can be used to assess indoor air quality is presented by Musser *et al.* [35]. The test compartment was a displacement ventilation test room that contained computers, furniture, and lighting fixtures as well as heated rectangular boxes intended to represent occupants. A detailed description of the test configuration is given by Yuan *et al.* [36]. The room is ventilated with cool supply air introduced via a diffuser that is mounted on a side wall near the floor. The air rises as it is warmed by heat sources and exits through a return duct located in the upper portion of the room. The flow pattern is intended

to remove contaminants by sweeping them upward at the source and removing them from the room. Sulphur hexafluoride, SF₆, was introduced into the compartment during the experiment as a tracer gas near the breathing zone of the occupants. Temperature, tracer concentration, and velocity were measured during the experiments. For temperature, the two finest grids (50 by 36 by 24 and 64 by 45 by 30) produced results in which the agreement between the measurement and prediction was considered “acceptable.” The agreement for the tracer concentrations were not as good. It was suggested that the difference could be related to the way the source of the tracer gas was modeled. The comparison of velocity data was deemed “reasonable,” given the limitations of the velocity probes at low velocities.

In another study, Musser and Tan [37] used FDS to assess the design of ventilation systems for facilities in which train locomotives operate. Although there is only a limited amount of validation, the study is useful in demonstrating a practical use of FDS for a non-fire scenario.

Mniszewski [38] used FDS to model the release of flammable gases in simple enclosures and open areas. In this work, the gases were not ignited.

Kerber and Walton provided a comparison between FDS version 1 and experiments on positive pressure ventilation in a full-scale enclosure without a fire. The model predictions of velocity were within 10 % to 20 % of the experimental values [39].

2.2.4 Wind Engineering

Most applications of FDS involve fires within buildings. However, it can be used to model thermal plumes in the open and wind impinging on the exterior of a building. Rehm, McGrattan, Baum and Simiu [40] used the LES solver to estimate surface pressures on simple rectangular blocks in a crosswind, and compared these estimates to experimental measurements. In a subsequent paper [41], they considered the qualitative effects of multiple buildings and trees on a wind field.

A different approach to wind was taken by Wang and Joulain [42]. They considered a small fire in a wind tunnel 0.4 m wide and 0.7 m tall with flow speeds of 0.5 m/s to 2.5 m/s. Much of the comparison with experiment is qualitative, including flame shape, lean, length. They also use the model to determine the predominant modes of heat transfer for different operating conditions. To assess the combustion, they implemented an “eddy break-up” combustion model [43] and compared it to the mixture fraction approach used by FDS. The two models performed better or worse, depending on the operating conditions. Some of the weaknesses of the mixture fraction model as implemented in FDS version 2 were addressed in subsequent versions.

Chang and Meroney [44] compared the results of FDS with the commercial CFD package FLUENT in simulating the transport of pollutants from steady point sources in an idealized urban environment. FLUENT employs a variety of RANS (Reynolds Averaged Navier-Stokes) closure methods, whereas FDS employs large eddy simulation (LES). The results of the numerical models were compared with wind tunnel measurements within a 1:50 scale physical model of an urban street “canyon.”

2.2.5 Atmospheric Dispersion

During the 1980s and 1990s, the Building and Fire Research Laboratory at NIST studied the burning of crude oil under the sponsorship of the US Minerals Management Service. The aim of the work was to assess the feasibility of using burning as a means to remove spilled oil from the sea surface. As part of the effort, Rehm and Baum developed a special application of the LES model called ALOFT. The model was a spin-off of the two-dimensional LES enclosure model, in which a three-dimensional steady-state plume was computed as a two-dimensional evolution of the lateral wind field generated by a large fire blown in a steady wind. The ALOFT model is based on large eddy simulation in that it attempts to resolve the relevant scales of a large, bent-over plume. Validation work was performed by simulating the plumes from

several large experimental burns of crude oil in which aerial and ground sampling of smoke particulate was performed [45]. Yamada [46] performed a validation of the ALOFT model for 10 m oil tank fire. The results indicate that the prediction of the plume cross section 500 m from the fire agree well with the experimental observations.

Mouilleau and Champassith [47] performed a validation study to assess the ability of FDS (version 4) to model atmospheric dispersion. They concluded that the best results were obtained for simulations done with explicitly-modeled wind fluctuations. Specific atmospheric flow characteristics were evaluated for passive releases in open and flat fields. The authors concluded that maximum downwind concentration were well-predicted, except for the case of unstable conditions where the model over-predicted the concentration, and that time-averaged “cloud shape” was well-predicted for stable atmospheric conditions, but less so for neutral and unstable conditions.

2.2.6 Growing Fires

Vettori [48] modeled two different fire growth rates in an obstructed ceiling geometry. The rectangular compartment was 9.2 m by 5.6 m by 2.4 m with a hollow steel door to the outside that remained closed during the tests. An open wooden stairway led to an upper floor with the same dimensions as the fire compartment below. Wooden joists measuring 0.038 m by 0.24 m were spaced at 0.41 m intervals across the ceiling and were supported by a single steel beam that spanned the width of the room. A rectangular methane gas burner measuring 0.7 m by 1.0 m by 0.31 m was placed in the corner of the chamber. Slow and fast burning fires that reached 1055 kW in 600 s and 150 s, respectively, were monitored. Four vertical arrays of Type K thermocouples were used to measure temperatures during the tests. The FDS model used four grid refinements and piecewise-linear grid spacing for each fire growth rate (slow and fast). For the fast growing fire, the predicted temperatures were within 20 % of the measured values and within 10 % for the slow growing fire. In general, finer grids produced better agreement.

In a follow-up report, Vettori [49] extended his study to include sloped ceilings, with and without obstructions. He found that the difference between predicted and measured sprinkler activation times varied between 4 % and 26 % for all cases studied. He also noted that FDS was able to predict the first activation of a sprinkler twice as far from the fire as another; caused presumably by the re-direction of smoke and heat by the beams on the ceiling.

Floyd [50, 51] validated FDS by comparing the modeling results with measurements from fire tests at the Heiss-Dampf Reaktor (HDR) facility. The structure was originally the containment building for a nuclear power reactor in Germany. The cylindrical structure was 20 m in diameter and 50 m in height topped by a hemispherical dome 10 m in radius. The building was divided into eight levels. The total volume of the building was approximately 11,000 m³. From 1984 to 1991, four fire test series were performed within the HDR facility. The T51 test series consisted of eleven propane gas tests and three wood crib tests. To avoid permanently damaging the test facility, a special set of test rooms were constructed, consisting of a fire room with a narrow door, a long corridor wrapping around the reactor vessel shield wall, and a curtained area centered beneath a maintenance hatch. The fire room walls were lined with fire brick. The doorway and corridor walls had the same construction as the test chamber. Six gas burners were mounted in the fire room. The fuel source was propane gas mixed with 10 % air fed at a constant rate to one of the six burners. The FDS model predicted the layer height and temperature of the space to within 10 % of the experimental values [50].

FDS predictions of fire growth and smoke movement in large spaces were presented by Kashef [52]. The experiments were conducted at the National Research Council Canada. The tests were performed in a compartment with dimensions of 9 m by 6 m by 5.5 m with 32 exhaust inlets and a single supply fan. A burner generated fires ranging in size from 15 kW to 1000 kW.

2.2.7 Flame Spread

Although FDS simulations have been compared to actual and experimental large-scale fires, it is difficult to *quantify* the accuracy because of the uncertainty associated with material properties. Most quantified validation work associated with flame spread have been for small, laminar flames with length scales ranging from millimeters to a few centimeters.

For example, FDS (or its core algorithms) have been used at a grid resolution of roughly 1 mm to look at flames spreading over paper in a micro-gravity environment [53, 54, 55, 56, 57, 58], as well as "g-jitter" effects aboard spacecraft [59]. Simulations have been compared to experiments performed aboard the Space Shuttle. The flames are laminar and relatively simple in structure, and the materials are relatively well-characterized.

The flame spread calculations from FDS were compared to the vertical flame spread over a 5 m slab of PMMA performed by Factory Mutual Research Corporation (FMRC). The predicted flame spread rate was within 0.3 m/s for any point in time during the analysis. The comparison at the quasi-steady burning rate once the full slab was burning shows that FDS over-estimated the burning rate [24, 25].

A charring model was implemented in FDS by Hostikka and McGrattan [60]. The model is a simplification of work done at NIST by Ritchie *et al.* [61]. The charring model was first used to predict the burning rate of a small wooden sample in the cone calorimeter. The results were more favorable for higher imposed heat fluxes. For low imposed fluxes, the heat transfer at the edge of the sample was more pronounced, and more difficult to model accurately. Full-scale room tests with wood paneling were modeled, but the results were judged to be grid-dependent. This was likely a consequence of the gas phase spatial resolution, rather than the solid phase. The authors concluded that it is difficult to predict the growth rate of a fire in a wood-lined room without "tuning" the pyrolysis rate coefficients. For real wood products, it is unlikely that all of the necessary properties can be obtained easily. Thus, grid sensitivity and uncertain material properties make *blind* predictions of fire growth on real materials beyond the reach of the current version of the model. However, the model can still be used for a qualitative assessment of fire behavior as long as the uncertainty in the flame spread rate is recognized.

Kwon *et al.* [62] performed three simulations to evaluate the capability of FDS, version 4, in predicting upward flame spread. The FDS predictions were compared with empirical correlations and experimental data for upward flame spread on a 5 m PMMA panel. A simplified flame spread model was also applied to assess the simulation results.

An extensive amount of flame spread validation work with FDS version 4 has been performed by Hietaniemi, Hostikka, and Vaari at VTT, Finland [34]. The case studies are comprised of fire experiments ranging in scale from the cone calorimeter (ISO 5660-1, 2002) to full-scale fire tests such as the room corner test (ISO 9705, 1993). Comparisons are also made between FDS 4 results and data obtained in the SBI (Single Burning Item) Euro-classification test apparatus (EN 13823, 2002) as well as data obtained in two *ad hoc* experimental configurations: one is similar to the room corner test but has only partial linings and the other is a space to study fires in building cavities. In the study of upholstered furniture, the experimental configurations are the cone and furniture calorimeters, and the ISO room. For liquid pool fires, comparison is made to data obtained by numerous researchers. The burning materials include spruce timber, MDF (Medium Density Fiber) board, PVC wall carpet, upholstered furniture, cables with plastic sheathing, and heptane. The scope of the VTT work is considerable. Assessing the accuracy of the model must be done on a case by case basis. In some cases, predictions of the burning rate of the material were based solely on its fundamental properties, as in the heptane pool fire simulations. In other cases, some properties of the material are unknown, as in the spruce timber simulations. Thus, some of the simulations are true predictions, some are calibrations. The intent of the authors was to provide guidance to engineers using the model as to appropriate grid sizes and material properties. In many cases, the numerical grid was made fairly coarse to account for the fact that in practice, FDS is used to model large spaces of which the fuel may only comprise

a small fraction.

2.2.8 Compartment Fires

As part of the NIST investigation of the World Trade Center fires and collapse, a series of large scale fire experiments were performed specifically to validate FDS [63]. The tests were performed in a rectangular compartment 7.2 m long by 3.6 m wide by 3.8 m tall. The fires were fueled by heptane for some tests and a heptane/toluene mixture for the others. The results of the experiments and simulations are included in detail in this Guide.

A second set of experiments to validate FDS for use in the World Trade Center investigation is documented in Ref. [64]. The experiments are not described as part of this Guide. The intent of these tests was to evaluate the ability of the model to simulate the growth of a fire burning three office workstations within a compartment of dimensions 11 m by 7 m by 4 m, open at one end to mimic the ventilation of windows similar to those in the WTC towers. Six tests were performed with various initial conditions exploring the effect of jet fuel spray and ceiling tiles covering the surface of the desks and carpet. Measurements were made of the heat release rate and compartment gas temperatures at four locations using vertical thermocouple arrays. Six different material samples were tested in the NIST cone calorimeter: desk, chair, paper, computer case, privacy panel, and carpet. Data for the carpet, desk and privacy panel were input directly into FDS, with the other three materials lumped together to form an idealized fuel type. Open burns of single workstations were used to calibrate the simplified fuel package. Details of the modeling are contained in Ref. [65].

The BRE Centre for Fire Safety Engineering at the University of Edinburgh conducted a series of large-scale fire tests in a real high rise building in Dalmarnock, Glasgow, Scotland [66, 67]. The experiments took place in July, 2006, with the close collaboration of the Strathclyde Fire Brigade and other partners. These experiments attempted to create realistic scenario in which a wide range of modern fire safety engineering tools could be put to a test. Jahn, Rein and Torero assessed the sensitivity of FDS when applied to these experiments [68]. Fire size and location, convection, radiation and combustion parameters were varied in order to determine the associated degree of sensitivity. Emphasis was put in the prediction of secondary ignition and time to flashover. In this context and while keeping the HRR constant, simulations of fire growth were significantly sensitive to location of the heat release rate, fire area, flame radiative fraction, and material thermal and ignition properties.

Students at Stord/Haugesund University College in Norway simulated full-scale experiments of temperature and smoke spread in a realistic multi-room setting using both CFAST and FDS [69]. Data from the top 0.5 m of the compartments was compared with measurements. The simulations were found to provide satisfying results in CFAST, as an alternative to FDS.

2.2.9 Sprinklers, Mist System, and Suppression by Water

A significant validation effort for sprinkler activation and suppression was a project entitled the International Fire Sprinkler, Smoke and Heat Vent, Draft Curtain Fire Test Project organized by the National Fire Protection Research Foundation [70]. Thirty-nine large scale fire tests were conducted at Underwriters Laboratories in Northbrook, IL. The tests were aimed at evaluating the performance of various fire protection systems in large buildings with flat ceilings, like warehouses and “big box” retail stores. All the tests were conducted under a 30 m by 30 m adjustable-height platform in a 37 m by 37 m by 15 m high test bay. At the time, FDS had not been publicly released and was referred to as the Industrial Fire Simulator (IFS), but it was essentially the same as FDS version 1. The first series of heptane spray burner fires have been simulated with the latest version of FDS and are included in this Guide under the heading “UL/NFPRF Test Series.” Most of the full-scale experiments performed during the project used a heptane spray burner to generate controlled fires of 1 MW to 10 MW. However, five experiments were performed with 6 m high

racks containing the Factory Mutual Standard Plastic Commodity, or Group A Plastic. To model these fires, bench scale experiments were performed to characterize the burning behavior of the commodity, and larger test fires provided validation data with which to test the model predictions of the burning rate and flame spread behavior [71, 72]. Two to four tier configurations were evaluated. For the period of time prior to application of water, the simulated heat release rate was within 20 % of the experimental heat release rates. It should be noted that the model was very sensitive to the thermal parameters and the numerical grid when used to model the fire growth in the piled commodity tests.

High rack storage fires of pool chemicals were modeled by Olenick *et al.* [73] to determine the validity of sprinkler activation predictions of FDS. The model was compared to full-scale fires conducted in January, 2000 at Southwest Research Institute in San Antonio, Texas.

FDS has been used to study the behavior of a fire undergoing suppression by a water mist system. Kim and Ryou [74, 75] compared FDS predictions to results of compartment fire tests with and without the application of a water mist. The cooling and oxygen dilution were predicted to within about 10 % of the measurements, but the simulations failed to predict the complete extinguishment of a hexane pool fire. The authors suggest that this is a result of the combustion model rather than the spray or droplet model.

Another study of water mist suppression using FDS was conducted by Hume at the University of Canterbury, Christchurch, New Zealand [76]. Full-scale experiments were performed in which a fine water mist was combined with a displacement ventilation system to protect occupants and electrical equipment in the event of a fire. Simulations of these experiments with FDS showed qualitative agreement, but the version of the model used in the study (version 3) was not able to predict accurately the decrease in heat release rate of the fire.

Hostikka and McGrattan [77] evaluated the absorption of thermal radiation by water sprays. They considered two sets of experimental data and concluded that FDS has the ability to predict the attenuation of thermal radiation “when the hydrodynamic interaction between the droplets is weak.” However, modeling interacting sprays would require a more costly coalescence model. They also note that the results of the model were sensitive to grid size, angular discretization, and droplet sampling.

O’Grady and Novozhilov [78] compared the predictions of FDS version 4 against full-scale fire tests performed at SP Sweden involving a 1.5 MW steady-state fire with two different sprinkler flow rates [79]. The authors reported results for gas temperatures and the tangential flow velocity in the ceiling jet. With the sprinkler off, the average relative prediction error away from the fire was of the order of 12 % for the temperature (with respect to excess temperature in the ceiling jet) and 6 % for velocity. For the two different sprinkler operating conditions, the relative errors were 7 % to 8 % for velocity and 10 % to 15 % for the temperature. Sensitivity of the model to a range of input parameters was investigated. The model demonstrated moderate sensitivity to the spray parameters, such as spray cone configuration, initial droplet velocities, and droplet sizes. On the other hand, the sensitivity to other parameters such as sprinkler atomization length and rms of droplet size distribution was low.

2.2.10 Airflows in Fire Compartments

Friday studied the use of FDS in large scale mechanically ventilated spaces. The ventilated enclosure was provided with air injection rates of 1 to 12 air changes per hour and a fire with heat release rates ranging from 0.5 MW to 2 MW. The test measurements and model output were compared to assess the accuracy of FDS [80]. These simulations have been repeated with the latest version of FDS and reported in this Guide under the heading “FM/SNL Test Series.”

Zhang *et al.* [81] utilized the FDS model to predict turbulence characteristics of the flow and temperature fields due to fire in a compartment. The experimental data was acquired through tests that replicated a half-scale ISO Room Fire Test. Two cases were explored – the heat source in the center of the room and the heat source adjacent to a wall. In both cases, the heat source was a heating element with an output of 12 kW/m².

The predicted intensity of the temperature fluctuation “agree[d] very well” at all points except those directly adjacent to the burner. The turbulent heat flux was found to be larger in the region above the heat source.

2.2.11 Tunnel Fires

Cochard [82] used FDS to study the ventilation within a tunnel. He compared the model results with a full-scale tunnel fire experiment conducted as part of the Massachusetts Highway Department Memorial Tunnel Fire Ventilation Test Program. The test consisted of a single point supply of fresh air through a 28 m² opening in a 135 m tunnel. The ventilation was started 2 min after the ignition of a 40 MW fire. Fifteen temperature measurement trees were placed within the tunnel and replicated within the model. Depending on location, the difference between predicted and measured temperature rise ranged from 10 % to 20 %.

McGrattan and Hamins [83] also applied FDS to simulate two of the Memorial Tunnel Fire Tests as validation for the use of the model in studying an actual fire in the Howard Street Tunnel, Baltimore, Maryland, July 2001. The experiments chosen for the comparison were unventilated. One experiment was a 20 MW fire; the other a 50 MW fire. FDS predictions of peak near-ceiling temperatures were within 50 °C of the measured peak temperatures, which were 600 °C and 800 °C, respectively.

Piergoirgio *et al.* [84] provided a qualitative analysis of FDS applied to a truck fire within a tunnel. The goal of their analysis was to describe the spread of the toxic gases within the tunnels, to determine the places not involved in the spreading of combustion products and to quantify the oxygen, carbon monoxide and hydrochloric acid concentrations during the fire.

Edwards *et al.* [85, 86] used FDS to determine the critical air velocity for smoke reversal in a tunnel as a function of the fire intensity, and his results compared favorably with experimental results. In a further study, Edwards and Hwang [87] applied FDS to study fire spread along combustibles in a ventilated mine entry. Analyses such as these are intended for planning and implementation of ventilation changes during mine fire fighting and rescue operations.

Bilson *et al.* [88] used FDS to evaluate the interaction of a deluge system with a tunnel ventilation and smoke exhaust system.

Harris [89] used FDS to determine the heat flux from a tunnel fire under varying water application rates. These results were qualitatively consistent with experimental results of Arvidson [90], who conducted burn tests for shielded and unshielded standard plastic commodities under a variety of spray conditions.

2.2.12 Smoke Detection

The ability of version 1 of FDS to accurately predict smoke detector activation was studied by D’Souza [91]. The smoke transport model within FDS was tested and compared with UL 217 test data. The second step in this research was to further validate the model with full-scale multi-compartment fire tests. The results indicated that FDS is capable of predicting smoke detector activation when used with smoke detector lag correlations that correct for the time delay associated with smoke having to penetrate the detector housing. A follow-up report by Roby *et al.* [92] and paper by Zhang *et al.* [93] describes the implementation and validation of the smoke detector algorithm currently incorporated in FDS.

Another study of smoke detector activation was carried out by Brammer at the University of Canterbury, New Zealand [94]. Two fire tests from a series performed in a two-story residence were simulated, and smoke detector activation times were predicted using three different methods. The methods consisted of either a temperature correlation, a time-lagged function of the optical density, or a thermal device much like a heat detector. The purpose was to identify ways to reliably predict smoke detector activation using typical model output like temperature and smoke concentration. It was remarked that simulating the early stage of the fire is critical to reliable prediction.

Cleary [95] also provided a comparison between FDS computed gas velocity, temperature and concentrations at various detector locations. The research concluded that multi-room fire simulations with the FDS model can accurately predict the conditions that a sensor might experience during a real fire event. The FDS model was able to predict the smoke and gas concentrations, heat, and flow velocities at various detector locations to within 15 % of measurements.

2.2.13 Combustion Model

A few studies have been performed comparing direct numerical simulations (DNS) of a simple burner flame to laboratory experiments [96]. Another study compared DNS calculations of a counterflow diffusion flames to experimental measurements and the results of a one-dimensional multi-step kinetics model [97].

Bundy, Dillon and Hamins [98, 99] studied the use of FDS in providing data and correlations for fire investigators to support their investigations. A paraffin wax candle was placed within a 0.61 m by 0.61 m by 0.76 m plexi-glass enclosure. The chamber was raised 20 mm off the surface to reveal 44 uniformly spaced 6 mm diameter holes. The holes provided oxygen to the flame without subjecting the flame to a draft. A 150 mm hole was provided at the top of the enclosure to allow for the heat and combustion products to exit the space. The heat flux from the candle flame was modeled with FDS. The model provides a prediction of the heat flux of the candle at a height of 56 mm above the base of the flame with an accuracy of 5 %. The flux is under predicted by 16 % at 76 mm above the base of the flame. The remainder of the predictions show flux measurements were under-predicted by 15 % to 40 % of the measured values.

Floyd *et al.* [100, 51] compared the radiation model of FDS version 2 with full-scale data from the Virginia Tech Fire Research Laboratory (VTFRL). The test compartment was outfitted with equipment capable of taking temperature, air velocity, gas concentrations, unburned hydrocarbon and heat flux measurements. The test facility consisted of a single compartment geometrically similar to the ISO 9705 standard compartment with dimensions of 1.2 m by 1.8 m by 1.2 m in height. The ceiling and walls were constructed of fiberboard over a steel shell with a floor of concrete. Three baseline experiments were completed with fires ranging in size from 90 kW to 440 kW. Overall, FDS predicted the temperatures to within 15 % of the measured temperatures. The FDS velocity measurements followed the trend of the test data but did not replicate it. The outgoing velocities were under-predicted by 30 % to 40 % and the incoming velocities were over-predicted by 40 %. FDS predicted the heat flux gauge response to within 10 % of the measured values. The radiation model in FDS predicted the measured fluxes to within 15 %.

Xin and Gore [101] compared FDS predictions and measurements of the spectral radiation intensities of small fires. The fuel flow rates for methane and ethylene burners were selected so that the Froude numbers matched that of liquid toluene pool fires. The heat release rate was 4.2 kW for the methane flame and 3.4 kW for the ethylene flame. Line of sight spectral radiation intensities were measured at six downstream locations. The spectral radiation intensity calculations were performed by post-processing the transient scalar distributions provided by FDS.

Zhang *et al.* [102] compared the experimental results of a circular methane gas burner to predictions computed by FDS. The compartment was 2.8 m by 2.8 m by 2.2 m high with natural ventilation from a standard door.

2.3 Reconstructions of Actual Fires

ASTM E 1355 states that a model may be evaluated by comparing it with “Documented Fire Experience” which includes

- eyewitness accounts of real fires,

- known behavior of materials in fires (for example, melting temperatures of materials), and
- observed post-fire conditions, such as the extent of fire spread.

Often the term “reconstruction” is applied to this type of simulation, because the model is used to reconstruct events based on evidence collected during and after the fire. The two most notable examples of fire reconstructions by NIST using FDS were the reconstructions of the fires within the World Trade Center towers and Building 7 on September 11, 2001 [65]; and the fire that occurred at the Station Nightclub in Rhode Island in February, 2003 [103]. Other examples of reconstructions by NIST staff are cited below.

Dan Madrzykowski and Bob Vettori examined a fire in a townhouse in Washington, D.C., where two fire fighters were killed and one severely injured during the evening hours of May 30, 1999 [104]. Questions arose about the injuries the fire fighters had sustained, the lack of thermal damage in the living room where a fallen fire fighter was found and why the fire fighters never opened their hose lines to protect themselves or to extinguish the fire. To answer some of the questions, a rectangular volume of 10 m by 6 m by 5.1 m was divided into 76,500 cells in the FDS model. The FDS results that best replicated the observed fire behavior indicated that the opening of the basement sliding glass door provided oxygen to a pre-heated, under-ventilated fire. Flashover was estimated to occur in less than 60 s following the entry of fire fighters into the basement. The resulting fire gases flowed up the basement stairs and moved across the living room ceiling towards the back wall of the townhouse. These hot gases came in direct contact with the fire fighters who were killed. The hot gases traversed the townhouse in less than 2 s, giving the fire fighters little time to respond. The model showed that the oxygen level was too low to support flaming and, therefore, the fire fighters did not have a visual cue of the thermal conditions until it was too late. Results of the FDS study were shared with the D.C. fire department and have been made available via a multi-media CD-ROM to other fire departments across the country.

Bob Vettori, Dan Madrzykowski, and Doug Walton simulated a fire in a Houston restaurant [105]. On the morning of February 14, 2000, a fire started in the office area of a fast food restaurant. Two fire fighters died when the roof collapsed. The FDS model was used to simulate the fire. The fuel was assumed to be the contents of a typical office, and the fire was assumed to have a slowly growing heat release rate peaking at 6 MW. Multiple vents were modeled and the time at which they opened replicated the fire fighters’ actions after arrival. The model provided a visual representation of the fire during the initial phases until the collapse of the roof.

Dan Madrzykowski, Glenn Forney and Doug Walton simulated a fire that killed three children and three fire fighters on the morning of December 22, 1999 in a two story duplex house in Iowa [106]. The fire started on top of a stove in a two-story residence. FDS was used to simulate the fire. The fuel packages consisted of several furniture items in the kitchen and living room with heat release rates reaching 5.2 MW. The model results indicated the critical event in the fire was flashover of the kitchen. The fire became a multi-room event after flashover with temperatures increasing to over 600 °C. The hot gases spread quickly from the living room to the stairway on the second floor trapping the fire fighters.

Dan Madrzykowski and Doug Walton investigated the fire in the Cook County (Chicago) Administration Building in October, 2003, that claimed the lives of six people trapped in a stairwell [107]. Issues addressed by the model were the movement of the fire from its room of origin and the movement of smoke up the stairwell.

Outside of NIST, FDS has been used to investigate many actual fires, but very few of these studies are documented in the literature. Exceptions include

- A large fire in a “cash & carry” warehouse in the UK was studied by Camp and Townsend using both hand calculations and FDS (version 1) [108].
- A study by Rein *et al.* [109] looked at several fire events using an analytical fire growth model, the NIST zone model CFAST, and FDS.

- A similar study was performed several years earlier by Spearpoint *et al.* [110] as a class exercise at the University of Maryland.
- During the SFPE Professional Development Week in the fall of 2001, a workshop was held in which several engineers related their experiences using FDS as a forensic tool [111].
- The role of carbon monoxide in the deaths of three fire fighters was studied by Christensen and Icove [112].

Chapter 3

Description of Experiments

This chapter contains a brief description of the experiments that were used for model validation. Only enough detail is included here to provide a general understanding of the model simulations. Anyone wishing to use the experimental measurements for validation ought to consult the cited test reports or other publications for a comprehensive description.

3.1 VTT Large Hall Tests

The experiments are described in Ref. [113]. The series consisted of 8 experiments, but because of replicates only three unique fire scenarios. The experiments were undertaken to study the movement of smoke in a large hall with a sloped ceiling. The tests were conducted inside the VTT Fire Test Hall, with dimensions of 19 m high by 27 m long by 14 m wide. Each test involved a single heptane pool fire, ranging from 2 MW to 4 MW. Four types of predicted output were used in the present evaluation – the HGL temperature and depth, average flame height and the plume temperature. Three vertical arrays of thermocouples (TC), plus two thermocouples in the plume, were compared to FDS predictions. The HGL temperature and height were reduced from an average of the three TC arrays using the standard algorithm described in Chapter 5. The ceiling jet temperature was not considered, because the ceiling in the test hall is not flat, and the standard model algorithm is not appropriate for this geometry.

The VTT test report lacks some information needed to model the experiments, which is why some information was based on private communications with the principal investigator, Simo Hostikka.

Surface Materials: The walls and ceiling of the test hall consist of a 1 mm thick layer of sheet metal on top of a 5 cm layer of mineral wool. The floor was constructed of concrete. The report does not provide thermal properties of these materials.

Natural Ventilation: In Cases 1 and 2, all doors were closed, and ventilation was restricted to infiltration through the building envelope. Precise information on air infiltration during these tests is not available. The scientists who conducted the experiments recommend a leakage area of about 2 m^2 , distributed uniformly throughout the enclosure. By contrast, in Case 3, the doors located in each end wall (Doors 1 and 2, respectively) were open to the external ambient environment. These doors are each 0.8 m wide by 4 m high, and are located such that their centers are 9.3 m from the south wall.

Mechanical Ventilation: The test hall has a single mechanical exhaust duct, located in the roof space, running along the center of the building. This duct had a circular section with a diameter of 1 m, and opened horizontally to the hall at a distance of 12 m from the floor and 10.5 m from the west wall. Mechanical exhaust ventilation was operational for Case 3, with a constant volume flow rate of $11 \text{ m}^3/\text{s}$ drawn through the exhaust duct.

Heat Release Rate: Each test used a single liquid fuel pan with its center located 16 m from the west wall and 7.4 m from the south wall. For all tests, the fuel was heptane in a circular steel pan that was partially filled with water. The pan had a diameter of 1.17 m for Case 1 and 1.6 m for Cases 2 and 3. In each case, the fuel surface was 1 m above the floor. The trays were placed on load cells, and the HRR was calculated from the mass loss rate. For the three cases, the fuel mass loss rate was averaged from individual replicate tests. In the HRR estimation, the heat of combustion (taken as 44,600 kJ/kg) and the combustion efficiency for n-heptane was used. Hostikka suggests a value of 0.8 for the combustion efficiency. Tewarson reports a value of 0.93 for a 10 cm pool fire [114]. For the calculations reported in the current study, a combustion efficiency of 0.85 is assumed. In general, an uncertainty of 15 % has been assumed for the reported HRR of most of the large scale fire experiments used.

Radiative Fraction: The radiative fraction was assumed to be 0.35, similar to many smoky hydrocarbons.

A diagram of the test structure is displayed in Figure 3.1.

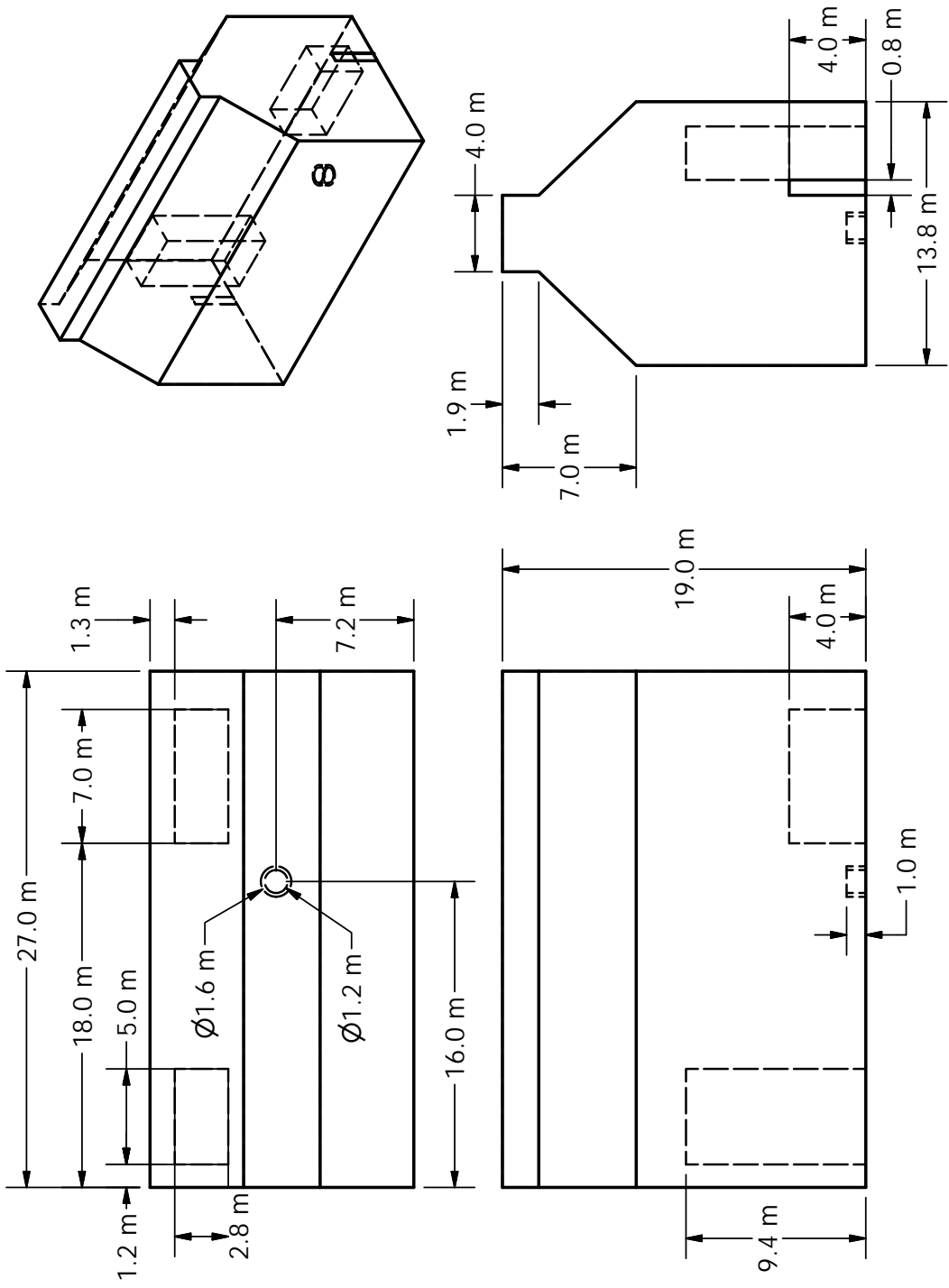


Figure 3.1: Geometry of the VTT Large Fire Test Hall.

3.2 UL/NFPRF Sprinkler, Vent, and Draft Curtain Study

In January, 1997, a series of 22 heptane spray burner experiments was conducted at the Large Scale Fire Test Facility at Underwriters Laboratories (UL) in Northbrook, Illinois [115]. The objective of the experiments was to characterize the temperature and flow field for fire scenarios with a controlled heat release rate in the presence of sprinklers, draft curtains and a single smoke & heat vent. The Large Scale Fire Test Facility at UL contains a 37 m by 37 m (120 ft by 120 ft) main fire test cell, equipped with a 30.5 m by 30.5 m (100 ft by 100 ft) adjustable height ceiling. The layout of the experiments is shown in Fig. 3.2. One 1.2 m by 2.4 m (4 ft by 8 ft) vent was installed among 49 upright sprinklers on a 3 m by 3 m (10 ft by 10 ft) spacing.

Ceiling: The ceiling was raised to a height of 7.6 m and instrumented with thermocouples and other measurement devices. The ceiling was constructed of 0.6 m by 1.2 m by 1.6 cm UL fire-rated Armstrong Ceramaguard (Item 602B) ceiling tiles. The manufacturer reported the thermal properties of the material to be: specific heat 753 J/(kg·K), thermal conductivity 0.0611 W/(m·K), and density 313 kg/m³.

Draft Curtains: Sheet metal, 1.2 mm thick and 1.8 m deep, was suspended from the ceiling for 16 of the 22 tests, enclosing an area of about 450 m² and 49 sprinklers.

Sprinklers: Central ELO-231 (Extra Large Orifice) uprights were used for all the tests. The orifice diameter of this sprinkler is reported by the manufacturer to be nominally 1.6 cm (0.64 in), the reference actuation temperature is reported by the manufacturer to be 74°C (165°F). The RTI (Response Time Index) and C-factor (Conductivity factor) were reported by UL to be $148 \text{ (m}\cdot\text{s)}^{\frac{1}{2}}$ and $0.7 \text{ (m/s)}^{\frac{1}{2}}$, respectively [115]. When installed, the sprinkler deflector was located 8 cm below the ceiling. The thermal element of the sprinkler was located 11 cm below the ceiling. The sprinklers were installed with nominal 3 m by 3 m (exact 10 ft by 10 ft) spacing in a system designed to deliver a constant $0.34 \text{ L/(s}\cdot\text{m}^2)$ (0.50 gpm/ft^2) discharge density when supplied by a 131 kPa (19 psi) discharge pressure

Vent: A single UL listed double leaf fire vent with steel covers and steel curb was installed in the adjustable height ceiling in the position shown in Fig. 3.2. The vent is designed to open manually or automatically. The vent doors were recessed into the ceiling about 0.3 m (1 ft).

Heat Release Rate: The heptane spray burner consisted of a 1 m by 1 m square of 1.3 cm pipe supported by four cement blocks 0.6 m off the floor. Four atomizing spray nozzles were used to provide a free spray of heptane that was then ignited. For all but one of the tests, the total heat release rate from the fire was manually ramped up following a “t-squared” curve to a steady-state in 75 s (150 s was used in Test I-16). The fire growth curve was followed until a specified fire size was reached or the first sprinkler activated. After either of these events, the fire size was maintained at that level until conditions reached roughly a steady state, *i.e.* the temperatures recorded near the ceilings remained steady and no more sprinkler activations occurred. The heat release rate from the burner was confirmed by placing it under the large product calorimeter at UL, ramping up the flow of heptane in the same manner as in the tests, and measuring the total and convective heat release rates. It was found that the convective heat release rate was 0.65 ± 0.02 of the total.

Instrumentation: The instrumentation for the tests consisted of thermocouples, gas analysis equipment, and pressure transducers. The locations of the instrumentation are referenced in the plan view of the facility (Fig. 3.2). Temperature measurements were recorded at 104 locations. Type K 0.0625 in diameter Inconel sheathed thermocouples were positioned to measure (i) temperatures near the ceiling, (ii) temperatures of the ceiling jet, and (iii) temperatures near the vent.

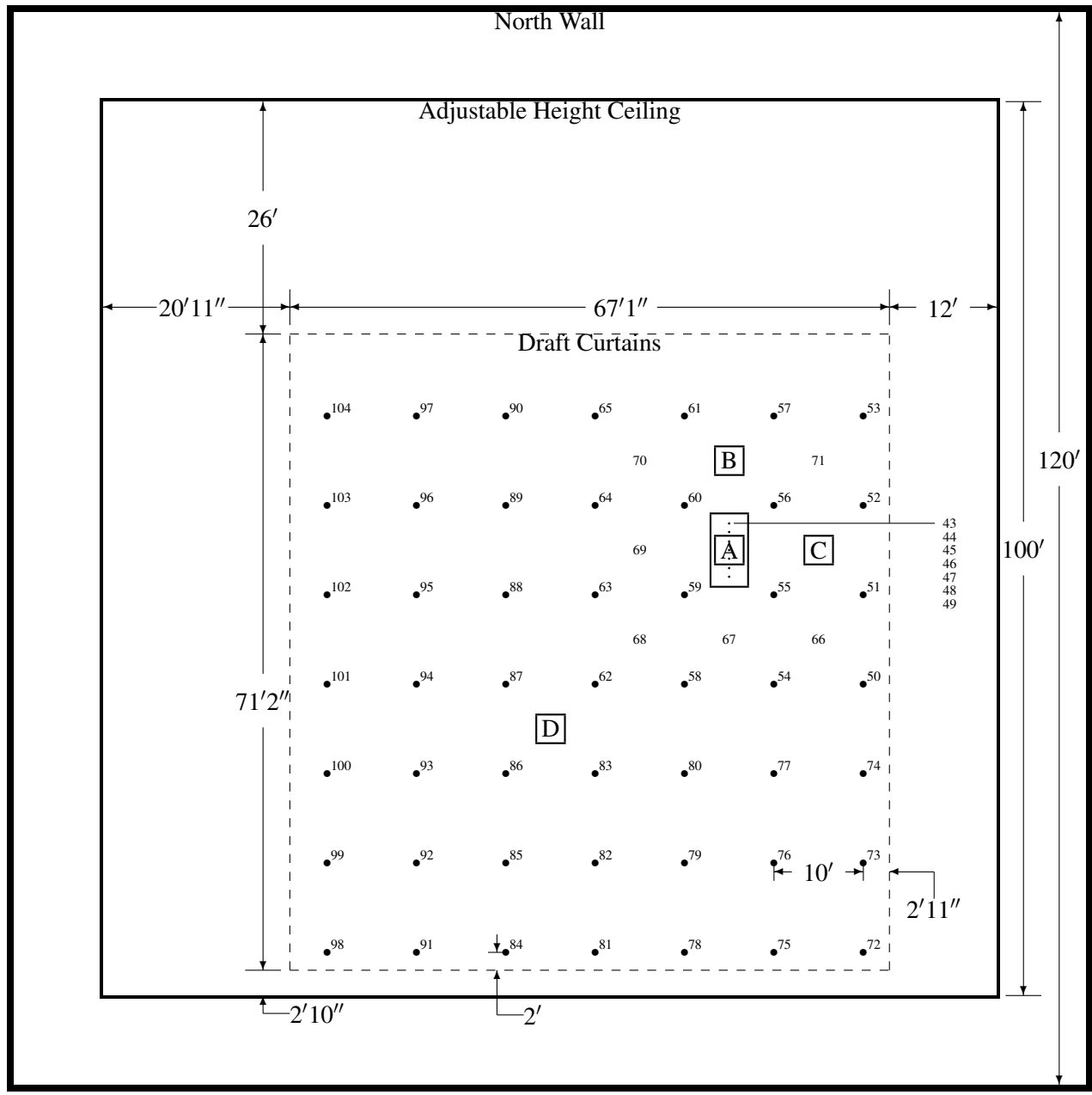


Figure 3.2: Plan view of the UL/NFPRF Experiments. The sprinklers are indicated by the solid circles and are spaced 3 m apart. The number beside each sprinkler location indicates the channel number of the nearest thermocouple. The vent dimensions are 4 ft by 8 ft. The boxed letters A, B, C and D indicate burner positions. Corresponding to each burner position is a vertical array of thermocouples. Thermocouples 1–9 hang 7, 22, 36, 50, 64, 78, 92, 106 and 120 in from the ceiling, respectively, above Position A. Thermocouples 10 and 11 are positioned above and below the ceiling tile directly above Position B, followed by 12–20 that hang at the same levels below the ceiling as 1–9. The same pattern is followed at Positions C and D, with thermocouples 21–31 at C and 32–42 at D.

Heptane Spray Burner Test Series I						
Test No.	Burner Pos.	Vent Operation	First Actuation (s)	Total Actuations	Draft Curtains	Heat Release Rate MW @ s
I-1	B	Closed	65	11	Yes	4.4 @ 50
I-2	B	Manual (0:40)	66	12	Yes	4.4 @ 50
I-3	B	Manual (1:30)	64	12	Yes	4.4 @ 50
I-4	C	Closed	60	10	Yes	4.4 @ 50
I-5	C	Manual (0:40)	72	9	Yes	4.4 @ 50
I-6	C	Manual (1:30)	62	8	Yes	4.4 @ 50
I-7	C	74°C link (DNO)	70	10	Yes	4.4 @ 50
I-8	B	74°C link (9:26)	60	11	Yes	4.4 @ 50
I-9	D	74°C link (DNO)	70	12	Yes	4.4 @ 50
I-10	D	Manual (0:40)	72	13	Yes	4.4 @ 50
I-11	D	74°C link (4:48)	N/A	N/A	Yes	4.4 @ 50
I-12	A	Closed	68	14	Yes	4.4 @ 50
I-13	A	74°C link (1:04)	69	5	Yes	6.0 @ 60
I-14	A	Manual (0:40)	74	7	Yes	5.8 @ 60
I-15	A	Manual (1:30)	64	5	Yes	5.8 @ 60
I-16	A	74°C link (1:46)	106	4	Yes	5.0 @ 110
I-17	B	100°C link (DNO)	58	4	No	4.6 @ 50
I-18	C	100°C link (DNO)	58	4	No	3.7 @ 50
I-19	A	100°C link (10:00)	56	10	No	4.6 @ 50
I-20	A	74°C link (1:20)	54	4	No	4.2 @ 50
I-21	C	74°C link (7:00)	58	10	No	4.6 @ 50
I-22	D	100°C link (DNO)	60	6	No	4.6 @ 50

Table 3.1: Results of the UL/NFPRF Experiments. Note that DNO means “Did Not Open”. Also note, the fires grew at a rate proportional to the square of the time until a certain flow rate of fuel was achieved at which time the flow rate was held steady. Thus, the “Heat Release Rate” was the size of the fire at the time when the fuel supply was leveled off.

The UL/NFPRF test results (Series I) are summarized in Table 3.1.

3.3 NIST/NRC Test Series

These experiments, sponsored by the US NRC and conducted at NIST, consisted of 15 large-scale experiments performed in June 2003. All 15 tests were included in the validation study. The experiments are documented in Ref. [116]. The fire sizes ranged from 350 kW to 2.2 MW in a compartment with dimensions 21.7 m by 7.1 m by 3.8 m high, designed to represent a compartment in a nuclear power plant containing power and control cables. The walls and ceiling were covered with two layers of marinate boards, each layer 0.0125 m thick. The floor was covered with one layer of gypsum board on top of a layer of plywood. Thermo-physical and optical properties of the marinate and other materials used in the compartment are given in Ref. [116]. The room had one door and a mechanical air injection and extraction system. Ventilation conditions, the fire size, and fire location were varied. Numerous measurements (approximately 350 per test) were made including gas and surface temperatures, heat fluxes and gas velocities.

Following are some notes provided by Anthony Hamins, who conducted the experiments:

Natural Ventilation: The compartment had a 2 m by 2 m door in the middle of the west wall. Some of the tests had a closed door and no mechanical ventilation (Tests 2, 7, 8, 13, and 17), and in those tests the measured compartment leakage was an important consideration. The test report lists leakage areas based on measurements performed prior to Tests 1, 2, 7, 8, and 13. For the closed door tests, the leakage area used in the simulations was based on the last available measurement. The chronological order of the tests differed from the numerical order. For Test 4, the leakage area measured before Test 2 was used. For Tests 10 and 16, the leakage area measured before Test 7 was used.

Mechanical Ventilation: The mechanical ventilation and exhaust was used during Tests 4, 5, 10, and 16, providing about 5 air changes per hour. The door was closed during Test 4 and open during Tests 5, 10, and 16. The supply duct was positioned on the south wall, about 2 m off the floor. An exhaust duct of equal area to the supply duct was positioned on the opposite wall at a comparable location. The flow rates through the supply and exhaust ducts were measured in detail during breaks in the testing, in the absence of a fire. During the tests, the flows were monitored with single bi-directional probes during the tests themselves.

Heat Release Rate: A single nozzle was used to spray liquid hydrocarbon fuels onto a 1 m by 2 m fire pan that was about 0.1 m deep. The test plan originally called for the use of two nozzles to provide the fuel spray. Experimental observation suggested that the fire was less unsteady with the use of a single nozzle. In addition, it was observed that the actual extent of the liquid pool was well-approximated by a 1 m circle in the center of the pan. For safety reasons, the fuel flow was terminated when the lower-layer oxygen concentration dropped to approximately 15 % by volume. The fuel used in 14 of the tests was heptane, while toluene was used for one test. The HRR was determined using oxygen consumption calorimetry. The recommended uncertainty values were 17 % for all of the tests.

Radiative Fraction: The value of the radiative fraction and its uncertainty were reported as 0.44 and 0.40 for heptane and toluene, respectively.

A diagram of the test structure is displayed in Figure 3.3.

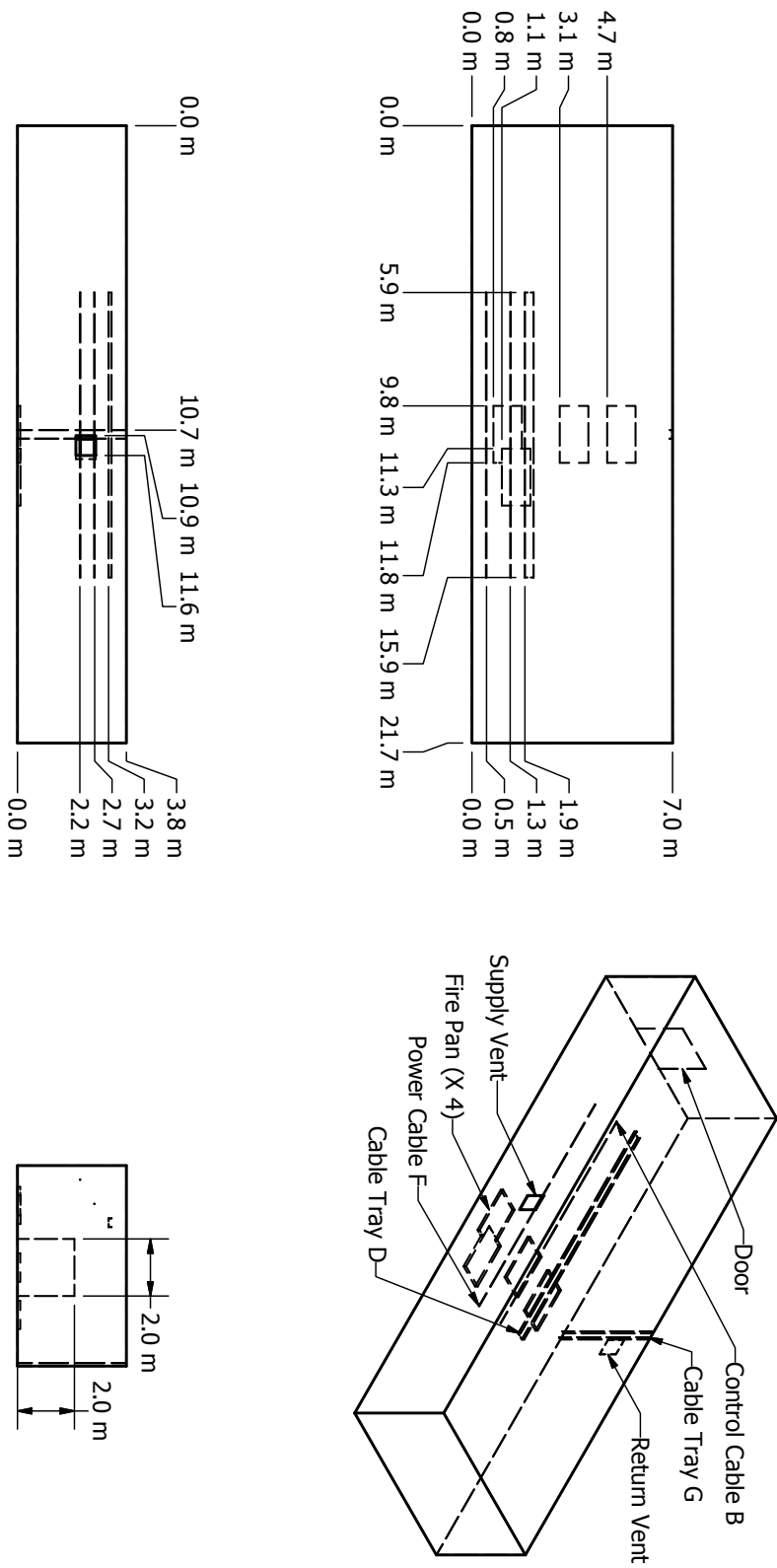


Figure 3.3: Geometry of the NIST/NRC Experiments.

3.4 WTC Spray Burner Test Series

As part of its investigation of the World Trade Center disaster, the Building and Fire Research Laboratory at NIST conducted several series of fire experiments to both gain insight into the observed fire behavior and also to validate FDS for use in reconstructing the fires. The first series of experiments involved a relatively simple compartment with a liquid spray burner and various structural elements with varying amounts of sprayed fire-resistive materials (SFRM). A diagram of the compartment is shown in Fig. 3.4. A complete description of the experiments can be found in the NIST WTC report NCSTAR 1-5B [63]. The overall enclosure was rectangular, as were the vents and most of the obstructions. The compartment walls and ceiling were made of 2.54 cm thick marinite. The manufacturer provided the thermal properties of the material used in the calculation. The density was 737 kg/m^3 , conductivity 0.12 W/m/K . The specific heat ranged from 1.17 kJ/kg/K at 93°C to 1.42 kJ/kg/K at 425°C . This value was assumed for higher temperatures. The steel used to construct the column and truss flanges was 0.64 cm thick. The density of the steel was assumed to be $7,860 \text{ kg/m}^3$; its specific heat 0.45 kJ/kg/K .

Two fuels were used in the tests. The properties of the fuels were obtained from measurements made on a series of unconfined burns that are referenced in the test report. The first fuel was a blend of heptane isomers, C_7H_{16} . Its soot yield was set at a constant 1.5 %. The second fuel was a mixture (40 % - 60 % by volume) of toluene, C_7H_8 , and heptane. Because FDS only considers the burning of a single hydrocarbon fuel, the mixture was taken to be C_7H_{12} with a soot yield of 11.2 %. The radiative fraction for the heptane blend was 0.44; for the heptane/toluene mixture it was 0.39. The heat release rate of the simulated burner was set to that which was measured in the experiments. The spray burner was modeled using reported properties of the nozzle and liquid fuel droplets.

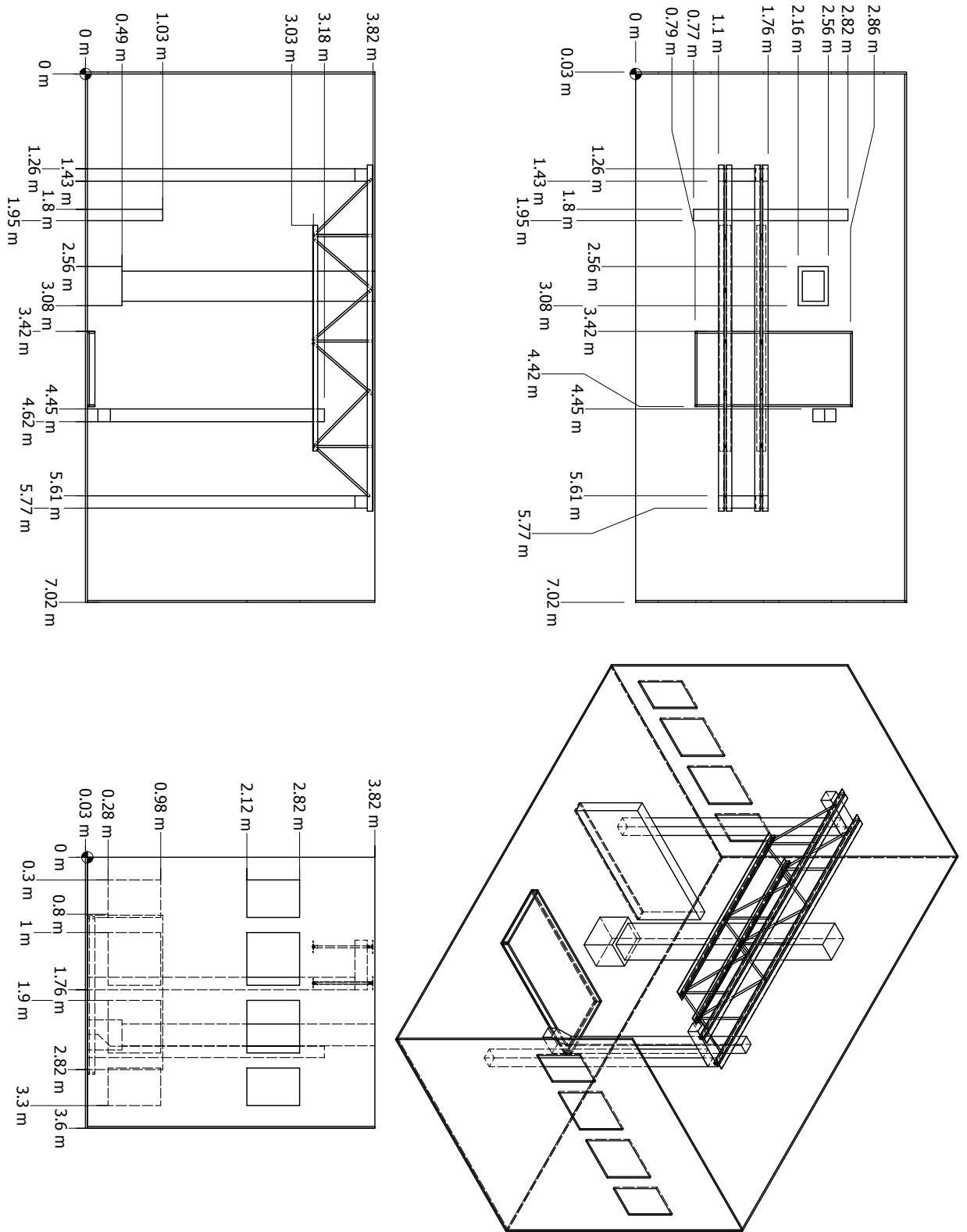


Figure 3.4: Geometry of the WTC Experiments.

3.5 FM/SNL Test Series

The Factory Mutual and Sandia National Laboratories (FM/SNL) test series was a series of 25 fire tests conducted in 1985 for the U.S. Nuclear Regulatory Commission (NRC) by Factory Mutual Research Corporation (FMRC), under the direction of Sandia National Laboratories (SNL) [117, 118]. The primary purpose of these tests was to provide data with which to validate computer models for various types of compartments typical of nuclear power plants. The experiments were conducted in an enclosure measuring approximately 18 m long x 12 m wide x 6 m high, constructed at the FMRC fire test facility in Rhode Island. All of the tests involved forced ventilation to simulate typical power plant operations. Four of the tests were conducted with a full-scale control room mockup in place. Parameters varied during the experiments included fire intensity, enclosure ventilation rate, and fire location.

The current study used data from three experiments (Tests 4, 5, and 21). In these tests, the fire source was a propylene gas burner with a diameter of approximately 0.9 m, with its rim located approximately 0.1 m above the floor. For Tests 4 and 5, the burner was positioned on the longitudinal axis centerline, 6.1 m from the nearest wall. For Test 21, the fire source was placed within a simulated electrical cabinet.

Following is supplemental information provided by the test director, Steve Nowlen of Sandia National Laboratory:

Heat Release Rate: The HRR was determined using oxygen consumption calorimetry in the exhaust stack with a correction applied for the carbon dioxide in the upper layer of the compartment. The uncertainty of the fuel mass flow was not documented. All three tests selected for this study had the same target peak heat release rate of 516 kW following a 4 min “t-squared” growth profile. The test report contains time histories of the measured HRR, for which the average, sustained HRR following the ramp up for Tests 4, 5, and 21 have been estimated as 510 kW, 480 kW, and 470 kW, respectively. Once reached, the peak HRR was maintained essentially constant during a steady-burn period of 6 min in Tests 4 and 5, and 16 min in Test 21. Note that in Test 21, Nowlen reports a “significant” loss of effluent from the exhaust hood that could lead to an under-estimate of the HRR towards the end of the experiment.

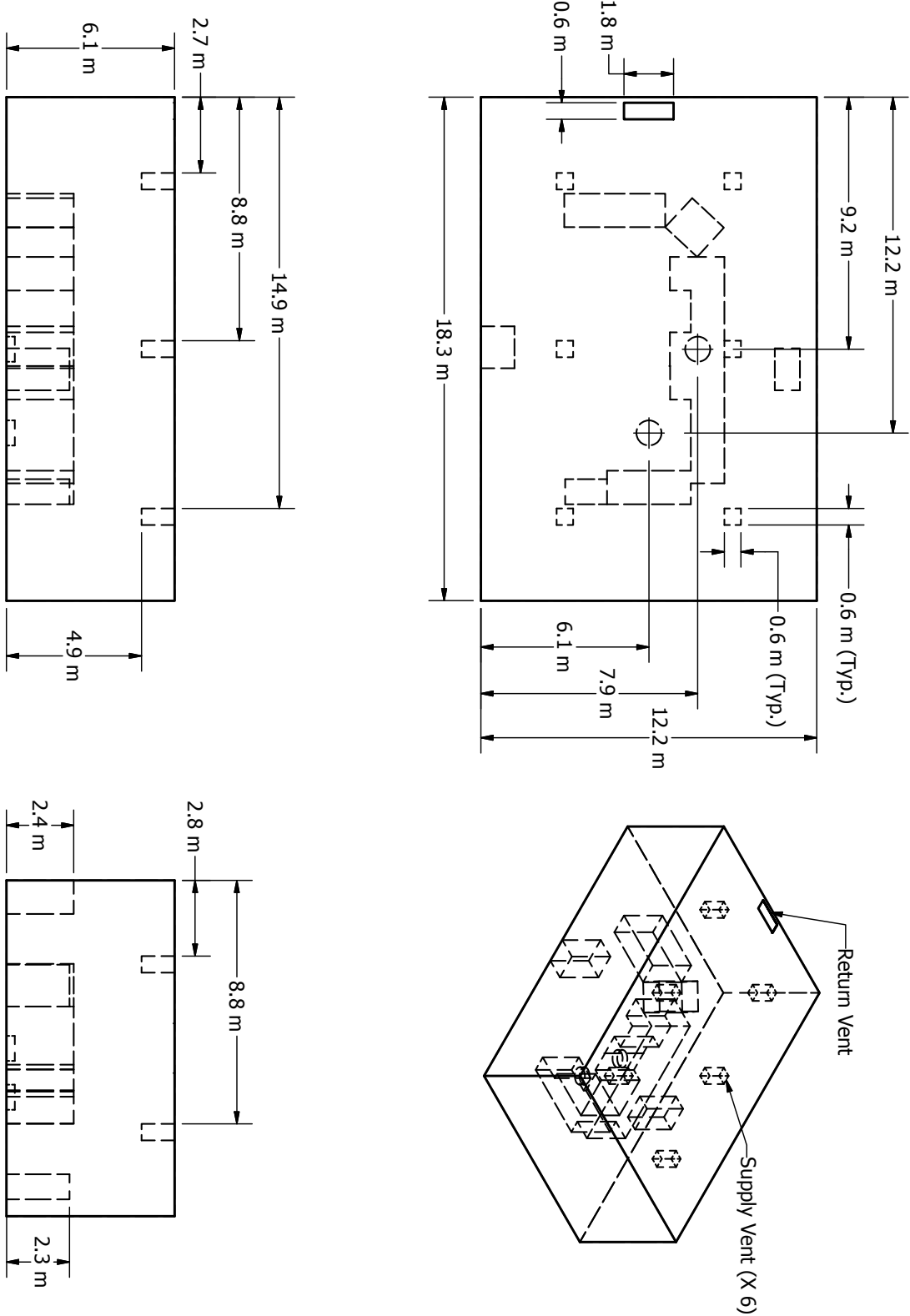
Radiative Fraction: The radiative fraction was not measured during the experiment, but in this study it is assumed to equal 0.35, which is typical for a smoky hydrocarbons. It was further assumed that the radiative fraction was about the same in Test 21 as the other tests, as fuel burning must have occurred outside of the electrical cabinet in which the burner was placed.

Measurements: Four types of measurements were conducted during the FM/SNL test series that are used in the current model evaluation study, including the HGL temperature and depth, and the ceiling jet and plume temperatures. Aspirated thermocouples (TCs) were used to make all of the temperature measurements. Generally, aspirated TC measurements are preferable to bare-bead TC measurements, as systematic radiative exchange measurement error is reduced.

HGL Depth and Temperature: Data from all of the vertical TC trees were used when reducing the HGL height and temperature. For the FM/SNL Tests 4 and 5, Sectors 1, 2, and 3 were used, all weighted evenly. For Test 21, Sectors 1 and 3 were used, evenly weighted. Sector 2 was partially within the fire plume in Test 21.

A diagram of the test structure is displayed in Figure 3.5.

Figure 3.5: Geometry of the FM/SNL Experiments.



3.6 NBS Multi-Room Test Series

The National Bureau of Standards (NBS, which is now called the National Institute of Standards and Technology, NIST) Multi-Room Test Series consisted of 45 fire tests representing 9 different sets of conditions were conducted in a three-room suite. The experiments were conducted in 1985 and are described in detail in Ref. [119]. The suite consisted of two relatively small rooms, connected via a relatively long corridor. The fire source, a gas burner, was located against the rear wall of one of the small compartments. Fire tests of 100 kW, 300 kW and 500 kW were conducted. For the current study, only three 100 kW fire experiments have been used, including Test 100A from Set 1, Test 100O from Set 2, and Test 100Z from Set 4. These tests were selected because they had been used in prior validation studies, and because these tests had the steadiest values of measured heat release rate during the steady-burn period.

Following is additional information provided by the test director, Richard Peacock of NIST:

Heat Release Rate: In the two tests for which the door was open, the HRR during the steady-burn period measured via oxygen consumption calorimetry was 110 kW with an uncertainty of about 15 %, consistent with the replicate measurements made during the experimental series and the uncertainty typical of oxygen consumption calorimetry. It was assumed that the closed door test (Test 100O) had the same HRR as the open door tests.

Radiative Fraction: Natural gas was used as the fuel in Test 100A. In Tests 100O and 100Z, acetylene was added to the natural gas to increase the smoke yield, and as a consequence, the radiative fraction increased. The radiative fraction of natural gas has been studied previously, whereas the radiative fraction of the acetylene/natural gas mixture has not been studied. The radiative fraction for the natural gas fire was assigned a value of 0.20, whereas a value of 0.30 was assigned for the natural gas/acetylene fires.

Measurements: Only two types of measurements conducted during the NBS test series were used in the evaluation considered here, because there was less confidence in the other measurements. The measurements considered here were the HGL temperature and depth, in which bare bead TCs were used to make these measurements. Single point measurements of temperature within the burn room were not used in the evaluation of plume or ceiling jet algorithms. This is because the geometry was not consistent in either case with the assumptions used in the model algorithms of plumes or jets. Specifically, the burner was mounted against a wall, and the room width-to-height ratio was less than that assumed by the various ceiling jet correlations.

A diagram of the test structure is displayed in Figure 3.6.

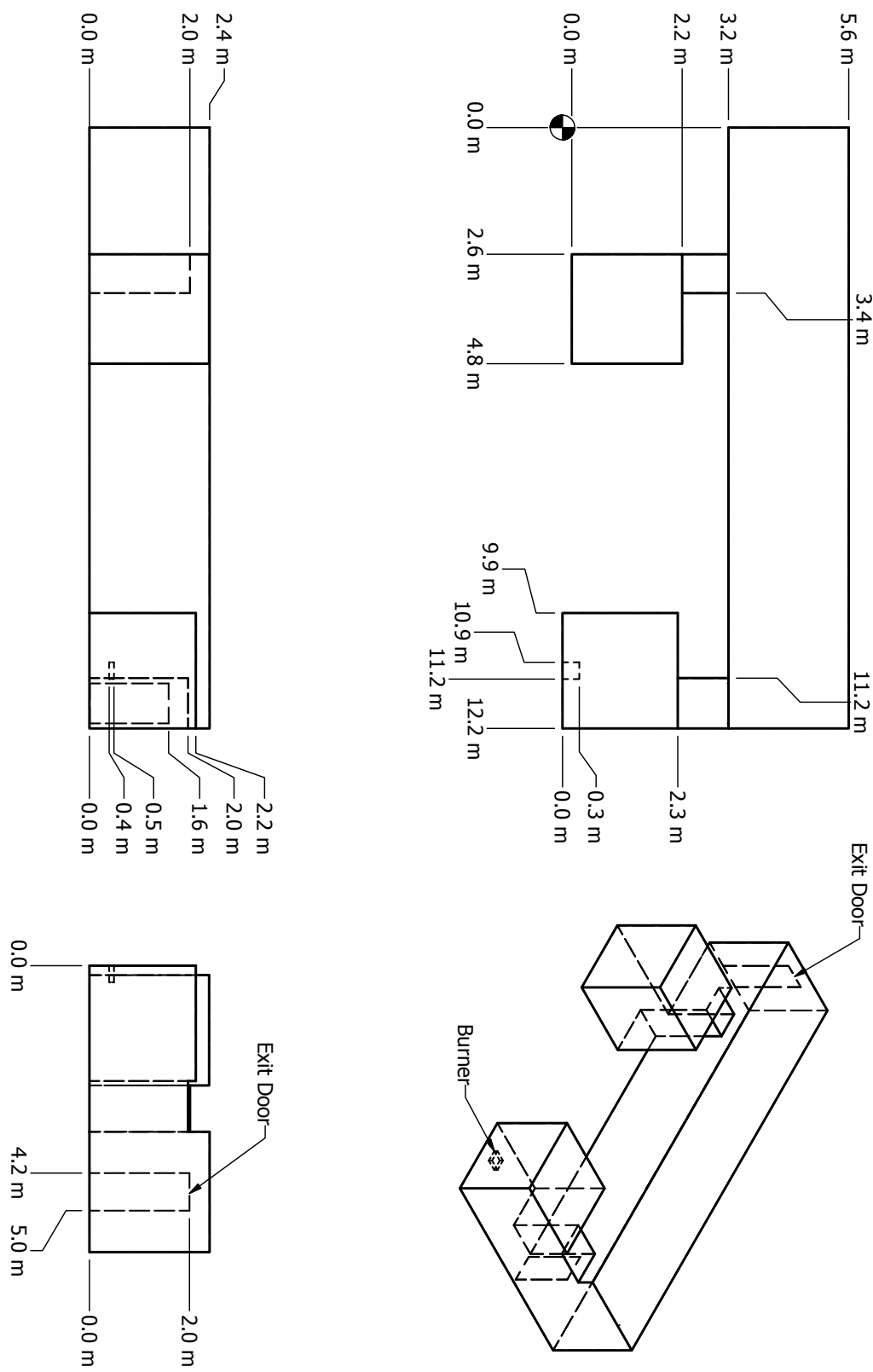


Figure 3.6: Geometry of the NBS Multi-Room Experiments.

3.7 Steckler Compartment Experiments

Steckler, Quintiere and Rinkinen performed a set of 55 compartment fire tests at NBS in 1979. The compartment was 2.8 m by 2.8 m by 2.13 m high¹, with a single door of various widths, or alternatively a single window with various heights. A 30 cm diameter methane burner was used to generate fires with heat release rates of 31.6 kW, 62.9 kW, 105.3 kW and 158 kW. Vertical profiles of velocity and temperature were measured in the doorway, along with a single vertical profile of temperature within the compartment. A full description and results are reported in Reference [120]. The basic test matrix is listed in Table 3.2. Note that the test report does not include a detailed description of the compartment. However, an internal report² by the test sponsor, Armstrong Cork Company, reports that the compartment floor was composed of 19 mm calcium silicate board on top of 12.7 mm plywood on wood joists. The walls and ceiling consisted of 12.7 mm ceramic fiber insulation board over 0.66 mm aluminum sheet attached to wood studs.

¹The test report gives the height of the compartment as 2.18 m. This is a misprint. The compartment was 2.13 m high.

² *Technical Research Report, Fire Induced Flows Through Room Openings - Flow Coefficients*, Project 203005-003, Armstrong Cork Company, Lancaster, Pennsylvania, May, 1981.

Table 3.2: Summary of Steckler compartment experiments.

Test	Opening Width (m)	Opening Height (m)	HRR \dot{Q} (kW)	Burner Location	Test	Opening Width (m)	Opening Height (m)	HRR \dot{Q} (kW)	Burner Location
10	0.24	1.83	62.9	Center	224	0.74	0.92	62.9	Back Corner
11	0.36	1.83	62.9	Center	324	0.74	0.92	62.9	Back Corner
12	0.49	1.83	62.9	Center	220	0.74	1.83	31.6	Back Corner
612	0.49	1.83	62.9	Center	221	0.74	1.83	105.3	Back Corner
13	0.62	1.83	62.9	Center	514	0.24	1.83	62.9	Back Wall
14	0.74	1.83	62.9	Center	544	0.36	1.83	62.9	Back Wall
18	0.74	1.83	62.9	Center	512	0.49	1.83	62.9	Back Wall
710	0.74	1.83	62.9	Center	542	0.62	1.83	62.9	Back Wall
810	0.74	1.83	62.9	Center	610	0.74	1.83	62.9	Back Wall
16	0.86	1.83	62.9	Center	510	0.74	1.83	62.9	Back Wall
17	0.99	1.83	62.9	Center	540	0.86	1.83	62.9	Back Wall
22	0.74	1.38	62.9	Center	517	0.99	1.83	62.9	Back Wall
23	0.74	0.92	62.9	Center	622	0.74	1.38	62.9	Back Wall
30	0.74	0.92	62.9	Center	522	0.74	1.38	62.9	Back Wall
41	0.74	0.46	62.9	Center	524	0.74	0.92	62.9	Back Wall
19	0.74	1.83	31.6	Center	541	0.74	0.46	62.9	Back Wall
20	0.74	1.83	105.3	Center	520	0.74	1.83	31.6	Back Wall
21	0.74	1.83	158.0	Center	521	0.74	1.83	105.3	Back Wall
114	0.24	1.83	62.9	Back Corner	513	0.74	1.83	158.0	Back Wall
144	0.36	1.83	62.9	Back Corner	160	0.74	1.83	62.9	Center*
212	0.49	1.83	62.9	Back Corner	163	0.74	1.83	62.9	Back Corner*
242	0.62	1.83	62.9	Back Corner	164	0.74	1.83	62.9	Back Wall*
410	0.74	1.83	62.9	Back Corner	165	0.74	1.83	62.9	Left Wall*
210	0.74	1.83	62.9	Back Corner	162	0.74	1.83	62.9	Right Wall*
310	0.74	1.83	62.9	Back Corner	167	0.74	1.83	62.9	Front Center*
240	0.86	1.83	62.9	Back Corner	161	0.74	1.83	62.9	Doorway*
116	0.99	1.83	62.9	Back Corner	166	0.74	1.83	62.9	Front Corner*
122	0.74	1.38	62.9	Back Corner					* Raised burner

3.8 Bryant Doorway Velocity Measurements

Rodney Bryant of the Fire Research Division at NIST performed a series of velocity measurements of the gas velocity within the doorway of a standard ISO 9705 compartment for fires ranging from 34 kW to 511 kW [121]. A doorway served as the only vent for the enclosure. It included a jamb of 30 cm extending outward to facilitate the laser measurements. The entire compartment was elevated 0.3 m off the floor of the laboratory.

The measurements were made using both bi-directional probes and PIV (Particle Image Velocimetry). The PIV measurements only cover the lower two-thirds of the doorway because of difficulties in seeding the hot outflow gases. The bi-directional probe measurements span the entire height of the doorway, but Bryant reports that these measurements were up to 20 % greater than the PIV measurements in certain regions of the flow. Consequently, only the PIV data was used for comparison to the model.

3.9 SP Adiabatic Surface Temperature Experiments

In 2008, three compartment experiments were performed at SP Technical Research Institute of Sweden under the sponsorship of Brandforsk, the Swedish Fire Research Board [122]. The objective of the experiments was to demonstrate how plate thermometer measurements in the vicinity of a simple steel beam can be used to supply the boundary conditions for a multi-dimensional heat conduction calculation for the beam. The adiabatic surface temperature was derived from the plate temperatures and used by TASEF, a finite-element thermal-structural program.

The experiments were performed inside a standard compartment designed for corner fire testing (ISO 9705). The compartment is 3.6 m deep, 2.4 m wide and 2.4 m high and includes a door opening 0.8 m by 2.0 m. The room was constructed of 20 cm thick light weight concrete blocks with a density of $600 \text{ kg/m}^3 \pm 100 \text{ kg/m}^3$. The heat source was a gas burner run at a constant power of 450 kW. The top of the burner, with a square opening 30 cm by 30 cm, was placed 65 cm above the floor, 2.5 cm from the walls. A single steel beam was suspended 20 cm below the ceiling along the centerline of the compartment. There were three measurement stations along the beam at lengths of 0.9 m (Position A), 1.8 m (Position B), and 2.7 m (Position C) from the far wall where the fire was either positioned in the corner (Tests 1 and 2), or the center (Test 3). The beam in Test 1 was a rectangular steel tube filled with an insulation material. The beam in Tests 2 and 3 was an I-beam.

3.10 ATF Corridors Experiments

A series of eighteen experiments were conducted in a two-story structure with long hallways and a connecting stairway in the large burn room of the ATF Fire Research Laboratory in Ammendale, Maryland, in 2008 [123]. The test enclosure consisted of two 17.0 m long hallways connected by a stairway consisting of two staircases and an intermediary landing. There was a door at the opposite end of the first floor hallway, which was closed during all tests. The end of the second floor hallway was open with a soffit near the ceiling.

The walls and ceilings of the test structure were constructed of 1.2 cm gypsum wallboard. The flooring throughout the structure, including the stairwell landing floor, consisted of one layer of 1.3 cm thick cement board on one layer of 1.9 cm thick plywood supported by wood joists. The first set of stairs, which had eight risers, led from the first floor up to the landing area. The second set of stairs, which had nine risers, led from the landing area up to the second floor. The stairs were constructed of 2.5 cm thick clear pine lumber. The two set of stairs were separated by an approximately 0.42 m wide gap in the middle of the stairwell. This gap was separated from the stairs by a 0.91 m tall barrier constructed of a single piece of gypsum board. The flue space was open to the first floor. The flue space was separated from the second floor by a 0.9 m tall

barrier constructed of gypsum board. There was a metal exterior type door at the end of the first floor near the burner. The door was closed during all experiments.

The fire source was a natural gas diffusion burner. The burner surface was horizontal, square and 0.45 m on each side, its surface was 0.37 m above the floor, and it was filled with gravel. The burner was located near the end of the first floor away from the stairs. A diagram of the test structure is displayed in Figure 3.7.

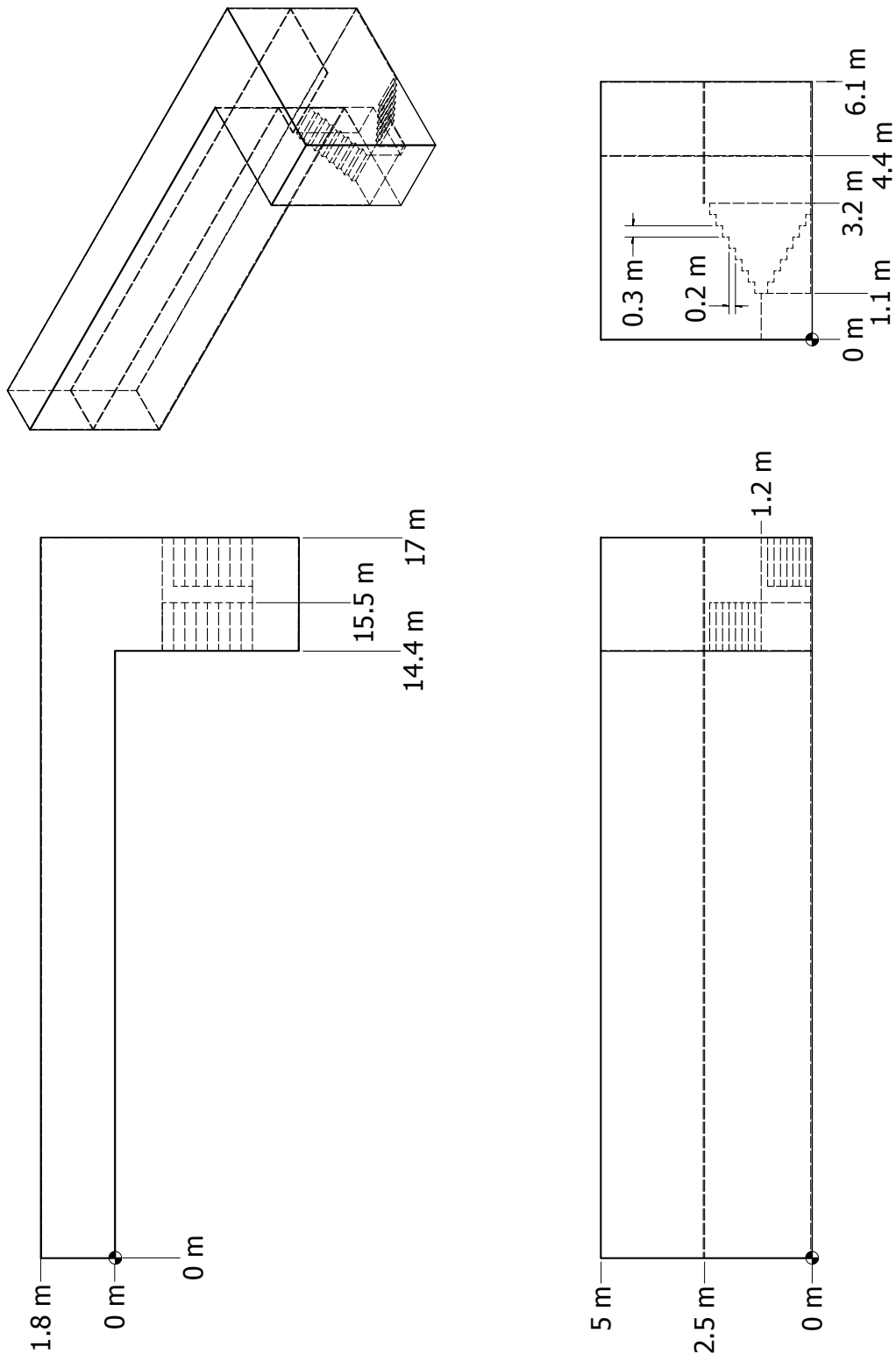


Figure 3.7: Geometry of the ATF Corridors Experiments

3.11 McCaffrey Plume Experiments

In 1979, at the National Bureau of Standards (now NIST), Bernard McCaffrey measured centerline temperature and velocity profiles above a porous, refractory burner. There were five distinct heat release rates, ranging from 14 kW to 57 kW. The fuel was natural gas. The burner was square, 0.3 m on each side. The results of the experiments are reported in Reference [124].

3.12 Sandia Plume Experiments

The Fire Laboratory for Accreditation of Models by Experimentation (FLAME) facility [125, 126] at Sandia National Laboratories in Albuquerque, New Mexico, is designed specifically for validating models of buoyant fire plumes. The plume source is 1 m in diameter surrounded by a 0.5 m steel ‘ground plane’. PIV/PLIF techniques are used to obtain instantaneous joint scalar and velocity fields. O’Hern *et al.* [125] studied a turbulent buoyant helium plume in the FLAME facility. Earlier work to model this experiment was performed by DesJardin *et al.* [127]. Tieszen *et al.* [128, 129] studied methane and hydrogen pool fires.

3.13 Smyth Slot Burner Experiment

Kermit Smyth *et al.* conducted diffusion flame experiments at NIST using a methane/air Wolfhard-Parker slot burner. The experiments are described in detail in Refs. [130, 131]. The Wolfhard-Parker slot burner consists of an 8 mm wide central slot flowing fuel surrounded by two 16 mm wide slots flowing dry air with 1 mm separations between the slots. The slots are 41 mm in length. Measurements were made of all major species and a number of minor species along with temperature and velocity. Experimental uncertainties have been reported as 5 % for temperature and 10 % to 20 % for the major species.

3.14 Beyler Hood Experiments

Craig Beyler performed a large number of experiments involving a variety of fuels, fire sizes, burner diameters, and burner distances beneath a hood [132]. The hood consisted of concentric cylinders separated by an air gap. The inner cylinder was shorter than the outer and this allowed combustion products to be removed uniformly from the hood perimeter. The exhaust gases were then analyzed to determine species concentrations. The burner could be raised and lowered with respect to the bottom edge of the hood. Based on the published measurement uncertainties, species errors are estimated at 6 %.

3.15 NIST Reduced Scale Enclosure Experiments

The CO production test series used the NIST Reduced Scale Enclosure (RSE) [133]. The RSE is a 40 % scaled version of the ISO 9705 compartment. It measures 0.98 m wide by 1.46 m deep by 0.98 m tall. The compartment contains a door centered on the small face that measures 0.48 m wide by 0.81 m tall. A 15 cm diameter natural gas burner was positioned in the center of the compartment. The burner was on a stand so that its top was 15 cm above the floor. Species measurements were made inside the upper layer of the compartment at the front near the door and near the rear of the compartment.

3.16 Hamins Methane Burner Experiments

Anthony Hamins *et al.* performed a series of tests on circular gas burners measuring the radial and vertical radiative heat flux profiles outside the flame region. The tests are described in [33]. Tests at three burner diameters, 0.10 m, 0.38 m and 1.0 m are used for validation.

3.17 Restivo Compartment Air Flow Experiment

Velocity measurements for forced airflow within a 9 m by 3 m by 3 m high compartment were made by Restivo [134]. These measurements have been widely used to validate CFD models designed for indoor air quality applications. It was also used to assess early versions of FDS [20, 21, 35]. In the experiment, air was forced into the compartment through a 16.8 cm vertical slot along the ceiling running the width of the compartment with a velocity of 0.455 m/s. A passive exhaust was located near the floor on the opposite wall, with conditions specified such that there was no buildup of pressure in the enclosure. The component of velocity in the lengthwise direction was measured in four arrays: two vertical arrays located 3 m and 6 m from the inlet along the centerline of the room, and two horizontal arrays located 8.4 cm above the floor and below the ceiling, respectively. These measurements were taken using hot-wire anemometers. While data on the specific instrumentation used are not readily available, hot-wire systems tend to have limitations at low velocities, with typical thresholds of approximately 0.1 m/s.

3.18 NRL/HAI Wall Heat Flux Measurements

Back, Beyler, DiNenno and Tatem [135] measured the heat flux from 9 different sized propane fires set up against a wall composed of gypsum board. The experiments were sponsored by the Naval Research Laboratory and conducted by Hughes Associates, Inc., of Baltimore, Maryland. The square sand burner ranged in size from 0.28 m to 0.70 m, and the fires ranged in size from 50 kW to 520 kW.

3.19 Ulster SBI Corner Heat Flux Measurements

Zhang *et al.* [136] measured the heat flux and flame heights from fires in the single burning item (SBI) enclosure at the University of Ulster, Northern Ireland. Thin steel plate probes were used to measure the surface heat flux, and flame heights were determined by analyzing the instantaneous images extracted from the videos of the experiments by a CCD camera. Three heat release rates were used – 30 kW, 45 kW, and 60 kW.

3.20 FM Parallel Panel Experiments

Patricia Beaulieu made heat flux measurements within a set of vertical parallel panels as part of a cooperative research program between Worcester Polytechnic Institute and FM Global (Factory Mutual) [137]. The experimental apparatus consisted of two vertical parallel panels, 2.4 m high and 0.6 m wide, with a sand burner at the base. The objective of the project was to measure the flame spread rate over various composite wall lining materials, but there were also experiments conducted with inert walls for the purpose of measuring the heat flux from two fuels, propane and propylene, at heat release rates of 30 kW, 60 kW, and 100 kW.

3.21 NRCC Facade Heat Flux Measurements

A series of experiments was conducted by the Fire Research Section of the Institute for Research in Construction, National Research Council of Canada (NRCC), to measure the heat flux to a mock exterior building facade due to a fire within a compartment [138, 139]. The experiments selected for model validation were conducted using a series of propane line burners within a compartment whose interior dimensions were 5.95 m wide, 4.4 m deep, and 2.75 m high (see Fig. 3.8). There were five different door/window sizes:

1. 0.94 m by 2.00 m high
2. 0.94 m by 2.70 m high (door)
3. 2.60 m by 1.37 m high (shown in Fig. 3.8)
4. 2.60 m by 2.00 m high
5. 2.60 m by 2.70 m high (door)

There were four fire sizes: 5.5 MW, 6.9 MW, 8.6 MW, and 10.3 MW. In all, 19 experiments were conducted, with the exception of the 10.3 MW fire with Window 1. In each experiment, heat flux measurements were made 0.5 m, 1.5 m, 2.5 m, and 3.5 m above the top of the door/window.

3.22 Cable Response to Live Fire – CAROLFIRE

CAROLFIRE was a project sponsored by the U.S. Nuclear Regulatory Commission to study the fire-induced thermal response and functional behavior of electrical cables [140]. The primary objective of CAROLFIRE was to characterize the various modes of electrical failure (*e.g.* hot shorts, shorts to ground) within bundles of power, control and instrument cables. A secondary objective of the project was to test a simple model to predict thermally-induced electrical failure (THIEF). The measurements used for these purposes were conducted at Sandia National Laboratories and are described in Volume II of the CAROLFIRE test report. In brief, there were two series of experiments. The first were conducted within a heated cylindrical enclosure known as the Penlight apparatus. Single and bundled cables were exposed to various heat fluxes and the electrical failure modes recorded. The second series of experiments involved cables within trays in a semi-enclosed space under which a gas-fueled burner created a hot layer to force cable failure.

Petra Andersson and Patrick Van Hees of the Swedish National Testing and Research Institute (SP) proposed that a cable's thermally-induced electrical failure can be predicted via a one-dimensional heat transfer calculation, under the assumption that the cable can be treated as a homogenous cylinder [141]. Their results for PVC cables were encouraging and suggested that the simplification of the analysis is reasonable and that it should extend to other types of cables. The assumptions underlying the THIEF model are as follows:

1. The heat penetration into a cable of circular cross section is largely in the radial direction. This greatly simplifies the analysis, and it is also conservative because it is assumed that the cable is completely surrounded by the heat source.
2. The cable is homogenous in composition. In reality, a cable is constructed of several different types of polymeric materials, cellulosic fillers, and a conducting metal, most often copper.
3. The thermal properties \bar{U} conductivity, specific heat, and density $\bar{\rho}$ of the assumed homogenous cable are independent of temperature. In reality, both the thermal conductivity and specific heat of polymers are temperature-dependent, but this information is very difficult to obtain from manufacturers. More discussion of this assumption is found below.

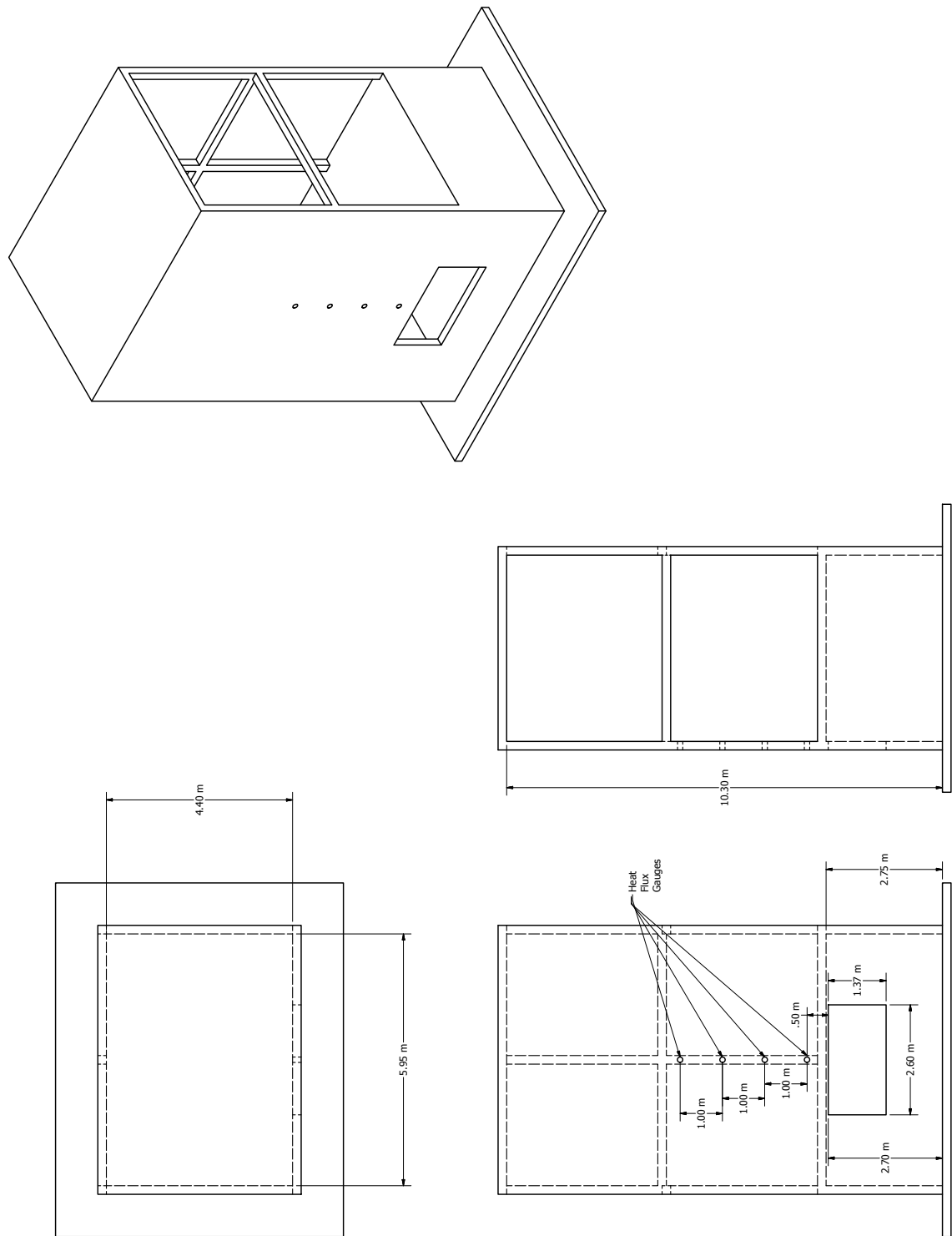


Figure 3.8: Geometry of the NRCC Facade Experiments

4. It is assumed that no decomposition reactions occur within the cable during its heating, and ignition and burning are not considered in the model. In fact, thermoplastic cables melt, thermosets form a char layer, and both off-gas volatiles up to and beyond the point of electrical failure.
5. Electrical failure occurs when the temperature just inside the cable jacket reaches an experimentally determined value.

Because the CAROLFIRE Penlight experiments tested single cables that were heated uniformly on all sides, the one-dimensional THIEF model accurately predicted the times for the temperature inside the cable jacket to reach “threshold” values that are typically observed when the cable fails electrically.

3.23 BRE Spray Test for Radiation Attenuation

Murrel *et al.* [142] measured the attenuation of thermal radiation passing through a water spray using a heat flux gauge. The radiation was produced by a heat panel, one meter square, at 900 °C. The horizontal distance from the radiation panel to the spray nozzle was 2 m and to the measurement point 4 m. The nozzles were positioned at a height 0.24 m above the panel upper edge. The heat flux gauge was positioned at the line passing through the center of the panel. The attenuation of radiation was defined as $(q_0 - q_s)/q_0$, where q_0 is the initial radiative heat flux, measured without a spray, and q_s is the heat flux measured during the spray operation.

Experimental results are used from three full-cone type nozzles, labeled A, B and D. The opening angles of the nozzles were between 90 and 108 degrees. The purpose of the simulation is to compare the measured and simulated attenuation of radiation at different flow conditions. The nozzles were specified in terms of median droplet size and mean vertical velocity using PDPA measurement in a single position, 0.7 m below the nozzle. The droplet boundary conditions were determined by assuming $d_m \propto p^{-1/3}$ and $v \propto p^{1/2}$ type of dependences between the droplet size, speed and pressure.

3.24 Vettori Flat Ceiling Experiments

Vettori [48] analyzed a series of 45 experiments conducted at NIST that were intended to compare the effects of different ceiling configurations on the activation times of quick response residential pendant sprinklers. The two ceiling configurations used consisted of an obstructed ceiling, with parallel beams 0.038 m wide by 0.24 m deep placed 0.41 m on center, and a smooth ceiling configuration, in which the beams were covered by a sheet of gypsum board. In addition to the two ceiling configurations, there were also three fire growth rates and three burner locations used – a total of 18 test configurations. The fire growth rate was provided by a computer controlled methane gas burner to mimic a standard t-squared fire growth rate with either a slow, medium, or fast ramp up. The burner was placed in a corner of the room, then against an adjacent wall, and then in a location removed from any wall. Measurements were taken to record sprinkler activation time, temperatures at varying heights and locations within the room, and the ceiling jet velocities at several other locations. A diagram of the test structure is displayed in Figure 3.9.

Ceiling.pdf

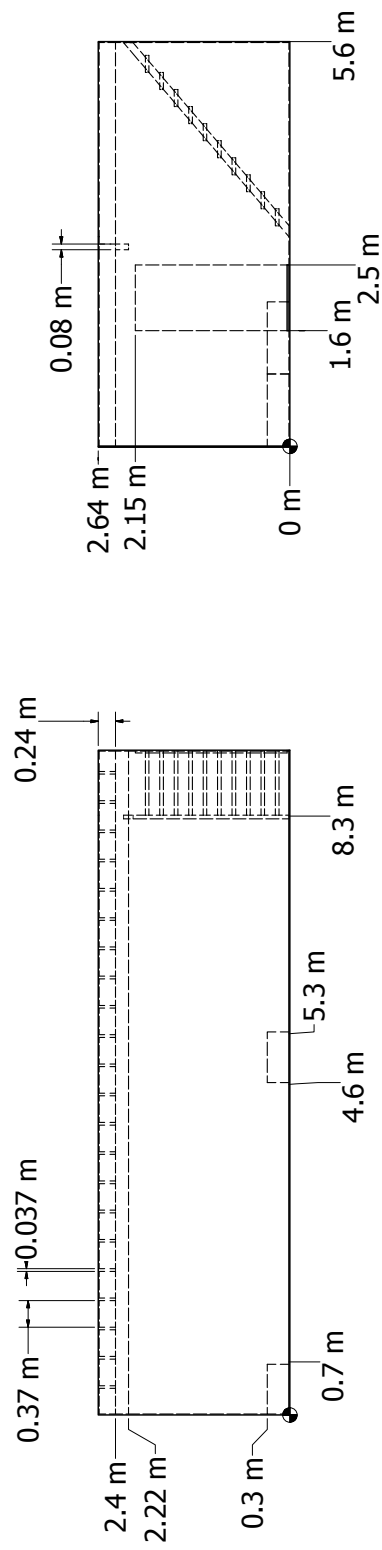
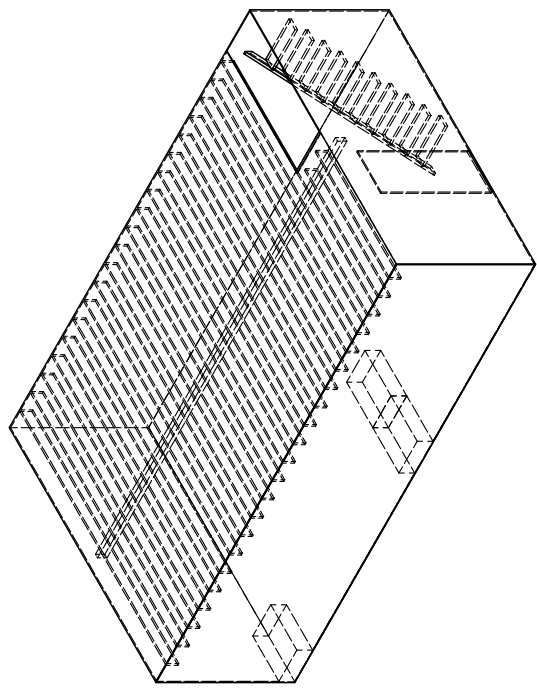
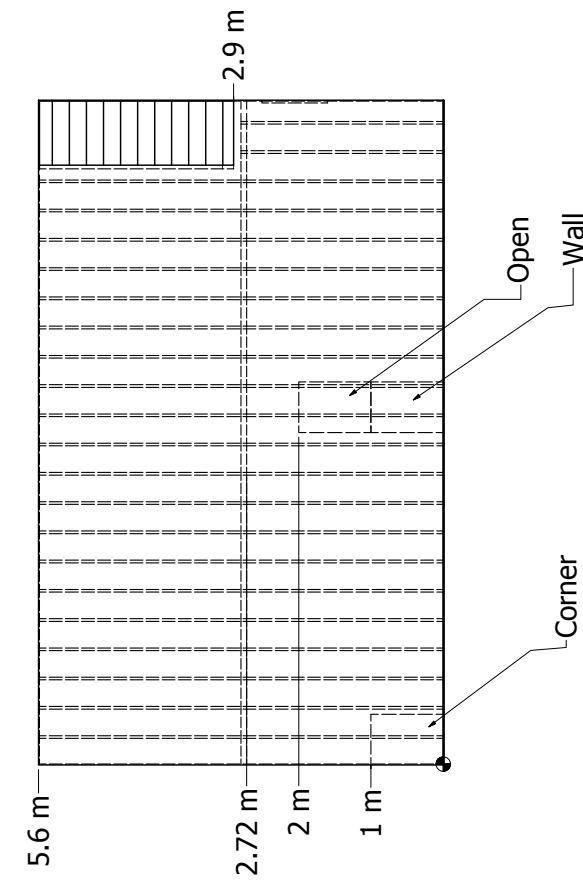


Figure 3.9: Geometry of the Vettori Flat Ceiling.

3.25 Vettori Sloped Ceiling Experiments

Vettori [49] performed a series of 72 compartment experiments to assess the effects of ceiling beams and slopes on the activation times of quick-response residential pendent sprinklers. There were 36 experiments (2 replicates of each) combining the following parameters:

- Flat, 13°, or 24° Sloped Ceiling
- Smooth or Obstructed Ceiling
- Fast or Slow Growth Fire
- Corner, Side Wall, or Detached Burner Location

3.26 Summary of Experiments

This section presents a summary of all the experiments described in this chapter in terms of quantities commonly used in fire protection engineering. This “parameter space” outlines the range of applicability of the validation performed to date. The parameters are explained below:

Heat Release Rate, \dot{Q} , is the range of peak heat release rates of the fires in the test series.

Fire Plume Parameter, Q^* , is a useful non-dimensional quantity for plume correlations and flame height estimates.

$$Q^* = \frac{\dot{Q}}{\rho_\infty c_p T_\infty \sqrt{g D D^2}} \quad (3.1)$$

Global Equivalence Ratio, ϕ , is the ratio of the mass flux of fuel to the mass flux of oxygen into the compartment, divided by the stoichiometric value.

Fire Diameter, D , is the equivalent diameter of the base of the fire.

Characteristic Fire Diameter, D^* , is a useful length scale that incorporates the heat release rate of the fire.

$$D^* = \left(\frac{\dot{Q}}{\rho_\infty c_p T_\infty \sqrt{g}} \right)^{2/5} \quad (3.2)$$

Non-dimensional Ceiling Height, H/D^* , reports the actual ceiling height, H , in terms of the fire’s characteristic length scale. This is a useful parameter in assessing the role that the fire plume plays in the simulation. A large value represents a relatively small fire in a relatively high space.

Non-dimensional Ceiling Jet Radius, r_{cj}/H , is mainly used in empirical correlations. It is not as useful for CFD.

Non-dimensional Radiation Radius, r_{rad}/D , is an appropriate measure of whether the radiation measurement is *near-field* or *far-field*.

Table 3.3: Summary of the major experimental parameters.

Test Series	\dot{Q} (kW)	Q^*	ϕ	D (m)	D^* (m)	H/D^*	r_{cj}/H	r_{rad}/D
ATF Corridors	50-500	0.25-2.5	N/A	0.5	0.3-0.7	8.0-3.4	7	N/A
FM/SNL	500	0.6	0.04-0.4	0.9	1.0-1.3	8.4	1.2-1.6	N/A
NBS Multi-Room	100	1.4	0.04	0.34	1.0-1.3	5.6	N/A	N/A
NIST/NRC	400-2300	0.4-2.1	0.1-0.6	1.0	1.0-1.3	2.9-5.7	1.3-1.7	2.2-5.7
NIST RSE	600	62	0.83	0.15	0.8	1.3	N/A	N/A
Steckler	63	1.1	0.02	0.30	0.32	6.7	N/A	N/A
UL/NFPRF	4400	3.9	0.11	1.0	1.7	4.4	0.86	N/A
VTT	1800-3600	1.0	0.10	1.2-1.6	1.0-1.3	12-16	N/A	N/A
WTC	3000	2.7	0.33	1.0	1.5	2.6	0.52	1.0

Chapter 4

Quantifying Model Uncertainty

4.1 Introduction

The most effective way of introducing the subject of uncertainty in fire modeling is by way of an example. Suppose that a fire model is used to estimate the likelihood that an electrical control cable could be damaged by a fire. It is assumed that the cable loses functionality when its surface temperature reaches 400 °C, and the model predicts that the cable temperature could reach as high as 350 °C. Does this mean that there is no chance of damage? The answer is no, because the input parameters, like the heat release rate of the fire, and the model assumptions, like the way the cables are modeled, are uncertain. The combination of the two – the *parameter uncertainty* and the *model uncertainty* – leave open the possibility that the cable temperature could exceed 400 °C.

This chapter addresses *model uncertainty* only and suggests a simple method to quantify it. While parameter uncertainty is certainly an important consideration in fire modeling, its treatment varies considerably depending on the particular application. For example, in what is often referred to as a “bounding analysis,” the model input parameters are chosen so as to simulate a “maximum credible” or “worst case” fire. In other cases, mean values of the input parameters constitute a “50th percentile” design scenario. Sometimes entire statistical distributions, rather than individual values, of the input parameters are “propagated” through the model in a variety of ways, leading to a statistical distribution of the model output. Notarianni and Parry survey these techniques in the SFPE Handbook [143]. Regardless of the method that is chosen for assessing the impact of the input parameters on the model prediction, there needs to be a way of quantifying the uncertainty of the model itself. In other words, how good is the prediction for a given set of input parameters?

The issue of model uncertainty has been around as long as the models themselves. The scenario above, for example, was considered by Siu and Apostolakis in the early 1980s [144] as part of their development of risk models for nuclear power plants. The fire models at the time were relatively simple. In fact, many were engineering correlations in the form of simple formulae. This made the methods for quantifying their uncertainty reasonably tractable because each formula consisted of only a handful of physical parameters. Over the past thirty years, however, both fire modeling and the corresponding methods of uncertainty analysis have become far more complex. The current generation of computational fluid dynamics fire models require such a large number of physical and numerical parameters that it is considered too cumbersome to estimate model uncertainty by systematically assessing their combined effect on the final prediction. The more practical approach is to compare model predictions with actual fire experiments in a validation study, the conclusions of which typically come in the form of statements like: “The model generally over-predicts the measured temperatures by about 10 %,” or “The model predictions are within about 20 % of the measured heat fluxes.” This information is helpful, at the very least to demonstrate that the model is appropriate for the given application. However, even the statement that the model over-predicts measured temperatures

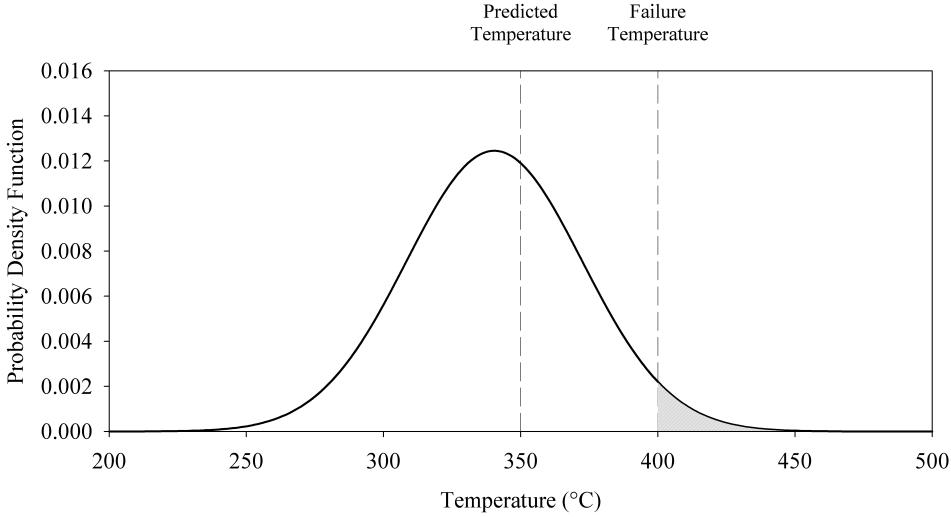


Figure 4.1: Plot showing a possible way of expressing the uncertainty of the model prediction.

by 10 % is useful not only to gain acceptance of the model but also to provide a better sense of the model's accuracy, and a greater level of assurance in answering the question posed above. Knowing that the model not only predicted a temperature of 350 °C, but also that the model tends to over-predict temperatures by a certain amount, increases the confidence that the postulated fire would not cause the cable to fail. The probability of cable failure could be quantified further via a statistical distribution like the one shown in Fig. 4.1. The area indicated by the shaded region is the probability that the temperature will exceed 400 °C, even though the model has predicted a peak temperature of only 350 °C.

This chapter suggests a method for expressing *model uncertainty* by way of a distribution like the one shown in Fig. 4.1. The procedure is not a dramatic departure from the current practice of fire model validation in that it relies entirely on comparisons of model predictions and experimental measurements. The advantage of the approach is that it does not demand advanced knowledge of statistics or details of the numerical model. The parameters of the distribution shown in Fig. 4.1, namely the mean and standard deviation, are not generated by the model user. Rather, they are reported as the results of the validation study. The calculation of the probability of exceeding some critical threshold (*i.e.* the area under the curve) is a simple table look-up or function call in data analysis software like Microsoft Excel®.

4.2 Sources of Model Uncertainty

A deterministic fire model is based on fundamental conservation laws of mass, momentum and energy, applied either to entire compartments or smaller control volumes that make up the compartments. A CFD model may use millions of control volumes to compute the solution of the Navier-Stokes equations. However, it does not actually solve the Navier-Stokes equations, but rather an approximate form of these equations. The approximation involves simplifying physical assumptions, like the various techniques for treating subgrid-scale turbulence. One critical approximation is the discretization of the governing equations. For example, the partial derivative of the density, ρ , with respect to the spatial coordinate, x , can be written in approximate form as:

$$\frac{\partial \rho}{\partial x} = \frac{\rho_{i+1} - \rho_{i-1}}{2\delta x} + O(\delta x^2) \quad (4.1)$$

where δx is the grid spacing chosen by the model user. The second term on the right represents all of the terms of order δx^2 and higher in the Taylor series expansion and are known collectively as the *discretization error*. These extra terms are simply dropped from the equation set, the argument being that they become smaller and smaller with decreasing grid cell size, δx . The effect of these neglected terms is captured, to some extent, by the subgrid-scale turbulence model, but that is yet another approximation of the true physics. What effect do these approximations have on the predicted results? It is very difficult to determine based on an analysis of the discretized equations. One possibility for estimating the magnitude of the discretization error is to perform a detailed convergence analysis, but this still does not answer a question like, “What is the uncertainty of the model prediction of the gas temperature at a particular location in the room at a particular point in time?”

To make matters worse, there are literally dozens of subroutines that make up a CFD fire model, from its transport equations, radiation solver, solid phase heat transfer routines, pyrolysis model, empirical mass, momentum and energy transfer routines at the wall, and so on. It has been suggested by some that a means to quantify the model uncertainty is to combine the uncertainties of all the model components in a way similar to that of the input parameters. However, such an exercise is very difficult, especially for a computational fluid dynamics (CFD) model, for a number of reasons. First, fire involves a complicated interaction of gas and solid phase phenomena that are closely coupled. Second, grid sensitivity in a CFD model or the error associated with a two-layer assumption in a zone model are dependent on the particular fire scenario. Third, fire is an inherently transient phenomenon in which relatively small changes in events, like a door opening or sprinkler actuation, can lead to significant changes in outcome.

Rather than attempt to decompose the model into its constituent parts and assess the uncertainty of each, the strategy adopted here is to compare model predictions to as many experiments as possible. This has been the traditional approach for quantifying model uncertainty in fire protection engineering because of the relative abundance of test data. Consider, for example, the plot shown in Fig. 4.2. This is the typical outcome of a validation study, where in this case a series of heat flux measurements are compared with model predictions. The diagonal line indicates where the prediction and measurement agree. But because there is uncertainty associated with each, it cannot be said that the model is perfect if its predictions agree exactly with measurements. There needs to be a way of quantifying the uncertainties of each before any conclusions can be drawn. Such an exercise would result in the uncertainty bars¹ shown in the figure. The horizontal bar associated with each point represents the uncertainty in the measurement itself. For example, the heat flux gauge is subject to uncertainty due to its design and fabrication. Because the horizontal bar represents the experimental uncertainty, it is assumed that the vertical bar represents the model uncertainty. This is only partially true. In fact the vertical bar represents the total uncertainty of the prediction, which is a combination of the *model* and *parameter* uncertainties. The physical input parameters, like the heat release rate and material properties, are based on measurements that are reported in the documentation of the experiment. The total *experimental uncertainty* is represented by all of the horizontal bar and part of the vertical. If the *experimental uncertainty* can be quantified, then the *model uncertainty* can be obtained as a result.

4.3 Quantifying the Experimental Uncertainty

As discussed in the previous section, the *experimental uncertainty* is a combination of the uncertainty in the measurement of the quantity of interest, like the gas temperature or heat flux, along with the propagated uncertainty of the measured test parameters, like the heat release rate or material properties. “Propagated uncertainty” is, in this case, what has been referred to above as the parameter uncertainty. It is not the

¹The data in Fig. 4.2 was extracted from Ref. [3]. The uncertainty bars are for demonstration only.

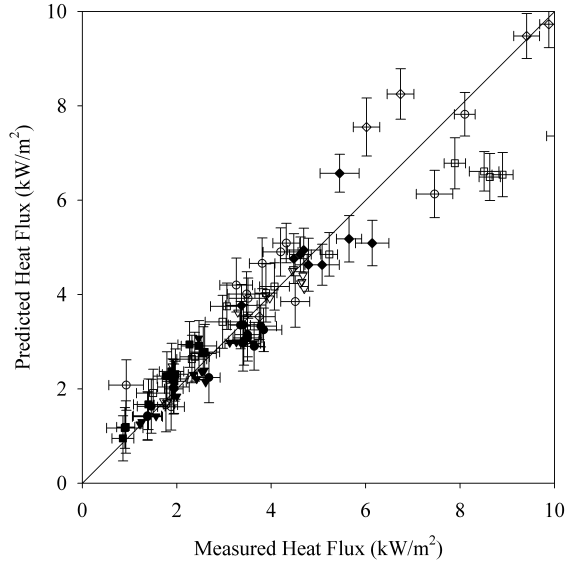


Figure 4.2: Example of a typical scatter plot of model predictions and experimental measurements.

uncertainty of the parameter itself, but rather the uncertainty in the predicted quantity resulting from the uncertainty of the parameter.

In a recent fire model validation study conducted by the U.S. Nuclear Regulatory Commission [3], Hamins estimated the experimental uncertainty for several full-scale fire experiments. There were two uncertainty estimates needed for each quantity of interest. The first was an estimate, expressed in the form of a 95 % confidence interval, of the uncertainty in the measurement of the quantity itself. For example, reported gas and surface temperatures were made with thermocouples of various designs (bare-bead, shielded, aspirated) with different size beads, metals, and so on. For each, one can estimate the uncertainty in the reported measurement.

Next, the uncertainty of the measurements of the reported test parameters was estimated, including the heat release rate, leakage area, ventilation rate, material properties, and so on. It was then necessary to calculate how the uncertainty in these parameters contributed to the uncertainty of the reported measurement. To do this, Hamins examined a number of empirical formulae that are widely used in fire protection engineering to determine the most important test parameters and their effect on the measured results. These formulae provided the means of propagating the parameter uncertainties through the experiment. For example, it has been shown [145] that the hot gas layer temperature rise, $T - T_0$, due to a compartment fire is proportional to the heat release rate, \dot{Q} , raised to the two-thirds power:

$$T - T_0 = C \dot{Q}^{\frac{2}{3}} \quad (4.2)$$

The constant, C , involves a number of geometric and thermo-physical parameters that are unique to the given fire scenario. By way of differentials, this empirical relationship can be expressed in the form:

$$\frac{\Delta T}{T - T_0} \approx \frac{2}{3} \frac{\Delta \dot{Q}}{\dot{Q}} \quad (4.3)$$

In words, the relative change in the temperature rise is approximately two-thirds the relative change in the heat release rate. Assuming that the numerical model exhibits the same functional relationship between the compartment temperature and the heat release rate, there is now a way to express the uncertainty of the model

Table 4.1: Sensitivity of model outputs from Volume 2 of NUREG-1824 [3].

Output Quantity	Input Parameter(s)	Power Dependence
HGL Temperature	HRR	2/3
HGL Depth	Door Height	1
Ceiling Jet Temperature	HRR	
Plume Temperature	HRR	
Gas Concentration	HRR	1/2
Smoke Concentration	HRR	1
	Soot Yield	1
Compartment Pressure	HRR	2
	Leakage Rate	2
	Ventilation Rate	2
Heat Flux	Heat Flux	4/3
Surface Temperature	HRR	2/3

prediction as a function of the uncertainty of this most important input parameter. Often, the uncertainty of a measurement is expressed in the form of a 95 % confidence interval, (two standard deviations or 2σ). Thus, if the heat release rate of a fire is assumed with 95 % confidence to be within 15 % of the reported measurement, then the temperature predicted by the model has an uncertainty² of at least 10 %.

The uncertainty of each measurement is expressed as a relative standard deviation. The uncertainty of the measured output quantity is denoted $\tilde{\sigma}_o$, and the uncertainty of each significant input parameter is denoted $\tilde{\sigma}_i$. Assuming that all the uncertainties are uncorrelated, they are combined via the expression:

$$\tilde{\sigma}_E^2 = \tilde{\sigma}_o^2 + \sum_i p_i^2 \tilde{\sigma}_i^2 \quad (4.4)$$

The factors, p_i , represent the power dependencies of the individual input parameters. Table 4.1 lists the most important physical parameters associated with various measured quantities in the experiments and their power dependence.

Hamins estimated the combined experimental uncertainties for ten quantities of interest in the U.S. NRC validation study. The results are summarized in Table 4.2, with each combined uncertainty reported in the form of a 95 % confidence interval (*i.e.* $2\tilde{\sigma}_E$). It is assumed throughout that both experiment and model uncertainties can be expressed in relative terms. The assumption is based on a qualitative assessment of dozens of scatter plots similar to that shown in Fig. 4.2 that show the scattered points to form an expanding “wedge” about the diagonal line, or some other off-diagonal line due to an assumed bias in the model predictions. This assessment is a critical component of the analysis described in the next section.

4.4 Calculating Model Uncertainty

This section describes a method for calculating the *model uncertainty*. In terms of the example given in the Introduction, this is the answer to the question, “350 °C plus or minus what?” Actually, the “plus or minus”

²An uncertainty that is expressed in the form of a percentage typically means one or two *relative* standard deviations, often denoted with a tilde, $\tilde{\sigma} = \sigma/\mu$.

Table 4.2: Summary of Hamins' uncertainty estimates [3].

Measured Quantity	Combined Relative Uncertainty, $2\tilde{\sigma}_E$
HGL Temperature	0.14
HGL Depth	0.13
Ceiling Jet Temperature	0.16
Plume Temperature	0.14
Gas Concentrations	0.09
Smoke Concentration	0.33
Pressure with Ventilation	0.80
Pressure without Ventilation	0.40
Heat Flux	0.20
Surface Temperature	0.14

uncertainty bounds are expressed as a statistical distribution. That is, the model prediction of the “true” temperature of the cable, θ , is expressed in the following way³:

$$\theta | 350 \sim N \left(\frac{350}{\delta}, \tilde{\sigma}_M^2 \left(\frac{350}{\delta} \right)^2 \right) \quad (4.5)$$

In words, given a model prediction of 350 °C, the expected value of the true temperature is assumed to be normally distributed with the given mean and standard deviation. The values of δ and $\tilde{\sigma}_M$ are calculated based on the comparison of model predictions with experimental measurements, and this calculation is discussed below. First, however, there are a few very important assumptions that need to be justified.

1. The distribution is assumed to be normal. Given the complexity of the models, it would be difficult to postulate a more precise functional relationship. The same is true of the form of the distribution. Given the complexity of the models and the experiments, it would be difficult to justify any particular distribution. In fact, the very reason for developing this method of quantifying model uncertainty based on validation experiments is because the model algorithm itself is too complicated to work with directly as a means of estimating the error. However, if the distributions were better characterized, the methodology presented here could be generalized appropriately.
2. The degree to which the model under or over-predicts the “truth” is expressed as a multiplicative bias factor, δ ; thus, the mean of the distribution in this case is $350/\delta$. If $\delta < 1$, the model tends to under-predict, in which case it is assumed that the true value would be greater than 350. If $\delta > 1$, it is assumed that the true value would be less than 350.
3. The standard deviation of the distribution is expressed as a fixed percentage of the mean, $\tilde{\sigma} = \sigma/\mu$. This is based on the observation that the results of past validation exercises, when plotted as shown in Fig. 4.2, suggest that the difference between predicted and measured values is roughly proportional to the magnitude of the measured value.

With these assumptions in mind, it remains to show how the two parameters, δ and $\tilde{\sigma}_M$, are calculated using the results of a model validation study. Such a study typically consists of comparing point measurements from a wide variety of fire experiments with corresponding model predictions. Figure 4.3 is a typical

³ $N(\mu, \sigma^2)$ denotes a normal (Gaussian) distribution with mean, μ , and standard deviation, σ .

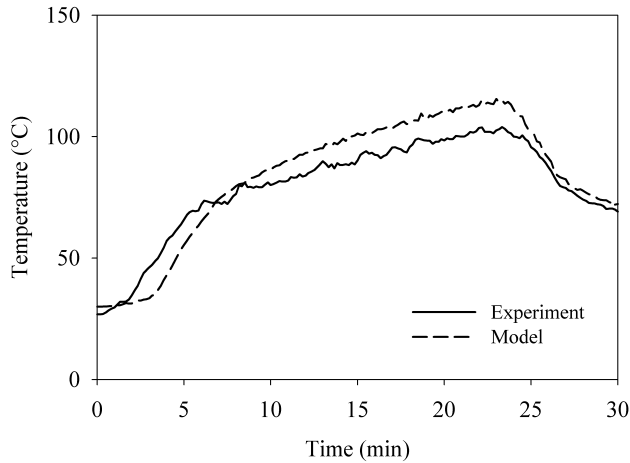


Figure 4.3: Example of a typical time history comparison of model prediction and experimental measurement.

result for a single point measurement, and given that usually dozens of such measurements are made during each experiment, and potentially dozens of experiments are conducted as part of a test series, hundreds of such plots can be produced for any given quantity of interest. Usually, the data is condensed into a more tractable form by way of a single metric with which to compare the two curves like the ones shown in Fig. 4.3. Peacock *et al.* [146] discuss various possible metrics. A commonly used metric is simply to compare the measured and predicted peak values. If the data is spiky, some form of time-averaging can be used. Regardless of the exact form of the metric, what results from this exercise is a pair of numbers for each plot, (E_i, M_i) , that can be depicted graphically as shown in Fig. 4.2.

With these assumptions in mind, a relatively simple method of analyzing the data can be developed. Assume that the set of model predictions and the corresponding set of experimental measurements are denoted M_i and E_i , respectively, where i ranges from 1 to n and both M_i and E_i are positive numbers expressing the increase in the value of a quantity above its ambient. As mentioned above, measurements from full-scale fire experiments often lack uncertainty estimates. In cases where the uncertainty is reported, it is usually expressed as either a standard deviation or confidence interval about the measured value. In other words, there is rarely a reported systematic bias in the measurement because if a bias can be quantified, the reported values are adjusted accordingly. For this reason, assume that a given experimental measurement, E_i , is normally distributed about the “true” value, θ_i , and there is no systematic bias:

$$E | \theta \sim N(\theta, \sigma_E^2) \quad (4.6)$$

The notation⁴ $E | \theta$ means that E is conditional on a particular value of θ . This is the usual way of defining a likelihood function. It is convenient to use the so-called delta method⁵ to obtain the approximate distribution

$$\ln E | \theta \sim N\left(\ln \theta - \frac{\tilde{\sigma}_E^2}{2}, \tilde{\sigma}_E^2\right) \quad (4.7)$$

⁴Note that the subscript, i , has been dropped merely to reduce the notational clutter.

⁵Given the random variable $X \sim N(\mu, \sigma^2)$, the delta method [147] provides a way to estimate the distribution of a function of X :

$$g(X) \sim N\left(g(\mu) + g''(\mu) \sigma^2/2, (g'(\mu) \sigma)^2\right)$$

The purpose of applying the natural log to the random variable is so that its variance can be expressed in terms of the relative uncertainty, $\tilde{\sigma}_E = \sigma_E/\theta$. This is convenient because it is assumed that the relative uncertainty is constant for each quantity of interest. The quantities and uncertainty values are listed in Table 4.2.

It cannot be assumed, as in the case of the experimental measurements, that the model predictions have no systematic bias. Instead, it is assumed that the model predictions are normally distributed about the true values multiplied by a bias factor, δ :

$$M | \theta \sim N(\delta\theta, \sigma_M^2) \quad (4.8)$$

The standard deviation, σ_M , and the bias factor, δ , represent the model uncertainty. Again, the delta method renders a distribution for $\ln M$ whose parameters can be expressed in terms of a relative standard deviation:

$$\ln M | \theta \sim N\left(\ln \delta + \ln \theta - \frac{\tilde{\sigma}_M^2}{2}, \tilde{\sigma}_M^2\right) ; \quad \tilde{\sigma}_M = \frac{\sigma_M}{\delta\theta} \quad (4.9)$$

Combining Eq. (4.7) with Eq. (4.9) yields:

$$\ln M - \ln E \sim N\left(\ln \delta - \frac{\tilde{\sigma}_M^2}{2} + \frac{\tilde{\sigma}_E^2}{2}, \tilde{\sigma}_M^2 + \tilde{\sigma}_E^2\right) \quad (4.10)$$

What is now needed is a way to estimate the mean and standard deviation of this combined distribution. First, define:

$$\overline{\ln M} = \frac{1}{n} \sum_{i=1}^n \ln M_i ; \quad \overline{\ln E} = \frac{1}{n} \sum_{i=1}^n \ln E_i \quad (4.11)$$

The least squares estimate⁶ of the standard deviation of the combined distribution is defined as:

$$\widehat{\tilde{\sigma}_M^2} + \widehat{\tilde{\sigma}_E^2} = \frac{1}{n-1} \sum_{i=1}^n [(\ln M_i - \overline{\ln M}) - (\overline{\ln M} - \overline{\ln E})]^2 \quad (4.12)$$

Recall that $\tilde{\sigma}_E$ is known and the expression on the right can be evaluated using the pairs of measured and predicted values. An estimate of δ can be found using the mean of the distribution:

$$\hat{\delta} = \exp\left(\overline{\ln M} - \overline{\ln E} + \frac{\widehat{\tilde{\sigma}_M^2}}{2} - \frac{\widehat{\tilde{\sigma}_E^2}}{2}\right) \quad (4.13)$$

Taking the assumed normal distribution of the model prediction, M , in Eq. (4.8) and using a Bayesian argument⁷ with a non-informative prior for θ , the posterior distribution can be expressed:

$$\delta\theta | M \sim N(M, \sigma_M^2) \quad (4.14)$$

The assumption of a non-informative prior implies that there is not sufficient information about the prior distribution (*i.e.* the true value) of θ to assume anything other than a uniform⁸ distribution. This is equivalent to saying that the modeler has not biased the model input parameters to compensate for a known bias in the model output. For example, if a particular model has been shown to over-predict compartment temperature,

⁶Note that $\hat{\sigma}$ denotes an estimate of σ .

⁷The form of Bayes theorem used here states that the posterior distribution is the product of the prior distribution and the likelihood function, normalized by their integral: $f(\theta|M) = p(\theta)f(M|\theta)/\int p(\theta)f(M|\theta)d\theta$. A constant prior is also known as a Jeffreys prior [148].

⁸A uniform distribution means that for any two equally sized intervals of the real line, there is an equal likelihood that the random variable takes a value in one of them.

and the modeler has reduced the specified heat release rate to better estimate the true temperature, then it can no longer be assumed that the prior distribution of the true temperature is uniform. Still another way to look at this is by analogy to target shooting. Suppose a particular rifle has a manufacturers defect such that, on average, it shoots 10 cm to the left of the target. It must be assumed that any given shot by a marksman without this knowledge is going to strike 10 cm to the left of the intended target. However, if the marksman knows of the defect, he or she will probably aim 10 cm to the right of the intended target to compensate for the defect. If that is the case, it can no longer be assumed that the intended target was 10 cm to the right of the bullet hole.

In summary, assuming that the modeler has not modified the input parameters to compensate for a known bias in the model, the true value of the model output quantity, θ , given the model prediction, M , is normally distributed with the following mean and standard deviation:

$$\theta | M \sim N\left(\frac{M}{\hat{\delta}}, \widehat{\sigma}_M^2 \left(\frac{M}{\hat{\delta}}\right)^2\right) \quad (4.15)$$

This formula has been obtained⁹ by dividing by the bias factor, $\hat{\delta}$, in Eq. (4.14). The two parameters, $\hat{\delta}$ and $\widehat{\sigma}_M$, indicate the accuracy of the model in comparison to experimental measurements. If $\hat{\delta} = 1$ and $\widehat{\sigma}_M = \widetilde{\sigma}_E$, then the model is of comparable accuracy to the measurements themselves. It is important to note that $\widehat{\sigma}_M$ cannot be less than $\widetilde{\sigma}_E$ because it is not possible to demonstrate that the model is more accurate than the measurements against which it is compared. This is not to say that the model cannot be more accurate than the measurements; rather, that the model cannot be shown to be more accurate than the measurements.

4.5 Verifying the Procedure

This section illustrates the meaning of the estimated parameters $\hat{\delta}$ and $\widehat{\sigma}_M$. Suppose that 1000 fire experiments are conducted, and that for each experiment the temperature at a given point and at a given time is known. For the sake of this exercise, assume that these values can be represented by 1000 uniformly distributed random numbers, θ_i , between 0 and 1000. These values have no uncertainty – they represent the “truth.” Of course, the true values can never be known, but for this hypothetical exercise they are assumed. Next, with θ_i as the mean, a normally-distributed random variable is chosen that represents a hypothetical measurement, E_i . The relative standard deviation of the distribution, $\widetilde{\sigma}_E$, is assumed known. In the same way, a normally-distributed random variable is chosen that represents a hypothetical model prediction, M_i . The mean of distribution $\delta\theta_i$ and the relative standard deviation, $\widehat{\sigma}_M$, is specified. This procedure creates 1000 pairs of (E_i, M_i) with which the procedure outlined in the previous section can be tested. Using the 1000 pairs of values and the experimental uncertainty, $\widetilde{\sigma}_E$, the specified model bias, $\hat{\delta}$, and relative error, $\widehat{\sigma}_M$, of the hypothetical model predictions should be accurately estimated.

Two examples are considered. For the first example, assume that the model has no bias ($\hat{\delta} = 1$) and that the relative uncertainty of the measurements and the relative error of the model are both 0.1, or 10 %. The scatter plot on the left side of Fig. 4.4 displays the model predicted values compared to the true values. The dashed lines indicate the 95 % confidence interval; that is, it is expected that 95 % of the points should fall between these lines, whose slopes are plus and minus 20 % ($2\widehat{\sigma}_M$) of the diagonal line. Of course, this plot cannot exist in a real situation, because the true values are never known. Instead, the only way to present the data is via the scatter plot on the right side of Fig. 4.4. Here, the measured values, E_i , are compared with the predicted values, M_i . The same dashed lines are carried over from the plot on the left. Because the predicted values are being compared with measurements that have uncertainty, it appears that the model

⁹Note that if $X \sim N(\mu, \sigma^2)$, then $cX \sim N(c\mu, (c\sigma)^2)$.

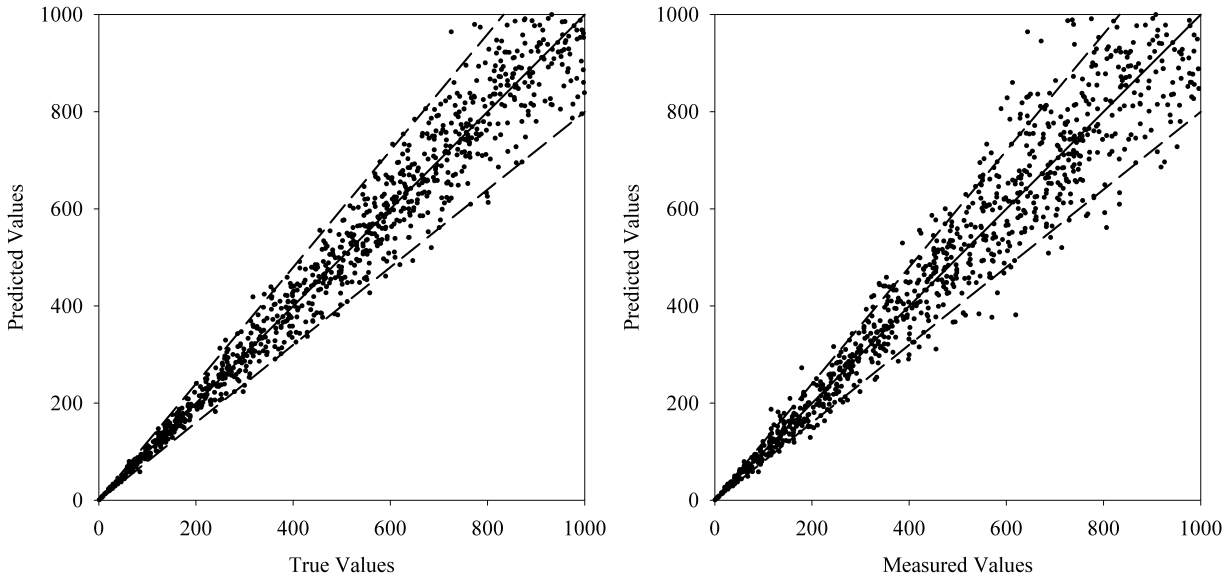


Figure 4.4: (Left) A comparison of predicted and “true” values for 1000 hypothetical experiments in which the model predictions and experimental measurements have the same accuracy. (Right) The same data, except now the predicted values are compared to measured values. On both plots, the uncertainty bounds apply to both the predicted and measured values.

uncertainty is greater than it actually is because the data points are now scattered noticeably beyond the original uncertainty bounds. In this hypothetical example, the model is assumed to be as accurate as the measurements, yet the comparison makes it seem as if the model is less accurate than the experiments. The procedure outlined above, which makes use of only the measured and predicted values, is able to extract from the data the fact that the hypothetical model has a relative error of 10 %, not the roughly 15 % that one would infer from the plot if the experimental uncertainty were not taken into account.

For the second example, the hypothetical model predictions and the experimental measurements are more realistic. Assume now that the measured quantity is surface temperature, and that the relative uncertainty of the measured values, $\tilde{\sigma}_E = 0.07$, is obtained from Table 4.2. We assume the model has a bias factor of 1.03 and its relative error is 0.10 in order to generate a set of hypothetical model predictions. A graphical representation of the data is shown in Fig. 4.5. Note that the experimental uncertainty bounds are represented by solid lines, and the model bias and relative error are represented by the dashed lines. Each are expressed as 95 % confidence intervals ($2\tilde{\sigma}$).

The statistical procedure outlined above ought to provide estimates of the bias factor, δ , and standard deviation, $\tilde{\sigma}_M$, for the hypothetical model predictions. The results of seven random trials are shown in Table 4.3. For each trial, values representing the model predictions and experimental measurements were randomly selected based on the assumed distributions. The calculation procedure discussed above was applied to these hypothetical values. The resulting estimates of the model bias and relative error were not exactly the same as those used to generate the data because the calculation procedure relies on truncated Taylor series approximations. However, given the fact that the experimental uncertainty estimate, $\tilde{\sigma}_E$, is often only a gross approximation in its own right, the accuracy of the procedure is more than adequate, as

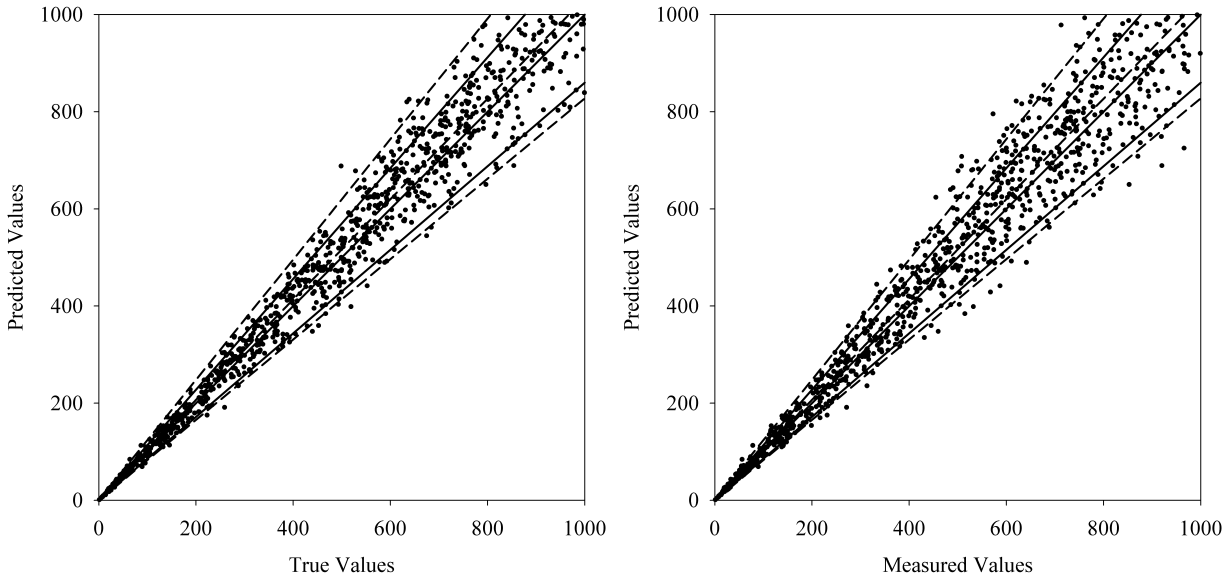


Figure 4.5: (Left) A comparison of predicted and “true” values for 1000 hypothetical experiments. The short dashed lines indicate the bias, $\delta = 1.03$, and the relative error, $2\tilde{\sigma}_M = 0.20$, of the model predictions. The solid, off-diagonal lines indicate the relative uncertainty, $2\tilde{\sigma}_E = 0.14$ of the experimental measurements. (Right) The same data, except now the predicted values are compared to measured values. On both plots, the uncertainty bounds are the same.

indicated by the average values of the seven trials.

4.6 Making Use of the Model Uncertainty

The previous sections describes a method of quantifying the model uncertainty by comparing its predictions with experimental measurements. But how does one make use of the computed model bias and relative error? This is best answered with an example. Suppose the model is being used to estimate the likelihood that electrical control cables could be damaged due to a fire in a compartment. Damage is assumed to occur when the surface temperature of any cable reaches 400°C . It is also assumed that the fire is ignited within an electrical cabinet and the heat release rate of the fire is a specified function of time, and that all other input parameters for the model are known and provided. Finally, it is assumed, for the time being, that there is no uncertainty associated with any of these assumptions. What is the likelihood that the cables would be damaged if that fire were to occur? The calculation is performed, and the model predicts that the maximum surface temperature of the cables is 350°C . Does this mean that there is no chance of damage, assuming that the input parameters and assumptions are not in question at the moment? The answer is no, because the model itself is subject to error. So what is the chance that the cables could actually reach temperatures greater than 400°C ?

Before answering this question, first consider past experiments for which model predictions have been compared to measured surface temperatures of objects with similar thermal characteristics as the cables in question. How “similar” the experiment is to the hypothetical scenario under study can be quantified by way of various parameters, like the thermal inertia of the object, the size of the fire, the size of the compartment, and so on. Next, the results of the validation study can be analyzed following the procedure spelled out

Table 4.3: Estimated bias and relative error from random trials used to verify the analysis.

Trial	Bias Factor	Relative Error
Exact	1.030	0.100
1	1.031	0.097
2	1.028	0.101
3	1.026	0.108
4	1.034	0.100
5	1.027	0.105
6	1.035	0.100
7	1.029	0.097
Average	1.030	0.101

above, which provides an estimate of the bias factor, δ , and relative error, $\tilde{\sigma}_M$, for the model predictions of this particular quantity. For the sake of argument, assume a bias factor is 1.03; that is, on average, the model has been shown to over-predict surface temperatures by 3 %. Also assume that the relative error has been calculated and it is 0.10 . These are the same values that were assumed in the second example of the previous section. Now, consider the graph shown in Fig. 4.1. The vertical lines indicate the “threshold” temperature at which damage is assumed to occur (400 °C), and the temperature predicted by the model (350 °C). Given an ambient temperature of 20 °C, the predicted temperature rise, M , is 330 °C. The bell curve is taken as a normal distribution whose mean and standard deviation are obtained from Eq. (4.15) and calculated here:

$$\mu = 20 + \frac{M}{\delta} = 20 + \frac{330}{1.03} = 340.4 \text{ } ^\circ\text{C} ; \quad \sigma = \tilde{\sigma}_M \frac{M}{\delta} = 0.10 \times \frac{330}{1.03} = 32 \text{ } ^\circ\text{C} \quad (4.16)$$

respectively. The shaded area beneath the bell curve is the probability (0.03 in this case) that the “true” temperature can exceed 400 °C. This means that there is a 3 % chance that the cables could become damaged *based solely on the fact that the model is not a perfect representation of reality*.

4.7 Limitations

The above verification exercises are valuable in assuring that the procedure works as designed, but it also points out a few issues that need to be addressed. First, any statistical procedure is based on the law of averages, or, in other words, more data is better than less. It is costly to conduct an extensive number of fire experiments to assess the accuracy of the model; thus, sometimes there just is not enough data to apply the above statistical procedure. Second, it has been assumed throughout the analysis that all of the relevant uncertainties can be characterized by normal distributions. Specifically, that the values of $\ln(M/E)$ are normally distributed. What if they are not? An examination of the results of the NRC/EPRI validation study discussed above [3] indicates that in cases where the number of pairs of M and E were greater than about 20, the values of $\ln(M/E)$ passed a test for normality¹⁰, whereas when there were less values, the values often did not pass the normality test. Figure 4.6 contains two sets of data for the model Fire Dynamics Simulator (FDS). There were 124 point comparisons of wall temperature, for which $\ln(M/E)$ conforms quite well

¹⁰The Kolmogorov-Smirnov test for normality was used with a p -value of 0.05. The p -value determines the probability of being incorrect in concluding that the data is not normally distributed.

to a normal distribution. However, there were only 9 point comparisons for plume temperature, for which $\ln(M/E)$ does not conform.

In cases where there is not enough data and/or the data cannot be considered normally distributed, it is preferable to present the data as is shown in Figure 4.6 for Plume Temperature with only uncertainty bounds for the experiments, assuming the information is available. The value of the validation process outlined above is that it is possible at any step to stop and accept the raw output of the study as the basis for making an assessment of the model. The uncertainty analysis is valid only to the extent that sufficient experimental data with quantified uncertainty estimates is available. It does more harm than good to attempt to quantify the model uncertainty with insufficient means to do so.

Another concern with the above procedure is that an over-estimate of the experimental uncertainty will result in an under-estimate of the model uncertainty. Keep in mind that the model can never be shown to be more accurate than the experimental measurements against which it is compared. The model may be, in fact, more accurate than a particular set of measurements, but these measurements cannot be used to prove it. This rule is demonstrated mathematically by Eq. (4.12) where it is observed that an over-estimate of the experimental uncertainty, $\tilde{\sigma}_E$, can result in the square root of a negative number, an imaginary number. In the case that the computed model uncertainty is less than the estimated experimental uncertainty, the latter must be re-evaluated, or the number of data points needs to be seriously questioned.

4.8 Conclusion

A procedure has been proposed to estimate model uncertainty by way of comparisons of model predictions with experimental measurements whose uncertainty has been quantified. For clarity of presentation, issues associated with the selection of experiments, metrics of comparison, and presentation of results, have not been discussed in detail because these decisions are application-specific and best left to the end user or AHJ.

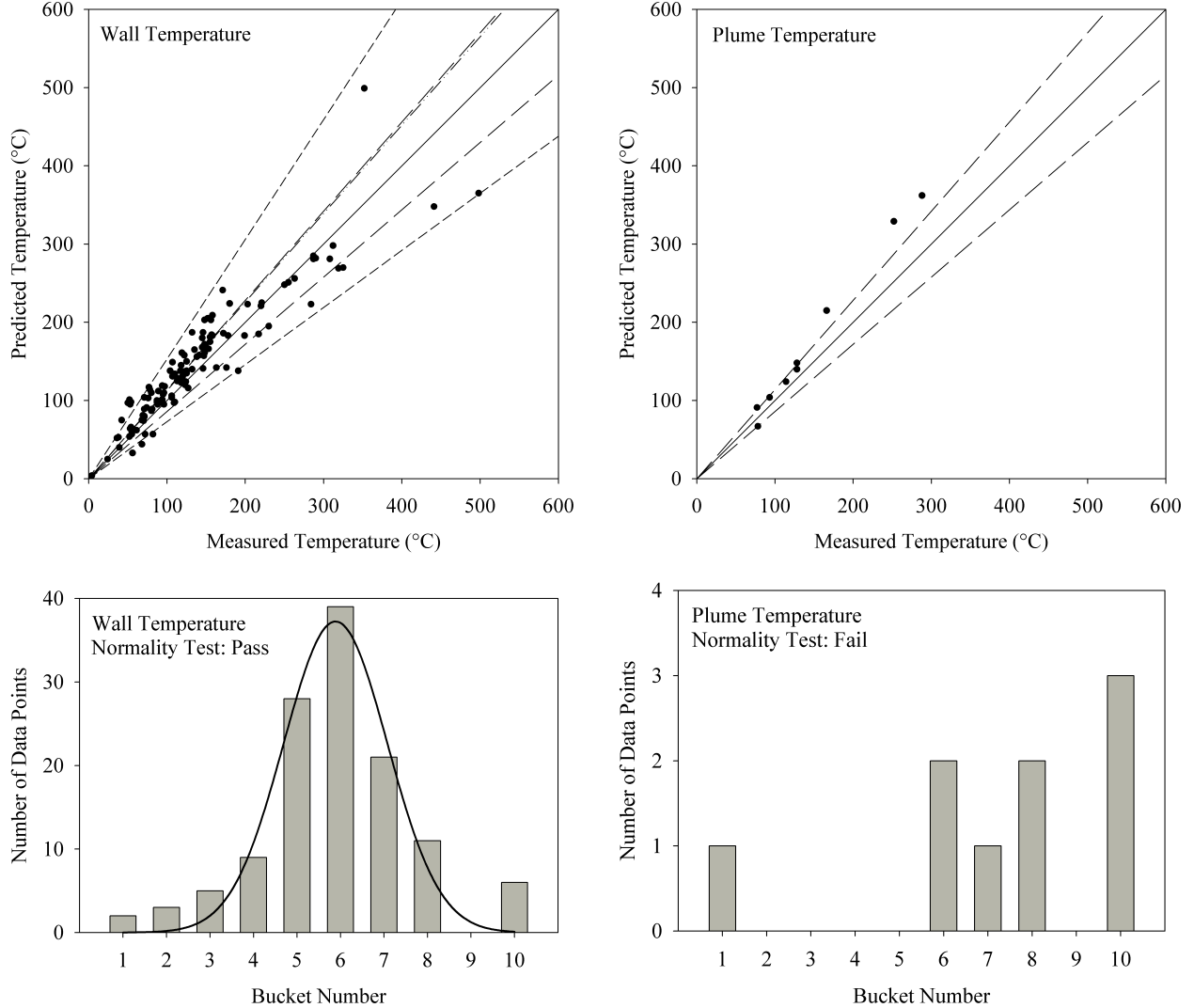


Figure 4.6: The results of normality testing for two sets of data taken from Reference [3]. On the left, measured vs predicted wall temperatures, and on the right, plume temperatures. Note that the off-diagonal lines in the scatter plot for Wall Temperature indicate the 2σ bounds for the experiments (long dash) and the model (short dash).

Chapter 5

HGL Temperature and Depth

FDS, like any CFD model, does not perform a direct calculation of the HGL temperature or height. These are constructs unique to two-zone models. Nevertheless, FDS does make predictions of gas temperature at the same locations as the thermocouples in the experiments, and these values can be reduced in the same manner as the experimental measurements to produce an “average” HGL temperature and height. Regardless of the validity of the reduction method, the FDS predictions of the HGL temperature and height ought to be representative of the accuracy of its predictions of the individual thermocouple measurements that are used in the HGL reduction. The temperature measurements from all six test series are used to compute an HGL temperature and height with which to compare to FDS. The same layer reduction method is used for five of the six test series. Only the NBS Multi-Room series uses another method.

A brief description of each test series is included below, followed by graphs comparing the predicted and measured HGL temperature and layer height.

5.1 HGL Reduction Method

Fire protection engineers often need to estimate the location of the interface between the hot, smoke-laden upper layer and the cooler lower layer in a burning compartment. Relatively simple fire models, often referred to as *two-zone models*, compute this quantity directly, along with the average temperature of the upper and lower layers. In a computational fluid dynamics (CFD) model like FDS, there are not two distinct zones, but rather a continuous profile of temperature. Nevertheless, there are methods that have been developed to estimate layer height and average temperatures from a continuous vertical profile of temperature. One such method [149] is as follows: Consider a continuous function $T(z)$ defining temperature T as a function of height above the floor z , where $z = 0$ is the floor and $z = H$ is the ceiling. Define T_u as the upper layer temperature, T_l as the lower layer temperature, and z_{int} as the interface height. Compute the quantities:

$$(H - z_{int}) T_u + z_{int} T_l = \int_0^H T(z) dz = I_1$$
$$(H - z_{int}) \frac{1}{T_u} + z_{int} \frac{1}{T_l} = \int_0^H \frac{1}{T(z)} dz = I_2$$

Solve for z_{int} :

$$z_{int} = \frac{T_l(I_1 I_2 - H^2)}{I_1 + I_2 T_l^2 - 2 T_l H} \quad (5.1)$$

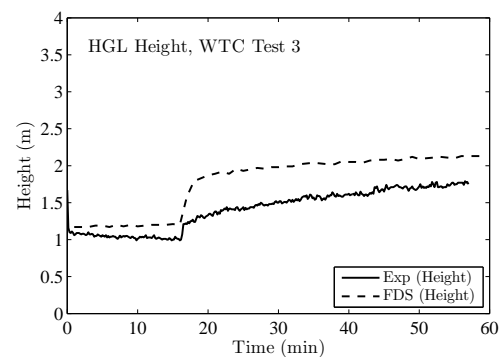
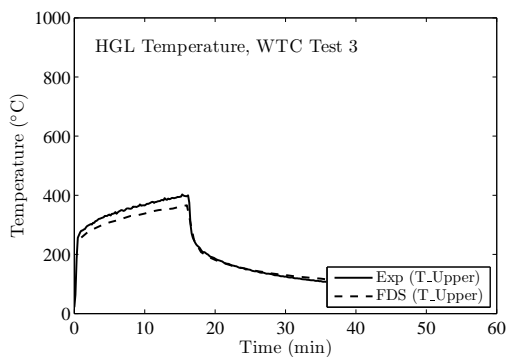
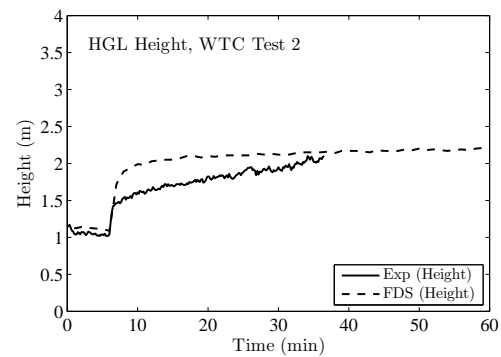
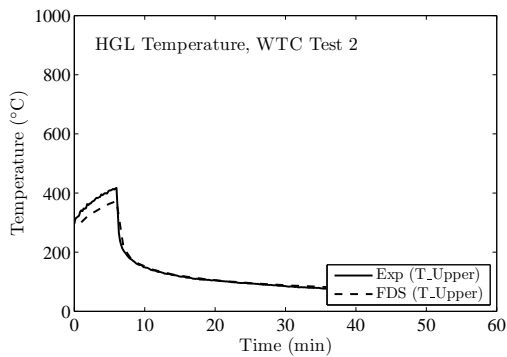
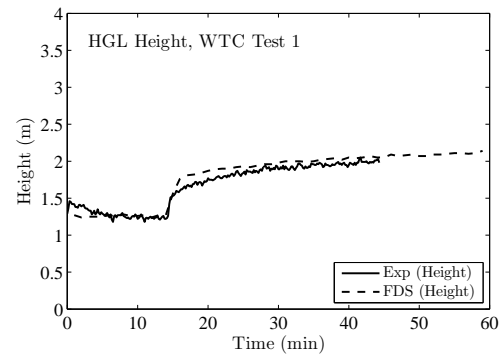
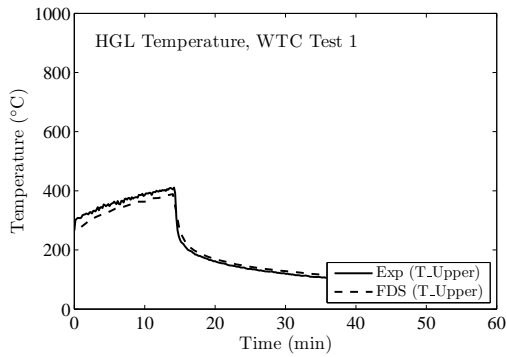
Let T_l be the temperature in the lowest mesh cell and, using Simpson's Rule, perform the numerical integration of I_1 and I_2 . T_u is defined as the average upper layer temperature via

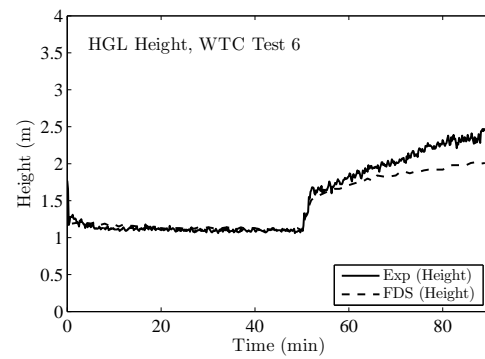
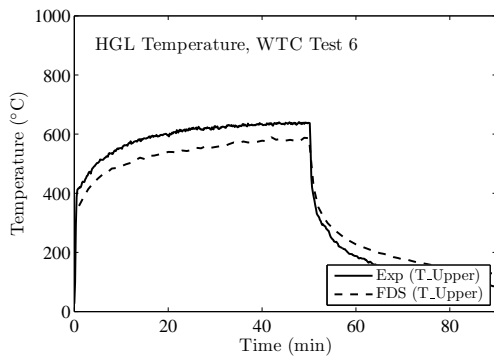
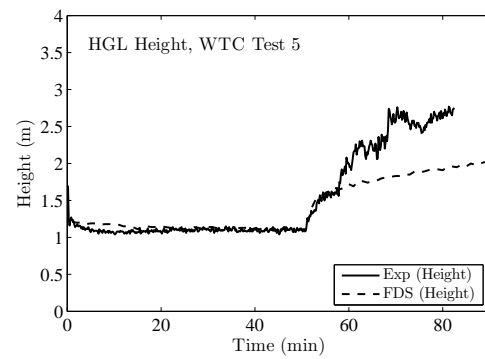
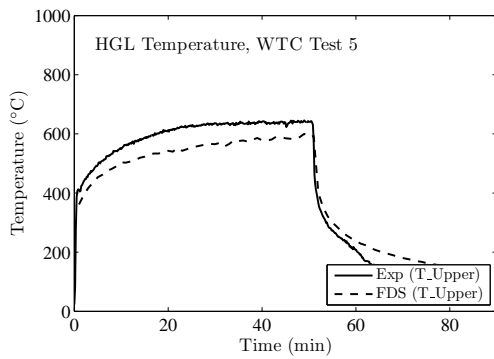
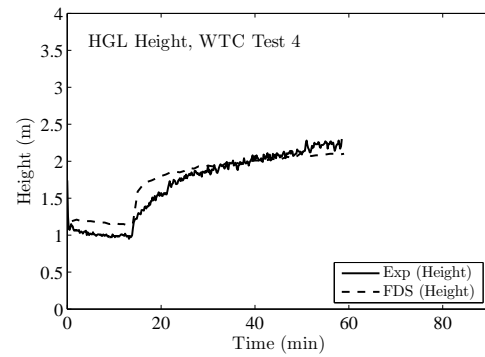
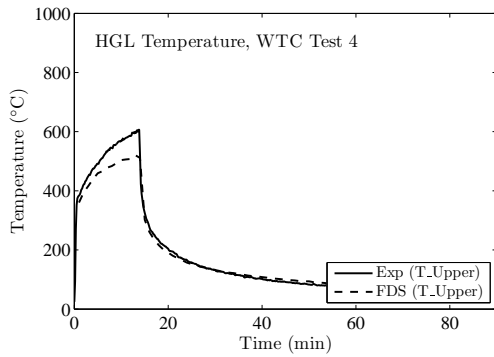
$$(H - z_{int}) T_u = \int_{z_{int}}^H T(z) dz \quad (5.2)$$

Further discussion of similar procedures can be found in Ref. [150].

5.2 WTC Test Series

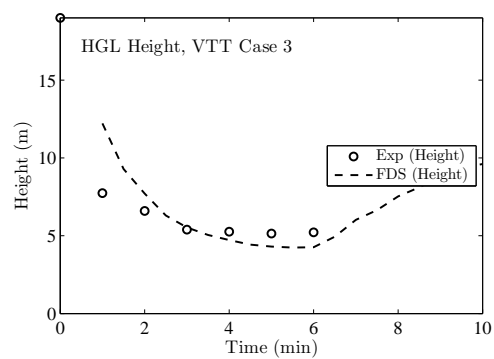
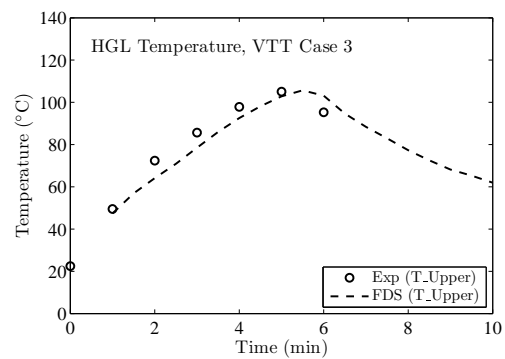
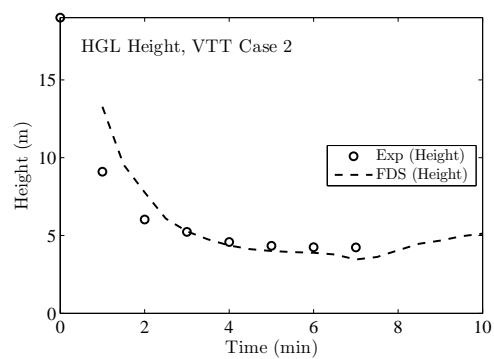
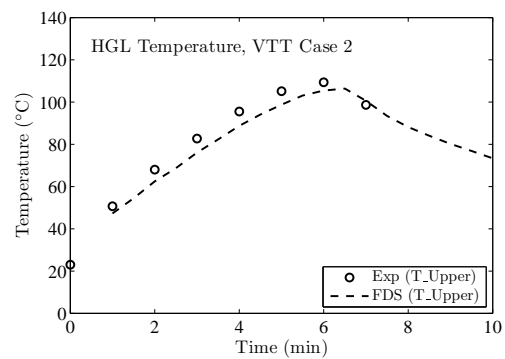
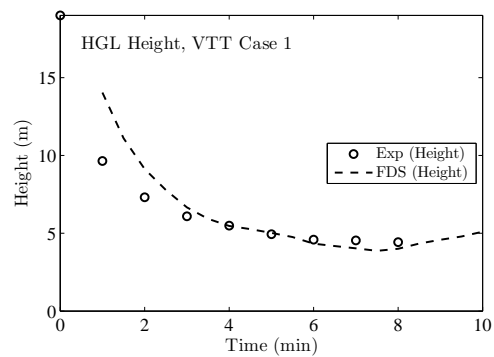
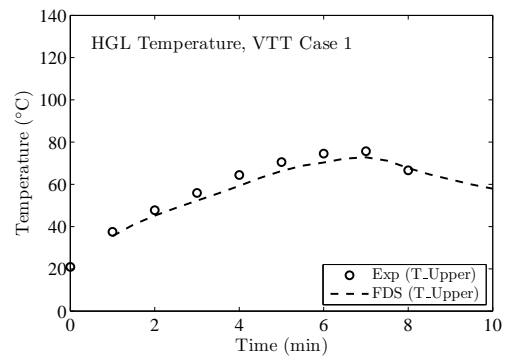
The HGL temperature and height for the WTC experiments were calculated from two TC trees, one that was approximately 3 m to the west and one 2 m to the east of the fire pan. Each tree consisted of 15 thermocouples, the highest point being 5 cm below the ceiling.





5.3 VTT Test Series

The HGL temperature and height are calculated from the (1 min) averaged gas temperatures from three vertical thermocouple arrays using the standard reduction method. There are 10 thermocouples in each vertical array, spaced 2 m apart in the lower two-thirds of the hall, and 1 m apart near the ceiling.

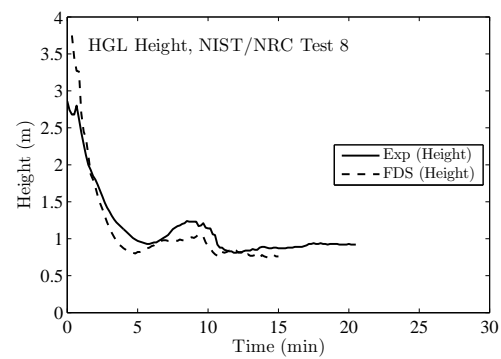
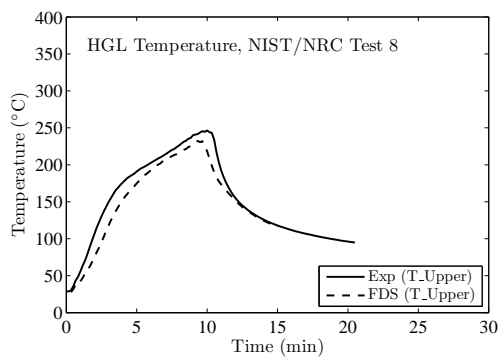
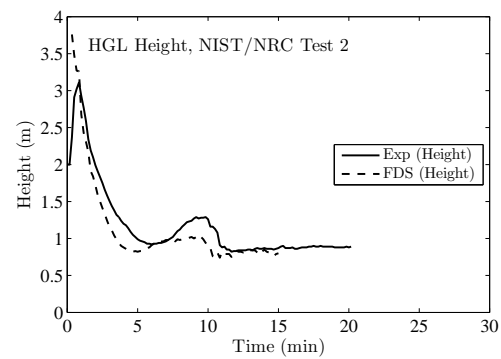
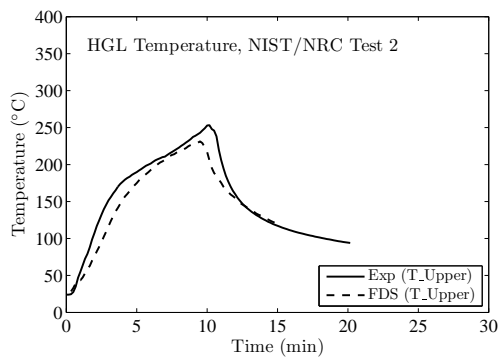
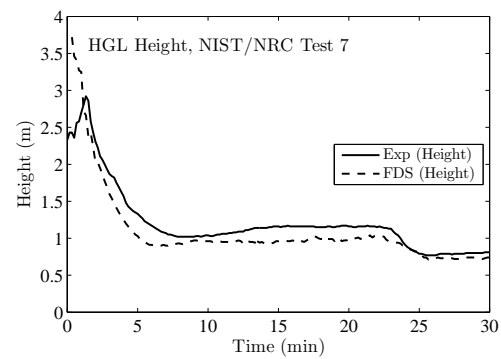
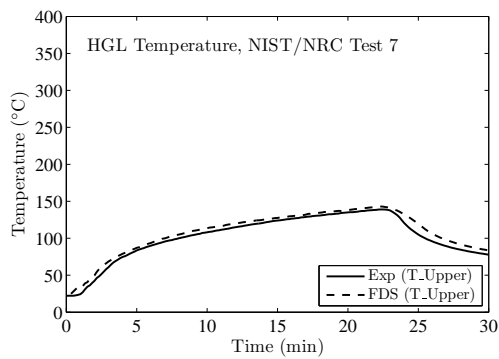
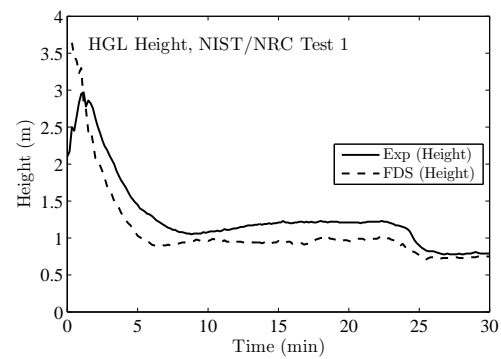
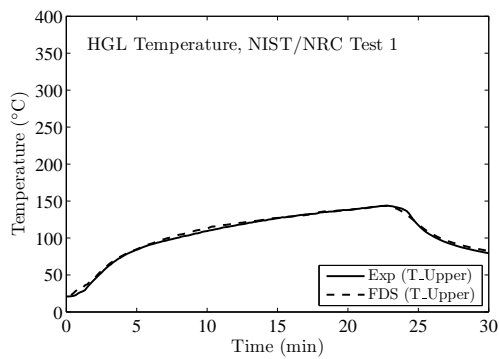


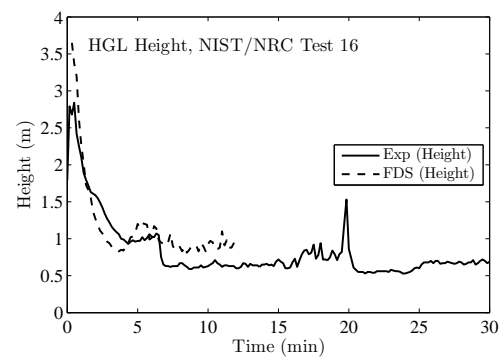
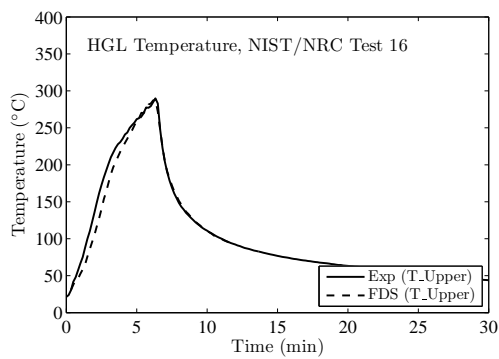
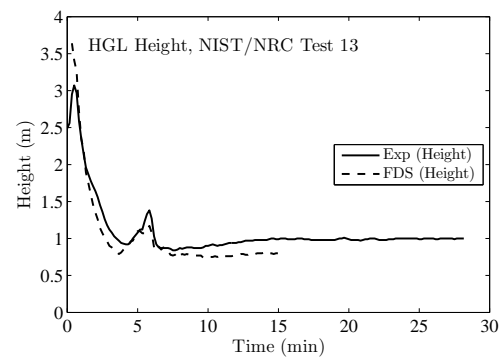
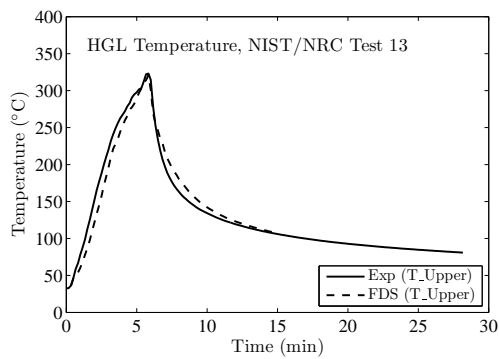
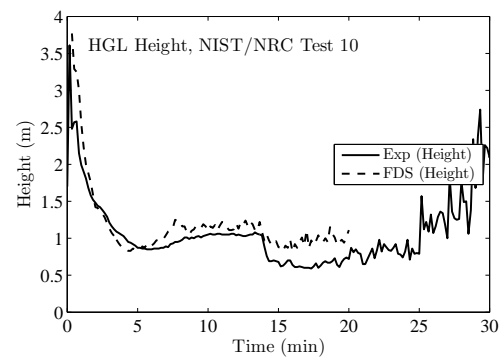
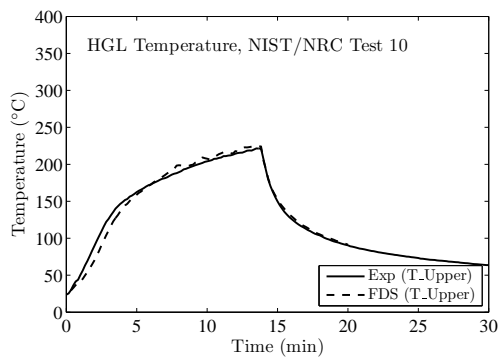
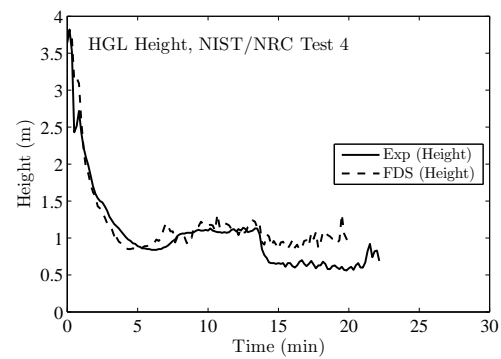
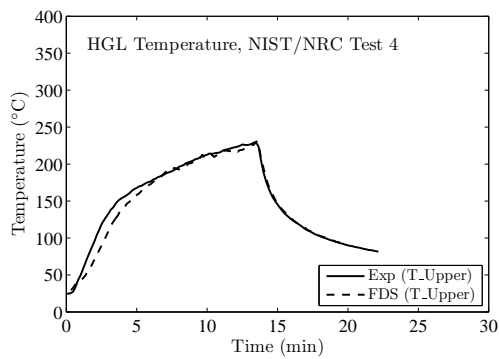
5.4 NIST/NRC Test Series

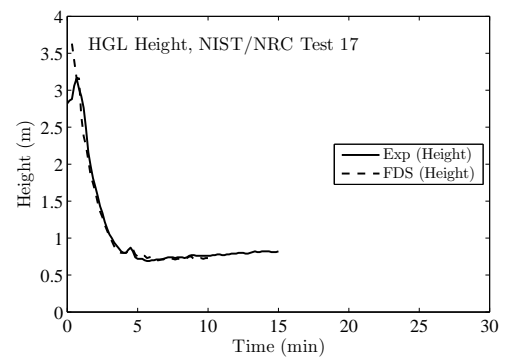
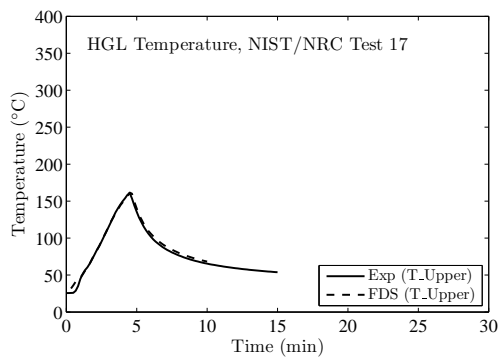
The NIST/NRC series consisted of 15 liquid spray fire tests with different heat release rates, pan locations, and ventilation conditions. Gas temperatures were measured using seven floor-to-ceiling thermocouple arrays (or “trees”) distributed throughout the compartment. The average hot gas layer temperature and height are calculated using thermocouple Trees 1, 2, 3, 5, 6 and 7. Tree 4 was not used because one of its thermocouples (TC 4-9) malfunctioned during most of the experiments.

A few observations about the simulations:

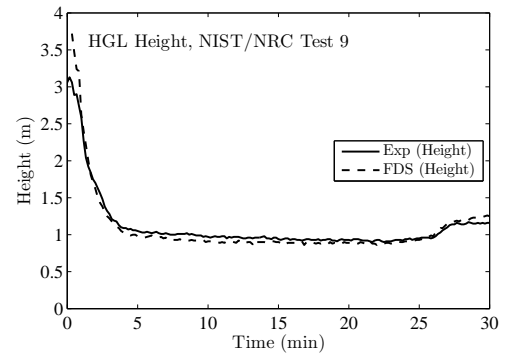
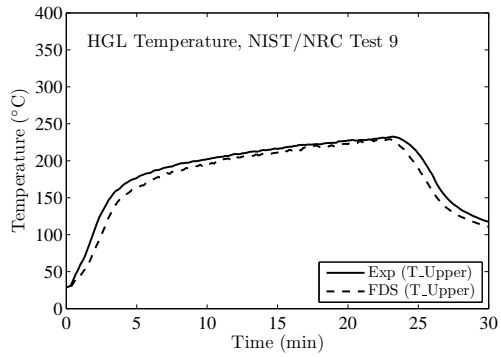
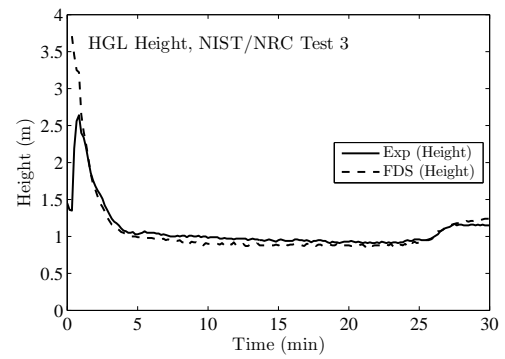
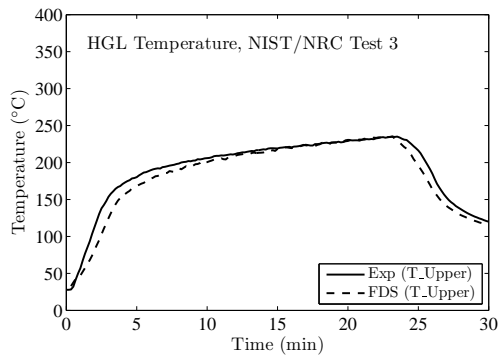
- During Tests 4, 5, 10 and 16 a fan blew air into the compartment through a vent in the south wall. The measured velocity profile of the fan is not uniform, with the bulk of the air blowing from the lower third of the duct towards the ceiling at a roughly 45° angle. The exact flow pattern is difficult to replicate in the model, thus, the results for Tests 4, 5, 10 and 16 should be evaluated with this in mind. The effect of the fan on the hot gas layer is small, but it does have a some effect on target temperatures near the vent.
- For all of the tests involving a fan, the predicted HGL height rises after the fire is extinguished, while the measured HGL drops. This appears to be a curious artifact of the layer reduction algorithm. It is not included in the calculation of the relative difference.
- In the closed door tests, the hot gas layer descends all the way to the floor. However, the reduction method, used on both the measured and predicted temperatures, does not account for the formation of a single layer, and therefore does not indicate that the layer drops all the way to the floor. This is neither a flaw in the measurements nor in FDS, but rather in the layer reduction method.
- The HGL reduction method produces spurious results in the first few minutes of each test because no clear layer has yet formed. These early times are not included in the relative difference calculation.

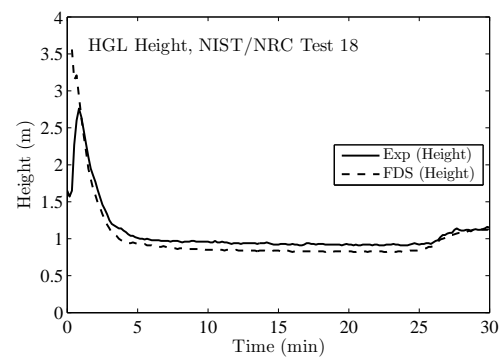
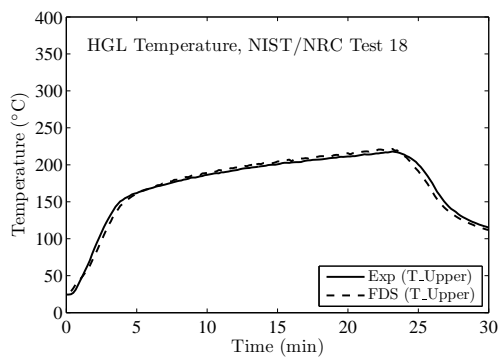
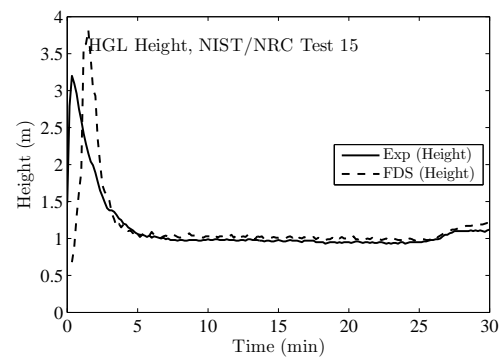
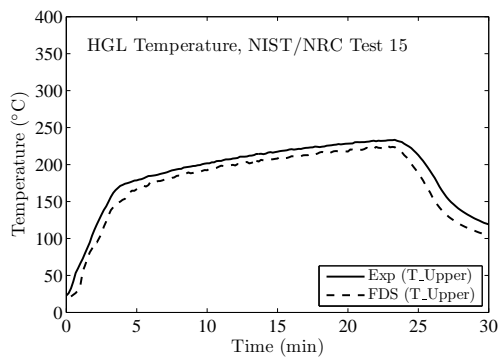
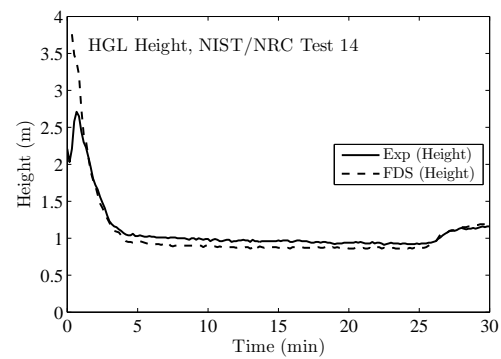
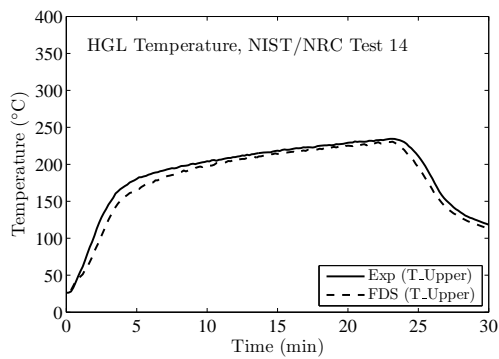
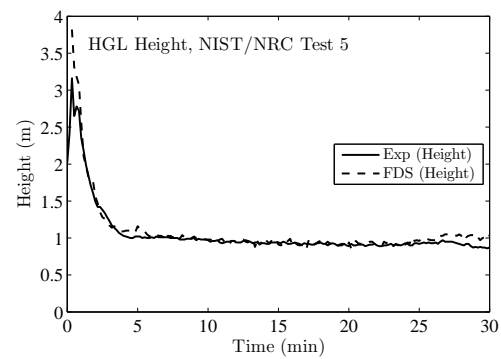
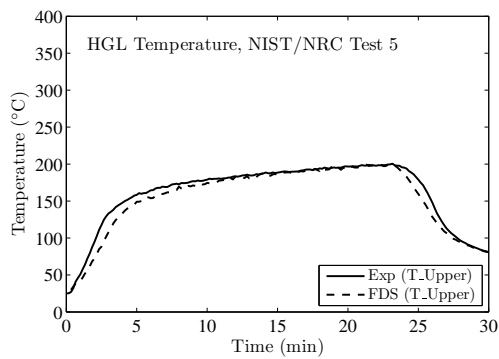






Open door tests to follow



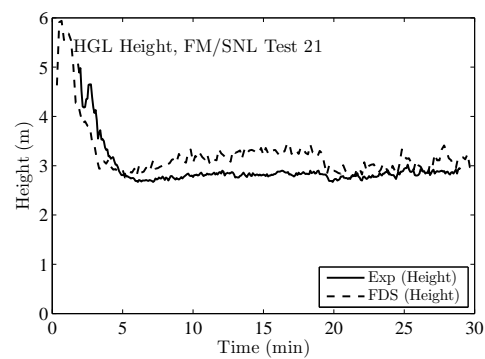
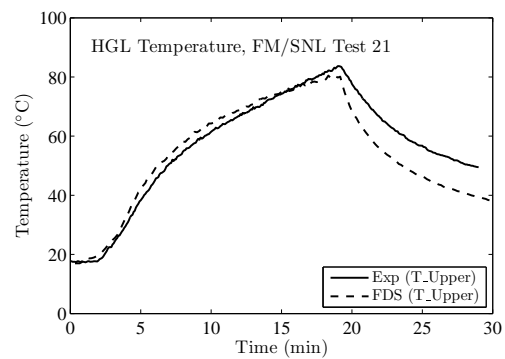
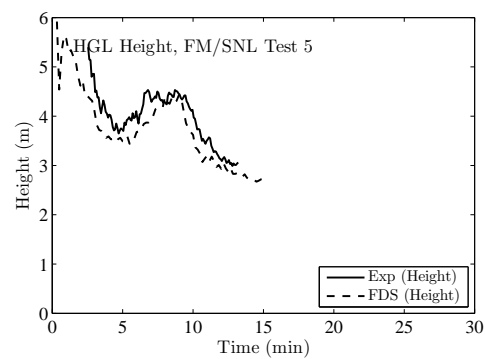
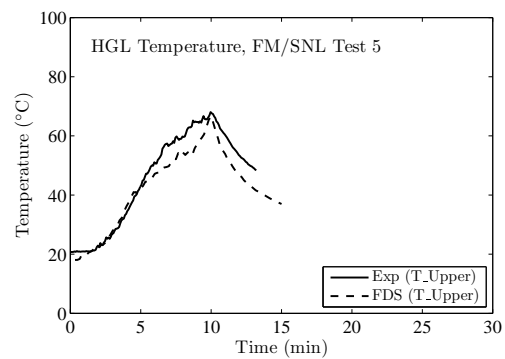
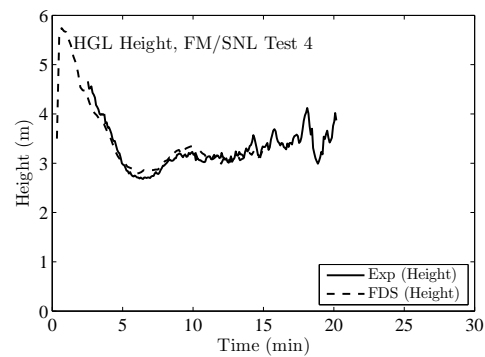
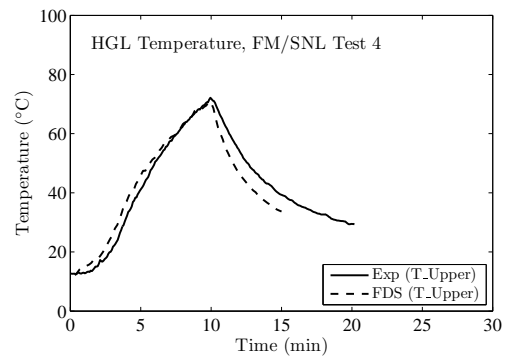


5.5 FM/SNL Test Series

Tests 4, 5, and 21 from the FM/SNL test series were selected for comparison. The hot gas layer temperature and height are calculated using the standard method. The thermocouple arrays that are referred to as Sectors 1, 2 and 3 are averaged (with an equal weighting for each) for Tests 4 and 5. For Test 21, only Sectors 1 and 3 are used, as Sector 2 falls within the smoke plume.

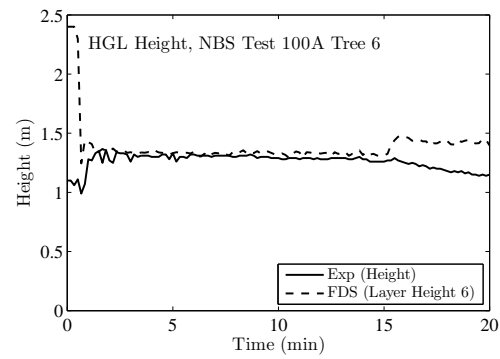
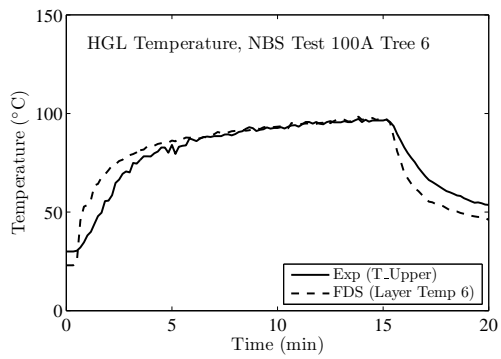
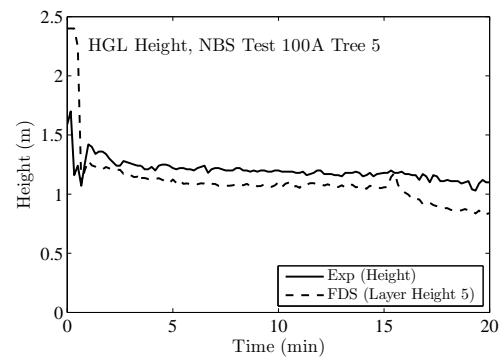
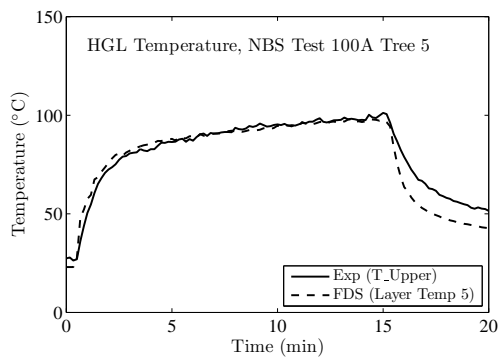
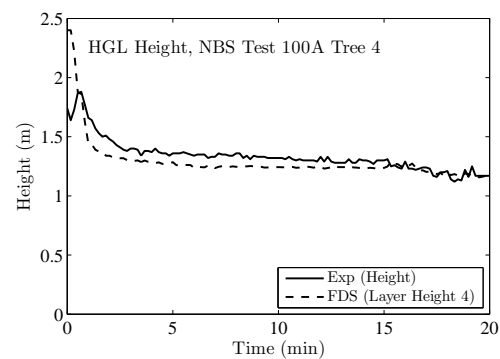
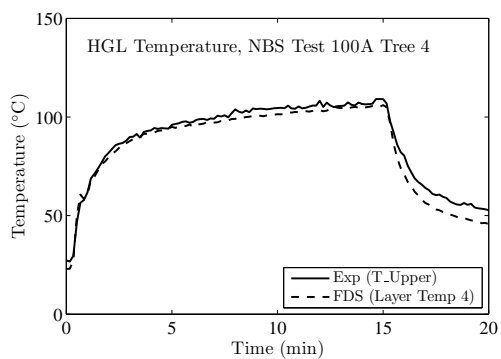
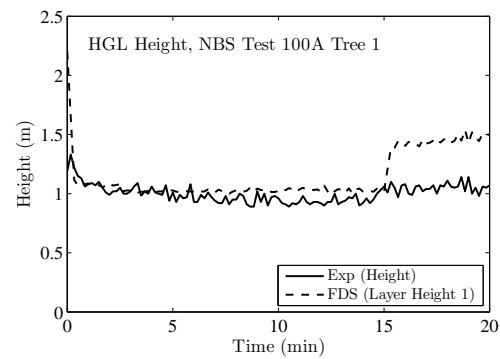
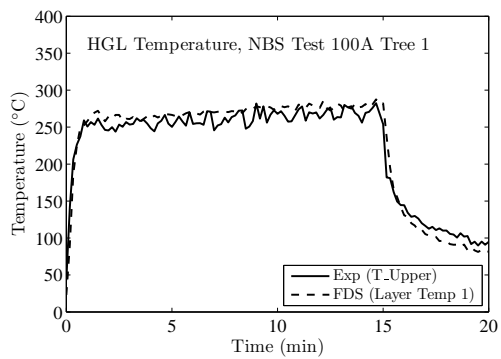
Note the following:

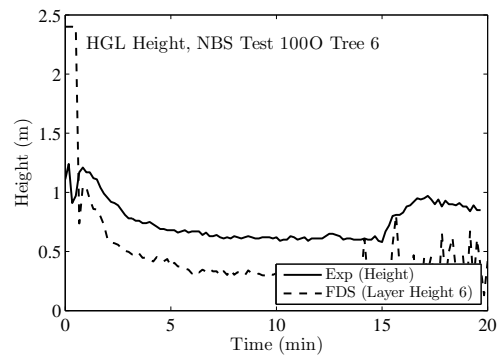
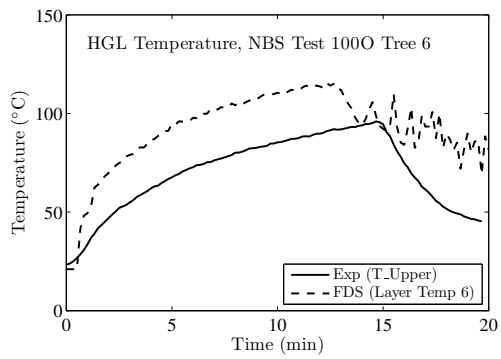
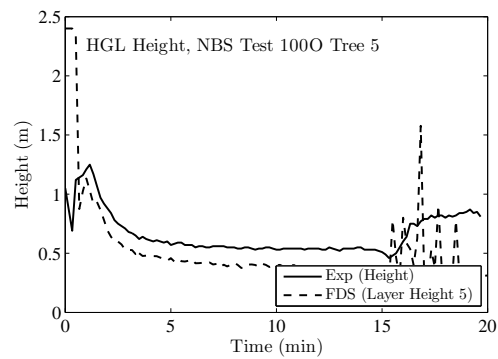
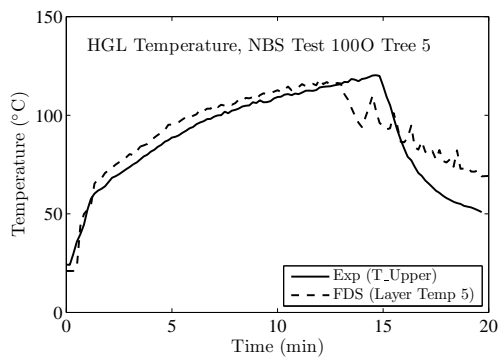
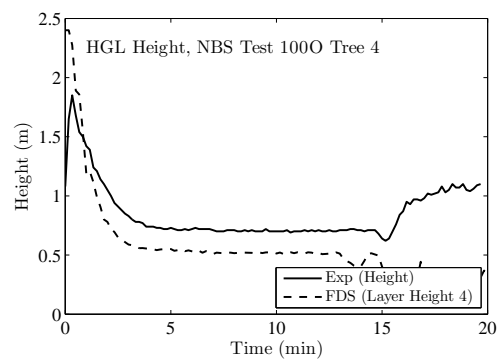
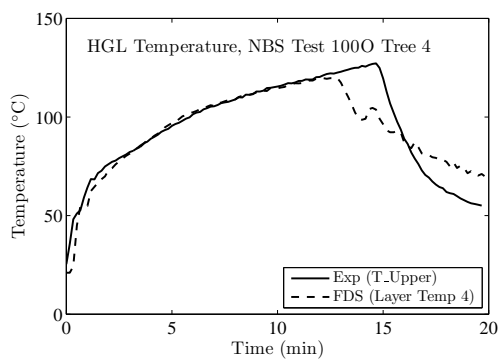
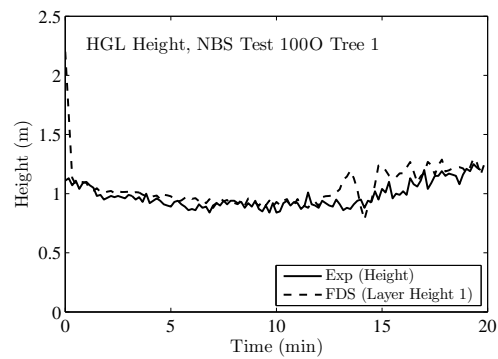
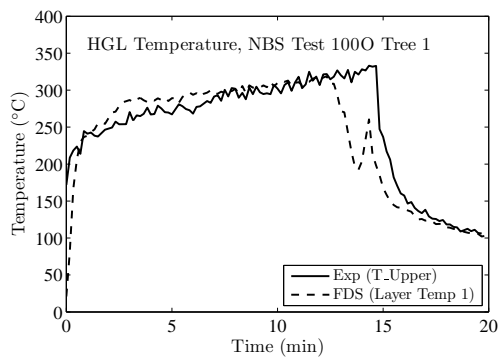
- The HGL heights, both the measured and predicted, are somewhat noisy due to the effect of ventilation ducts in the upper layer.
- The ventilation was turned off after 9 min in Test 5, the effect of which was a slight increase in both the measured and predicted HGL temperature.
- The measured HGL temperature is noticeably greater than the prediction in Test 21. This is possibly due to an increase in the HRR towards the end of the test. The simulations all used fixed HRRs after the 4 min ramp up.

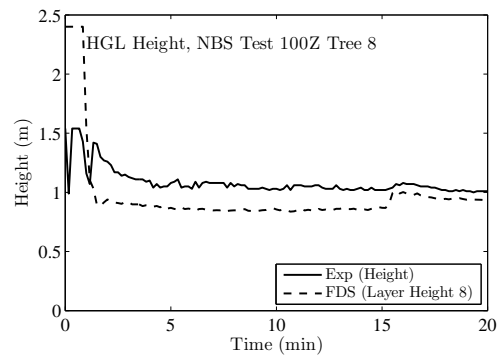
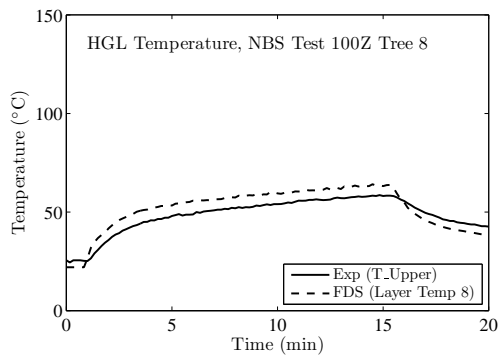
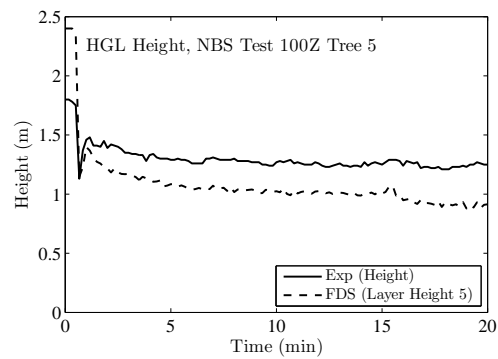
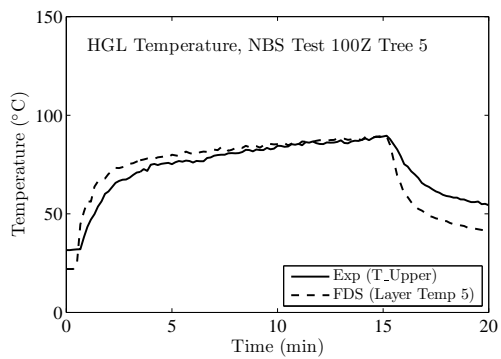
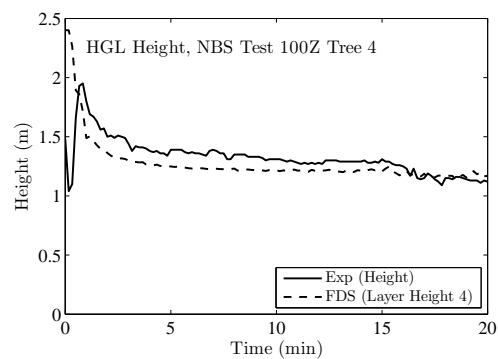
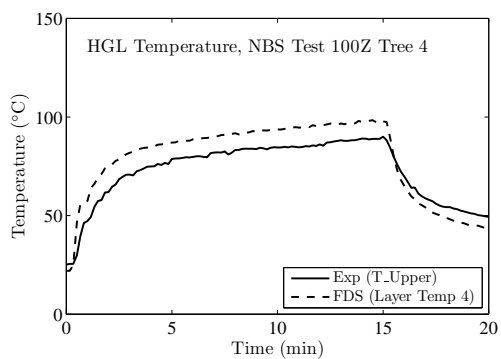
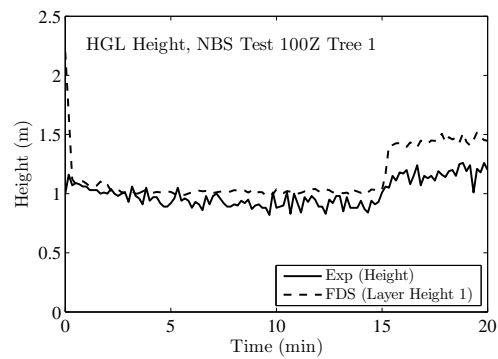
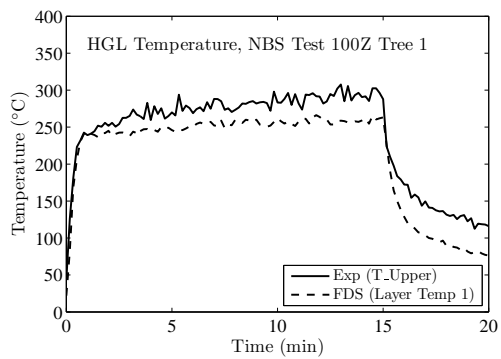


5.6 NBS Multi-Room Test Series

This series of experiments consists of two relatively small rooms connected by a long corridor. The fire is located in one of the rooms. Eight vertical arrays of thermocouples are positioned throughout the test space: one in the burn room, one near the door of the burn room, three in the corridor, one in the exit to the outside at the far end of the corridor, one near the door of the other or “target” room, and one inside the target room. Four of the eight arrays have been selected for comparison with model prediction: the array in the burn room (BR), the array in the middle of the corridor (18 ft from the BR), the array at the far end of the corridor (38 ft from the BR), and the array in the target room (TR). In Tests 100A and 100O, the target room is closed, in which case the array in the exit (EXI) doorway is used. The test director reduced the layer information individually for the eight thermocouple arrays using an alternative method. These results are included in the original data sets. However, for the current validation study, the selected TC trees were reduced using the conventional method common to all the experiments considered. The results are presented below.







5.7 Summary of Hot Gas Layer Temperature and Height

A summary scatter plot of the HGL predictions is given in Fig. 5.1. Most of the predictions fall within the experimental uncertainty bounds. Note, however, that both of these quantities represent spatial averages. At any given point in the compartment, a specific prediction of temperature may not fall within the uncertainty bounds. Point to point comparisons of temperature can be found in the chapters for plumes and ceiling jets.

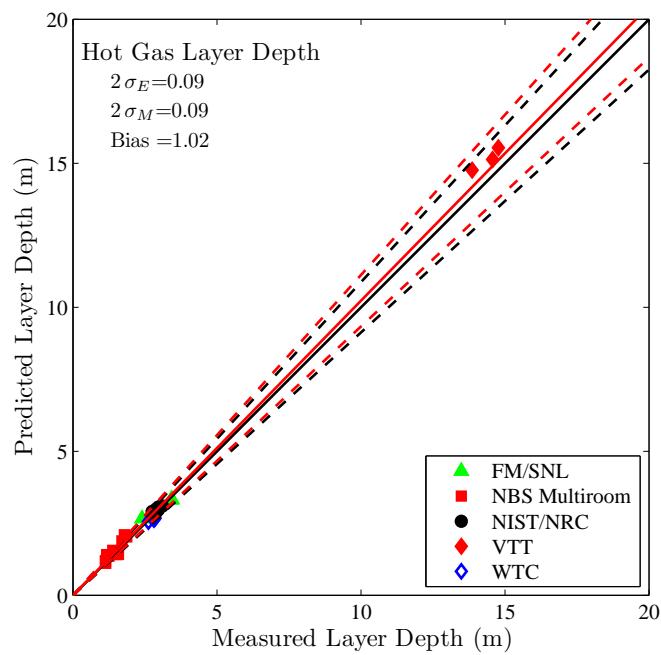
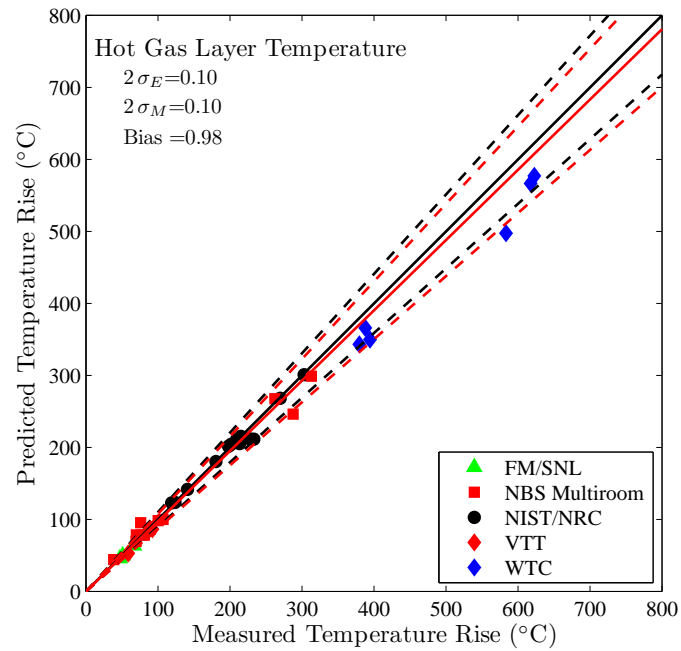
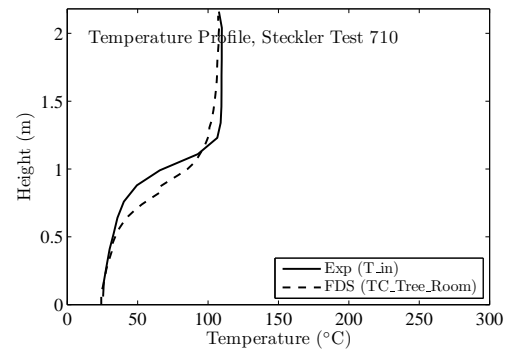
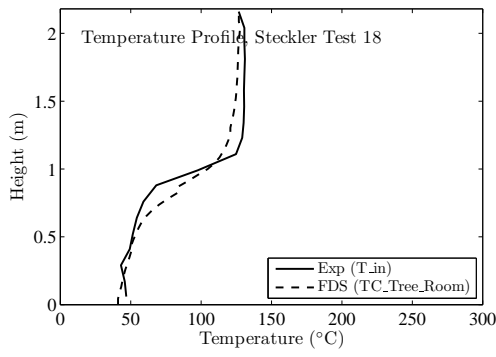
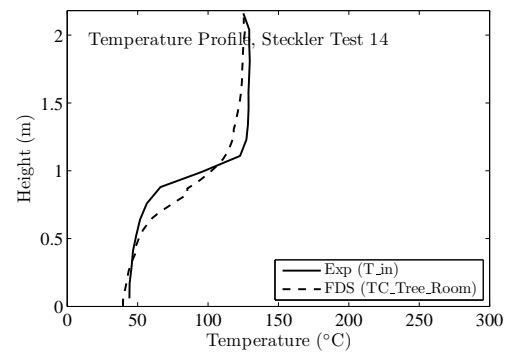
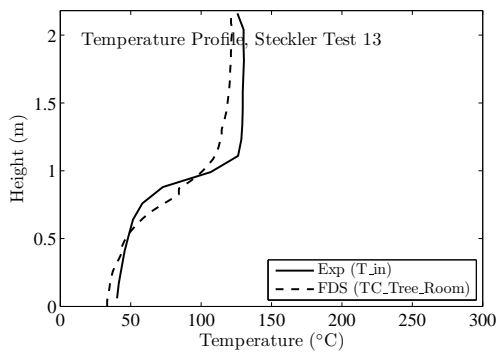
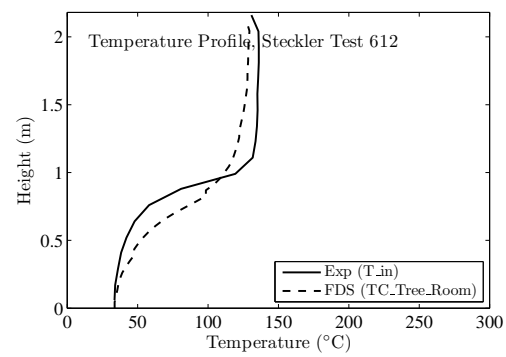
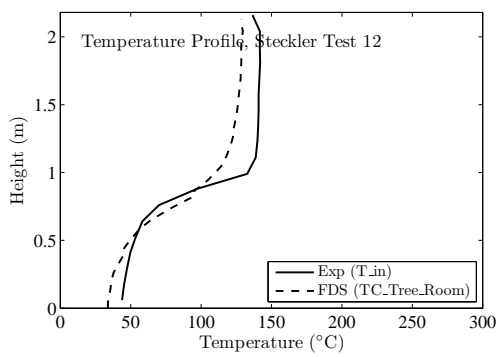
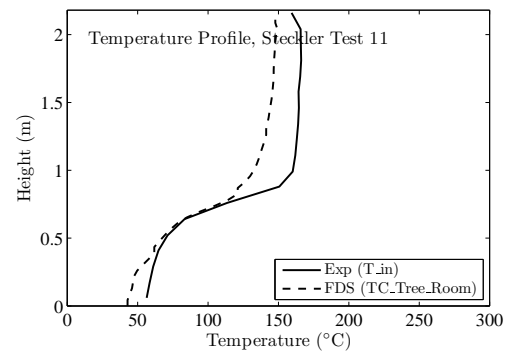
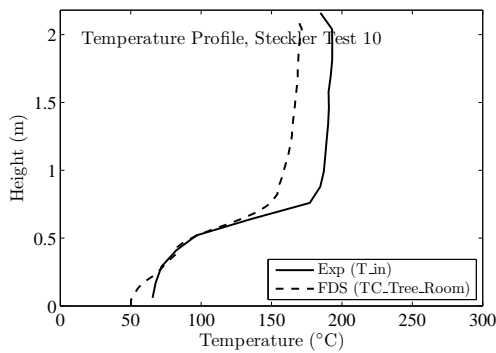
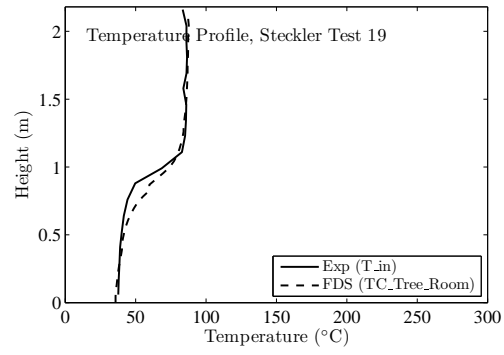
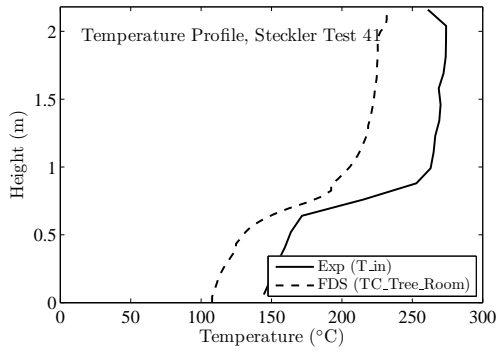
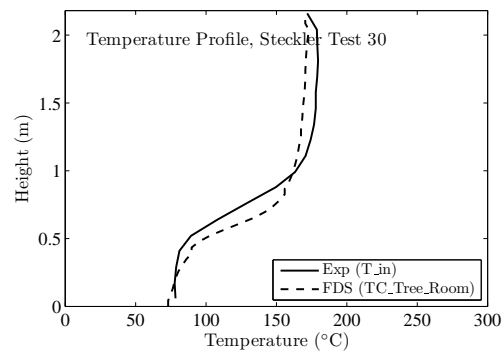
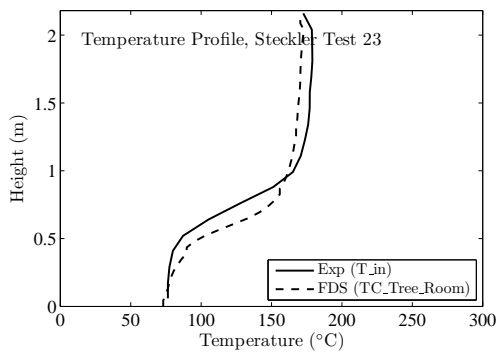
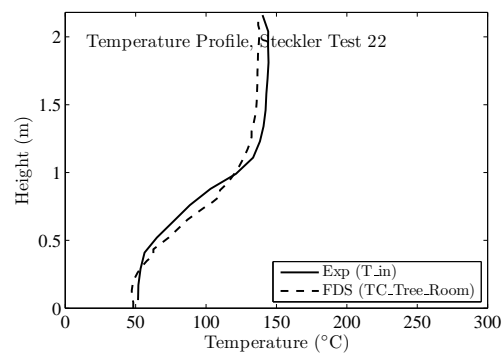
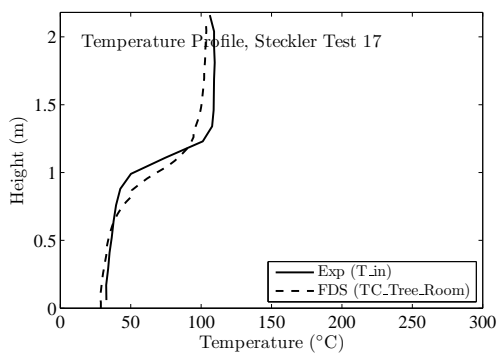
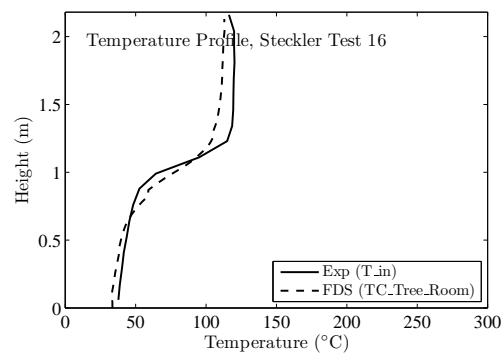
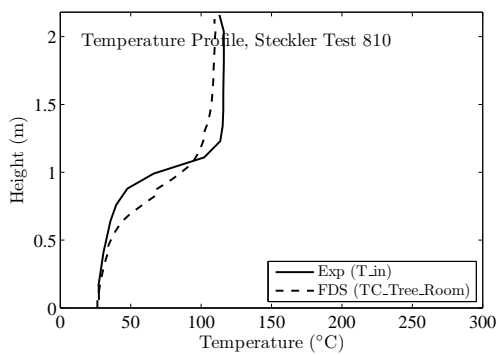


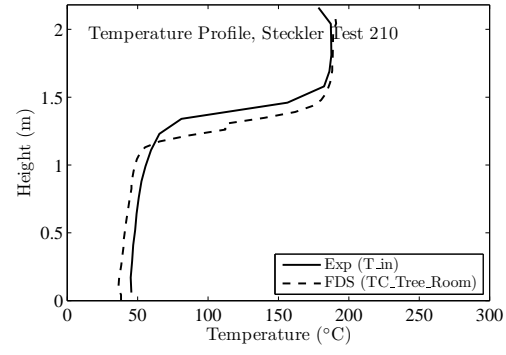
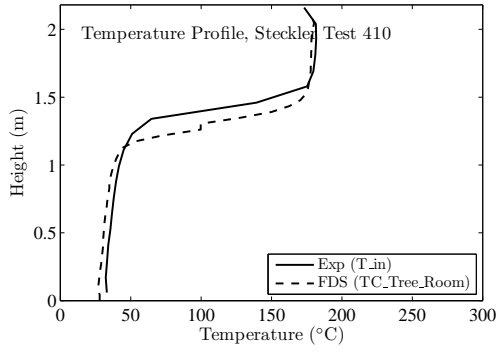
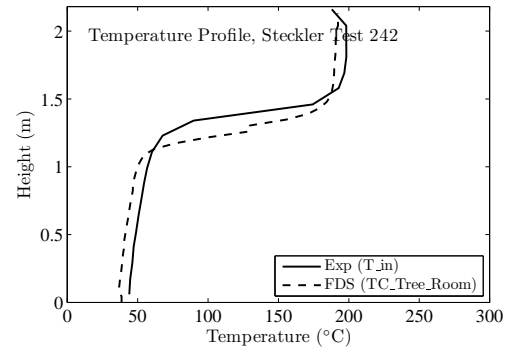
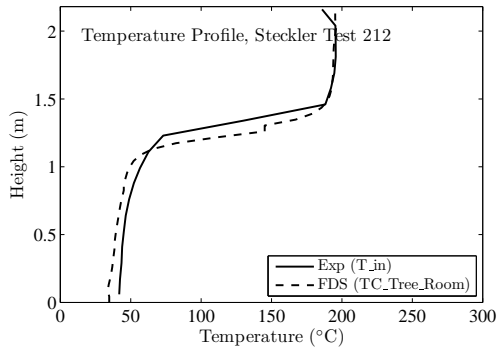
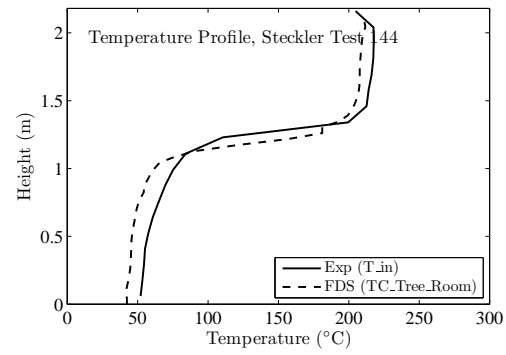
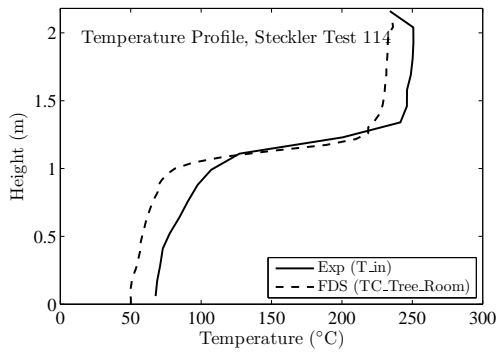
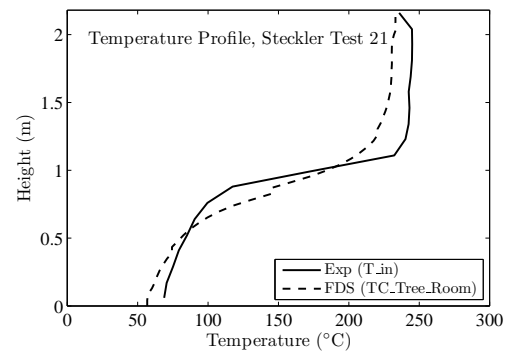
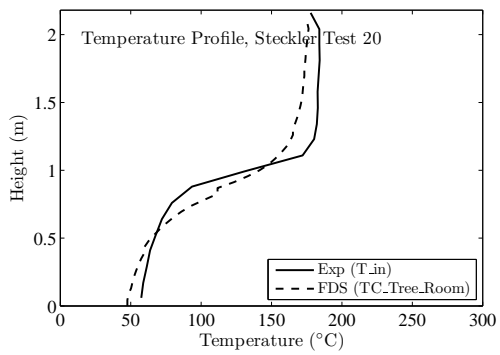
Figure 5.1: Summary of the HGL temperature and height predictions for the VTT, NIST/NRC, WTC, NBS and FM/SNL series.

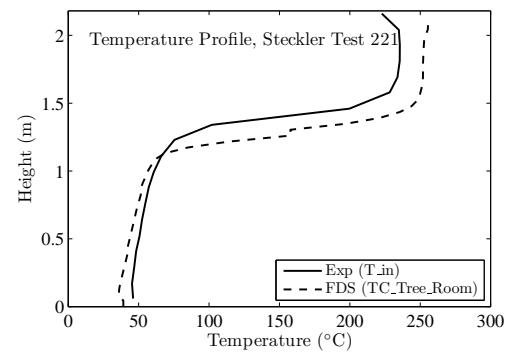
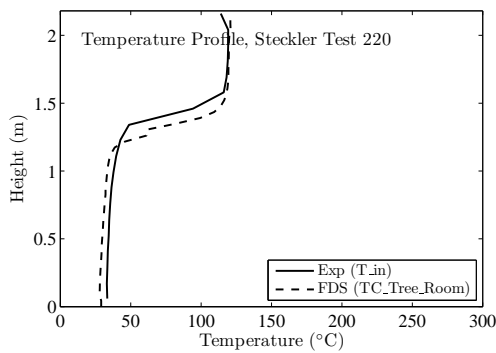
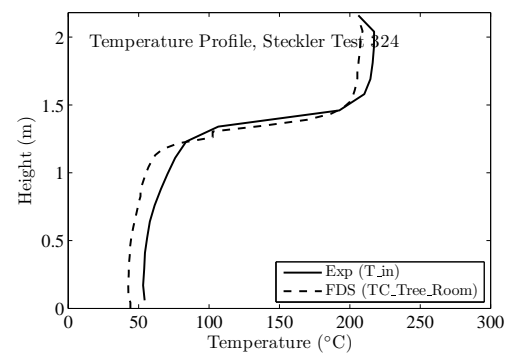
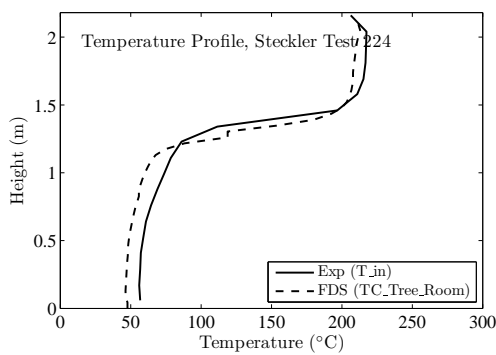
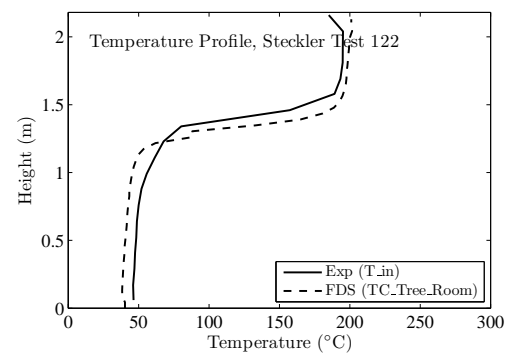
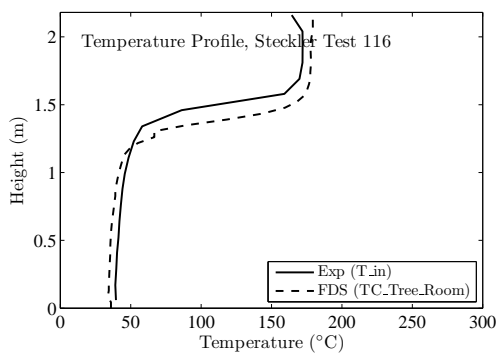
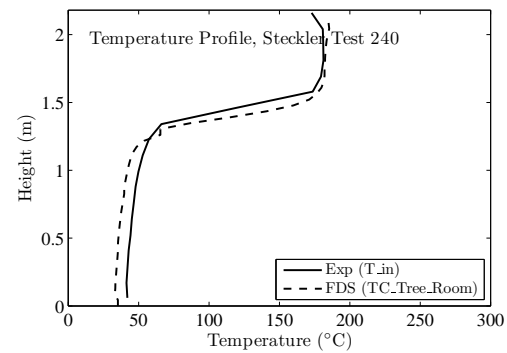
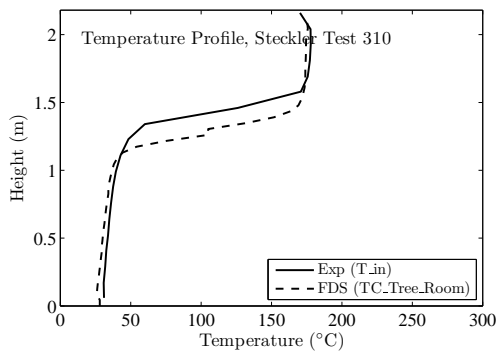
5.8 Steckler Compartment Experiments

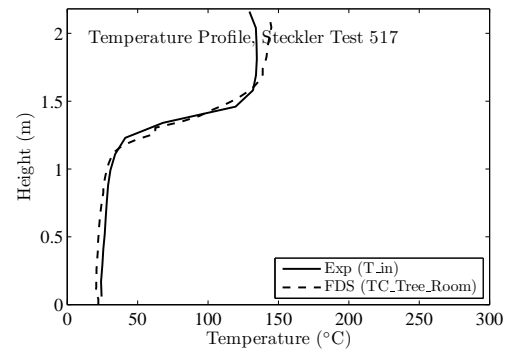
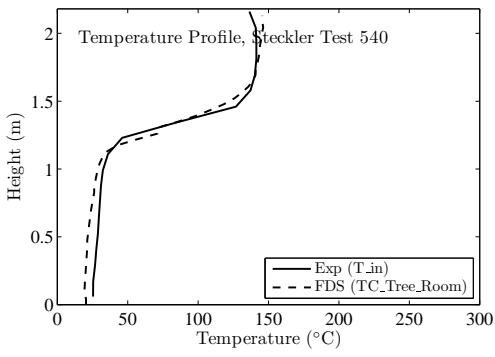
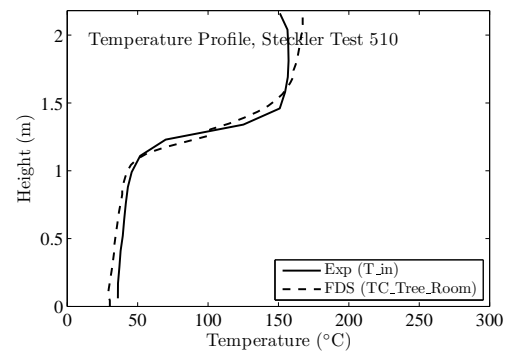
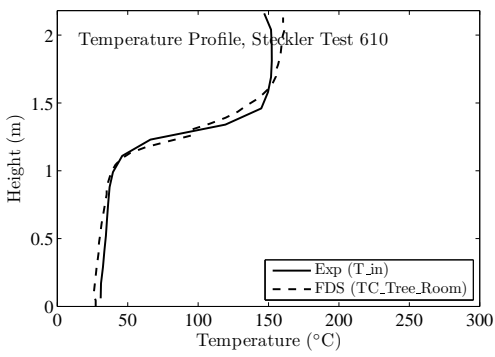
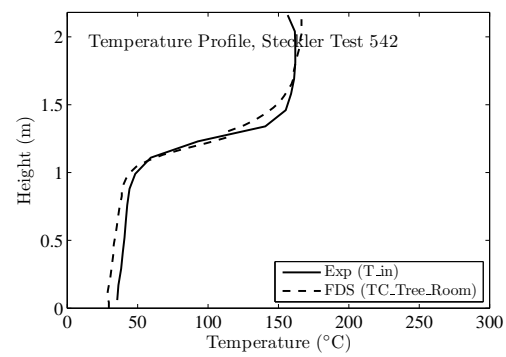
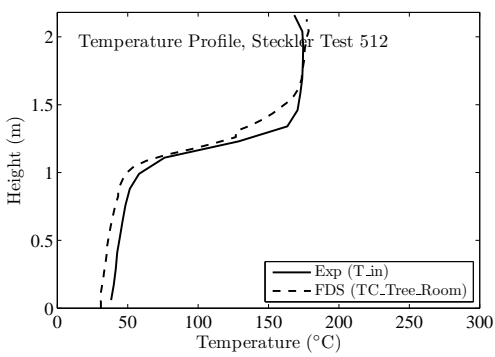
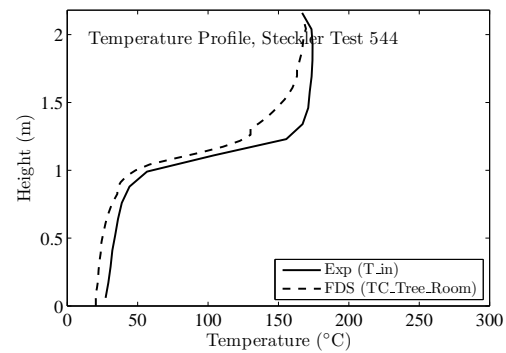
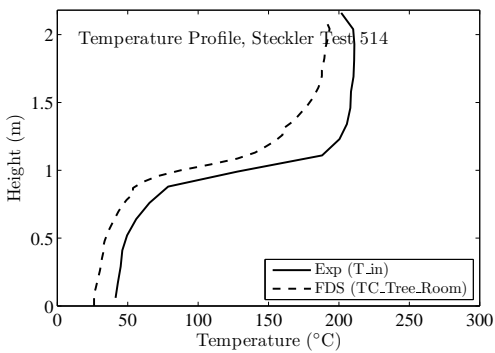
Steckler *et al.* [120] mapped the doorway/window flows in 55 compartment fire experiments. The test matrix is presented in Table 3.2. Shown on the following pages are the temperature profiles inside the compartment compared with model predictions. The FDS simulations were uniformly gridded with cells of 5 cm on each side. To quantify the difference between prediction and measurement, the maximum temperatures were compared.

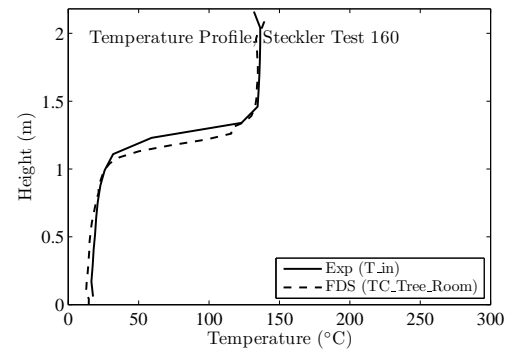
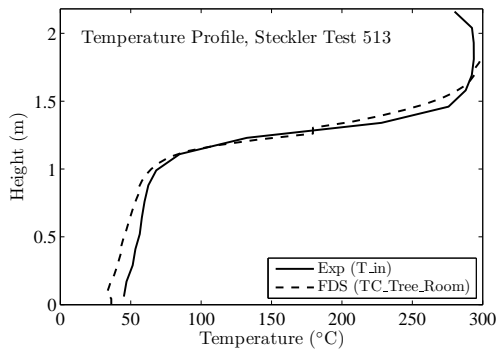
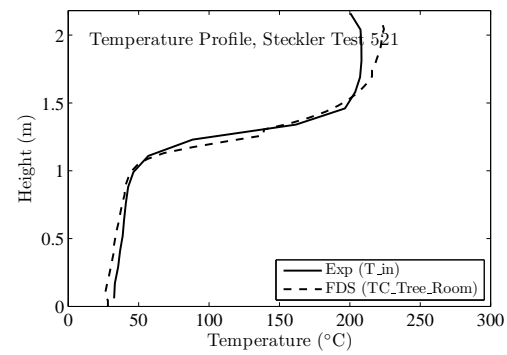
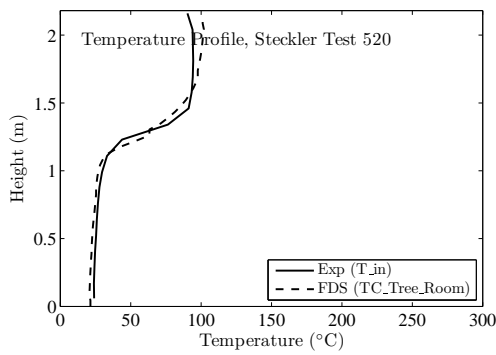
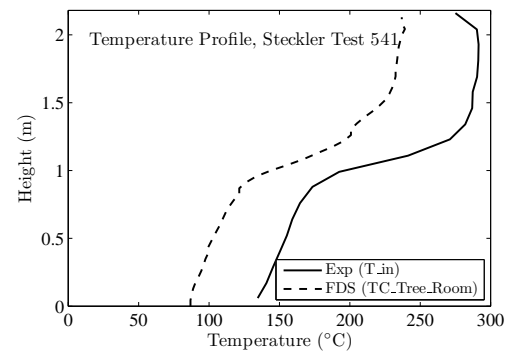
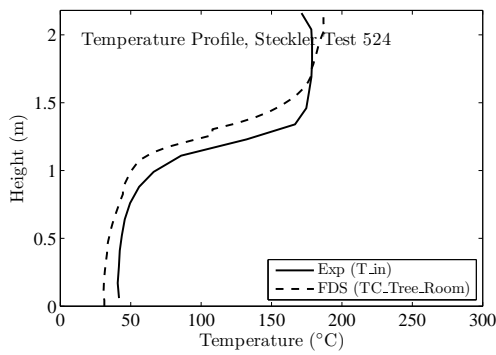
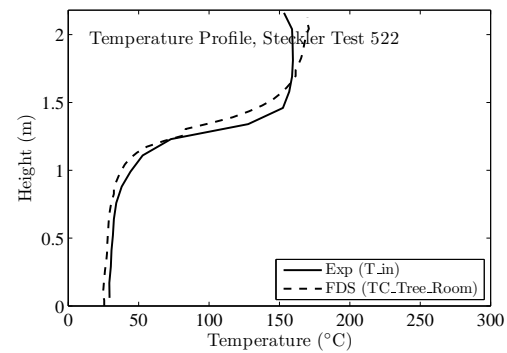
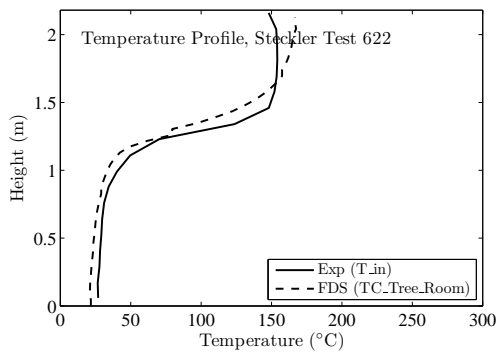


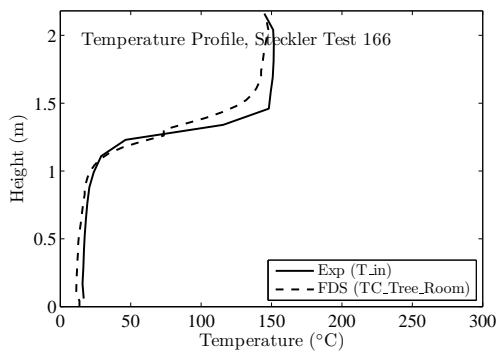
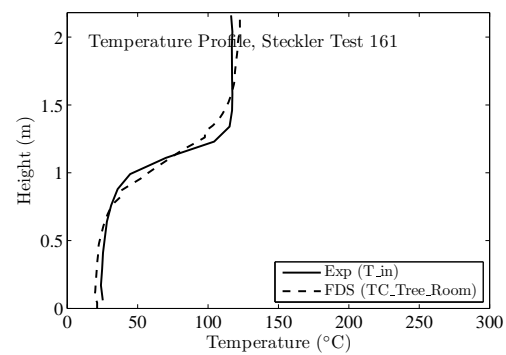
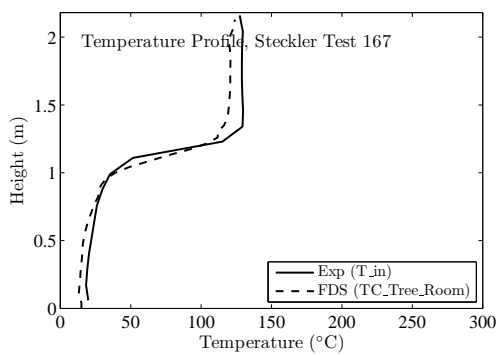
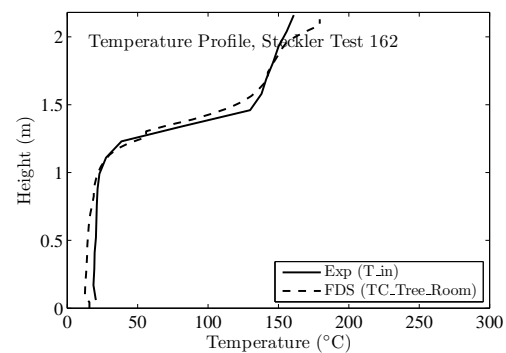
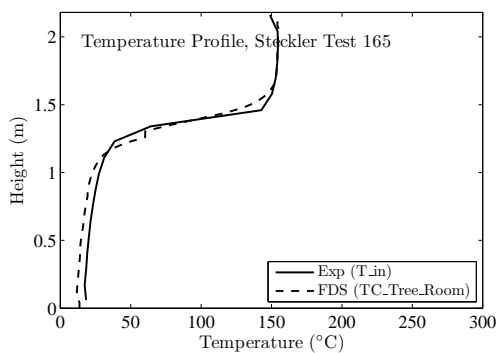
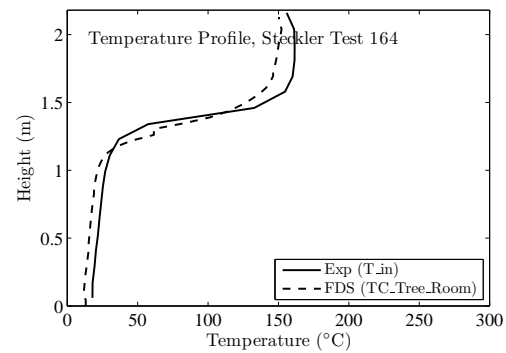
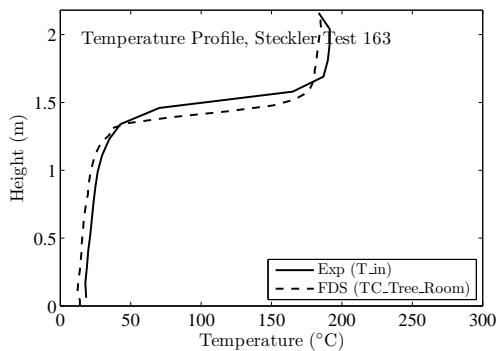












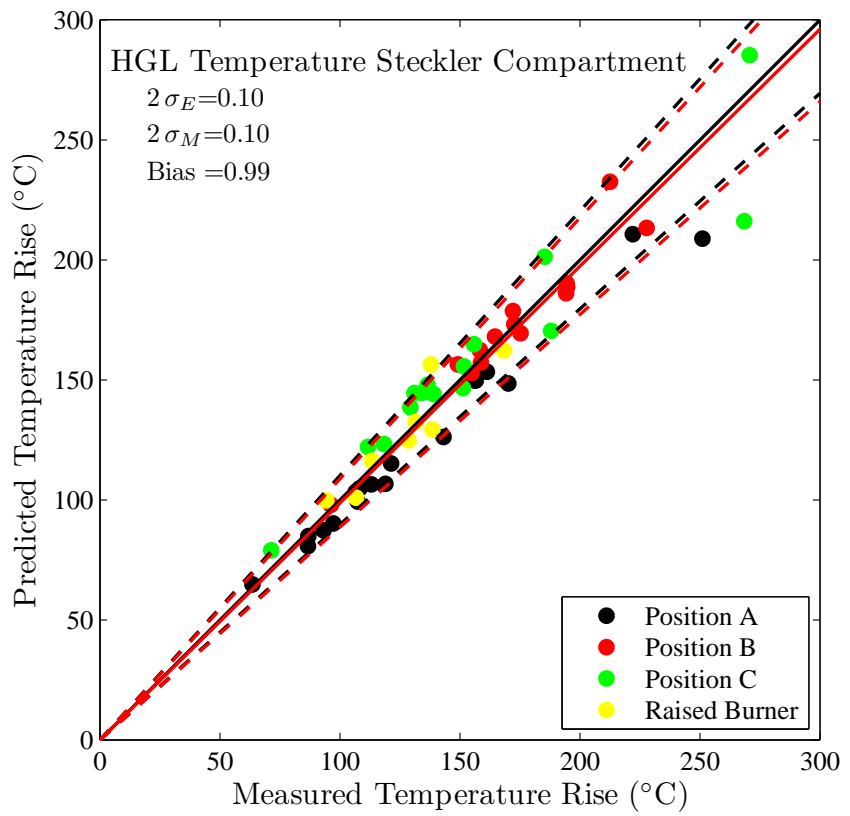


Figure 5.2: Summary of peak temperature predictions for the Steckler Compartment Experiments.

Chapter 6

Fire Plumes

For FDS simulations involving buoyant plumes, a measure of how well the flow field is resolved is given by the non-dimensional expression $D^*/\delta x$, where D^* is a characteristic fire diameter

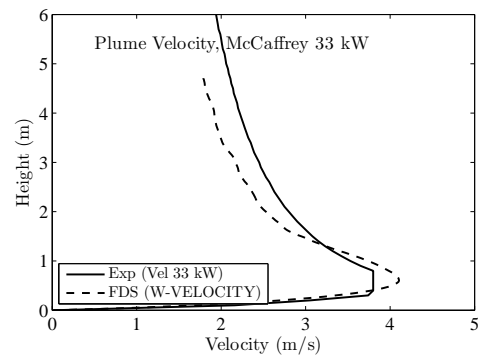
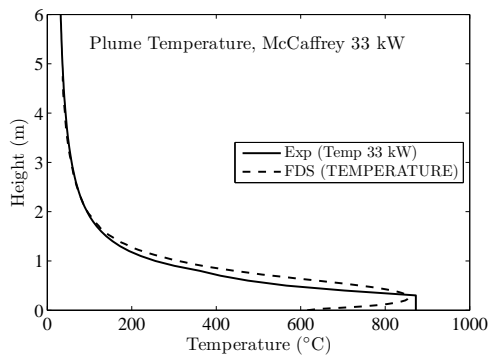
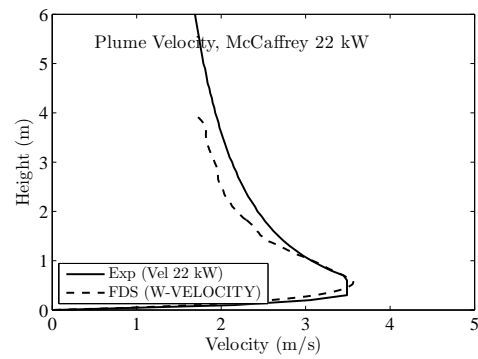
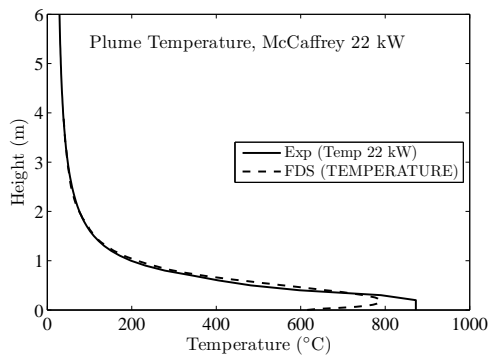
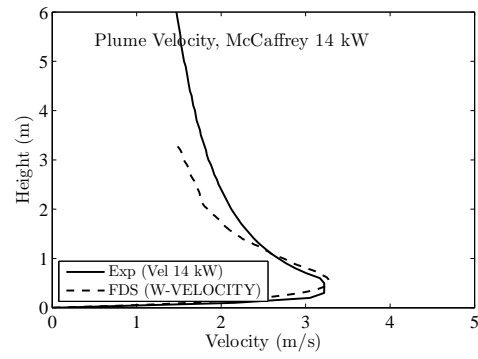
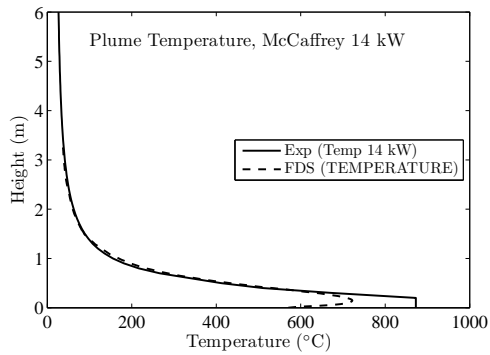
$$D^* = \left(\frac{\dot{Q}}{\rho_\infty c_p T_\infty \sqrt{g}} \right)^{\frac{2}{5}} \quad (6.1)$$

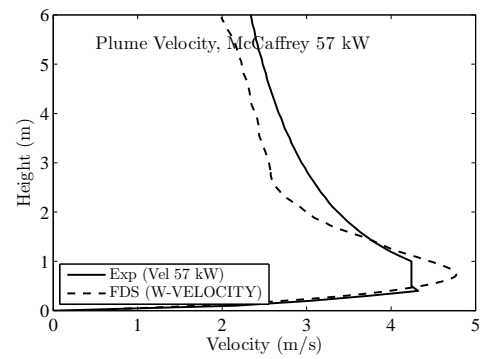
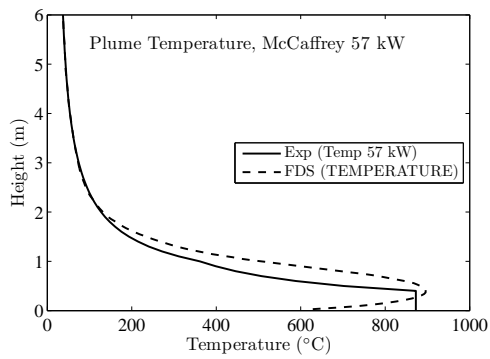
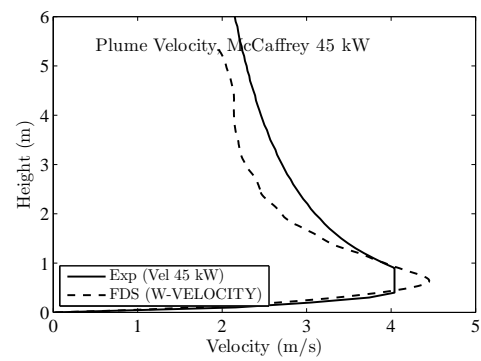
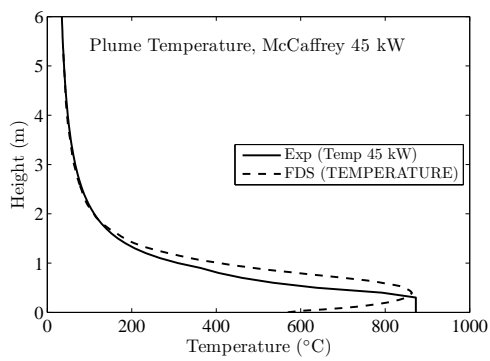
and δx is the nominal size of a mesh cell¹. The quantity $D^*/\delta x$ can be thought of as the number of computational cells spanning the characteristic (not necessarily the physical) diameter of the fire. The more cells spanning the fire, the better the resolution of the calculation. It is better to assess the quality of the mesh in terms of this non-dimensional parameter, rather than an absolute mesh cell size. For example, a cell size of 10 cm may be “adequate,” in some sense, for evaluating the spread of smoke and heat through a building from a sizable fire, but may not be appropriate to study a very small, smoldering source.

6.1 McCaffrey’s Plume Correlation

The following pages show the results of simulations of McCaffrey’s five fires with a grid resolution such that $D^*/\delta x = 10$. The mesh cells were all cubes, and no stretching was used.

¹The characteristic fire diameter is related to the characteristic fire size via the relation $Q^* = (D^*/D)^{5/2}$, where D is the physical diameter of the fire.





6.2 Heskestad's Flame Height Correlation

A widely used experimental correlation for flame height is given by the expression [26]:

$$\frac{L_f}{D} = 3.7 (Q^*)^{2/5} - 1.02 \quad (6.2)$$

where

$$Q^* = \frac{\dot{Q}}{\rho_\infty c_p T_\infty \sqrt{g} D^{5/2}} \quad (6.3)$$

is a non-dimensional quantity that relates the fire's heat release rate, \dot{Q} , with the diameter of its base, D . The greater the value of Q^* , the higher the flame height relative to its base diameter. Table 6.1 lists the parameters for 16 FDS calculations of a fire in a 1 m by 1 m square pan², and Fig. 6.1 compares the FDS predictions with Heskestad's empirical correlation. Note that the flame height for the FDS simulations is defined as the distance above the pan, on average, at which 99 % of the fuel has been consumed. Note also that the simulations were run at three different grid resolutions. A convenient length scale is given by

$$D^* = (Q^*)^{2/5} D \quad (6.4)$$

Given a grid cell size, δx , the three resolutions can be characterized by the non-dimensional quantity, $D^*/\delta x$, whose values in this case are 5, 10 and 20.

Table 6.1: Summary of parameters for the flame height predictions. The grid cell size, δx_{10} , refers to the case where $D^*/\delta x=10$.

Q^*	\dot{Q} (kW)	D^* (m)	δx_{10} (m)
0.1	151	0.45	0.045
0.2	303	0.59	0.059
0.5	756	0.86	0.086
1	1513	1.13	0.113
2	3025	1.49	0.149
5	7564	2.15	0.215
10	15127	2.84	0.284
20	30255	3.75	0.375
50	75636	5.40	0.540
100	151273	7.13	0.713
200	302545	9.41	0.941
500	756363	13.6	1.36
1000	1512725	17.9	1.79
2000	3025450	23.6	2.36
5000	7563625	34.1	3.41
10000	15127250	45.0	4.50

²The effective diameter, D , of a 1 m square pan is 1.13 m, obtained by equating the area of a square and circle.

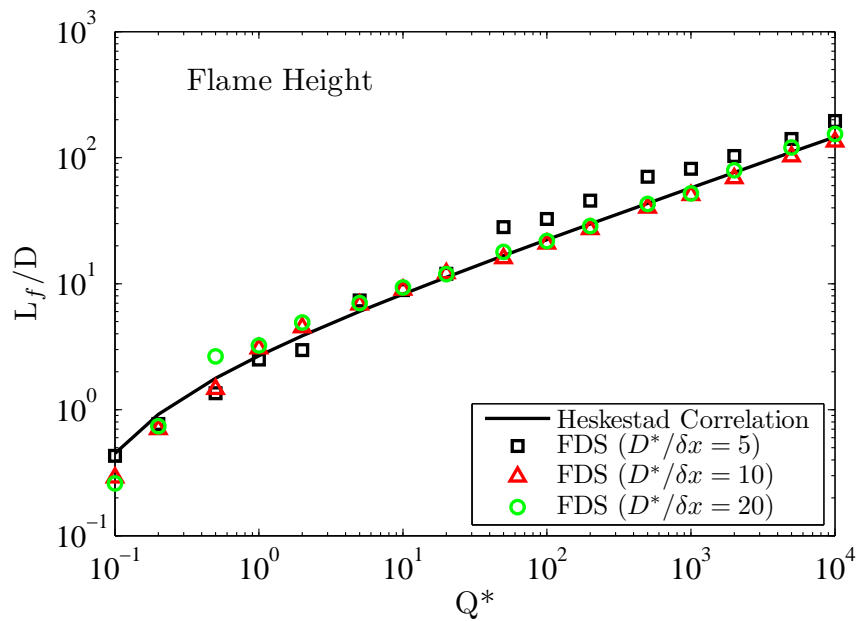


Figure 6.1: Comparison of FDS predictions of flame height from a 1 m square pan fire for Q^* values ranging from 0.1 to 10000.

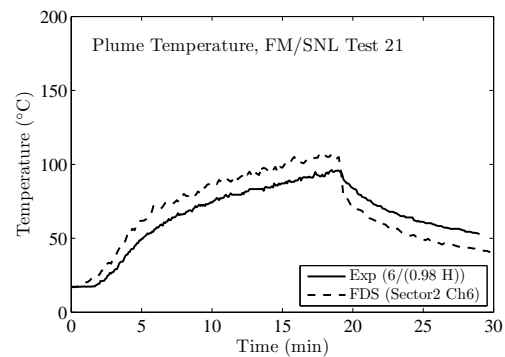
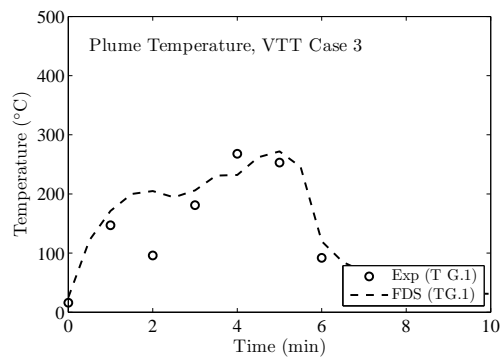
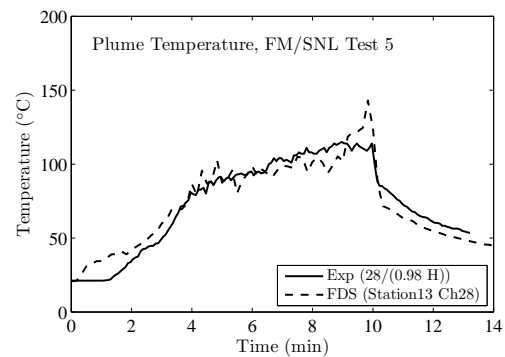
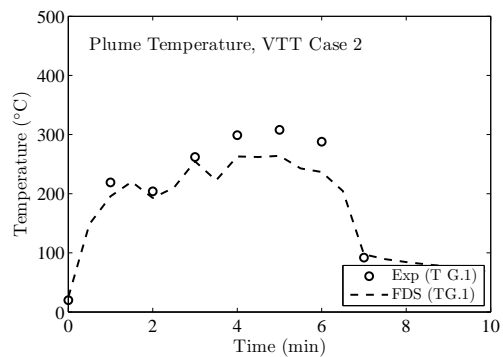
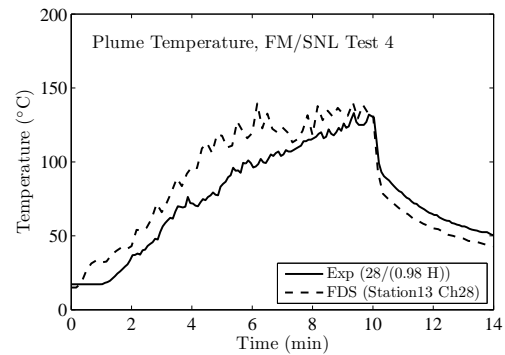
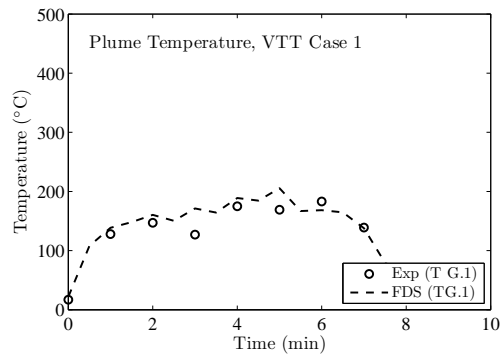
6.3 VTT Large Hall and FM/SNL Test Series

Plume temperature measurements are available from the VTT Large Hall and the FM/SNL series. For all the other full-scale experiments, the temperature above the fire has not been reported, or the fire plume leans because of the flow pattern within the compartment, or the fire is positioned against a wall. Only for the VTT and the FM/SNL series are the plumes relatively free from perturbations.

The VTT experiments consist of liquid fuel pan fires positioned in the middle of a large fire test hall. Plume temperatures are measured at two heights above the fire, 6 m and 12 m. The flames were observed to extend to about 4 m above the fire pan.

In the FM/SNL experiments, in Tests 4 and 5, thermocouples were positioned near the ceiling directly over the fire pan. In Test 21, the fire was positioned within an empty electrical cabinet, and the closest near ceiling thermocouple was used to assess the plume temperature prediction.

Comparisons of the predicted and measured plume temperatures for the VTT and FM/SNL tests are found on the following pages, including a summary plot at the end of the chapter.



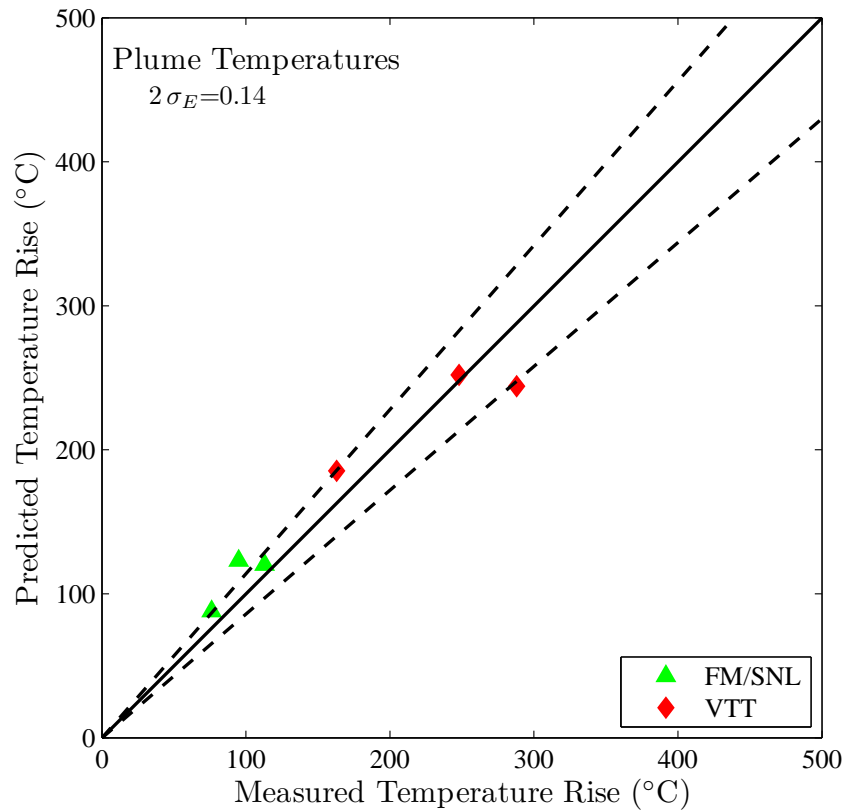


Figure 6.2: Summary of plume temperature predictions, VTT and FM/SNL test series.

6.4 Sandia 1 m Helium Plume

Calculations of the Sandia 1 m helium plume are run at three grid resolutions: 6 cm, 3 cm, and 1.5 cm. To give the reader with a qualitative feel for the results, Fig. 6.3 provides a snapshot of density contours from the simulation. The calculations are run in parallel on 16 processors; the outlined blocks indicate the domain decomposition. Data for vertical velocity, radial velocity, and helium mass fraction are recorded at three levels downstream from the base of the plume, $z = [0.2, 0.4, 0.6]$ m, corresponding to the experimental measurements of O’Hern et al. [125]. Results for the mean profiles are given in Figs. 6.4 and 6.5. The means are taken between $t = 10$ and $t = 20$ seconds in the simulation.

The domain is $3 \text{ m} \times 3 \text{ m} \times 4 \text{ m}$. The boundary conditions are open on all sides with a smooth solid surface surrounding the 1 m diameter helium pool. The ambient and helium mixture temperature is set to 12°C and the background pressure is set to 80900 Pa to correspond to the experimental conditions. The helium/acetone/oxygen mixture molecular weight is set to 5.45 kg/kmol. The turbulent Schmidt and Prandtl numbers are left at the FDS default value of 0.5. The helium mixture mass flux is specified as 0.0605 kg/s/m^2 . One noteworthy difference between this calculation and previous work modeling the Sandia helium plume [127] is that here the pool is depressed by 6 cm (one cell thickness for the coarsest case) which allows for variation in the inlet velocity profile at the $z = 0$ m plane, the plume baseline. This modification is justified based on the $\pm 6\%$ flow variation reported in [126] and is significant to the results. Further, the variation reported in [126] was based on hot wire probe measurements with air flowing through the honeycomb flow straighteners at the plume source. The variation might be greater for helium flows due to the buoyant accelerations which were not present in the air/air test case (S. Tieszen, personal communication).

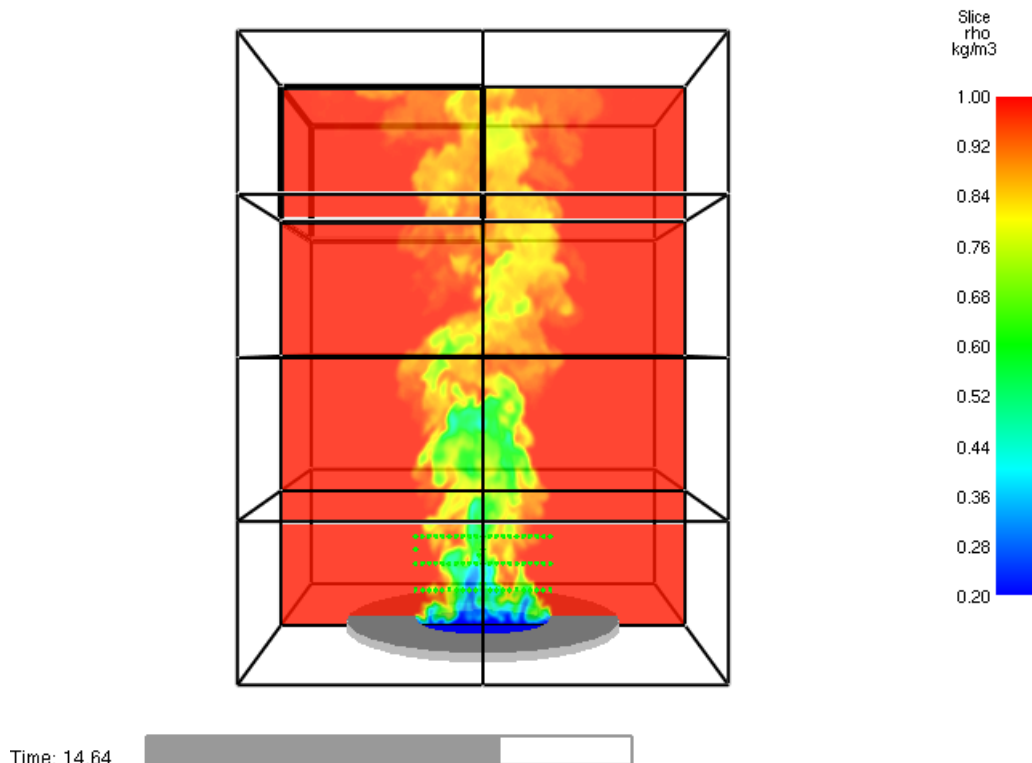


Figure 6.3: A snapshot of FDS 6 results at 1.5 cm resolution for the Sandia 1 m helium plume showing density contours. The rows of measurement devices are visible near the base.

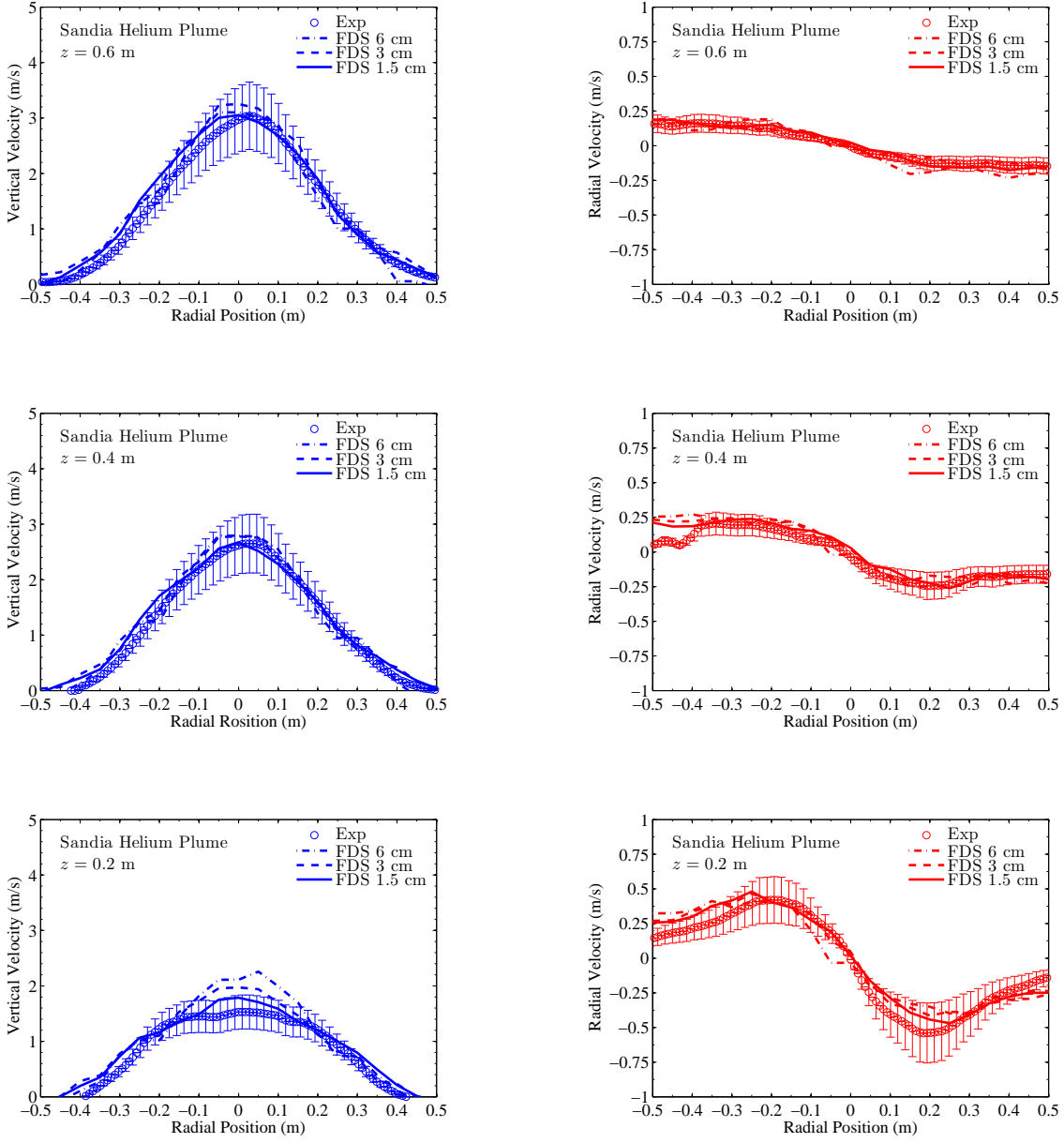


Figure 6.4: FDS 6 predictions of mean velocity profiles for the Sandia 1 m helium plume experiment. Results are shown for 6 cm, 3 cm, and 1.5 cm grid resolutions. With z being the streamwise coordinate, the bottom row is at $z = 0.2$ m, the middle row is at $z = 0.4$ m, and the top row is at $z = 0.6$ m.

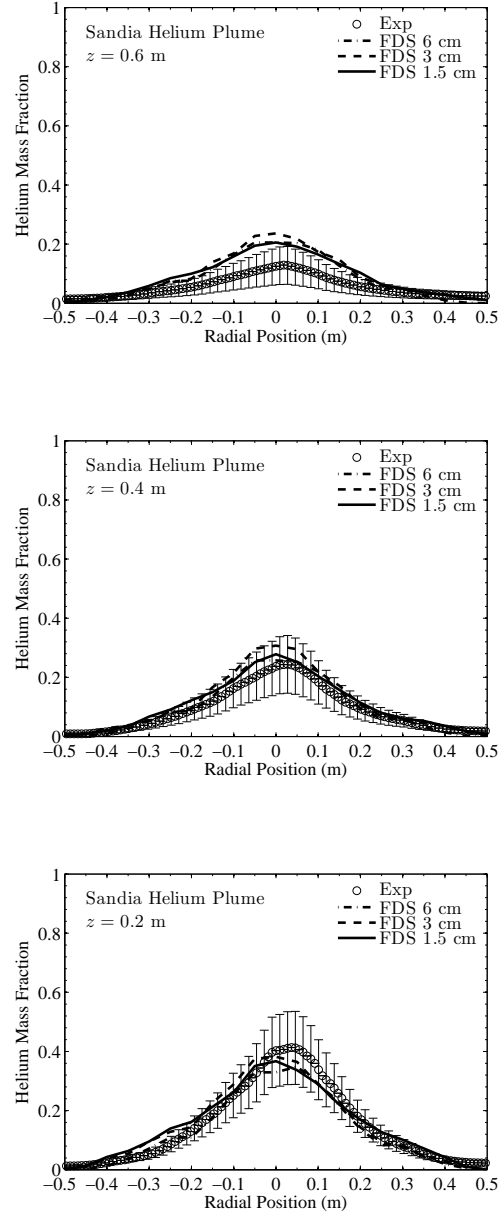


Figure 6.5: FDS 6 predictions of mean helium mass fraction profiles for the Sandia 1 m helium plume experiment. Results are shown for 6 cm, 3 cm, and 1.5 cm grid resolutions. With z being the streamwise coordinate, the bottom row shows data at $z = 0.2 \text{ m}$, the middle row shows data at $z = 0.4 \text{ m}$, and the top row shows data at $z = 0.6 \text{ m}$.

6.5 Sandia 1 m Methane Pool Fire

The Sandia 1 m methane pool fire series provides data for three methane flow rates: Test 14 (low flow rate), Test 24 (medium flow rate), and Test 17 (high flow rate) [128]. The experiments are simulated using three grid resolutions: 6 cm, 3 cm, and 1.5 cm. Fig. 6.6 provides a snapshot of temperature contours from the 1.5 cm Test 17 simulation. The calculations are run in parallel on 16 processors: a similar computational set up as the helium case (the experiments were run in the same facility at Sandia). Data for vertical velocity and radial velocity are recorded at three levels downstream from the base of the plume, $z = [0.3, 0.5, 0.9]$ m. Results for the mean profiles are given in Figs. 6.7 - 6.9. The means are taken between $t = 10$ and $t = 20$ seconds in the simulation.

For Test 17, we recorded the vertical velocity as a time series in four locations in the plume, at two positions along the centerline and at two positions on the edge. The time series from our 1.5 cm simulation at $x = 0$ m and $z = 0.5$ m, corresponding to Fig. 6 in [129], is shown in Fig. 6.10 along with the power spectrum from the average of the four time series locations. The eddy dissipation constant in the turbulent combustion model is tuned to a value of $C = 0.1$ based on comparison of the simulated large scale puffing mode with the experimentally obtained value of 1.65 Hz [129].

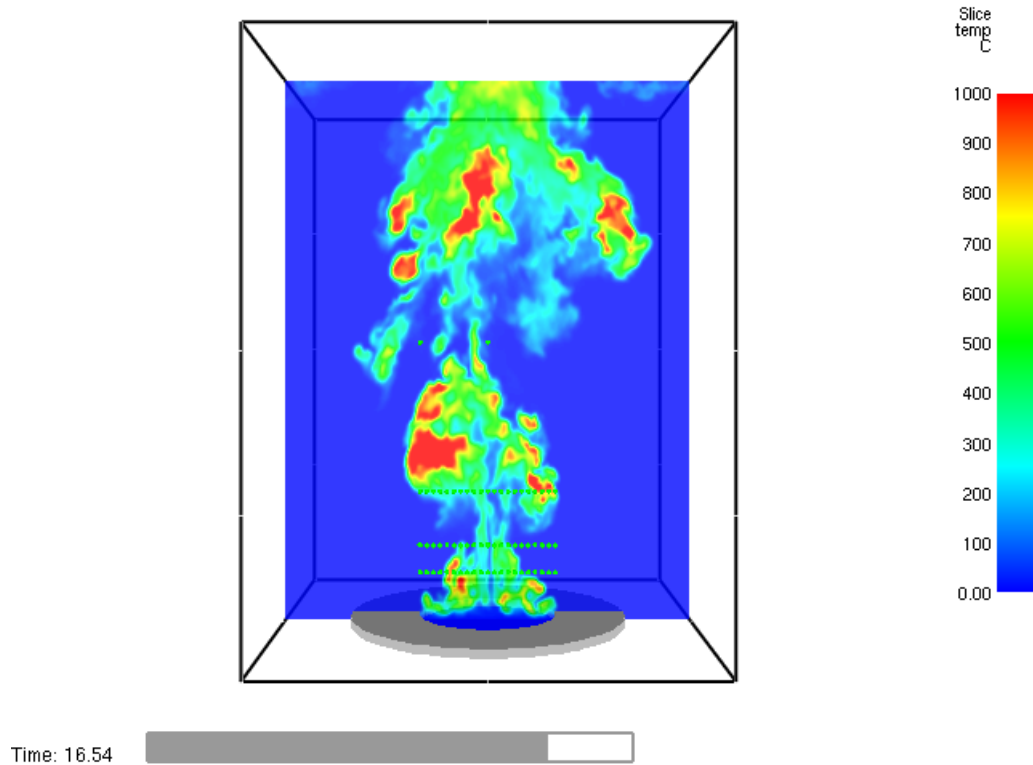


Figure 6.6: A snapshot of FDS 6 results at 1.5 cm resolution for the Sandia 1 m methane pool fire (Test 17 – high flow rate) showing instantaneous contours of temperature. The rows of measurement devices (green) are visible near the base.

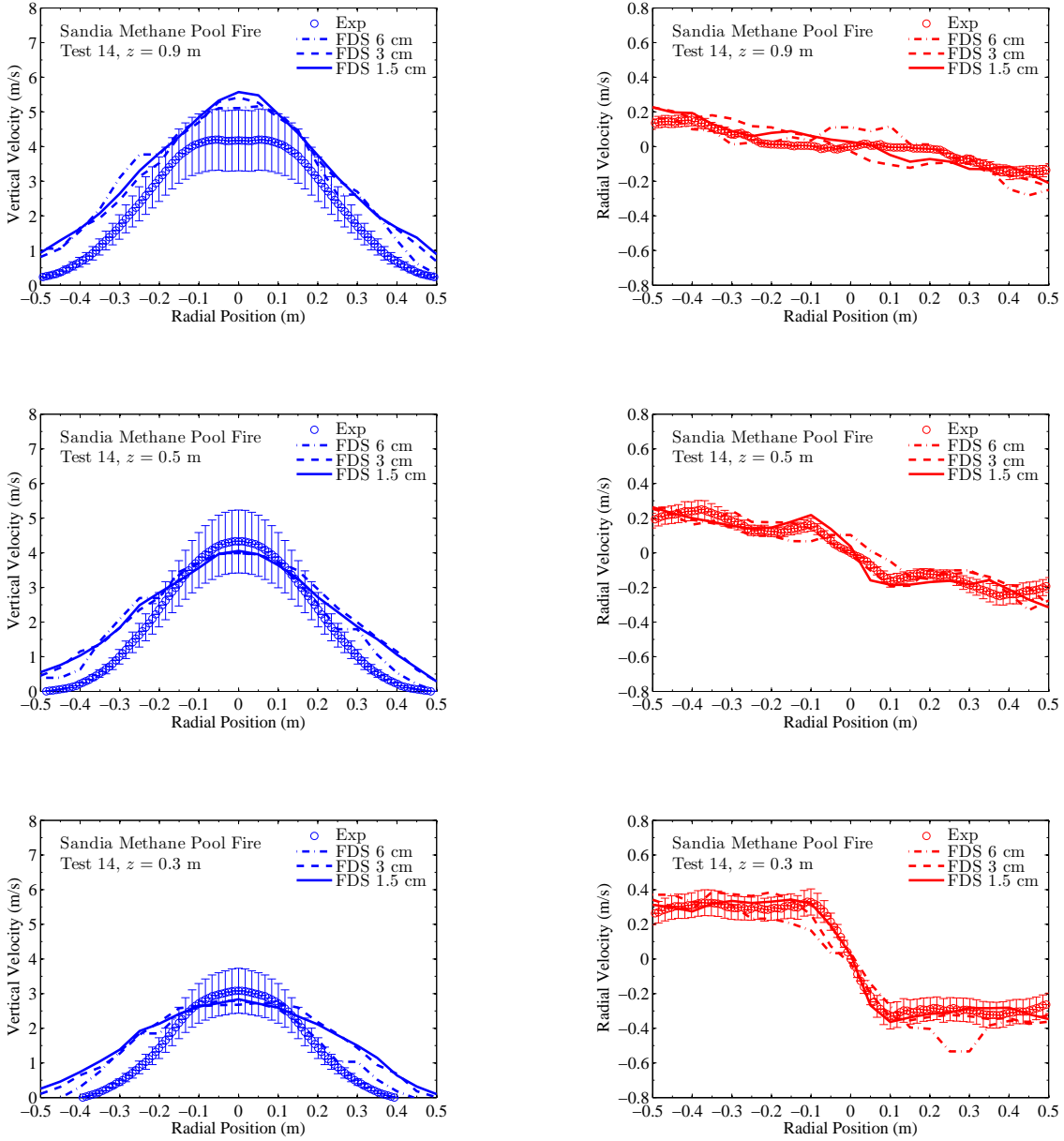


Figure 6.7: FDS 6 predictions of mean velocity profiles for the Sandia 1 m methane pool fire experiment (Test 14 – low flow rate). Results are shown for 6 cm, 3 cm, and 1.5 cm grid resolutions. The z coordinate represents height above the methane pool; bottom row: $z = 0.3\text{ m}$, middle row: $z = 0.5\text{ m}$, and top row: $z = 0.9\text{ m}$.

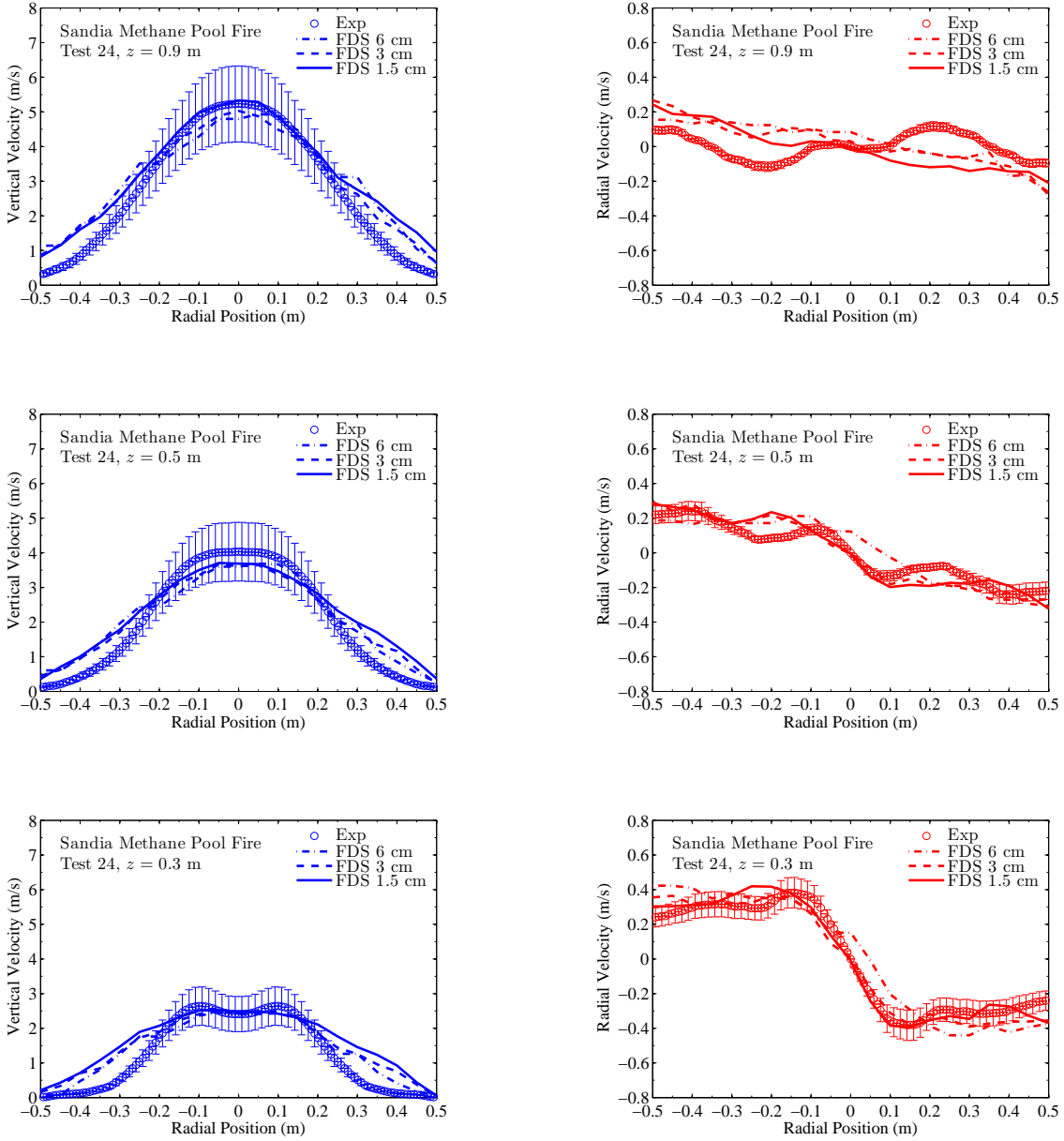


Figure 6.8: FDS 6 predictions of mean velocity profiles for the Sandia 1 m methane pool fire experiment (Test 24 – medium flow rate). Results are shown for 6 cm, 3 cm, and 1.5 cm grid resolutions. The z coordinate represents height above the methane pool; bottom row: $z = 0.3 \text{ m}$, middle row: $z = 0.5 \text{ m}$, and top row: $z = 0.9 \text{ m}$.

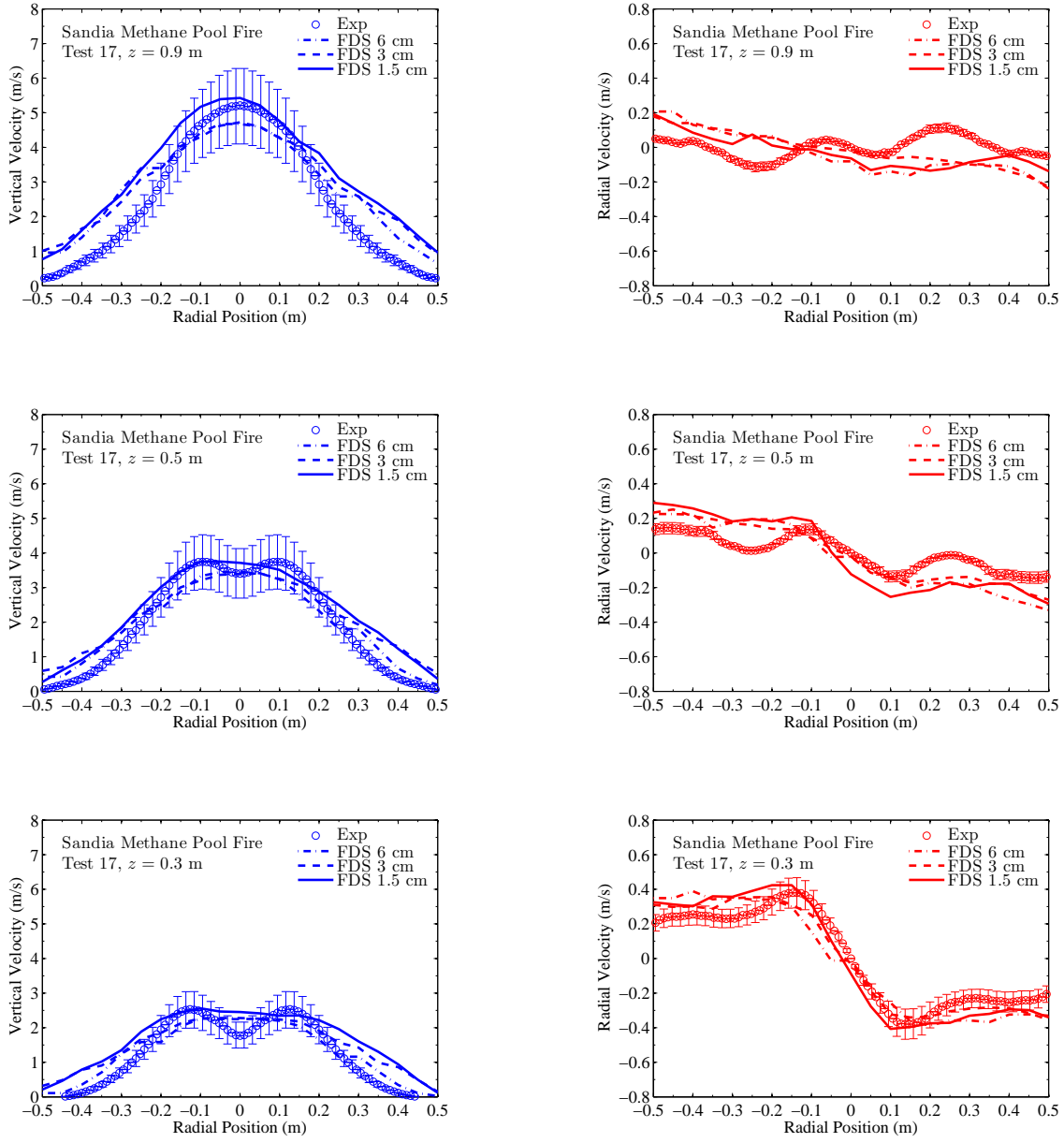


Figure 6.9: FDS 6 predictions of mean velocity profiles for the Sandia 1 m methane pool fire experiment (Test 17). Results are shown for 3 cm and 1.5 cm grid resolutions. The z coordinate represents height above the methane pool; bottom row: $z = 0.3$ m, middle row: $z = 0.5$ m, and top row: $z = 0.9$ m.

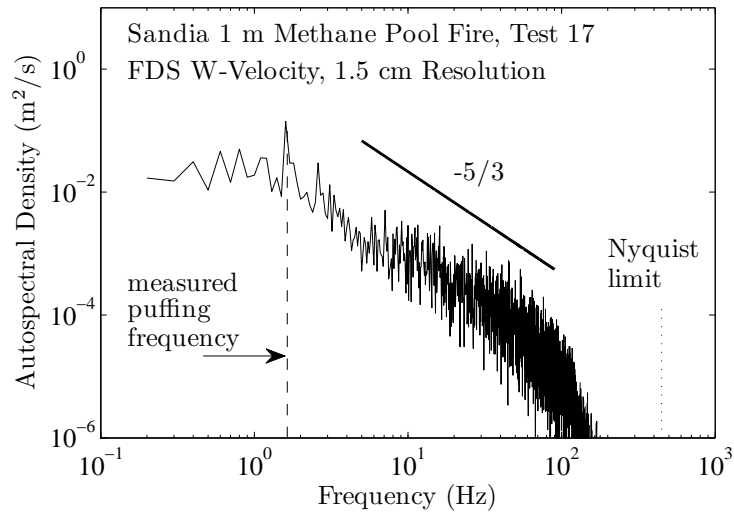
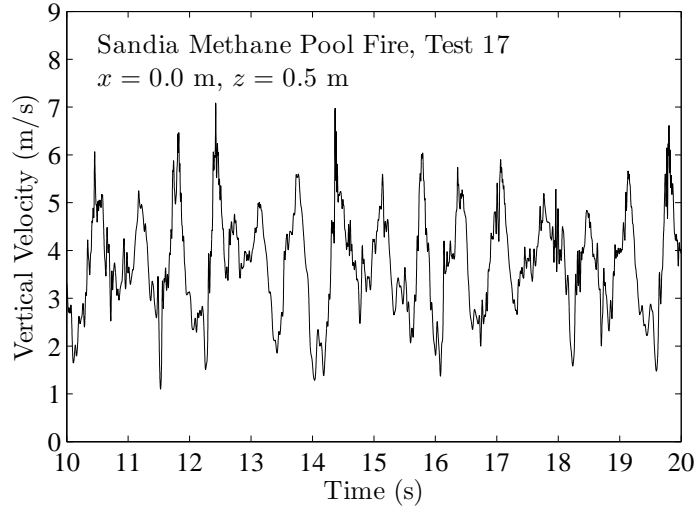


Figure 6.10: FDS 6 velocity signal and power spectrum for the Sandia 1 m methane pool fire experiment (Test 17). The vertical velocity signal (top plot) is output from FDS on the centerline at $z = 0.5 \text{ m}$ downstream of the fuel source. The power spectrum of vertical velocity is measured at four locations and averaged. Two of the measurement locations are along the centerline, at $z = [0.5, 2.0] \text{ m}$, and two are along the edge of the plume, $x = 0.5 \text{ m}$ and $z = [0.5, 2.0] \text{ m}$. The measured puffing frequency of the plume is 0.61 Hz [129]. The temporal Nyquist limit is $1/(2\delta t)$ where roughly $\delta t = \delta x / \max(W) = 0.015/7.0 = 0.002 \text{ s}$ (500 Hz).

6.6 Sandia 1 m Hydrogen Pool Fire

Sandia Test 35 [128] is simulated at three grid resolutions: 6 cm, 3 cm, and 1.5 cm. The computational set up is nearly identical to the methane cases. Results for mean vertical and radial velocity are given in Figs. 6.12. Means are taken from a time average between $t = 10$ and $t = 20$ seconds in the simulation.

By examining movies of the simulation results we can see a qualitative difference between the methane and hydrogen cases. The dynamics of the hydrogen case tend to dominated by near total consumption events which create blowback on the pool followed by streaks of accelerating buoyant flow which increase the mean vertical velocity. An example of the consumption event is seen near the end of the case shown in Fig. 6.11. It is possible that we have not run the simulation long enough for accurate statistics and that streaking events early in the time window (between 10-20 seconds) are biasing the mean vertical velocity to be too high, as is clear from the top-left plot in Fig. 6.12.

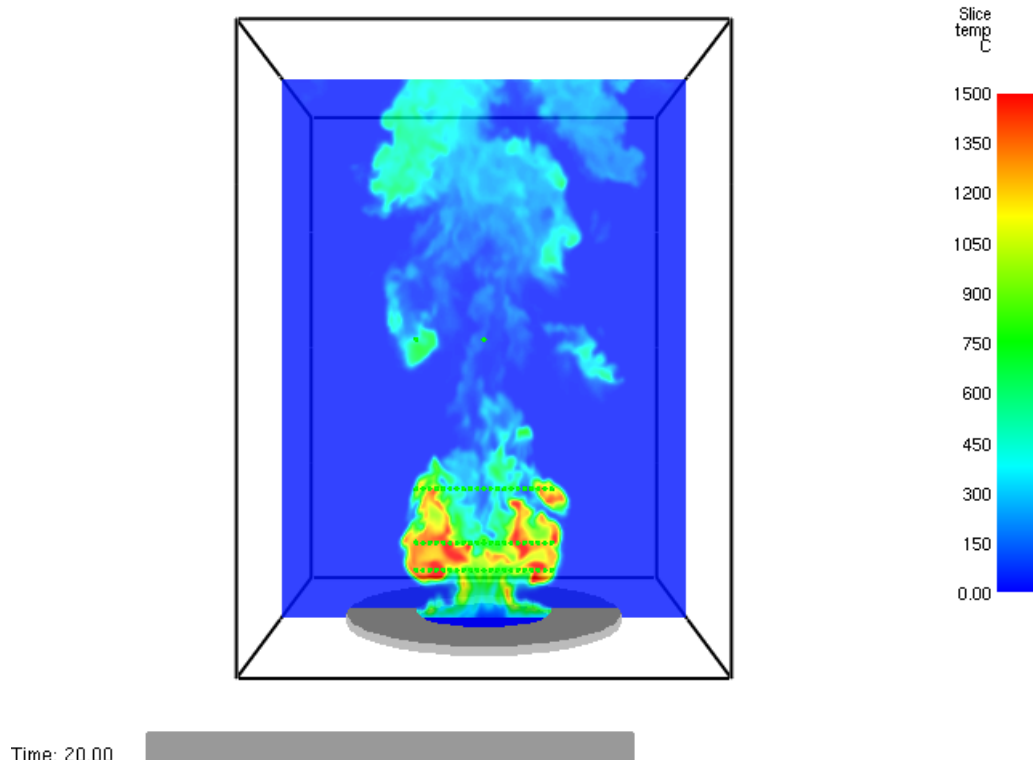


Figure 6.11: A snapshot of FDS 6 results at 1.5 cm resolution for the Sandia 1 m hydrogen pool fire (Test 35) showing instantaneous contours of temperature. The rows of measurement devices (green) are visible near the base.

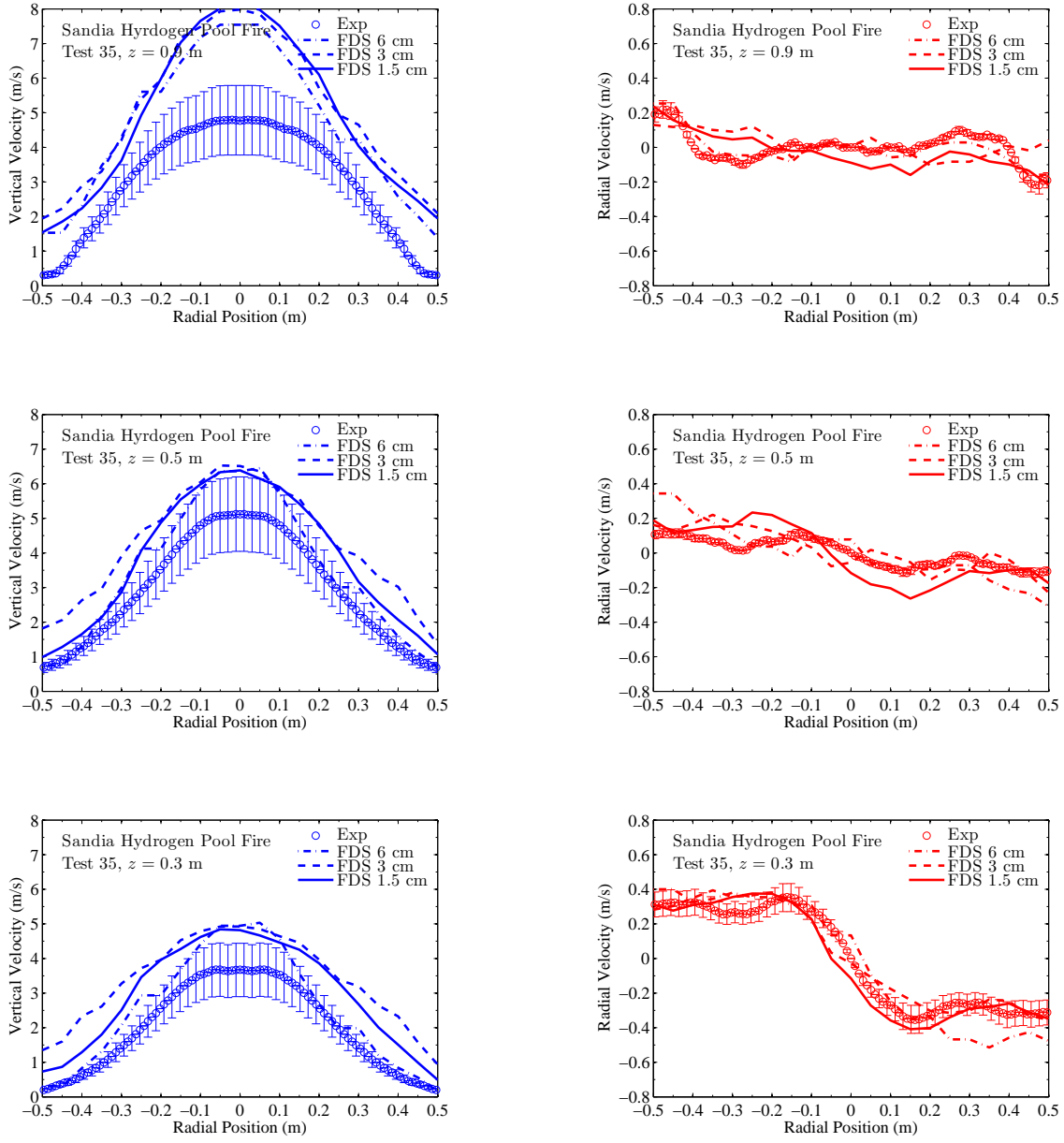


Figure 6.12: FDS 6 predictions of mean velocity profiles for the Sandia 1 m hydrogen pool fire experiment (Test 35). Results are shown for 6 cm, 3 cm, and 1.5 cm grid resolutions. The z coordinate represents height above the pool; bottom row: $z = 0.3 \text{ m}$, middle row: $z = 0.5 \text{ m}$, and top row: $z = 0.9 \text{ m}$.

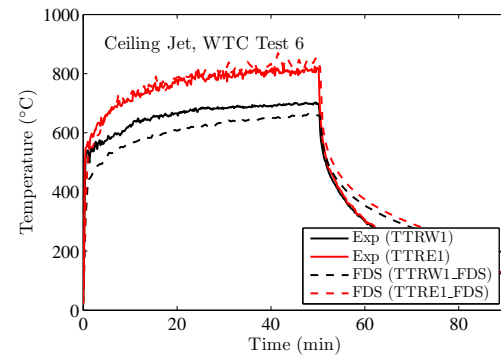
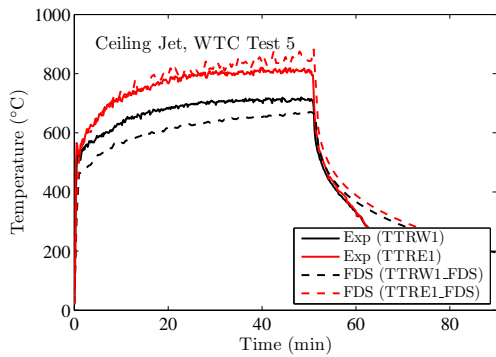
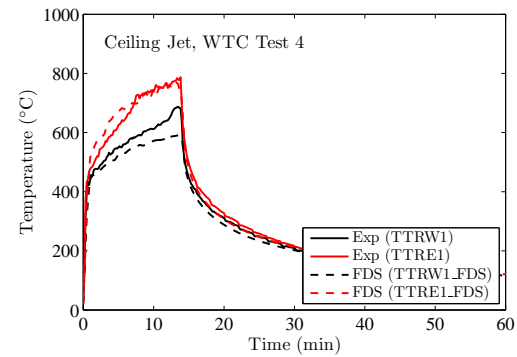
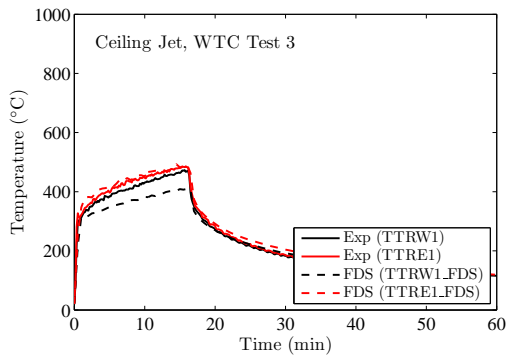
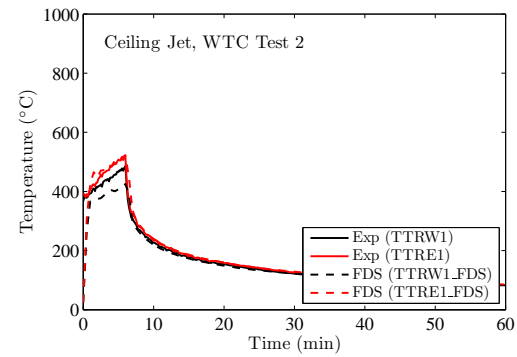
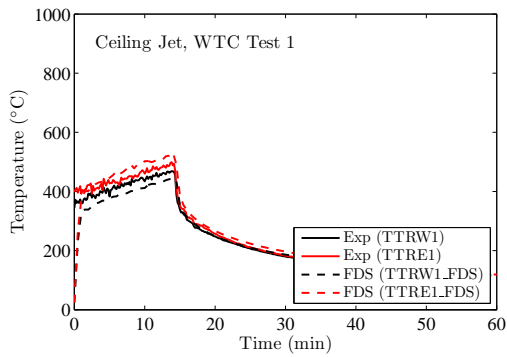
Chapter 7

Ceiling Jets and Device Activation

FDS is a computational fluid dynamics (CFD) model and has no explicit ceiling jet model. Rather, temperatures throughout the fire compartment are computed directly from the governing conservation equations. Nevertheless, temperature measurements near the ceiling can be used to evaluate the model's ability to predict the flow of hot gases across a relatively flat ceiling. Measurements for this category are available from the NIST/NRC and the FM/SNL series.

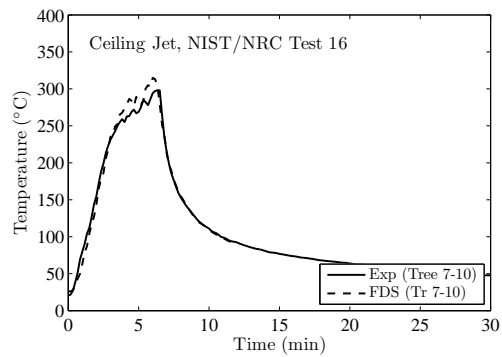
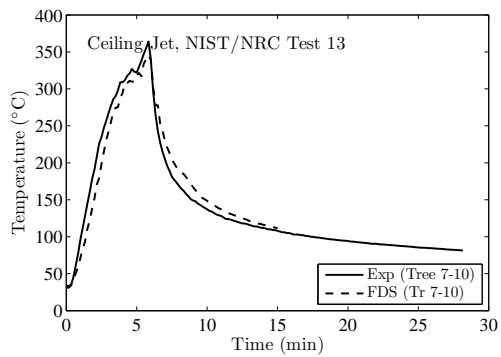
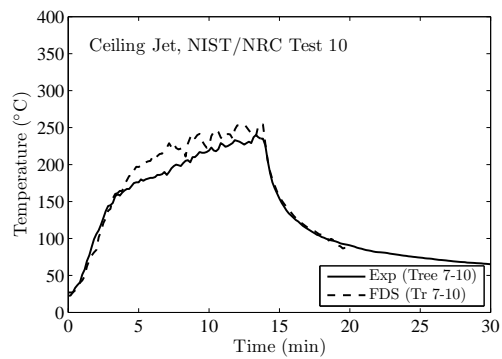
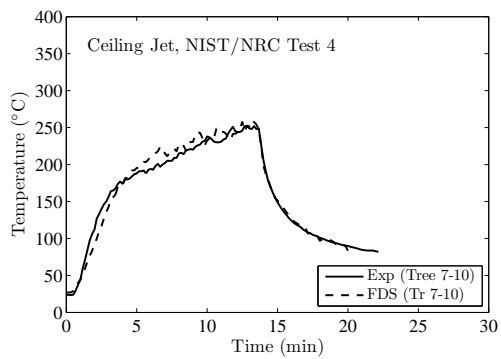
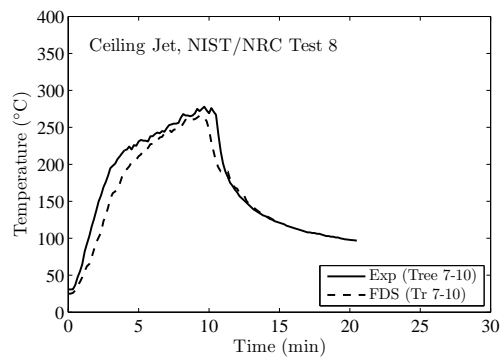
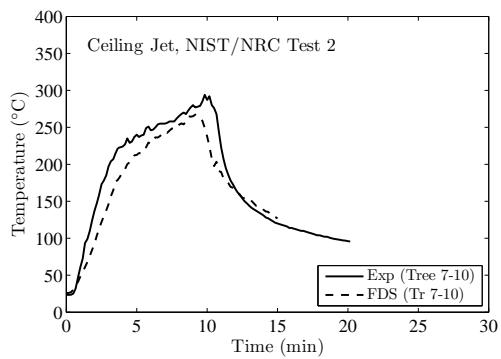
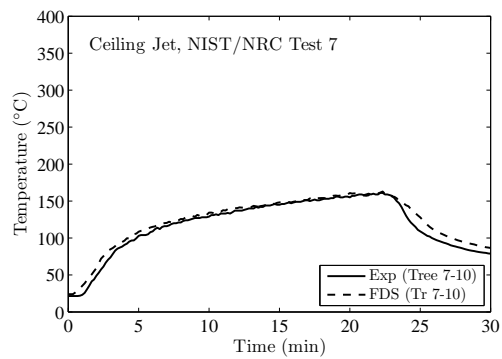
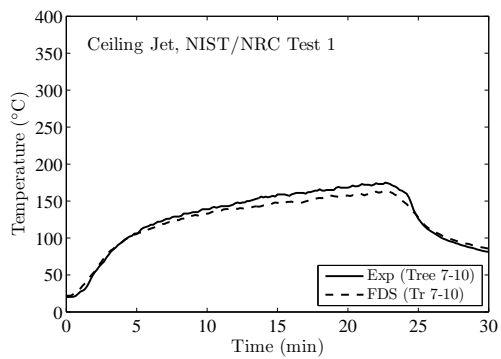
7.1 WTC Test Series

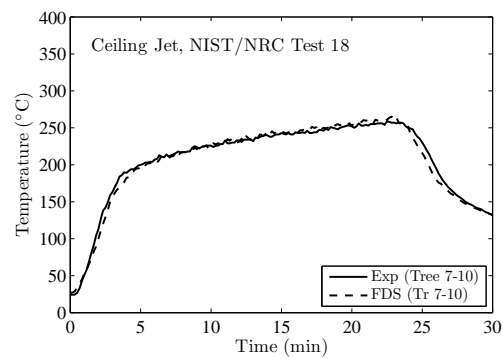
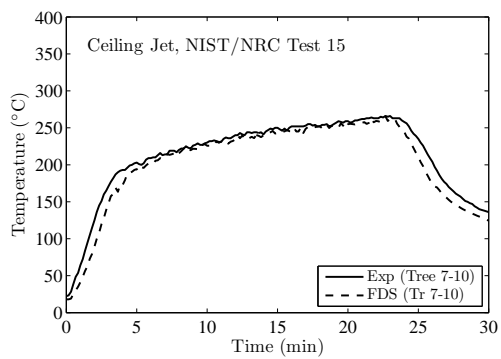
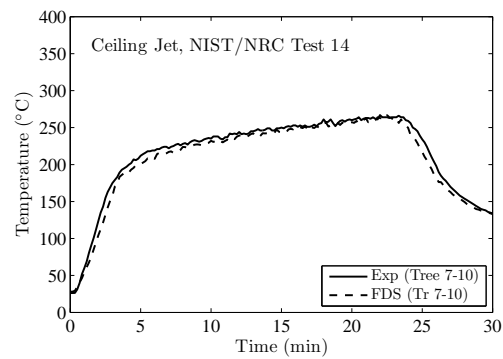
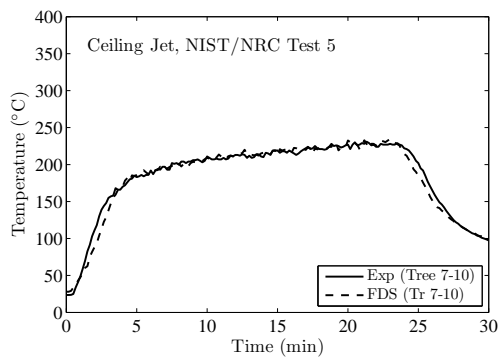
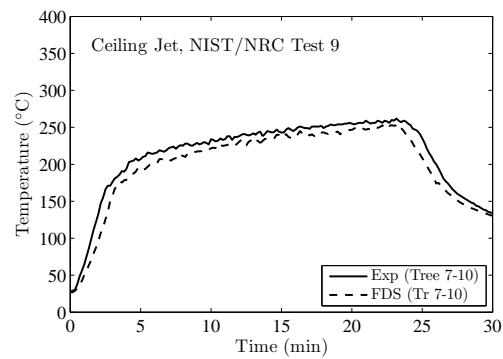
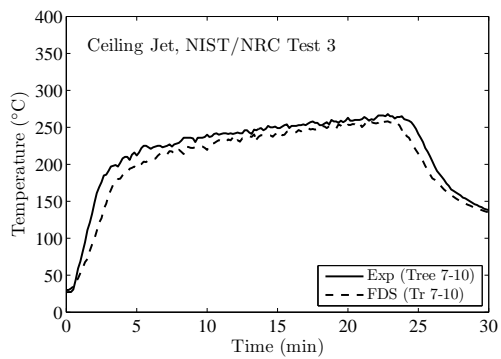
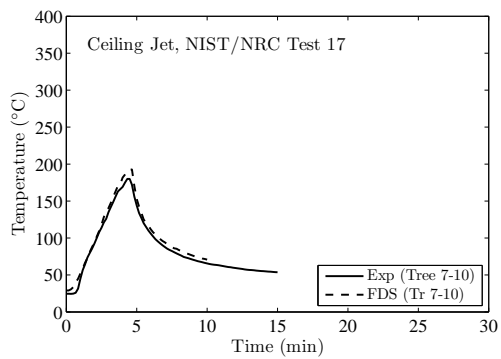
Aspirated thermocouples were positioned 3 m to the west (TTRW1) and 2 m to the east (TTRE1) of the fire pan, 18 cm below the ceiling.



7.2 NIST/NRC Test Series

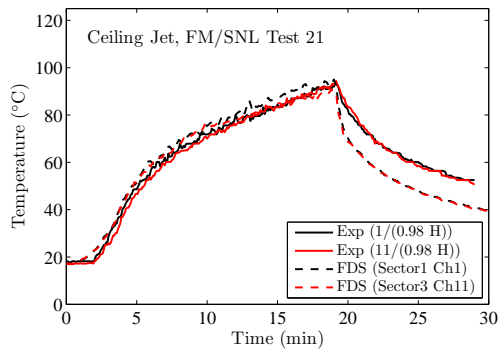
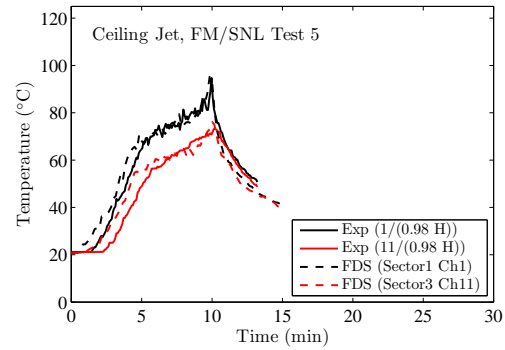
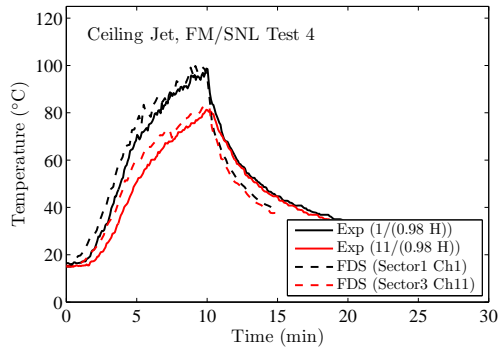
The thermocouple nearest the ceiling in Tree 7, located towards the back of the compartment, has been chosen as a surrogate for the ceiling jet temperature. Curiously, the difference between measured and predicted temperatures is noticeably greater for the open door tests. Certainly, the open door changes the flow pattern of the exhaust gases. However, the predicted HGL heights for the open door tests, shown in the previous section, do not show a noticeable difference from their closed door counterparts. The predicted HGL temperatures are only slightly less than those measured in the open door tests, due in large part to the contribution of Tree 7 in the layer reduction calculation.





7.3 FM/SNL Test Series

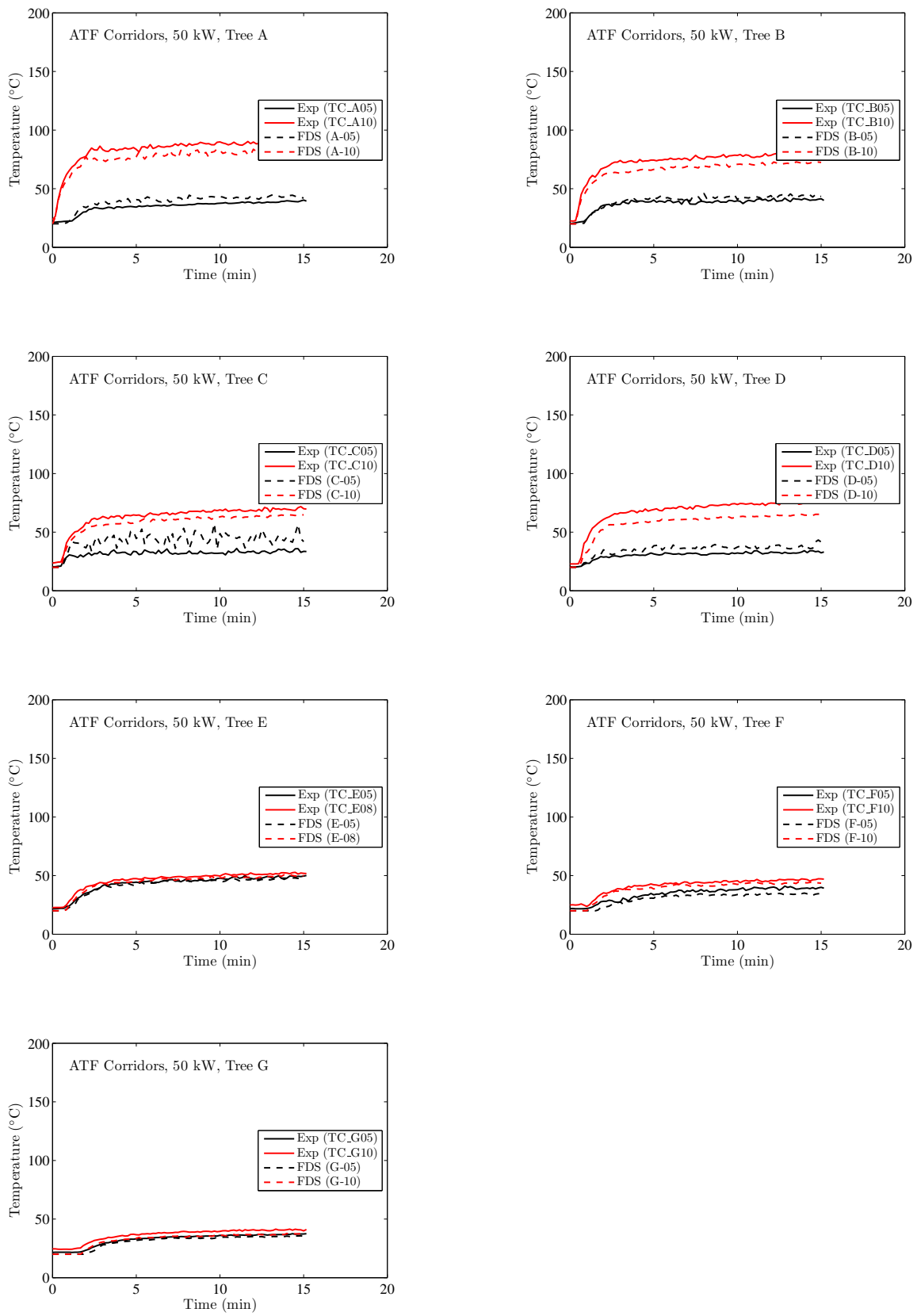
The near-ceiling thermocouples in Sectors 1 and 3 have been chosen as surrogates for the ceiling jet temperature. The results are shown below. The only noticeable discrepancy is in Test 21, and it is the same pattern that was observed in the HGL temperature comparison for this test.

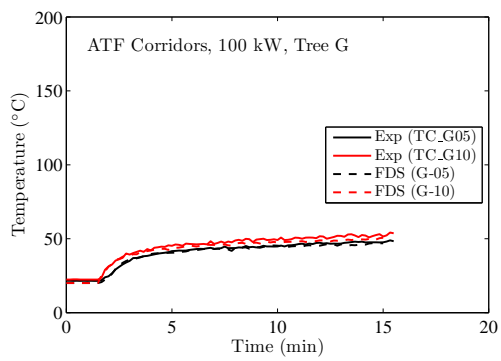
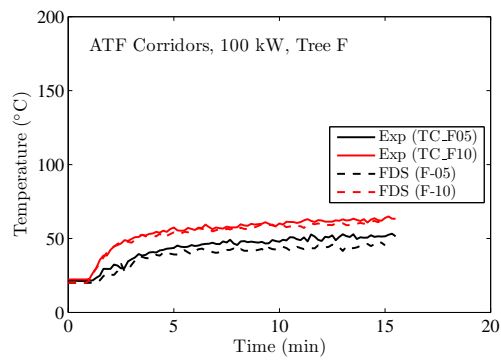
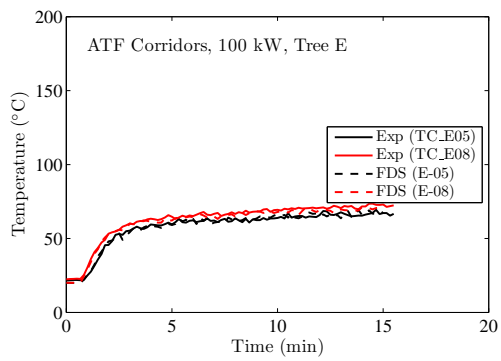
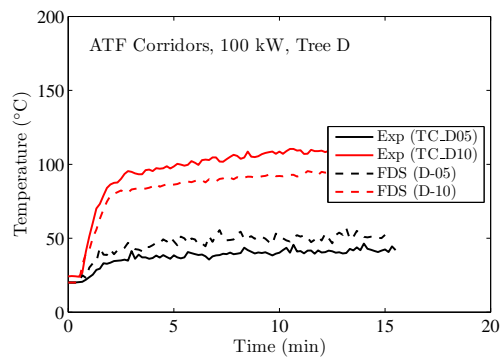
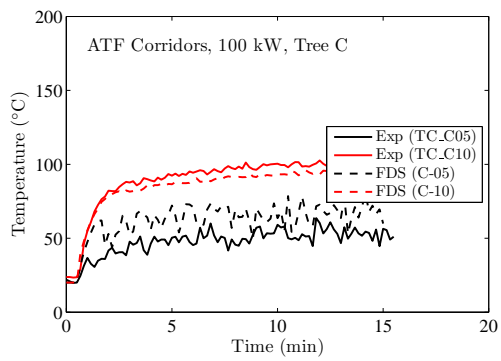
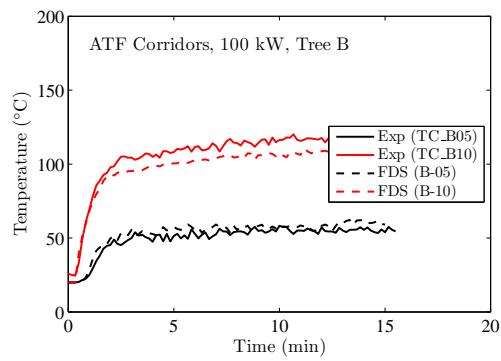
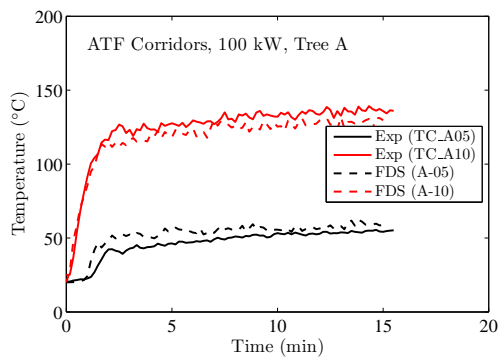


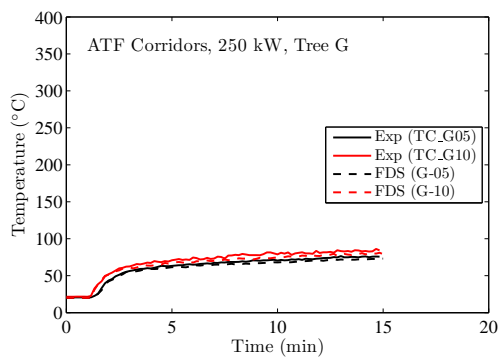
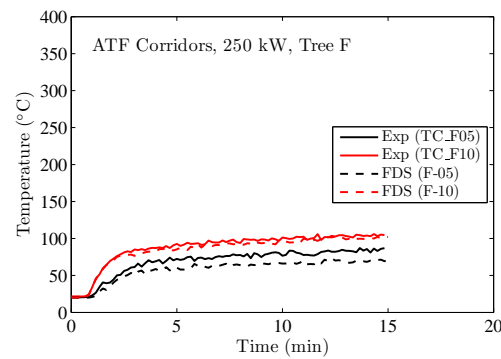
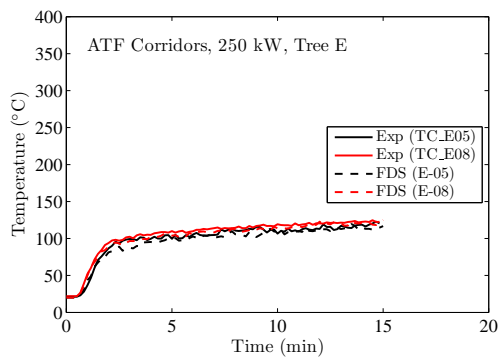
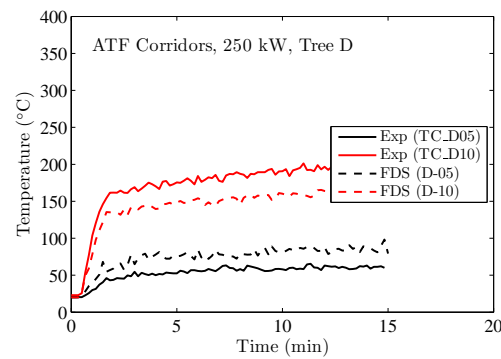
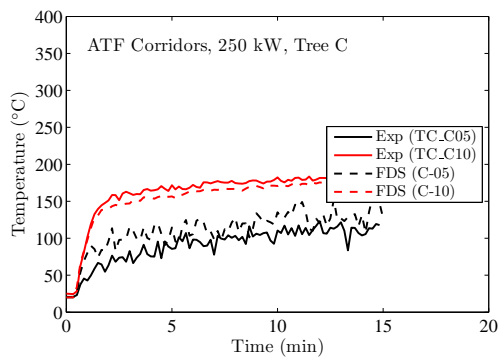
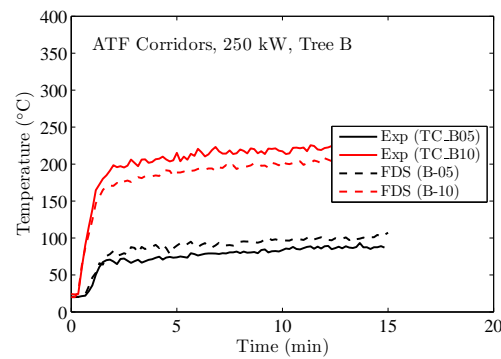
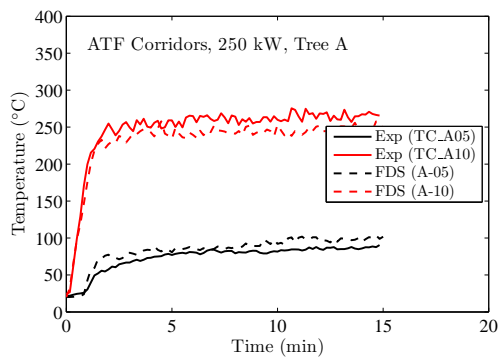
7.4 ATF Corridors Series

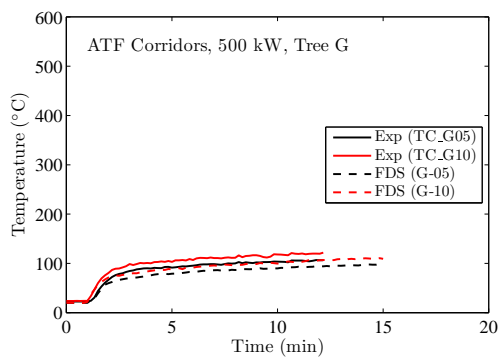
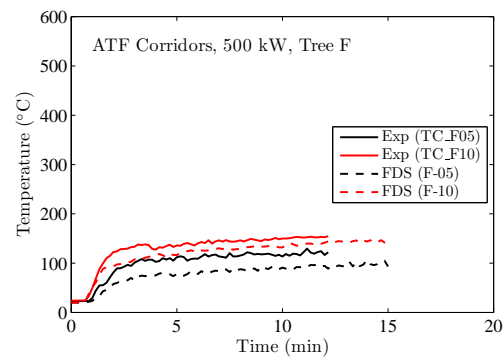
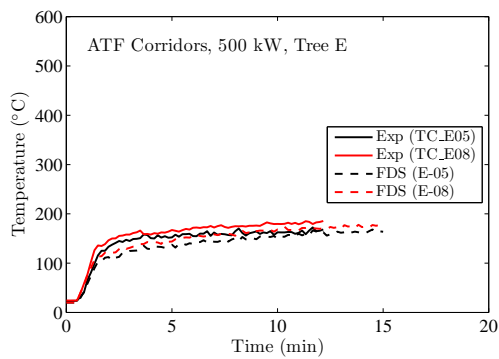
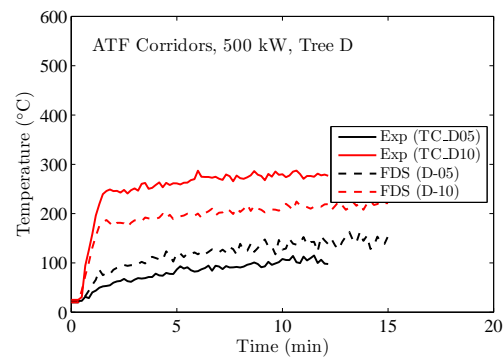
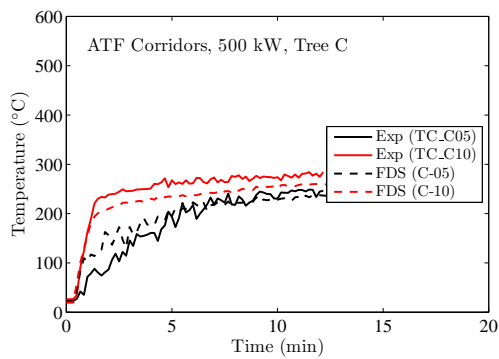
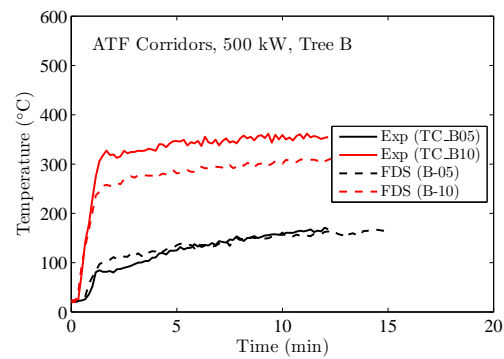
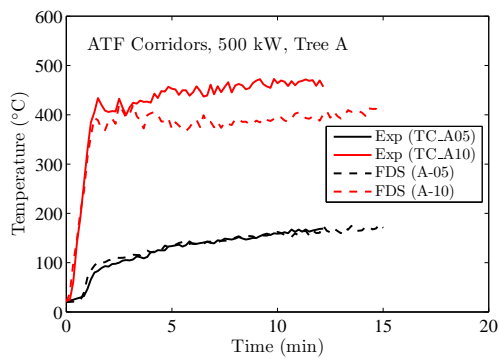
This series of experiments involved two fairly long corridors connected by a staircase. The fire, a natural gas sand burner, was located on the first level at the end of the corridor away from the stairwell, which was located at the other end. The corridor was closed at the end where the fire was located, and open at the same position on the second level. Two-way flow occurred on both levels because make-up air flowed from the opening on the second level down the stairs to the first. The only opening to the enclosure was the open end of the second-level corridor.

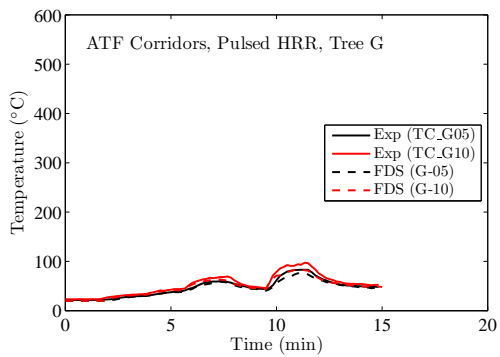
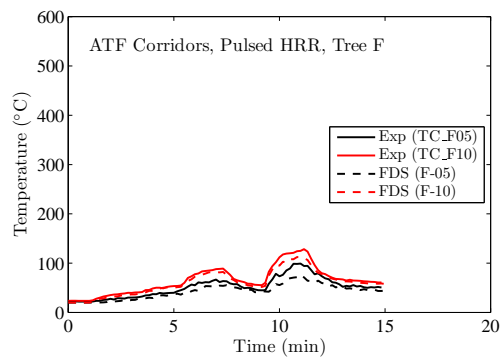
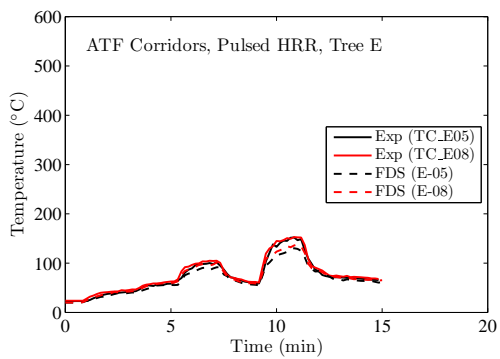
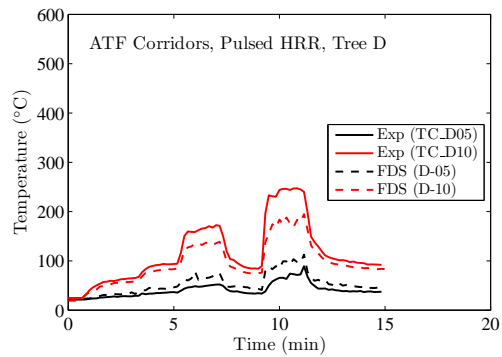
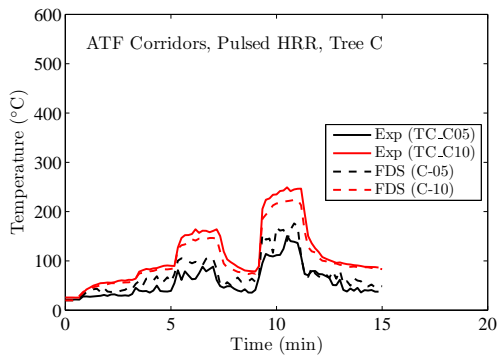
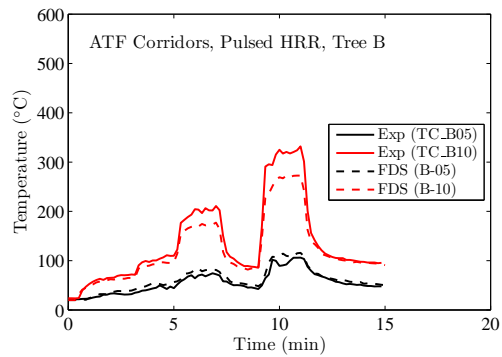
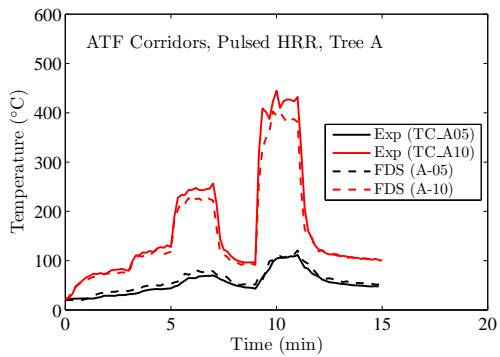
Temperatures were measured with 7 thermocouple trees. Tree A was located fairly close to the fire on the first level. Tree B was located halfway down the first-level corridor. Tree C was close to the stairwell entrance on the first level. Tree D was located in the doorway of the stairwell on the first level. Tree E was located roughly along the vertical centerline of the stairwell. Tree F was located near the stairwell opening on the second level. Tree G was located near the exit at the other end of the second-level corridor. The graphs on the following pages show the top and bottom TC from each tree for the given fire sizes of 50 kW, 100 kW, 250 kW, 500 kW, and a mixed HRR “pulsed” fire.











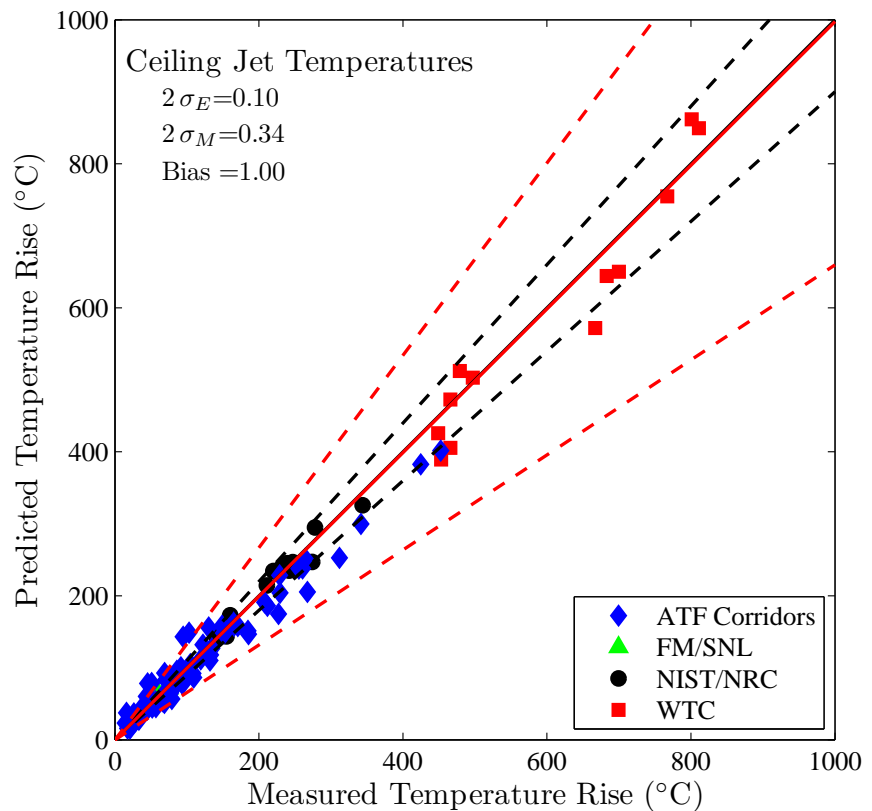
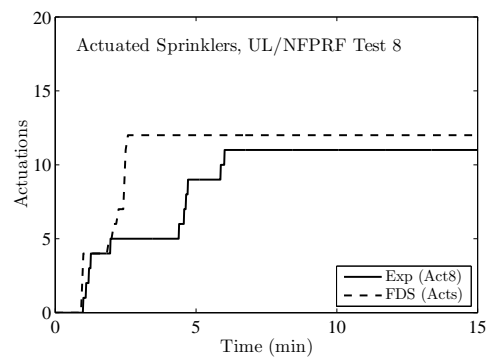
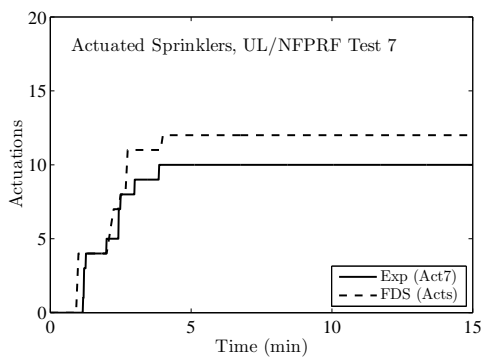
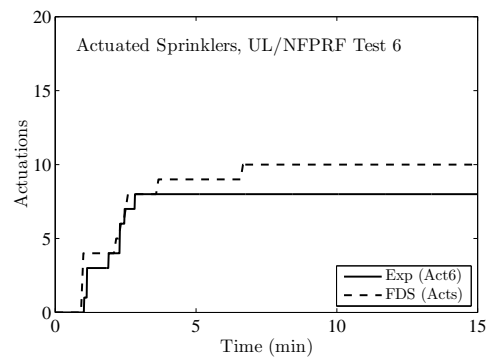
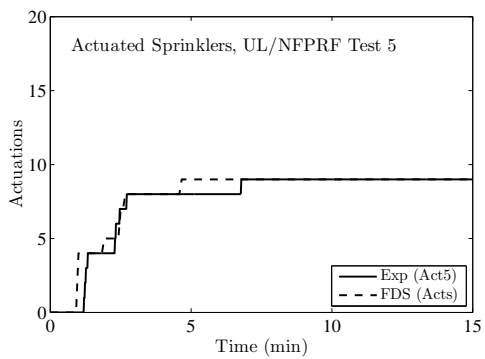
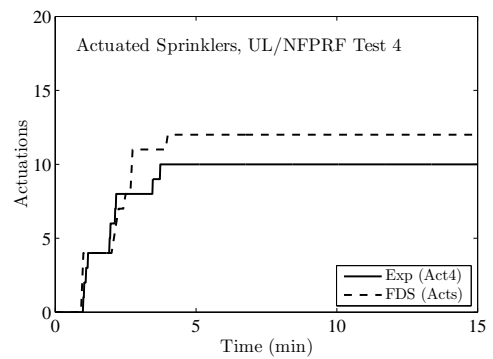
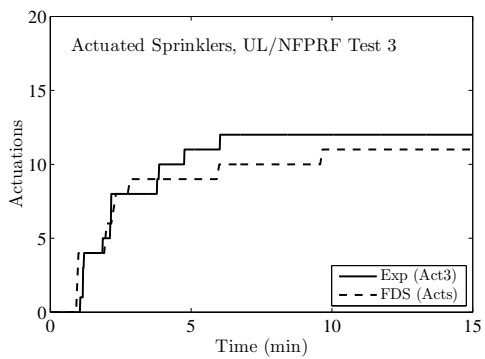
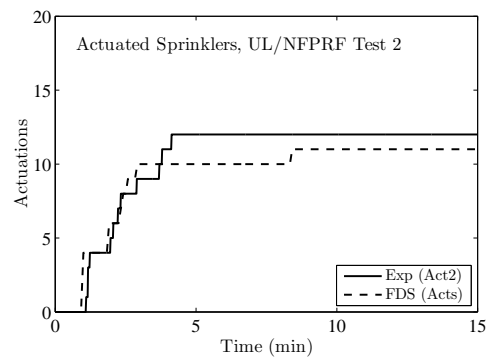
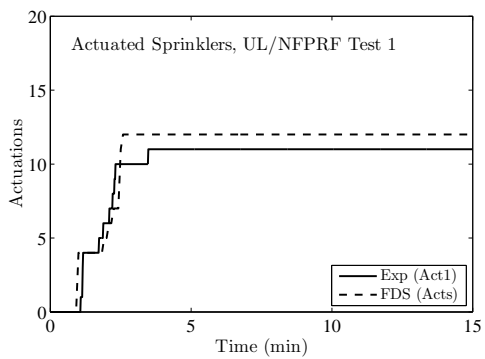


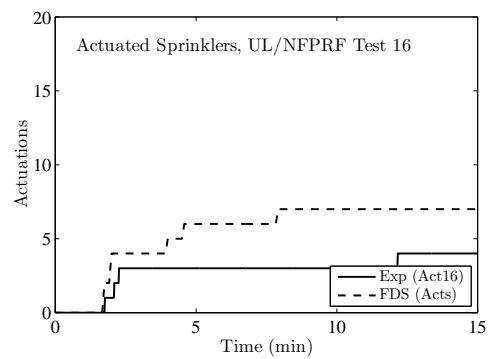
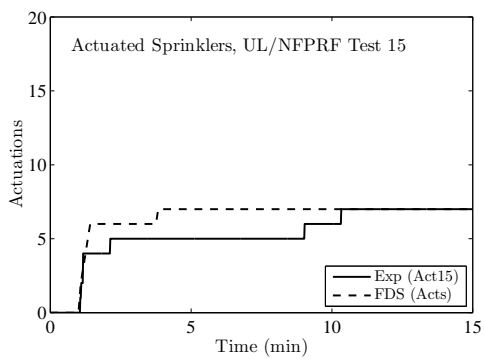
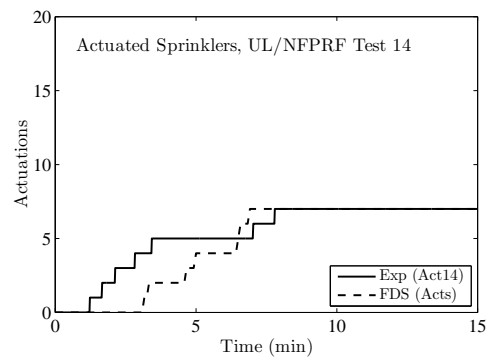
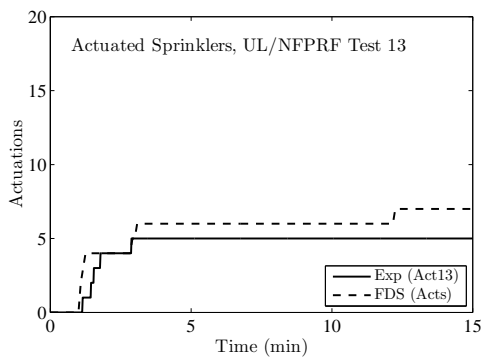
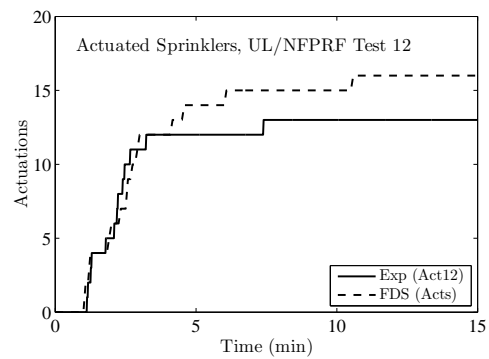
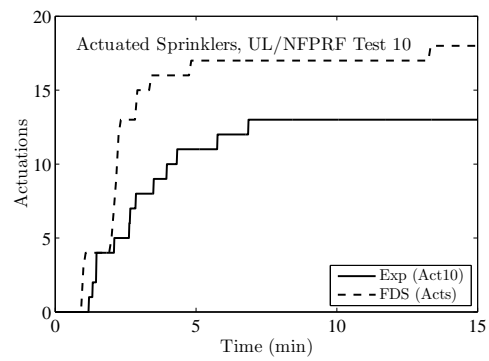
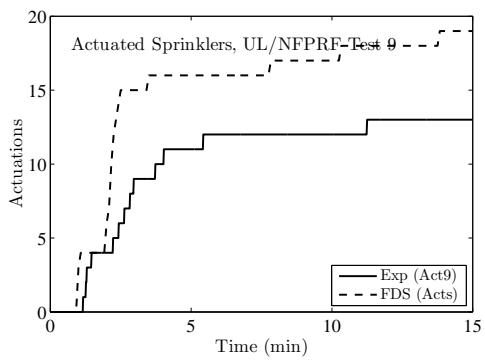
Figure 7.1: Summary of ceiling jet temperature predictions, WTC, NIST/NRC and FM/SNL test series.

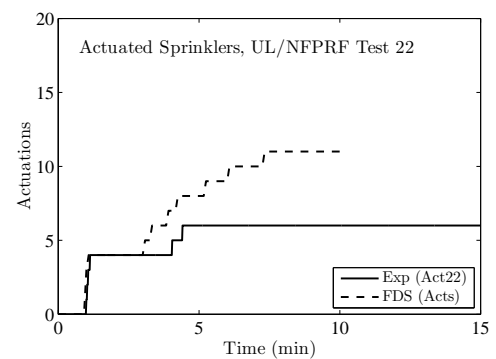
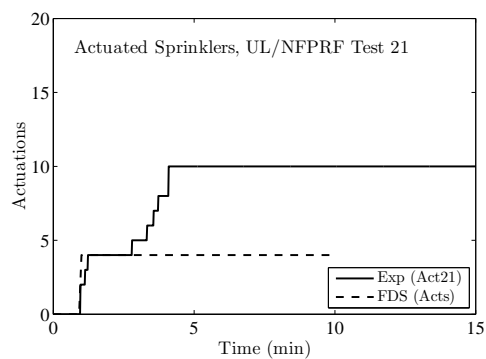
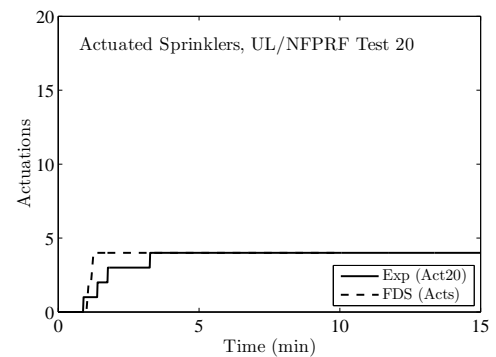
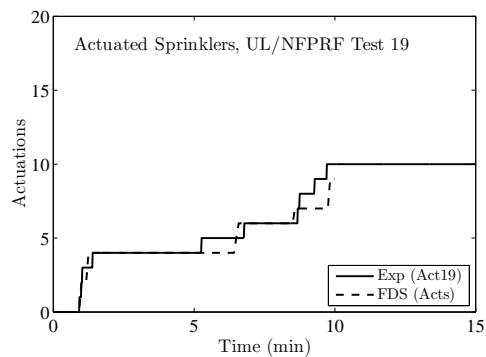
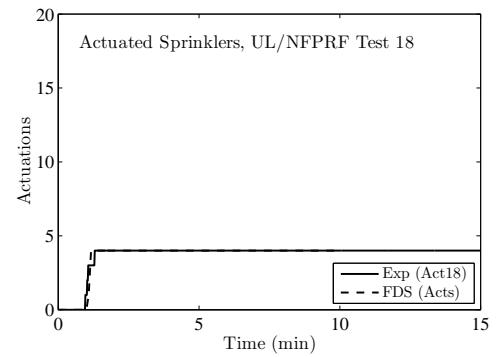
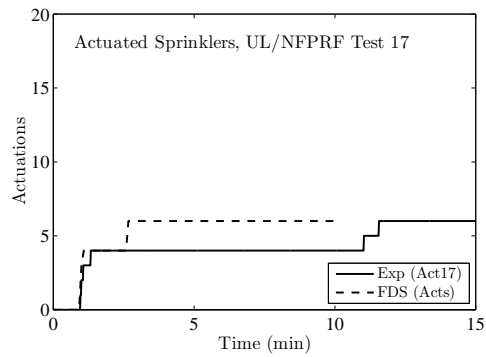
7.5 UL/NFPRF Sprinkler, Vent, and Draft Curtain Experiments

The ceiling jet is an important fire phenomenon because of the presence of automatic fire protection devices at the ceiling, like sprinklers and smoke/heat vents. The results of the UL/NFPRF experiments provide useful data to assess the accuracy of FDS in predicting the velocity and temperature near the ceiling, and consequently the resulting activation of sprinklers. The UL/NFPRF test results (Series I) are summarized in Table 3.1.

The figures on the following pages display the number of sprinklers actuated as a function of time. The results are then summarized in Fig. 7.2. Note that there are no experimental uncertainty bounds on the plot because it is difficult to estimate the combined uncertainty related to the various parameters that are input into the model. At the bottom of Fig. 7.2, the results of three replicate experiments demonstrate that the total number of actuated sprinklers in each experiment is repeatable, even though individual actuation times may vary. Based on these three replicates, there is very little, if any, uncertainty in the total number of actuated sprinklers for each test. However, the test report [115] does not include uncertainty estimates for the heat release rate, thermal properties of the ceiling, sprinkler RTI, conductivity factor, actuation temperature, median droplet diameter, and various other parameters that have been input into the model. Consequently, it is not possible to estimate the uncertainty in the total number of actuated sprinklers due to the uncertainty in the reported parameters. The only sensitivity analysis conducted for this set of experiments was to change the median volumetric droplet size from 1000 μm to 750 μm , which led to a reduction of approximately 50 % in the number of predicted sprinkler actuations.







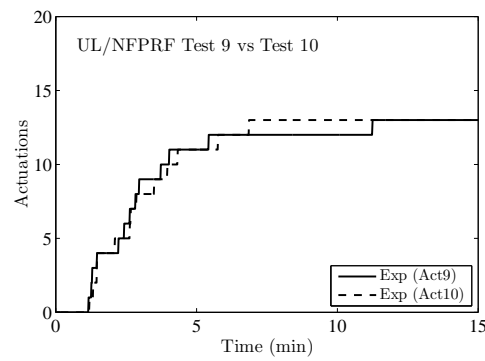
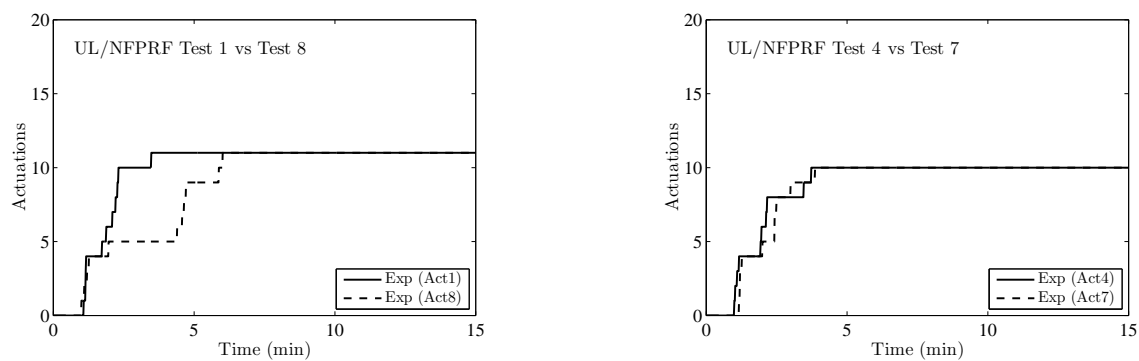
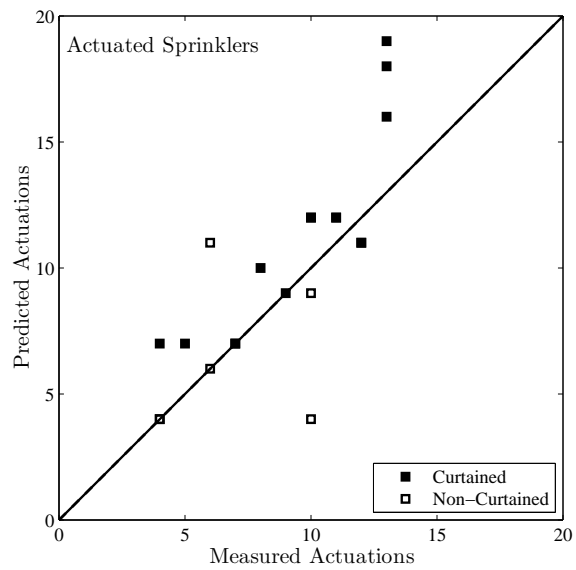
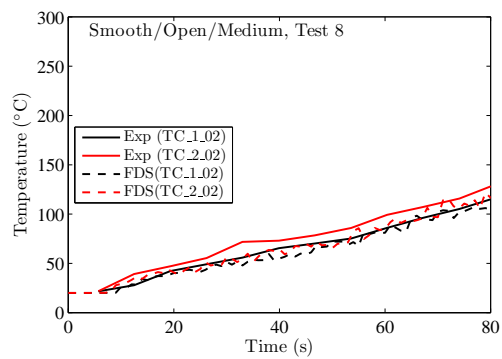
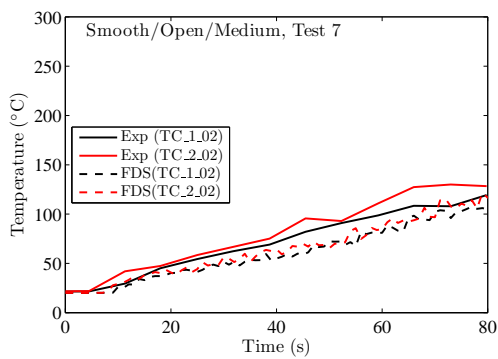
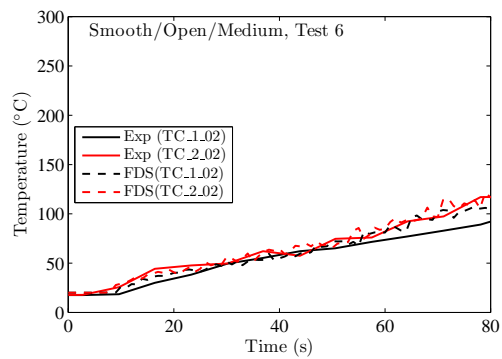
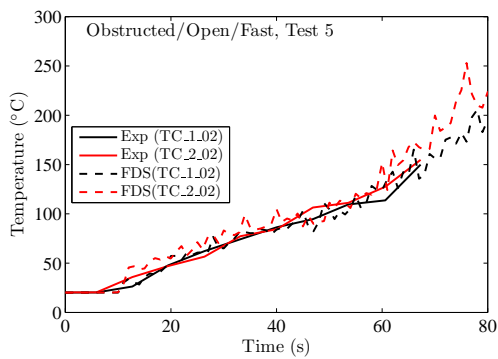
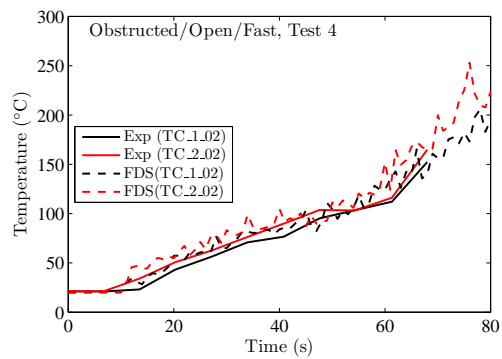
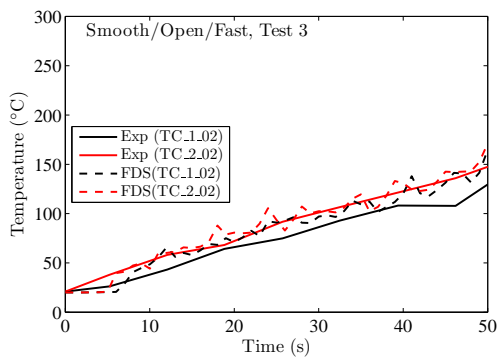
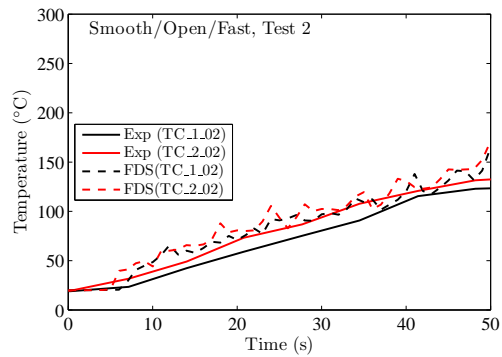
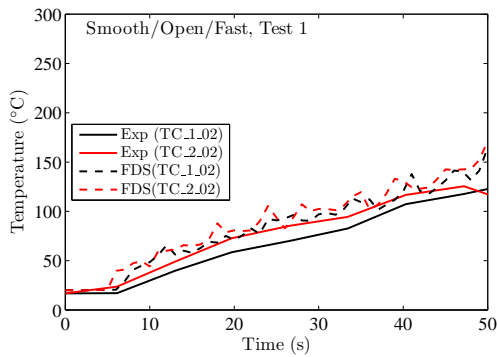


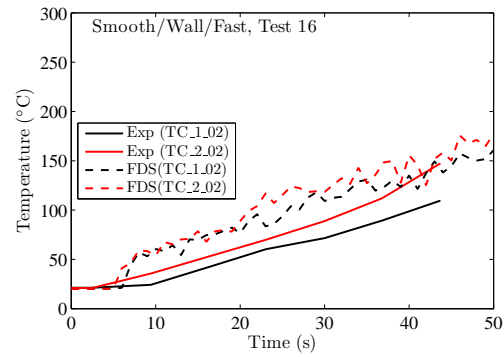
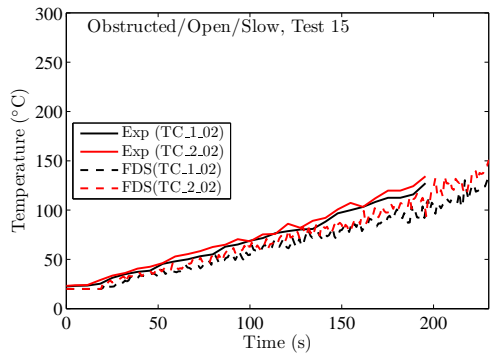
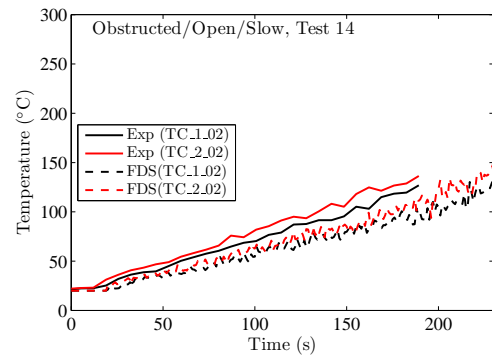
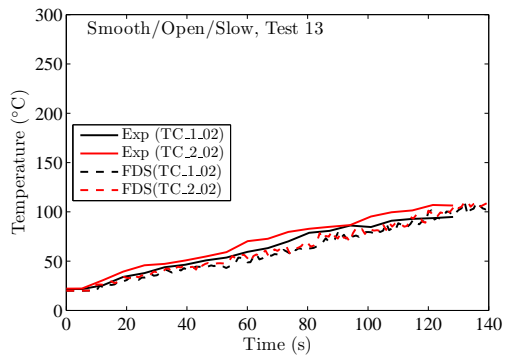
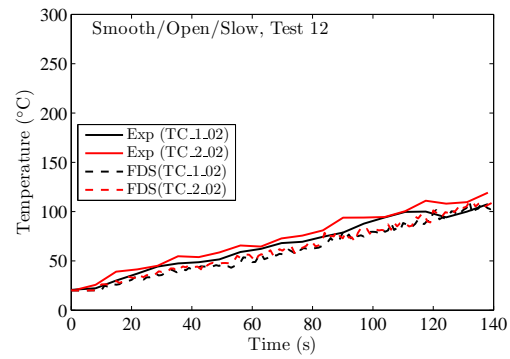
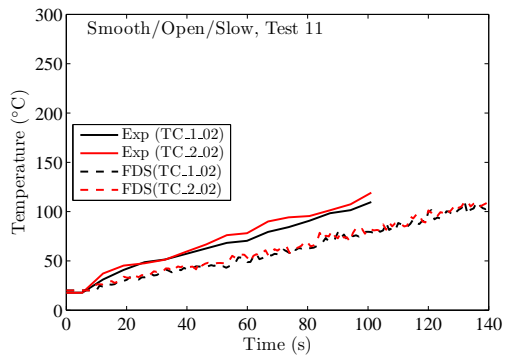
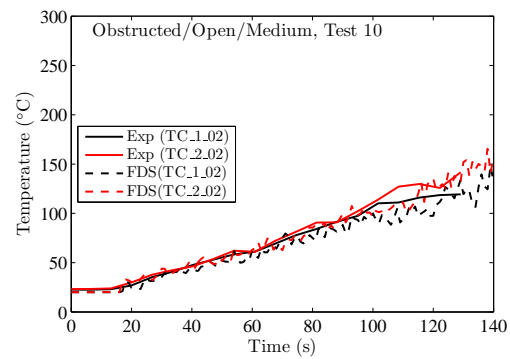
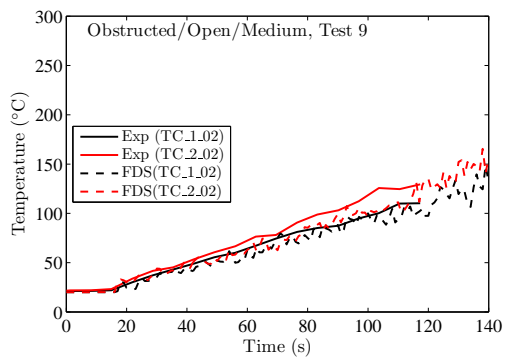
Figure 7.2: Above: Comparison of predicted and measured sprinkler activation times for the UL/NFPRF Test Series I. Below: The results of three replicate experiments.

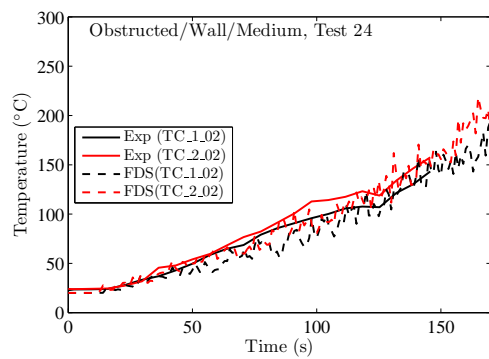
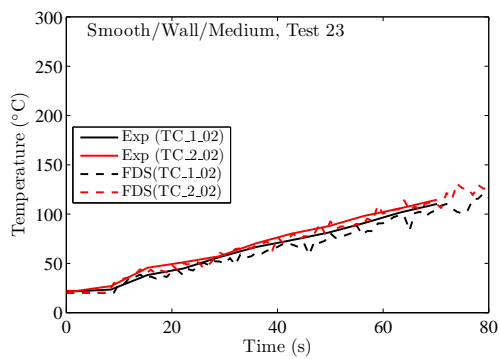
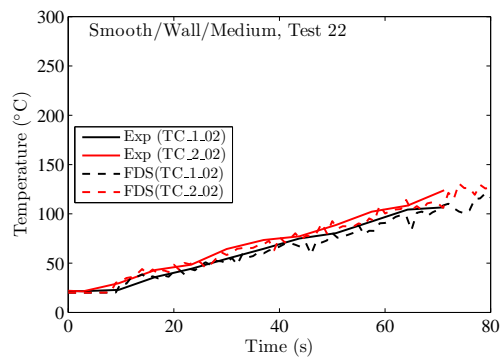
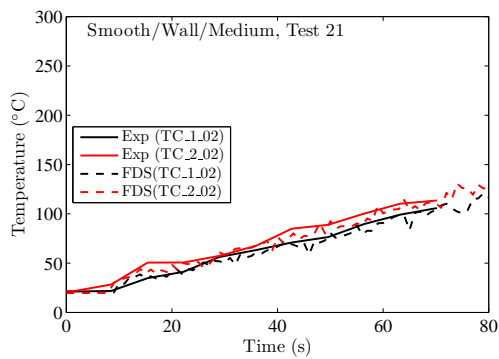
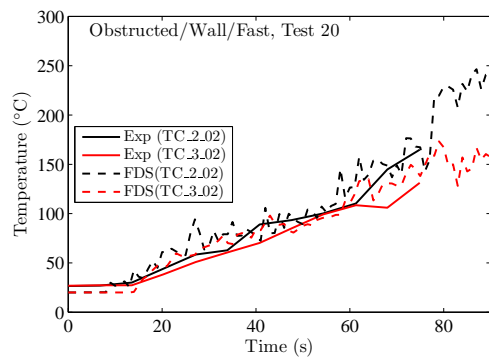
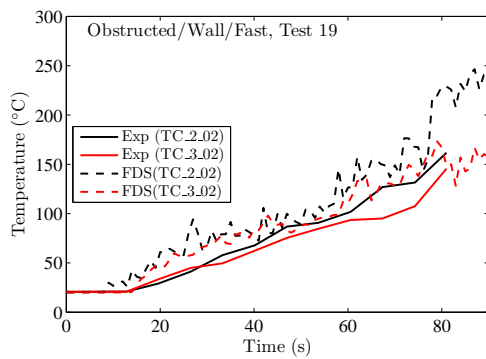
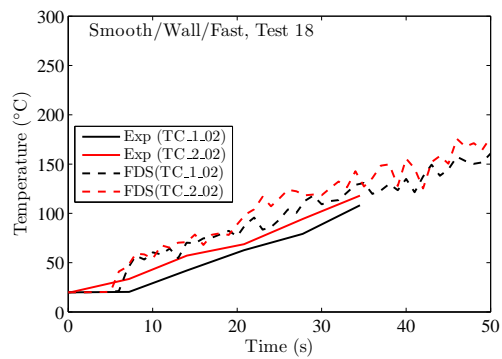
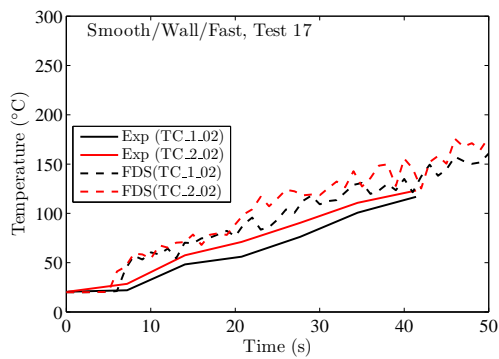
7.6 Vettori Flat Ceiling Experiments

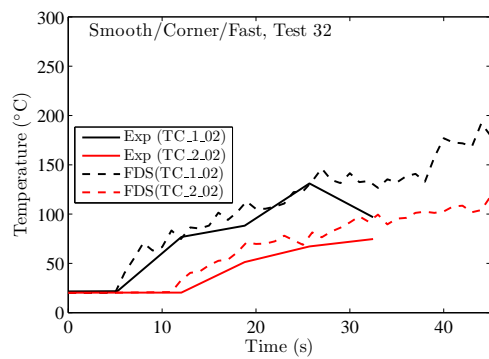
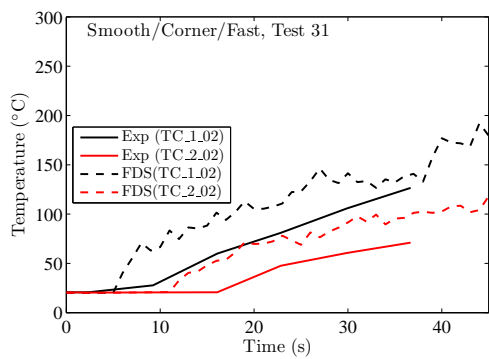
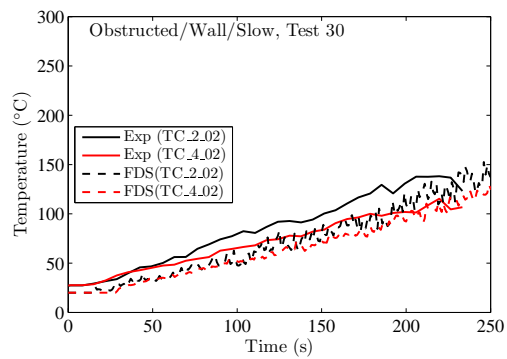
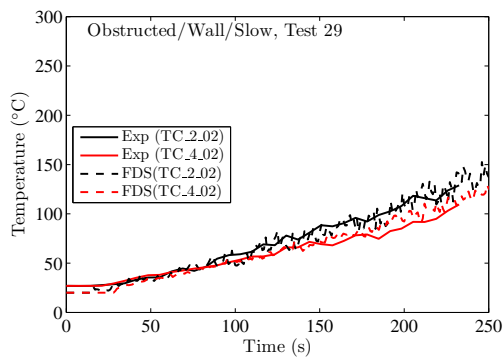
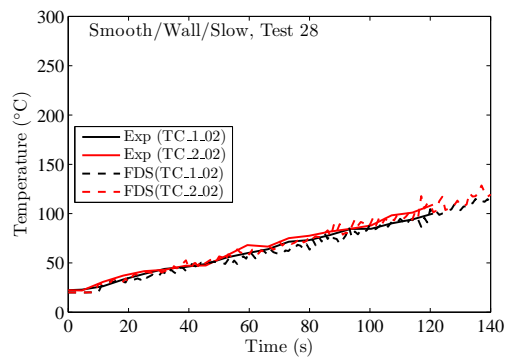
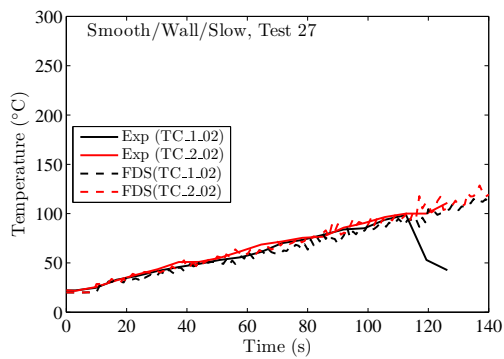
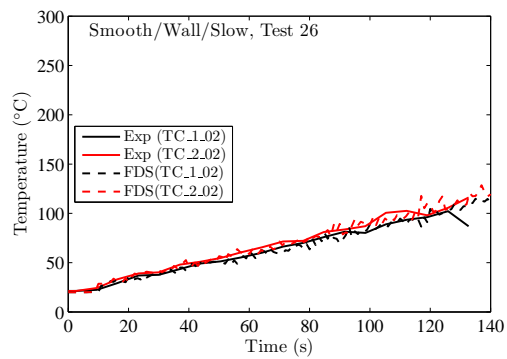
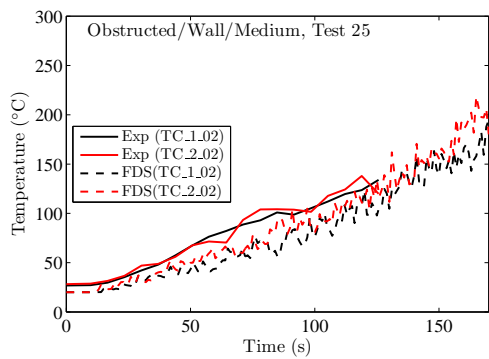
The behavior of ceiling jets is an important component in the design of automatic fire suppression systems, such as sprinklers. The Vettori cases examine the effects of fire location, fire growth rate, and ceiling obstructions on the temperature of ceiling jets and activation time of sprinklers. The results that follow provide useful data as to the predictive capacity of FDS with regards to ceiling jet behavior.

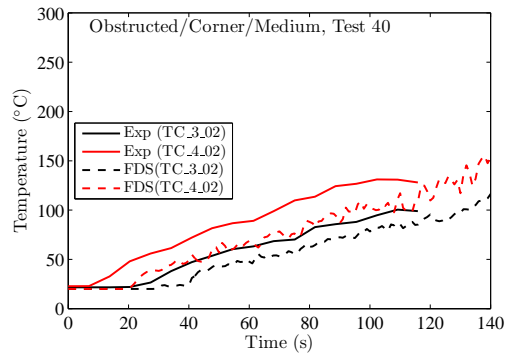
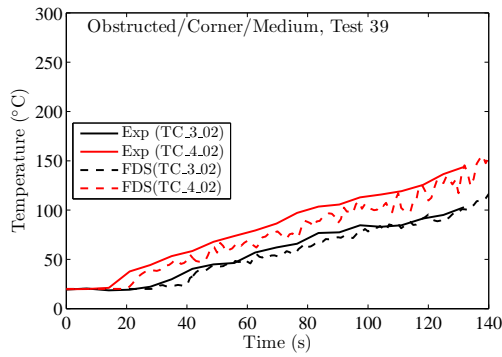
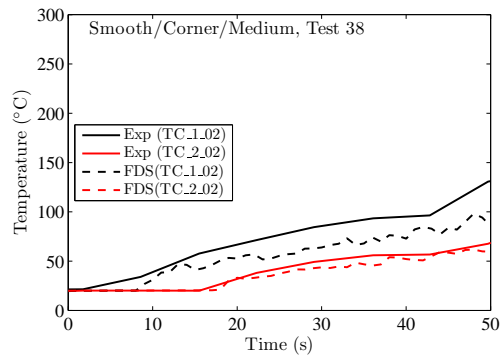
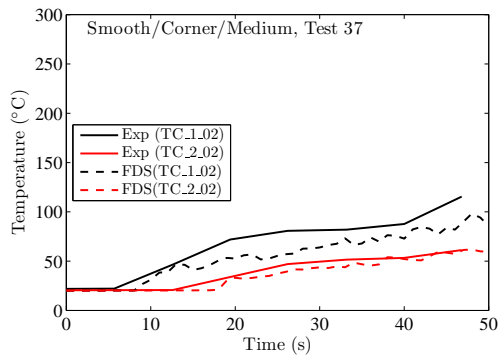
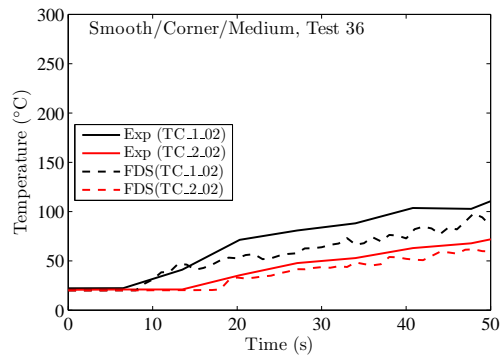
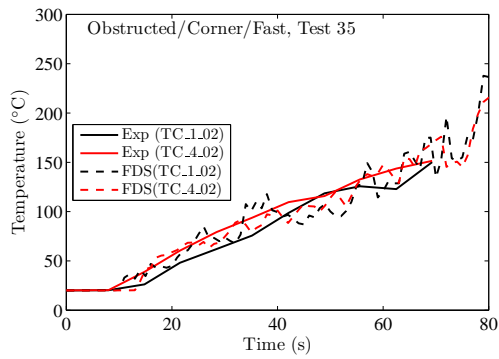
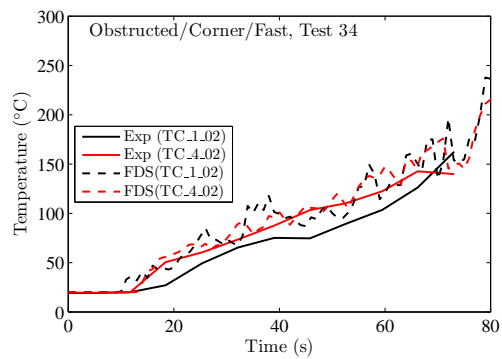
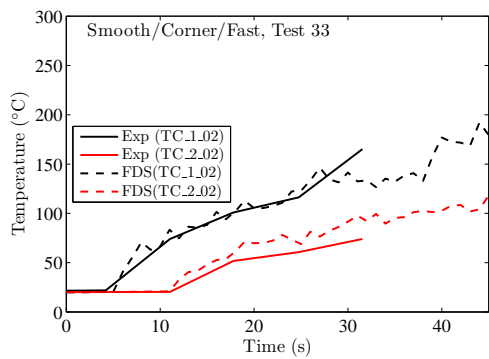
The following figures display the temperature of the ceiling jet at the location of the first two activating sprinklers for each of the 18 scenarios compared with the appropriate experimental data. The experiments consisted of either Smooth or Obstructed ceilings; Slow, Medium or Fast fires; and a burner in the Open, at the Wall, or in the Corner. The experiments performed included three replicates of each of the smooth ceiling configurations and two replicates of each of the obstructed ceiling configurations. Also included is a plot comparing predicted sprinkler activation times with the experimental results.

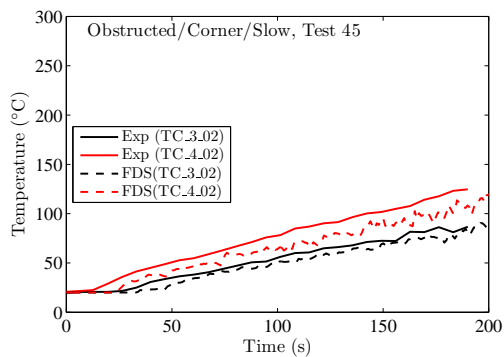
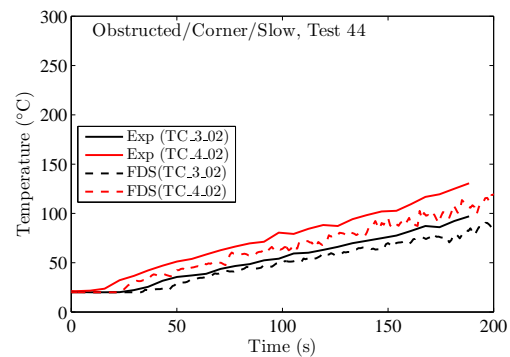
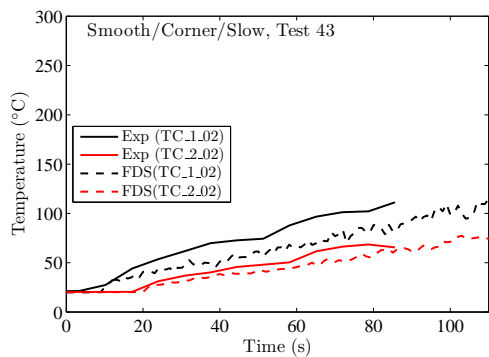
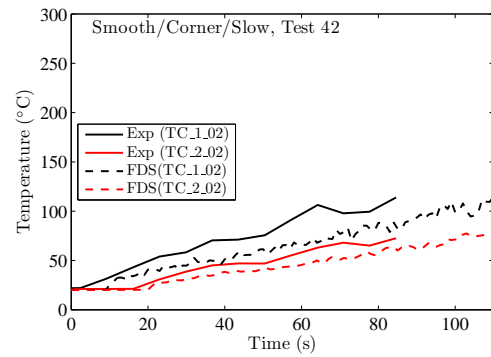
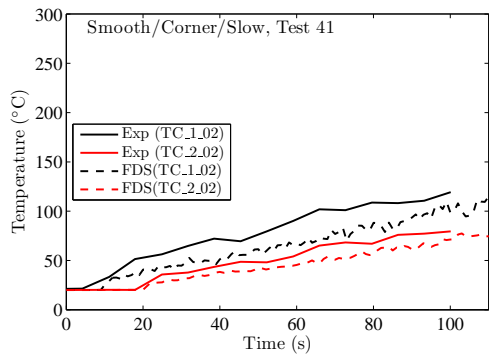












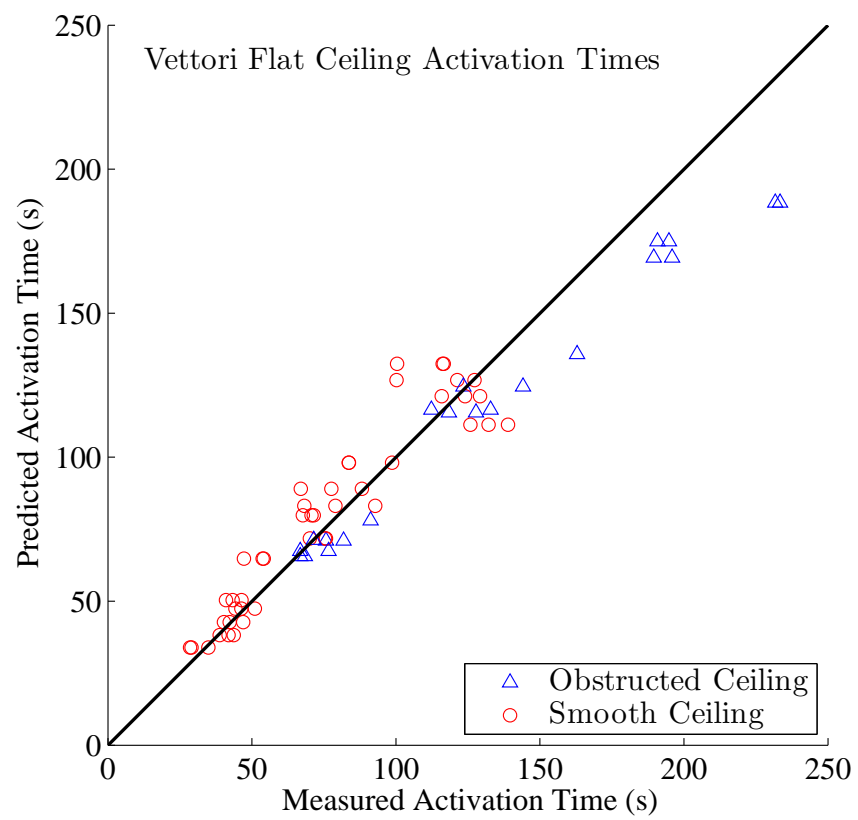
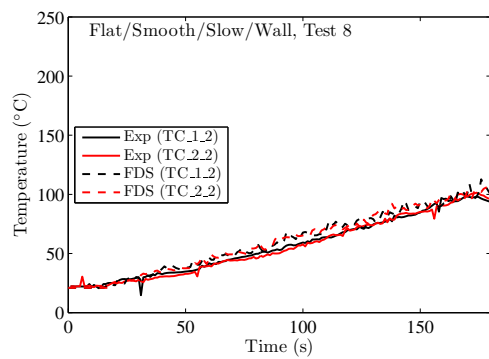
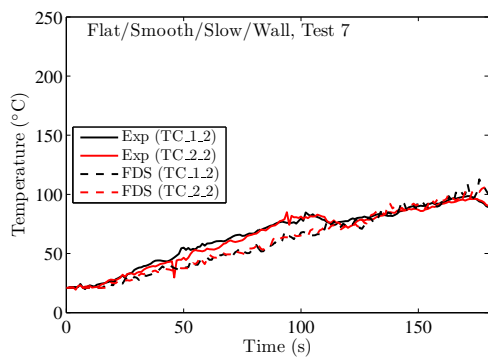
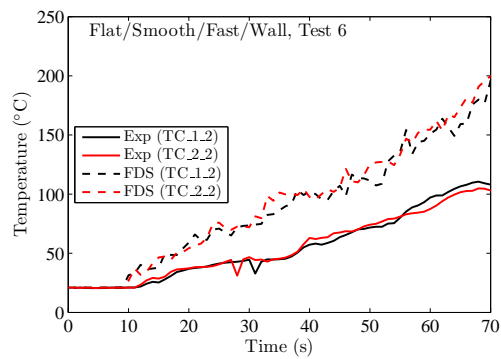
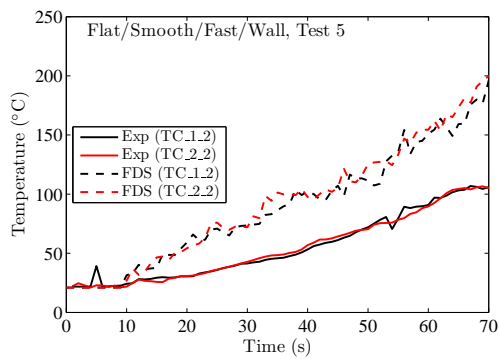
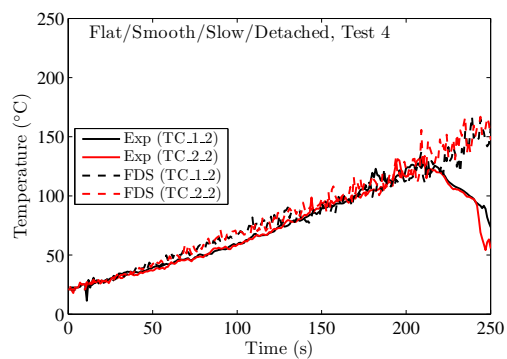
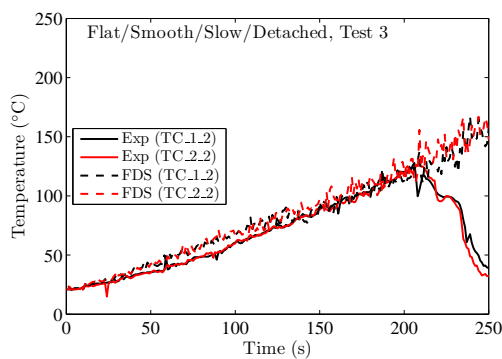
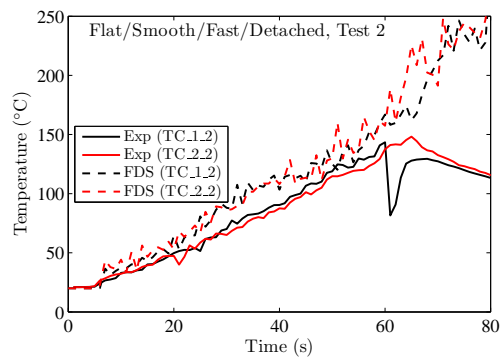
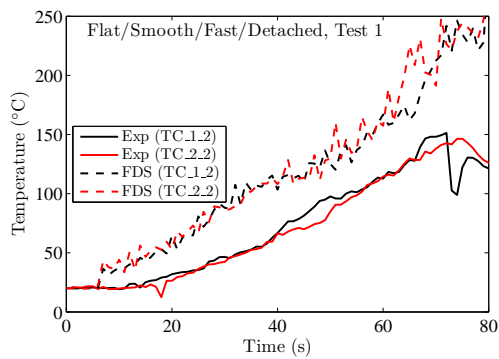
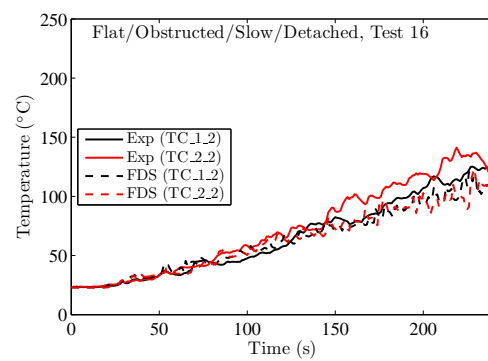
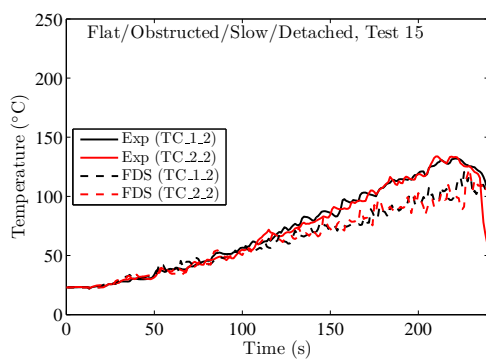
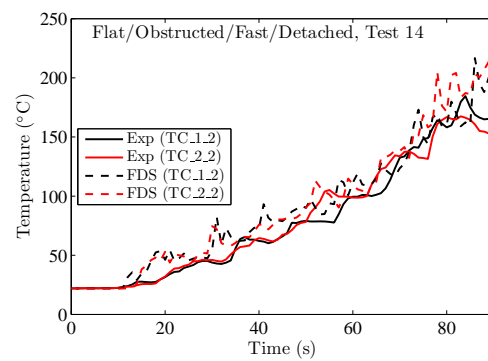
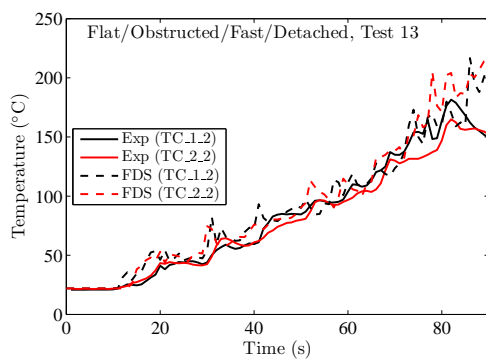
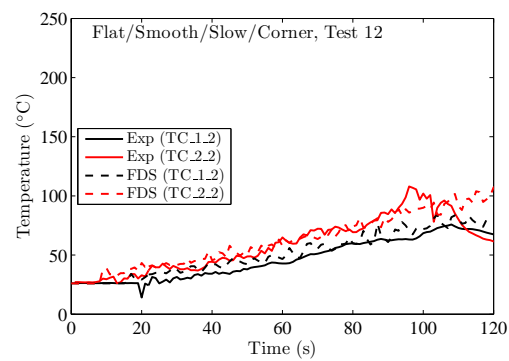
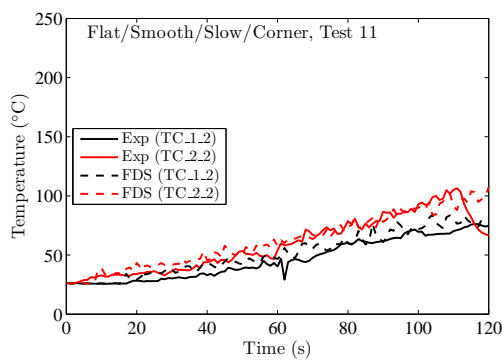
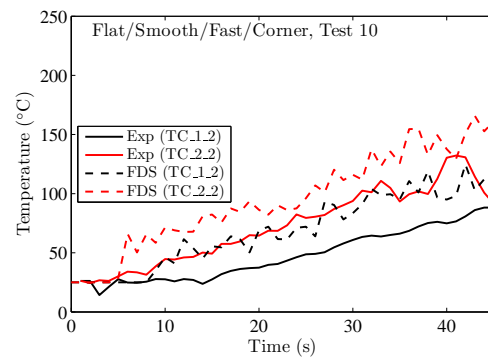
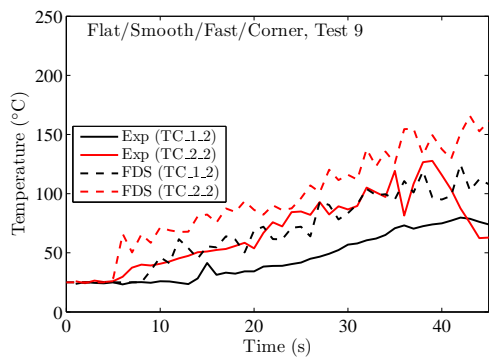


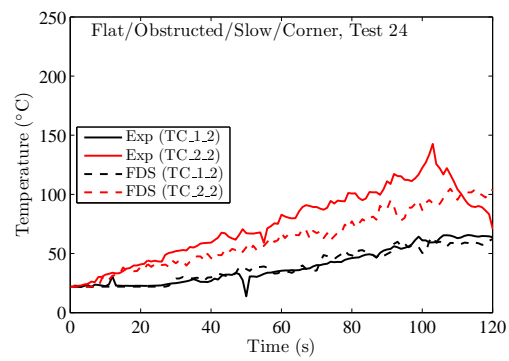
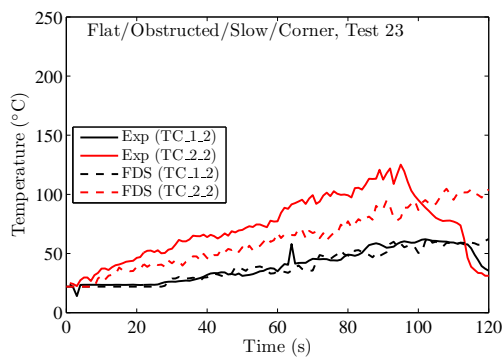
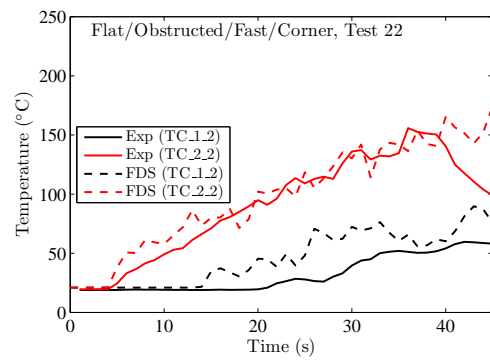
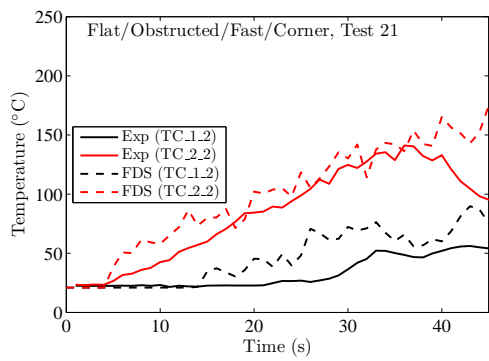
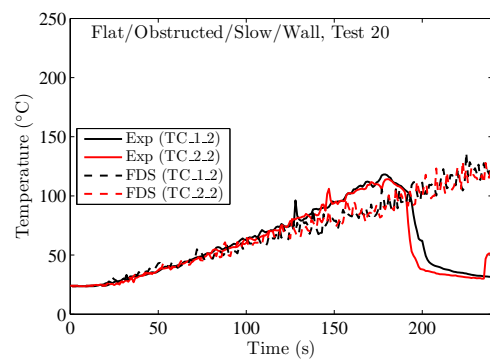
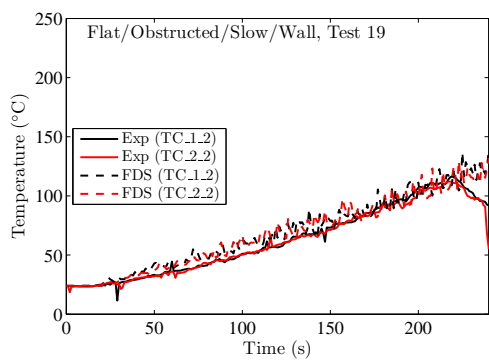
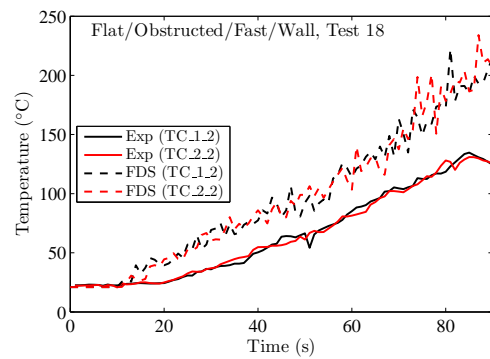
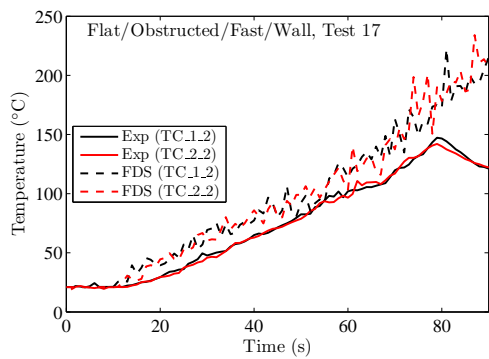
Figure 7.3: Predicted vs. Measured Activation Times of all the Vettori Cases

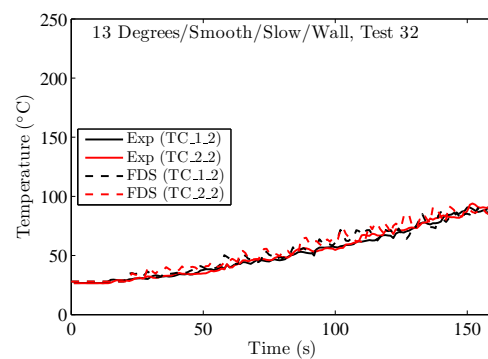
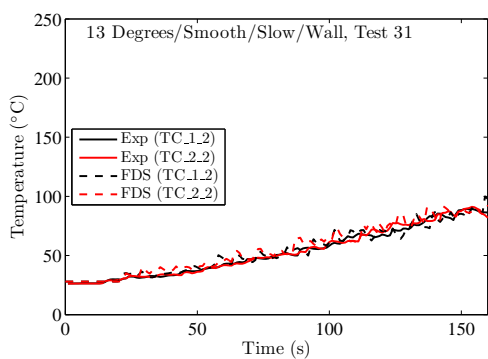
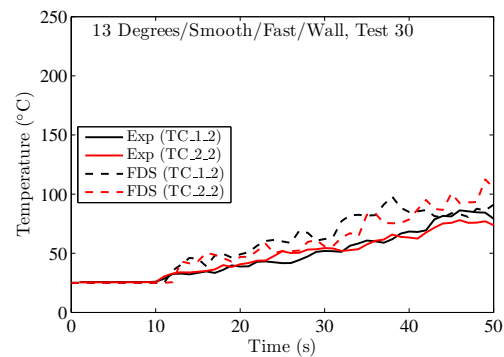
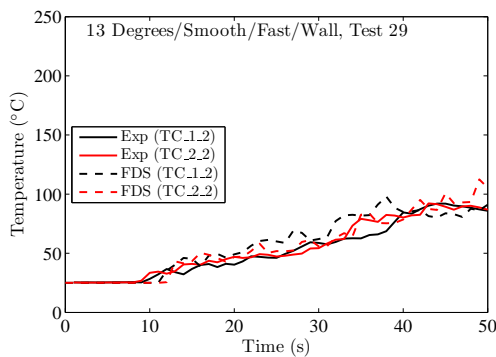
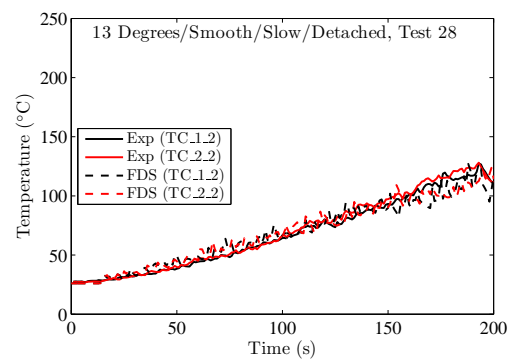
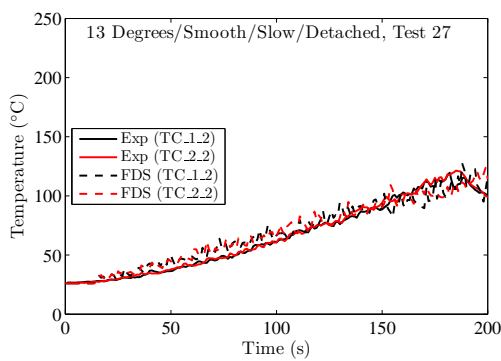
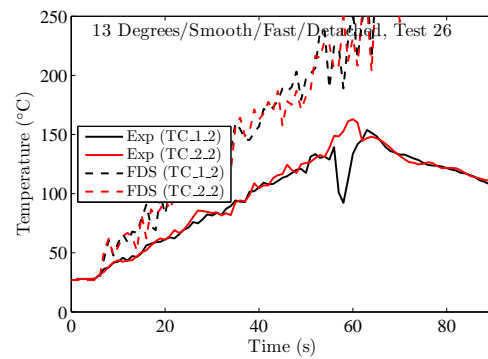
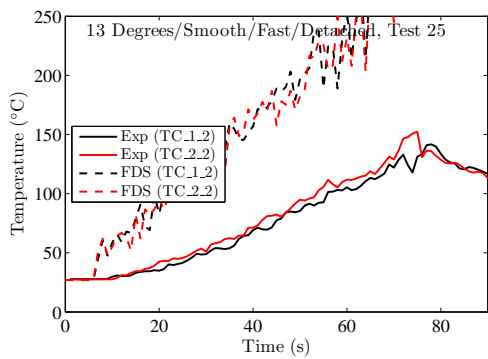
7.7 Vettori Sloped Ceiling Experiments

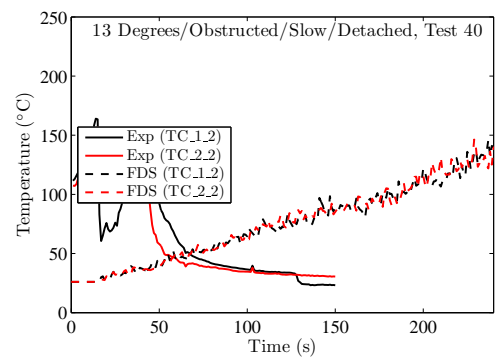
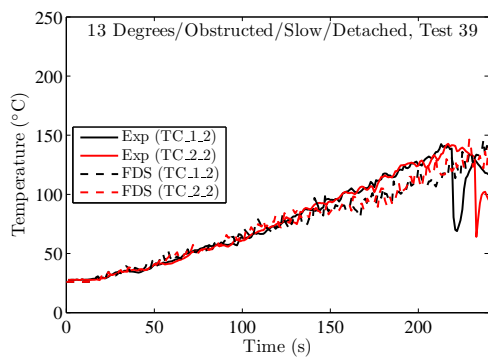
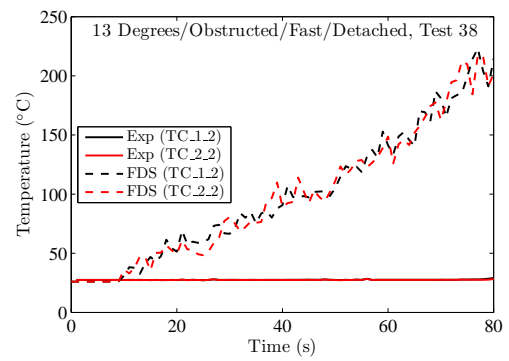
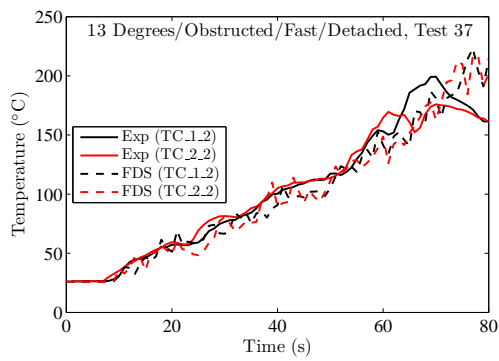
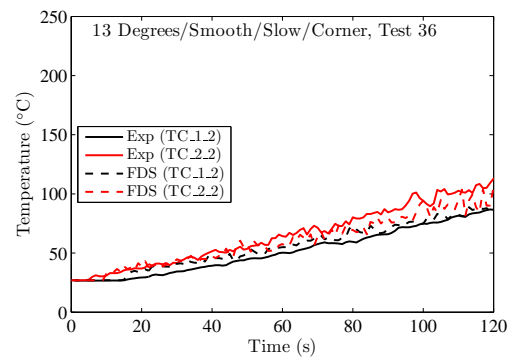
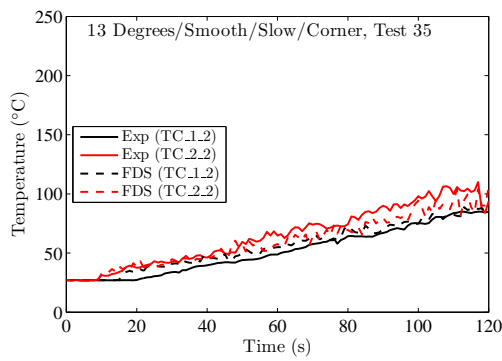
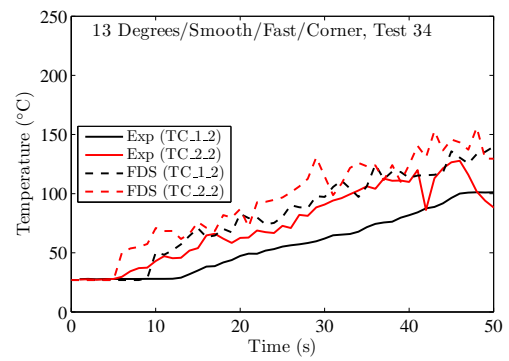
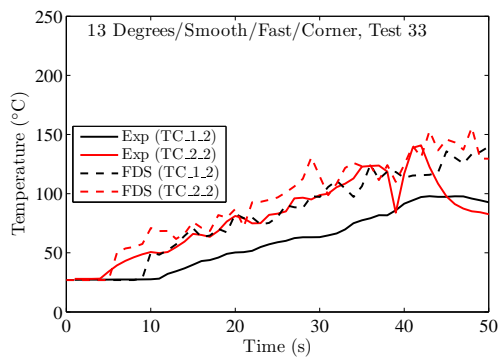
The plots on the following pages display the temperature of the ceiling jet at the location of the first two activating sprinklers for each of the 36 scenarios in the Vettori Sloped Ceiling series. The replicate results are shown side by side. The experiments consisted of either Smooth or Obstructed ceilings; Slow or Fast fires; a burner that is Detached from the wall, at the Wall, or in the Corner, and a Flat, 13°, or 24° sloped ceiling. Also included is a plot comparing predicted sprinkler activation times with the experimental results.

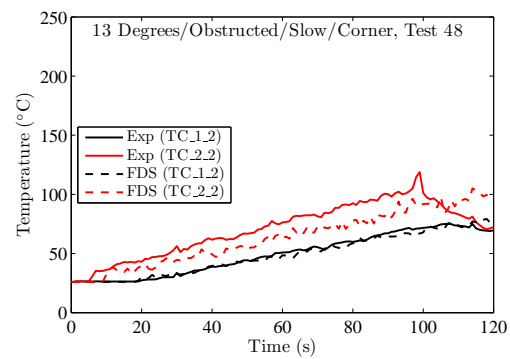
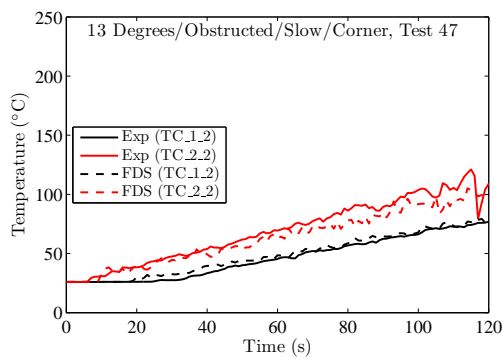
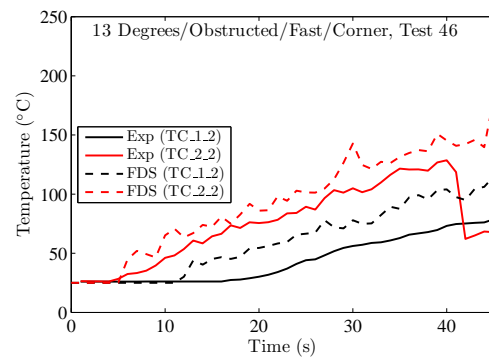
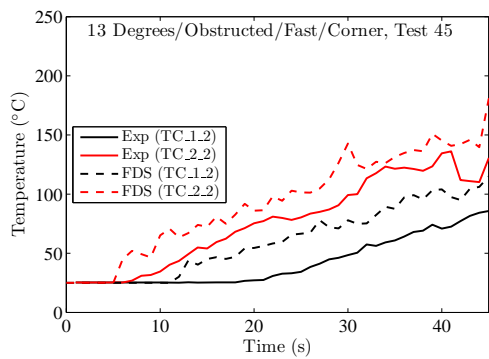
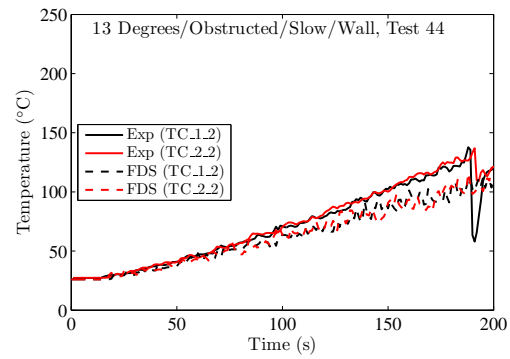
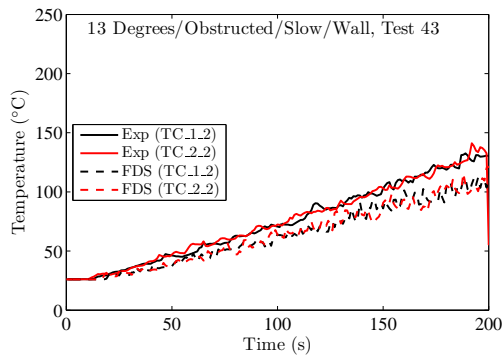
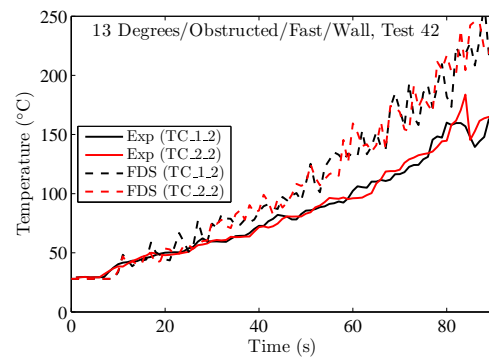
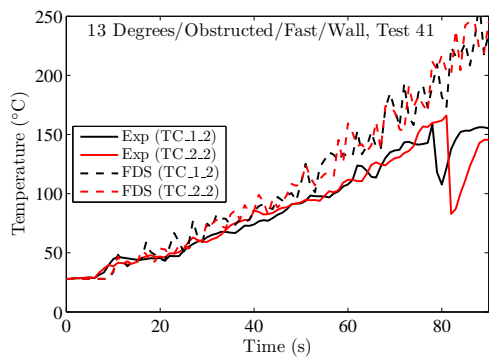


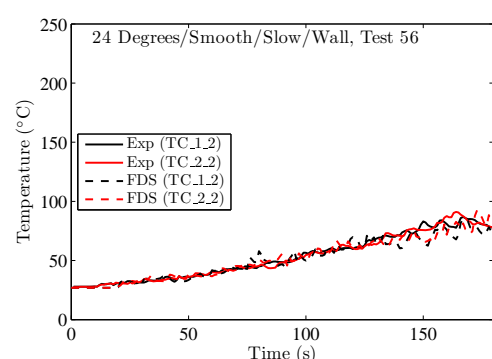
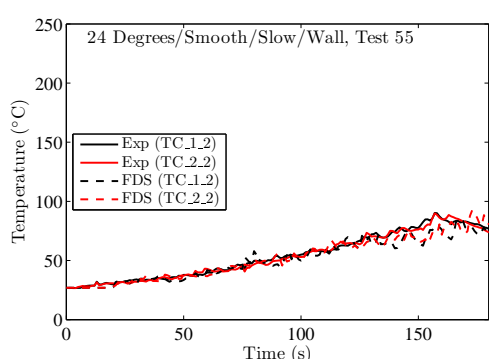
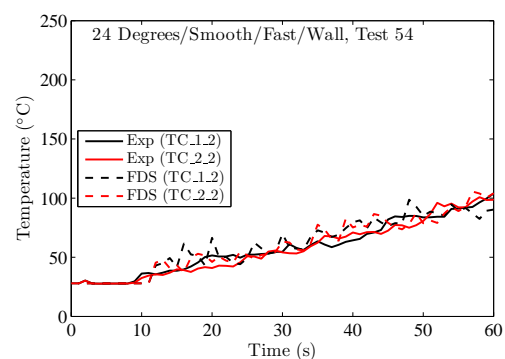
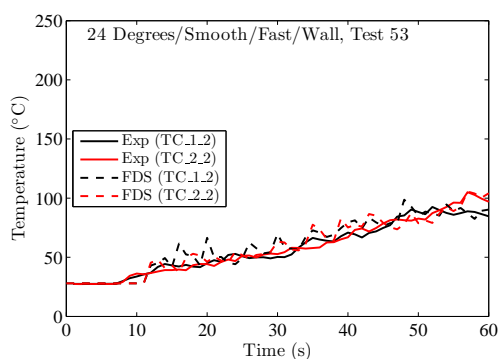
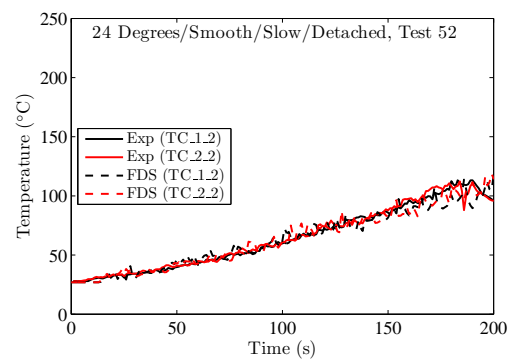
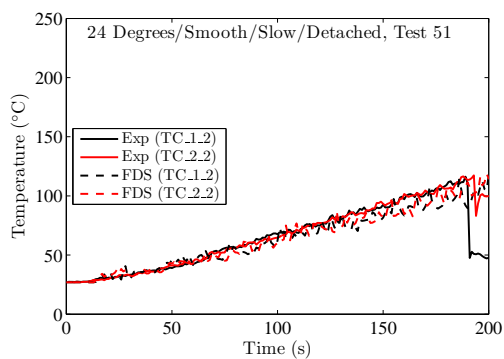
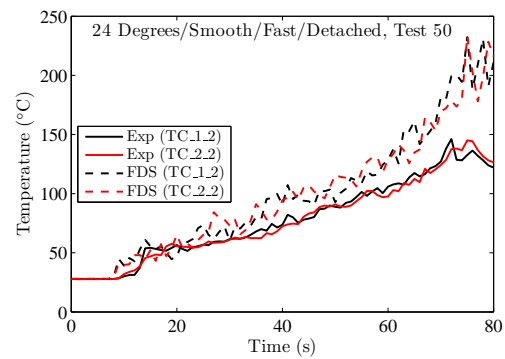
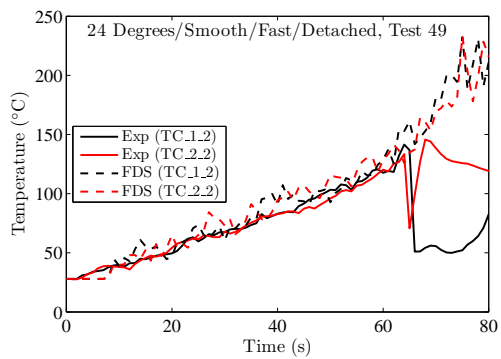


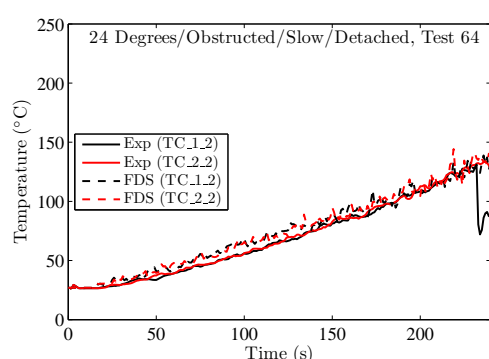
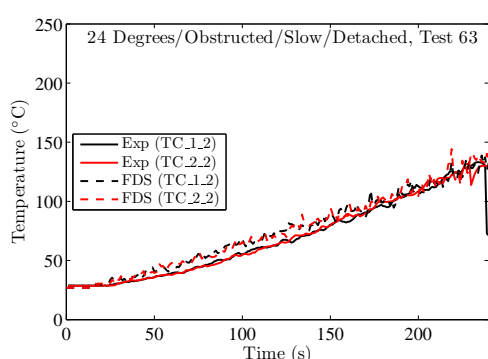
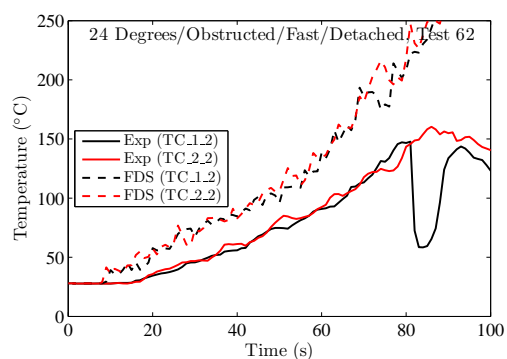
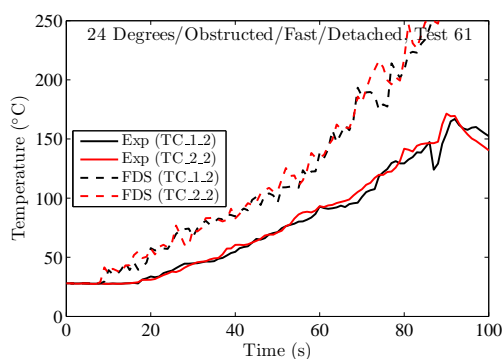
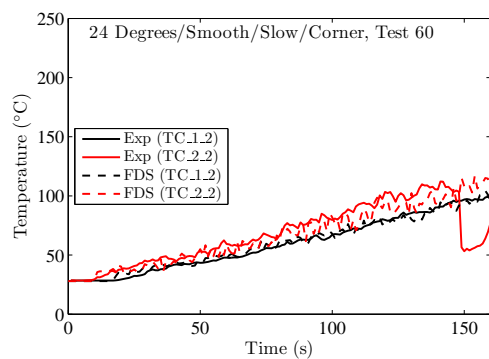
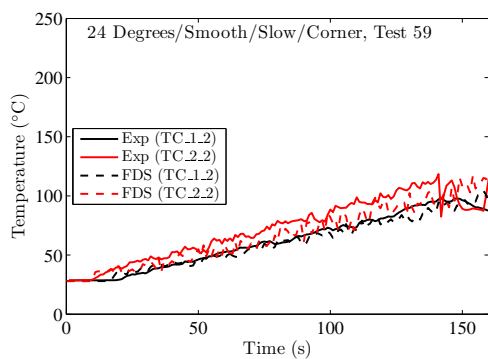
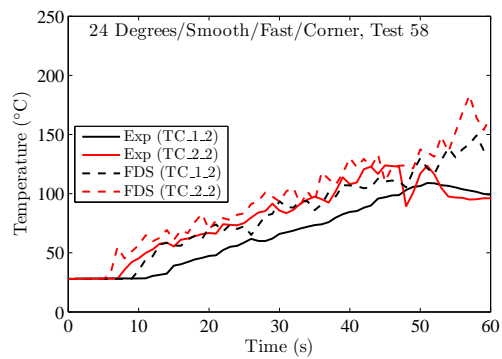
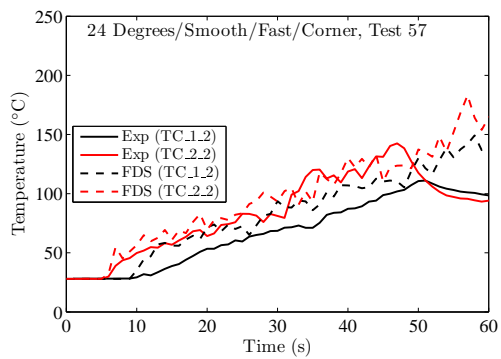


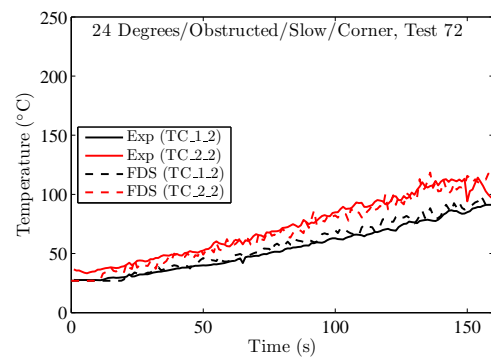
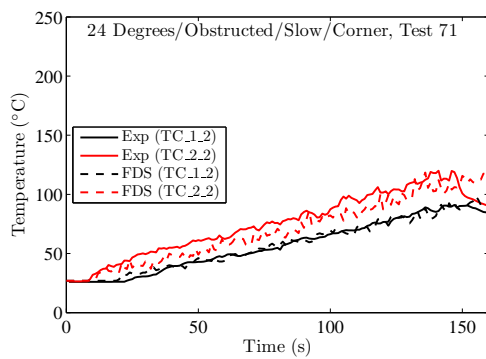
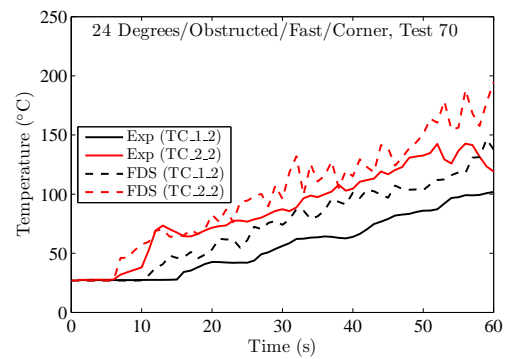
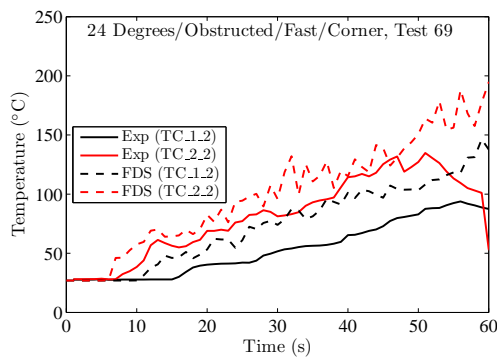
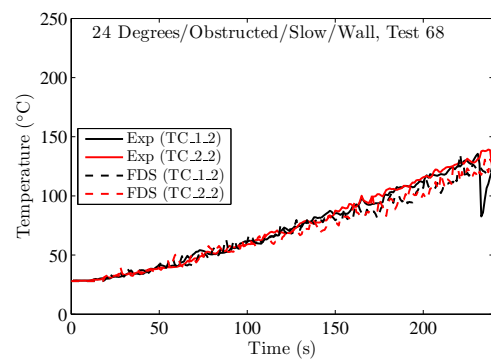
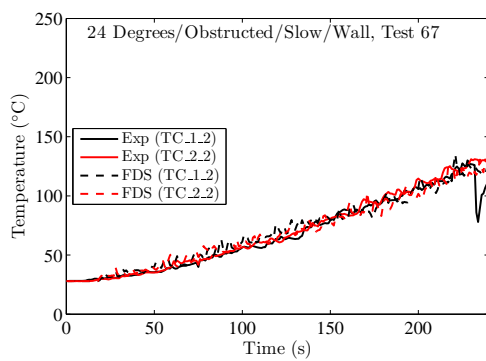
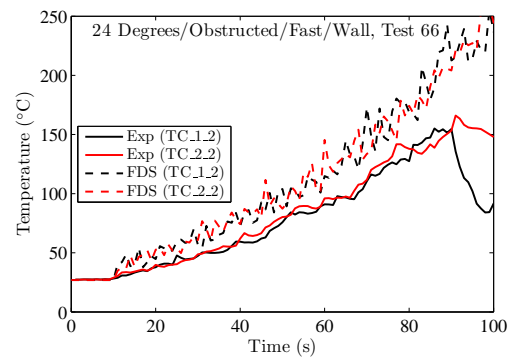
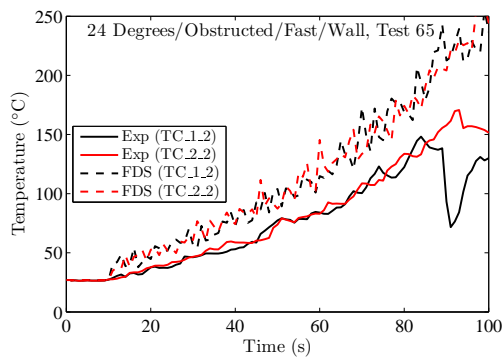












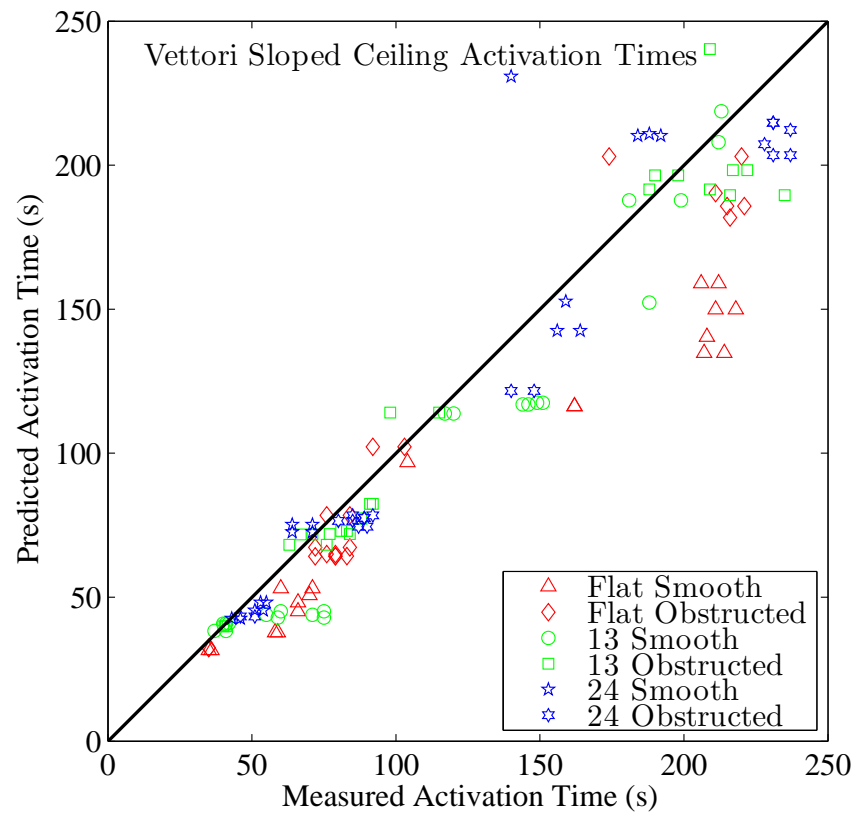


Figure 7.4: Predicted vs. Measured Activation Times of all the Vettori Sloped Ceiling Cases

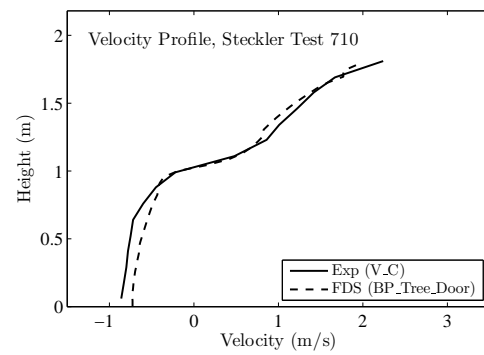
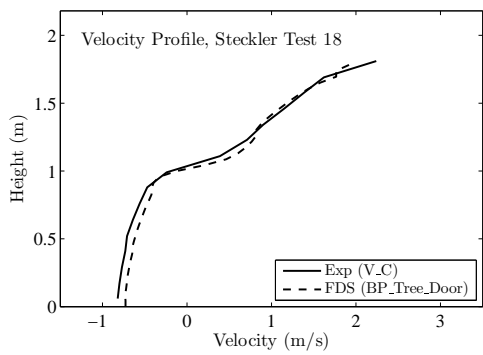
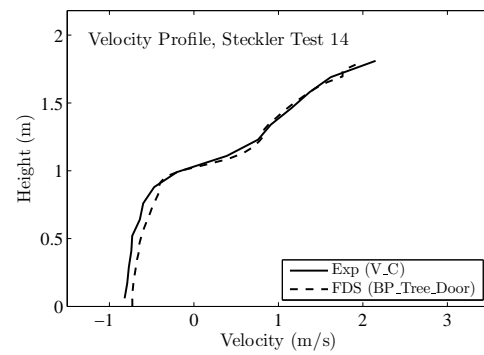
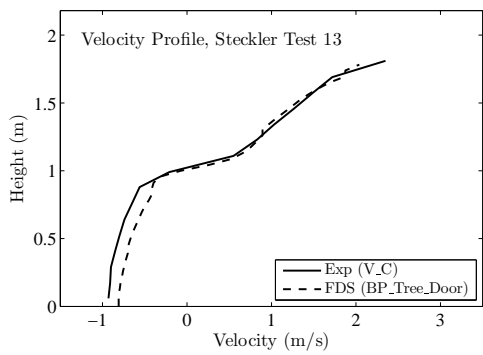
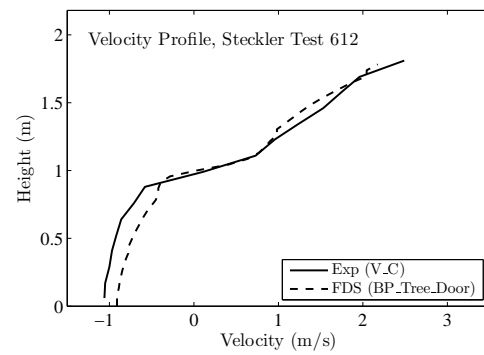
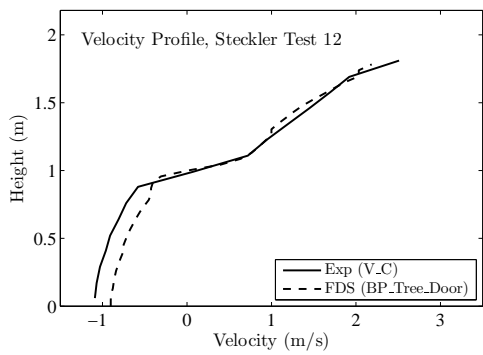
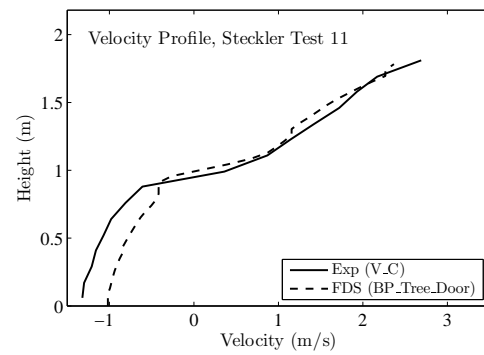
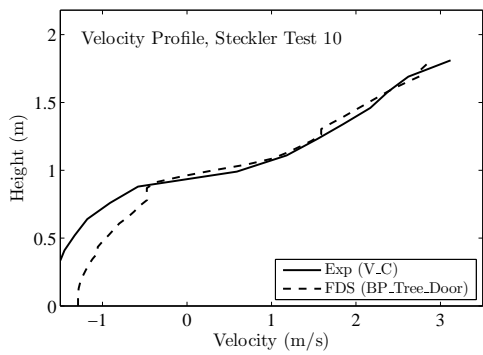
Chapter 8

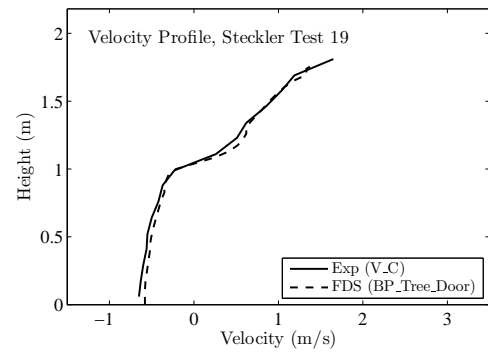
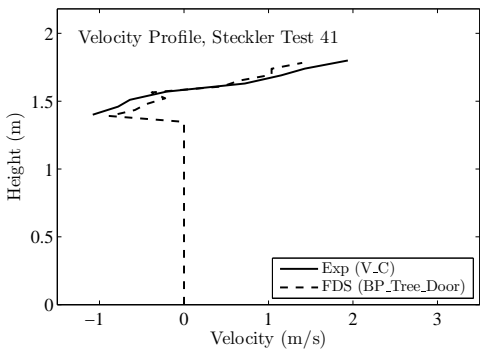
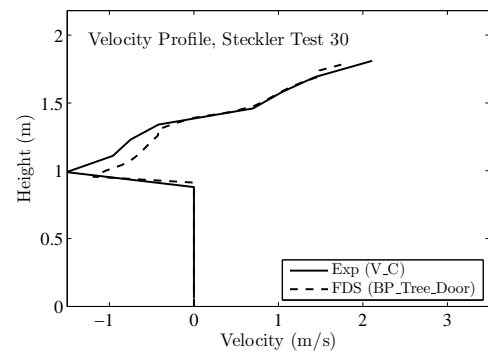
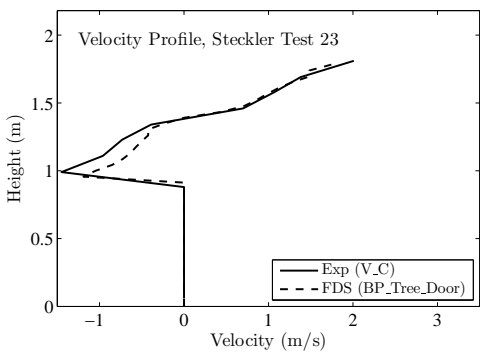
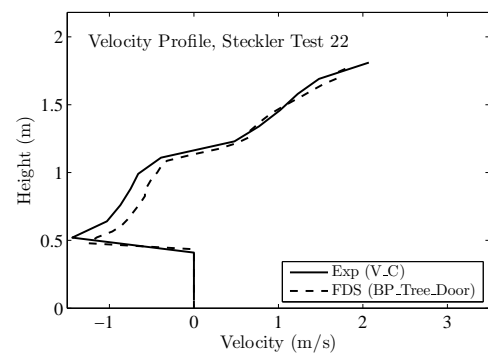
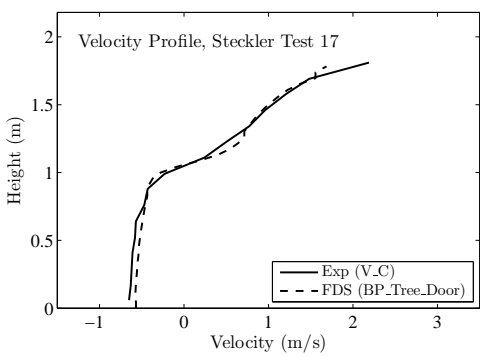
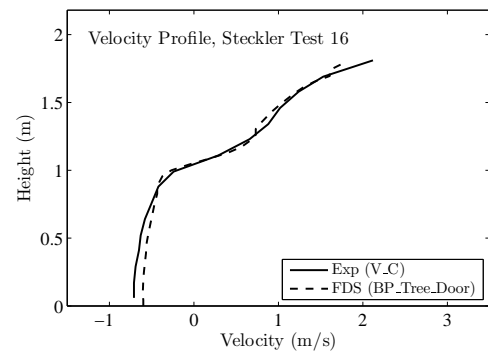
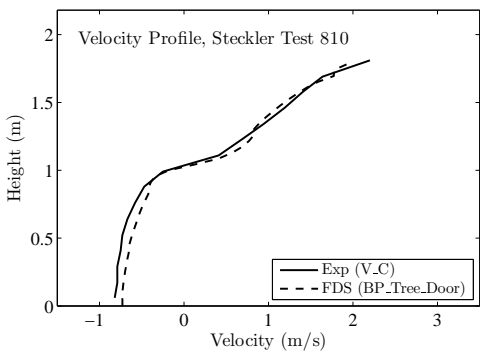
Gas Velocity

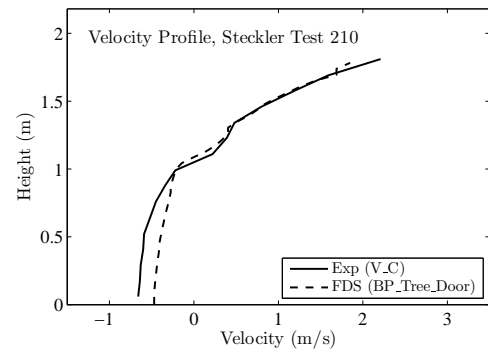
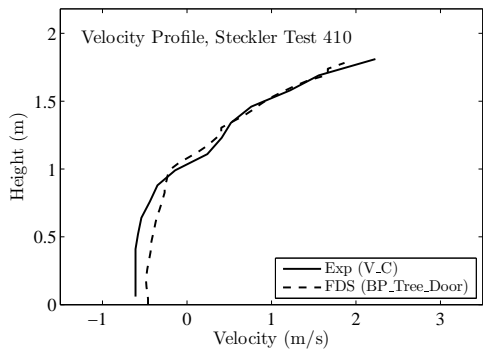
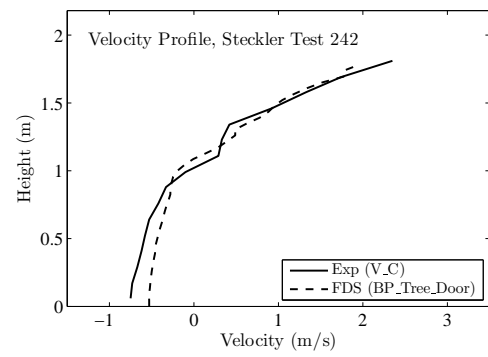
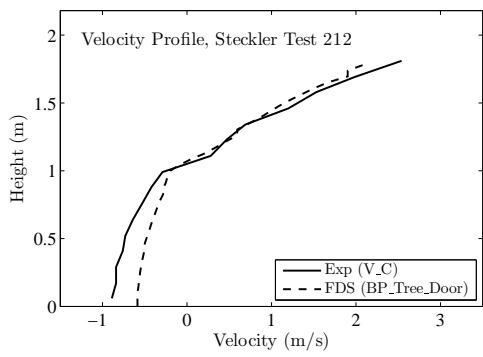
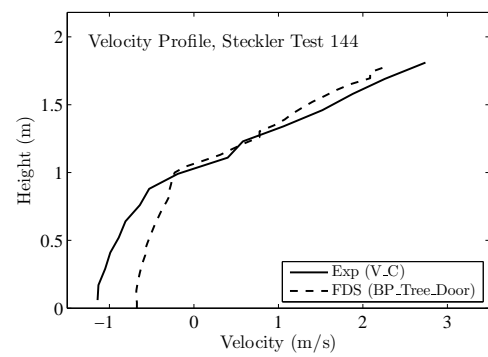
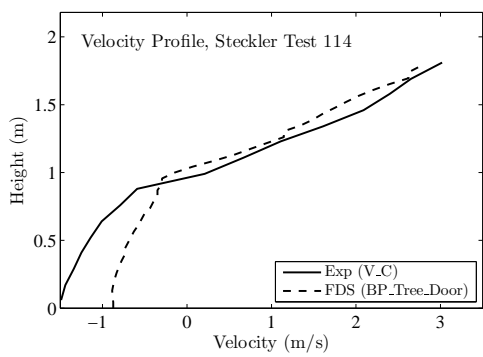
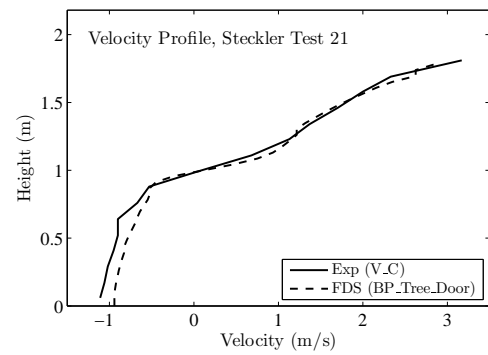
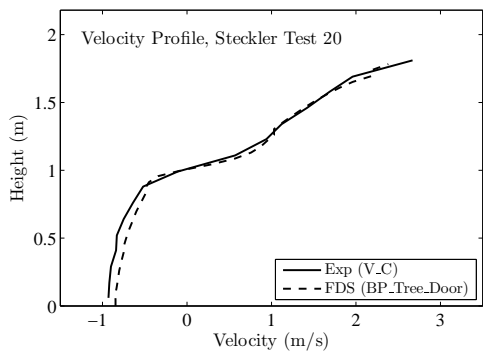
Gas velocity is often measured at compartment inlets and outlets as part of a global assessment of mass and energy conservation. This chapter contains measurements of gas velocity and related quantities.

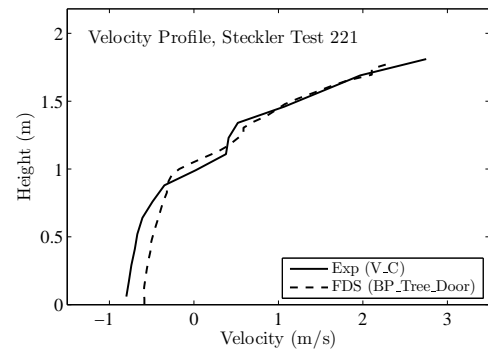
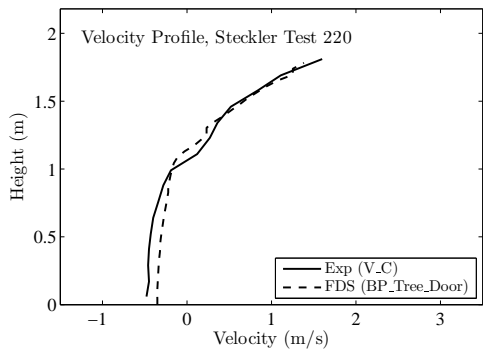
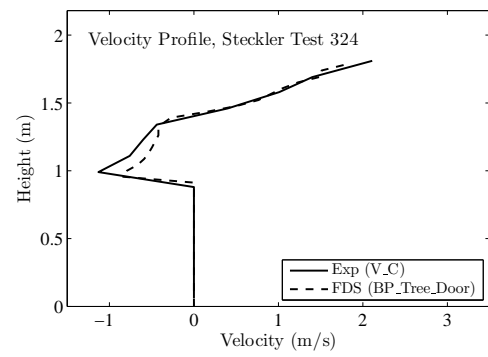
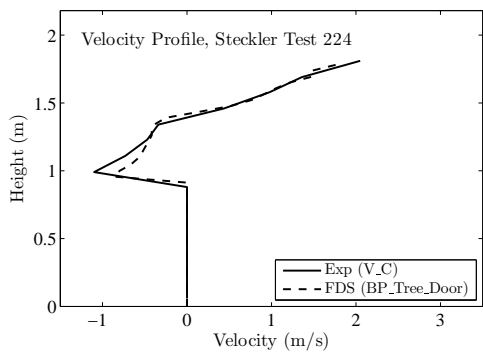
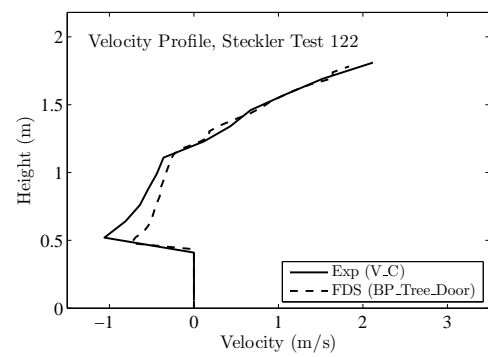
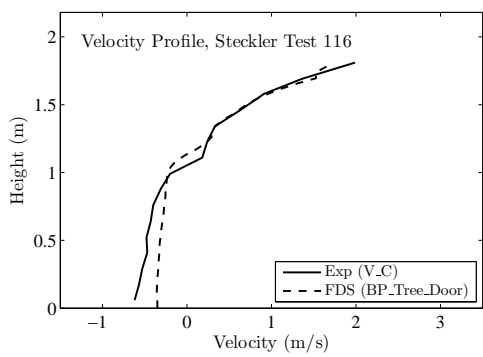
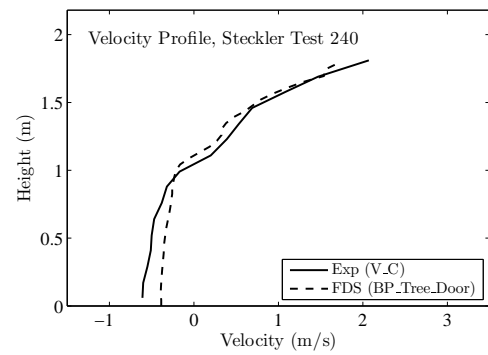
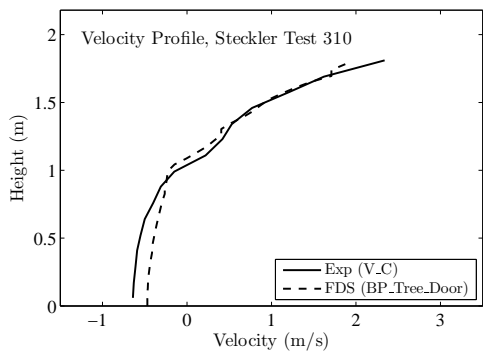
8.1 Steckler Compartment Doorway Velocity Profiles

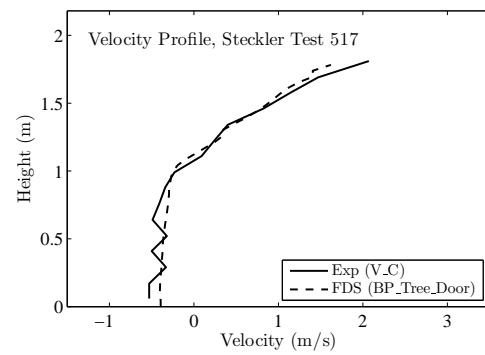
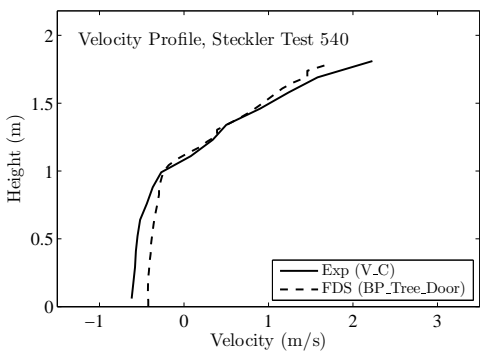
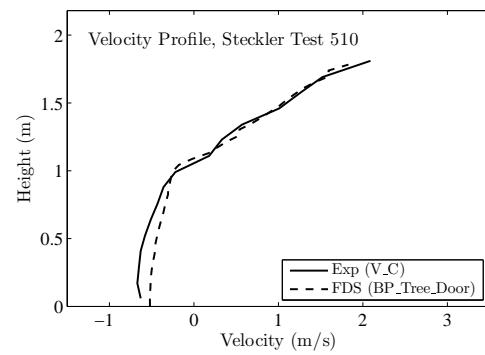
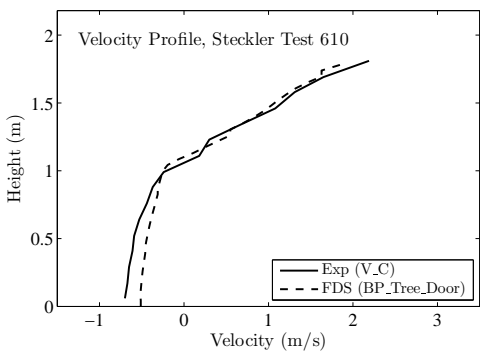
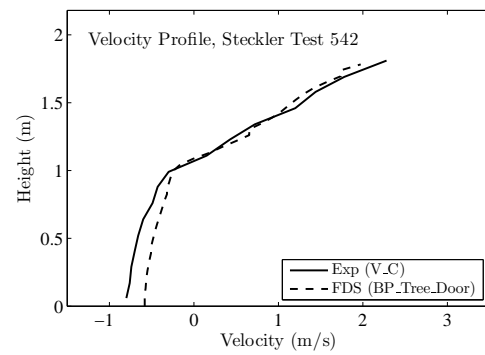
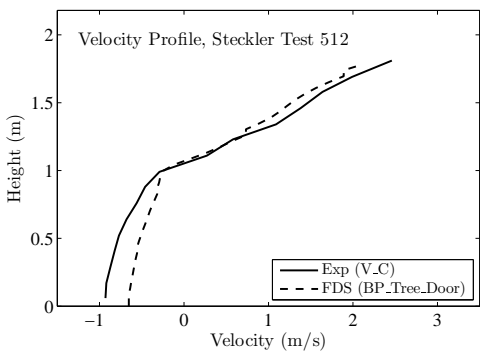
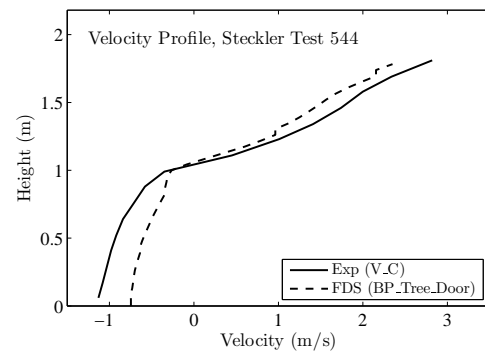
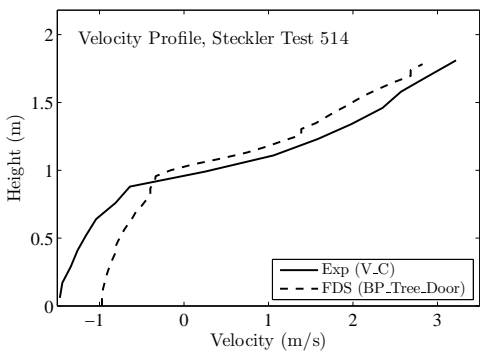
Steckler *et al.* [120] mapped the doorway/window flows in 55 compartment fire experiments. The test matrix is presented in Table 3.2. Shown on the following pages are the centerline profiles, compared with model predictions. Off-center profiles are not shown. The vertical spacing of the measurements was approximately 11 cm, with the uppermost velocity probe centered 5.7 cm below the 10 cm thick soffit. The FDS simulations were uniformly gridded with cells of 5 cm on each side. To quantify the difference between prediction and measurement, the maximum outward velocities, which always occurred at the uppermost measurement location, were compared. As can be seen in Fig. 8.1, the uppermost velocity measurement is under-predicted by FDS. It has been found that relatively minor changes in the velocity boundary conditions at the edges and bottom of the door soffit can have a noticeable impact on these results. It is believed that the resolution of the grid is not fine enough to capture the steep gradients in the velocity profile in the uppermost grid cell. Work is on-going to improve the situation.

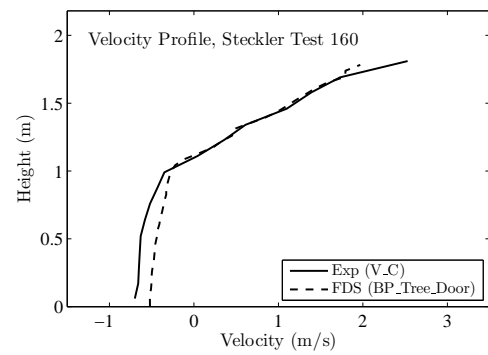
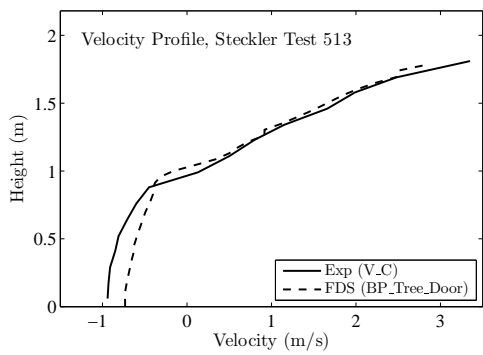
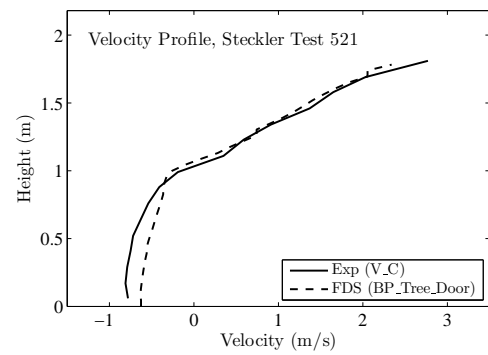
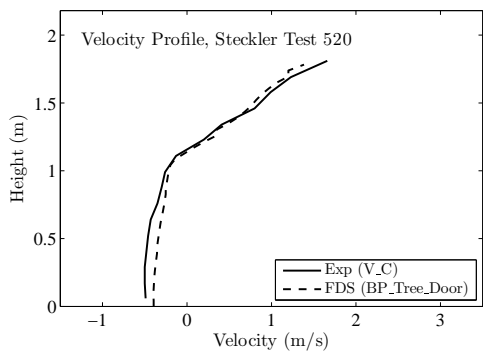
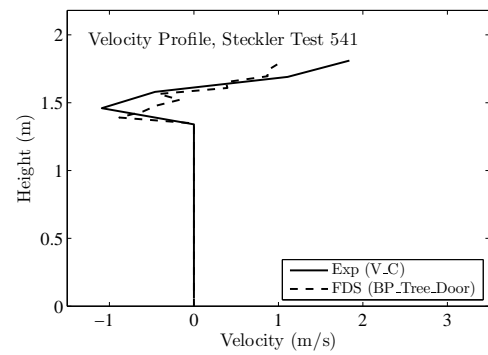
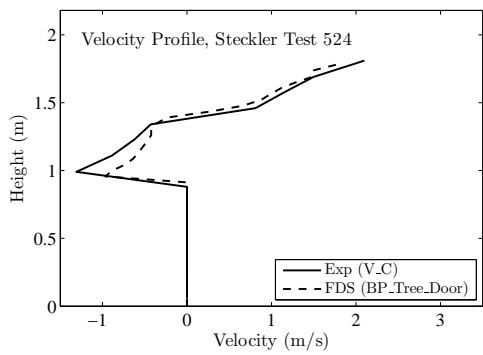
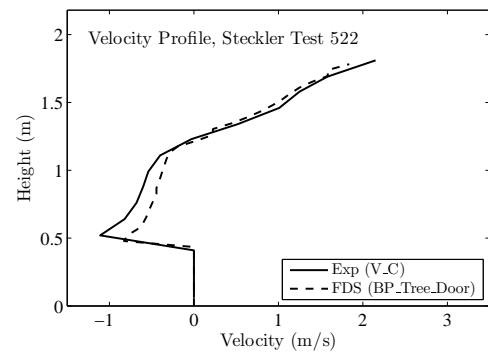
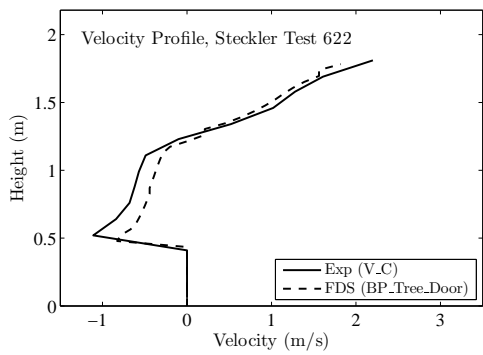


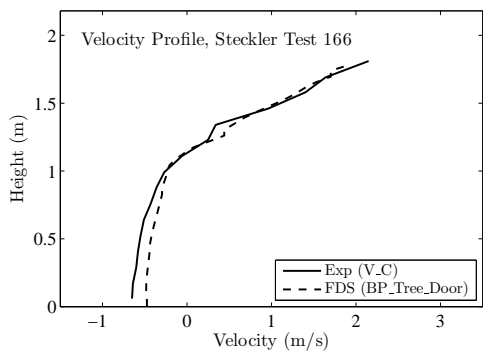
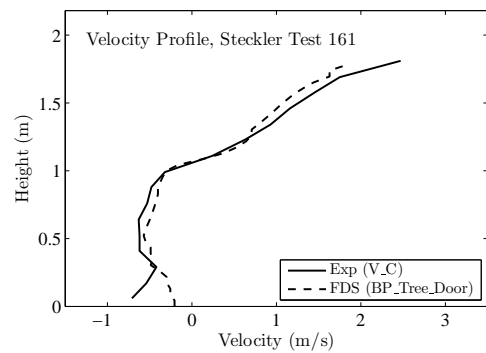
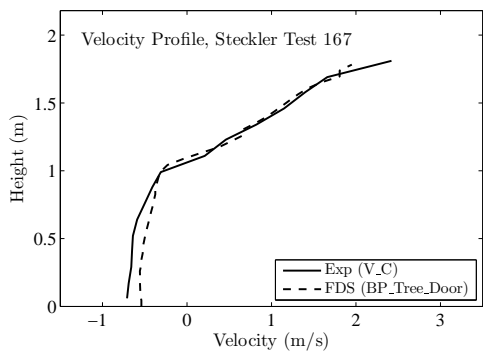
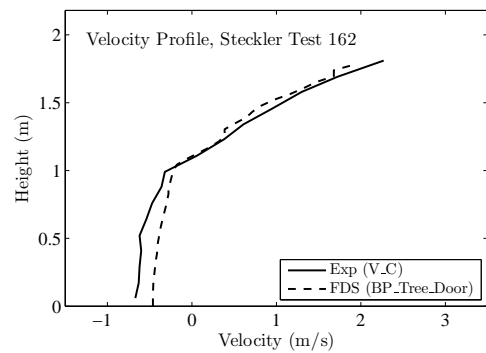
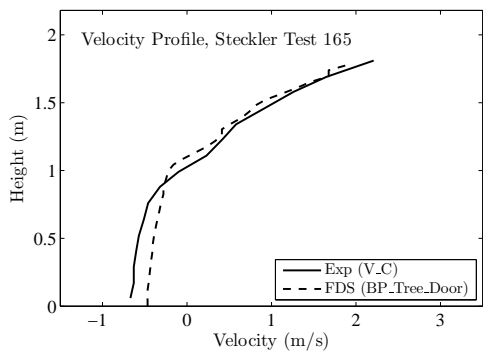
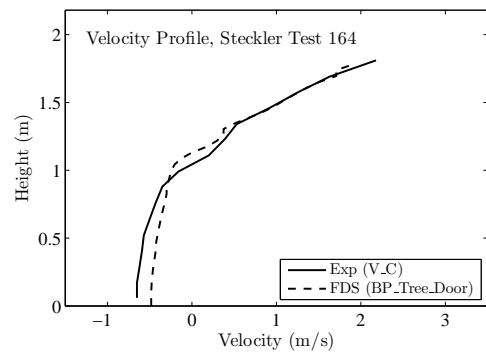
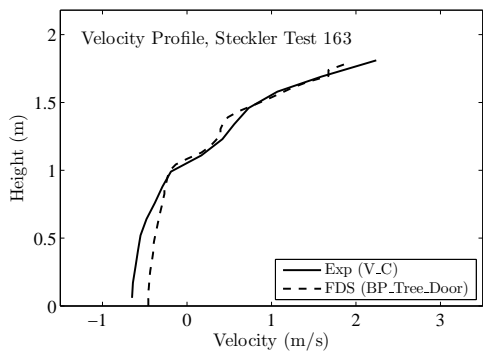












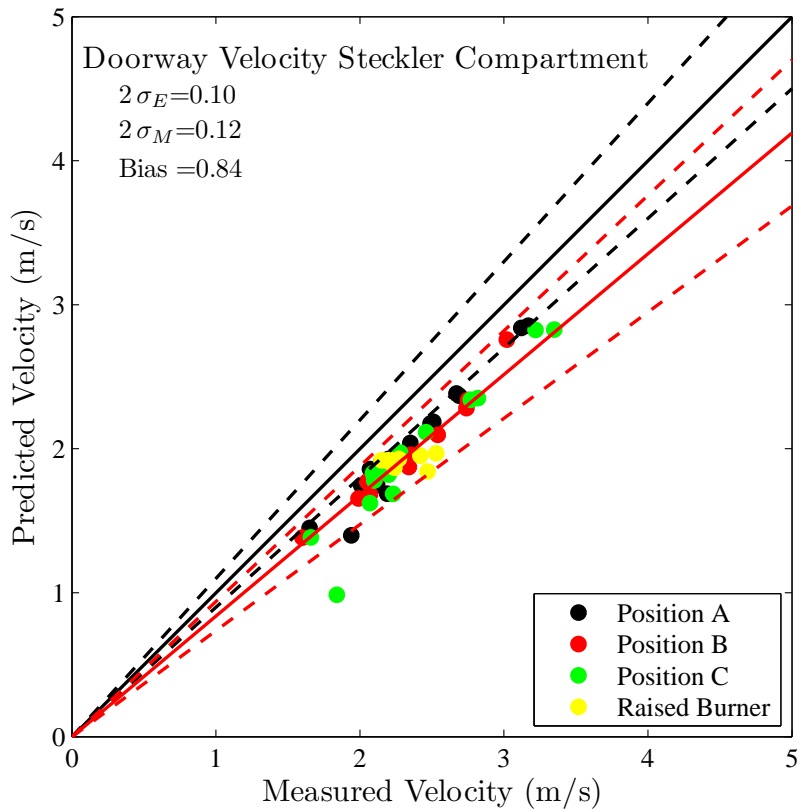
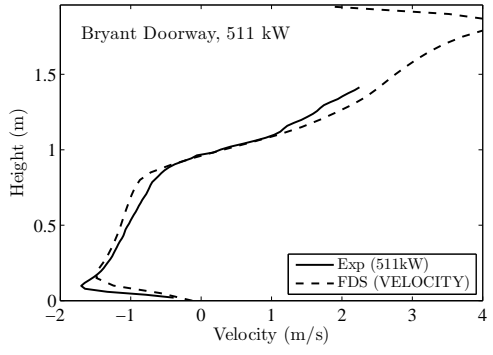
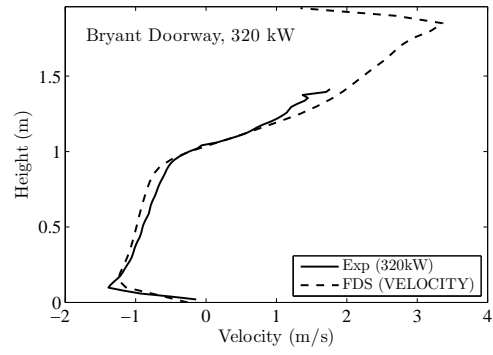
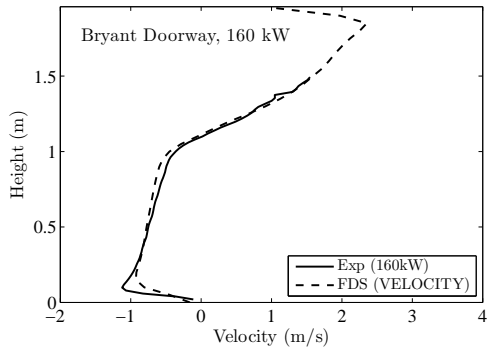
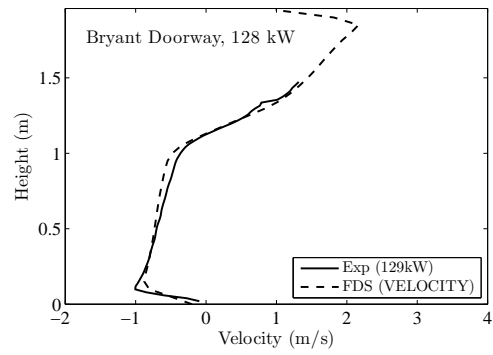
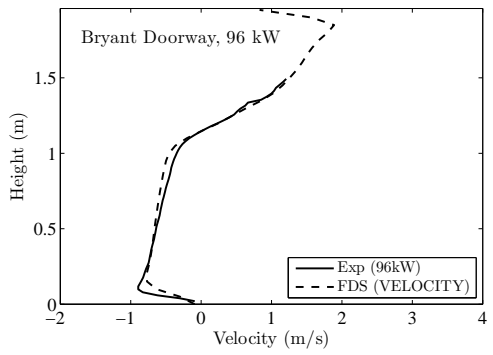
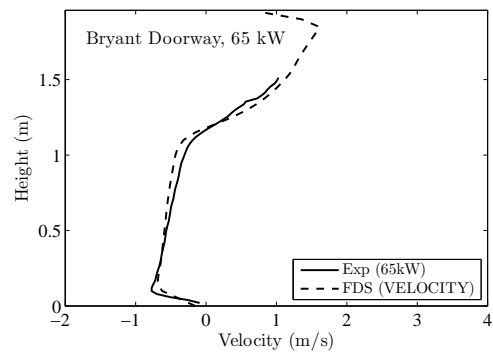
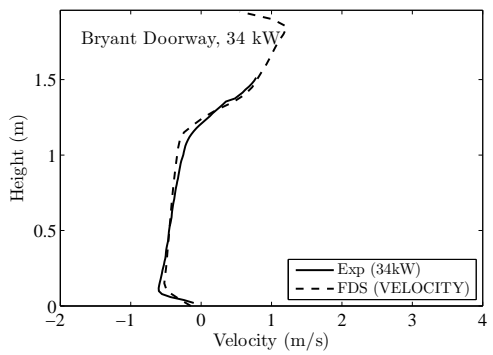


Figure 8.1: Summary of comparisons of predicted and measured maximum velocities in the doorway/window of the Steckler compartment experiments. The uncertainty in the measurements (dotted lines) were reported by Steckler to be about 10 %.

8.2 Bryant Doorway Experiments

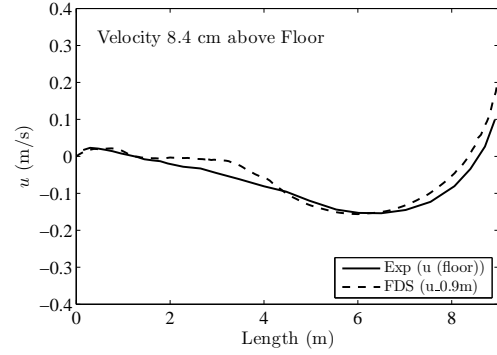
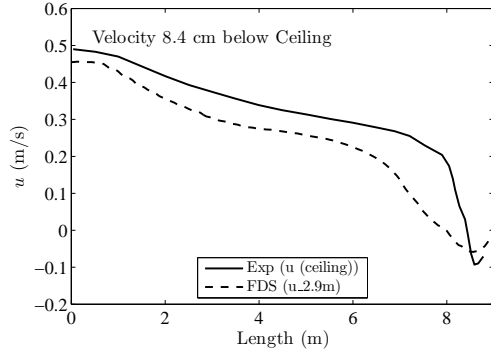
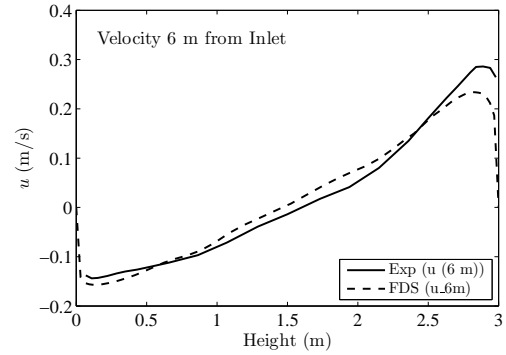
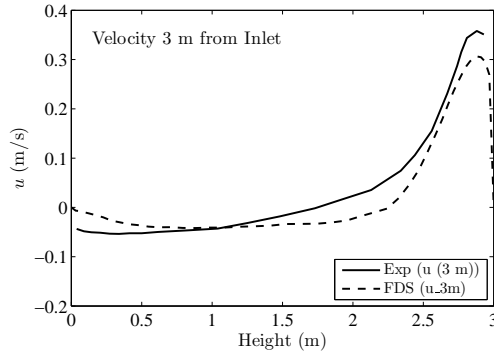
On the following page there are seven plots comparing the predicted and measured centerline velocity¹ profiles in a doorway of a standard ISO 9705 compartment. The measurements shown are based on PIV (Particle Image Velocimetry). Note that the measurements do not extend to the top of the doorway 1.96 m above the compartment floor because the heat from the fire prevented adequate laser resolution of the particles. Velocity measurements were also made using bi-directional probes [121], but these measurements were shown to be up to 20 % greater in magnitude than the comparable PIV measurement.

¹Note that the quantity that is being compared is the total velocity multiplied by the sign of its normal component.



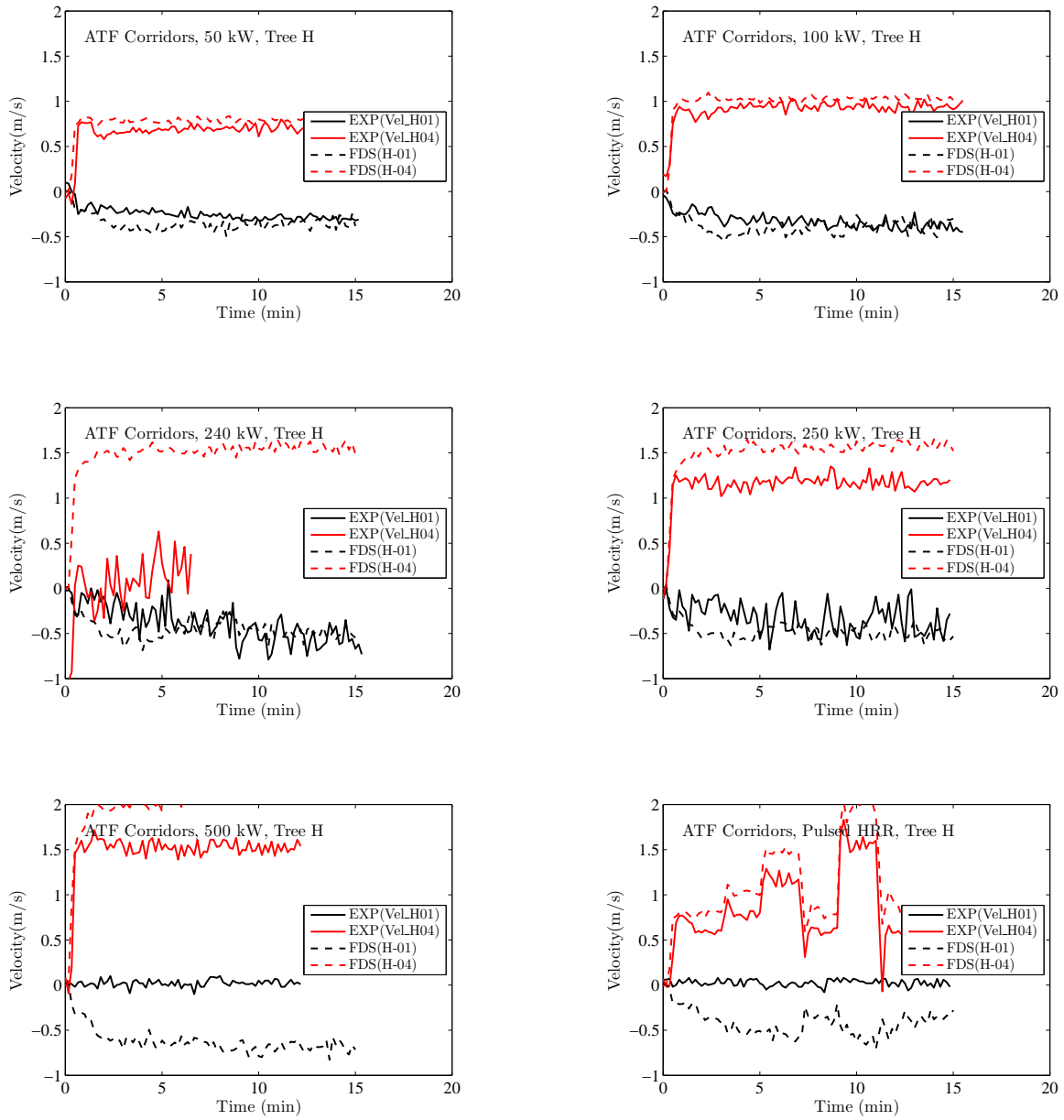
8.3 Restivo Experiment

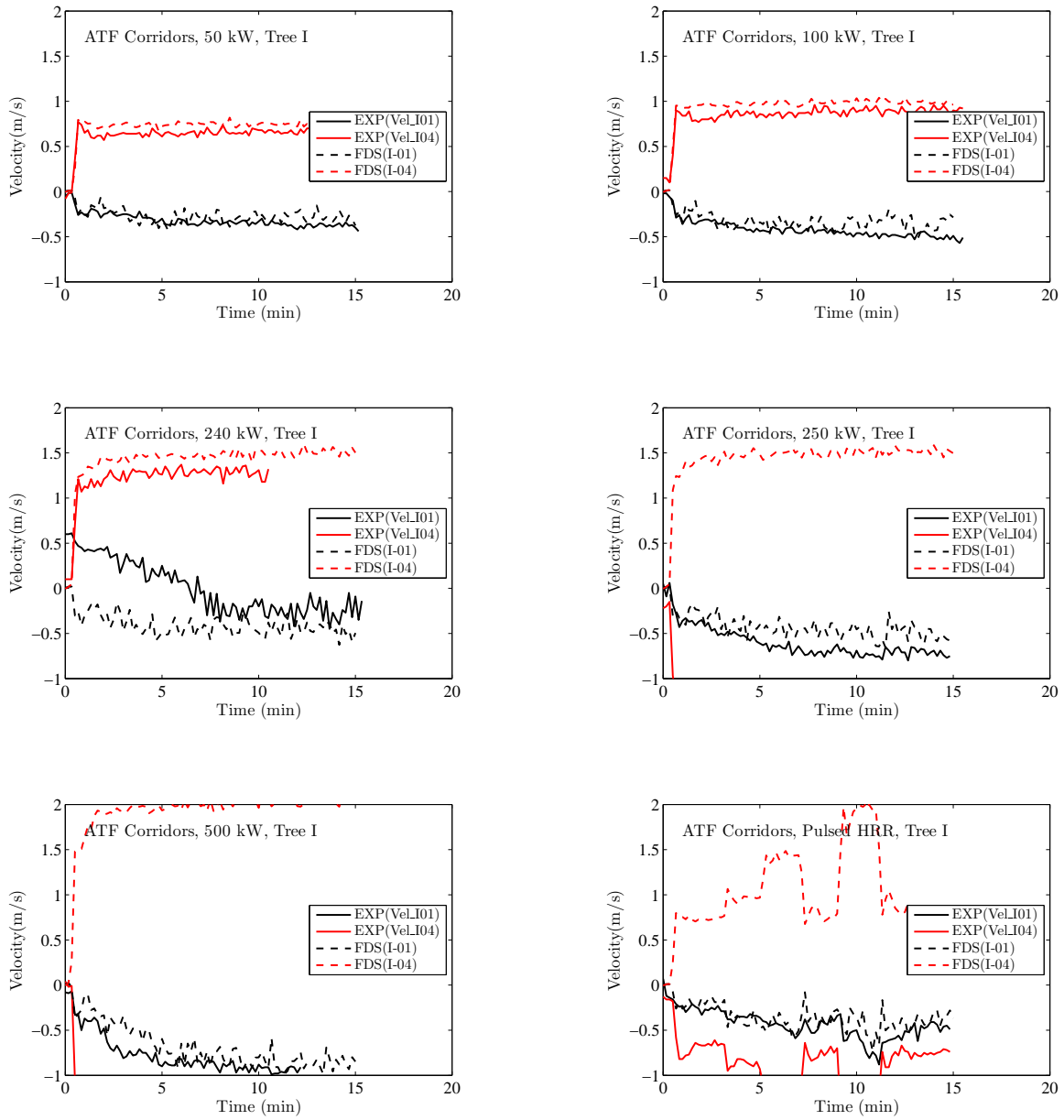
The results of a simulation of Restivo's room ventilation experiment are presented below. To capture the forced inlet flow, the volume near the supply slot needs a fairly fine grid to capture the mixing of air at the shear layer. For the results shown here, the height of the inlet was spanned with 6 grid cells, roughly 3 cm in the vertical dimension, 6 cm in the other two. Finer grids were used in the Musser study [35], but with no appreciable change in results. The component of velocity in the lengthwise direction was measured in four arrays: two vertical arrays located 3 m and 6 m from the inlet along the centerline of the room, and two horizontal arrays located 8.4 cm above the floor and below the ceiling, respectively. These measurements were taken using hot-wire anemometers. While data on the specific instrumentation used are not readily available, hot-wire systems tend to have limitations at low velocities, with typical thresholds of approximately 0.1 m/s.

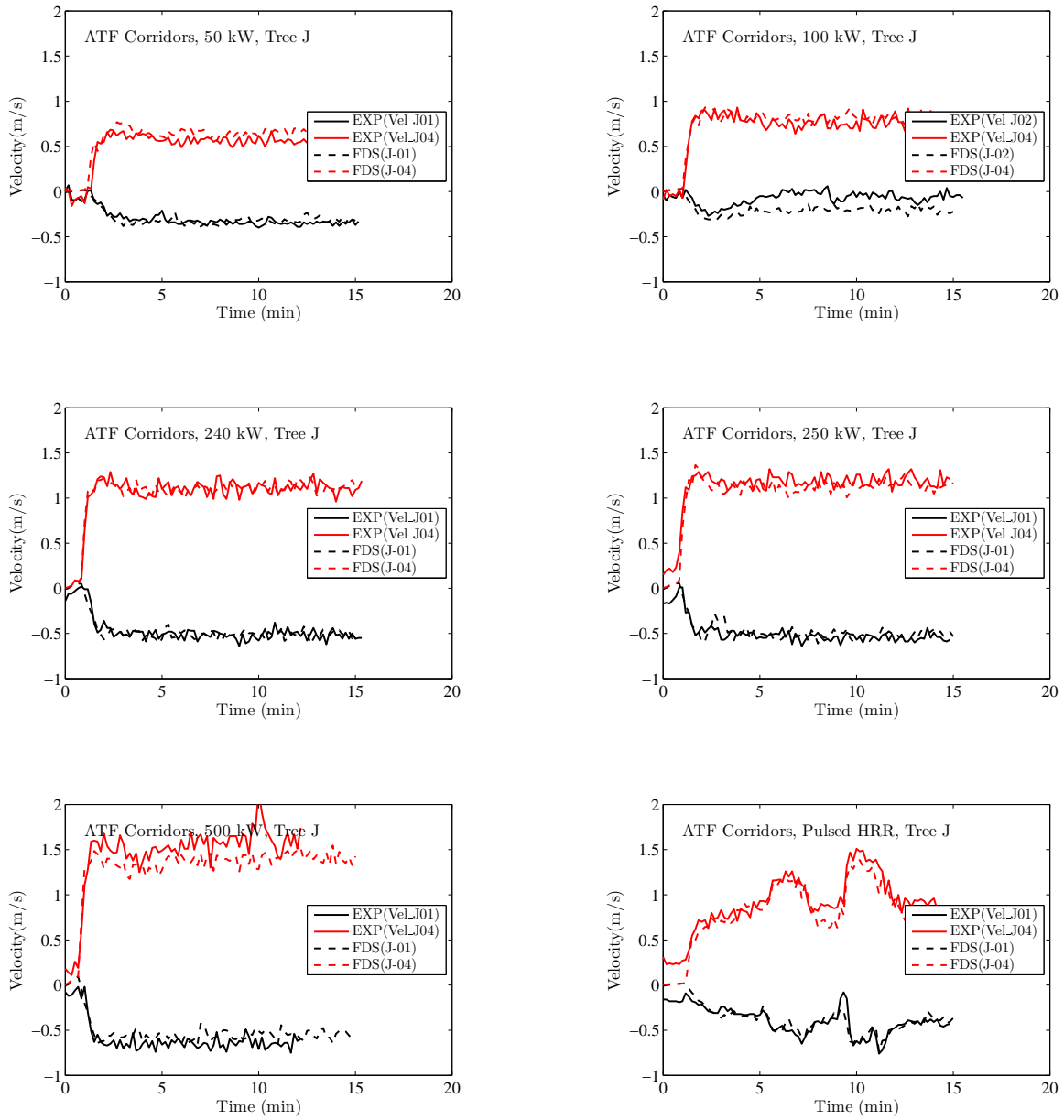


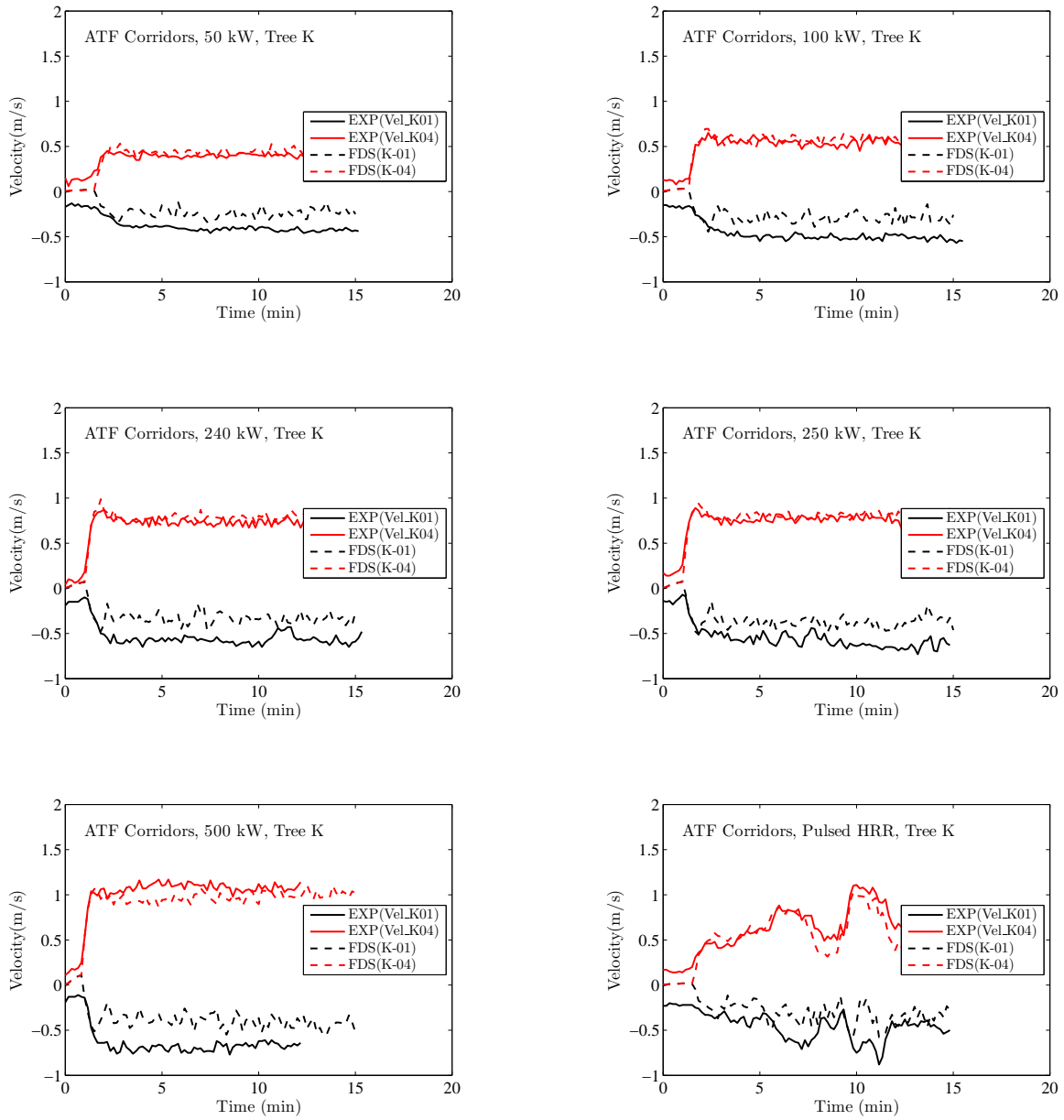
8.4 ATF Corridor

Comparisons of bi-directional velocity measurements with FDS predictions for the ATF Corridor experiments are presented on the following pages. Velocity measurements were made at four locations, two on the first level (Trees H and I) and two on the second level (Trees J and K). Shown are the upper-most and lower-most probe for each vertical array. Typically there were four probes per tree, with the number 1 indicating the upper-most probe.









Chapter 9

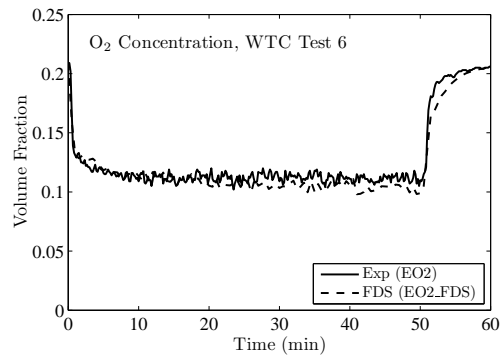
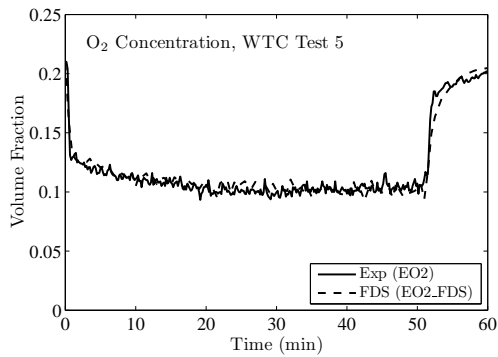
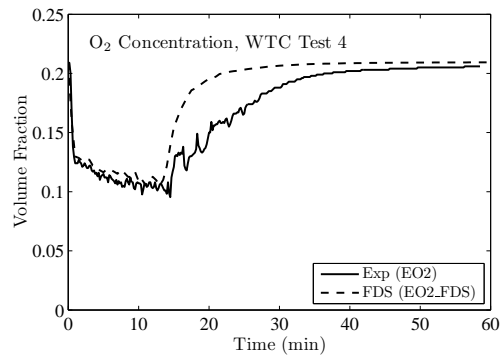
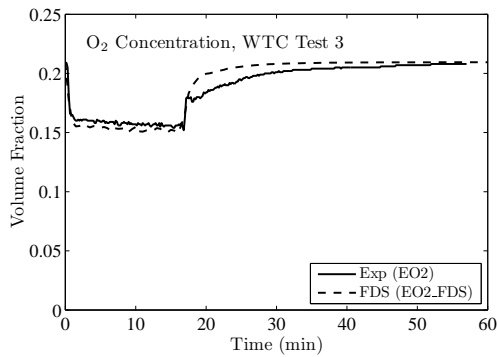
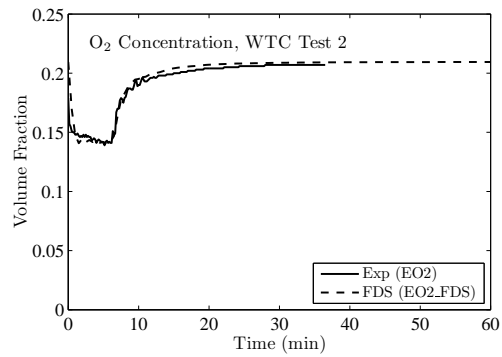
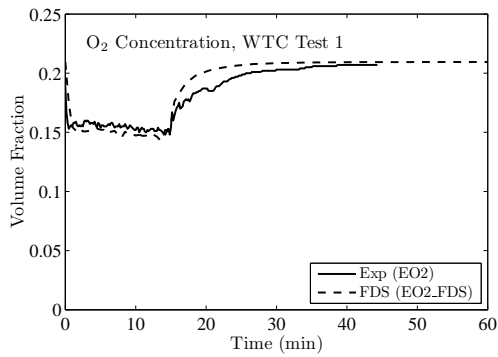
Gas Species and Smoke

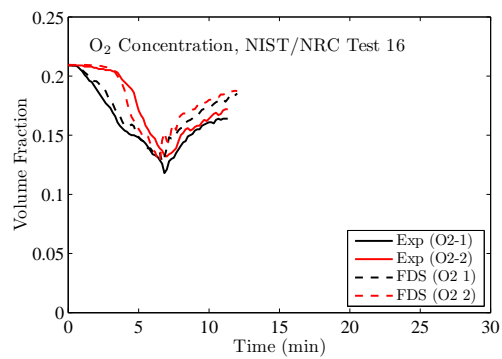
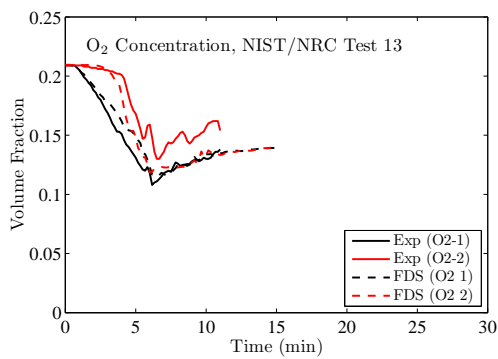
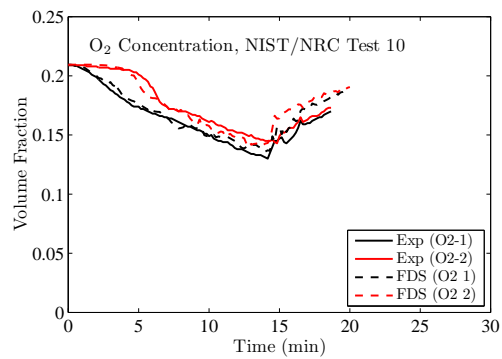
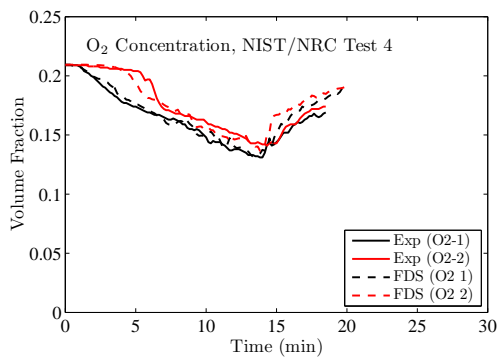
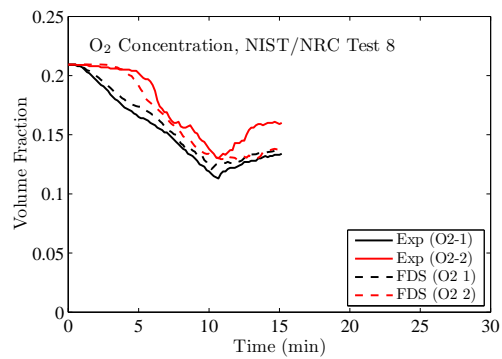
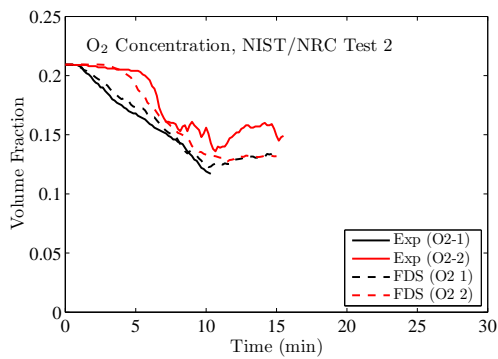
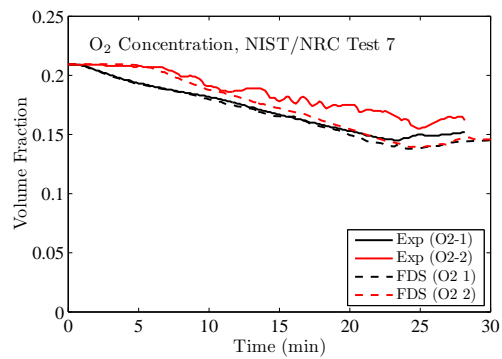
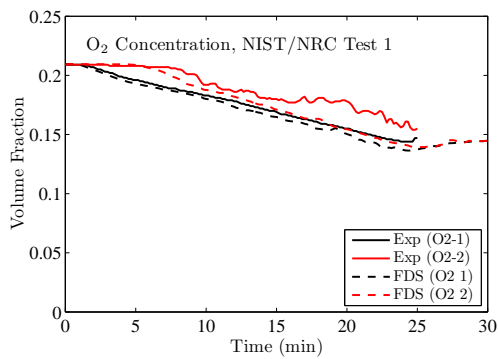
For most applications, FDS uses a single step chemical reaction whose products are tracked via a two-parameter mixture fraction model. The mixture fraction is a conserved scalar quantity that represents the mass fraction of one or more components of the gas at a given point in the flow field. By default, two components of the mixture fraction are explicitly computed. The first is the mass fraction of unburned fuel and the second is the mass fraction of burned fuel (i.e. the mass of the combustion products that originated as fuel). When the default model is used, O₂, CO₂ and smoke concentrations are obtained from the explicitly computed mixture fraction variables. Their yields are specified by the user and do not change.

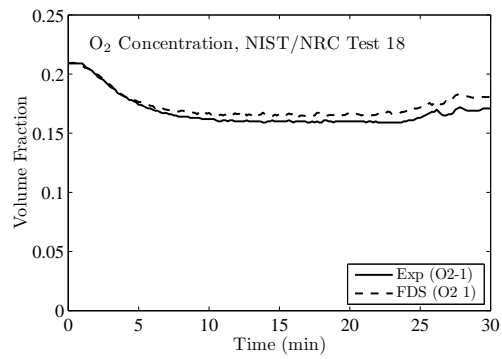
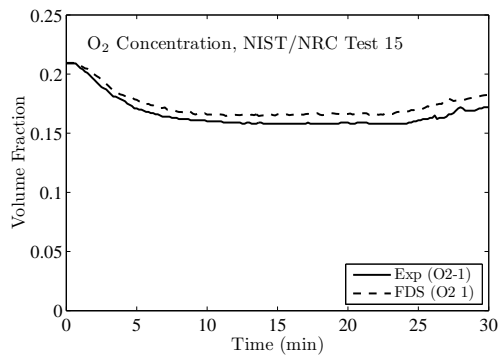
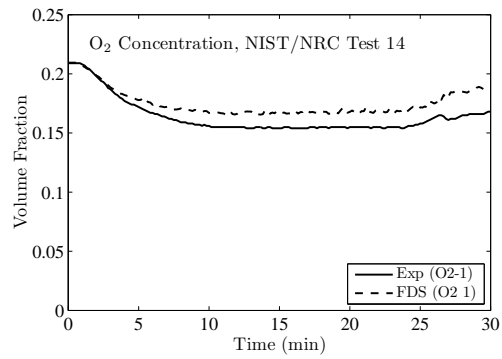
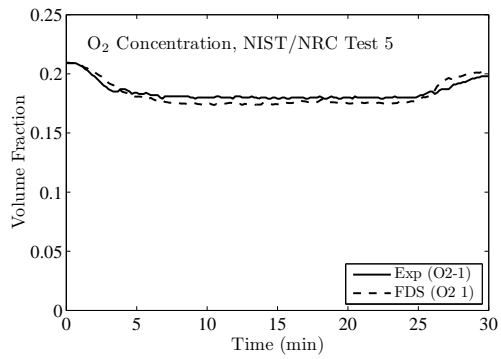
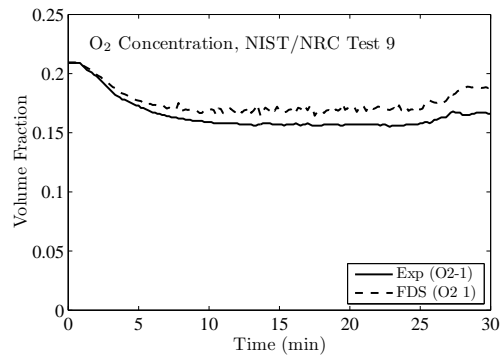
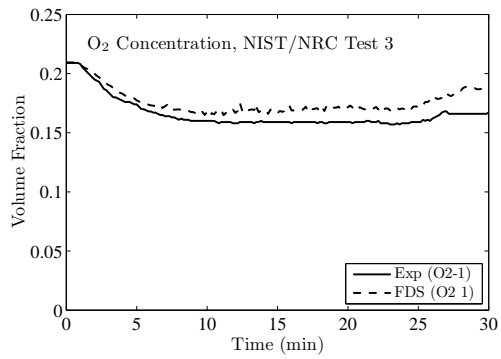
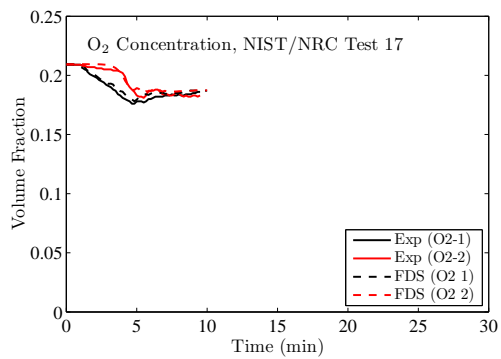
FDS has an optional two-step chemical reaction with a three parameter mixture fraction decomposition with the first step being oxidation of fuel to carbon monoxide and the second step the oxidation of carbon monoxide to carbon dioxide. The three mixture fraction components for the two step reaction are unburned fuel, mass of fuel that has completed the first reaction step, and the mass of fuel that has completed the second reaction step. The mass fractions of all of the major reactants and products can be derived from the mixture fraction parameters by means of “state relations.” Examples of this more detailed model can be found later in this chapter.

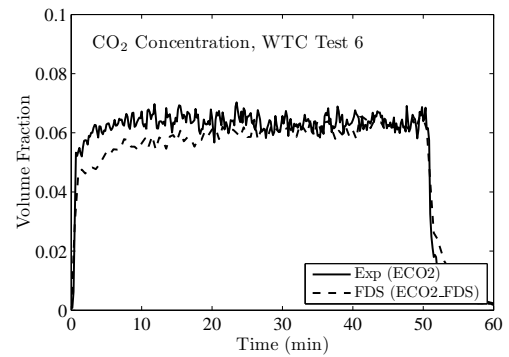
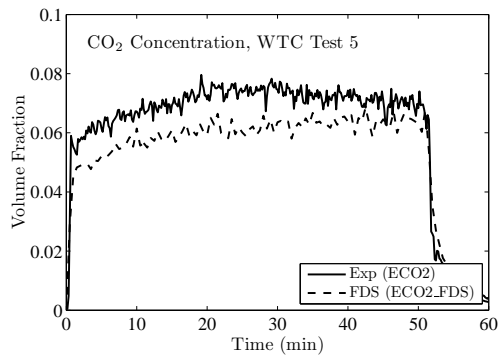
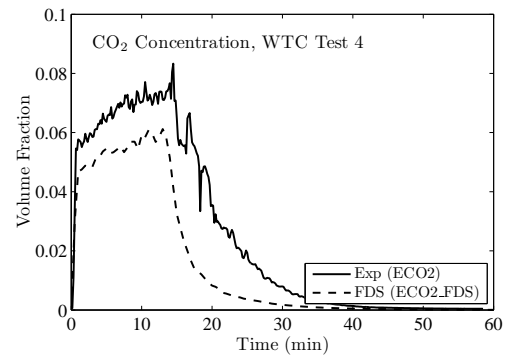
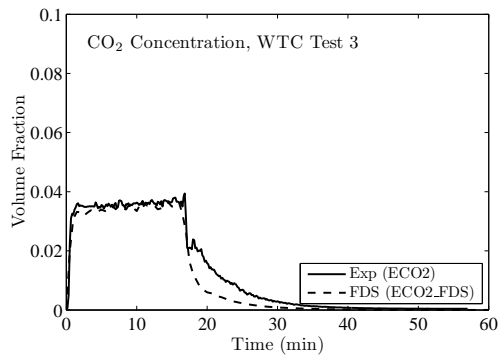
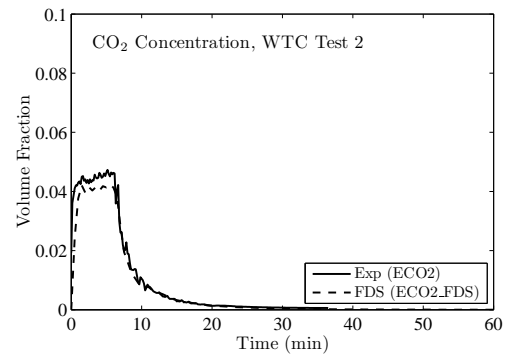
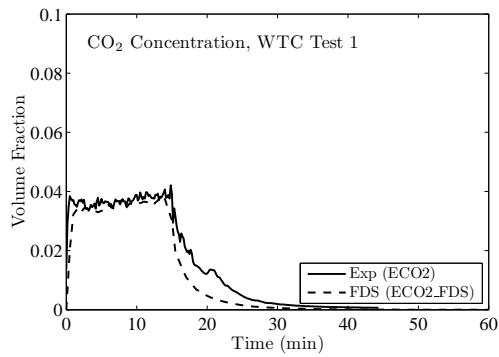
9.1 WTC and NIST/NRC Test Series, Oxygen and CO₂

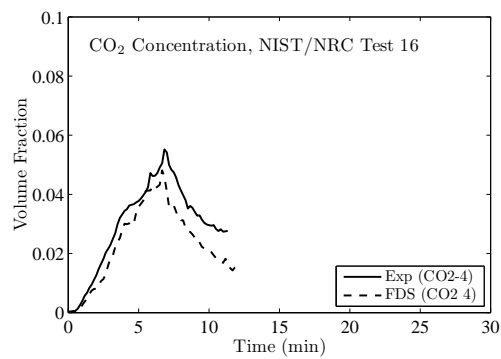
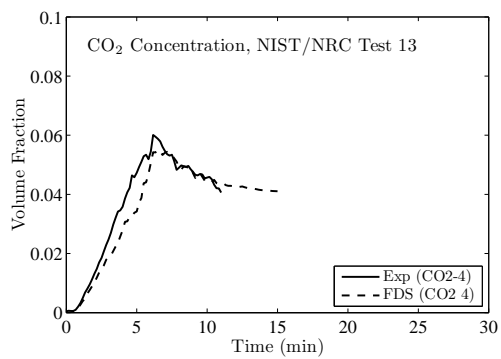
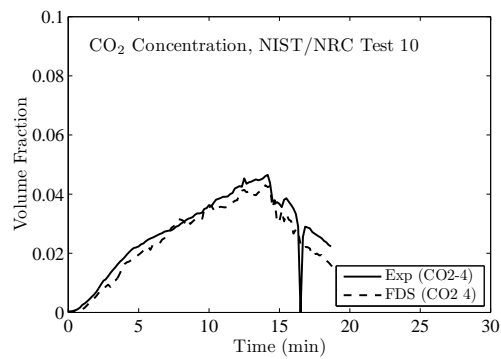
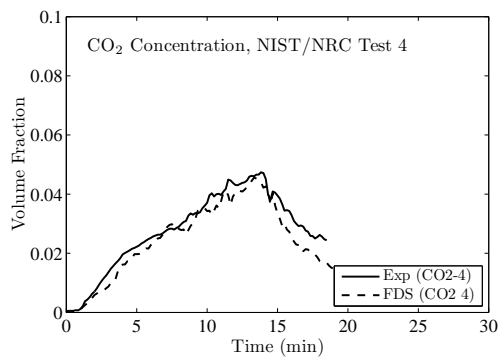
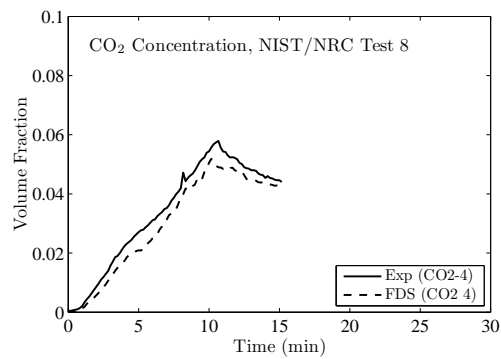
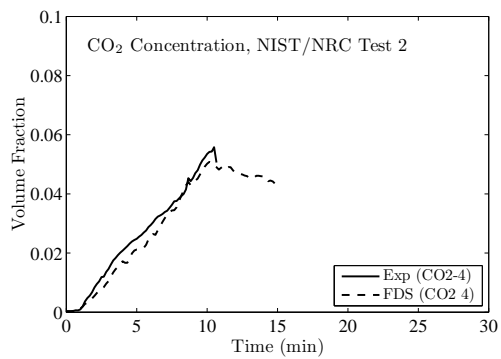
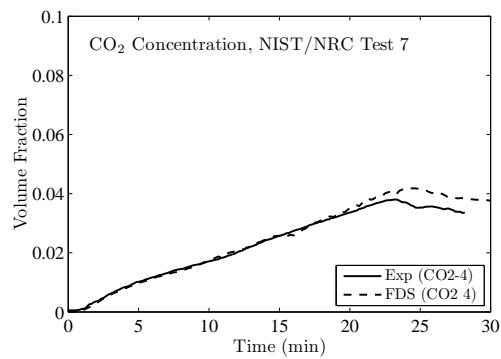
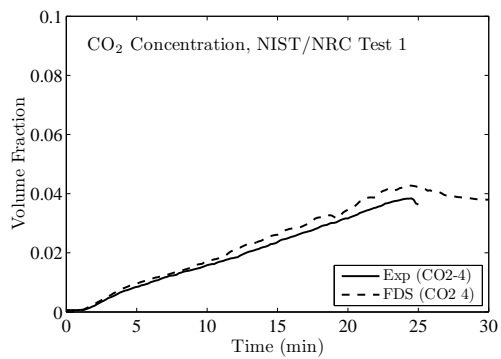
The following pages present comparisons of oxygen and carbon dioxide concentration predictions and measurements for the WTC and NIST/NRC series. In the WTC tests, there was only one measurement of each made near the ceiling of the compartment roughly 2 m from the seat of the fire. In the NIST/NRC tests, there were two oxygen measurements, one in the upper layer, one in the lower. There was only one carbon dioxide measurement in the upper layer.

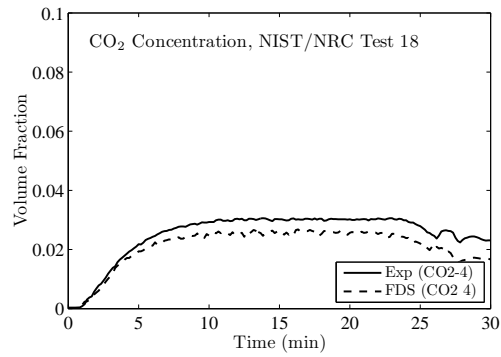
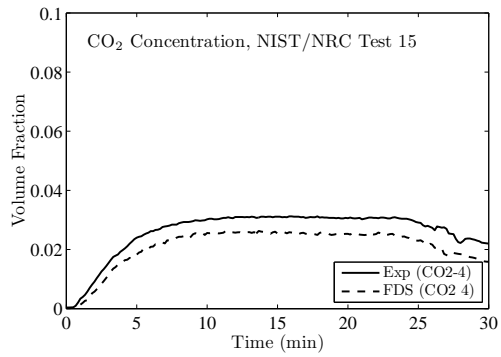
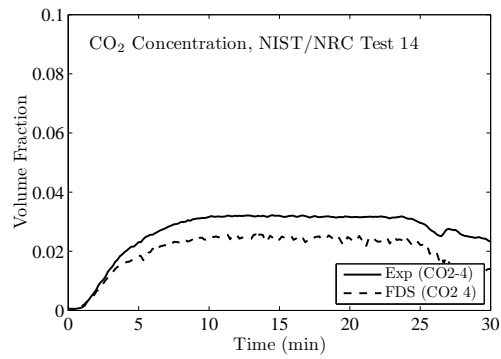
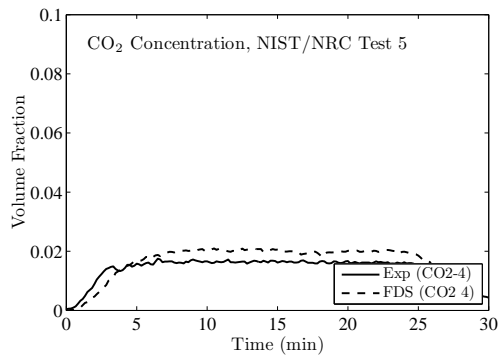
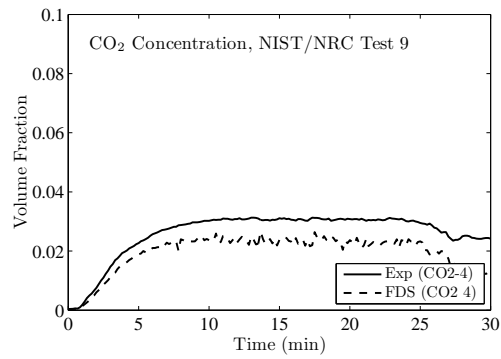
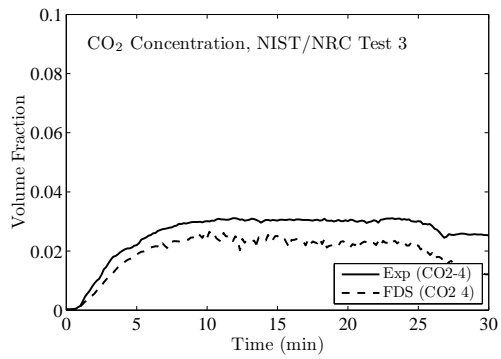
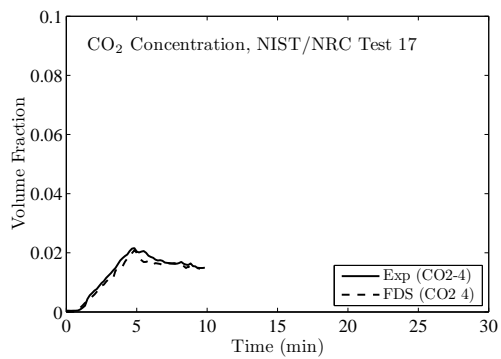












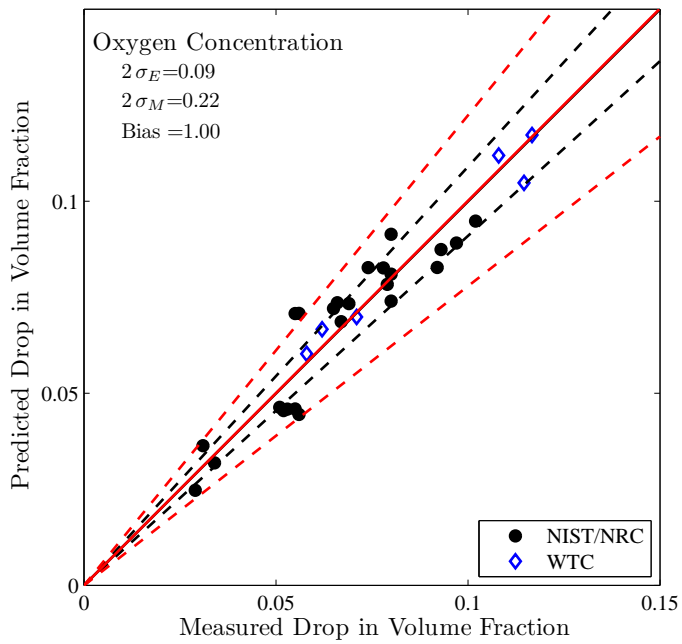
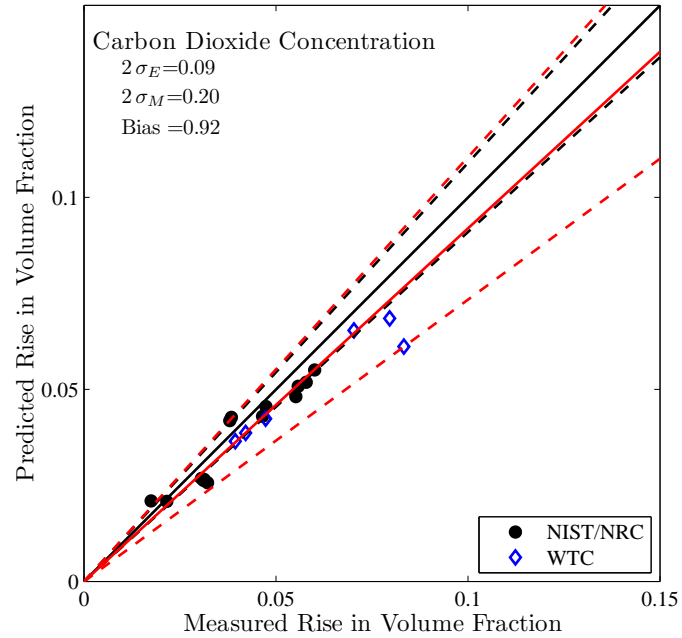
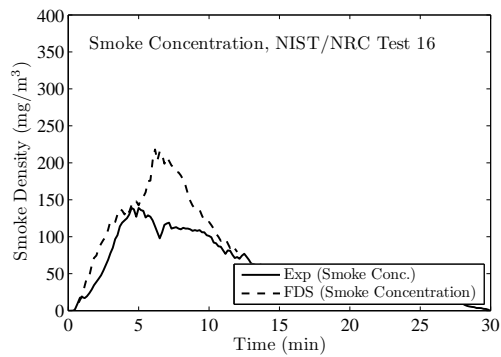
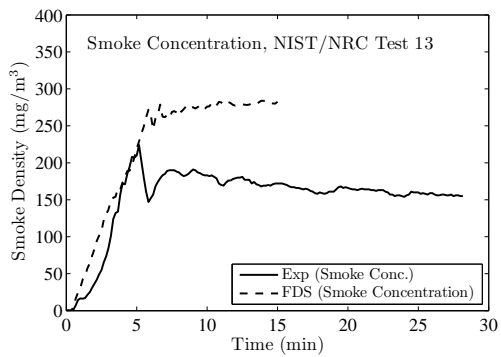
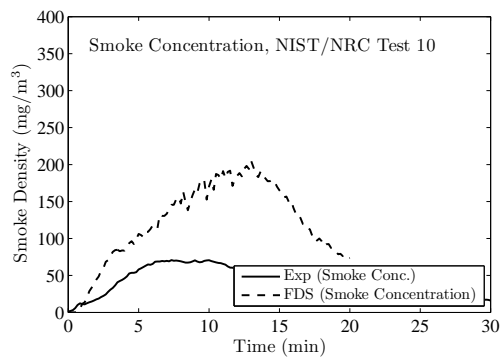
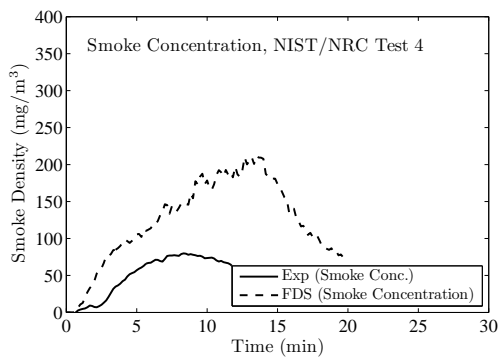
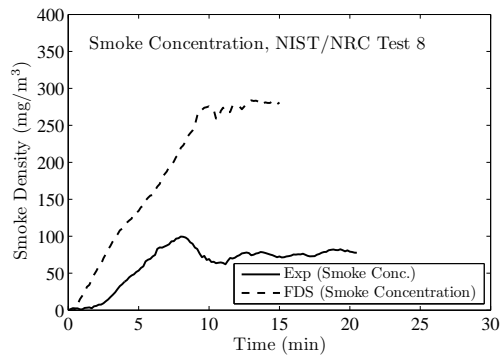
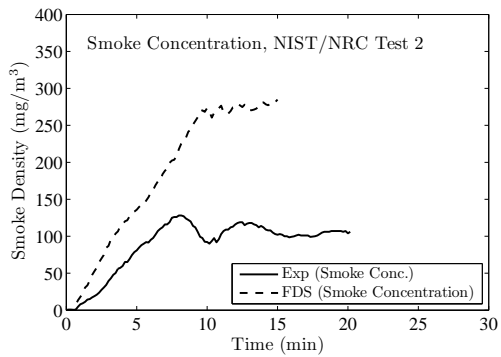
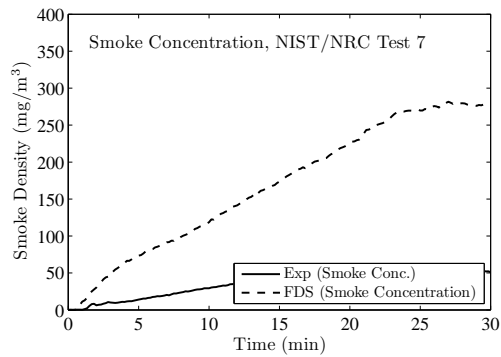
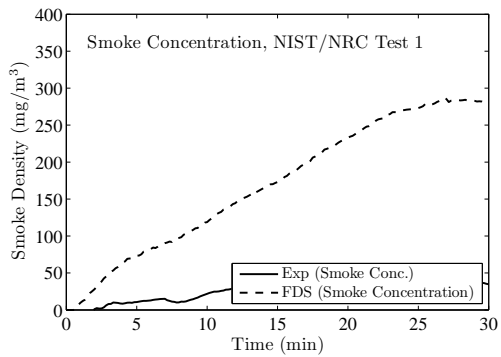
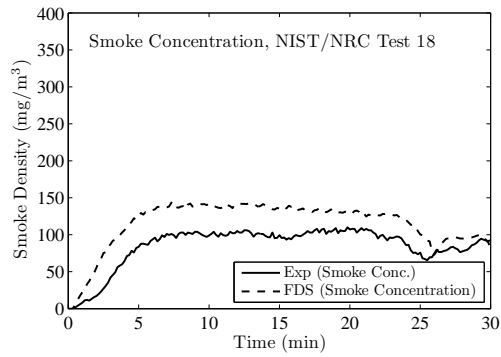
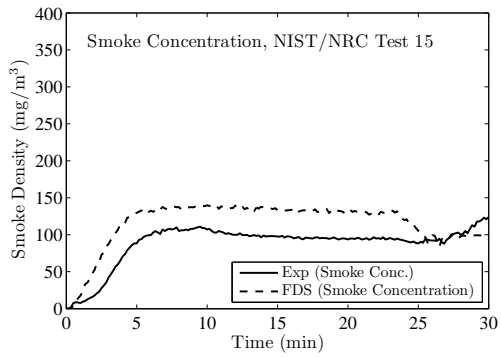
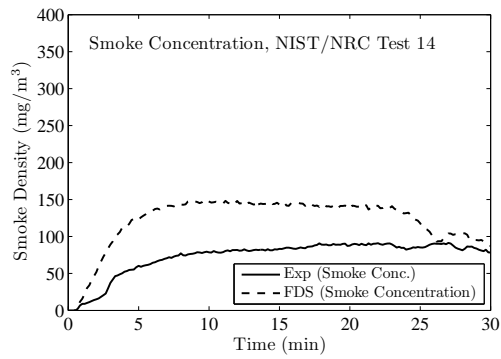
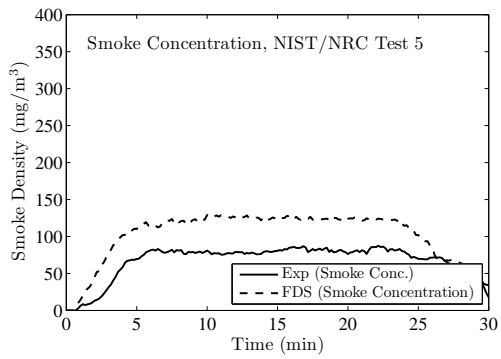
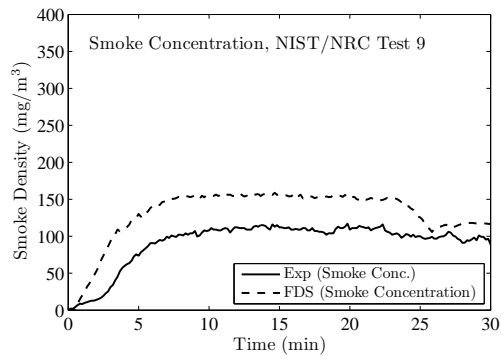
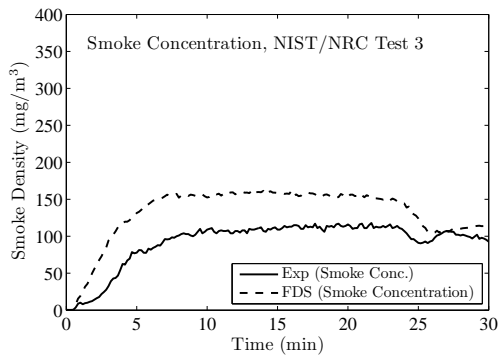
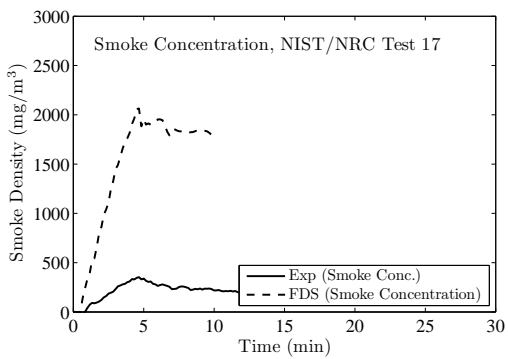


Figure 9.1: Summary of gas species predictions for the NIST/NRC and WTC test series.

9.2 NIST/NRC Test Series, Smoke

FDS treats smoke like all other combustion products, basically a tracer gas whose mass fraction is a function of the mixture fraction. To model smoke movement, the user need only prescribe the smoke yield, that is, the fraction of the fuel mass that is converted to smoke particulate. For the simulations of the NIST/NRC tests, the smoke yield is specified as one of the test parameters. The figures on the following pages contain comparisons of measured and predicted smoke concentration at one measuring station in the upper layer. There are two obvious trends in the figures: first, the predicted concentrations are about 50 % higher than the measured in the open door tests. Second, the predicted concentrations are roughly three times the measured concentrations in the closed door tests. As a contrast, Figure displays the time history of CO concentration for 6 of the NIST/NRC tests. Like smoke, the CO is specified in FDS via a fixed yield, measured along with smoke and reported in the test document. The large differences between model and measurement seen in the smoke data do not appear in the CO data.





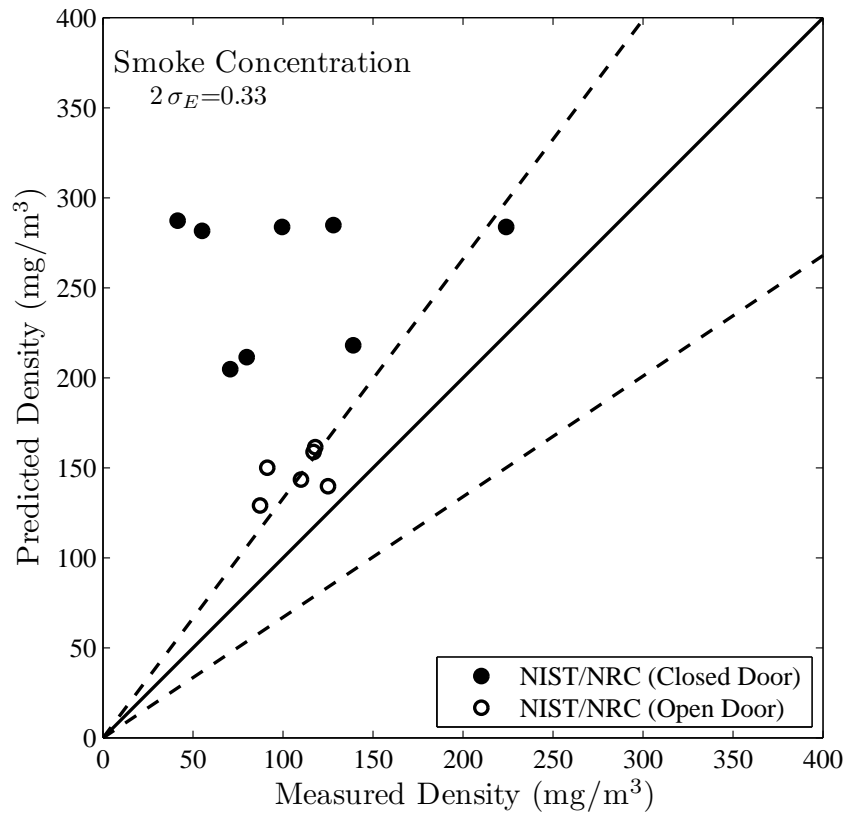


Figure 9.2: Summary of smoke concentration predictions for the NIST/NRC test series.

9.3 Smyth Slot Burner Experiment

The two-step, CO production model in FDS was used to simulate a methane/air slot burner diffusion flame. Figures 9.3 through 9.5 show predicted and measured temperatures at three elevations above the burner. The model predicts a flame that is slightly narrower and cooler than measured. The model also predicts higher centerline temperatures. These results are not surprising. The two-step combustion model considers the first step, $F \rightarrow CO$, to be infinitely fast, assuming that the local oxygen concentration satisfies a flammability criterion. This is true in the vicinity of the lip of the burner. In reality, the cold fuel and air streams do not react infinitely fast at this location and some oxygen penetrates the flame at the base, resulting in cooler gases being entrained into the core of the flame with a resulting drop in the centerline temperature.

Figures 9.3 through 9.5 also show predicted and measured values of CH_4 , O_2 , CO , and CO_2 at three elevations above the burner along. Note that the test data shows a small quantity of oxygen along the burner centerline which is not captured in the simulation. Along the centerline, the model predicts higher values of fuel and higher values of products than measured. The species profiles are also slightly narrower than measured, consistent with the temperature prediction. The reported uncertainty in the species concentration measurements ranges from 10 % to 20 %.

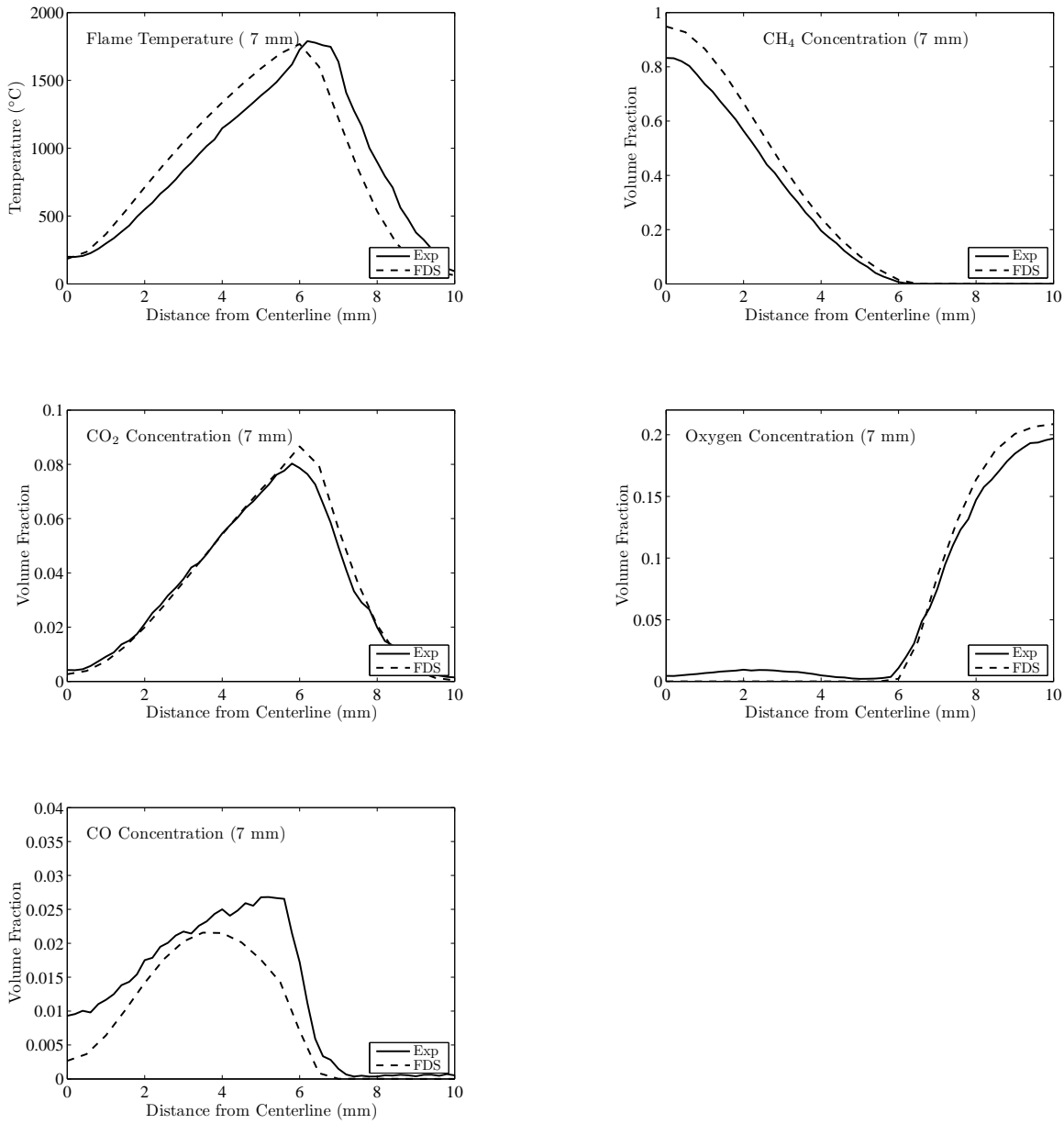


Figure 9.3: Predicted and measured temperature and gas species 7 mm above a methane-air slot burner.

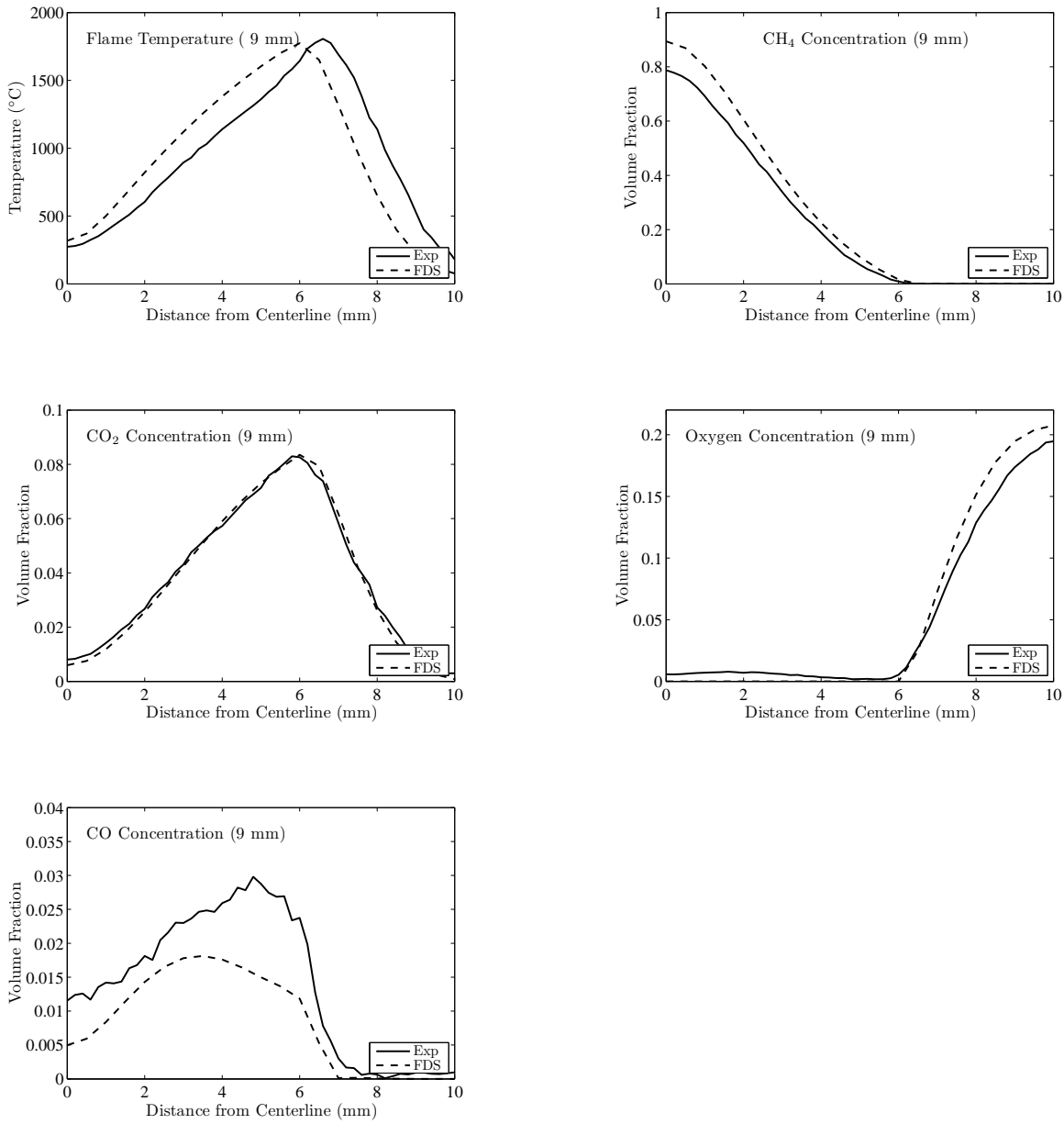


Figure 9.4: Predicted and measured temperature and gas species 9 mm above a methane-air slot burner.

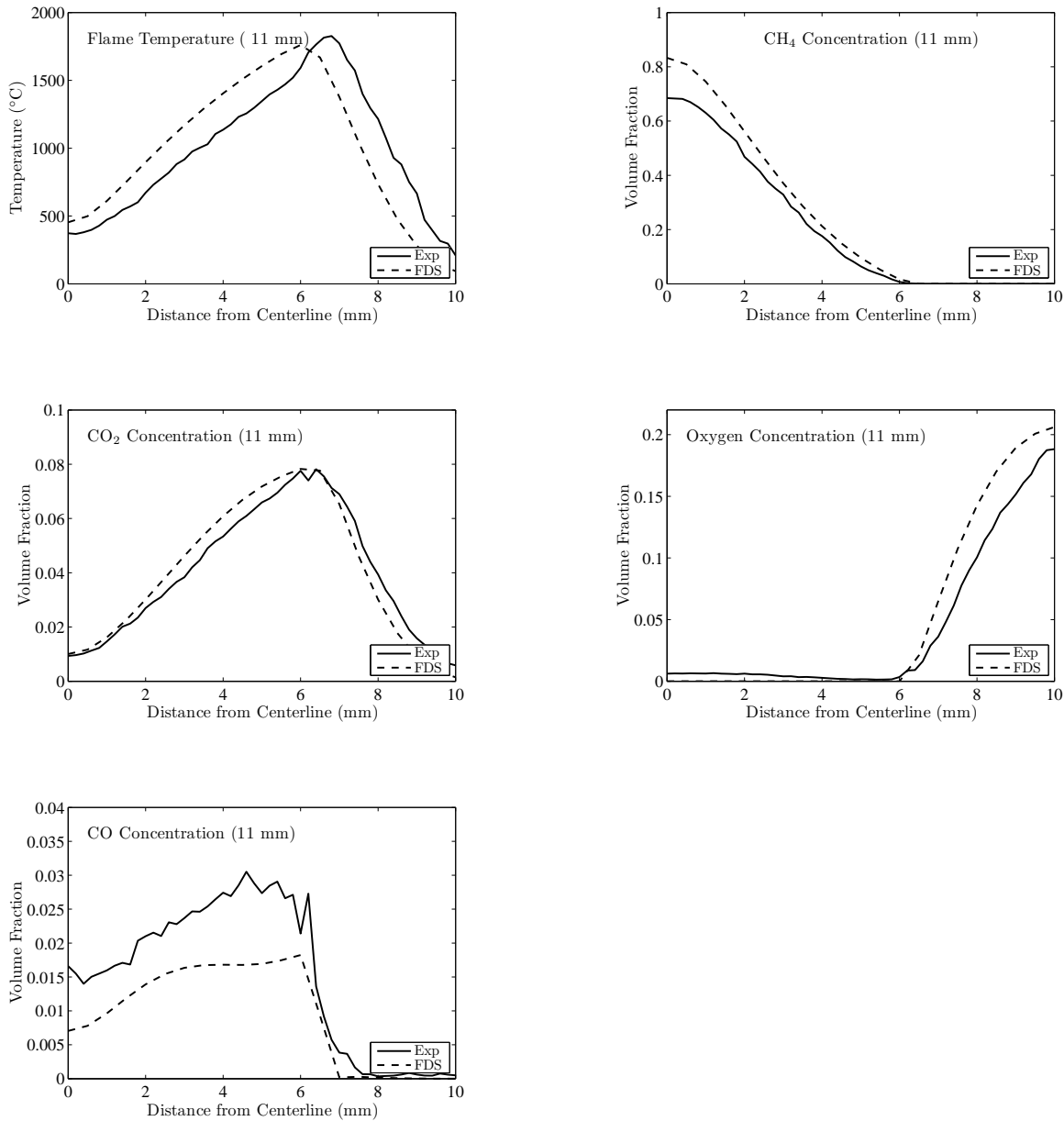


Figure 9.5: Predicted and measured temperature and gas species 11 mm above a methane-air slot burner.

9.4 Beyler Hood Experiments

Fig. 9.6 shows species predictions made by the two-step model compared with measured data for a range of fire sizes and burner positions. The dotted lines indicate the estimated measurement uncertainty. The model predicts the time-averaged species concentration at the hood exhaust vent. CO₂ predictions are within the measurement uncertainty for all but one of the simulations performed. For the well-ventilated fires (burner 10 cm below the edge of the hood), CO, CO₂, and unburned fuel predictions match the data. As the fires become under-ventilated, CO is over-predicted while fuel and O₂ are under-predicted. The most likely explanation for the discrepancy is that the model assumes fuel and oxygen react infinitely fast in the vicinity of near ambient conditions. This occurs at the lower edge of the hood where the vitiated layer is adjacent to the ambient air below the hood, and as a result layer burning is occurring in the model which depletes the fuel and O₂ and creates CO. This is not unexpected, and indicates that more work is required to establish the conditions under which combustion in the first step, conversion of fuel to CO, will be allowed.

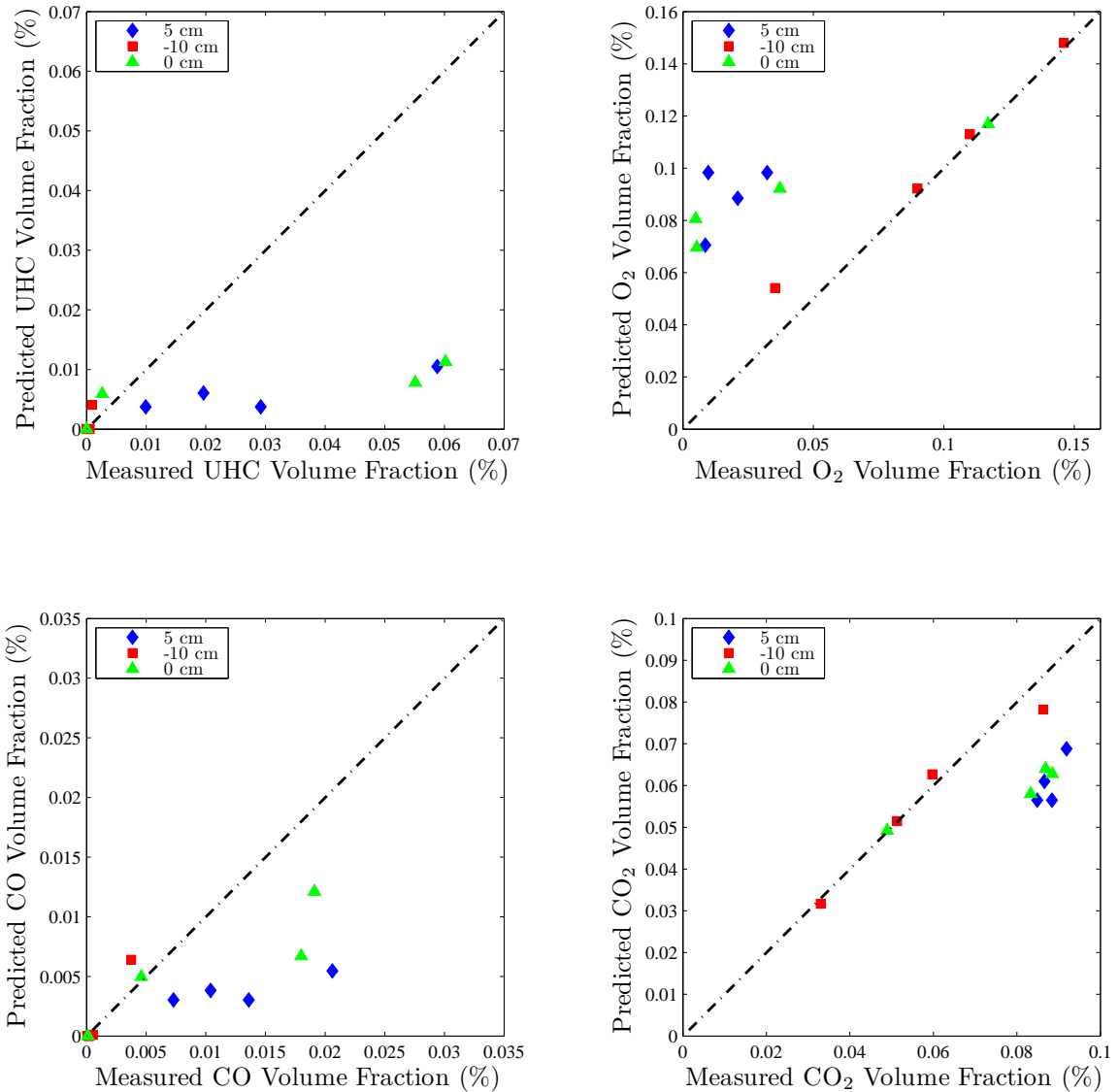


Figure 9.6: Comparison of measured and predicted species concentrations in the Beyler hood experiments, dotted lines show experimental uncertainty.

9.5 NIST Reduced Scale Enclosure (RSE) Test Series, 1994

The RSE natural gas experiments were selected to assess the CO production capability rather than soot production. Nine fire sizes were simulated: 50 kW, 75 kW, 100 kW, 150 kW, 200 kW, 300 kW, 400 kW, 500 kW, and 600 kW. The experiments were modeled using properties of the natural gas supplied to the test facility. The model geometry included the compartment interior along with a 0.6 m deep region outside the door. Figure 9.7 shows the measured and predicted CO, CO₂ and O₂ concentrations. The measured values are from the test series performed by Bryner, Johnsson, and Pitts [133].

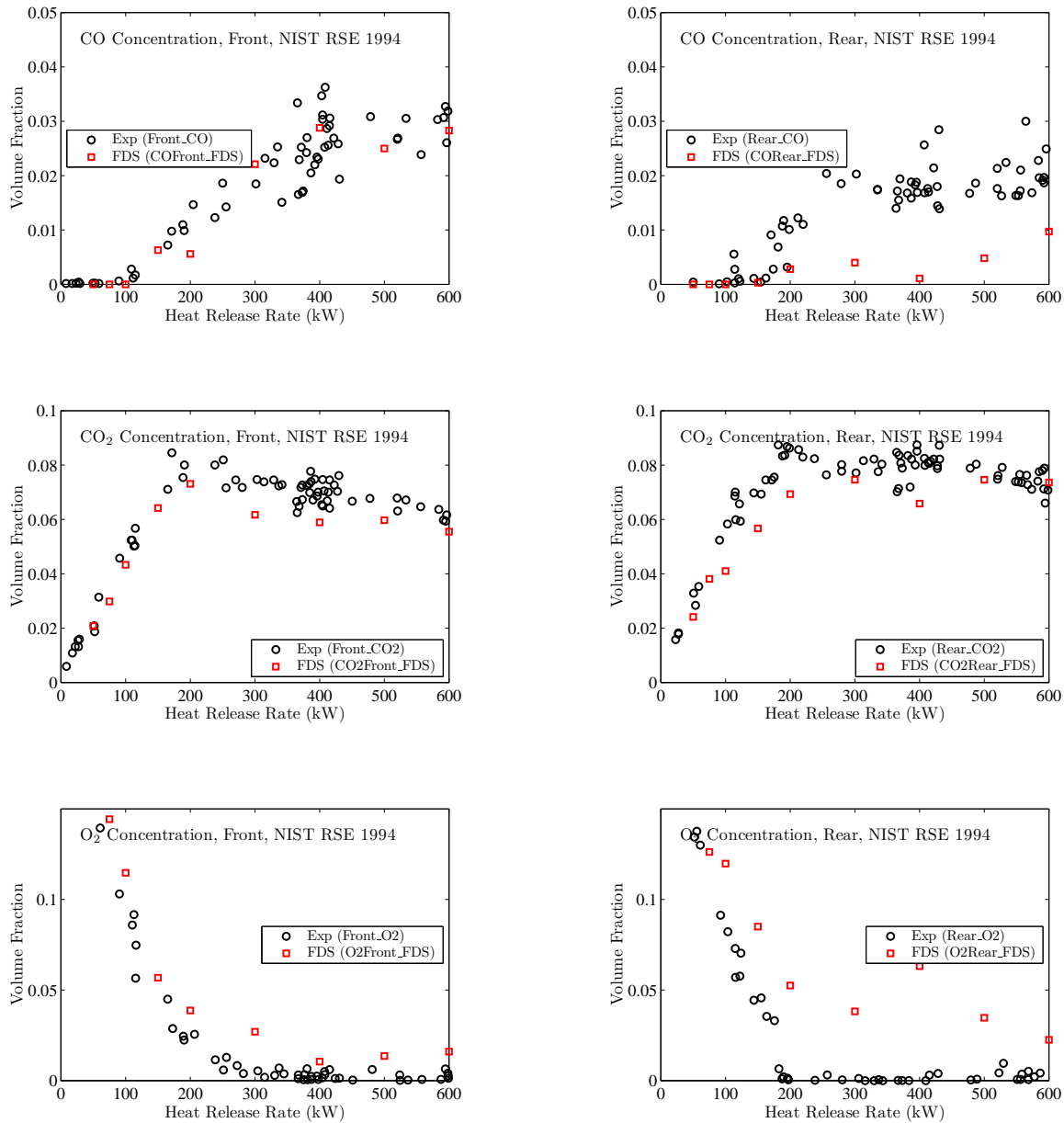


Figure 9.7: Summary of NIST Reduced Scale Enclosure (1994) experiments.

Chapter 10

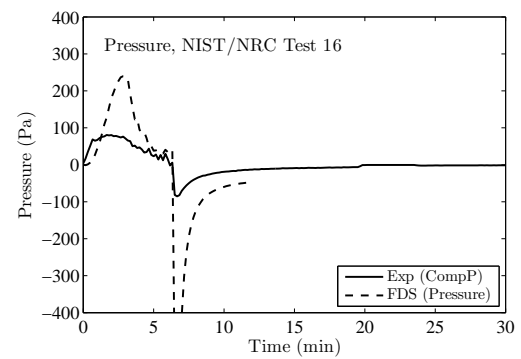
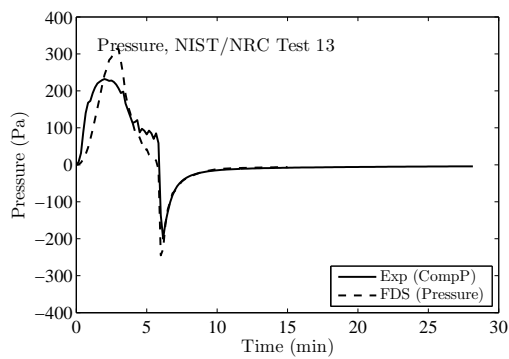
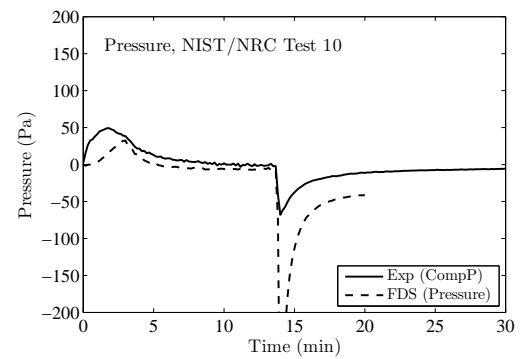
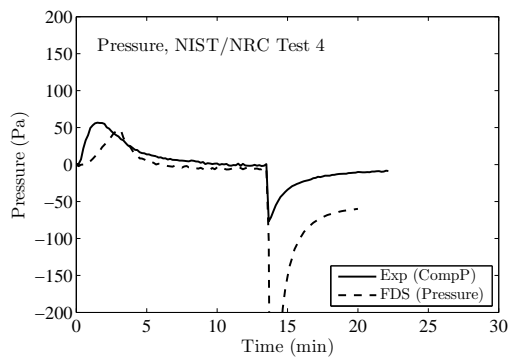
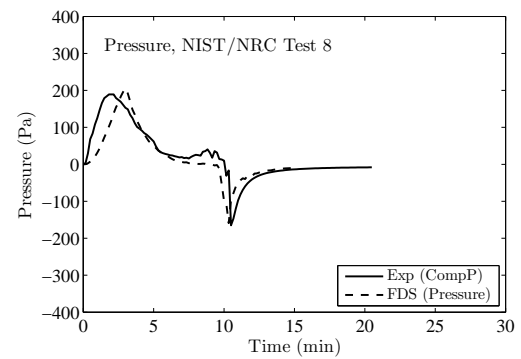
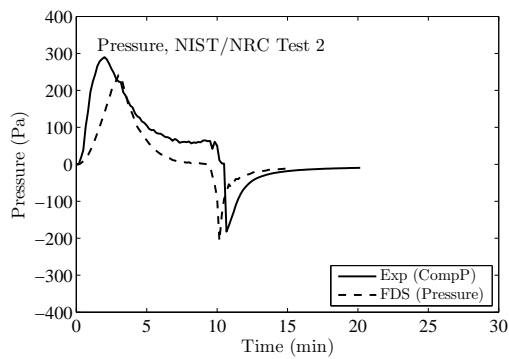
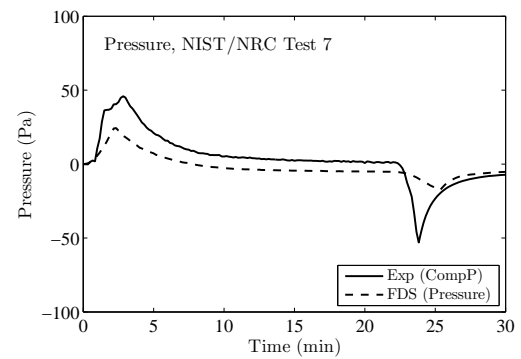
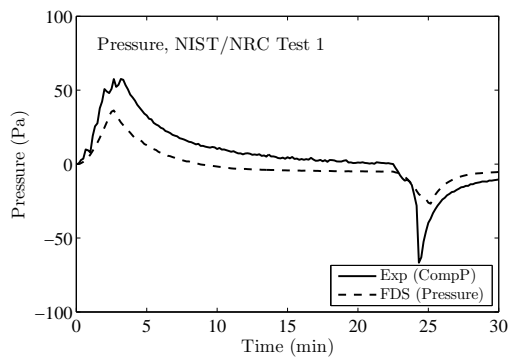
Compartment Pressure

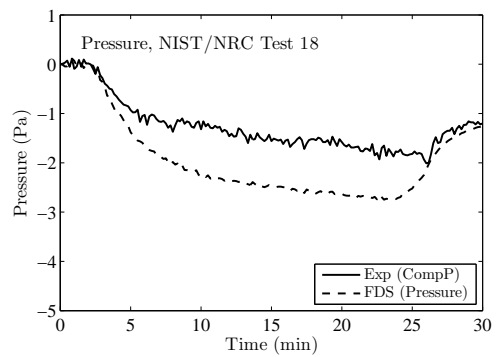
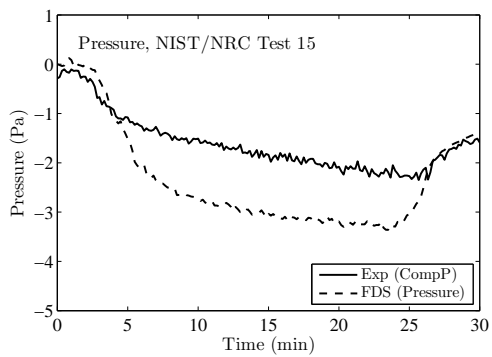
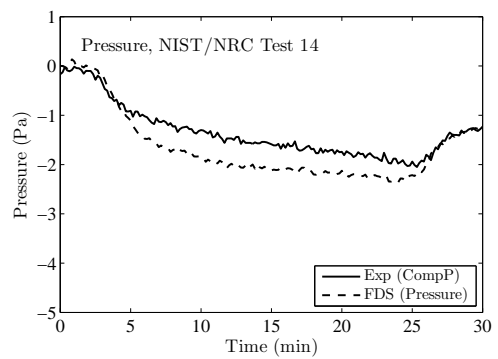
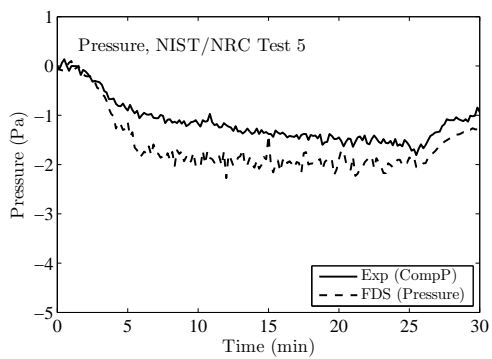
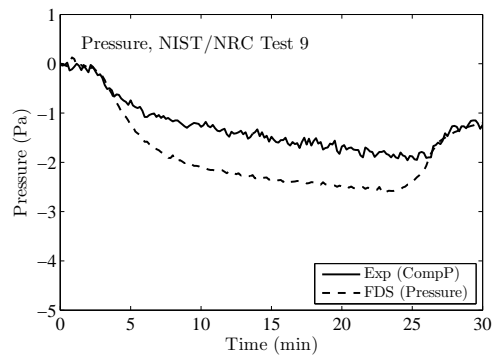
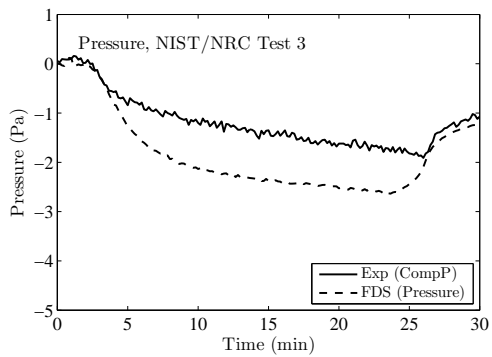
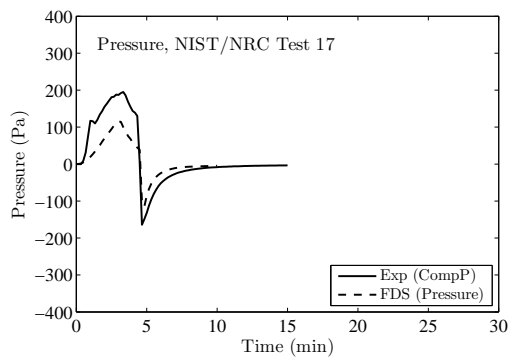
In FDS, the pressure is decomposed into a temporally-varying background pressure and a spatially-varying perturbation that drives the flow. The former can be thought of as the “over-pressure,” and it is essentially a check on global mass and energy balances; whereas the latter has most to do with momentum conservation. In real buildings, leakage and ventilation affect the compartment “over-pressure” along with the fire, which also affects the pressure perturbation.

10.1 NIST/NRC Test Series

Comparisons between measured and predicted pressures for the NIST/NRC Test Series are shown in on the following pages. For those tests in which the door to the compartment is open, the over-pressures are only a few Pascals, whereas when the door is closed, the over-pressures are several hundred Pascals. The pressure within the compartment was measured at a single point, near the floor. In the simulations of the closed door tests, the compartment was assumed to leak via a small uniform flow spread over the walls and ceiling. The flow rate was calculated based on the assumption that the leakage rate is proportional to the measured leakage area times the square root of compartment over-pressure.

Note that in the closed door tests, there is often a dramatic drop in the predicted compartment pressure. This is the result of the assumption in FDS that the heat release rate is decreased to zero in one second at the time in the experiment when the fuel flow was stopped for safety reasons. In reality, the fire did not extinguish immediately because there was an excess of fuel in the pan following the flow stoppage. For the purpose of model comparison, the peak over-pressures are differenced in the closed door tests, and the peak (albeit small) under-pressures are compared in the open door tests.





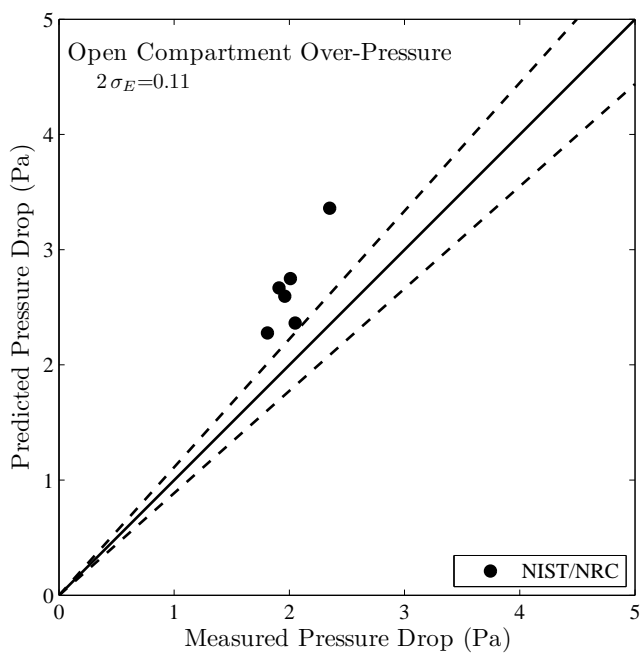
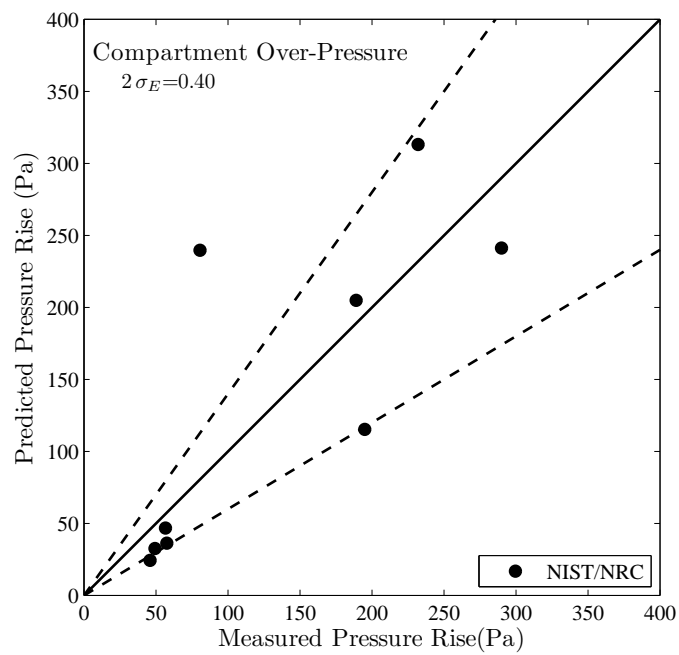


Figure 10.1: Summary of Pressure Results. The top graph shows the compartment “over-pressure” in closed door tests; the lower graph shows the small pressure perturbation in the open door tests.

Chapter 11

Surface Temperature

All solid surfaces in an FDS model are assigned thermal boundary conditions. Heat and mass transfer to and from solid surfaces is usually handled with empirical correlations, although it is possible to compute directly the heat and mass transfer when performing a Direct Numerical Simulation (DNS). Heat conduction into a solid surface is calculated via a one-dimensional solution of the heat equation in either cartesian or cylindrical coordinates. The latter is useful for cables.

11.1 WTC Test Series, Steel Structural Members and “Slug” Calorimeters

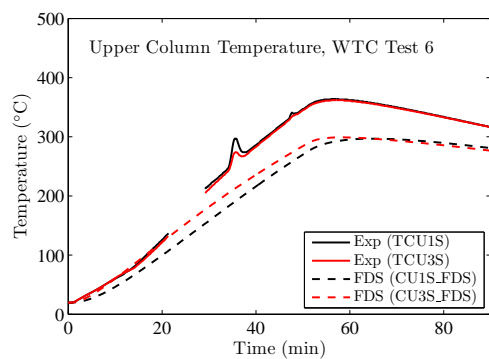
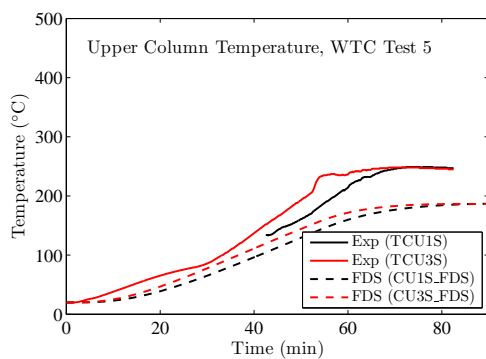
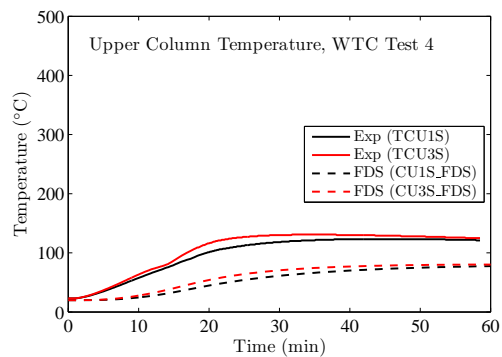
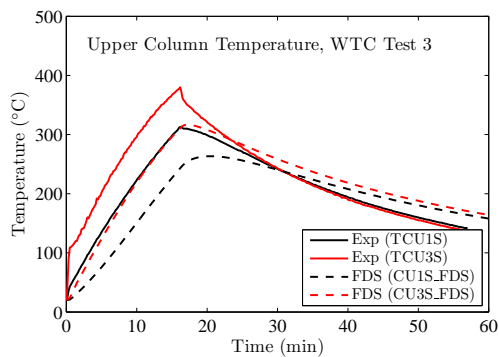
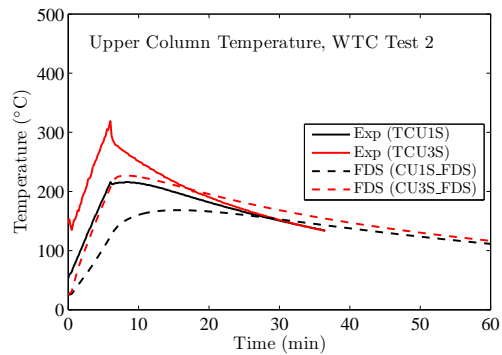
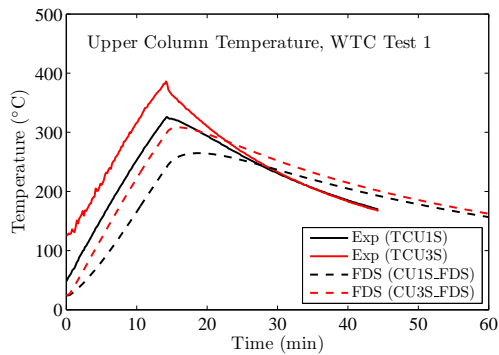
The compartment for the WTC experiments contained a hollow box column roughly 0.5 m from the fire pan, two trusses over the top of the pan, and one or two steel bars resting on the lower truss flanges. In Tests 1, 2 and 3, the steel was bare, and in Tests 4, 5 and 6, the steel was coated with various thicknesses of sprayed fire-resistive materials.

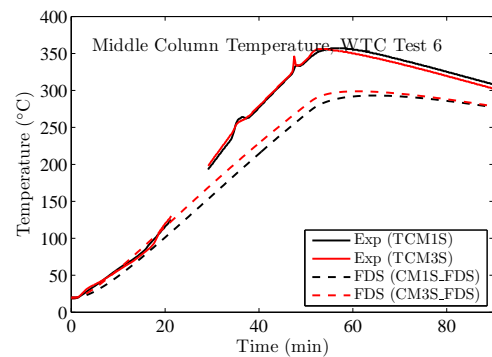
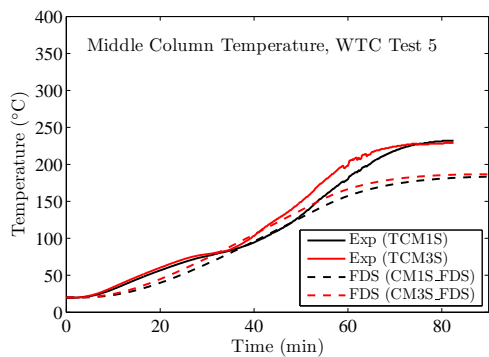
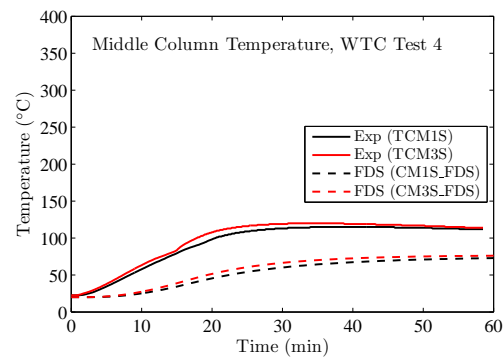
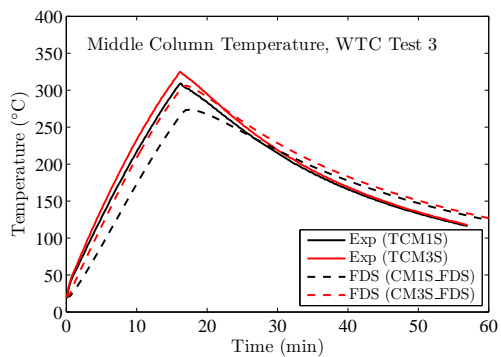
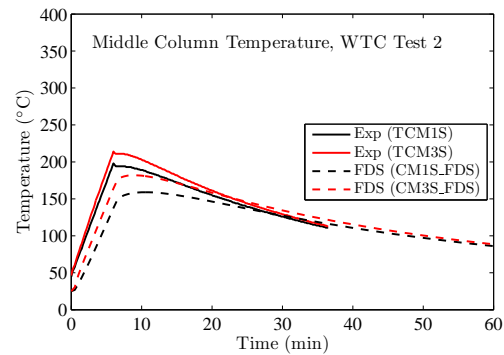
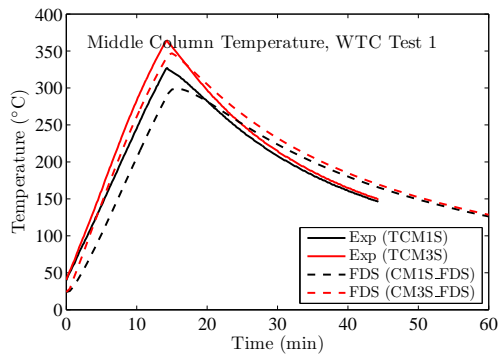
The column was instrumented near its base (about 0.5 m from the floor, middle (1.5 m), and upper (2.5 m)). Four measurements of steel (and insulation) temperatures were made at each location, for each of its four sides.

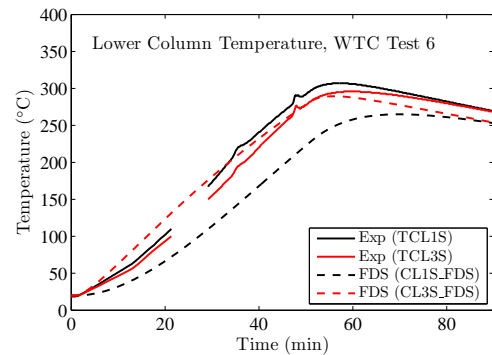
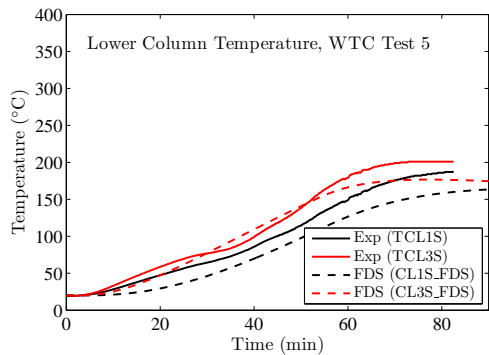
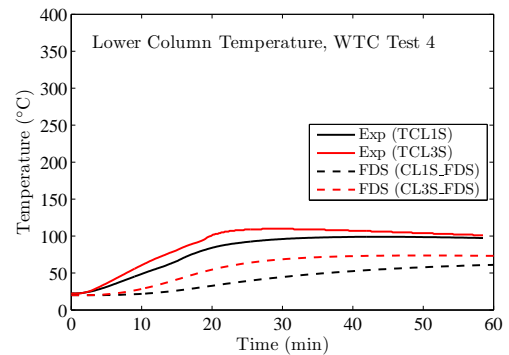
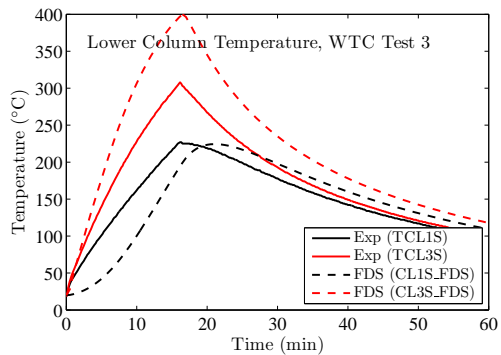
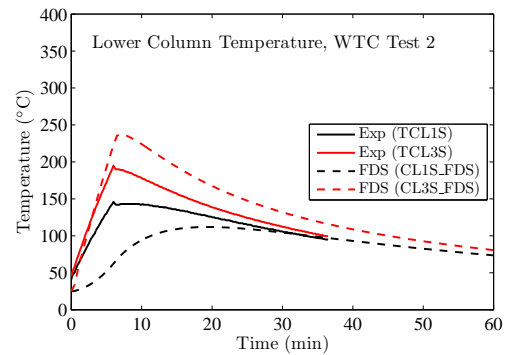
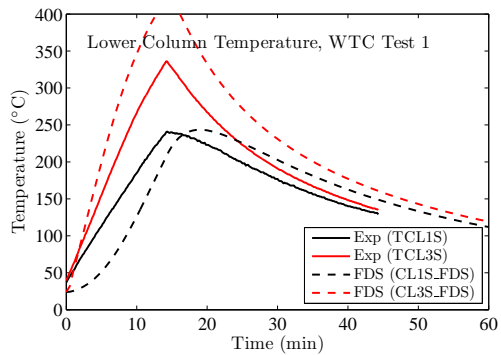
In FDS, these elements were modeled using thin sheet obstructions with a resolution of 10 cm.

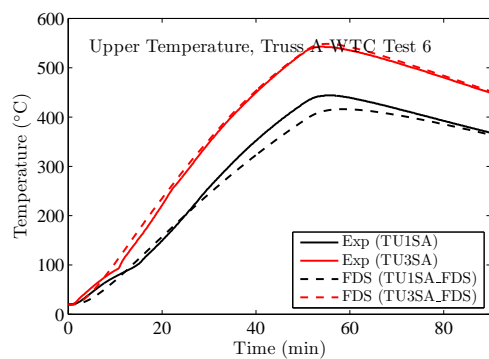
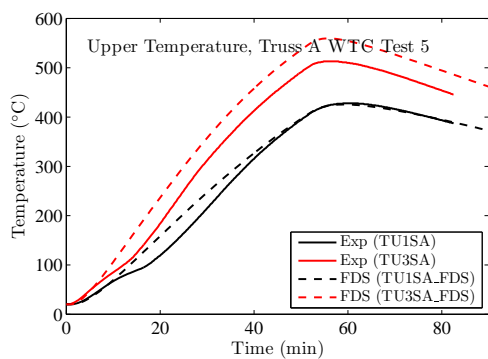
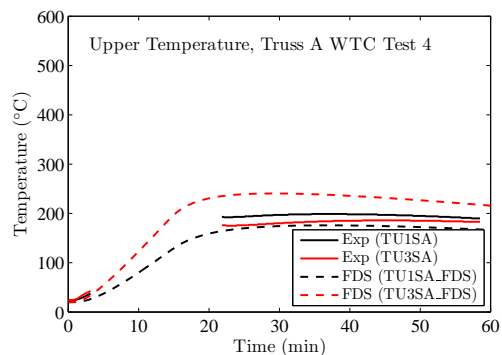
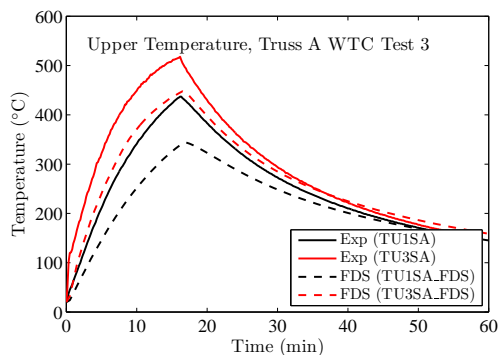
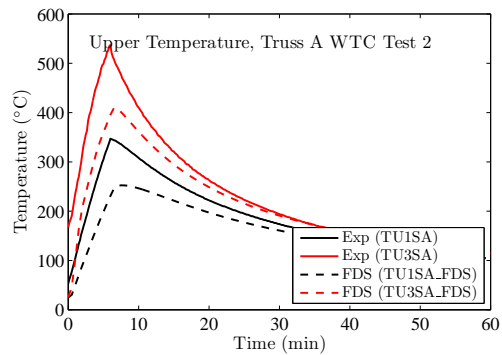
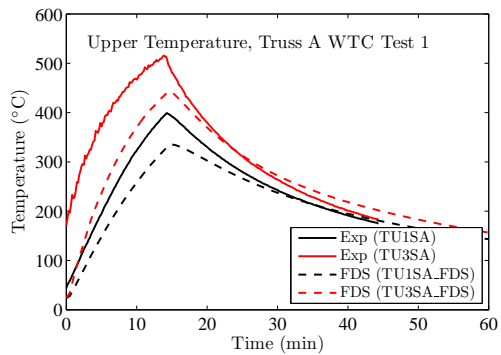
Five cylinders (“slugs”) of nickel 200 ($\geq 99\%$ nickel), 25.4 cm long and 10.2 cm in diameter, were positioned 50 cm north of the centerline in the WTC experiments. Slugs 1 through 5 were 2.92 m, 1.82 m, 0.57 m, 0.05 m, and 1.56 m, respectively, from the longitudinal axis of the fire pan. All the slugs were 50 cm north of the lateral axis. The fire pan measured 2 m by 1 m. Four thermocouples were inserted into each slug at various locations. All four temperatures for each slug were virtually indistinguishable.

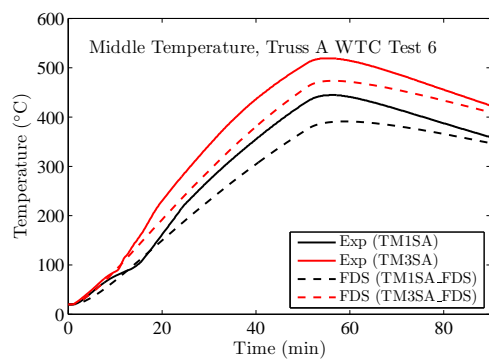
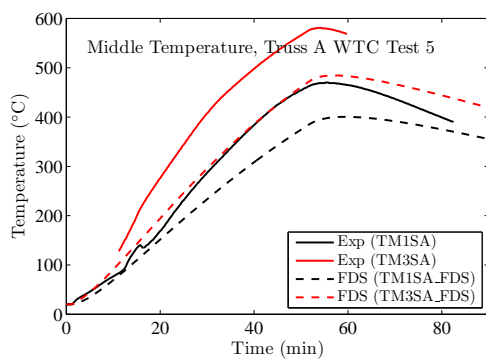
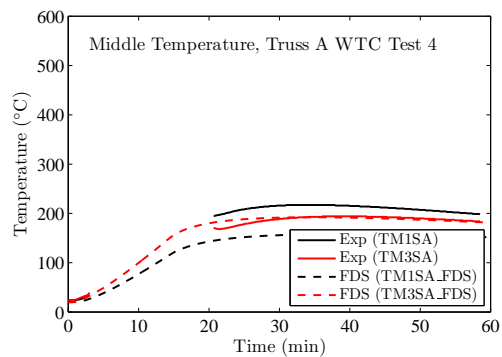
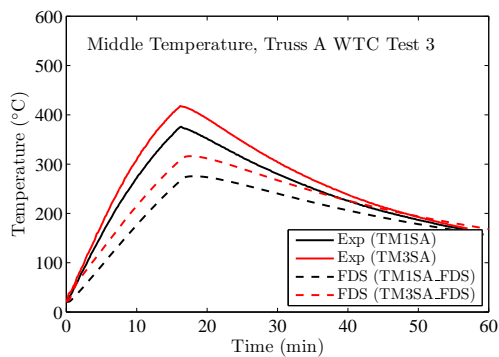
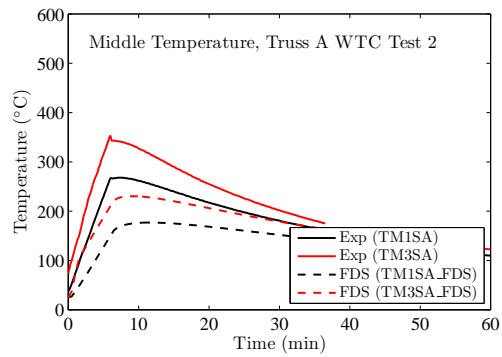
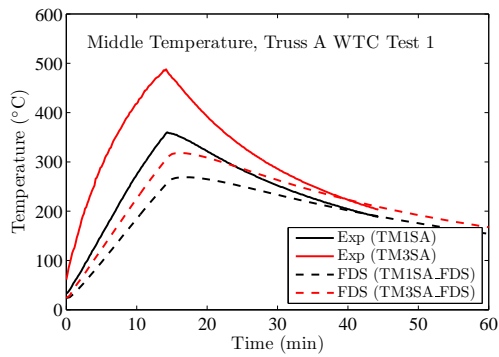
In FDS, rectangular obstructions were used to model the slugs, but the one-dimensional heat conduction calculation was performed using cylindrical coordinates.

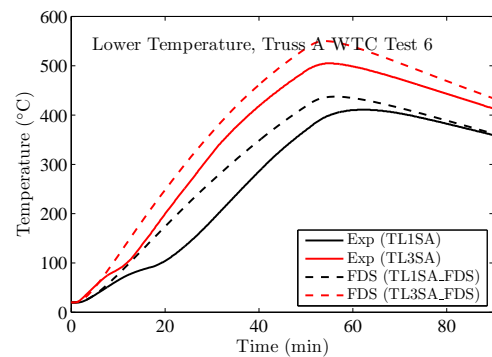
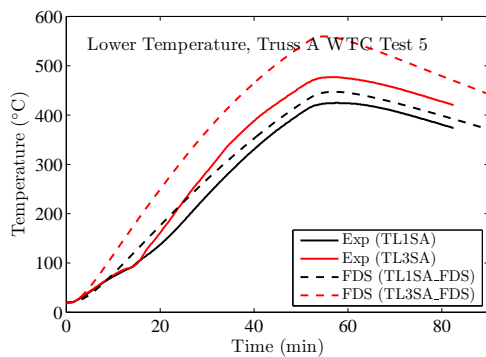
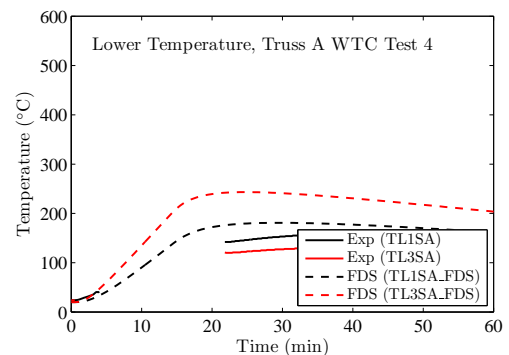
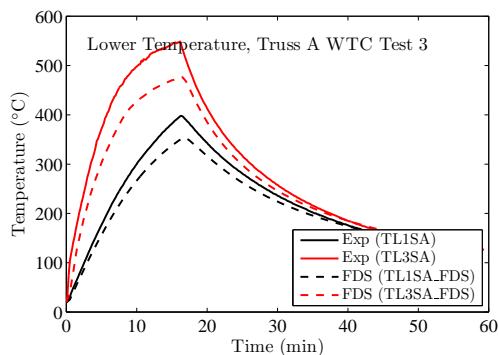
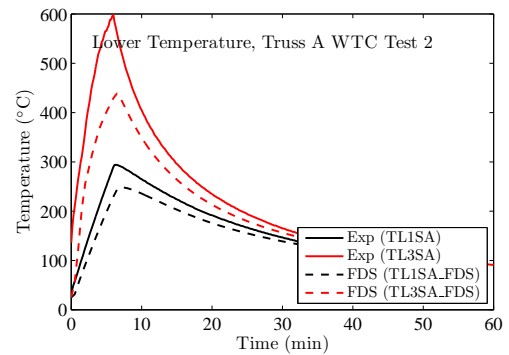
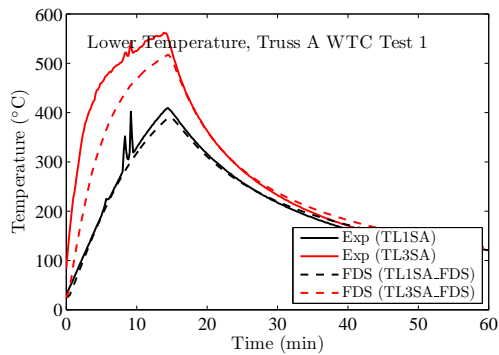


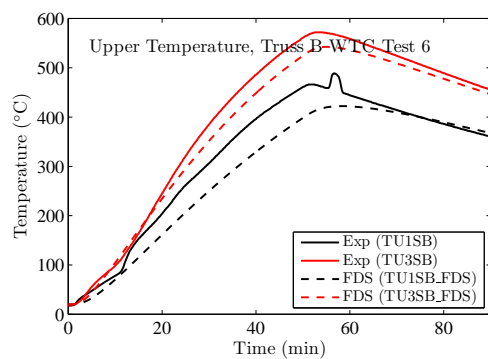
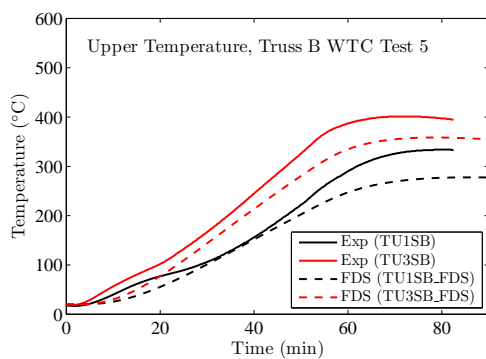
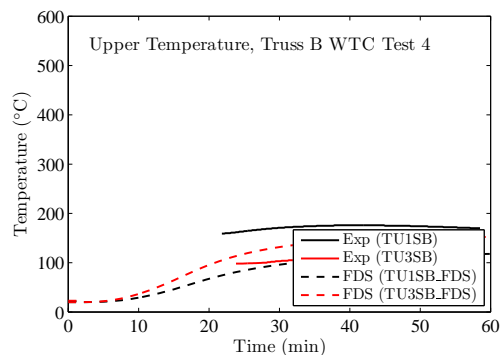
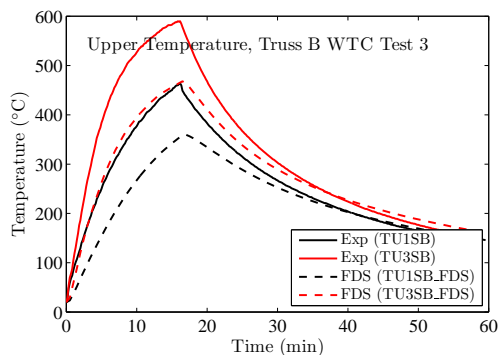
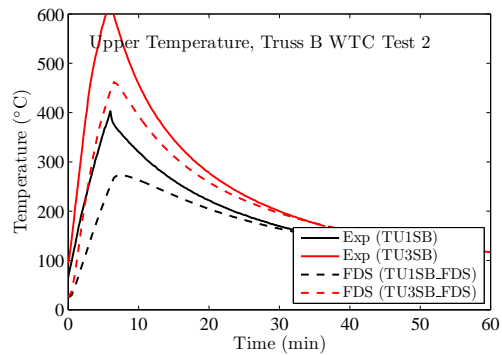
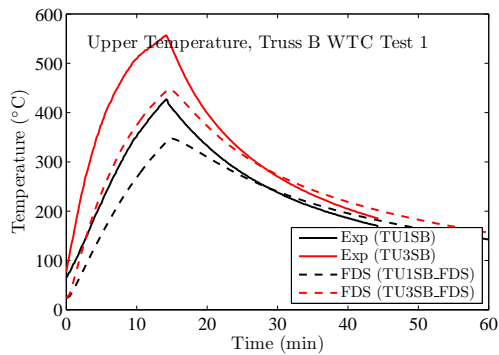


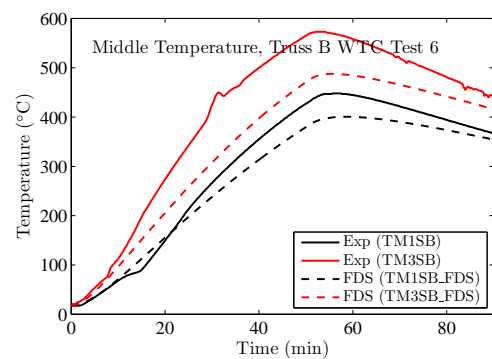
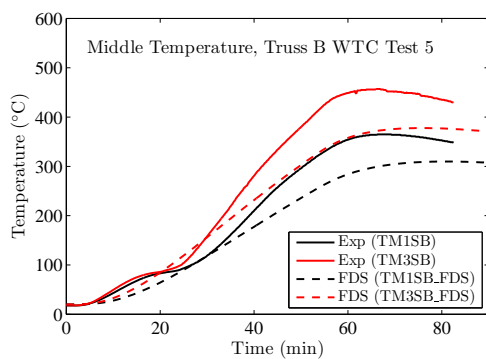
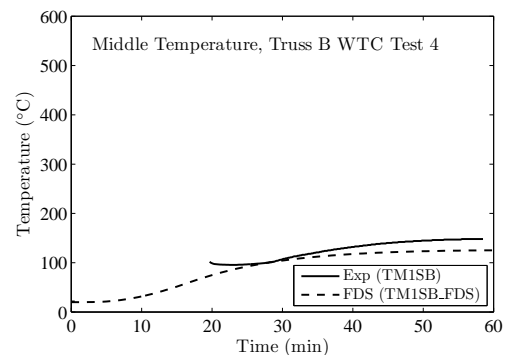
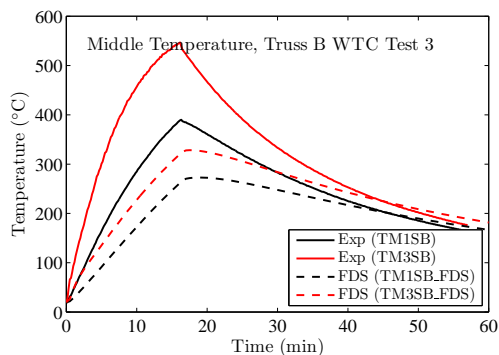
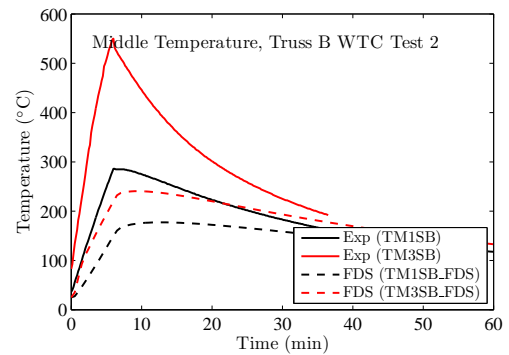
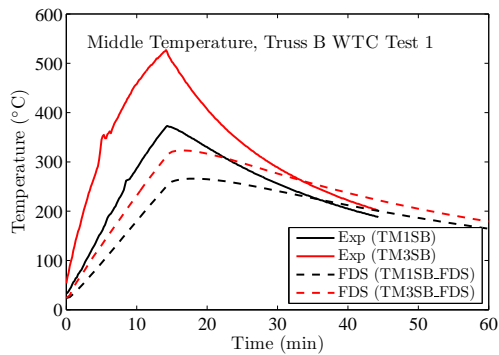


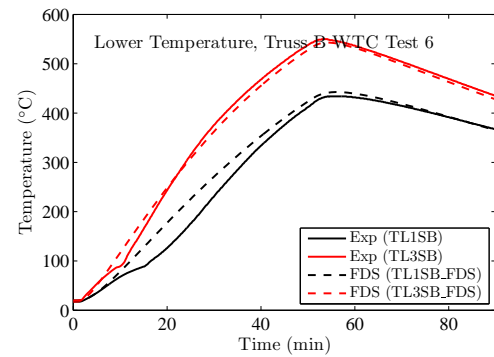
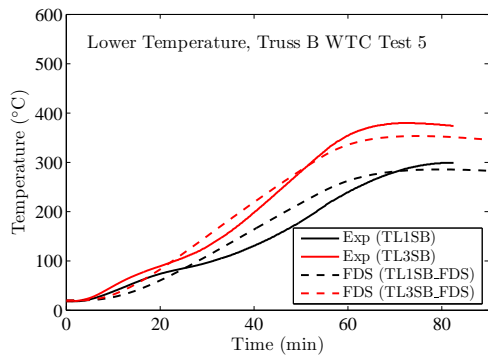
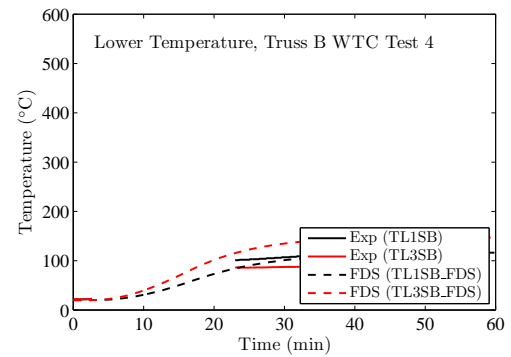
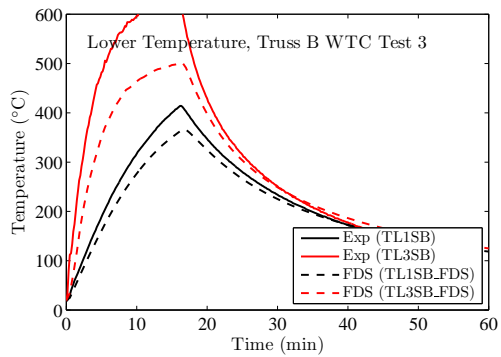
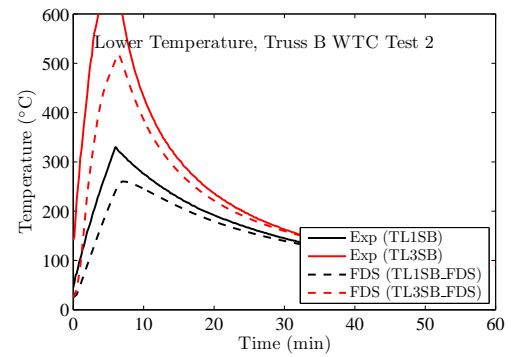
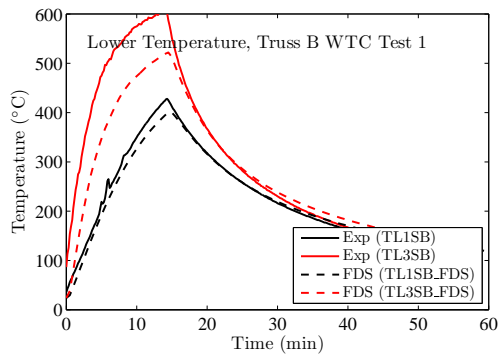


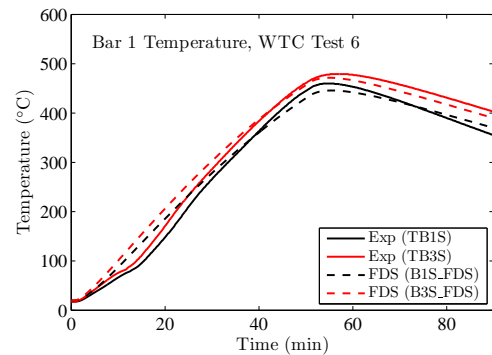
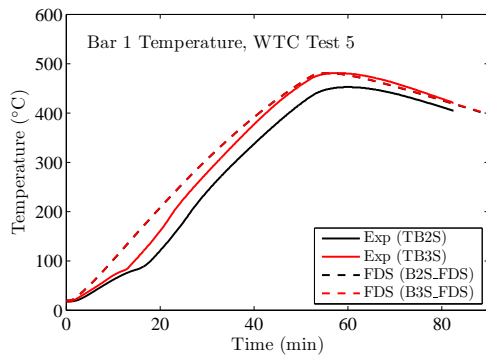
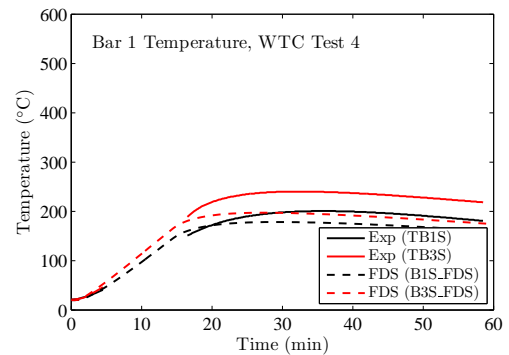
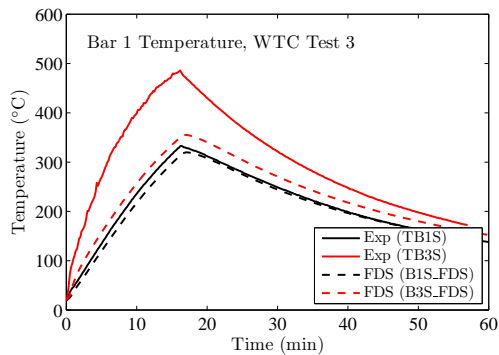
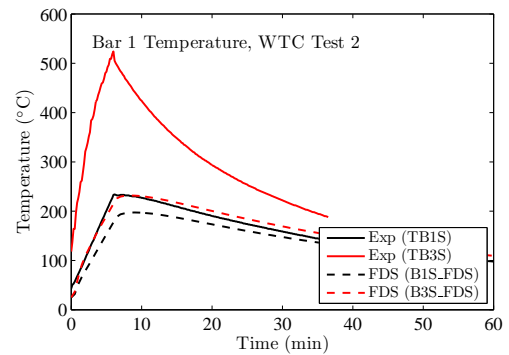
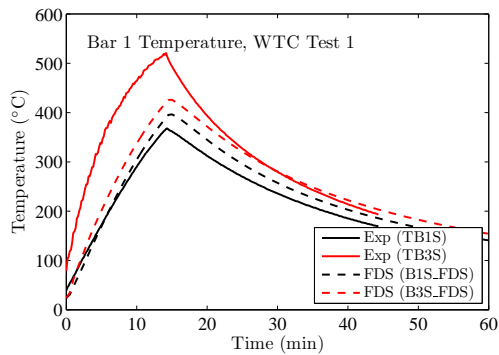


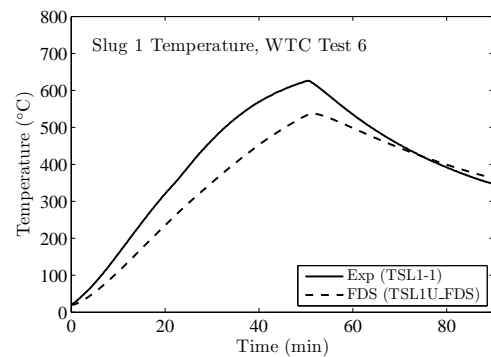
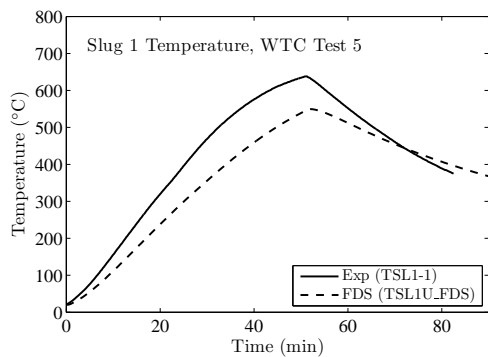
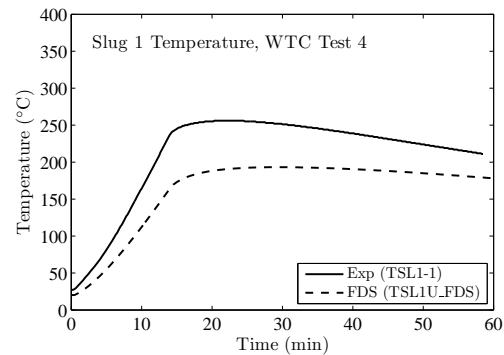
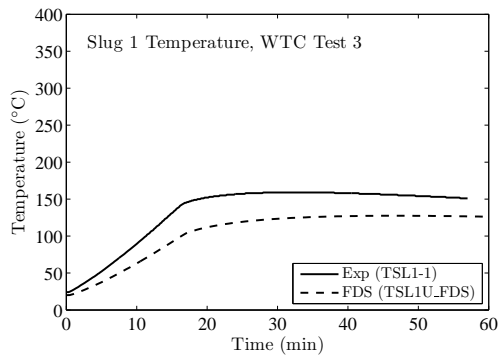
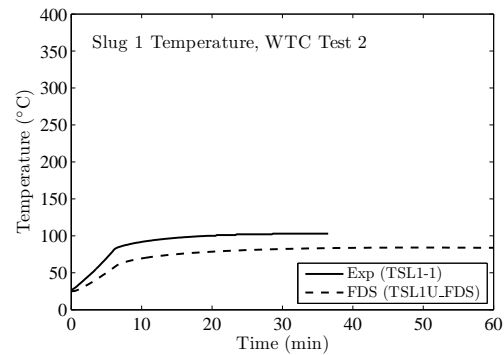
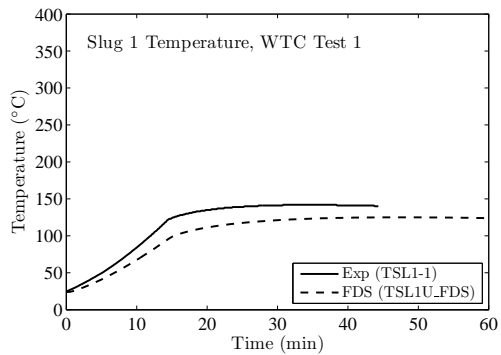


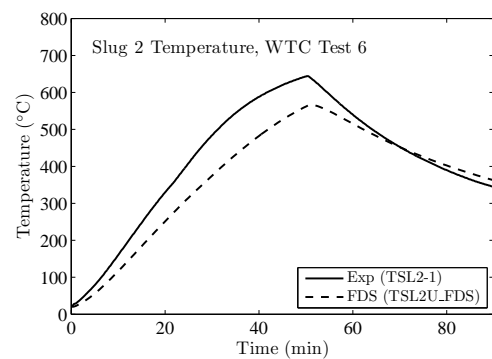
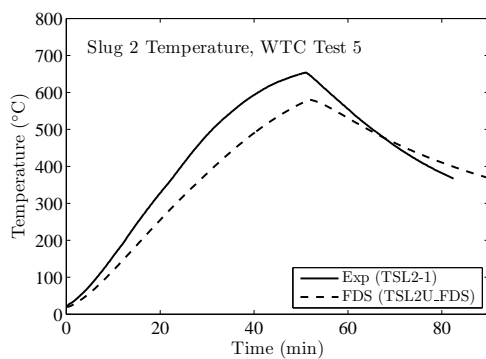
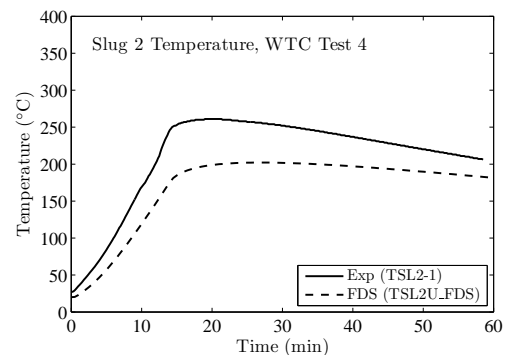
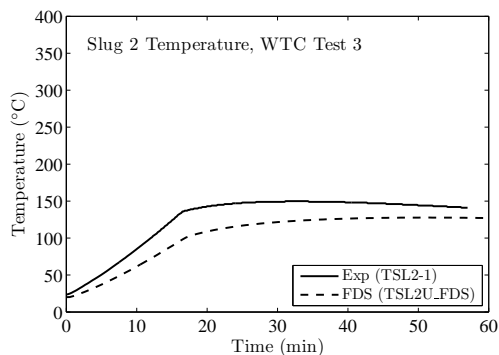
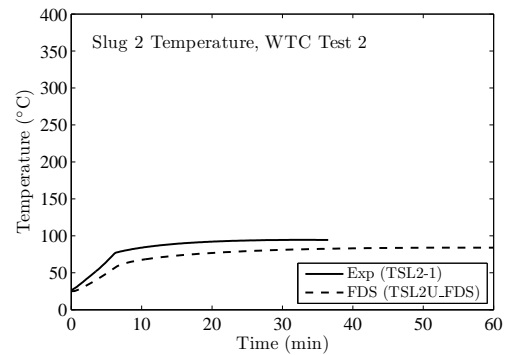
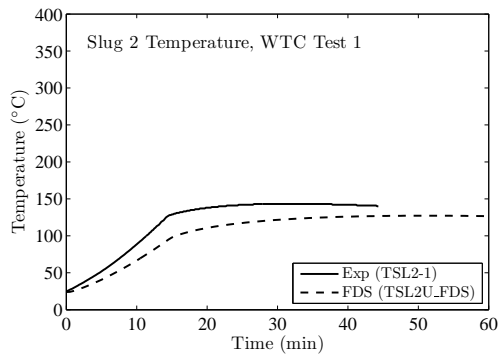


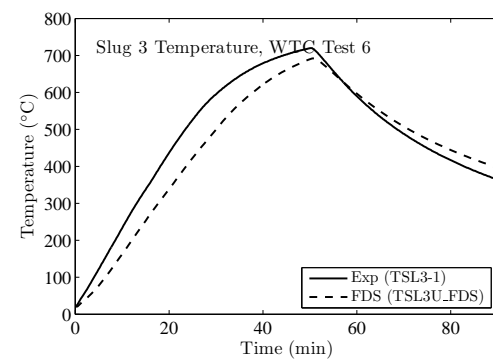
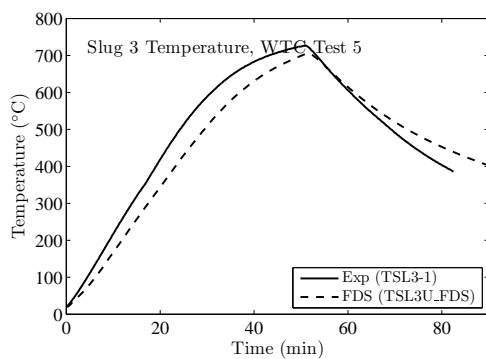
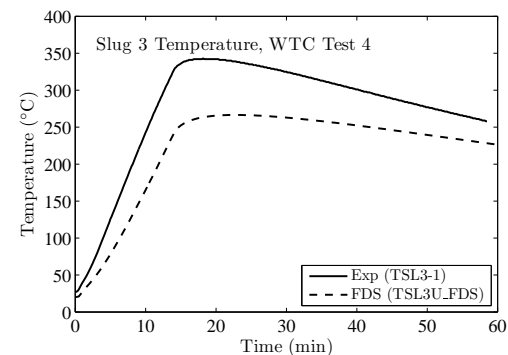
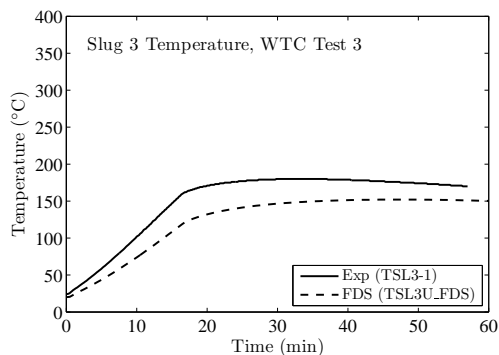
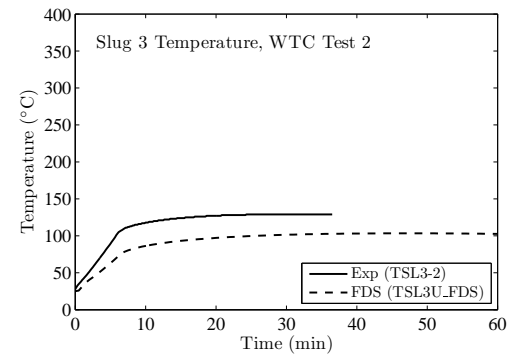
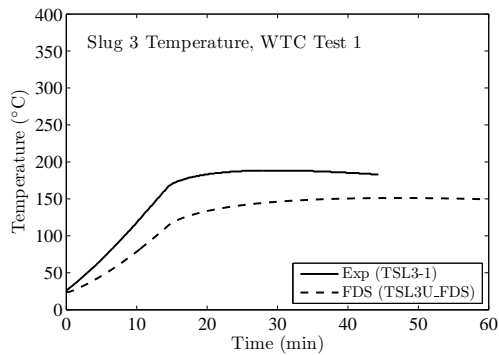


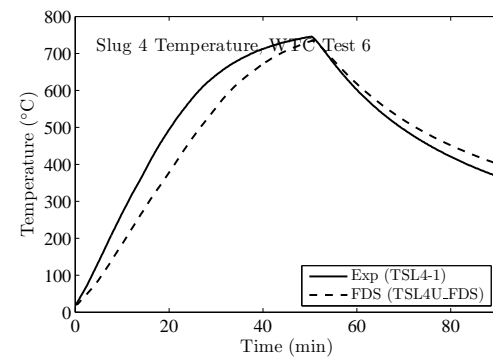
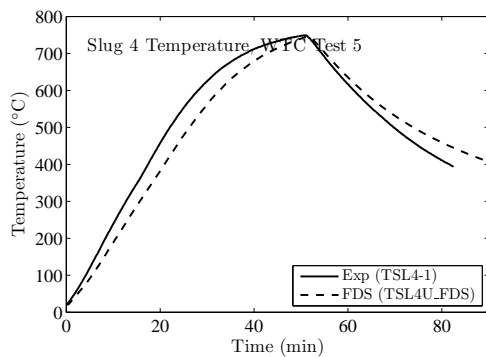
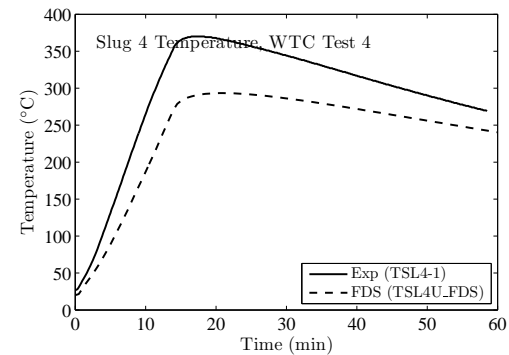
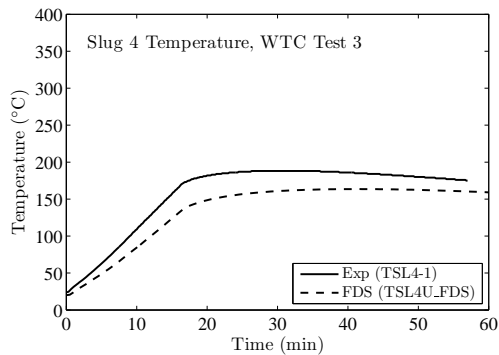
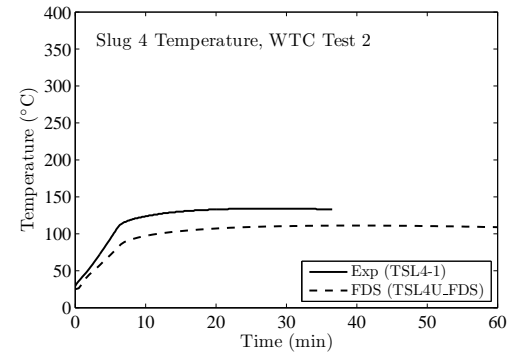
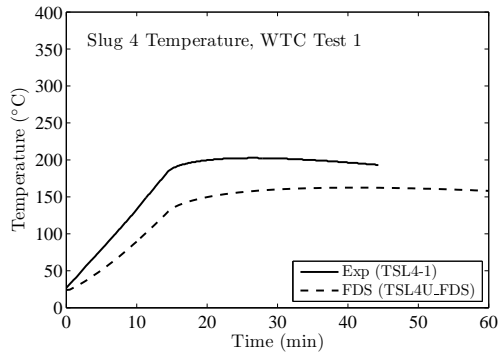


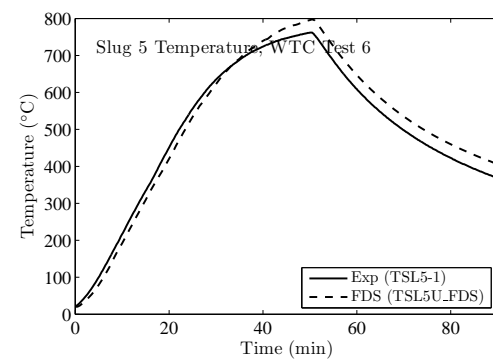
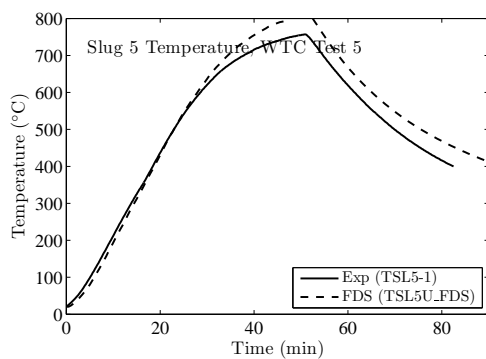
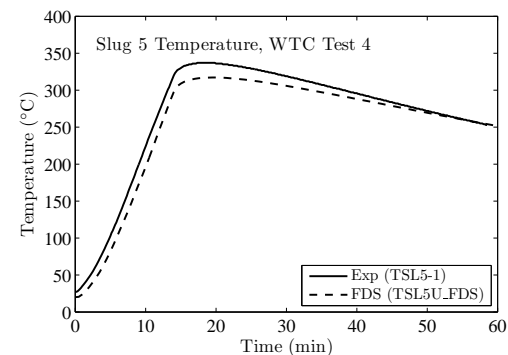
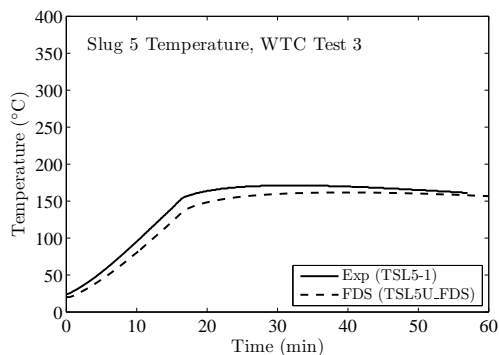
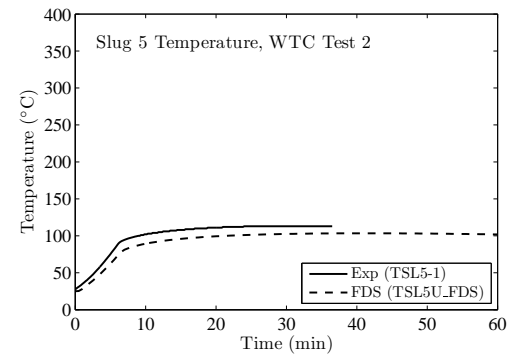
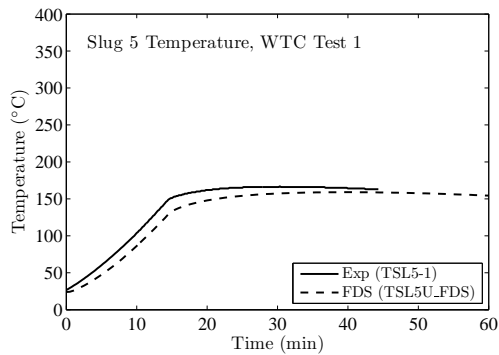












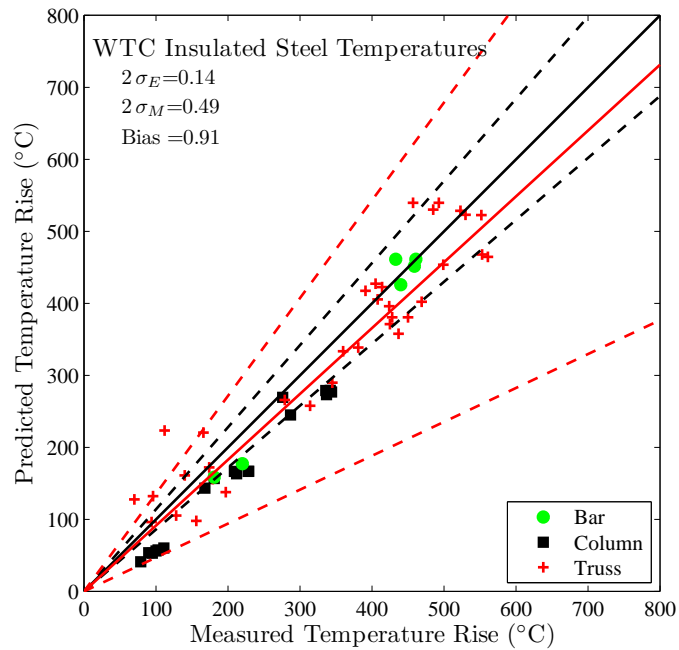
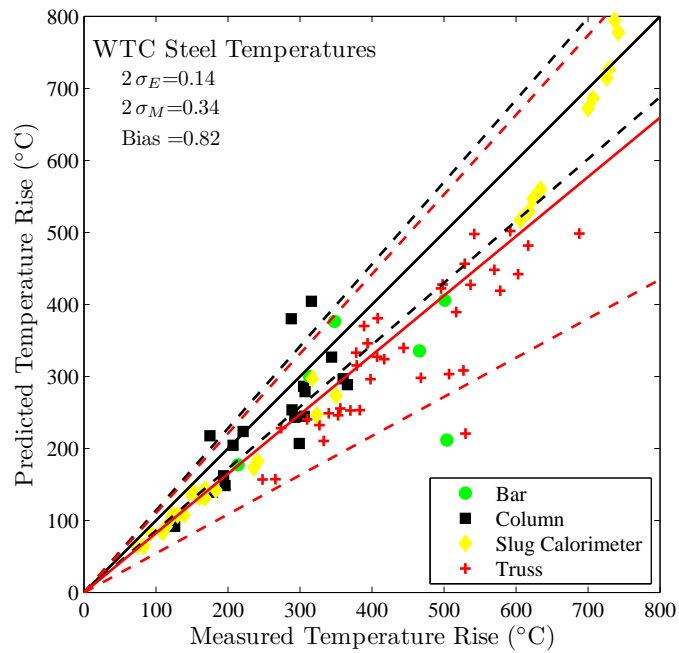


Figure 11.1: Summary of steel temperature predictions for the WTC test series.

11.2 SP Adiabatic Surface Temperature Experiments

Comparisons of FDS predictions of gas, plate thermometer, and steel temperatures for three compartment experiments conducted at SP, Sweden, are presented on the following pages. Each experiment was conducted in a standard compartment, 3.6 m long by 2.4 m wide by 2.4 m high, with a 0.8 m wide by 2.0 m high door centered on the narrow wall. Each experiment used a constant 450 kW propane burner and a single beam suspended 20 cm below the ceiling along the centerline of the compartment. There were three measurement stations along the beam at lengths of 0.9 m (Position A), 1.8 m (Position B), and 2.7 m (Position C) from the far wall where the fire was either positioned in the corner (Tests 1 and 2), or the center (Test 3). The beam in Test 1 was a rectangular steel tube filled with an insulation material. The beam in Tests 2 and 3 was an I-beam. Details can be found in the test report [122].

Each page to follow contains the results for a single experiment and measuring station. There are nine in all. In addition to predictions of the gas, plate thermometer, and steel temperatures, there are predictions of the adiabatic surface temperature (AST) for the locations and orientations of the plate thermometers. The AST is a useful quantity that serves as a boundary condition for thermal resistance calculations of structures. The basic idea is as follows. The *net* heat flux to the solid surface is given as the sum of radiative and convective components:

$$\dot{q}_r'' + \dot{q}_c'' = \epsilon (\dot{q}_{r,inc}'' - \sigma T_s^4) + h(T_g - T_s) \quad (11.1)$$

where $\dot{q}_{r,inc}''$ is the incident radiative flux, T_s the surface temperature, T_g the gas temperature near the surface, and h the convective heat transfer coefficient. Following the idea proposed by Wickström [151], the AST is defined as the surface temperature of a perfectly insulated solid. This is equivalent to saying that the net heat flux to this (hypothetical) surface is zero:

$$0 = \epsilon (\dot{q}_{r,inc}'' - \sigma T_{AST}^4) + h(T_g - T_{AST}) \quad (11.2)$$

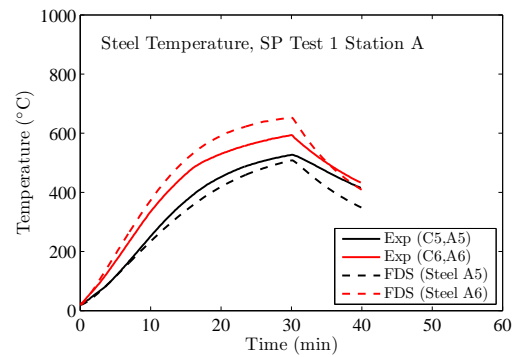
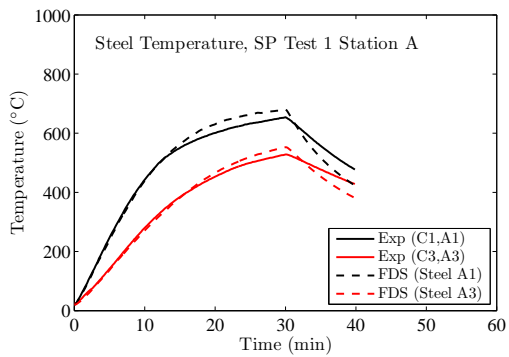
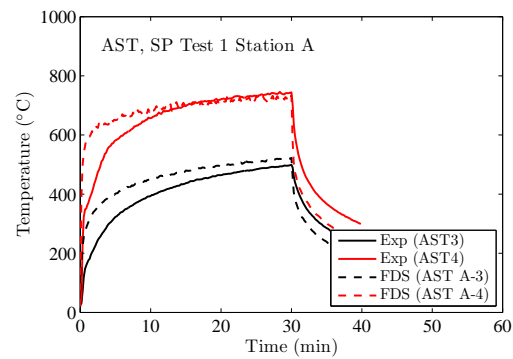
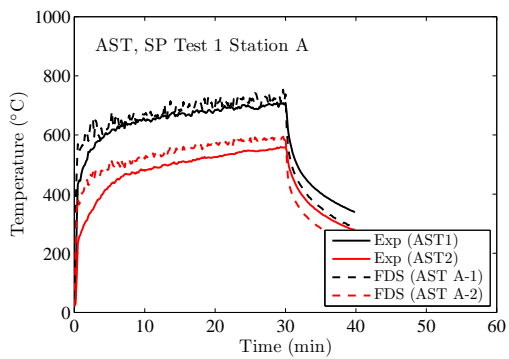
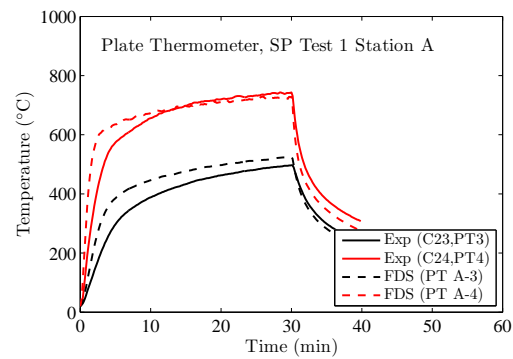
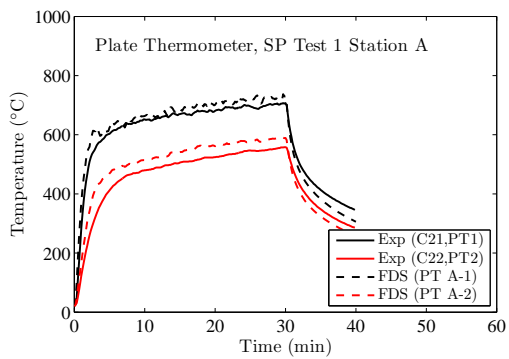
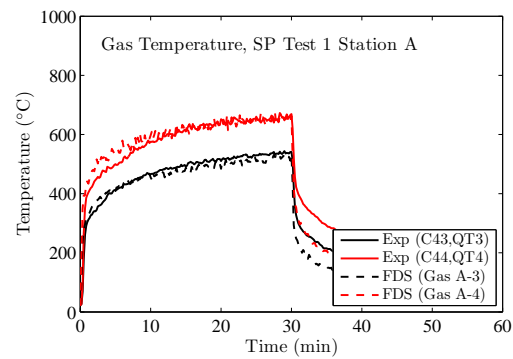
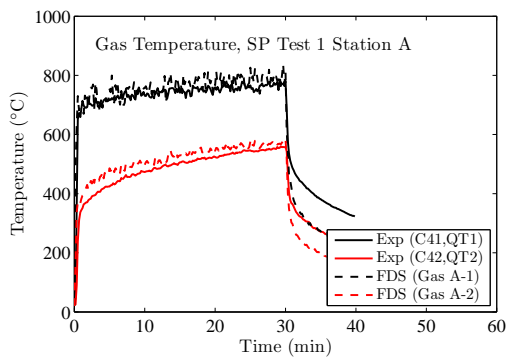
This definition of the AST forms the theory behind the plate thermometer, a 10 cm by 10 cm thin metal plate with an insulated backing that is designed to measure the AST, albeit with a slight time lag due to the fact that it is not a perfect insulator.

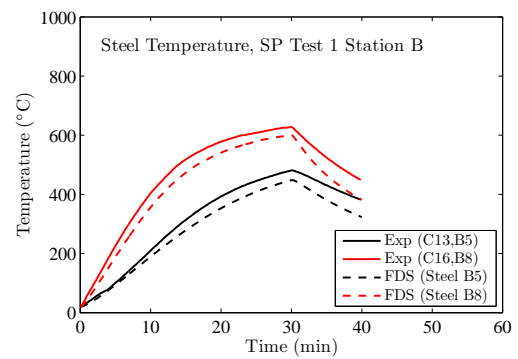
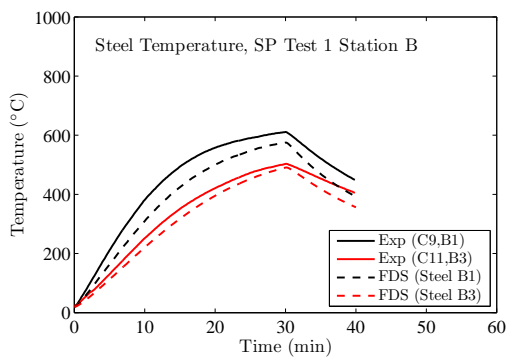
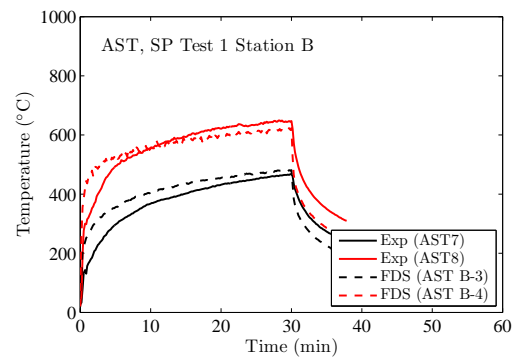
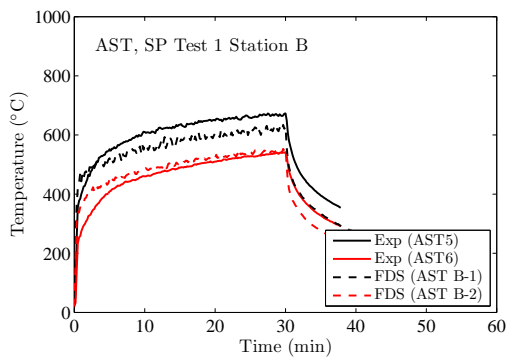
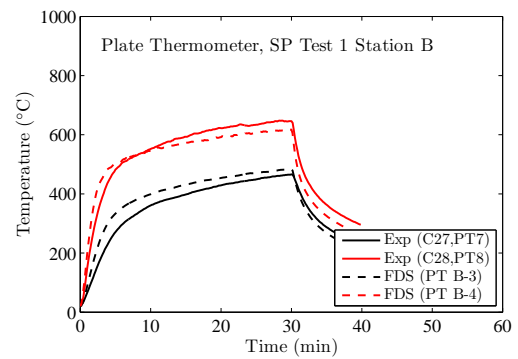
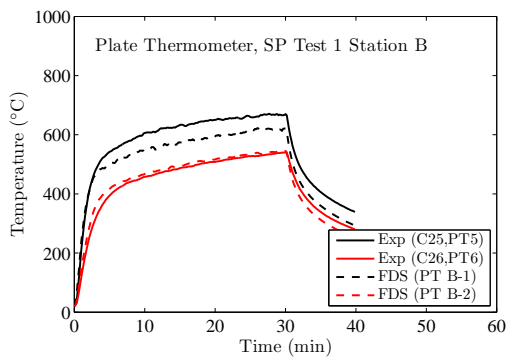
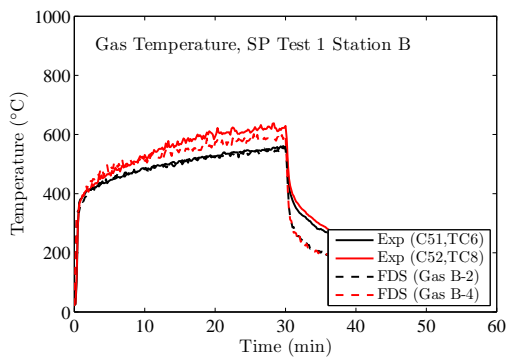
FDS calculates the AST by solving the following equation implicitly for T_{AST} :

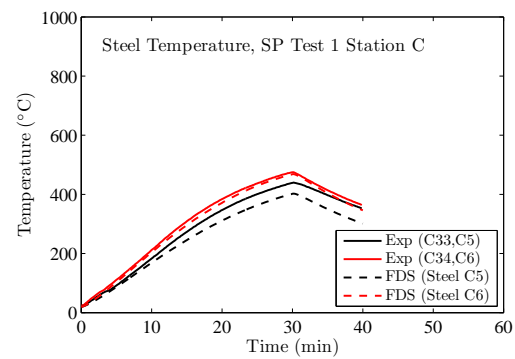
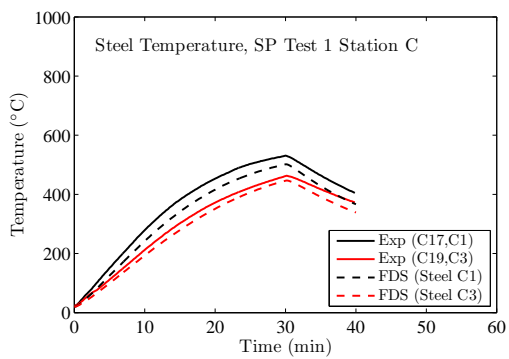
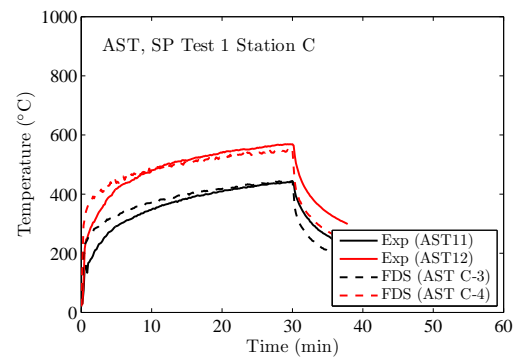
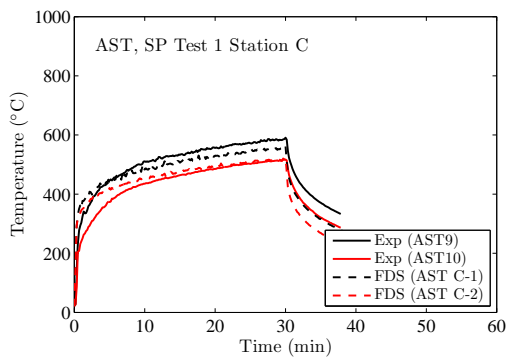
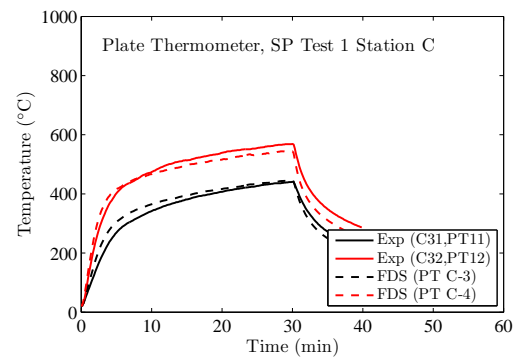
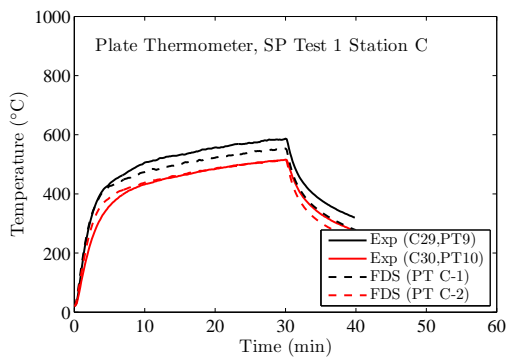
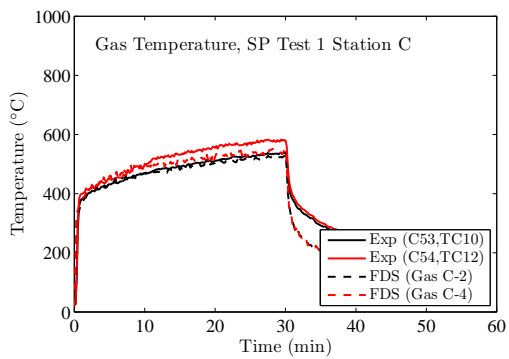
$$\dot{q}_r'' + \dot{q}_c'' = \epsilon (\sigma T_{AST}^4 - \sigma T_s^4) + h(T_{AST} - T_s) \quad (11.3)$$

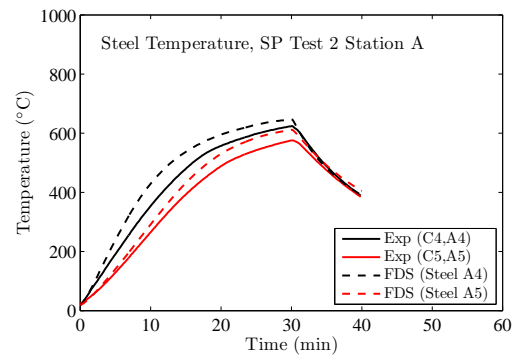
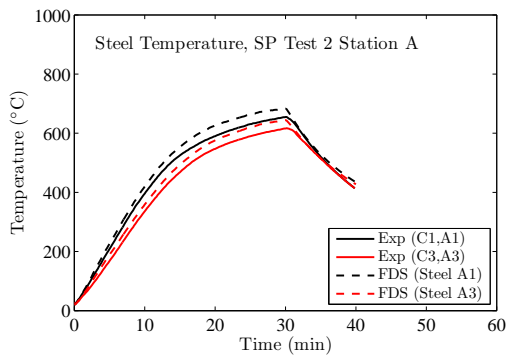
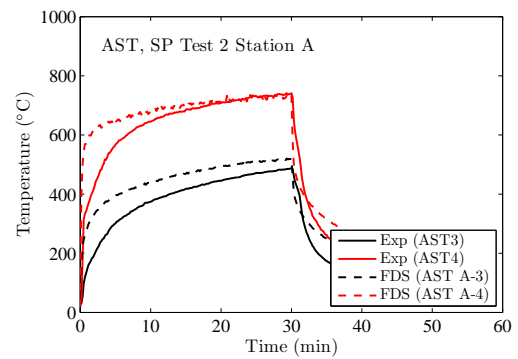
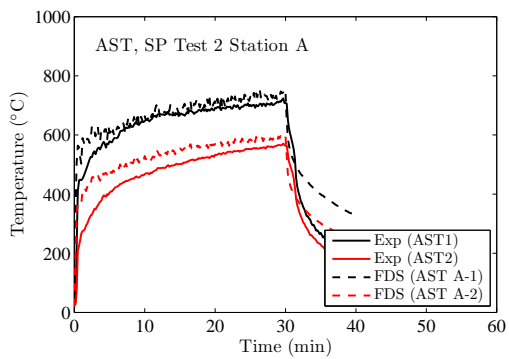
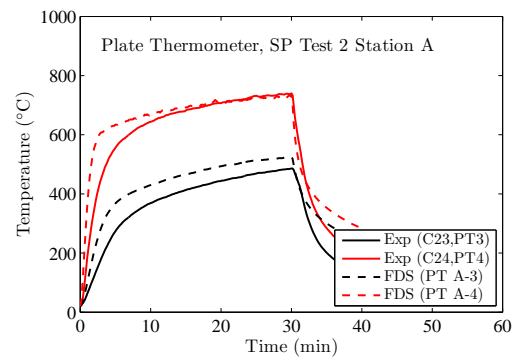
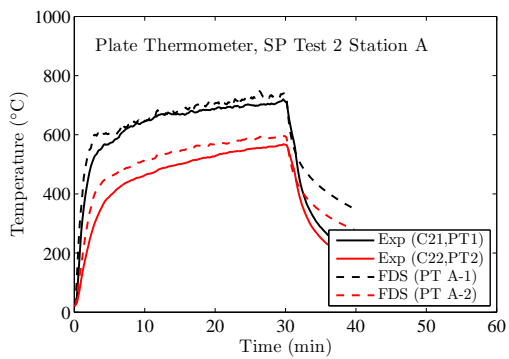
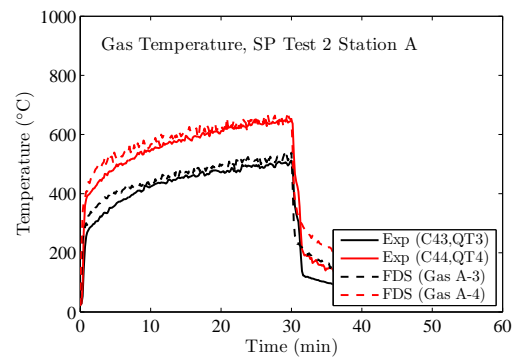
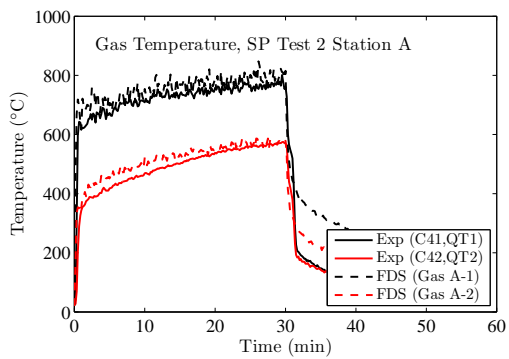
Equation (11.3) is simply Eq. (11.1) minus Eq. (11.2). As such, it shows that the AST can be regarded as an *effective* gas temperature for the purpose of providing boundary conditions for a detailed heat conduction calculation within the solid.

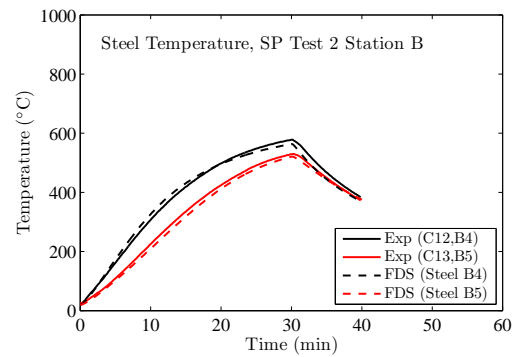
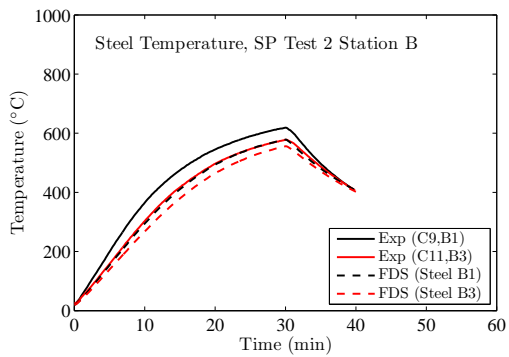
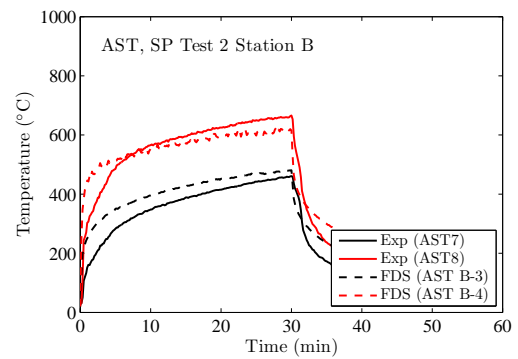
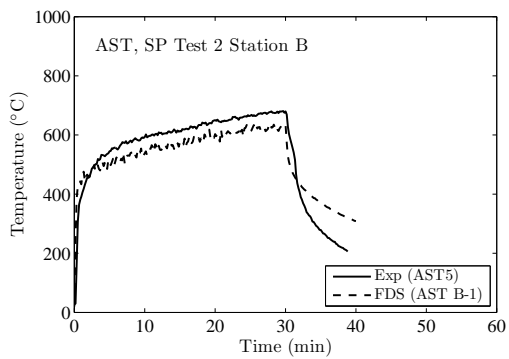
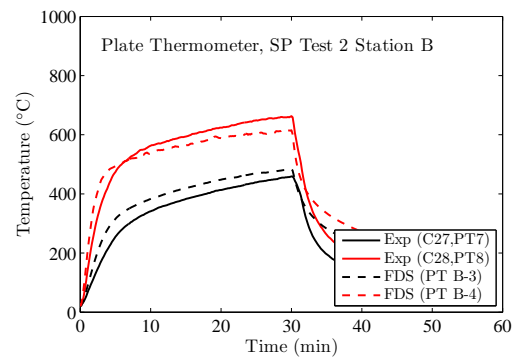
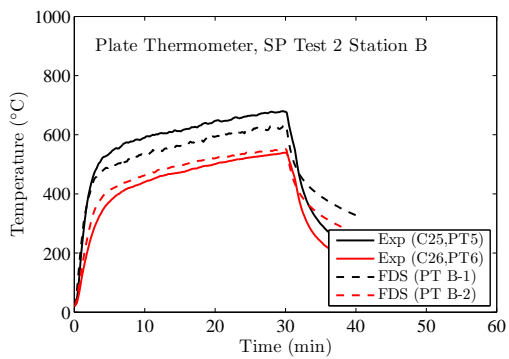
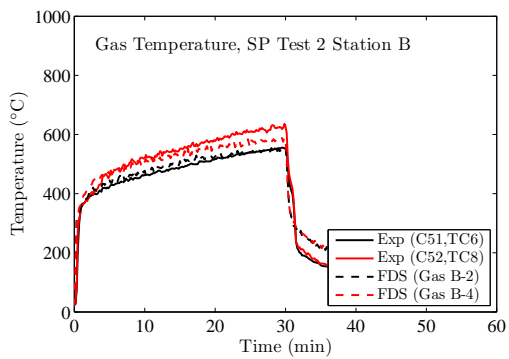
FDS calculates the AST using Eq. (11.3) and the plate thermometer temperature via its standard one-dimensional heat conduction calculation for a two layer solid of metal and insulating material. In the experiments, the plate thermometer temperature was obtained from a thermocouple attached to the back side of the thin metal plate, and the AST was derived from the measured plate thermometer temperature by a back calculation involving only the thermal lag due to the plate, not the insulation material.

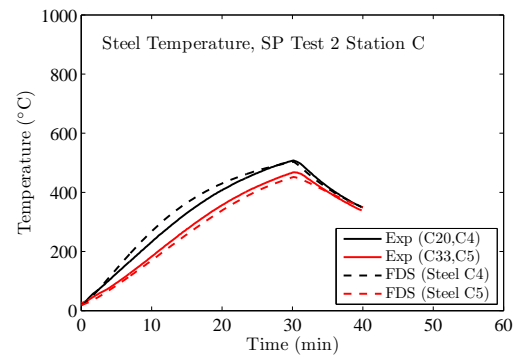
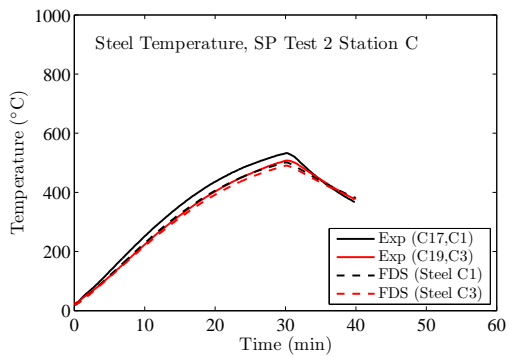
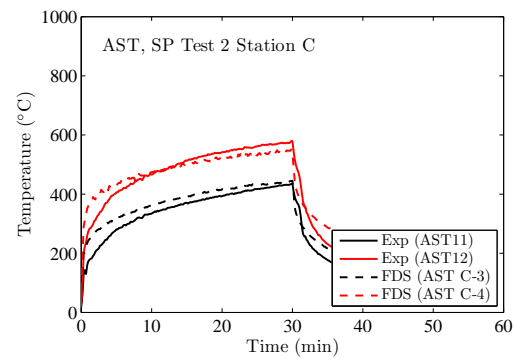
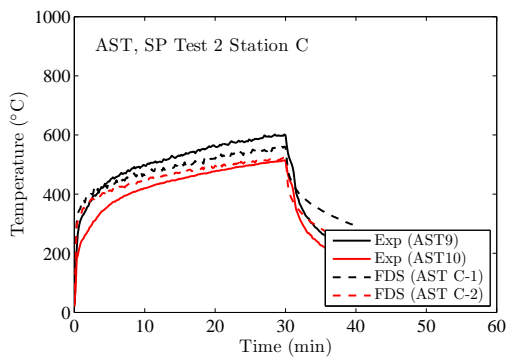
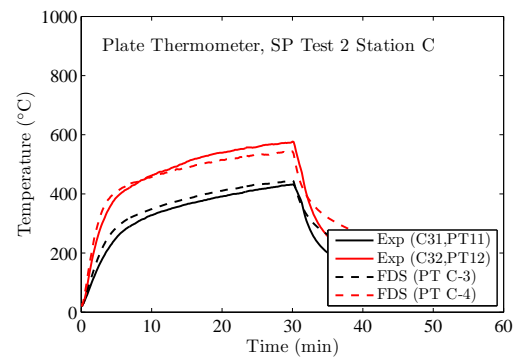
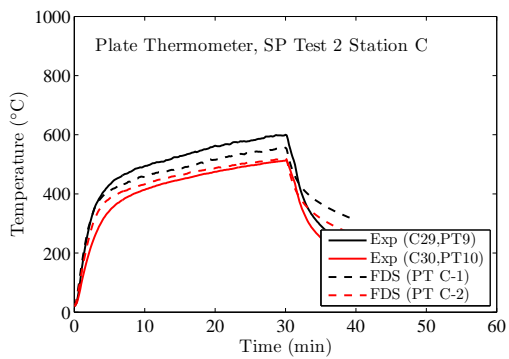
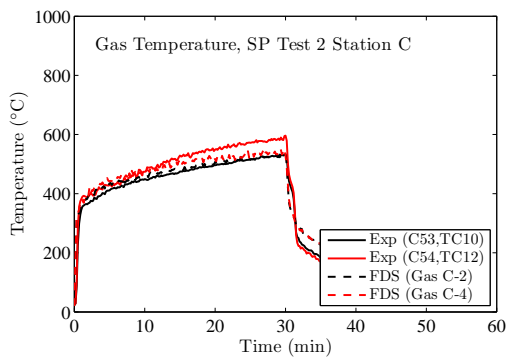


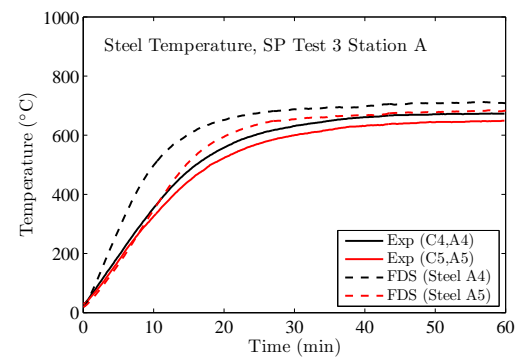
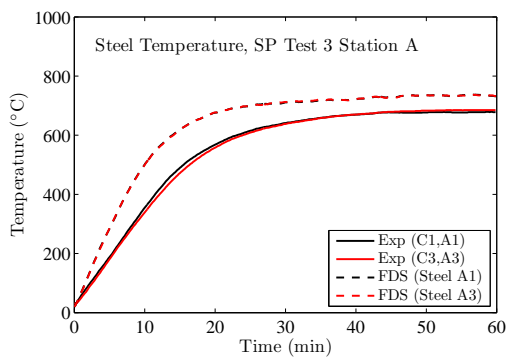
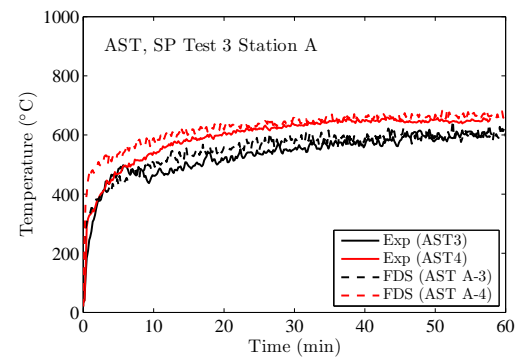
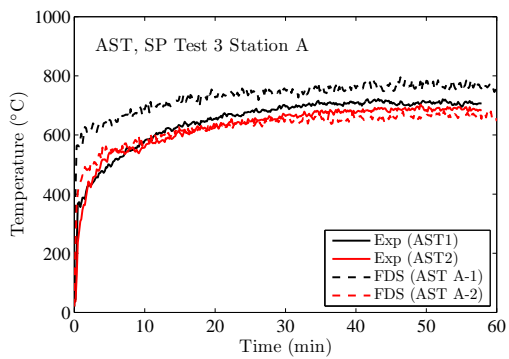
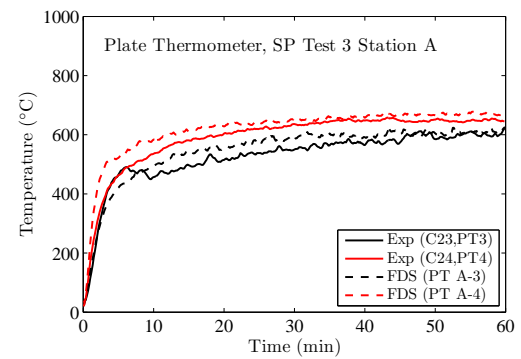
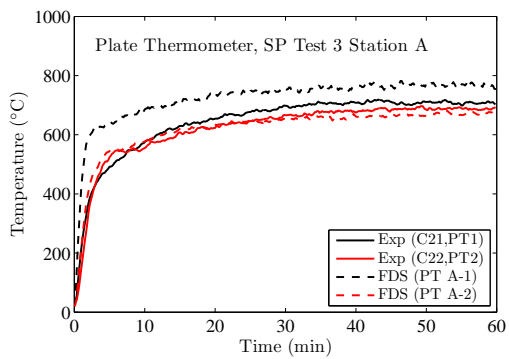
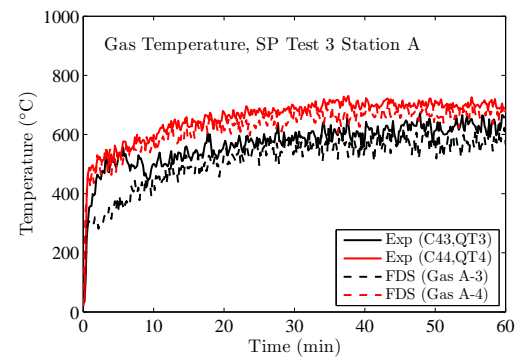
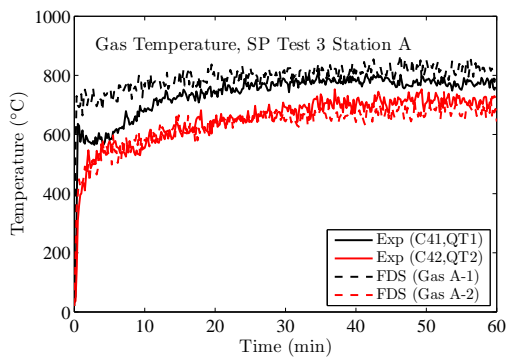


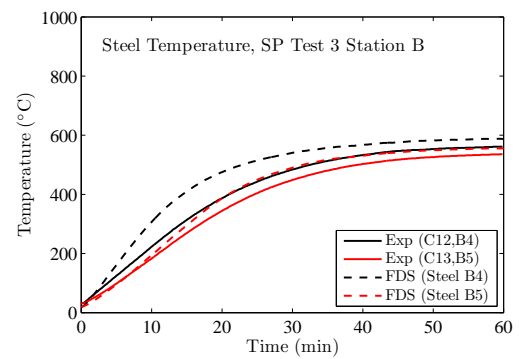
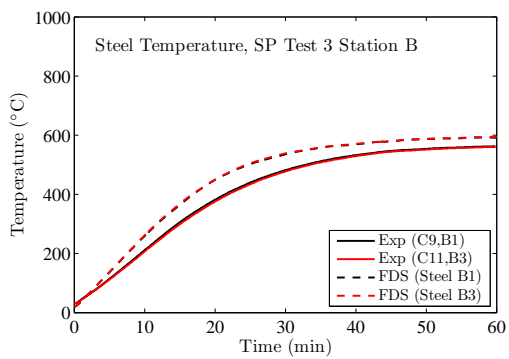
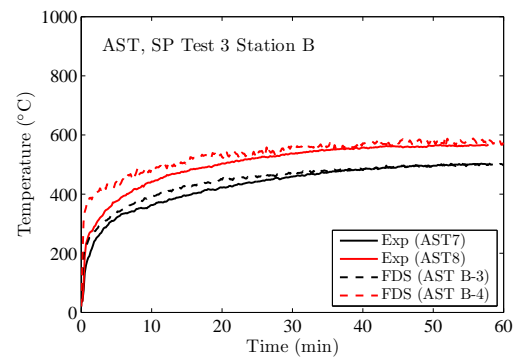
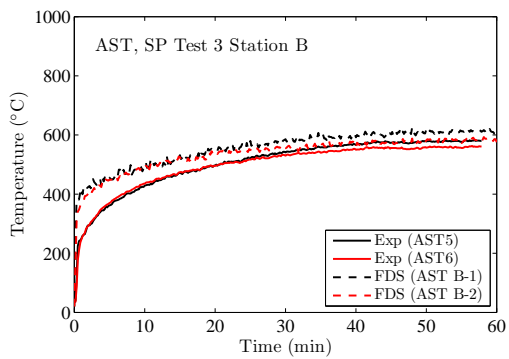
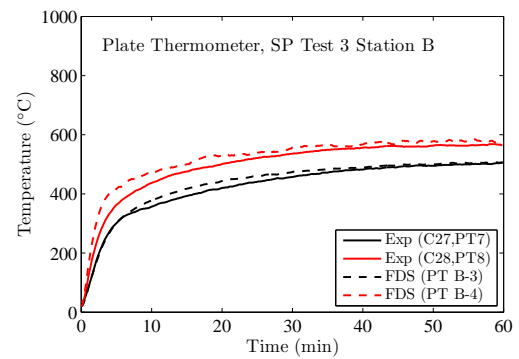
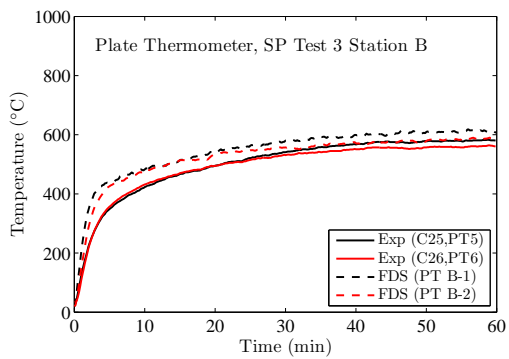
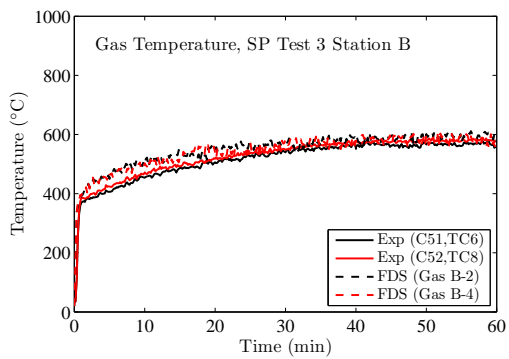


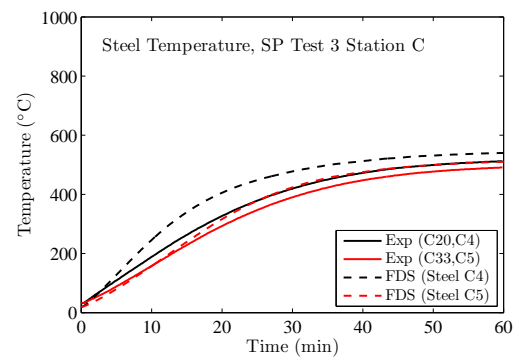
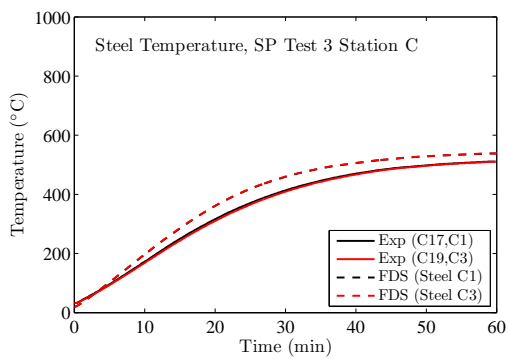
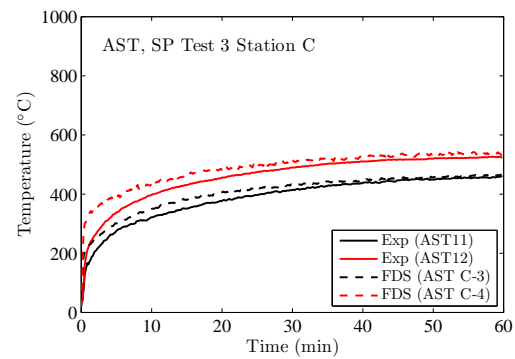
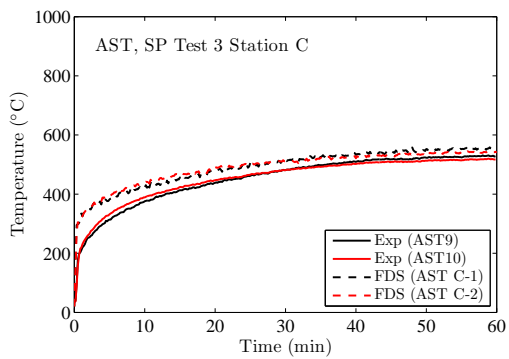
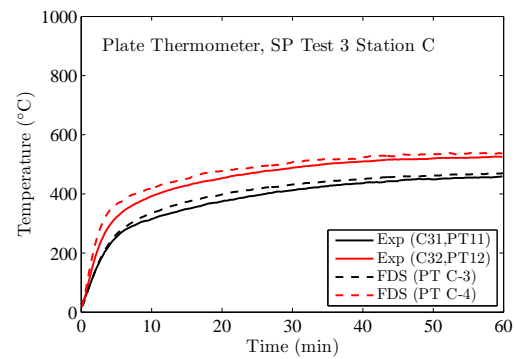
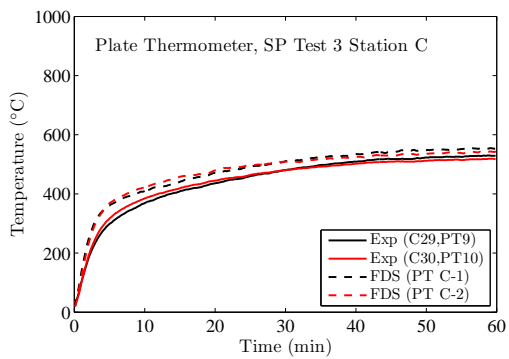
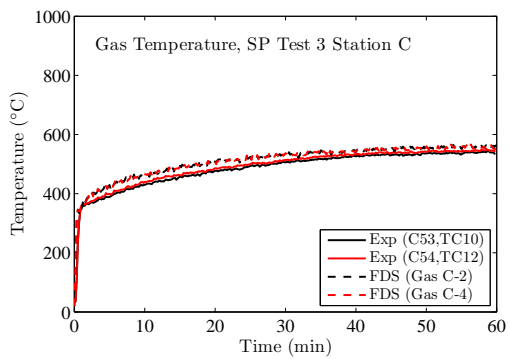












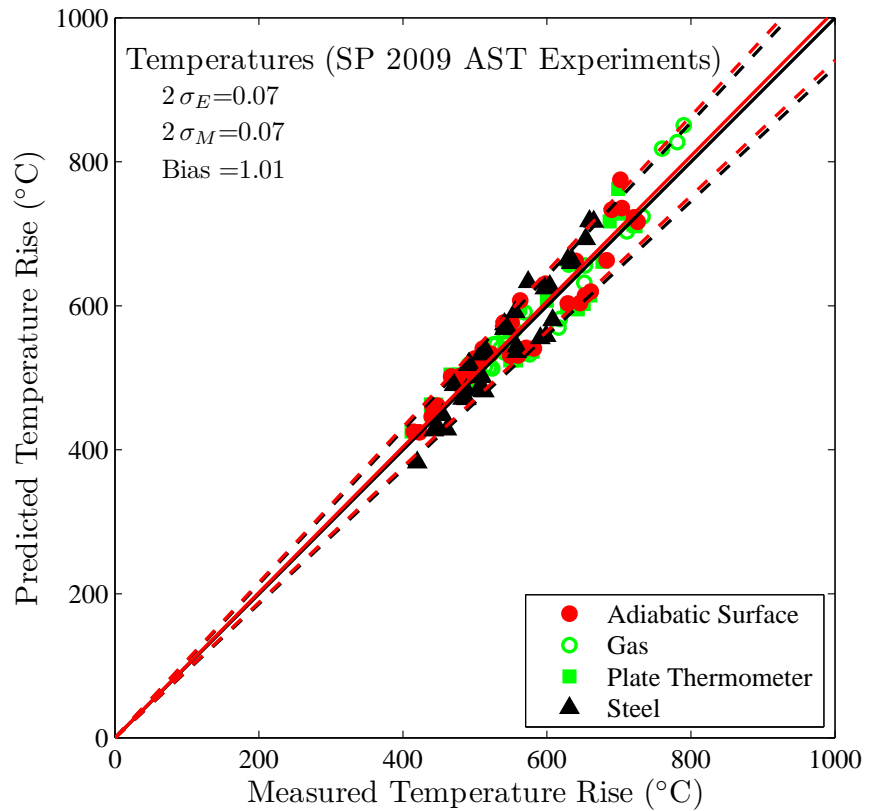
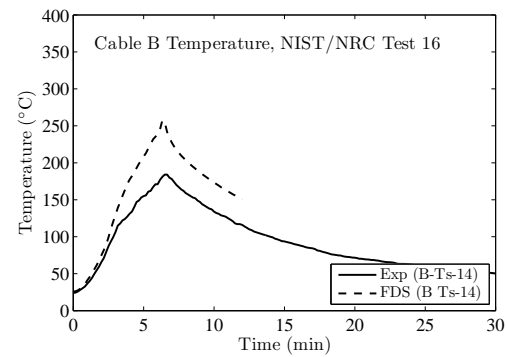
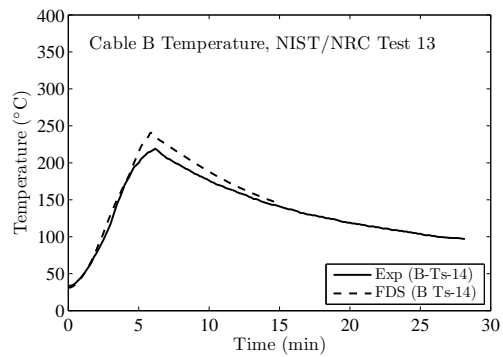
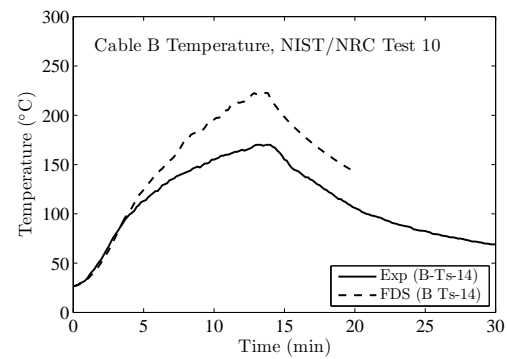
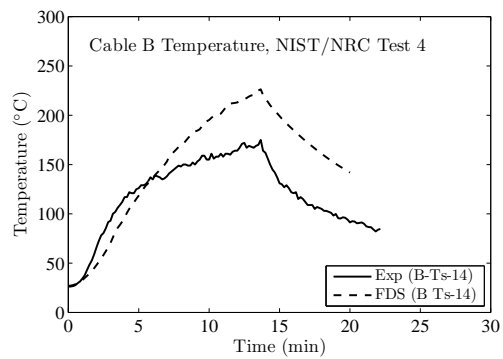
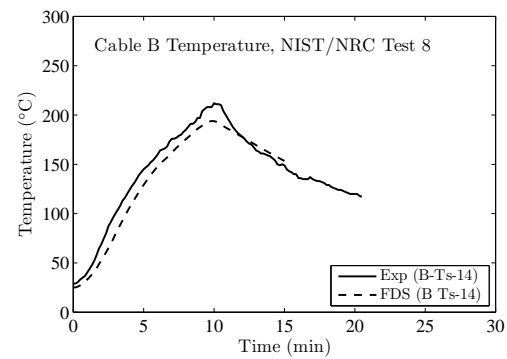
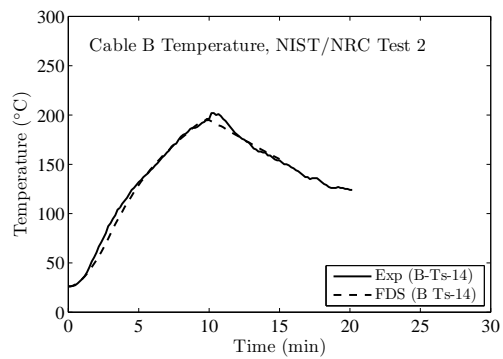
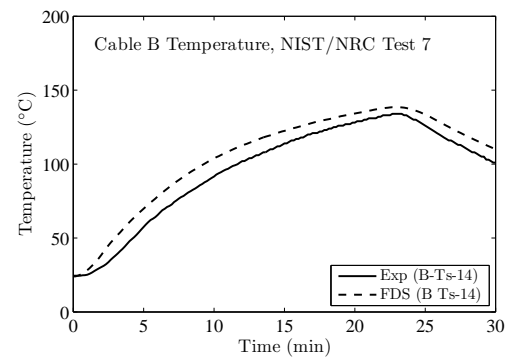
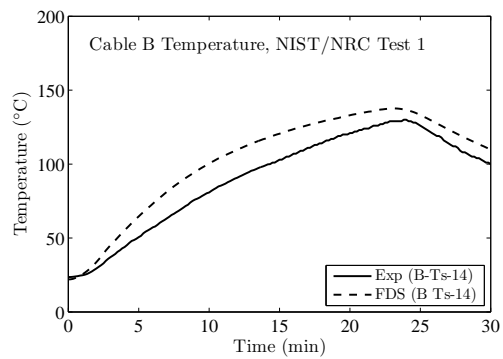
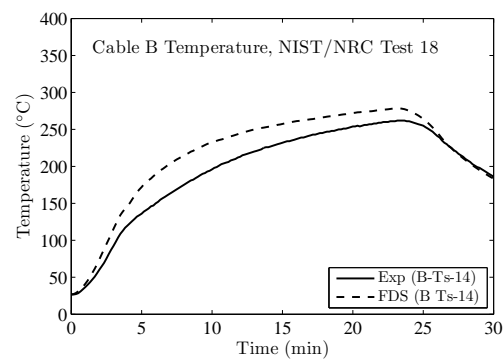
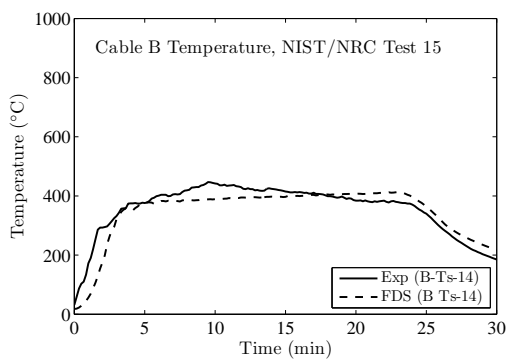
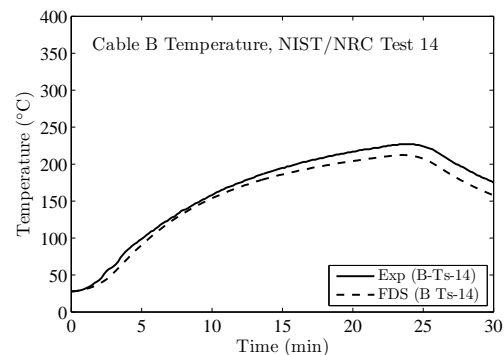
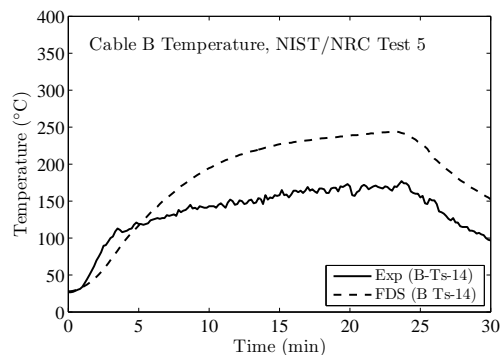
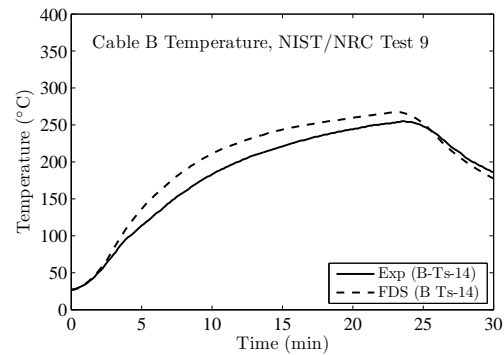
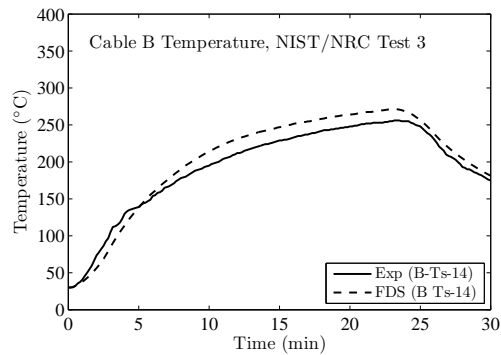


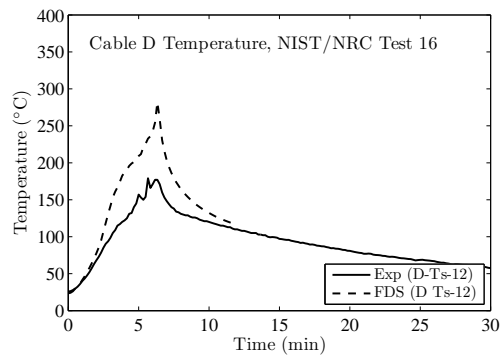
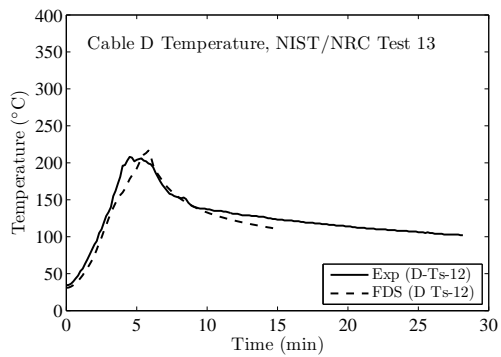
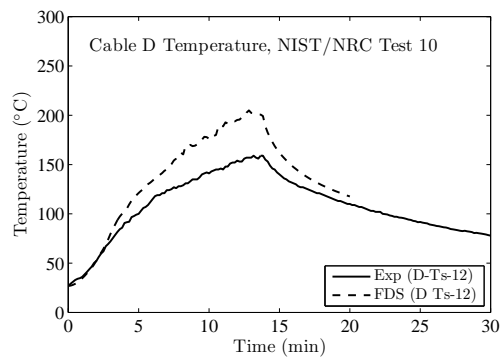
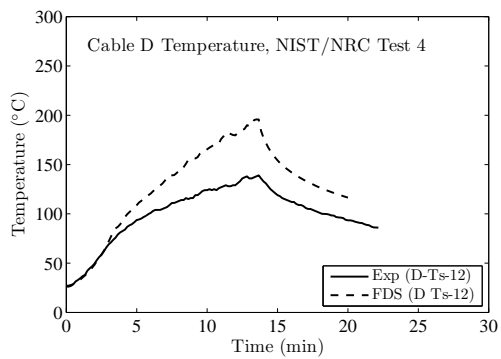
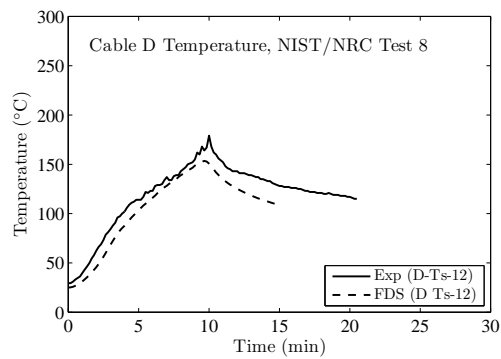
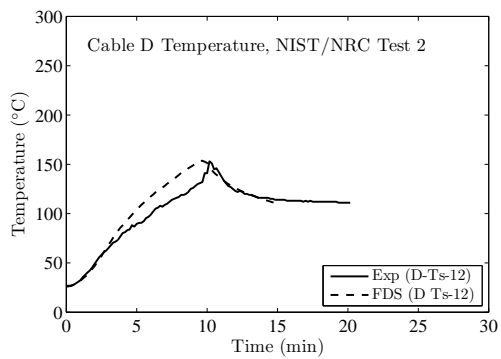
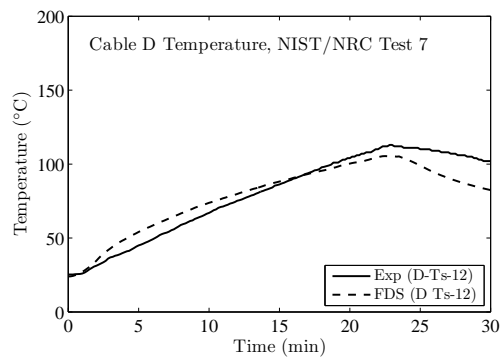
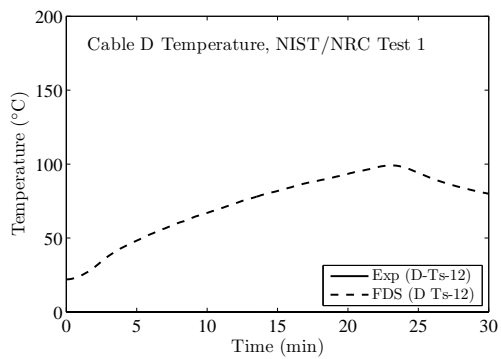
Figure 11.2: Summary of gas, plate thermometer, and steel temperatures, SP2009 AST Experiments.

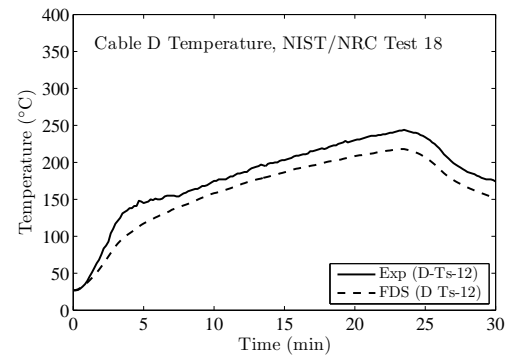
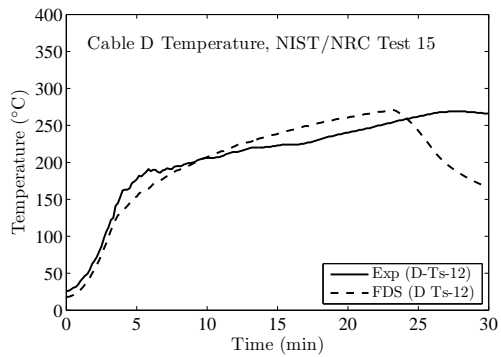
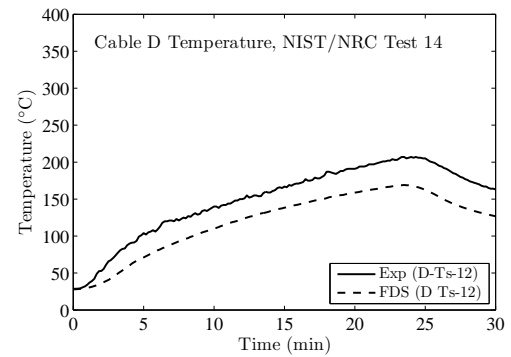
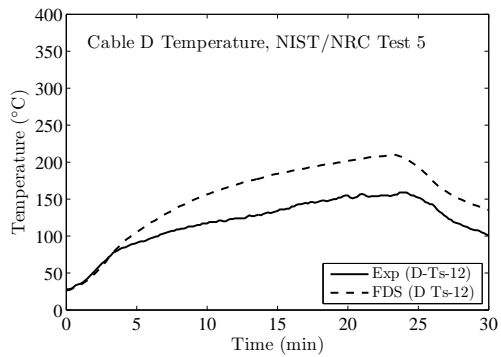
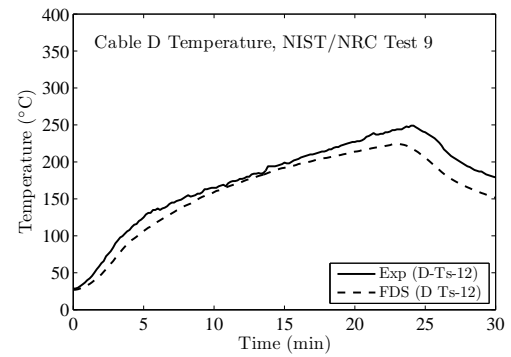
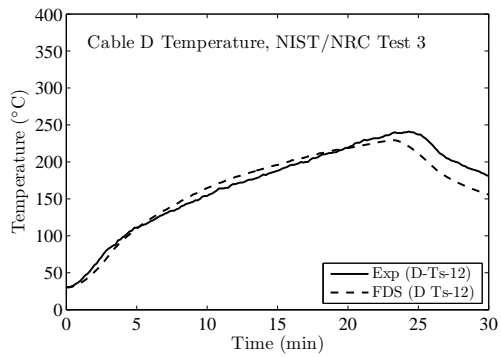
11.3 NIST/NRC Test Series, Cables

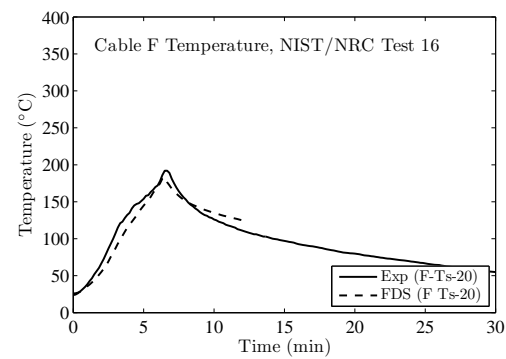
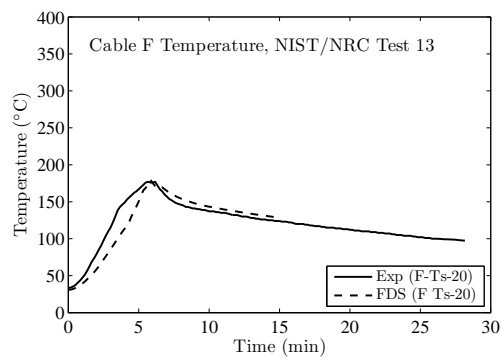
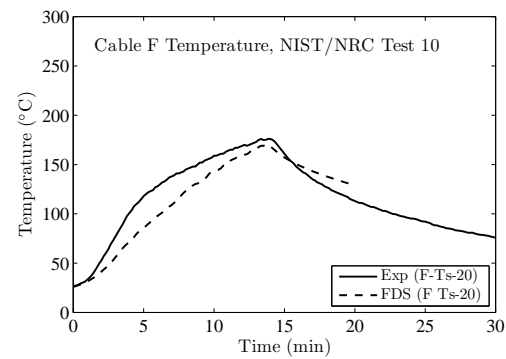
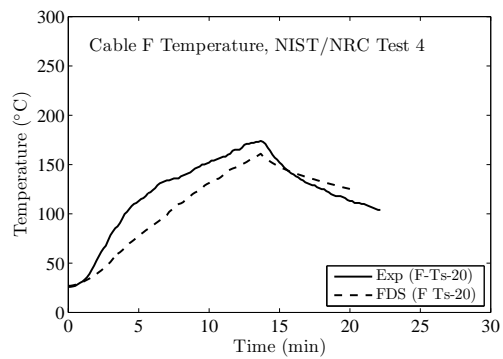
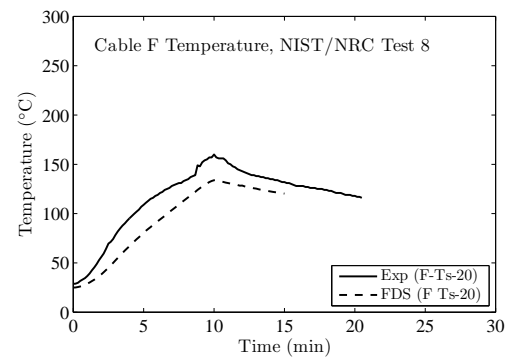
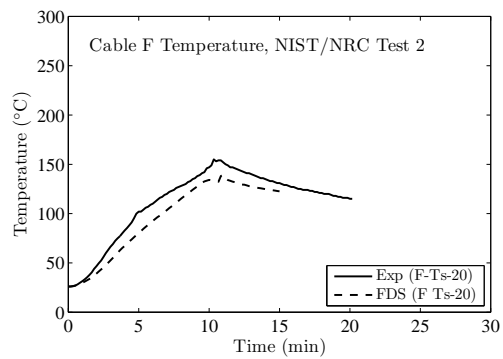
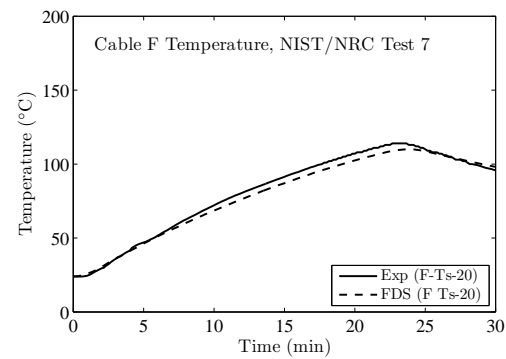
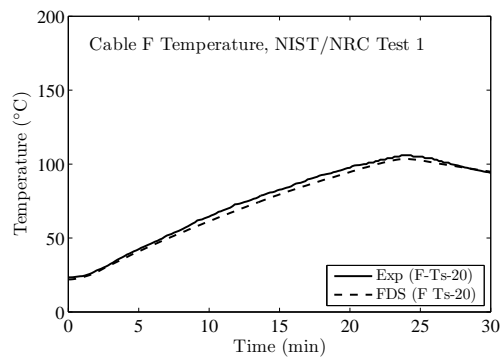
Cables in various types (power and control), and configurations (horizontal, vertical, in trays or free-hanging), were installed in the test compartment. For each of the four cable targets considered, measurements of the local gas temperature, surface temperature, radiative heat flux, and total heat flux are available. The following pages display comparisons of these quantities for Control Cable B, Horizontal Cable Tray D, Power Cable F and Vertical Cable Tray G. FDS does not have a detailed solid phase model that can account for the heat transfer within the bundled, cylindrical, non-homogenous cables. For the bundled cables within horizontal and vertical trays (Targets D and G), FDS assumes them to be rectangular slabs of thickness comparable to the diameter of the individual cables. For the free-hanging cables B and F, FDS assumes them to be cylinders of uniform composition into which it computes the radial heat transfer as a function of the heat flux to a designated location. The superposition of gas temperature, heat flux and surface temperature in the figures on the following pages provides information about how cables heat up in fires. Favorable or unfavorable predictions of cable surface temperatures can often be explained in terms of comparable errors in the prediction of the thermal environment in the vicinity of the cable.

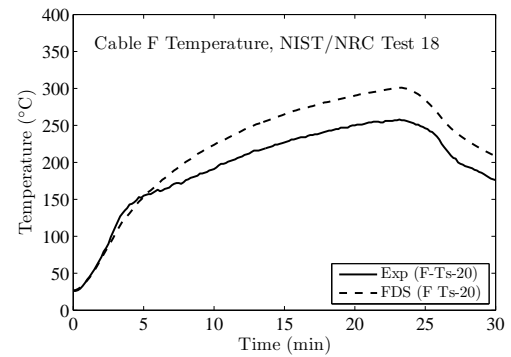
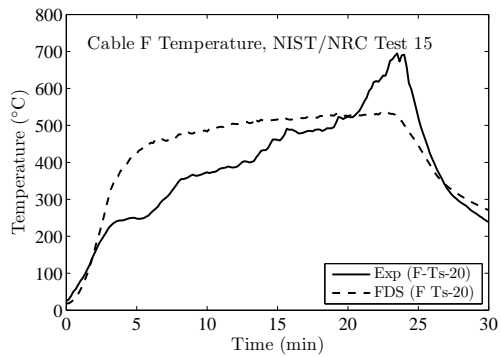
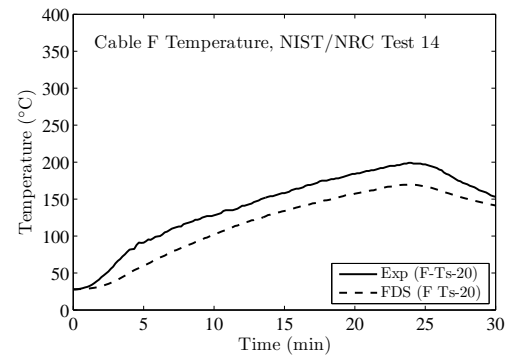
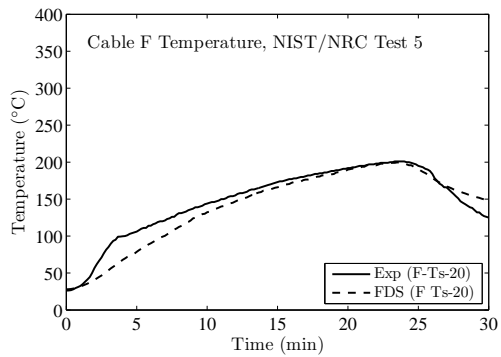
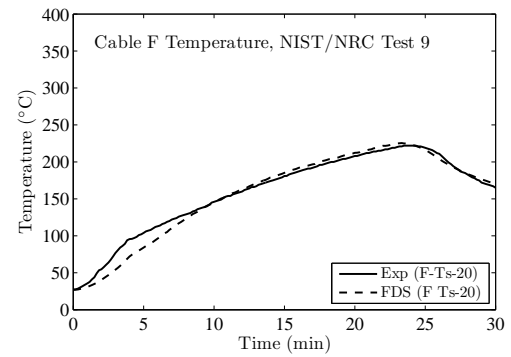
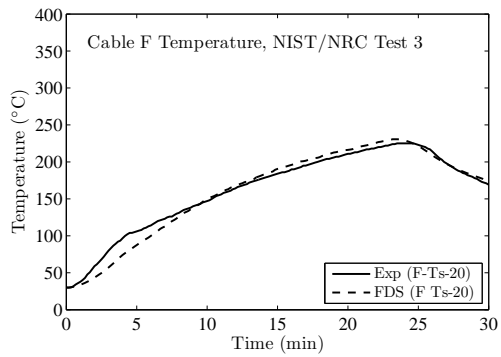


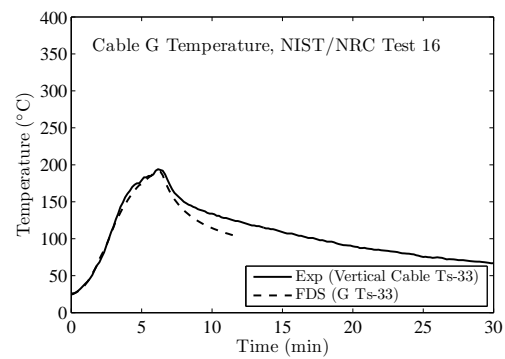
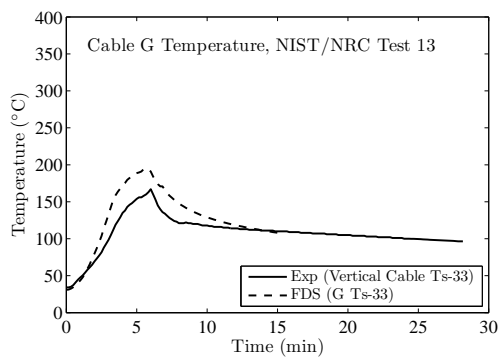
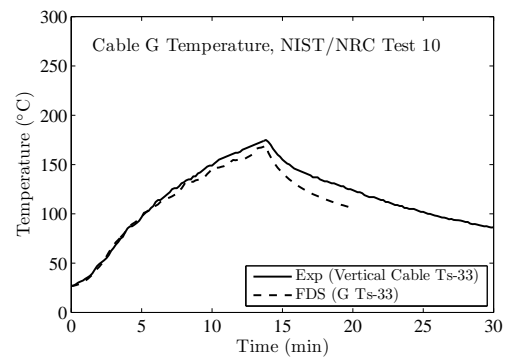
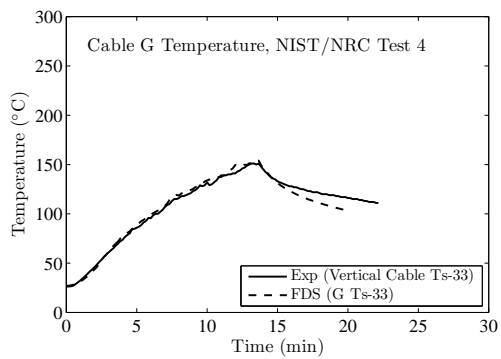
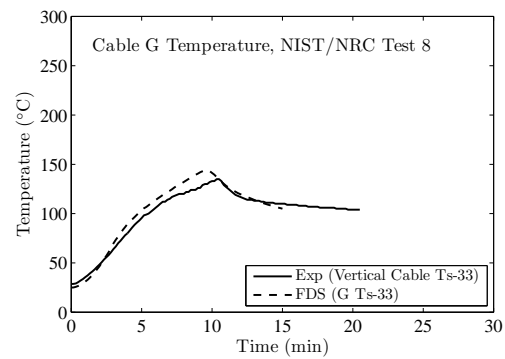
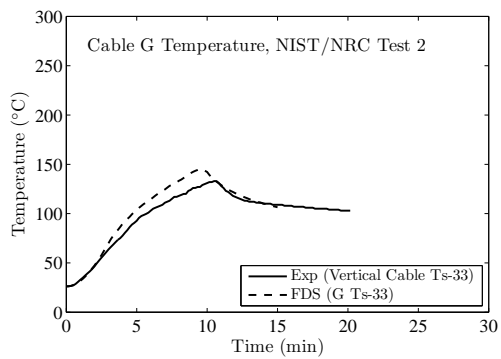
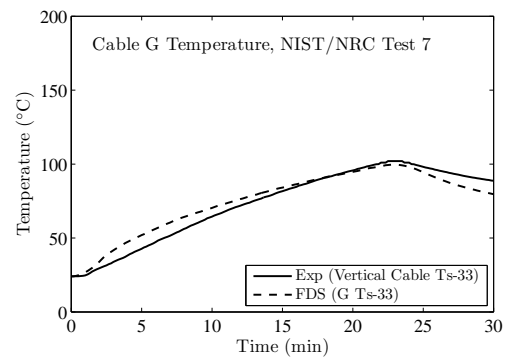
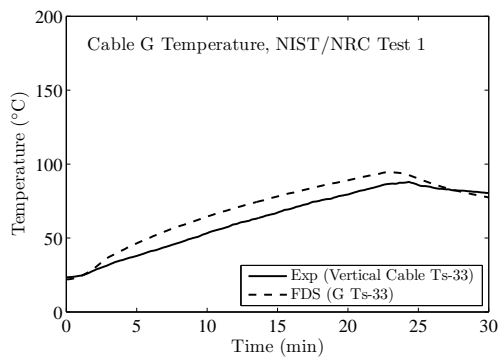


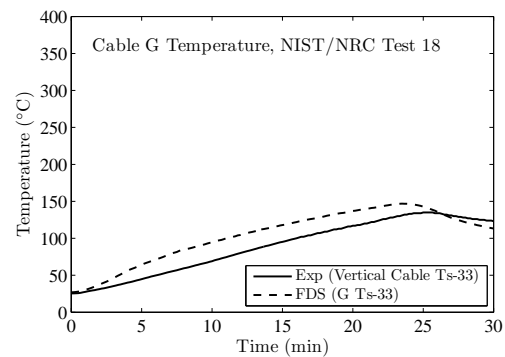
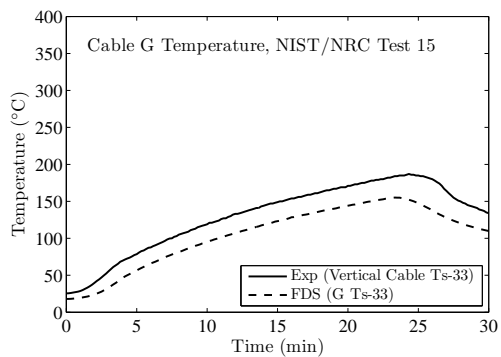
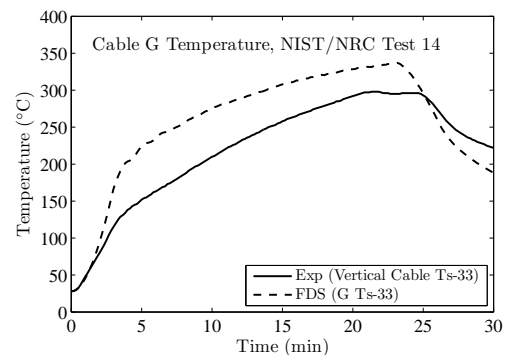
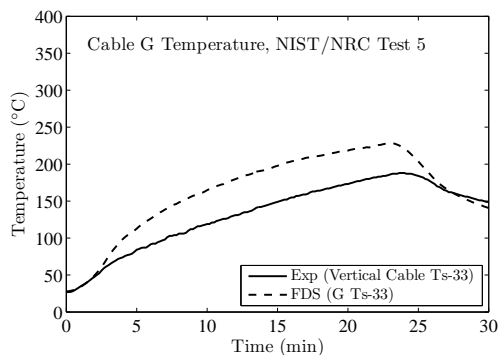
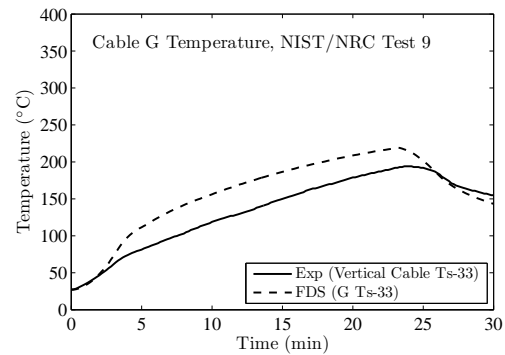
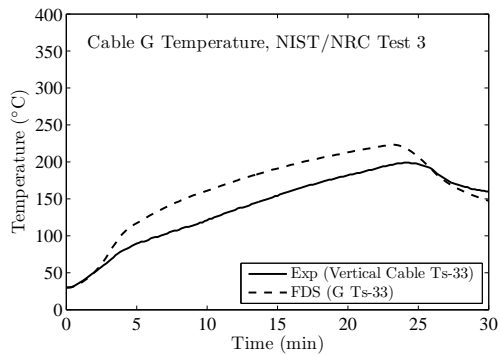












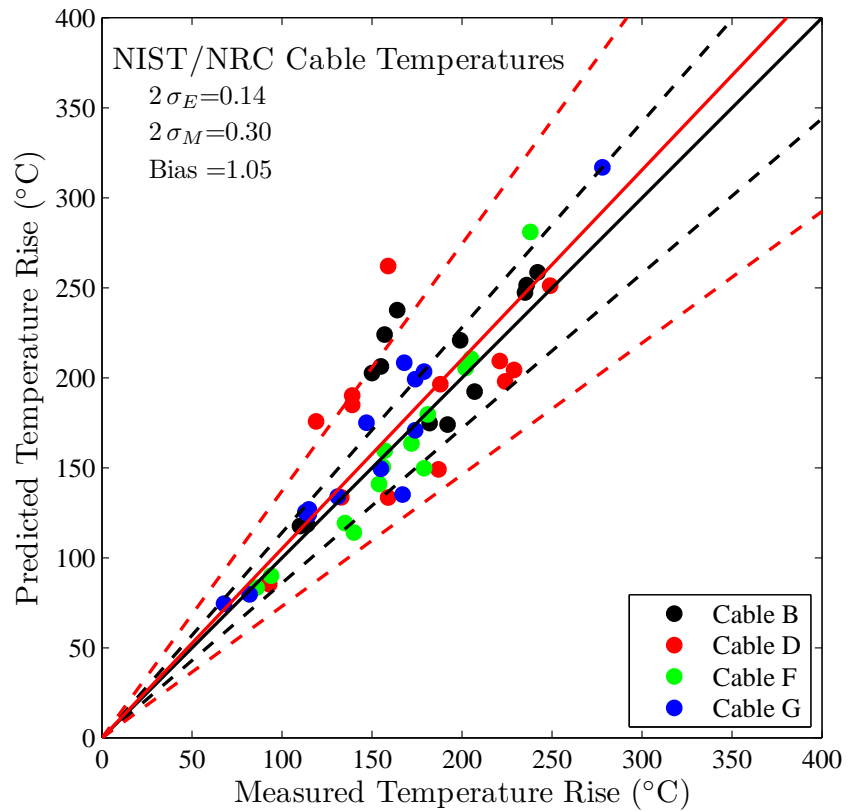
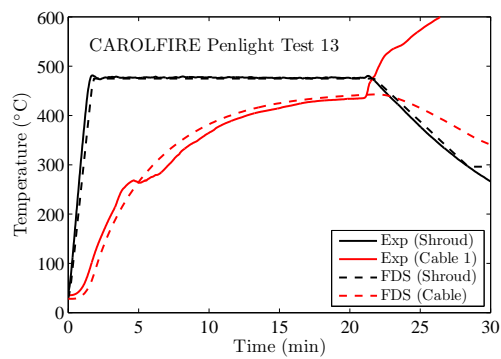
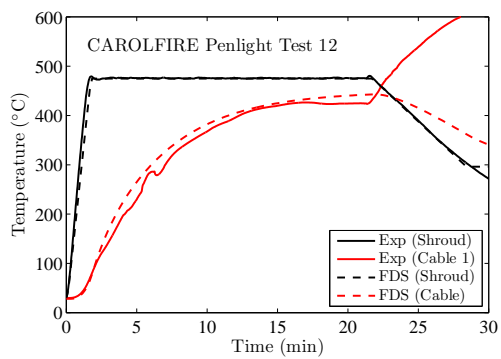
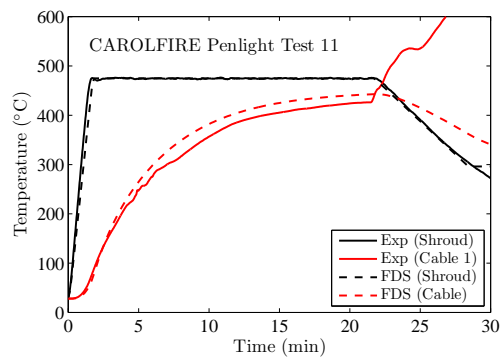
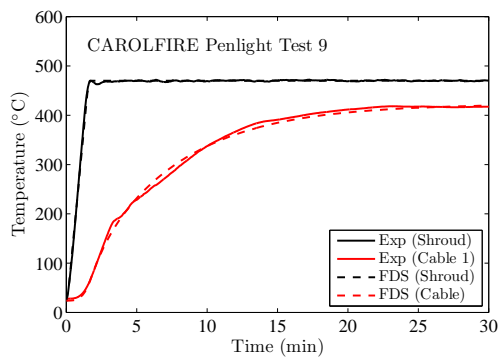
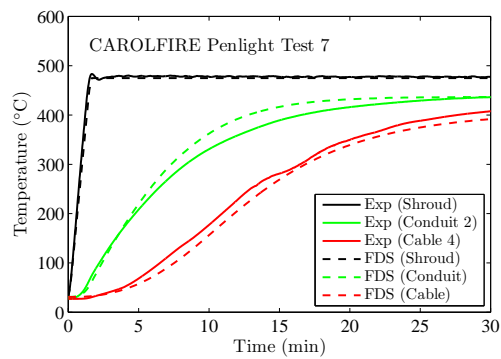
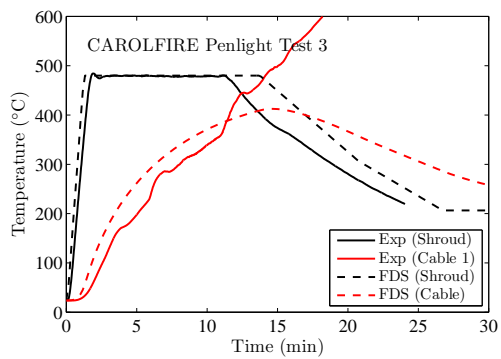
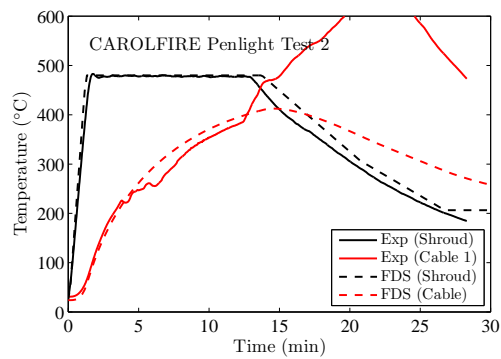
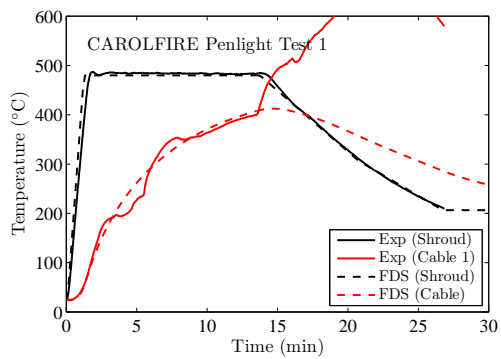


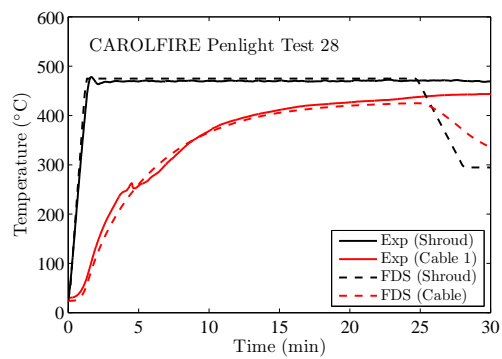
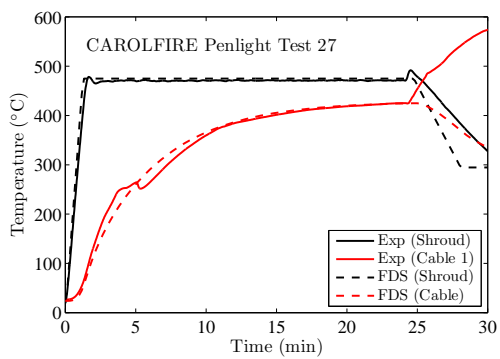
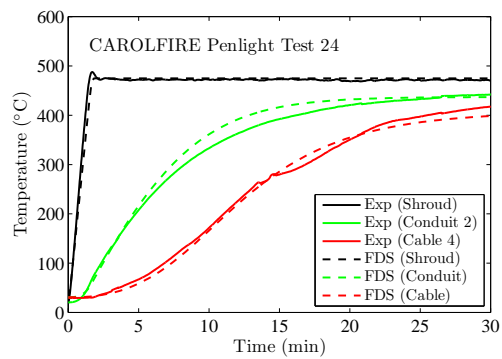
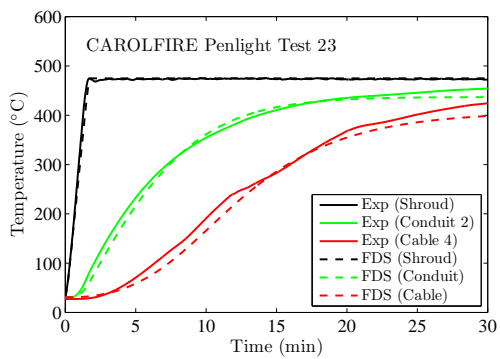
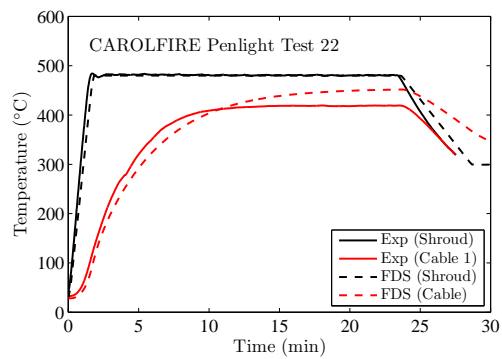
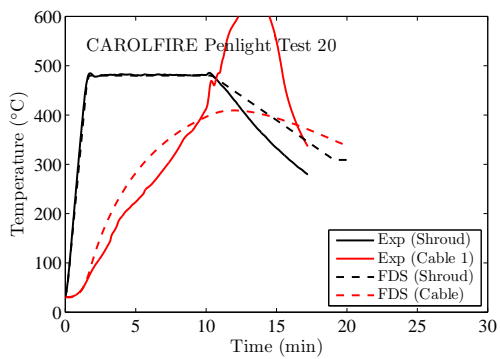
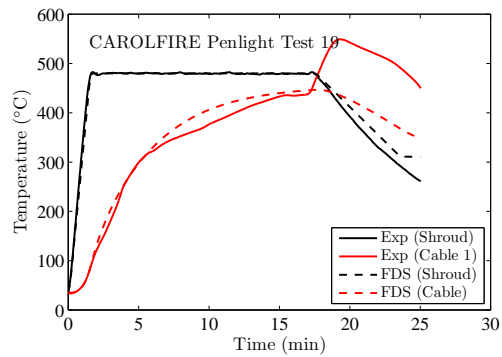
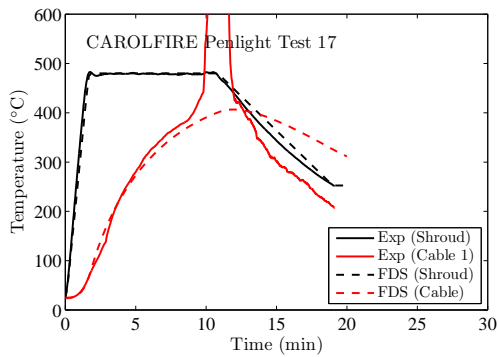
Figure 11.3: Summary of cable surface temperature predictions for the NIST/NRC test series.

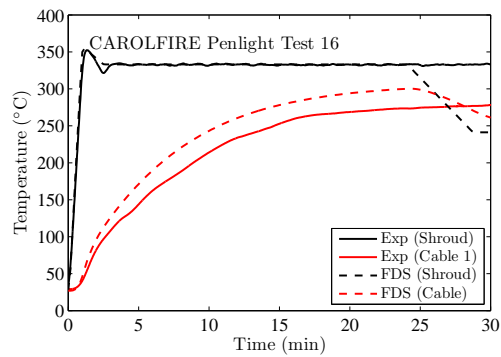
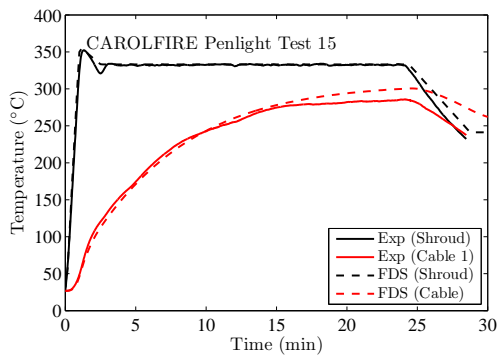
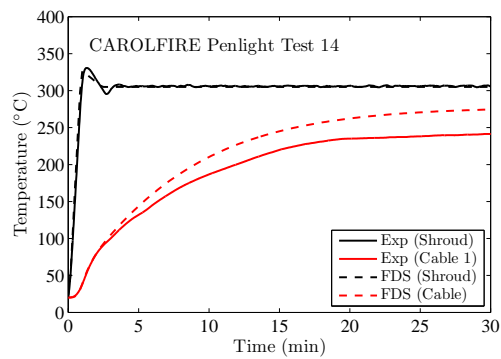
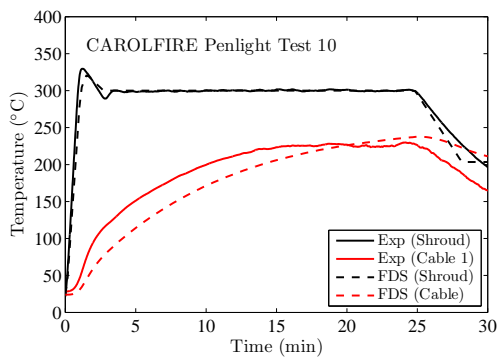
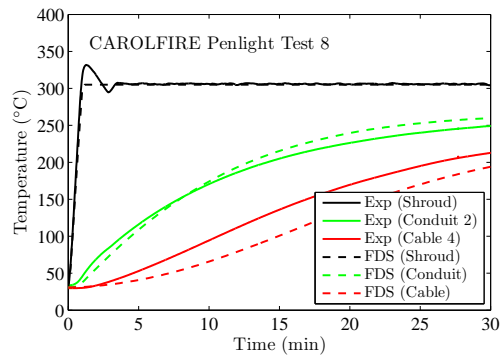
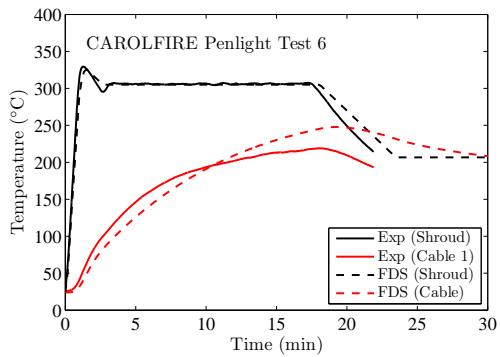
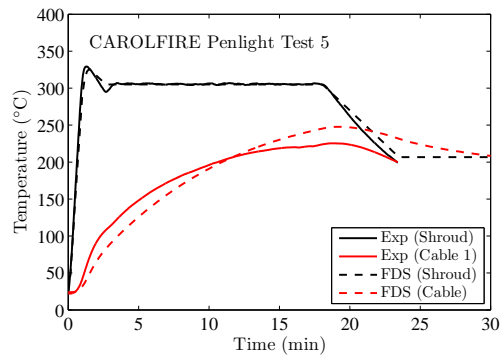
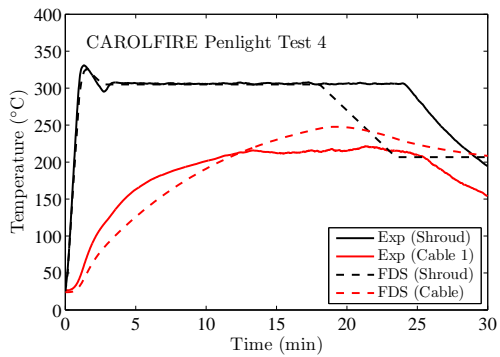
11.4 CAROLFIRE Cable Temperatures

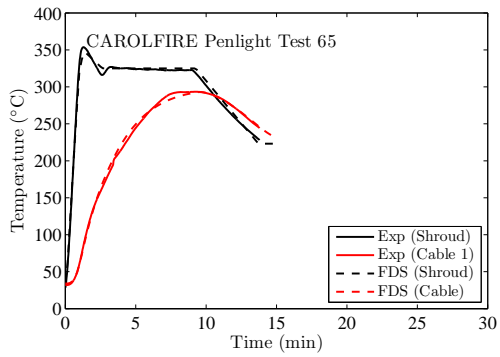
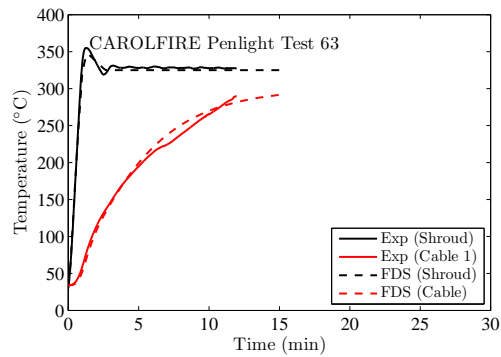
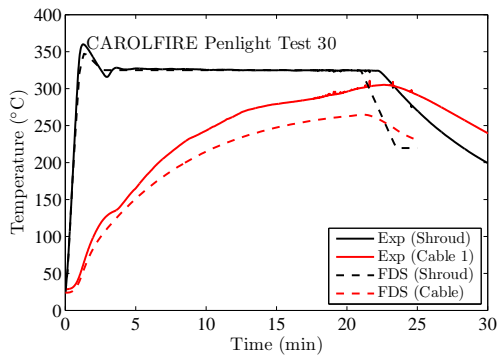
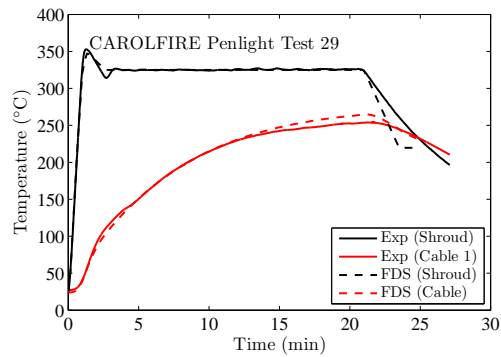
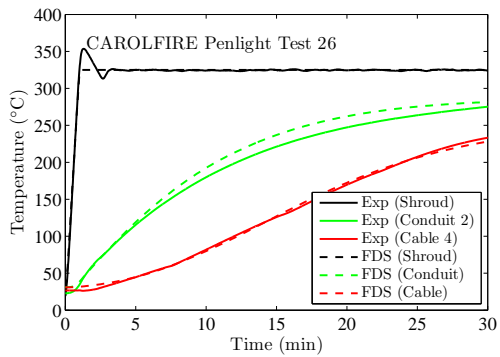
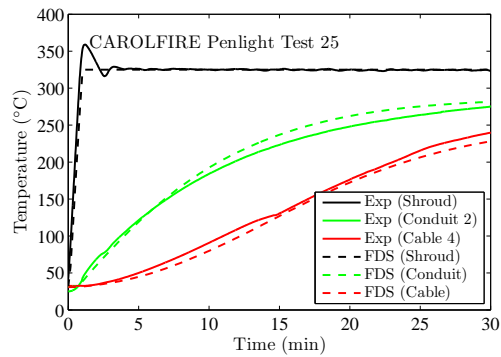
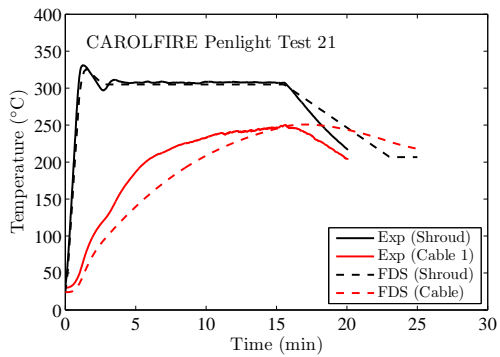
On the following pages are predictions of the THIEF (thermally-induced electrical failure) model compared to 35 experiments conducted in a heated cylindrical “shroud.” The shroud temperature is input into the model, and the cable temperature (and in some cases that of the steel conduit enclosing the cable) is predicted. Note that the cables generally fall into two categories – thermoset and thermoplastic. Thermoset cables form a char layer when burned and typically fail electrically at temperatures near 400 °C. Thermoplastic cables typically melt and then burn, leaving little residue behind except the conductors. These cables typically fail at about 250 °C [140]. Some cables, as in Tests 18 and 31, do not fall into either category. The thermoset cables were exposed to temperatures in the neighborhood of 480 °C, and the thermoplastics were exposed to temperatures near 300 °C.

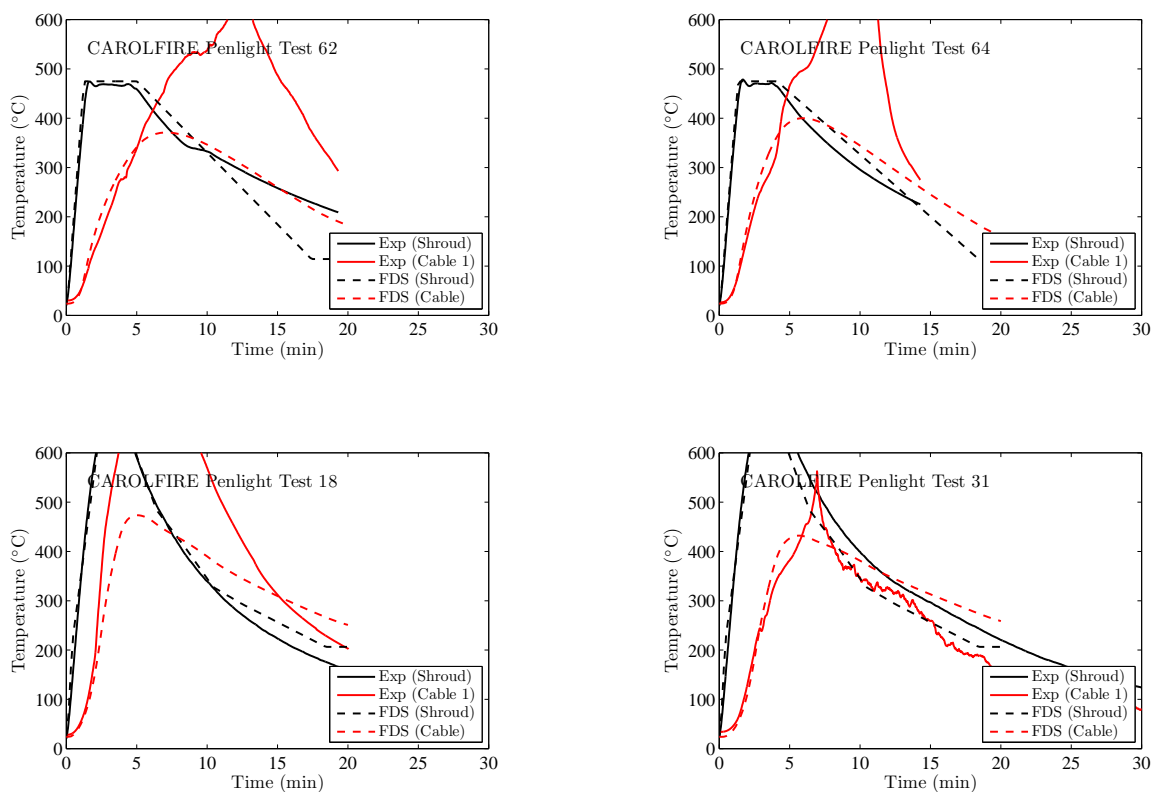
Note in the plots to follow that the objective of the calculation is to predict the cable temperature just inside of the jacket until the cable fails electrically. In some experiments, the short-circuiting of the cable led to ignition of the pyrolyzates. This behavior is not captured in the model, which is why some of the experimental data shows a rapid rise in temperature at a certain point in the test. In almost all cases, electrical failure occurred very shortly, or at about the same time, as ignition.









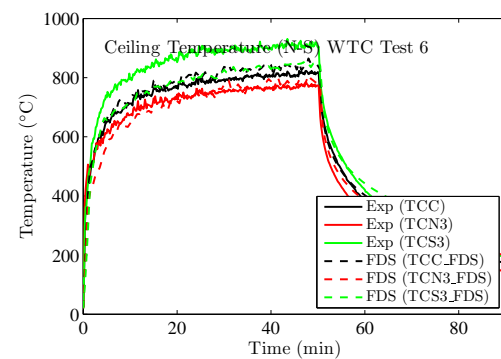
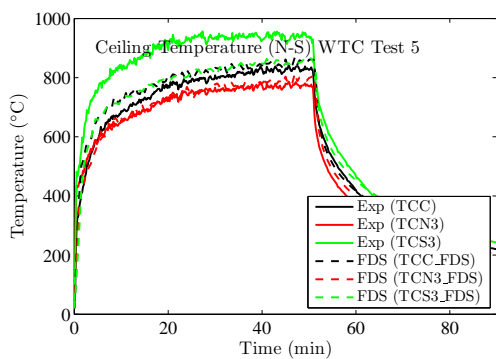
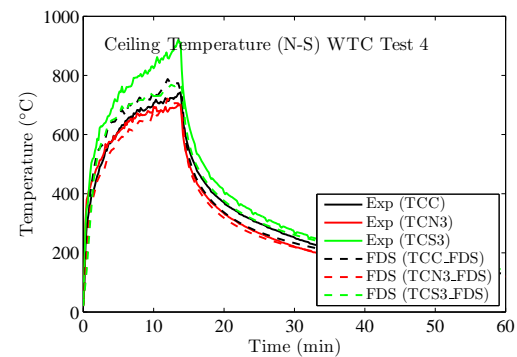
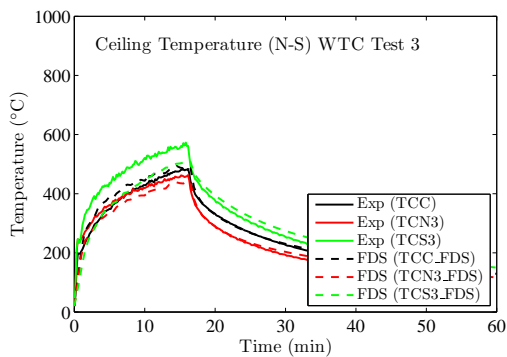
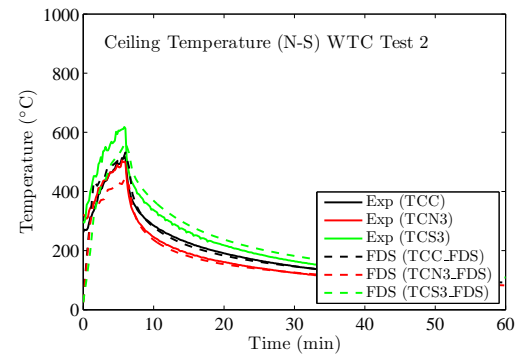
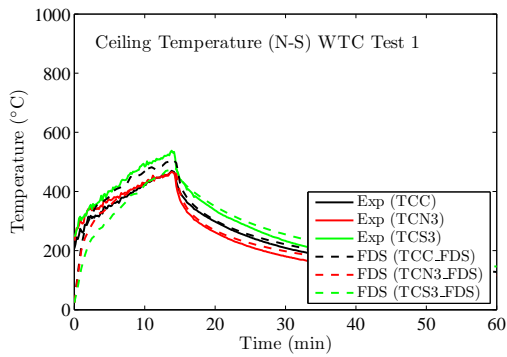


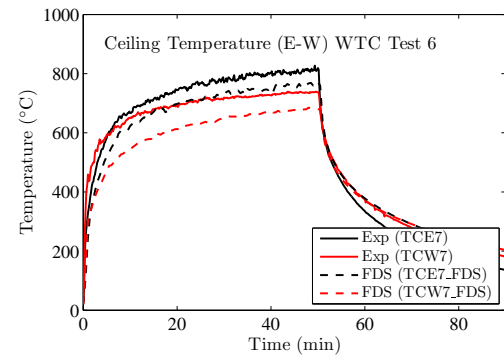
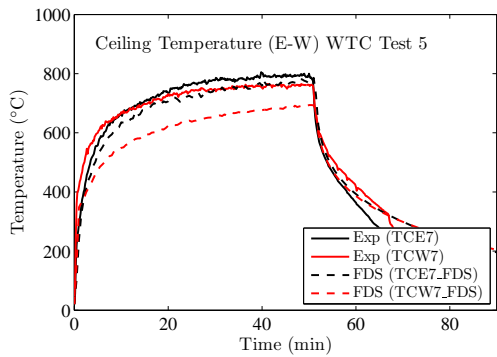
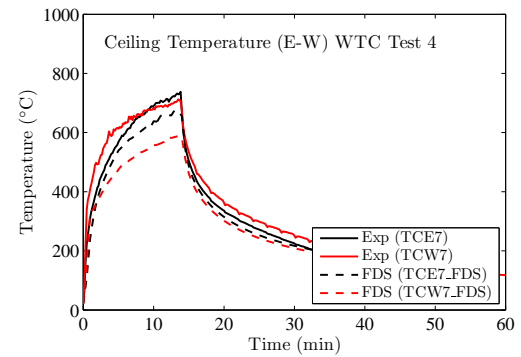
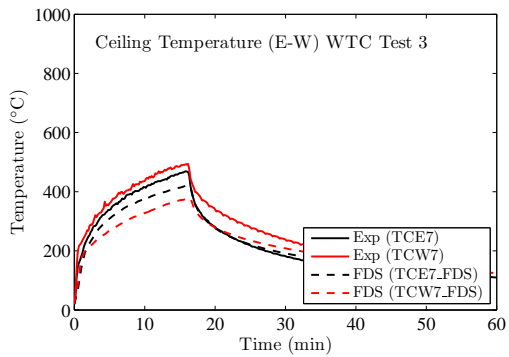
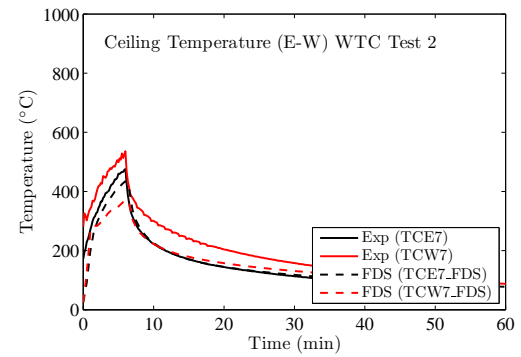
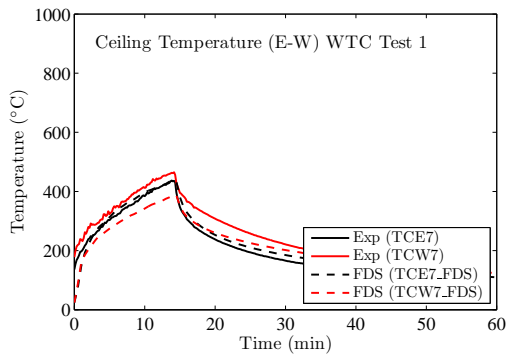
11.5 WTC Ceiling and Wall Temperatures

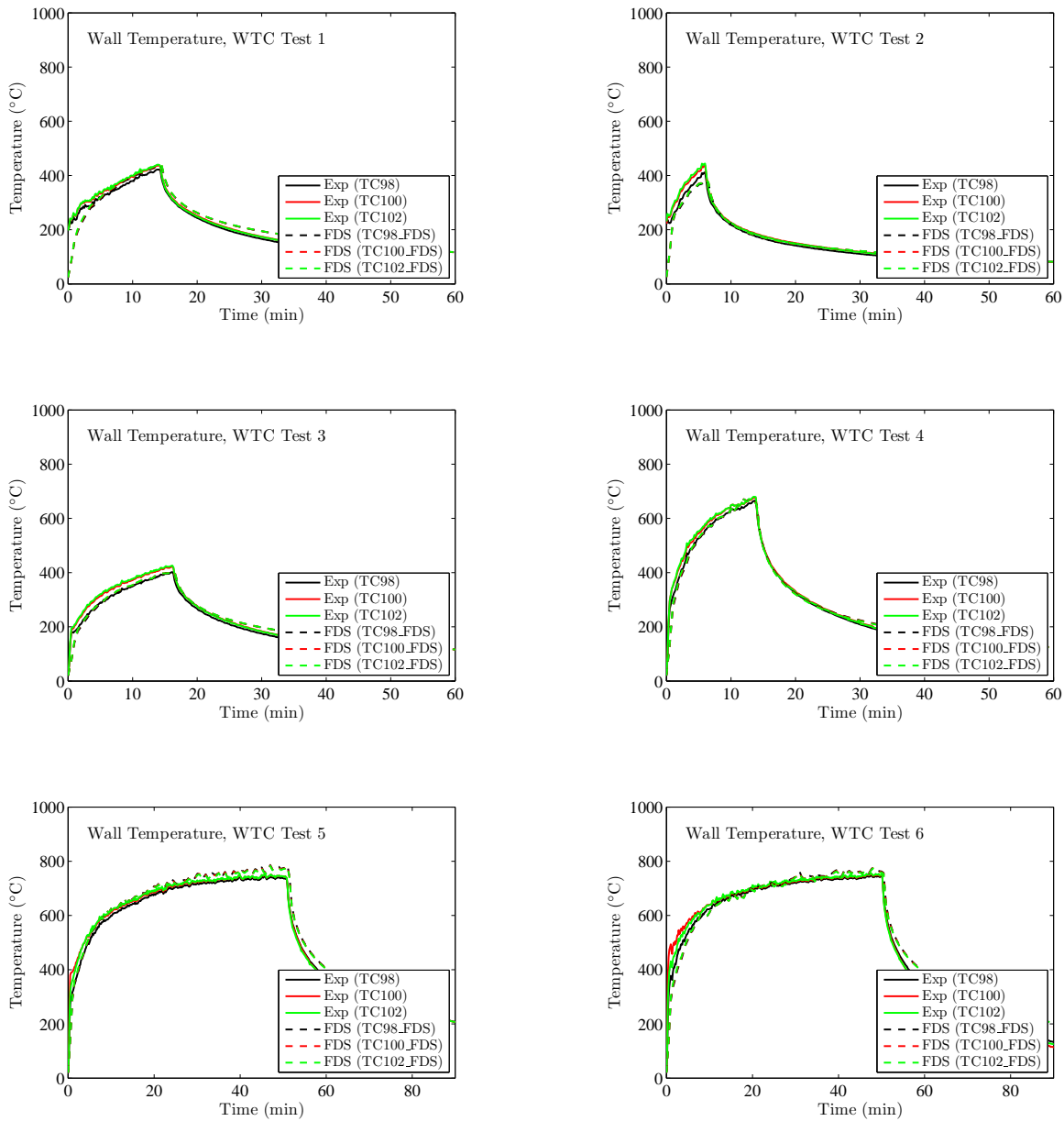
The following pages contain comparisons of predicted and measured ceiling temperatures, both at the surface and beneath a layer of marinite board. Table 11.1 below lists the coordinates of the measurement locations relative to the center of the fire pan. Names with “IN” appended are measurements made under the marinite board.

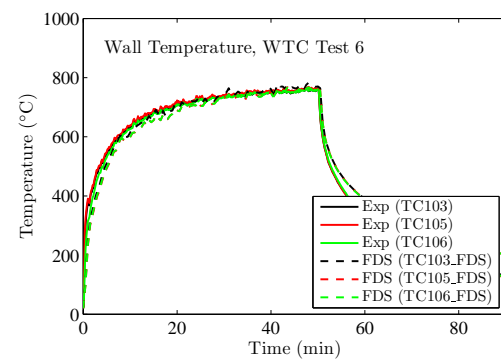
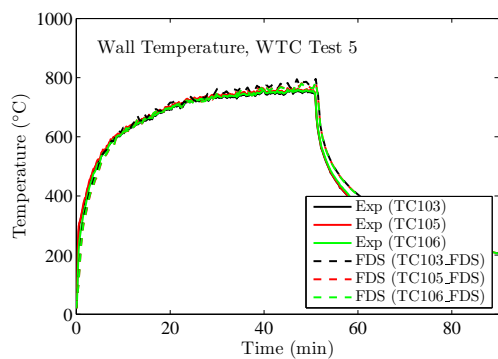
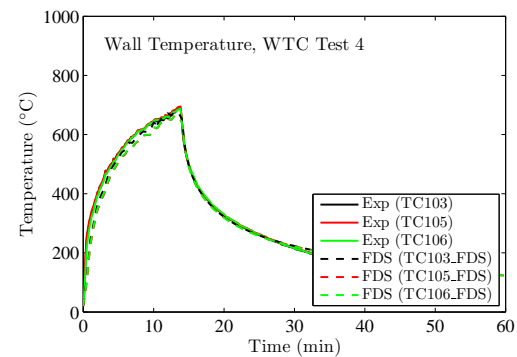
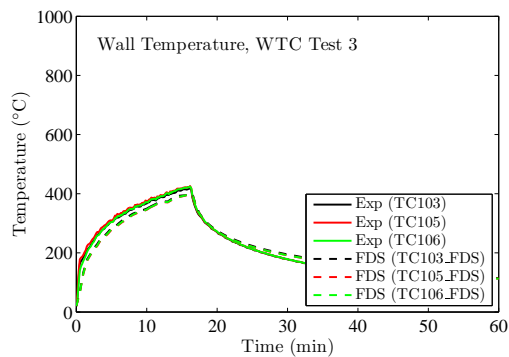
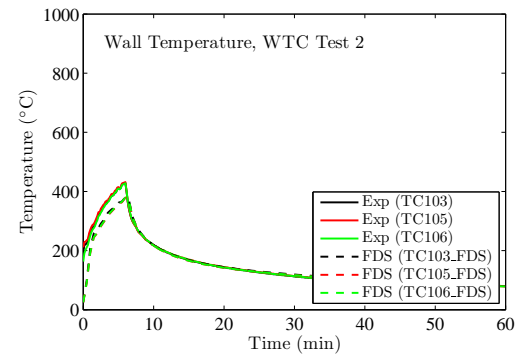
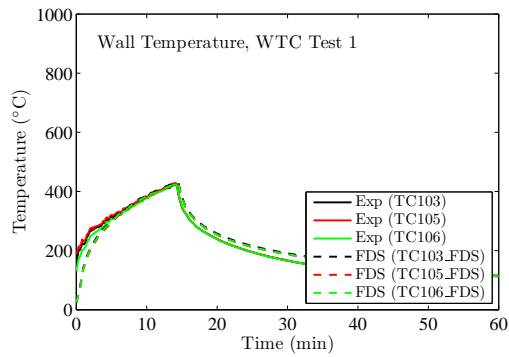
Table 11.1: Locations of ceiling surface temperature measurements relative to the fire pan in the WTC series.

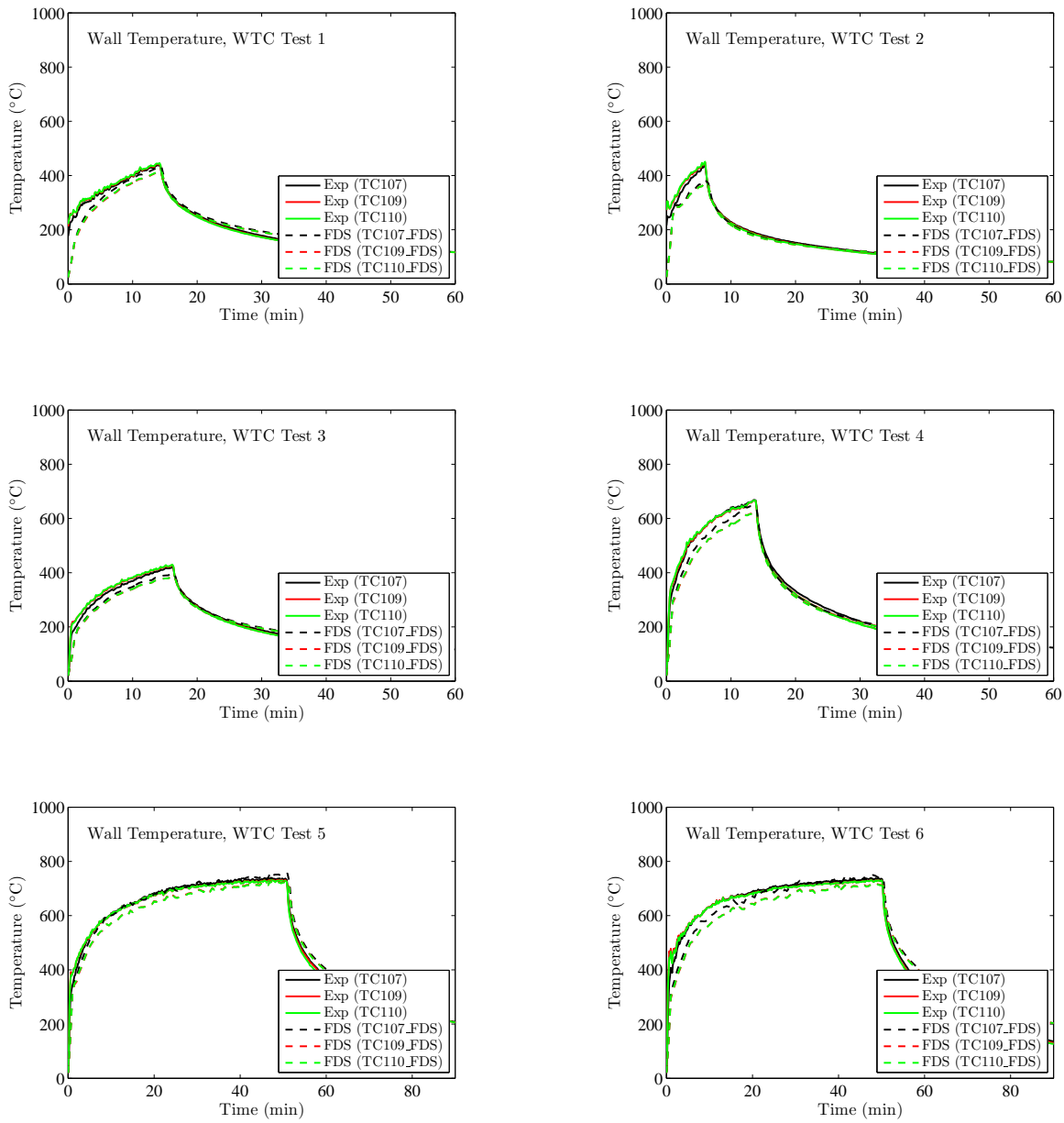
Name	x (m)	y (m)	z (m)
TCC	0.62	0.07	3.82
TCN3	0.62	0.67	3.82
TCS3	0.62	-0.53	3.82
TCE7	2.18	0.07	3.82
TCW7	-1.15	0.07	3.82
TCCIN	0.62	0.07	3.83
TCN3IN	0.62	0.67	3.83
TCS3IN	0.62	-0.53	3.83
TCE4IN	1.28	0.07	3.83
TCW4IN	0.05	0.07	3.83

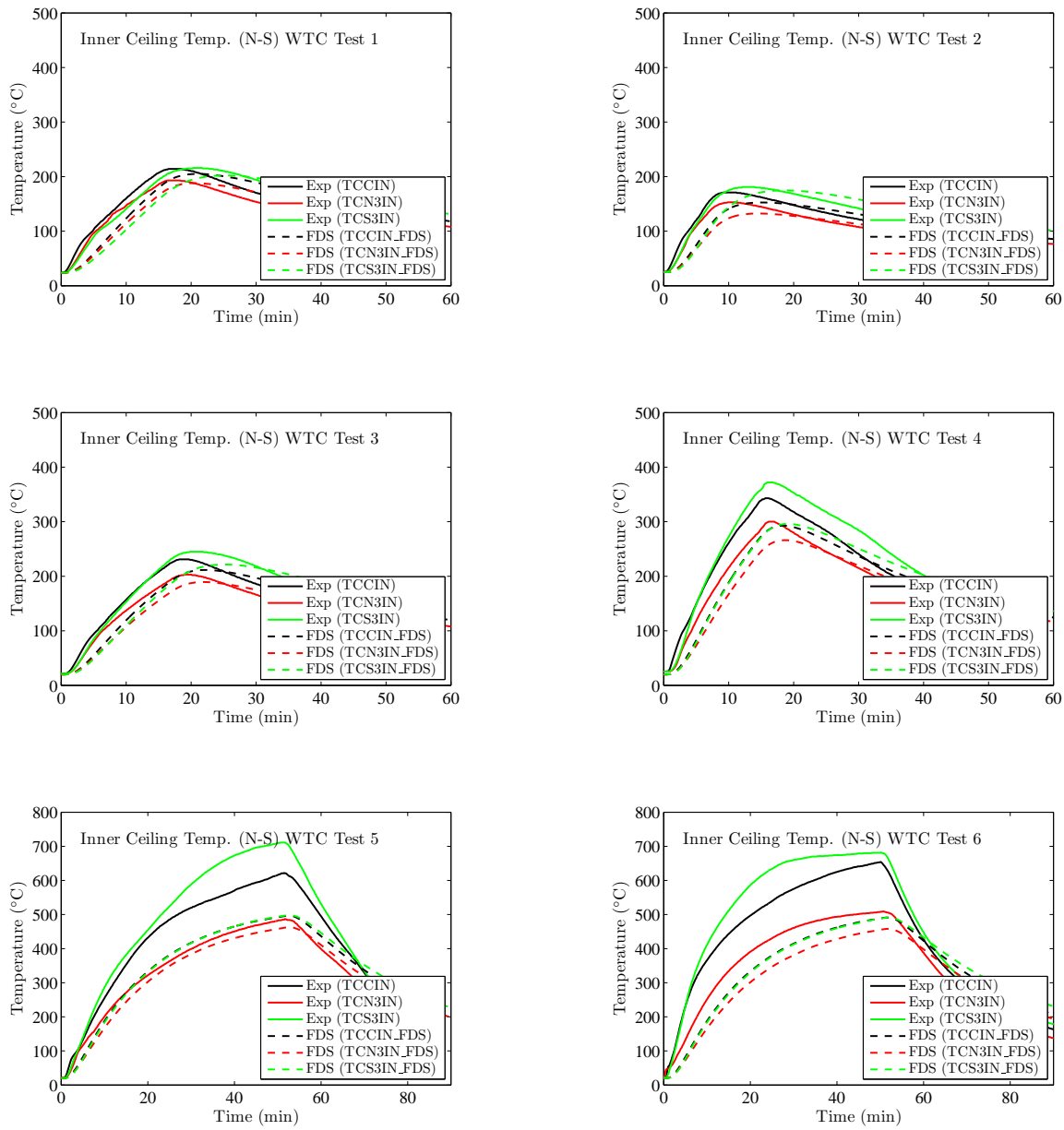


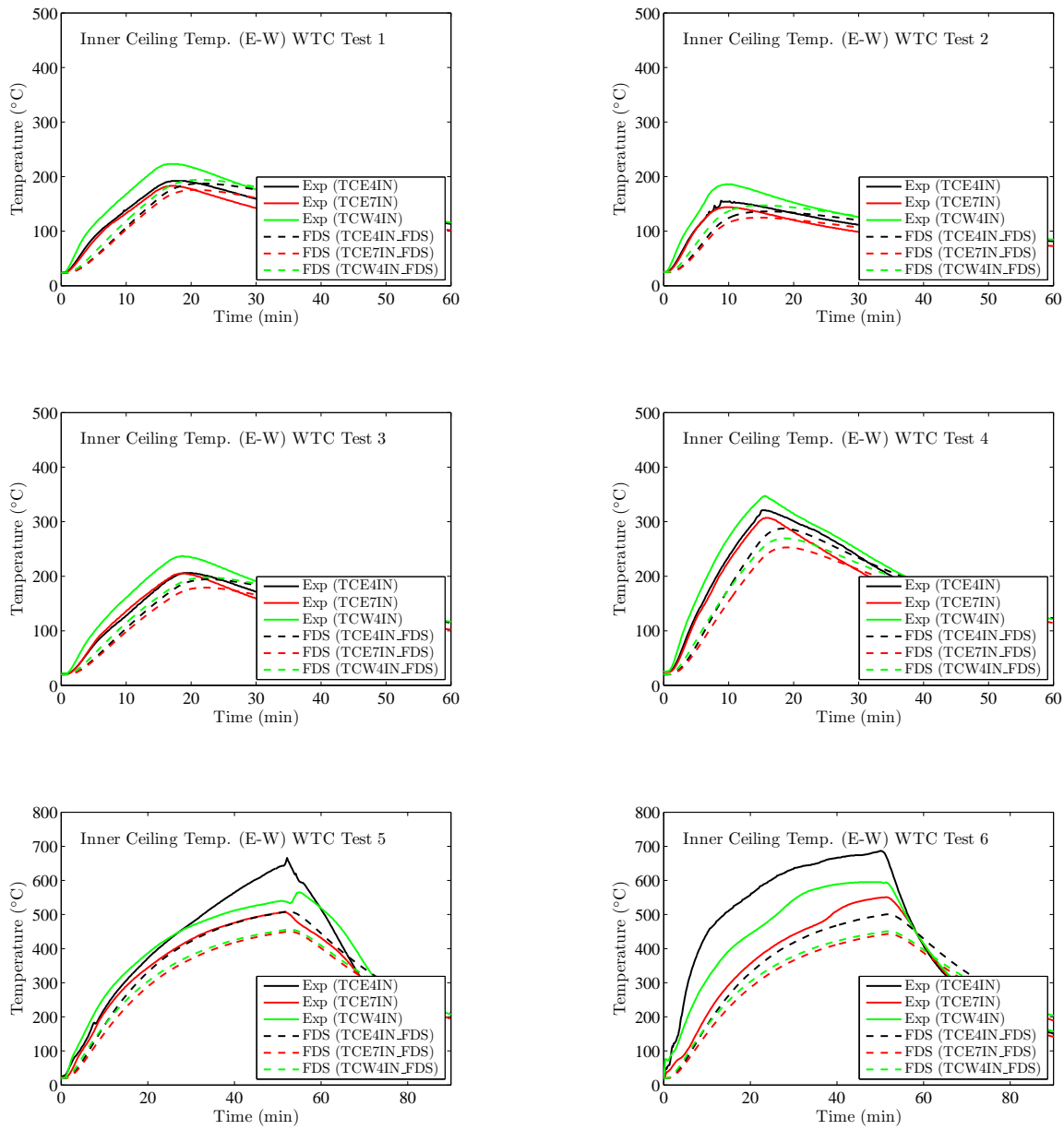


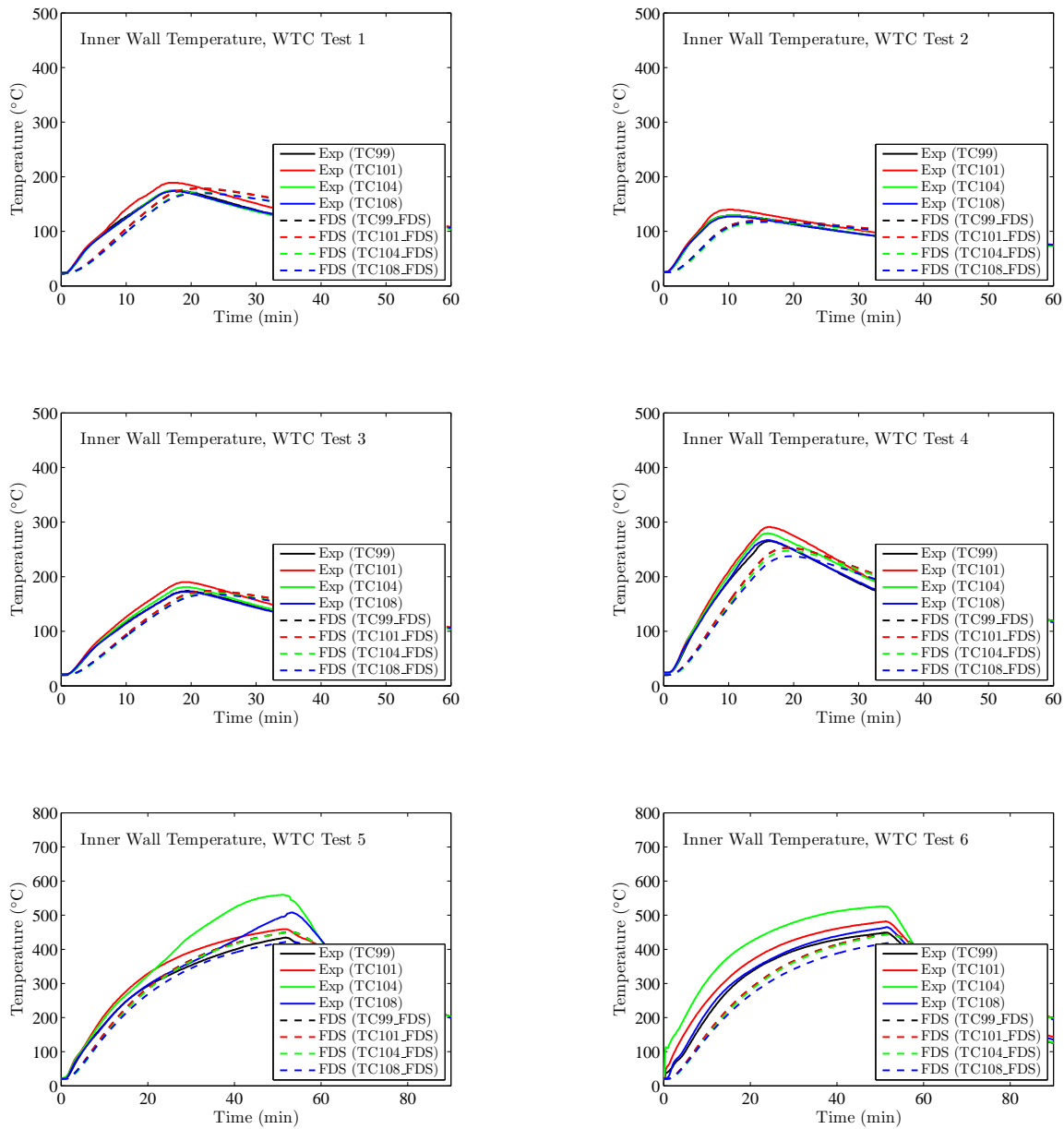












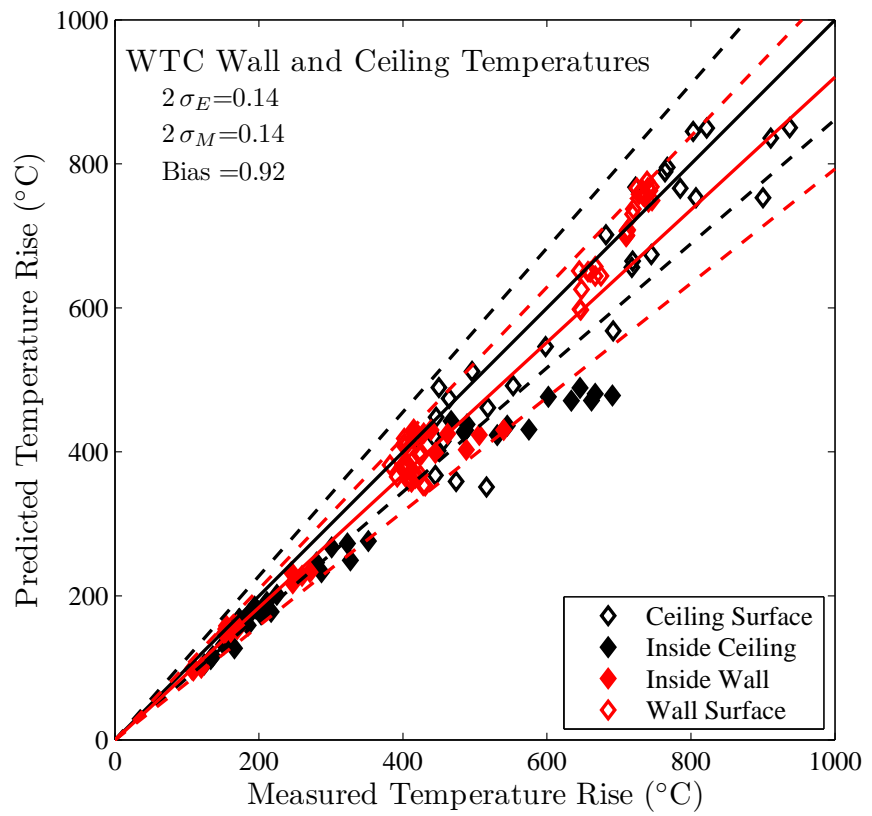


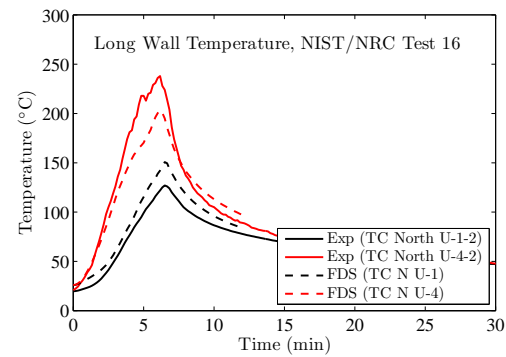
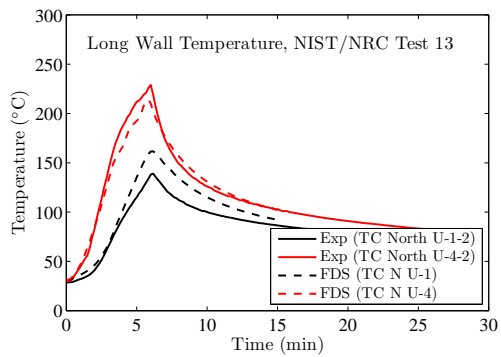
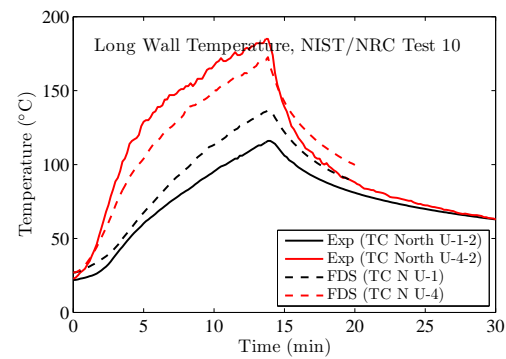
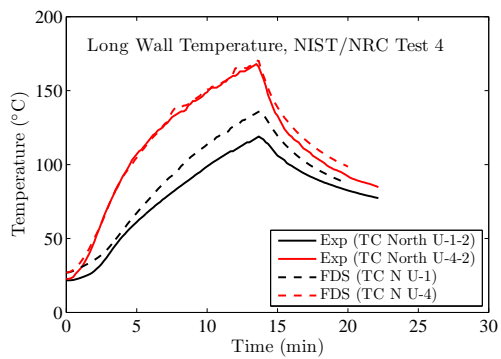
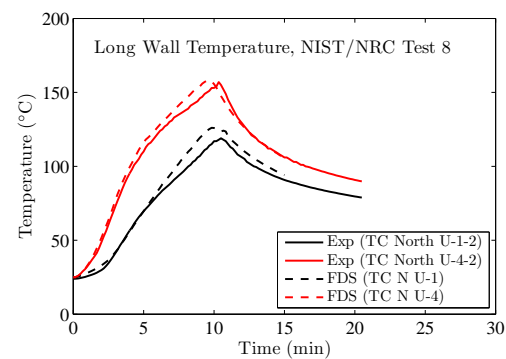
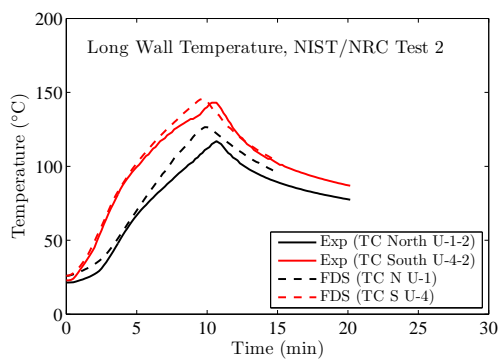
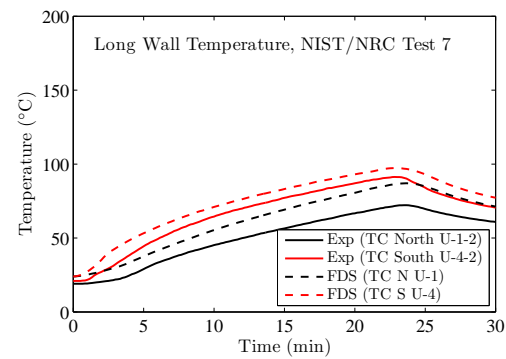
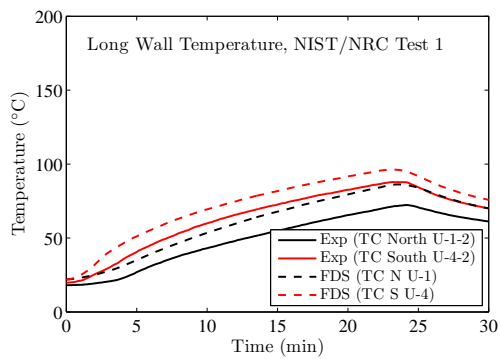
Figure 11.4: Summary of wall and ceiling temperature predictions for the WTC test series.

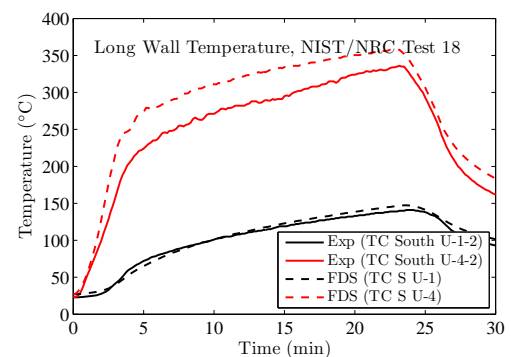
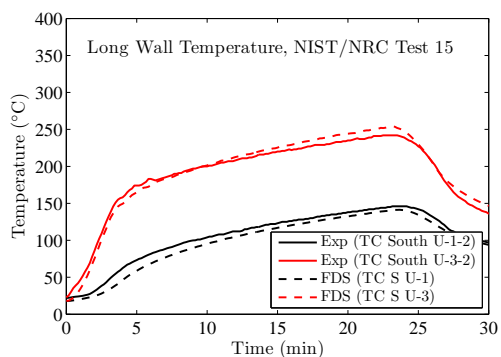
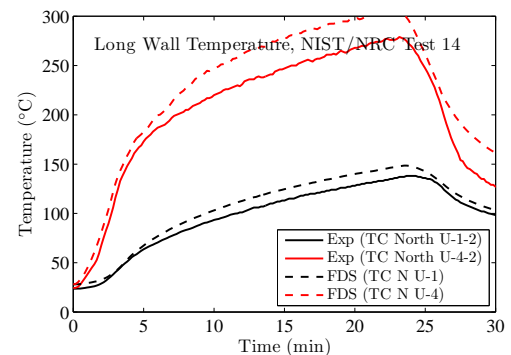
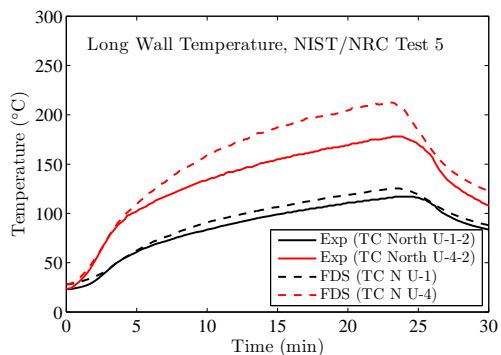
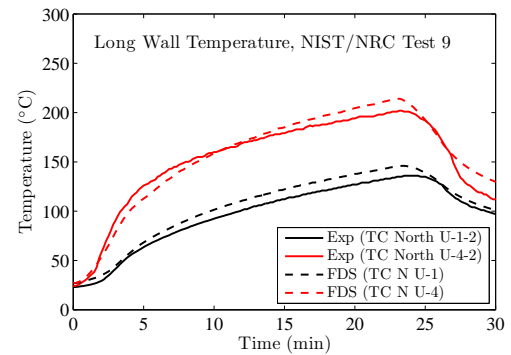
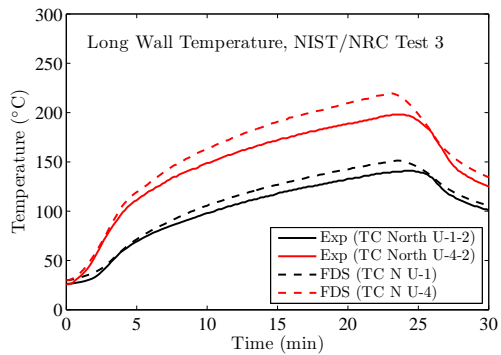
11.6 NIST/NRC Test Series, Compartment Walls, Floor and Ceiling

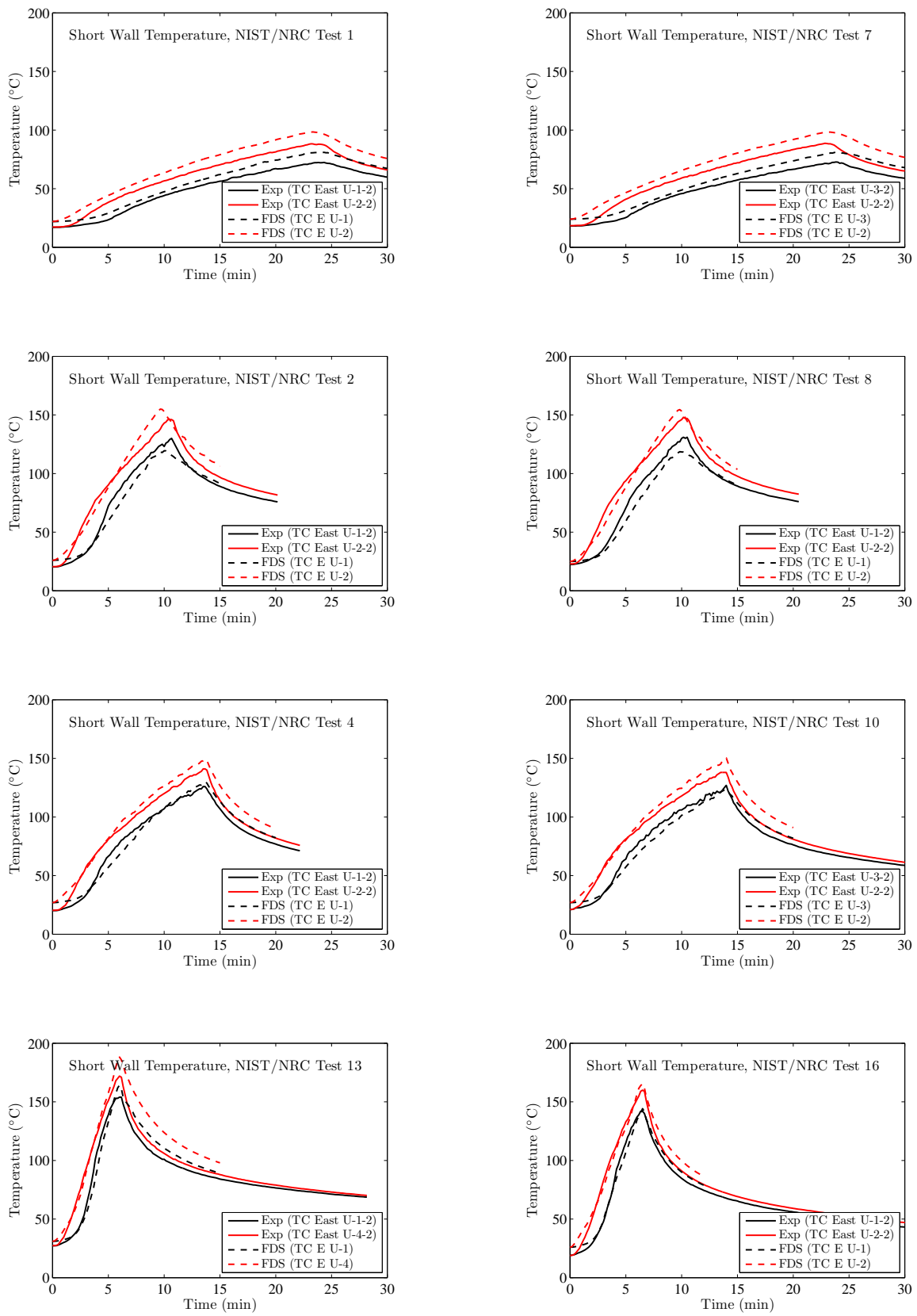
Thirty-six heat flux gauges were positioned at various locations on all four walls of the compartment, plus the ceiling and floor. Comparisons between measured and predicted heat fluxes and surface temperatures are shown on the following pages for a selected number of locations. Over half of the measurement points are in roughly the same relative location to the fire and hence the measurements and predictions are similar. For this reason, data for the east and north walls are shown because the data from the south and west walls are comparable. Data from the south wall is used in cases where the corresponding instrument on the north wall failed, or in cases where the fire is positioned close to the south wall. For each test, eight locations are used for comparison, two on the long (mainly north) wall, two on the short (east) wall, two on the floor, and two on the ceiling. Of the two locations for each panel, one is considered in the far-field, relatively remote from the fire; one is in the near-field, relatively close to the fire. How close or far varies from test to test. The two short wall locations are equally remote from the fire; thus, one location is in the lower layer, one in the upper. Table 11.2 lists the locations for each test.

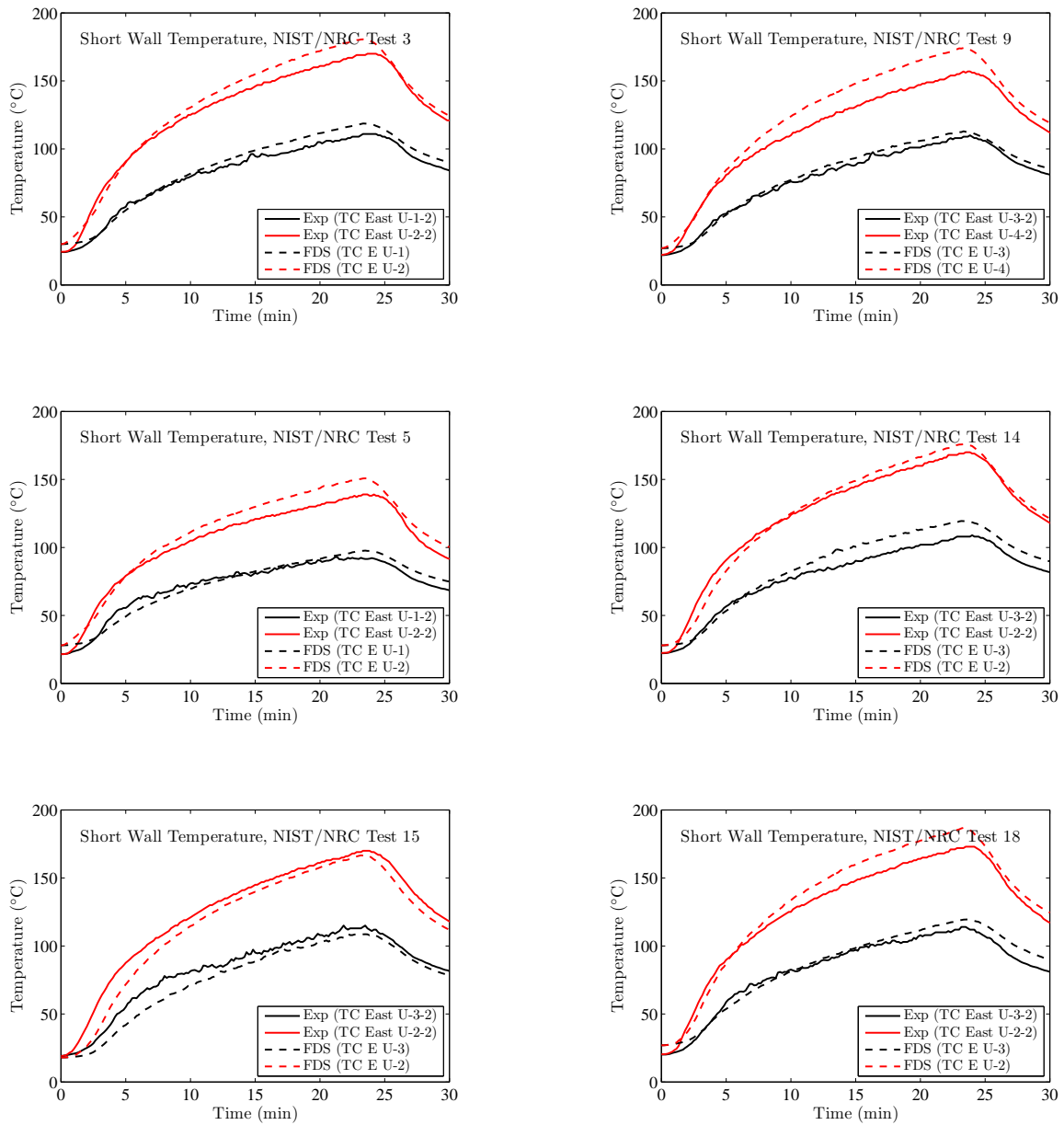
Table 11.2: Wall thermocouple positions for the NIST/NRC series. The origin of the coordinate system at the floor in the southwest corner of the compartment.

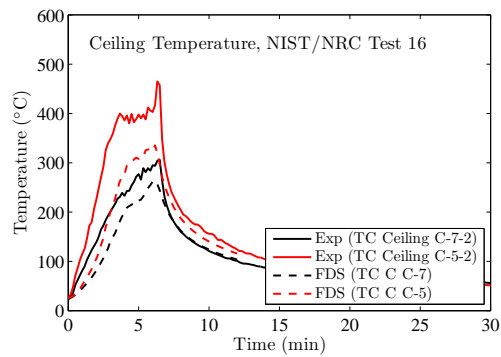
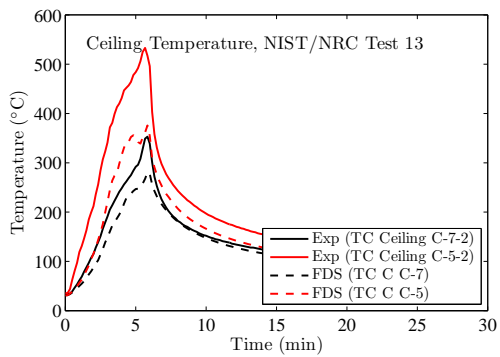
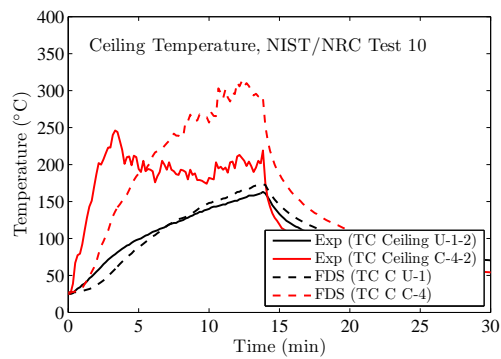
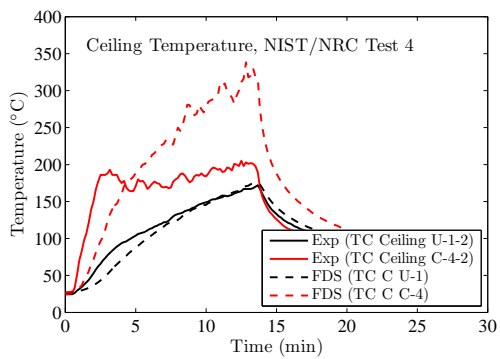
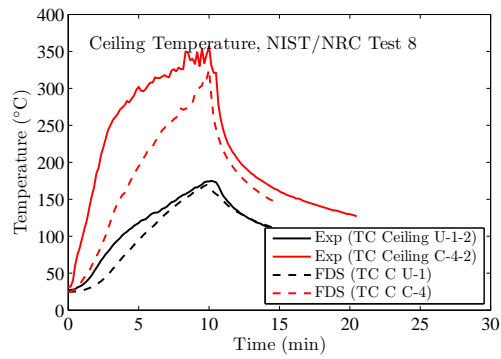
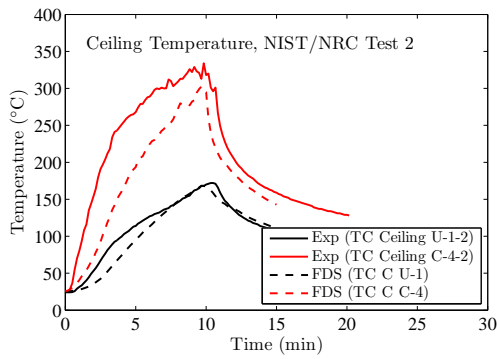
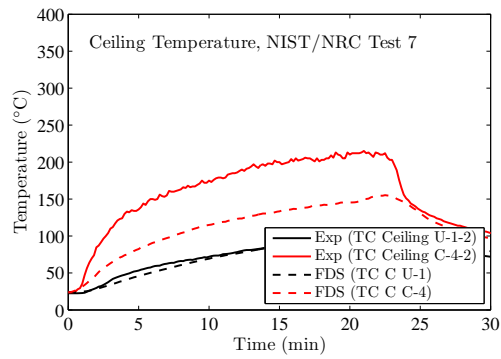
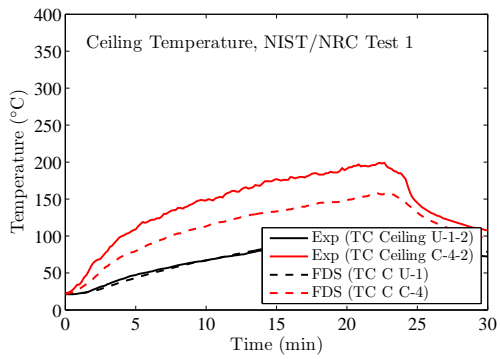
Name	<i>x</i>	<i>y</i>	<i>z</i>	Name	<i>x</i>	<i>y</i>	<i>z</i>
TC North U-1-2	3.85	7.04	1.49	TC Floor U-1-2	3.08	3.51	0
TC North U-2-2	3.86	7.04	3.71	TC Floor U-2-2	9.08	1.94	0
TC North U-3-2	9.48	7.04	1.86	TC Floor U-3-2	9.06	5.97	0
TC North U-4-2	12.07	7.04	1.88	TC Floor U-4-2	10.86	2.38	0
TC North U-5-2	17.69	7.04	1.49	TC Floor C-5-2	10.93	5.20	0.01
TC North U-6-2	17.69	7.04	3.69	TC Floor U-6-2	13.13	1.99	0
TC South U-1-2	3.86	0	1.49	TC Floor U-7-2	13.00	5.92	0
TC South U-2-2	3.86	0	3.82	TC Floor U-8-2	18.63	3.54	0
TC South U-3-2	9.54	0	1.86	TC Ceiling U-1-2	3.04	3.60	3.82
TC South U-4-2	12.08	0	1.86	TC Ceiling C-2-2	8.99	2.00	3.82
TC South U-5-2	17.69	0	1.50	TC Ceiling C-3-2	9.03	5.97	3.82
TC South U-6-2	17.74	0	3.70	TC Ceiling C-4-2	10.79	2.38	3.82
TC East U-1-2	21.66	1.52	1.12	TC Ceiling C-5-2	10.79	5.20	3.82
TC East U-2-2	21.66	1.52	2.40	TC Ceiling C-6-2	13.00	2.07	3.82
TC East U-3-2	21.66	5.68	1.13	TC Ceiling C-7-2	12.84	5.98	3.82
TC East U-4-2	21.66	5.70	2.42	TC Ceiling U-8-2	18.71	3.54	3.82

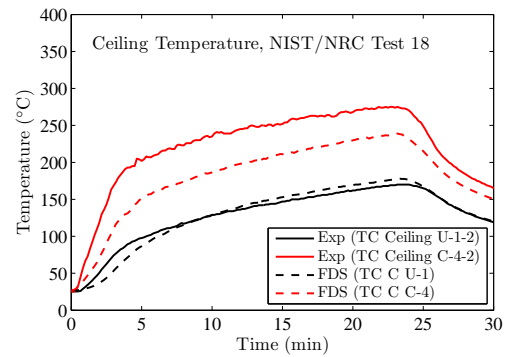
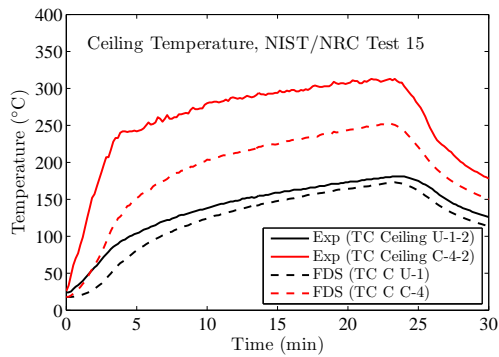
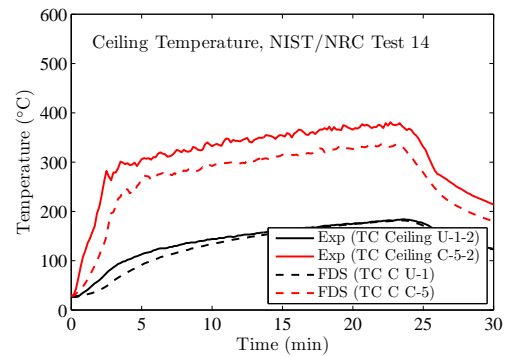
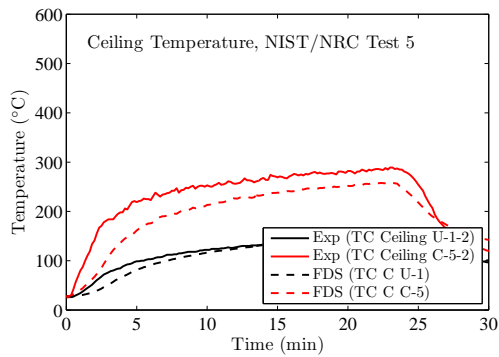
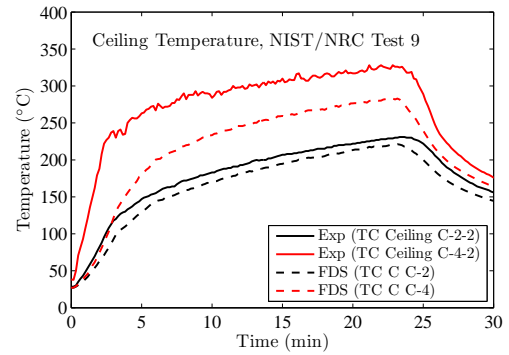
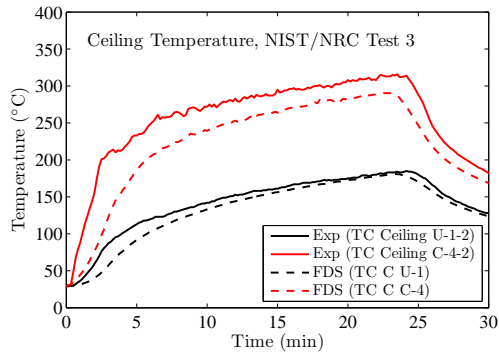


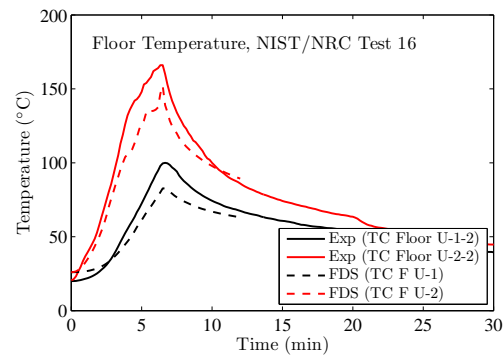
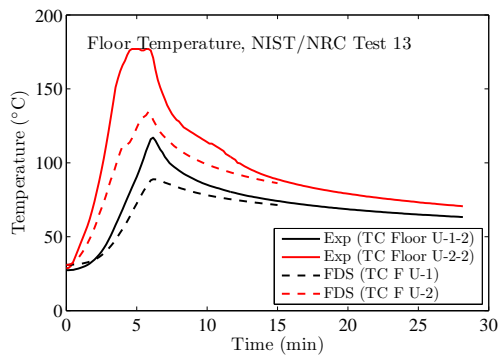
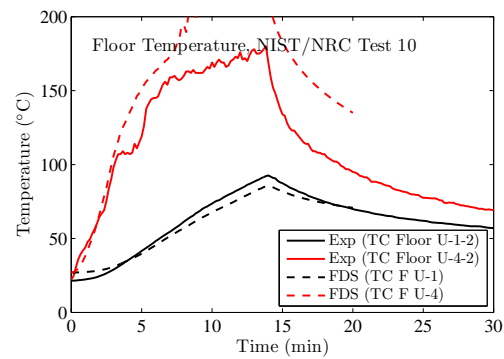
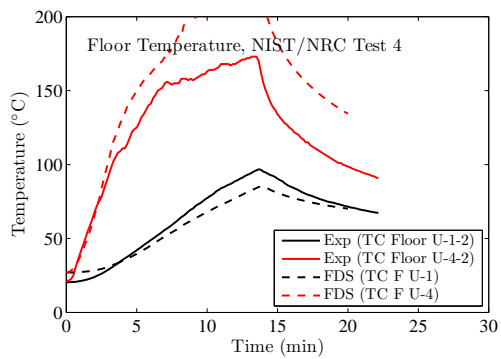
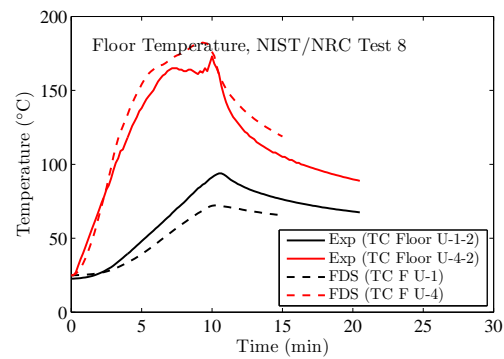
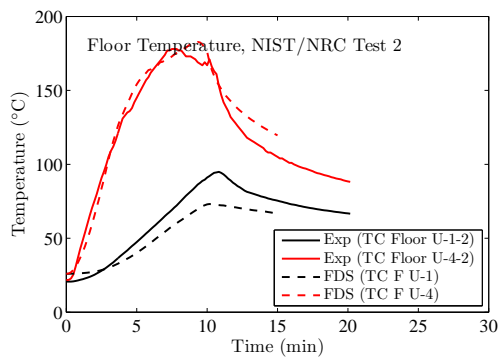
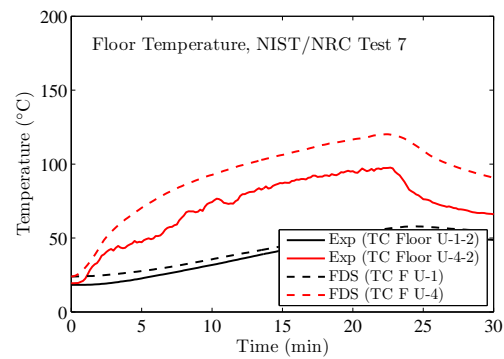
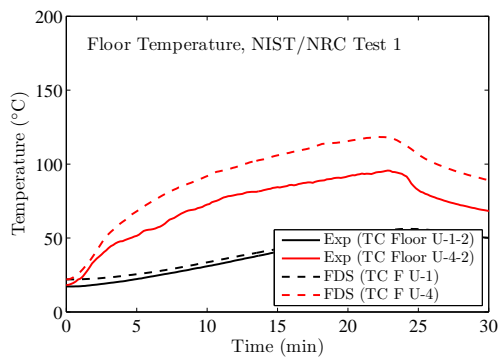


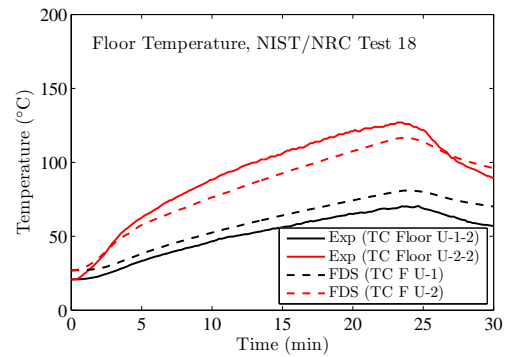
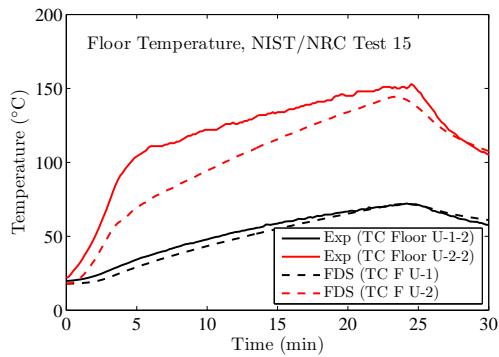
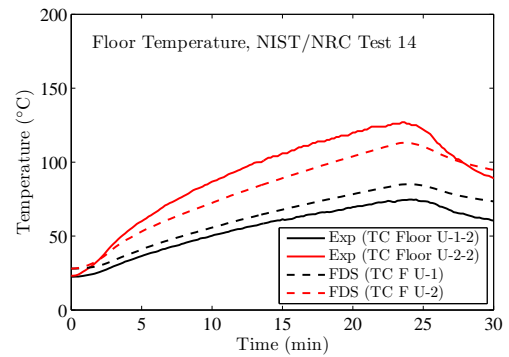
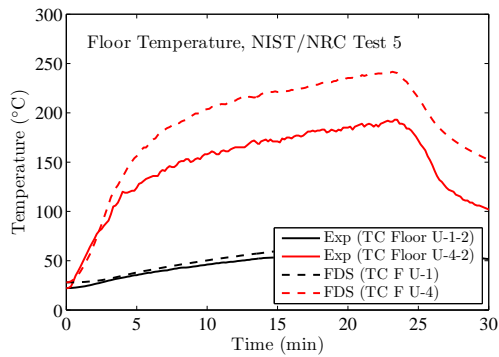
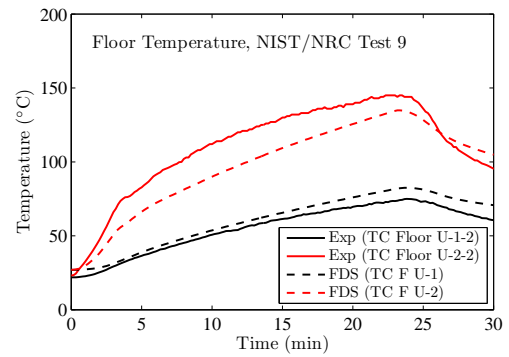
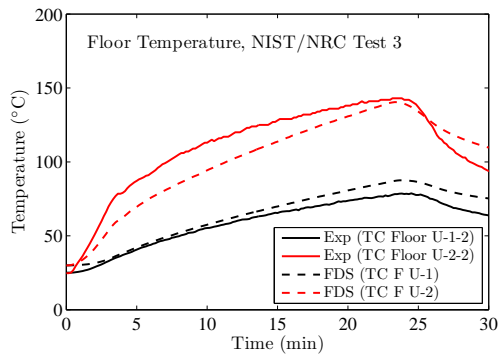












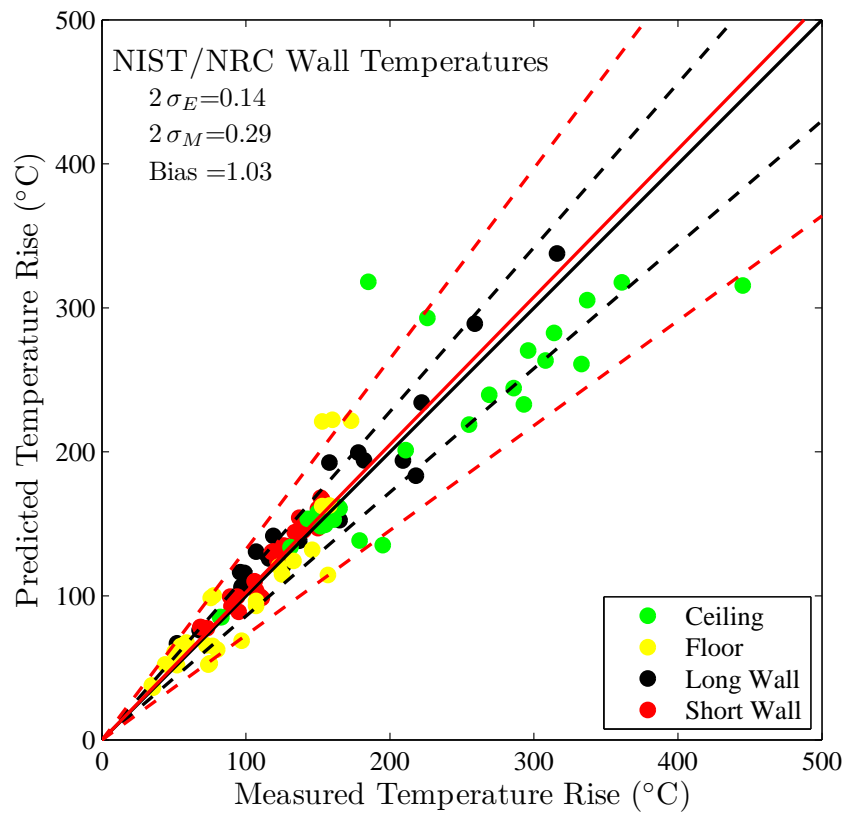


Figure 11.5: Summary of wall, floor and ceiling temperature predictions for the NIST/NRC test series.

Chapter 12

Heat Flux

Radiative heat transfer is included in FDS via the solution of the radiation transport equation for a gray gas, and in some limited cases using a wide band model. The equation is solved using a technique similar to finite volume methods for convective transport, thus the name given to it is the Finite Volume Method (FVM). Using approximately 100 discrete angles, the finite volume solver requires about 20 % of the total CPU time of a calculation, a modest cost given the complexity of radiation heat transfer. The absorption coefficients of the gas-soot mixtures are computed using RADCAL narrow-band model. Liquid droplets can absorb and scatter thermal radiation. This is important in cases involving mist sprinklers, but also plays a role in all sprinkler cases. The absorption and scattering coefficients are based on Mie theory.

This chapter contains a wide variety of heat flux measurements, ranging from less than a kW/m² from very small methane gas burners up to about 150 kW/m² in full-scale compartment fires.

12.1 Hamins Methane Burner Heat Flux Measurements

Predicted and measured radial and vertical heat flux profiles from six experiments conducted by Anthony Hamins at NIST are shown on the following pages. The relevant information about the fires is included in Table 12.1. These are challenging simulations because the neither the gray gas assumption nor the radiative fraction is assumed. Rather, the model is calculating the temperature and species concentrations necessary to predict the radiant energy from the fire.

Table 12.1: Summary of Hamins methane burner experiments.

Case	Test Number	D (m)	\dot{Q} (kW)	\dot{Q}'' (kW/m ²)	Q^*
A	1	0.10	0.42	53.8	0.12
B	5	0.10	1.88	240	0.53
C	23	0.38	33.5	295	0.34
D	21	0.38	175	1550	1.8
E	7	1.0	49.0	62.4	0.044
F	19	1.0	162	206	0.14

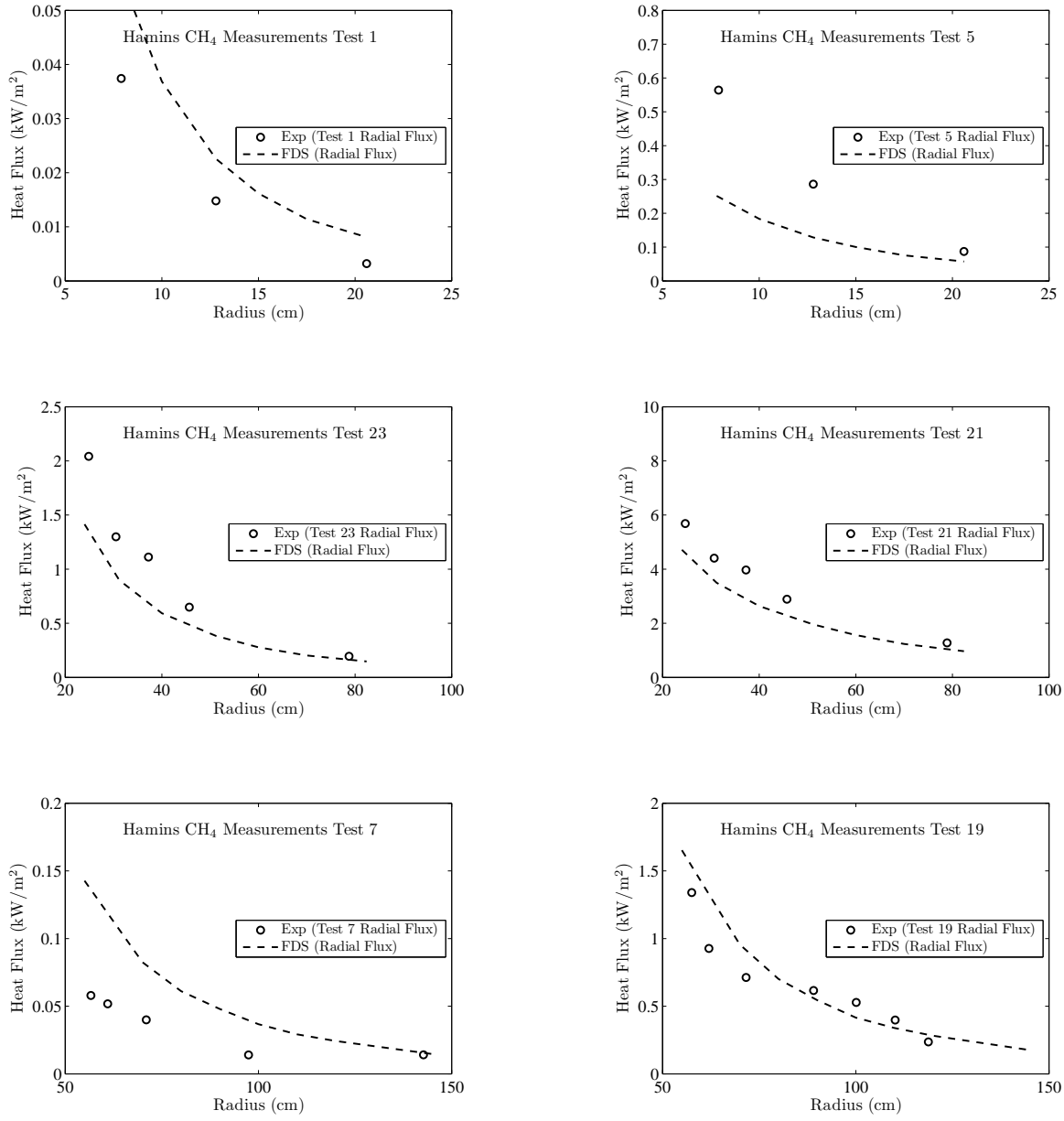


Figure 12.1: Comparison of predicted and measured heat fluxes to the “floor” as a function of radial distance from a methane burner, Hamins experiments.

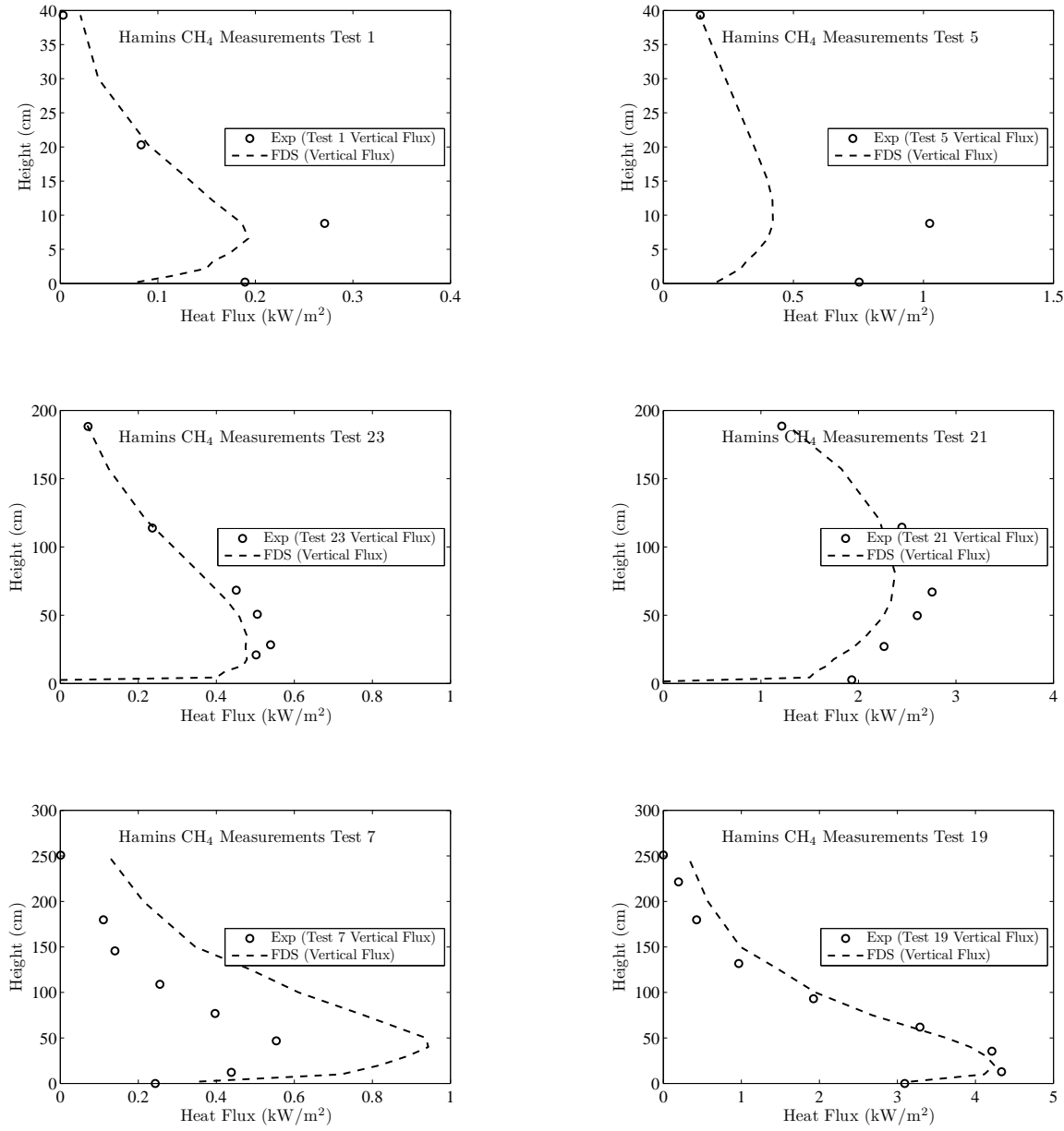


Figure 12.2: Comparison of predicted and measured heat fluxes from a methane burner to a “wall” as a function of the height from the burner surface, Hamins experiments.

12.2 NRL/HAI Wall Heat Flux Measurements

Predicted and measured vertical heat flux profiles from 9 propane sand burner fires are shown on the following pages. The parameters for each experiment are listed in Table 12.2 below. Note that all the FDS simulations were performed with a grid resolution such that $D^*/\delta x = 10$.

Table 12.2: Summary of the NRL/HAI Wall Heat Flux Measurements.

Test Number	D (m)	D^* (m)	\dot{Q} (kW)	Q^*	Observed Flame Height (m)
1	0.28	0.30	53	0.85	0.79
2	0.70	0.30	56	0.09	0.36
3	0.48	0.33	68	0.28	0.60
4	0.37	0.39	106	0.84	1.00
5	0.48	0.43	136	0.57	0.87
6	0.48	0.51	204	0.85	1.45
7	0.70	0.52	220	0.36	1.20
8	0.57	0.60	313	0.85	2.20
9	0.70	0.74	523	0.85	2.9 (based on 500 °C)

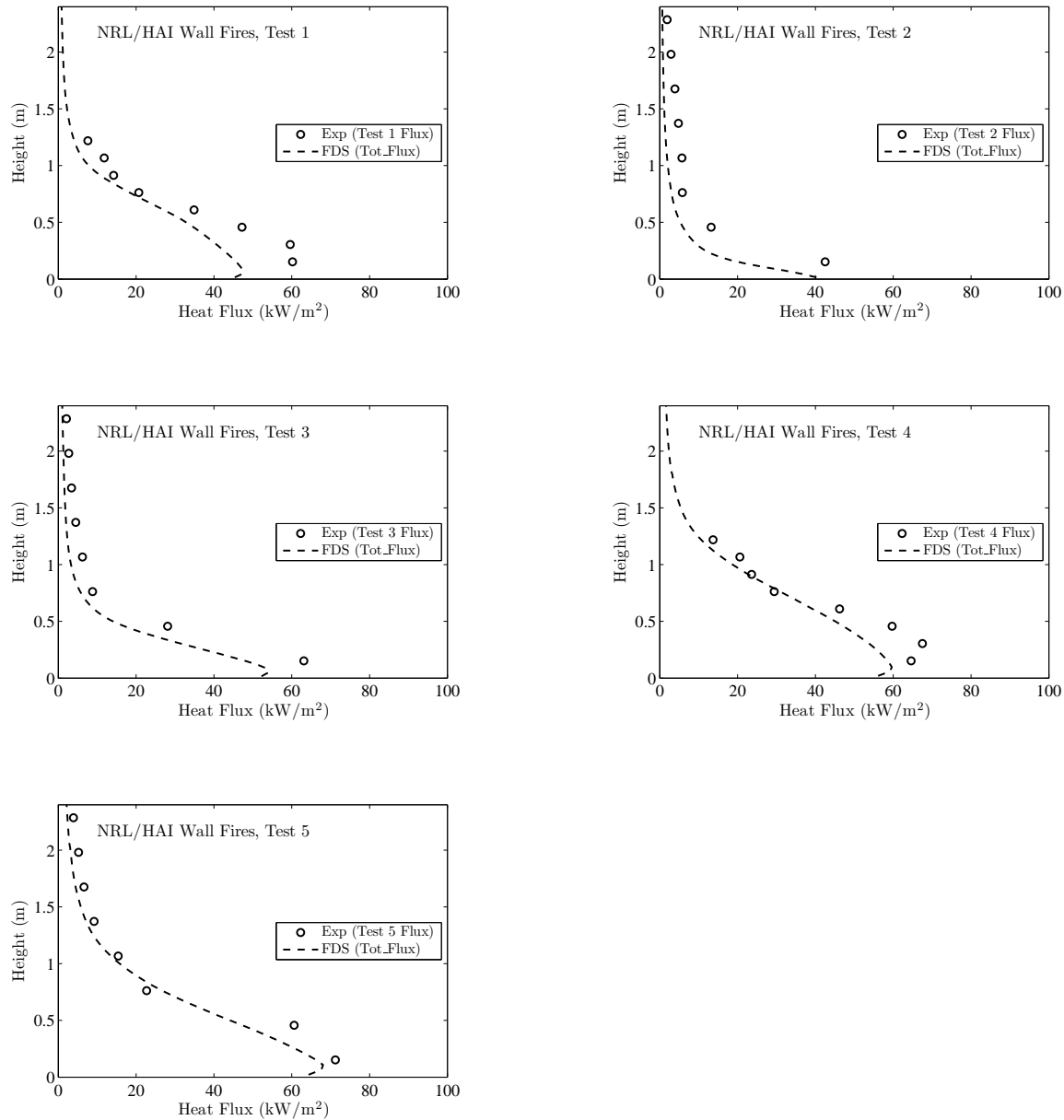


Figure 12.3: Comparison of predicted and measured heat fluxes to the wall from an adjacent propane sand burner, NRL/HAI experiments.

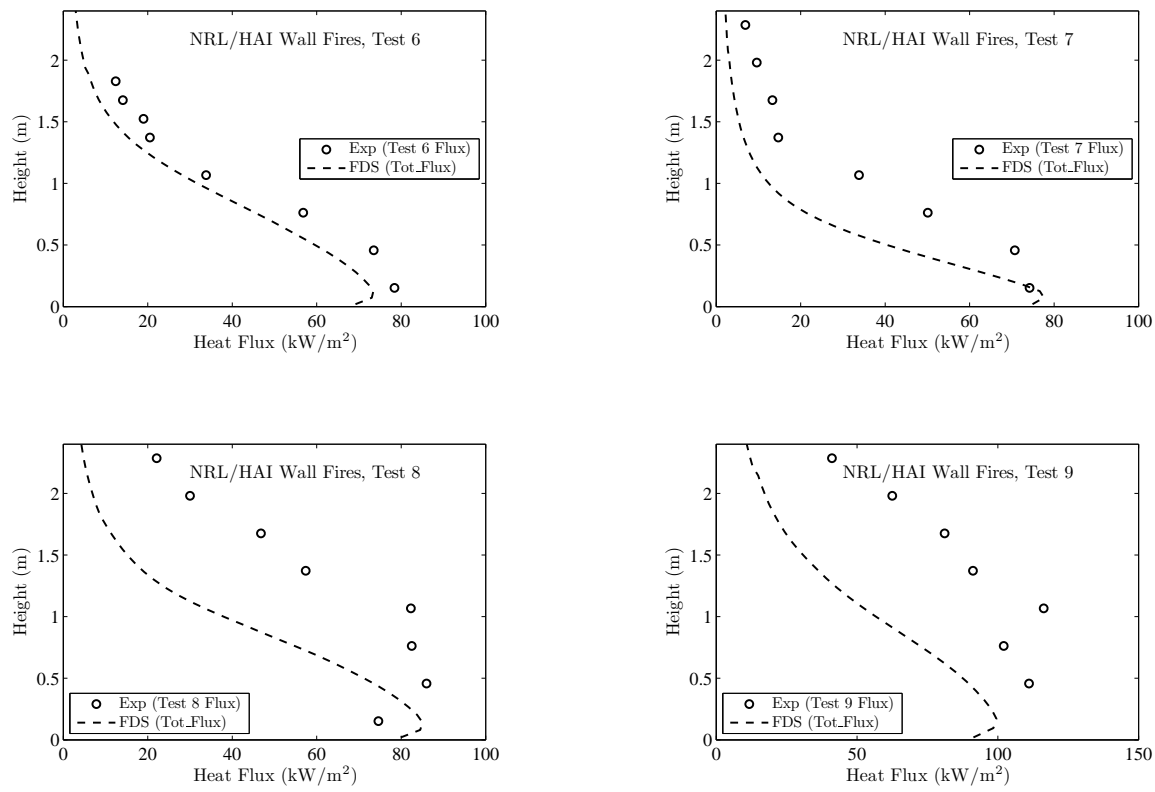


Figure 12.4: Comparison of predicted and measured heat fluxes to the wall from an adjacent propane sand burner, NRL/HAI experiments.

12.3 Ulster SBI Heat Flux Measurements

Predicted and measured vertical heat flux profiles for three propane fire sizes in the single burning item (SBI) enclosure at the University of Ulster are shown on the following page. Measurements were made on two vertical panels that form a corner, at the base of which was a triangular-shaped burner with sides of length 25 cm. Three vertical profiles were measured on each panel at distances of 3.25 cm, 16.5 cm, and 29 cm from the corner.

Note that all the FDS simulations were performed with a grid resolution of 2 cm, and note also that the parameter `RADIATIVE_FRACTION` has been set to zero, meaning that FDS is basing the source term of the radiation transport equation on the temperature rather than the heat release rate. In addition, the soot yield has been set to 0.05 as a crude way to represent the excess soot that is present in the flames but is eventually oxidized. The version of FDS used does not have a soot model to account for higher levels of soot in the flame region.

These results should be regarded as preliminary because FDS is being used in a way that one would ordinarily not use it.

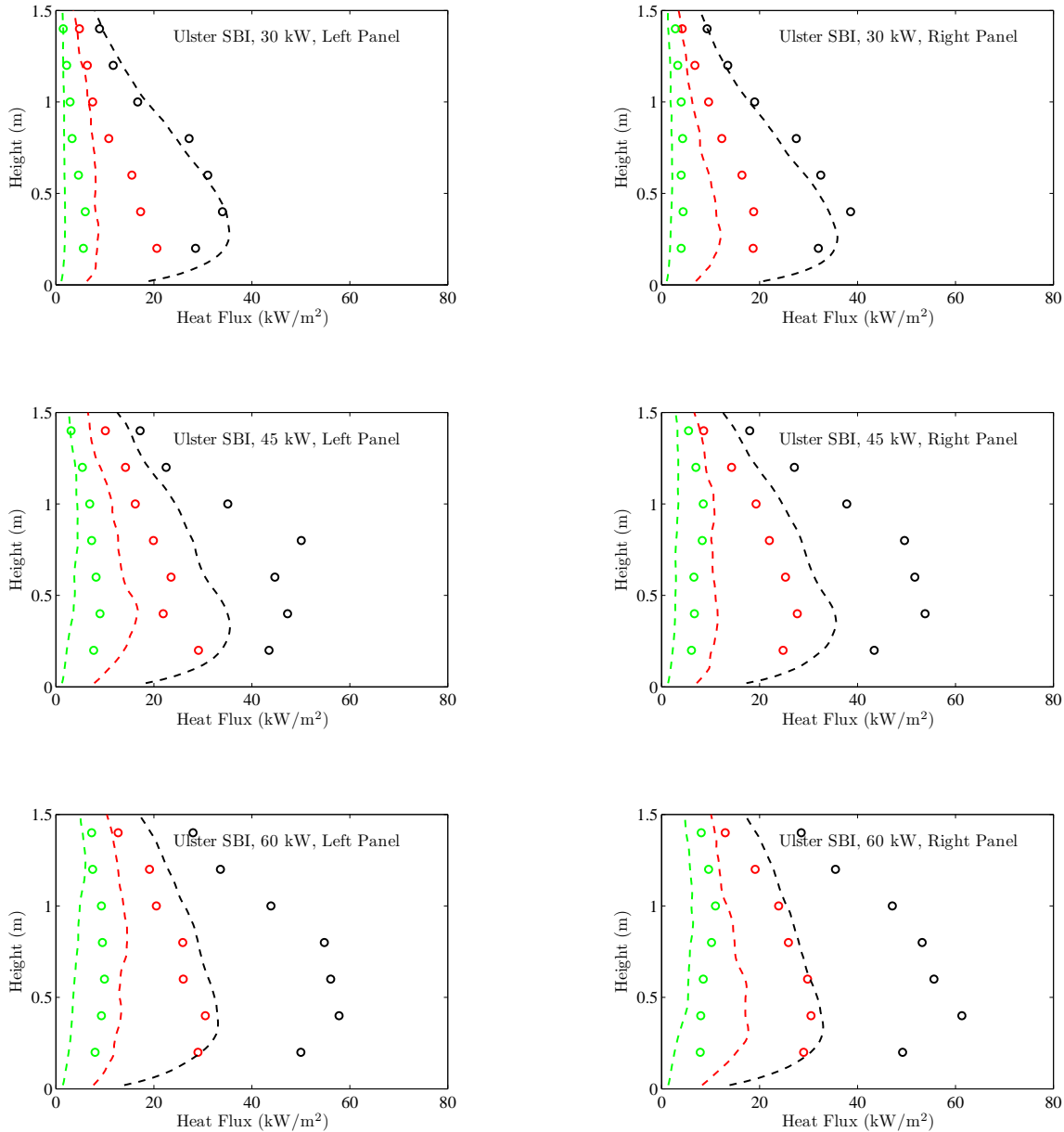


Figure 12.5: Comparison of predicted and measured heat fluxes to adjacent panels forming a corner in the single burning item (SBI) apparatus at the University of Ulster.

12.4 FM Parallel Panel Heat Flux Measurements

Predicted and measured vertical heat flux profiles for three propane and three propylene fires (30 kW, 60 kW, and 100 kW) sandwiched between two 2.4 m high, 0.6 m wide panels are presented on the following page. Note that all the FDS simulations were performed with a grid resolution of 2 cm, and note also that the parameter RADIATIVE_FRACTION has been set to 0.37 for propylene and 0.29 for propane. In addition, the soot yield has been set to 0.095 for propylene and 0.024 for propane. There is no soot growth or extinction model used.

These results should be regarded as preliminary because features of the next major release (FDS 6) are used.

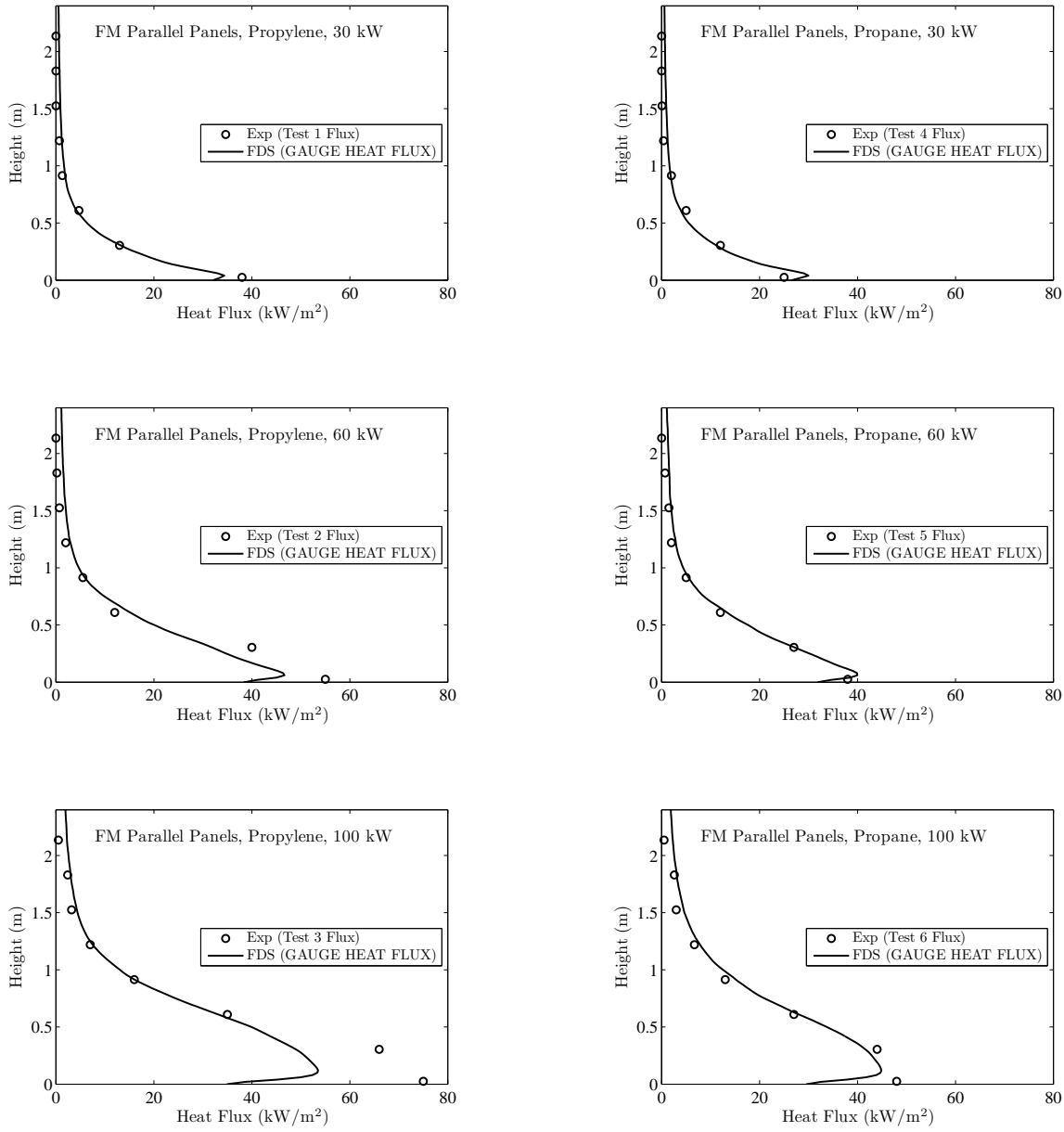


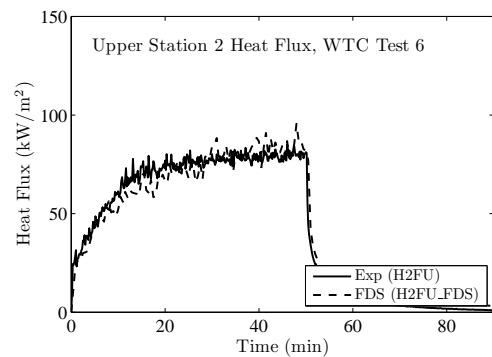
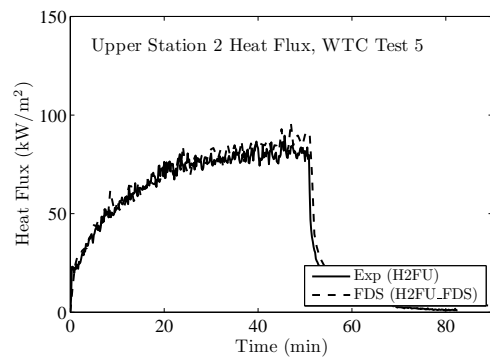
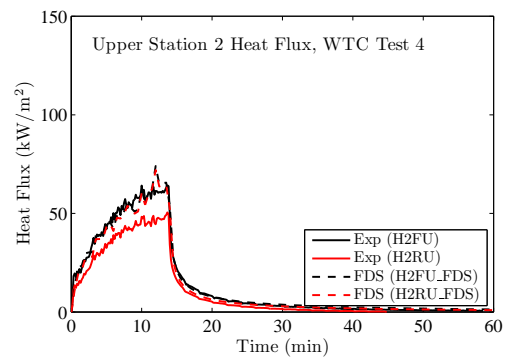
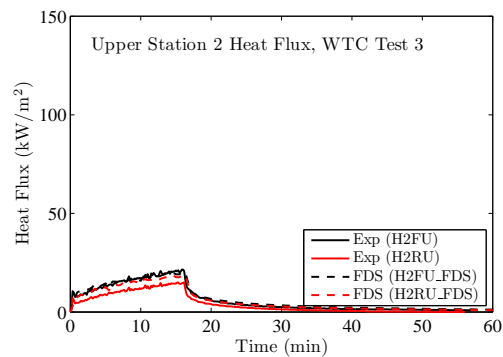
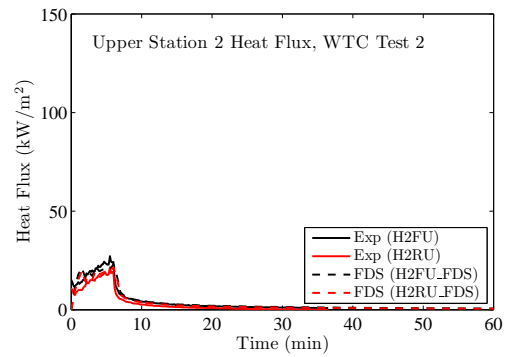
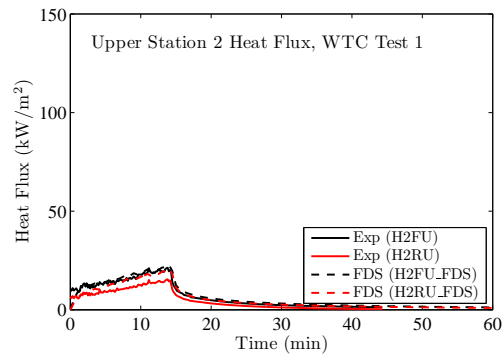
Figure 12.6: Comparison of predicted and measured heat fluxes to parallel panels.

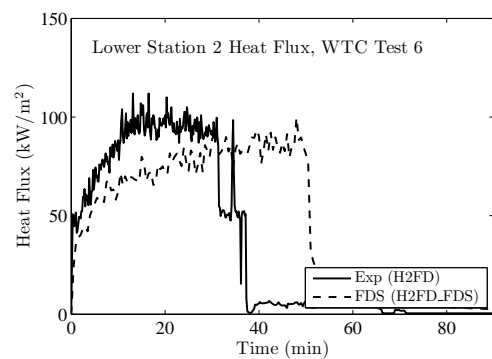
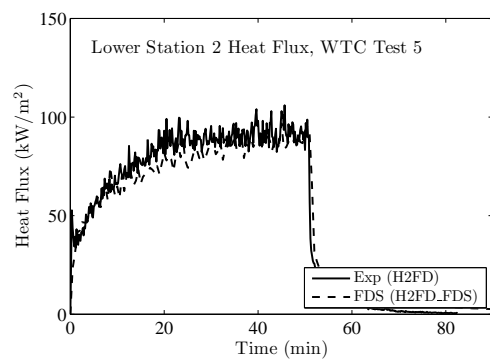
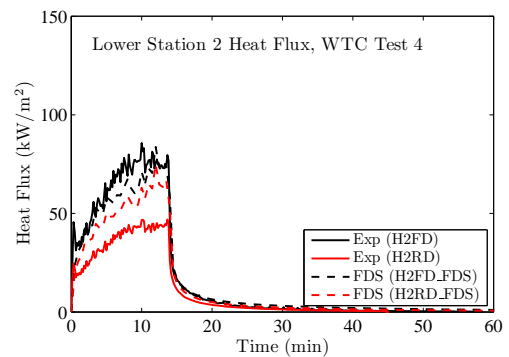
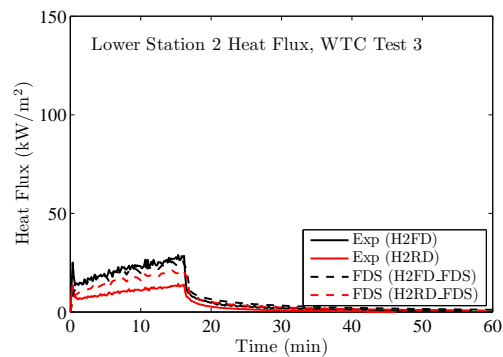
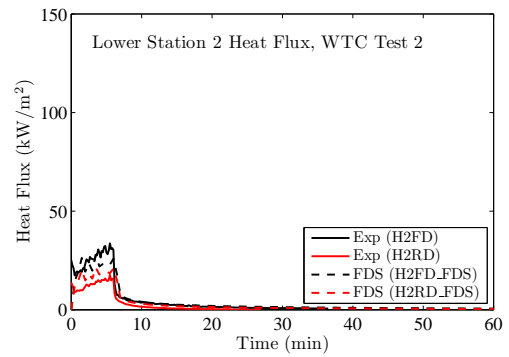
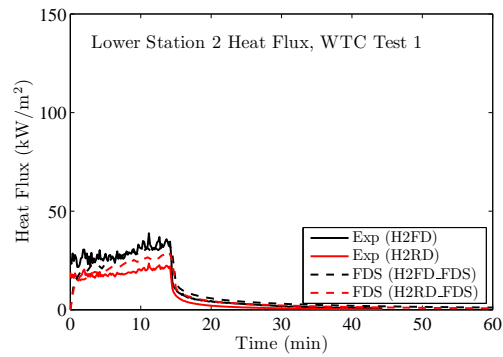
12.5 WTC Heat Flux Measurements

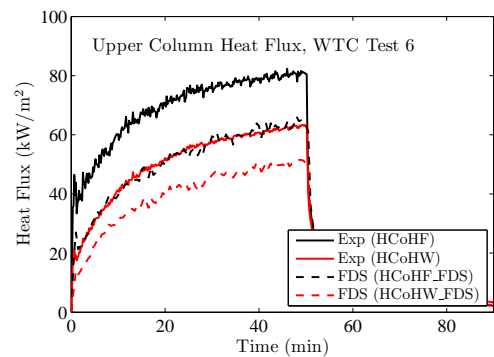
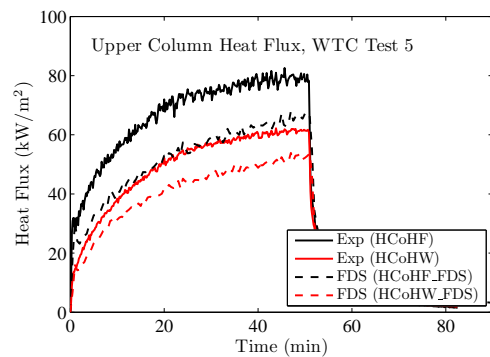
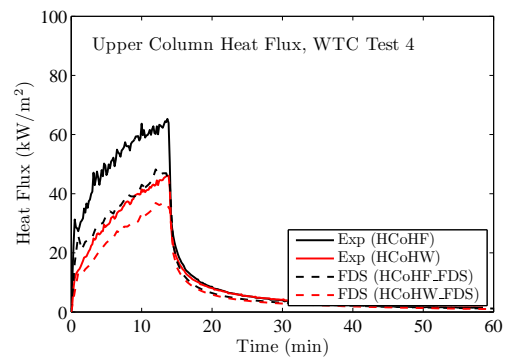
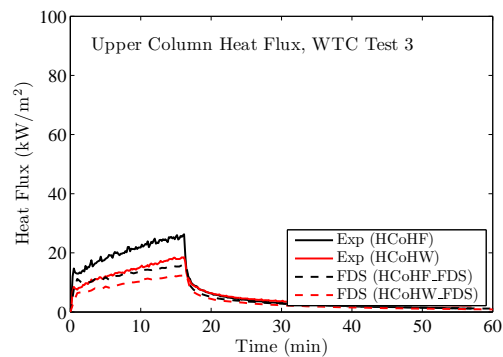
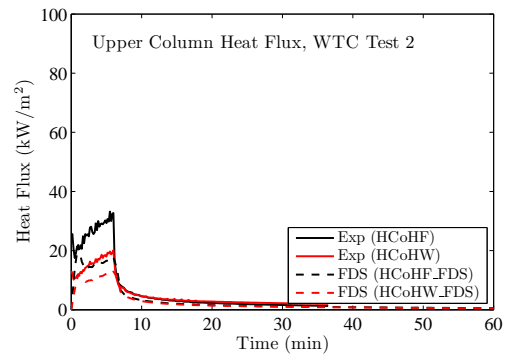
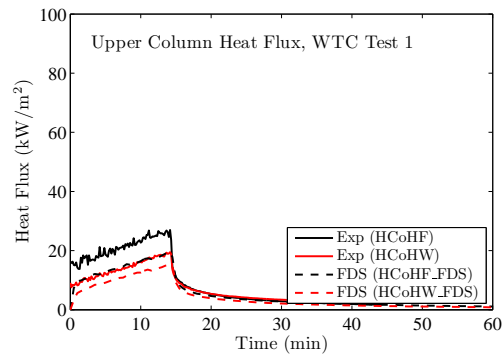
There were a variety of heat flux gauges installed in the test compartment. Most were within 2 m of the fire. Their locations and orientations are listed in Table 12.3.

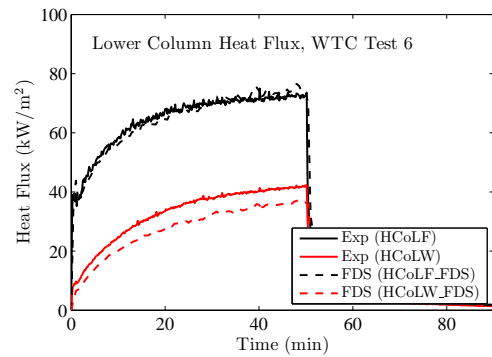
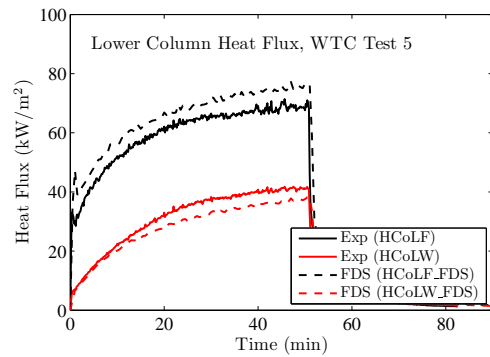
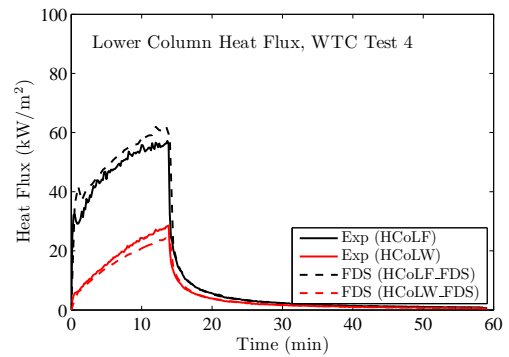
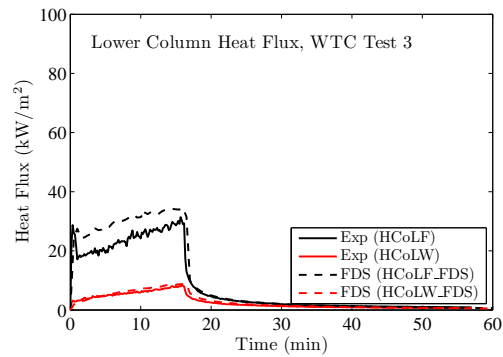
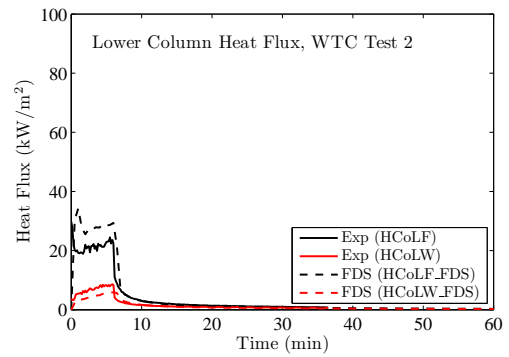
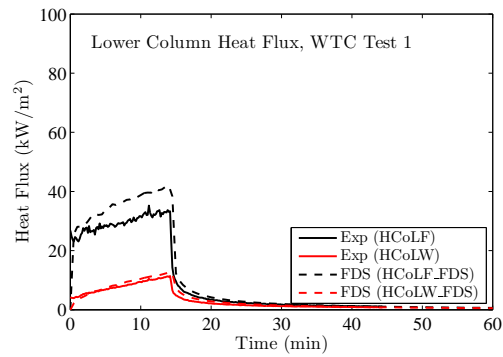
Table 12.3: Heat flux gauge positions relative to the center of the fire pan in the WTC series.

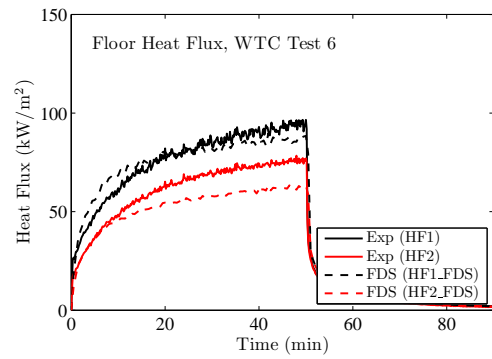
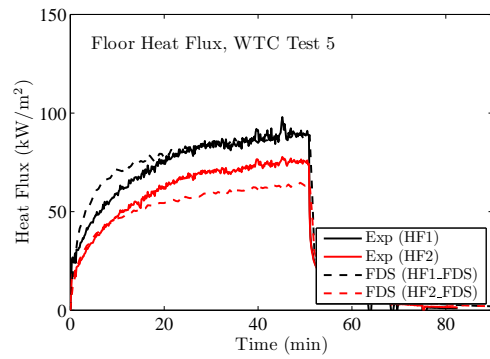
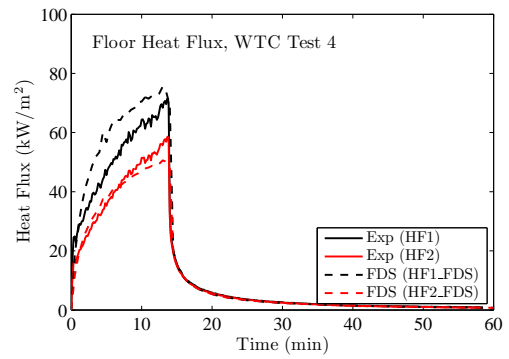
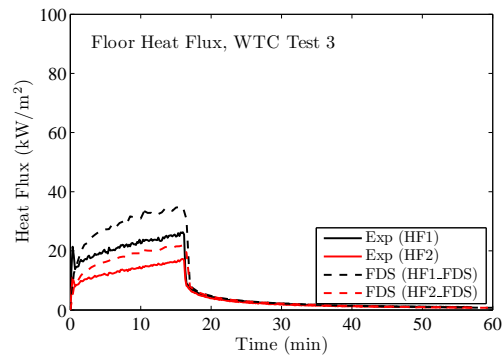
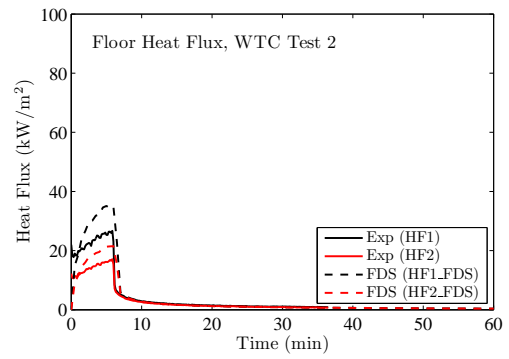
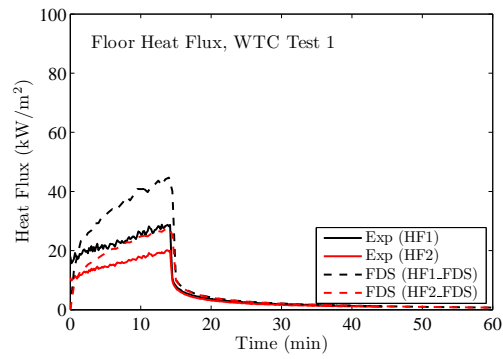
Name	x (m)	y (m)	z (m)	Orientation	Location
H2FU	0.64	0.63	3.30	$+z$	Truss Support
H2RU	0.64	0.51	3.30	$+z$	Truss Support
H2FD	0.64	0.30	3.15	$-z$	Truss Support
H2RD	0.64	0.42	3.15	$-z$	Truss Support
HCoHF	-0.90	0.84	3.46	$+x$	Column, facing fire
HCoHW	-0.97	0.92	3.27	$+y$	Column, facing north
HCoLF	-0.90	0.84	0.92	$+x$	Column, facing fire
HCoLW	-0.97	0.92	1.02	$+y$	Column, facing north
HF1	1.06	0.13	0.13	$+z$	Floor
HF2	1.56	0.10	0.13	$+z$	Floor
HCe1	-0.45	0.35	3.82	$-z$	Ceiling
HCe2	0.05	0.35	3.82	$-z$	Ceiling
HCe3	0.80	0.35	3.82	$-z$	Ceiling
HCe4	2.56	0.35	3.82	$-z$	Ceiling

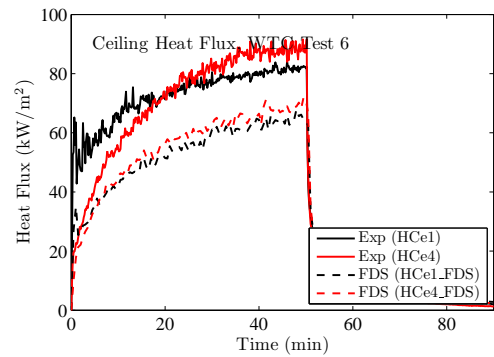
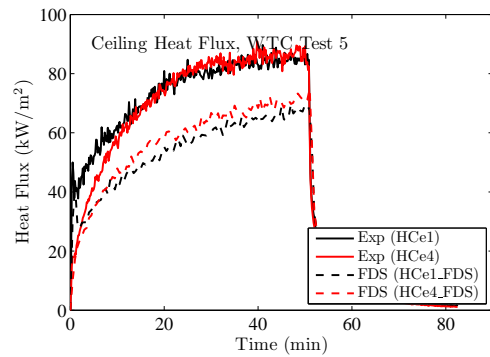
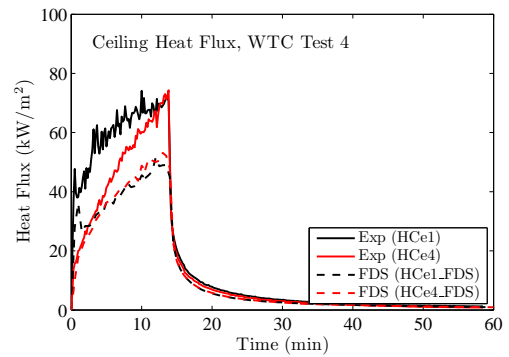
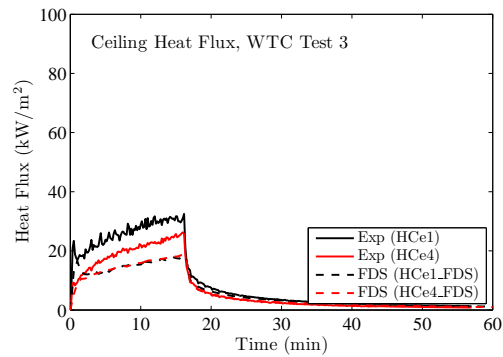
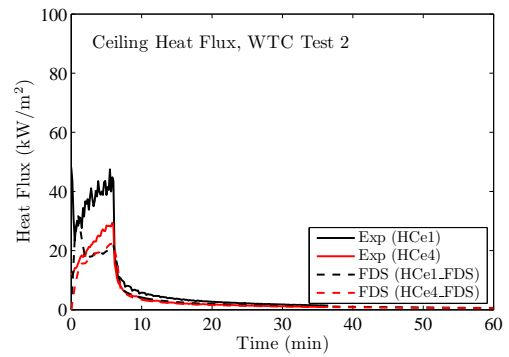
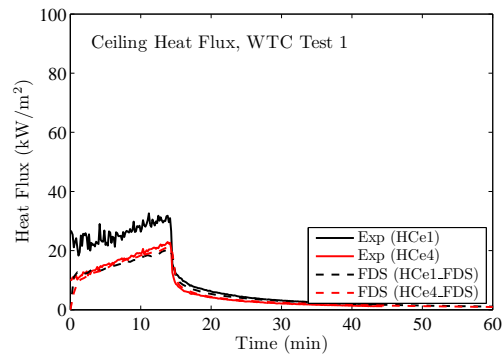


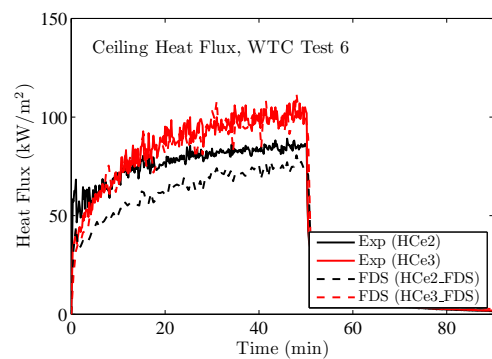
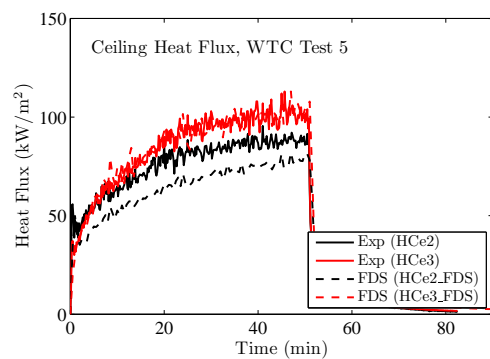
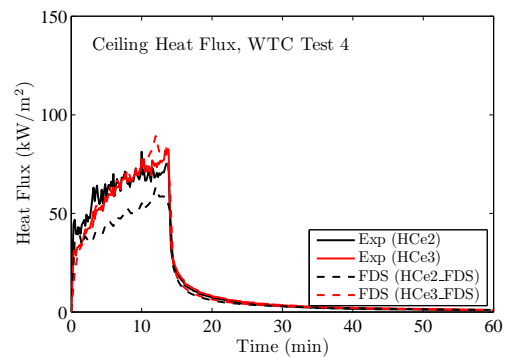
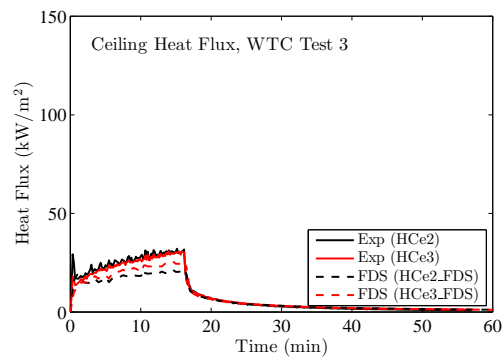
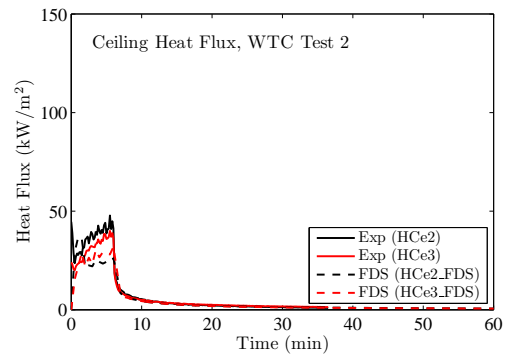
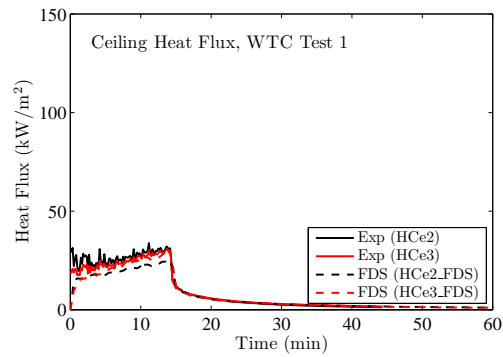












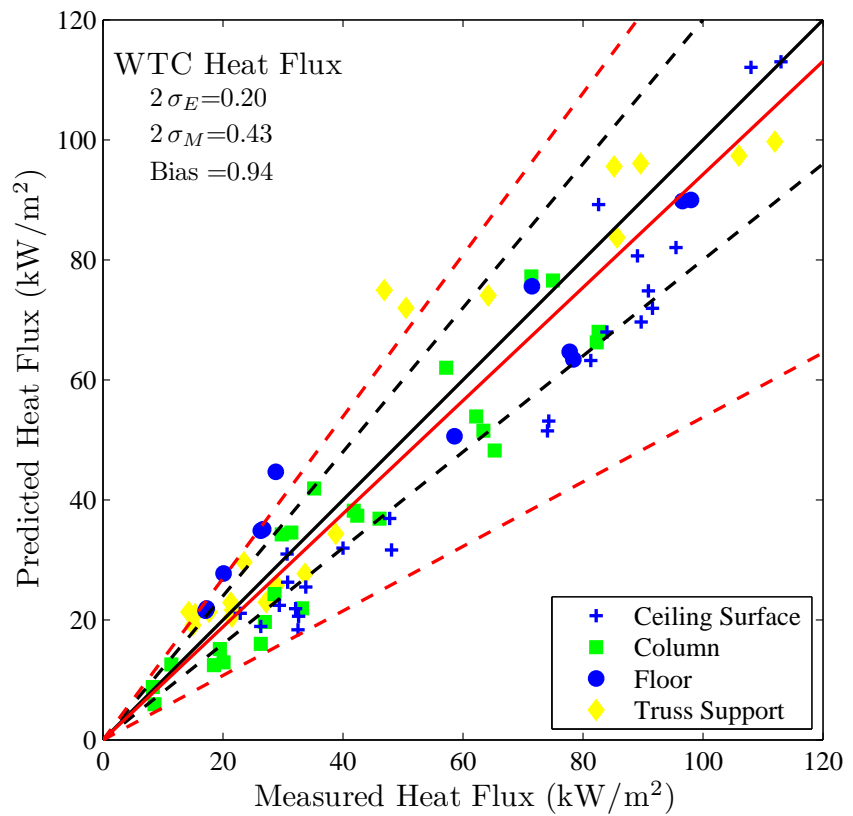
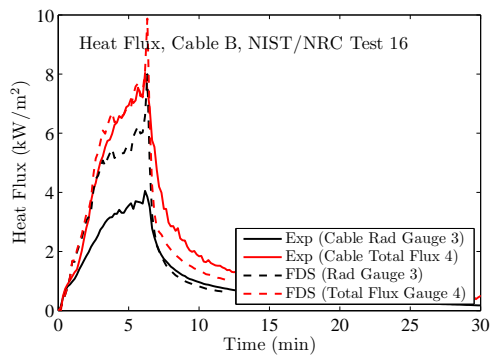
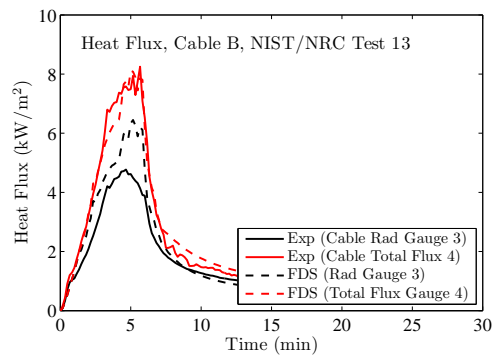
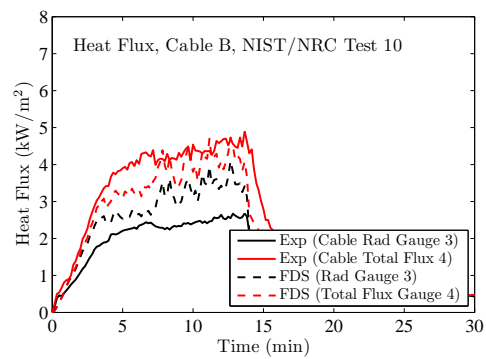
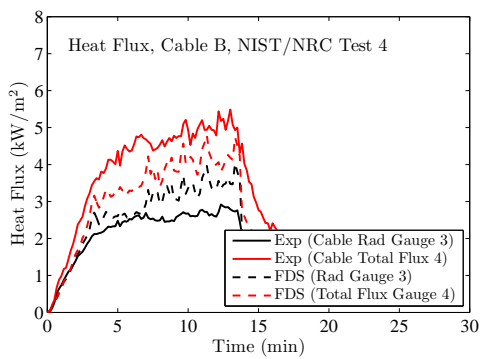
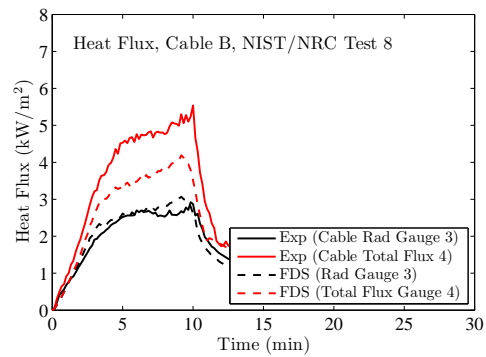
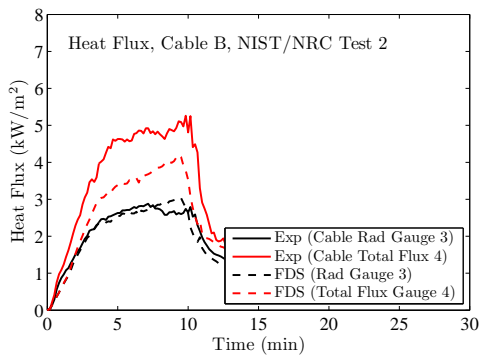
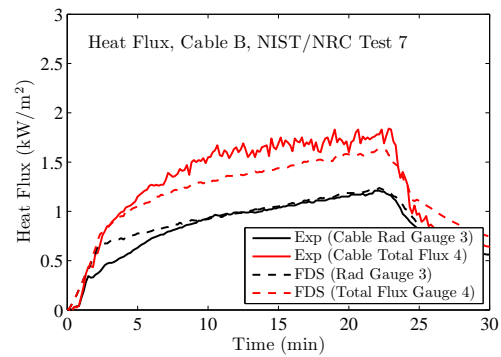
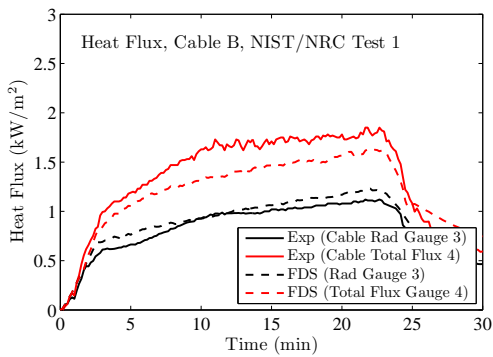
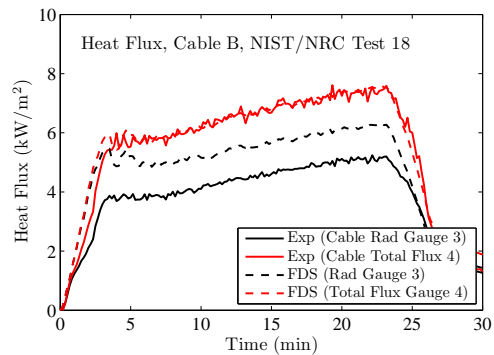
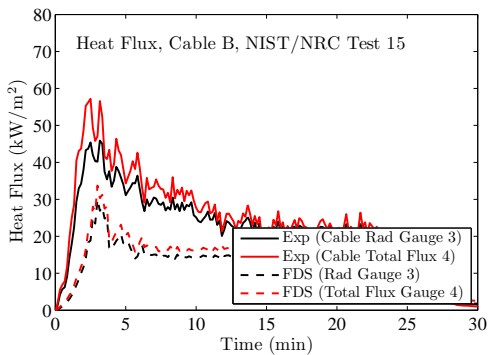
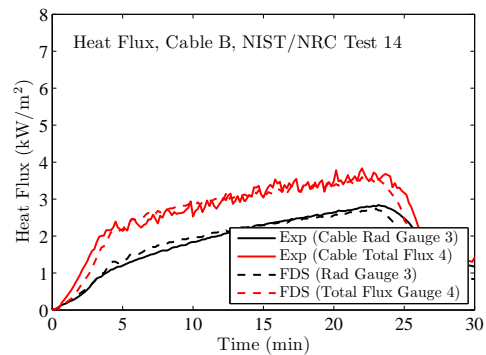
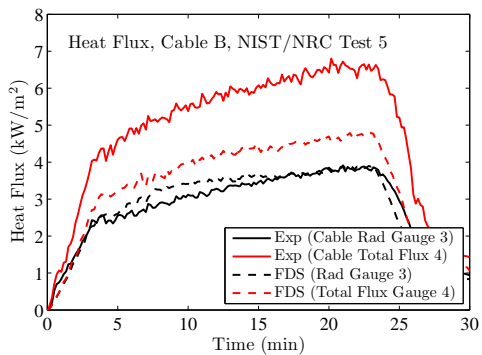
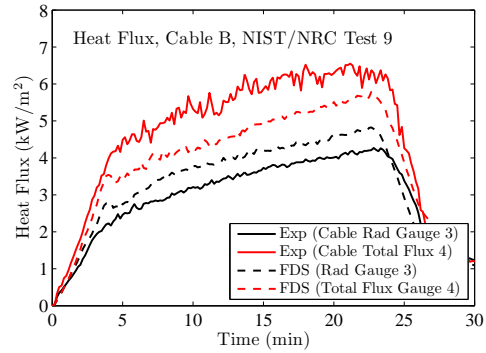
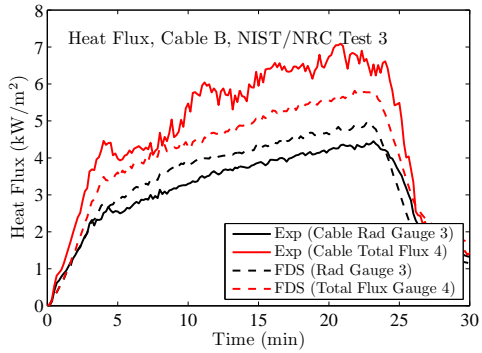


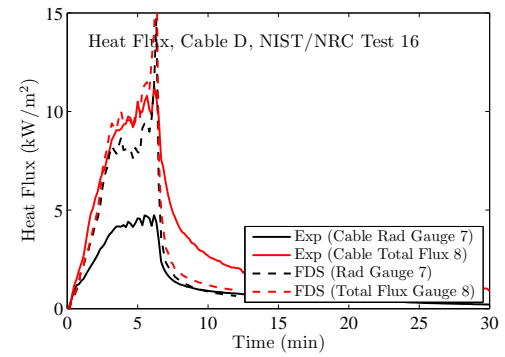
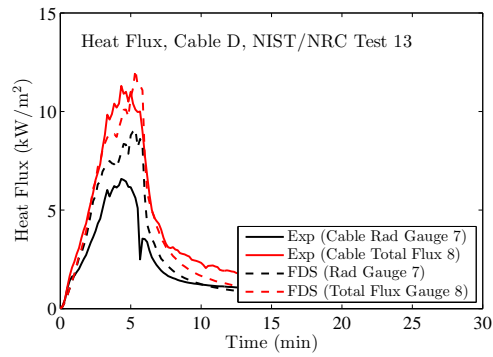
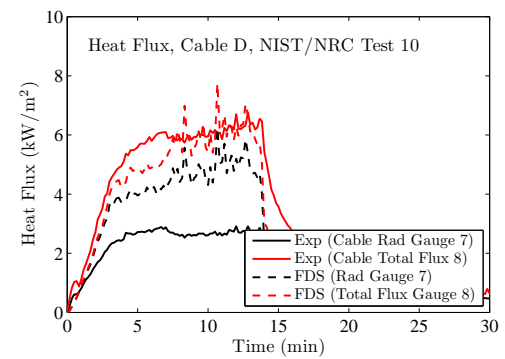
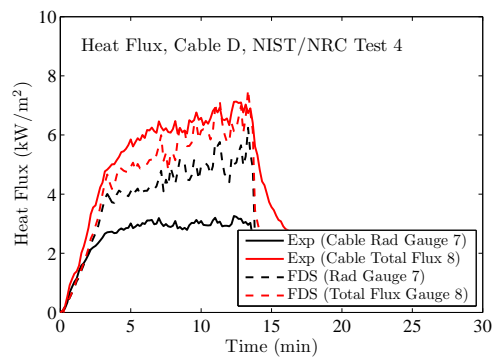
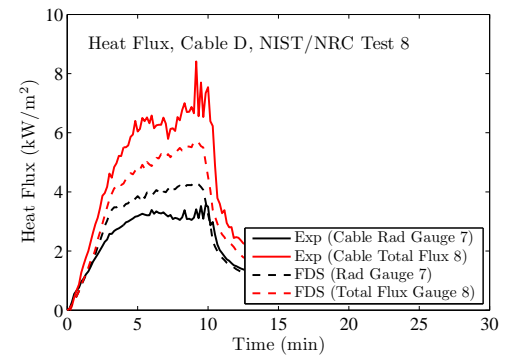
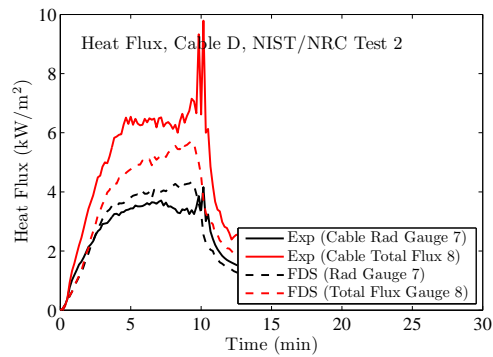
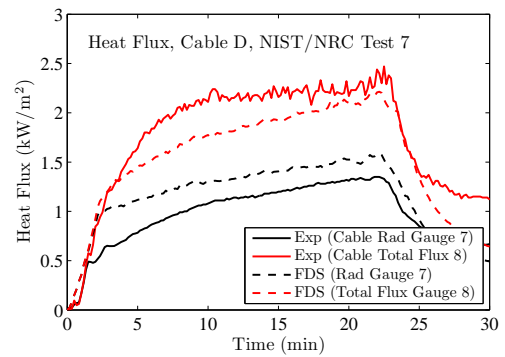
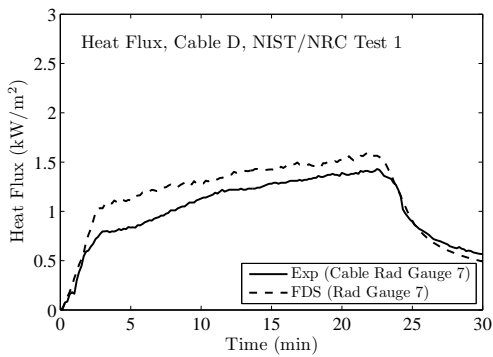
Figure 12.7: Summary of heat flux predictions for the WTC test series.

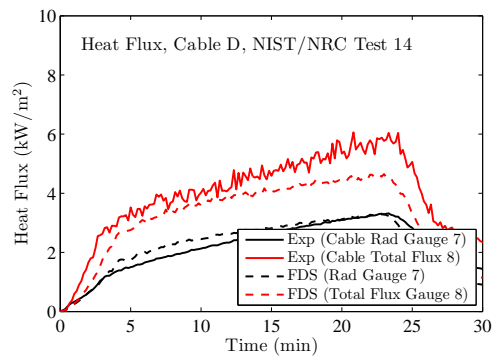
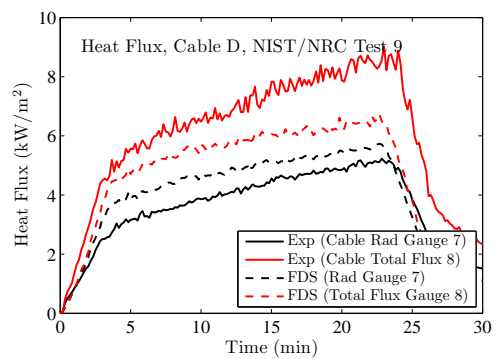
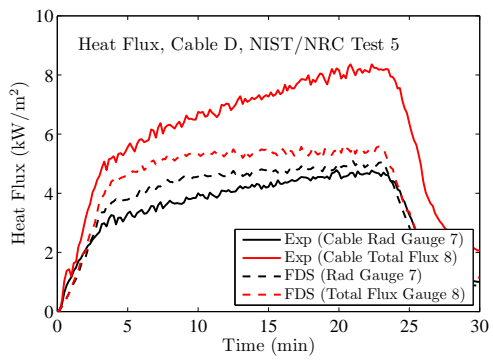
12.6 NIST/NRC Test Series, Heat Flux to Cables

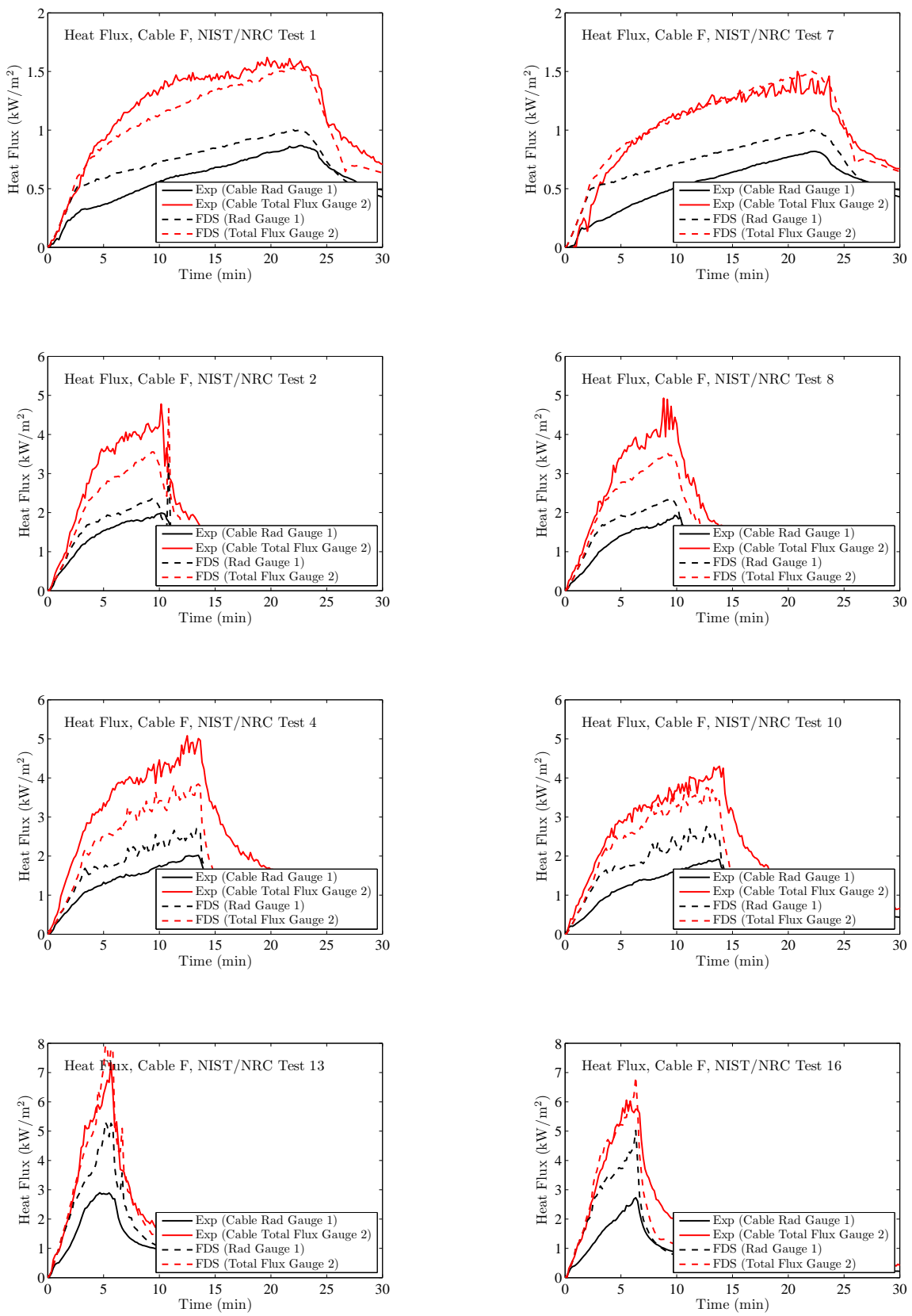
Cables in various types (power and control), and configurations (horizontal, vertical, in trays or free-hanging), were installed in the test compartment. For each of the four cable targets considered, measurements of the radiative and total heat flux were made with gauges positioned near the cables themselves. The following pages display comparisons of these heat flux predictions and measurements for Control Cable B, Horizontal Cable Tray D, Power Cable F and Vertical Cable Tray G.

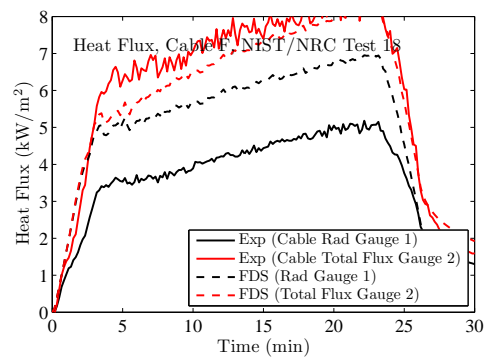
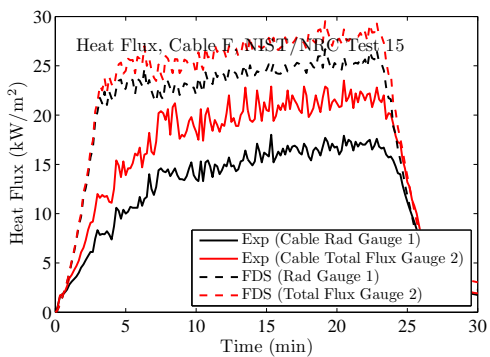
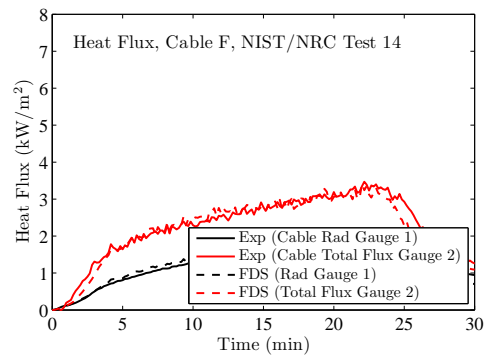
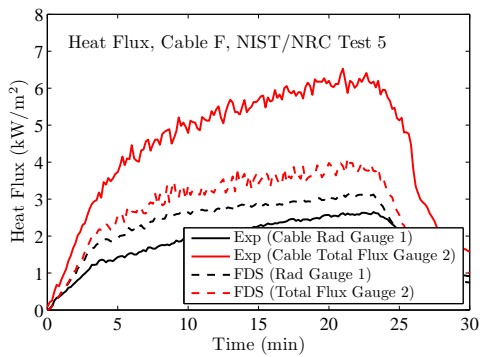
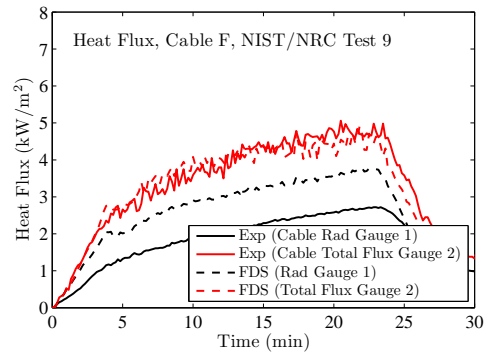
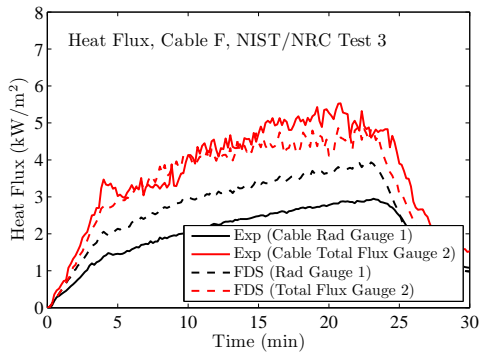


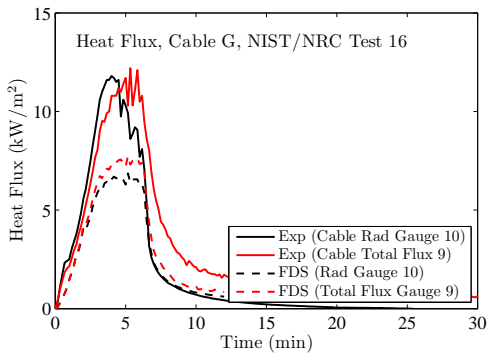
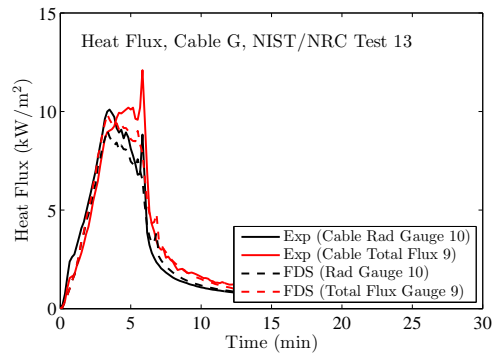
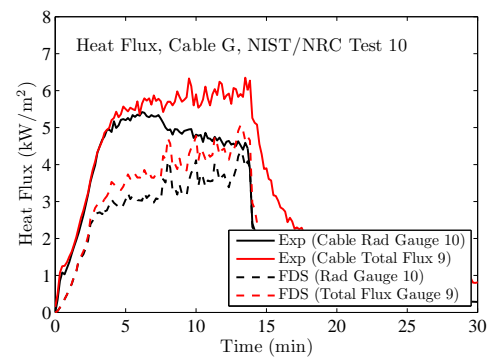
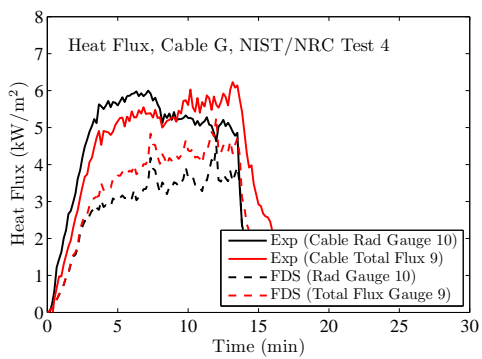
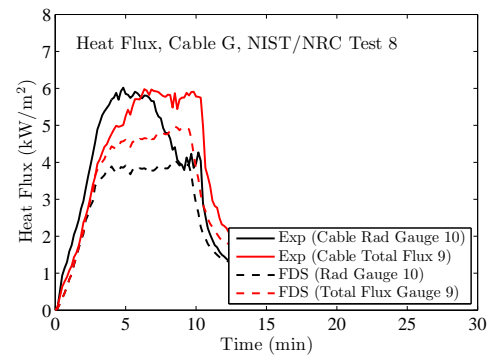
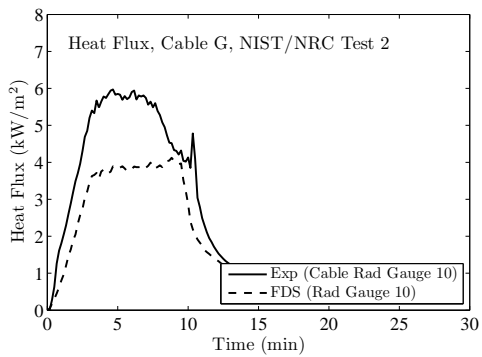
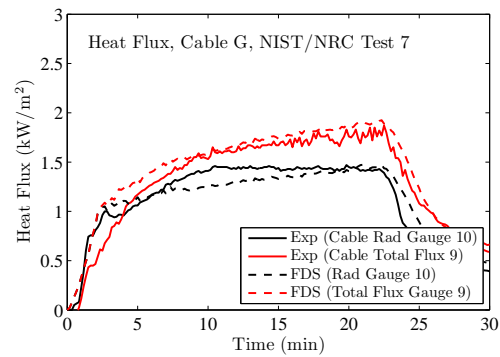
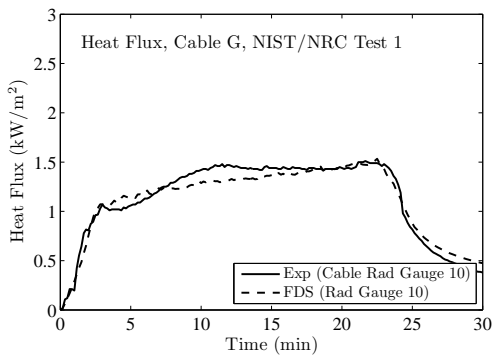


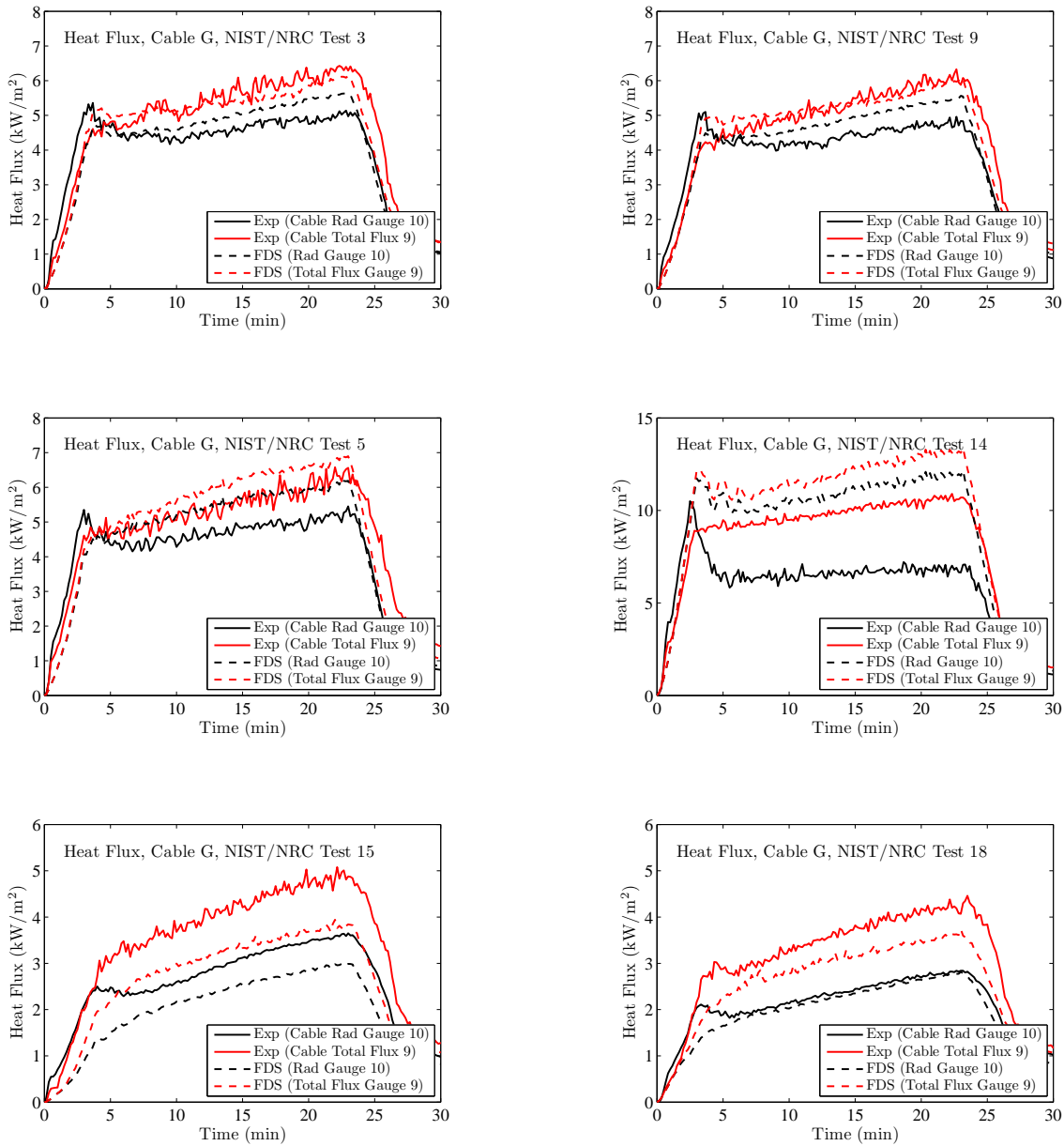












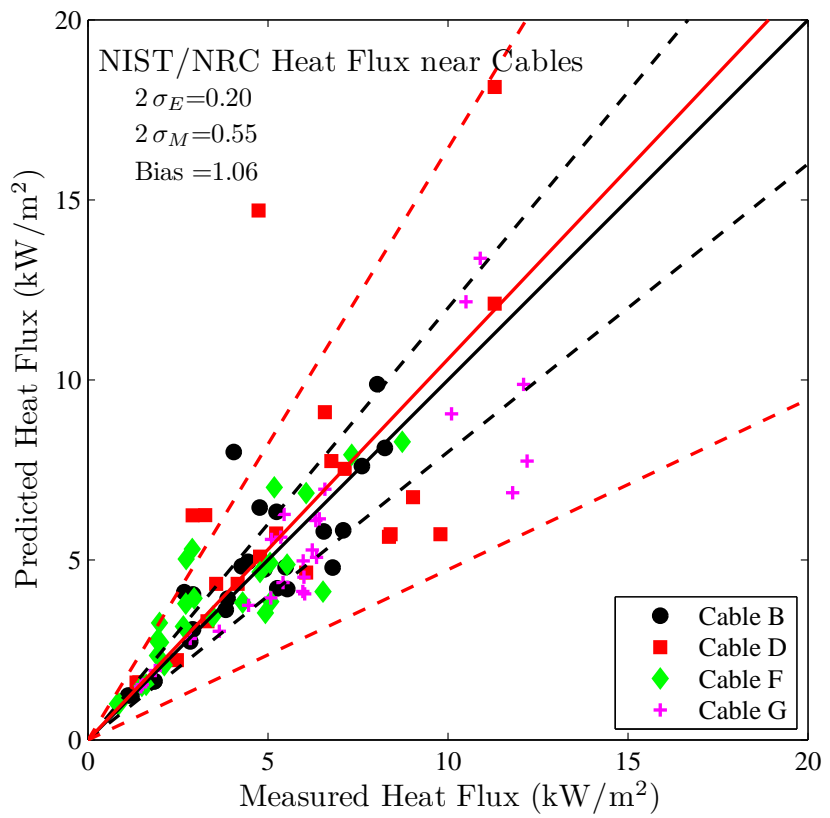


Figure 12.8: Summary of heat flux predictions to the cables in the NIST/NRC test series.

12.7 NRCC Facade Heat Flux Measurements

Figure 12.9 displays the simulation of a 10.3 MW fire inside and outside of a small enclosure. The purpose of the experiment was to measure the heat flux to the exterior facade. The FDS heat flux predictions are made at the location of the green points.

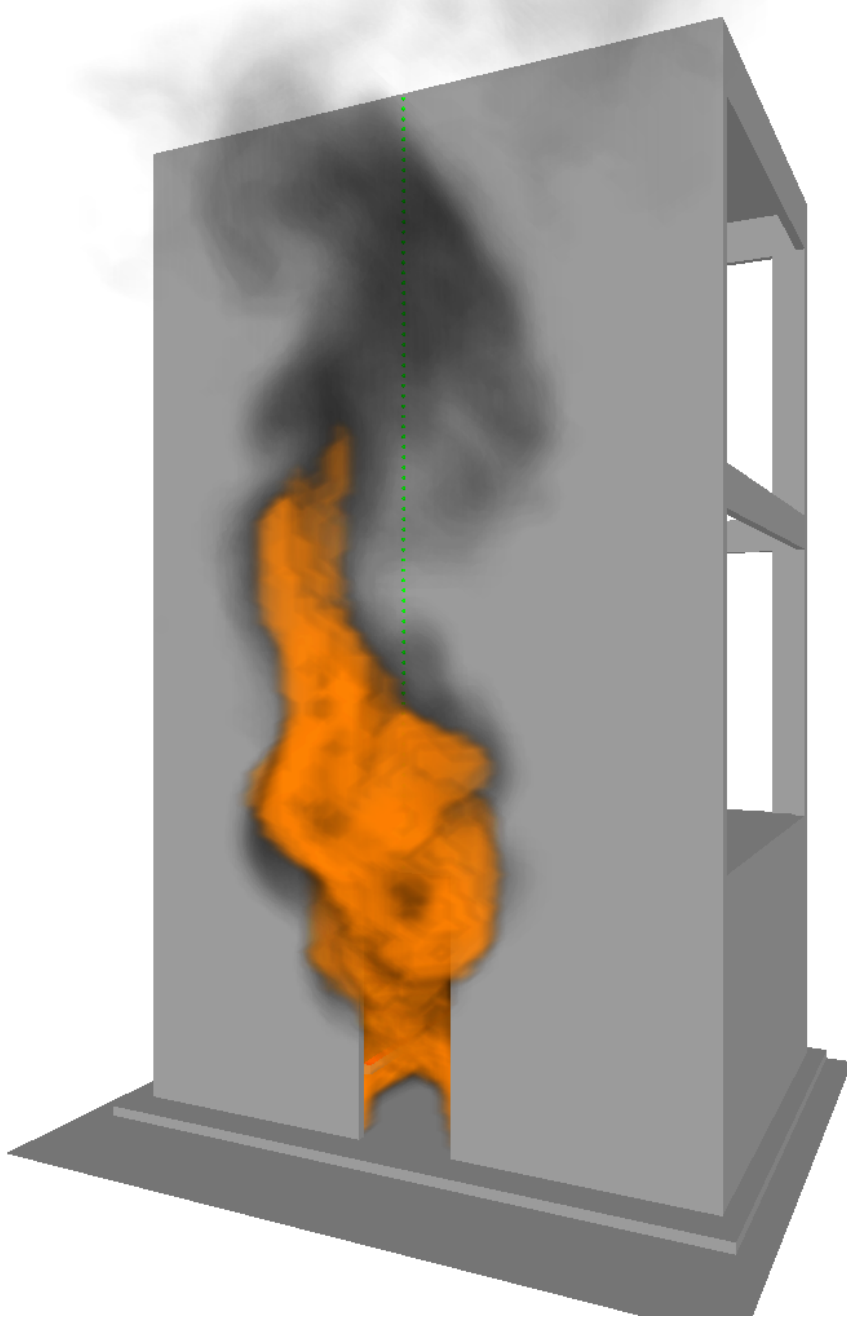
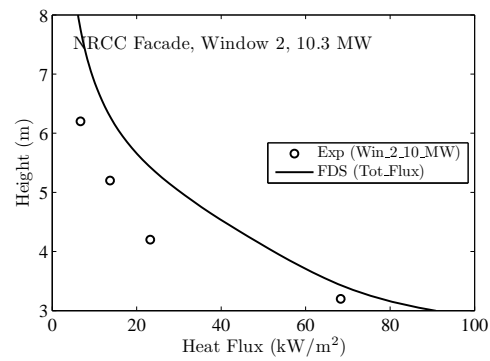
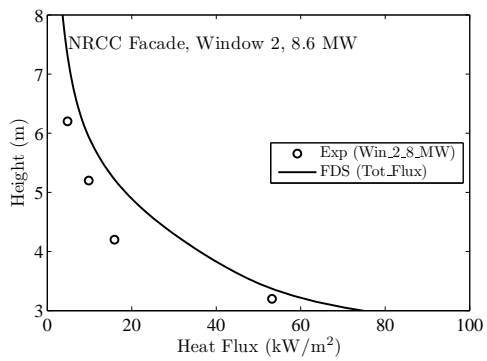
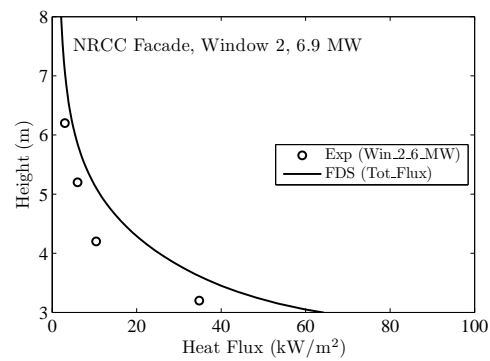
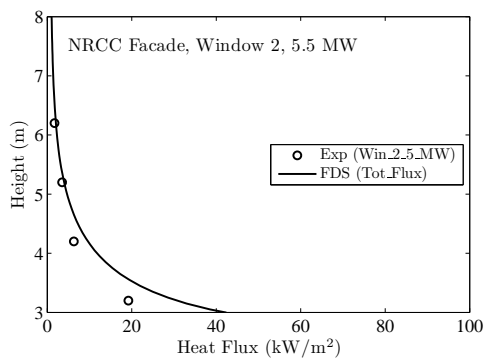
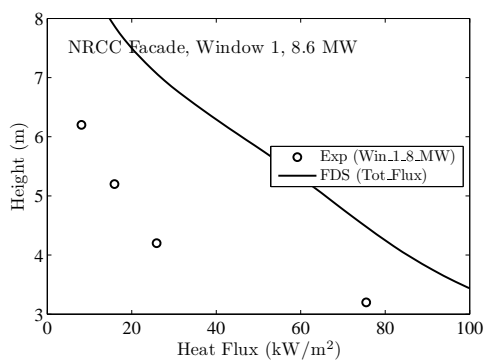
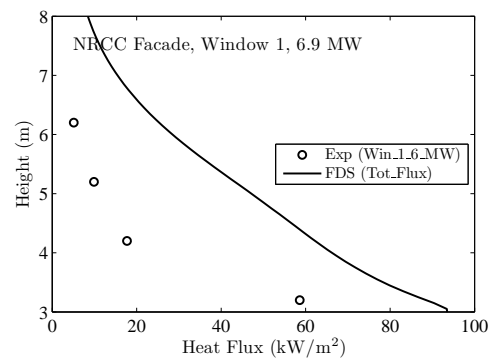
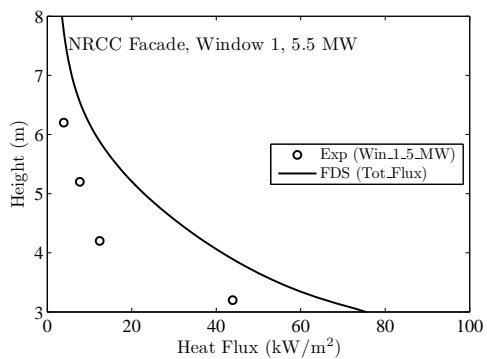
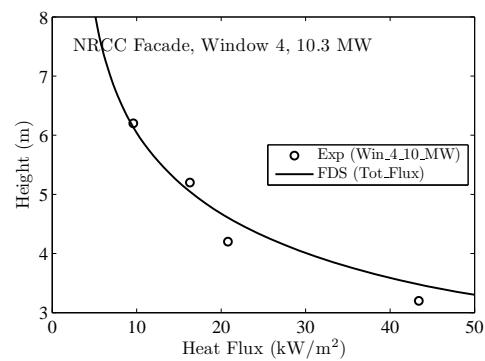
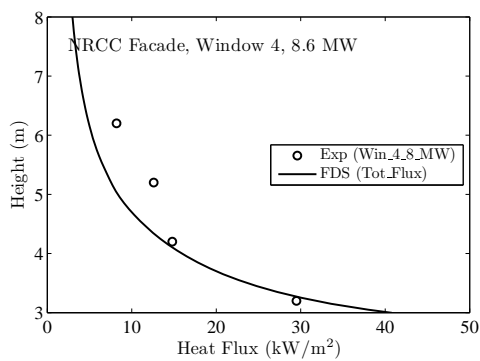
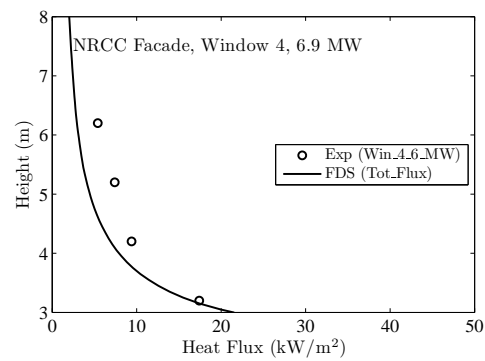
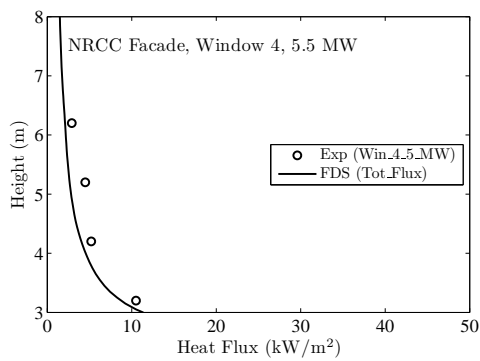
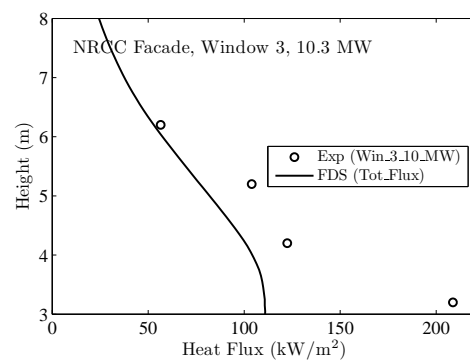
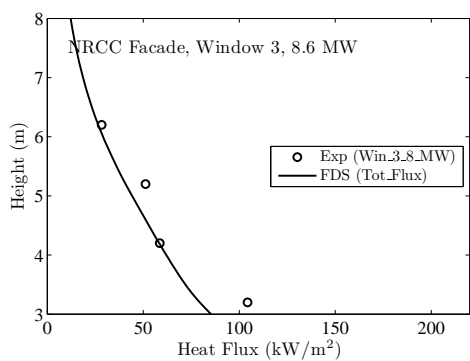
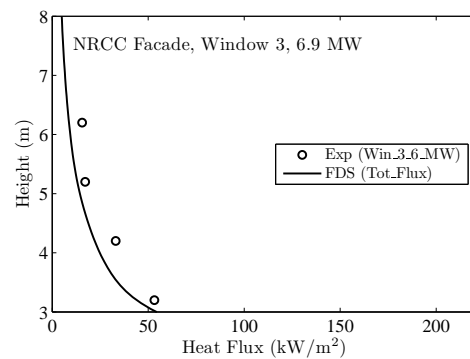
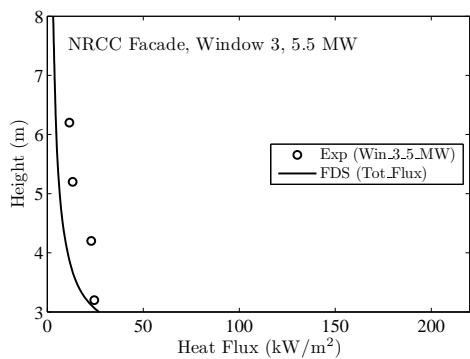
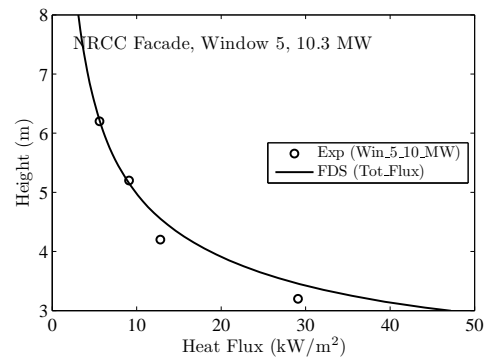
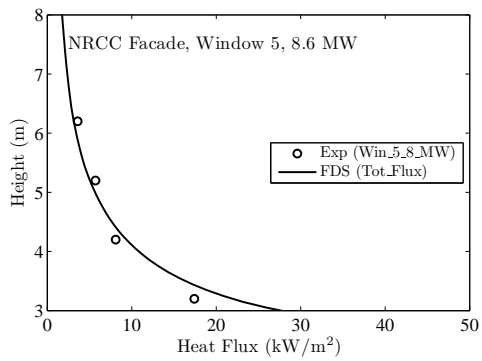
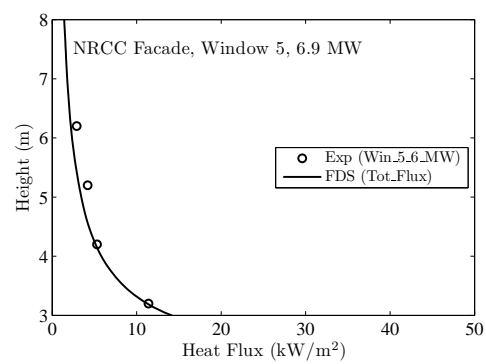
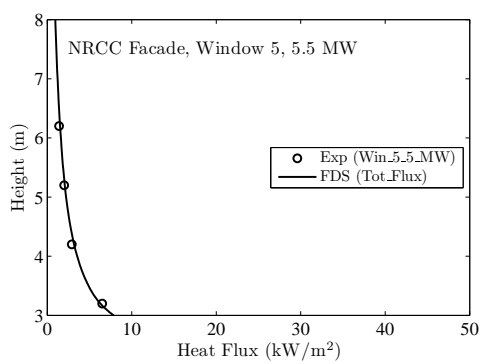


Figure 12.9: Smokeview rendering of one of the NRCC Facade experiments. The door is 0.94 m by 2.70 m tall (referred to as “Window 2” in the comparison plots). The fire is 10.3 MW.







12.8 BRE Spray Tests, Attenuation of Thermal Radiation in Water Spray

Attenuation of thermal radiation in water sprays was measured using three full-cone type hydraulic nozzles and eight pressures for each nozzle. The droplet boundary conditions were determined by assuming $d_m \propto p^{-1/3}$ and $v \propto p^{1/2}$ type of dependences between the droplet size, speed and pressure, and by comparing the predicted and measured results at the PDPA measurement location 0.7 m below the nozzles. For practical reasons, measured median diameter d_{v50} is compared against mean diameter d_{43} . For the vertical velocity, arithmetic mean of the droplets is used. These results represent a validation of the boundary conditions. The actual validation of radiation attenuation is performed by comparing the experimental and measured attenuations.

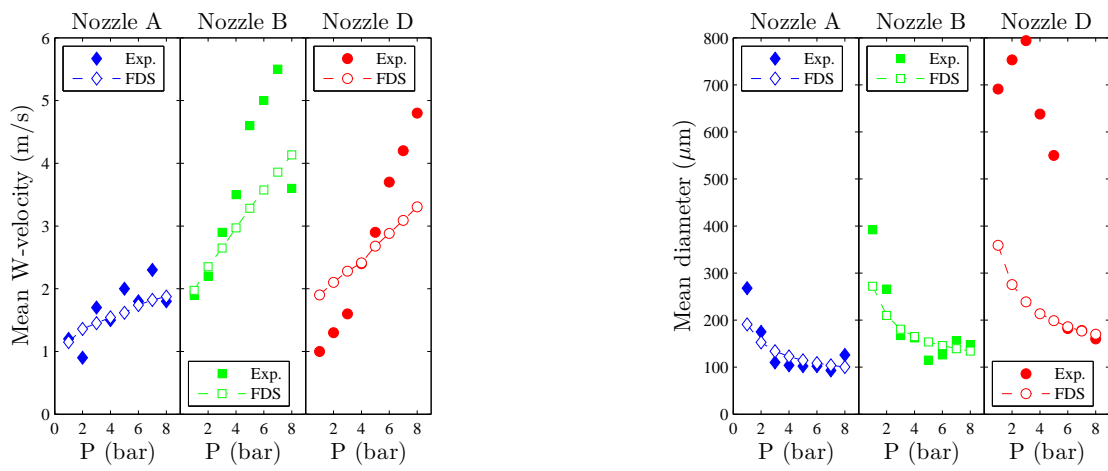


Figure 12.10: Comparison of experimental and predicted droplet speeds and mean diameters for the three nozzles and different pressures.

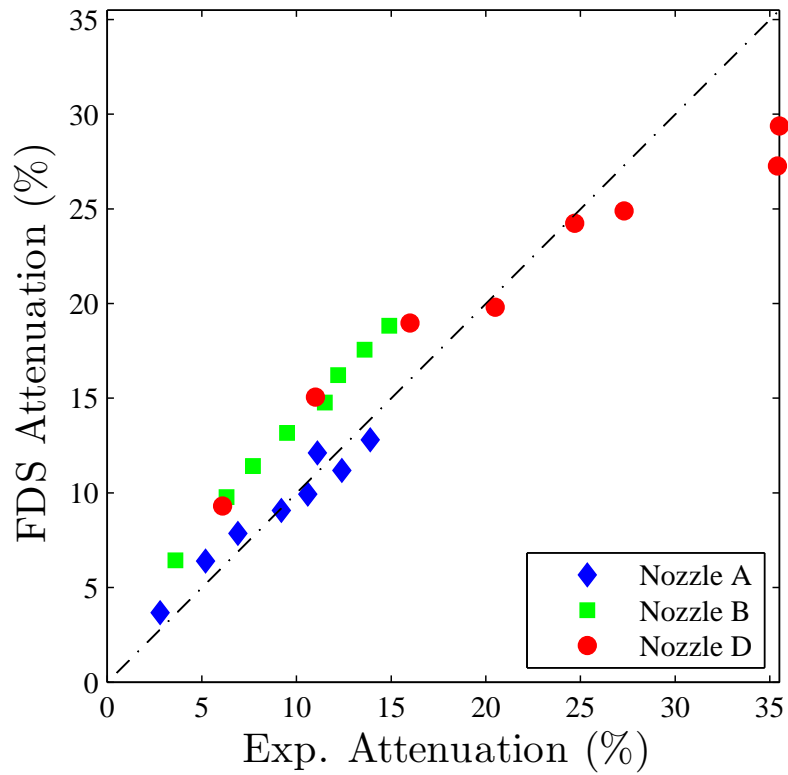


Figure 12.11: Summary radiation attenuations in the BRE Spray test series.

Bibliography

- [1] K.B. McGrattan, S. Hostikka, and J.E. Floyd. Fire Dynamics Simulator (Version 5), User's Guide. NIST Special Publication 1019-5, National Institute of Standards and Technology, Gaithersburg, Maryland, October 2007. [i](#)
- [2] American Society for Testing and Materials, West Conshohocken, Pennsylvania. *ASTM E 1355-04, Standard Guide for Evaluating the Predictive Capabilities of Deterministic Fire Models*, 2004. [i](#), [1](#)
- [3] K. Hill, J. Dreisbach, F. Joglar, B. Najafi, K. McGrattan, R. Peacock, and A. Hamins. Verification and Validation of Selected Fire Models for Nuclear Power Plant Applications. NUREG 1824, United States Nuclear Regulatory Commission, Washington, DC, 2007. [xiii](#), [47](#), [48](#), [49](#), [50](#), [56](#), [58](#)
- [4] R.G. Rehm and H.R. Baum. The Equations of Motion for Thermally Driven, Buoyant Flows. *Journal of Research of the NBS*, 83:297–308, 1978. [5](#)
- [5] H.R. Baum, R.G. Rehm, P.D. Barnett, and D.M. Corley. Finite Difference Calculations of Buoyant Convection in an Enclosure, Part I: The Basic Algorithm. *SIAM Journal of Scientific and Statistical Computing*, 4(1):117–135, March 1983. [5](#)
- [6] R.G. Rehm, P.D. Barnett, H.R. Baum, and D.M. Corley. Finite Difference Calculations of Buoyant Convection in an Enclosure: Verification of the Nonlinear Algorithm. *Applied Numerical Mathematics*, 1:515–529, 1985. [5](#)
- [7] R.G. Rehm, H.R. Baum, D.W. Lozier, H. Tang, and J. Sims. Buoyant Convection in an Inclined Enclosure. In *Fire Safety Science – Proceedings of the Third International Symposium*, pages 313–323. International Association for Fire Safety Science, 1991. [5](#)
- [8] H.R. Baum, O.A. Ezekoye, K.B. McGrattan, and R.G. Rehm. Mathematical Modeling and Computer Simulation of Fire Phenomenon. *Theoretical and Computational Fluid Dynamics*, 6:125–139, 1994. [5](#)
- [9] K.B. McGrattan, R.G. Rehm, and H.R. Baum. Fire-Driven Flows in Enclosures. *Journal of Computational Physics*, 110(2):285–291, 1994. [5](#)
- [10] R.G. Rehm, K.B. McGrattan, H.R. Baum, and K.W. Cassel. Transport by Gravity Currents in Building Fires. In *Fire Safety Science – Proceedings of the Fifth International Symposium*, pages 391–402. International Association for Fire Safety Science, 1997. [5](#)
- [11] H.R. Baum, K.B. McGrattan, and R.G. Rehm. Three Dimensional Simulations of Fire Plume Dynamics. In *Fire Safety Science – Proceedings of the Fifth International Symposium*, pages 511–522. International Association for Fire Safety Science, 1997. [5](#)

- [12] H.R. Baum, K.B. McGrattan, and R.G. Rehm. Large Eddy Simulations of Smoke Movement in Three Dimensions. In *Proceedings of the Seventh International Interflam Conference*, pages 189–198. Interscience Communications, London, 1996. [5](#)
- [13] H.R. Baum and B.J. McCaffrey. Fire Induced Flow Field – Theory and Experiment. In *Fire Safety Science – Proceedings of the Second International Symposium*, pages 129–148. International Association for Fire Safety Science, 1989. [5](#)
- [14] H.R. Baum, K.B. McGrattan, and R.G. Rehm. Three Dimensional Simulations of Fire Plume Dynamics. *Journal of the Heat Transfer Society of Japan*, 35(139):45–52, 1997. [5](#)
- [15] J.M. Clement and C.M. Fleischmann. Experimental Verification of the Fire Dynamics Simulator Hydrodynamic Model. In *Fire Safety Science – Proceedings of the Seventh International Symposium*, pages 839–862. International Association for Fire Safety Science, 2002. [5](#)
- [16] K.B. McGrattan, H.R. Baum, and R.G. Rehm. Large Eddy Simulations of Smoke Movement. *Fire Safety Journal*, 30:161–178, 1998. [5](#)
- [17] W. Mell, K.B. McGrattan, and H. Baum. Numerical Simulation of Combustion in Fire Plumes. In *Twenty-Sixth Symposium (International) on Combustion*, pages 1523–1530. Combustion Institute, Pittsburgh, Pennsylvania, 1996. [5](#)
- [18] T. Cleary, M. Anderson, J. Averill, and W. Grosshandler. Evaluating Multi-Sensor Fire Detectors in the Fire Emulator/Detector Evaluator. In *Proceedings of the Eighth International Interflam Conference*, pages 453–464. Interscience Communications, June 1999. [5](#)
- [19] W. Davis, K. Notarianni, and K. McGrattan. Comparison of Fire Model Predictions with Experiments Conducted in a Hangar with a 15 Meter Ceiling. NISTIR 5927, National Institute of Standards and Technology, Gaithersburg, Maryland, December 1996. [6](#)
- [20] S.J. Emmerich and K.B. McGrattan. Application of a Large Eddy Simulation Model to Study Room Airflow. *ASHRAE Transactions*, 104(1):1–9, 1998. [6](#), [37](#)
- [21] S.J. Emmerich. Use of Computational Fluid Dynamics to Analyze Indoor Air Quality Issues. NISTIR 5997, National Institute of Standards and Technology, Gaithersburg, Maryland, April 1997. [6](#), [37](#)
- [22] W.K. Chow and R. Yin. Discussion on Two Plume Formulae with Computational Fluid Dynamics. *Journal of Fire Sciences*, 20:179–201, May 2002. [6](#)
- [23] F. Battaglia, K. McGrattan, R. Rehm, and H. Baum. Simulating Fire Whirls. *Combustion Theory and Modeling*, 4:123–138, 2000. [6](#)
- [24] K.M. Liang, T. Ma, J.G. Quintiere, and D. Rouson. Application of CFD Modeling to Room Fire Growth on Walls. NIST GCR 03-849, National Institute of Standards and Technology, Gaithersburg, Maryland, April 2003. [6](#), [10](#)
- [25] T. Ma and J. Quintiere. Numerical Simulation of Axi-Symmetric Fire Plumes: Accuracy and Limitations. *Fire Safety Journal*, 38:467–492, 2003. [6](#), [10](#)
- [26] G. Hesketh. *SFPE Handbook of Fire Protection Engineering*, chapter Fire Plumes, Flame Height and Air Entrainment. National Fire Protection Association, Quincy, Massachusetts, 3rd edition, 2002. [6](#), [90](#)

- [27] C. Gutiérrez-Montes, E. Sanmiguel-Rojas, A. Viedma, and G. Rein. Experimental data and numerical modelling of 1.3 and 2.3 MW fires in a 20 m cubic atrium. *Building and Environment*, 44:1827–1839, 2009. ([Web Link](#)). [7](#)
- [28] M. Hurley and A. Munguia. Analysis of FDS Thermal Detector Response Prediction Capability. NIST GCR 09-921, National Institute of Standards and Technology, Gaithersburg, Maryland, 2009. [7](#)
- [29] M. Hurley and A. Munguia. Analysis of FDS Thermal Detector Response Prediction Capability. *J. Fire Protection Engineering*, 20, 2009. [7](#)
- [30] Y. Xin. Baroclinic Effects on Fire Flow Field. In *Proceedings of the Fourth Joint Meeting of the U.S. Sections of the Combustion Institute*. Combustion Institute, Pittsburgh, Pennsylvania, March 2005. [7](#)
- [31] Y. Xin, J.P. Gore, K.B. McGrattan, R.G. Rehm, and H.R. Baum. Fire dynamics simulation of a turbulent buoyant flame using a mixture-fraction-based combustion model. *Combustion and Flame*, 141:329–335, 2005. [7](#)
- [32] Y. Xin, J.P. Gore, K.B. McGrattan, R.G. Rehm, and H.R. Baum. Large Eddy Simulation of Buoyant Turbulent Pool Fires. In *Twenty-Ninth Symposium (International) on Combustion*, pages 259–266. Combustion Institute, Pittsburgh, Pennsylvania, 2002. [7](#)
- [33] S. Hostikka, K.B. McGrattan, and A. Hamins. Numerical Modeling of Pool Fires using Large Eddy Simulation and Finite Volume Method for Radiation. In *Fire Safety Science – Proceedings of the Seventh International Symposium*, pages 383–394. International Association for Fire Safety Science, 2002. [7, 37](#)
- [34] J. Hietaniemi, S. Hostikka, and J. Vaari. FDS Simulation of Fire Spread – Comparison of Model Results with Experimental Data. VTT Working Papers 4, VTT Building and Transport, Espoo, Finland, 2004. [7, 10](#)
- [35] A. Musser, K. B. McGrattan, and J. Palmer. Evaluation of a Fast, Simplified Computational Fluid Dynamics Model for Solving Room Airflow Problems. NISTIR 6760, National Institute of Standards and Technology, Gaithersburg, Maryland, June 2001. [7, 37, 154](#)
- [36] X. Yuan, Q. Chen, L.R. Glicksman, Y. Hu, and X. Yang. Measurements and Computations of Room Airflow with Displacement Ventilation. Technical Report RP-949, American Society of Heating, Refrigerating, Air-Conditioning Engineers, 1999. [7](#)
- [37] A. Musser and L. Tan. Control of Diesel Exhaust Fumes in Enclosed Locomotive Facilities. Technical Report RP-1191, American Society of Heating, Refrigerating, Air-Conditioning Engineers, 2003. [8](#)
- [38] K. Mniszewski. The Use of FDS for Estimation of Flammable Gas/Vapor Concentrations. In *Proceedings of the 3rd Technical Symposium on Computer Applications in Fire Protection Engineering*, pages 143–155. Society for Fire Protection Engineers, Bethesda, Maryland, September 2001. [8](#)
- [39] S. Kerber and W. Walton. Characterizing Positive Pressure Ventilation using Computational Fluid Dynamics. NISTIR 7065, National Institute of Standards and Technology, Gaithersburg, Maryland, February 2003. [8](#)
- [40] R. Rehm, K. McGrattan, H. Baum, and E. Simiu. An Efficient Large Eddy Simulation Algorithm for Computational Wind Engineering: Application to Surface Pressure Computations on a Single Building. NISTIR 6371, National Institute of Standards and Technology, August 1999. [8](#)

- [41] R.G. Rehm, K.B. McGrattan, and H.R. Baum. Large Eddy Simulation of Flow over a Wooded Building Complex. *Wind & Structures*, 5(2):291–300, 2002. [8](#)
- [42] H.Y. Wang and P. Joulain. Numerical Simulation of Wind-Aided Turbulent Fires in a Ventilated Model Tunnel. In *Fire Safety Science – Proceedings of the Seventh International Symposium*, pages 161–172. International Association for Fire Safety Science, 2002. [8](#)
- [43] F. Magnussen and B.H. Hjertager. On Mathematical Modeling of Turbulent Combustion with Special Emphasis on Soot Formation and Combustion. In *Proceedings of the Sixteenth Symposium (International) on Combustion*, pages 719–729. Combustion Institute, Pittsburgh, Pennsylvania, 1977. [8](#)
- [44] C.H. Chang and R.N. Meroney. Concentration and flow distributions in urban street canyons: wind tunnel and computational data. *Journal of Wind Engineering and Industrial Aerodynamics*, 91:1141–1154, 2003. [8](#)
- [45] K.B. McGrattan, H.R. Baum, and R.G. Rehm. Numerical Simulation of Smoke Plumes from Large Oil Fires. *Atmospheric Environment*, 30(24):4125–4136, 1996. [9](#)
- [46] T. Yamada. Smoke Plume Trajectory from In-Situ Burning of Crude Oil in Tomakomai. Technical report, National Research Institute of Fire and Disaster, Japan, November 1998. [9](#)
- [47] Y. Mouilleau and A. Champassith. CFD simulations of atmospheric gas dispersion using the Fire Dynamics Simulator (FDS). *Journal of Loss Prevention in the Process Industries*, 22:316–323, 2009. published by Elsevier. [9](#)
- [48] R. Vettori. Effect of an Obstructed Ceiling on the Activation Time of a Residential Sprinkler. NISTIR 6253, National Institute of Standards and Technology, Gaithersburg, Maryland, November 1998. [9](#), [40](#)
- [49] R. Vettori. Effect of a Beamed, Sloped, and Sloped Beamed Ceilings on the Activation Time of a Residential Sprinkler. NISTIR 7079, National Institute of Standards and Technology, Gaithersburg, Maryland, December 2003. [9](#), [42](#)
- [50] J. Floyd. Comparison of CFAST and FDS for Fire Simulation with the HDR T51 and T52 Tests. NISTIR 6866, National Institute of Standards and Technology, Gaithersburg, Maryland, March 2002. [9](#)
- [51] J.E. Floyd, K.B. McGrattan, S. Hostikka, and H.R. Baum. CFD Fire Simulation Using Mixture Fraction Combustion and Finite Volume Radiative Heat Transfer. *Journal of Fire Protection Engineering*, 13:11–26, February 2003. [9](#), [14](#)
- [52] A. Kashef, N. Benichou, G.D. Lougheed, and C. McCartney. A Computational and Experimental Study of Fire Growth and Smoke Movement in Large Spaces. Technical Report NRCC-45201, National Research Council Canada, 2002. [9](#)
- [53] K.B. McGrattan, T. Kashiwagi, H.R. Baum, and S.L. Olson. Effects of Ignition and Wind on the Transition to Flame Spread in a Microgravity Environment. *Combustion and Flame*, 106:377–391, 1996. [10](#)
- [54] T. Kashiwagi, K.B. McGrattan, S.L. Olson, O. Fujita, M. Kikuchi, and K. Ito. Effects of Slow Wind on Localized Radiative Ignition and Transition to Flame Spread in Microgravity. In *Twenty-Sixth Symposium (International) on Combustion*, pages 1345–1352. Combustion Institute, Pittsburgh, Pennsylvania, 1996. [10](#)

- [55] W. Mell and T. Kashiwagi. Dimensional Effects on the Transition from Ignition to Flame Spread in Microgravity. In *Twenty-Seventh Symposium (International) on Combustion*, pages 2635–2641. Combustion Institute, Pittsburgh, Pennsylvania, 1998. 10
- [56] W. Mell, S.L. Olson, and T. Kashiwagi. Flame Spread Along Free Edges of Thermally-Thin Samples in Microgravity. In *Twenty-Eighth Symposium (International) on Combustion*, pages 2843–2849. Combustion Institute, Pittsburgh, Pennsylvania, 2000. 10
- [57] K. Prasad, Y. Nakamura, S.L. Olson, O. Fujita, K. Nishizawa, K. Ito, and T. Kashiwagi. Effect of Wind Velocity on Flame Spread in Microgravity. In *Twenty-Ninth Symposium (International) on Combustion*, pages 2553–2560. Combustion Institute, Pittsburgh, Pennsylvania, 2002. 10
- [58] Y. Nakamura, T. Kashiwagi, K.B. McGrattan, and H.R. Baum. Enclosure Effects on Flame Spread over Solid Fuels in Microgravity. *Combustion and Flame*, 130:307–321, 2002. 10
- [59] W.E. Mell, K.B. McGrattan, and H.R. Baum. g-Jitter Effects on Spherical Diffusion Flames. *Microgravity Science and Technology*, 15(4):12–30, 2004. 10
- [60] S. Hostikka and K.B. McGrattan. Large Eddy Simulations of Wood Combustion. In *Proceedings of the Ninth International Interflam Conference*, pages 755–762. Interscience Communications, London, 2001. 10
- [61] S.J. Ritchie, K.D. Steckler, A. Hamins, T.G. Cleary, J.C. Yang, and T. Kashiwagi. The Effect of Sample Size on the Heat Release Rate of Charring Materials. In *Fire Safety Science - Proceedings of the 5th International Symposium*, pages 177–188. International Association For Fire Safety Science, 1997. 10
- [62] J.W. Kwon, N.A. Dembsey, and C.W. Lautenberger. Evaluation of FDS V.4: Upward Flame Spread. *Fire Technology*, 43:255–284, 2007. 10
- [63] A. Hamins, A. Maranghides, K.B. McGrattan, E. Johnsson, T. Ohlemiller, M. Donnelly, J. Yang, G. Mulholland, K. Prasad, S. Kukuck, R. Anleitner, and T. McAllister. Federal Building and Fire Safety Investigation of the World Trade Center Disaster: Experiments and Modeling of Structural Steel Elements Exposed to Fire. NIST NCSTAR 1-5B, National Institute of Standards and Technology, Gaithersburg, Maryland, September 2005. 11, 25
- [64] A. Hamins, A. Maranghides, K.B. McGrattan, Ohlemiller, and R. Anletiner. Federal Building and Fire Safety Investigation of the World Trade Center Disaster: Experiments and Modeling of Multiple Workstations Burning in a Compartment. NIST NCSTAR 1-5E, National Institute of Standards and Technology, Gaithersburg, Maryland, September 2005. 11
- [65] K. McGrattan, C. Bouldin, and G. Forney. Federal Building and Fire Safety Investigation of the World Trade Center Disaster: Computer Simulation of the Fires in the WTC Towers. NIST NCSTAR 1-5F, National Institute of Standards and Technology, Gaithersburg, Maryland, September 2005. 11, 15
- [66] G. Rein, C. Abecassis Empis, and R. Carvel, editors. *The Dalmarnock Fire Tests: Experiments and Modelling*. University of Edinburgh, 2007. 11
- [67] G. Rein, J.L. Torero, W. Jahn, J. Stern-Gottfried, N.L. Ryder, S. Desanghere, M. Lázaro, F. Mowrer, A. Coles, D. Joyeux, D. Alvear, J.A. Capote, A. Jowsey, C. Abecassis-Empis, and P. Reszka. Round-Robin Study of a priori Modelling Predictions of The Dalmarnock Fire Test One. *Fire Safety Journal*, 44(4):590–602, 2009. ([Web Link](#)). 11

- [68] W. Jahn, G. Rein, and J.L. Torero. The Effect of Model Parameters on the Simulation of Fire Dynamics. In *Proceedings of the Ninth Symposium on Fire Safety Science*, September 2008. Karlsruhe, Germany ([Web Link](#)). 11
- [69] B.M. Storm and M.R. Pantesjö. The use of simulation in fire investigation. Bachelors thesis, Stord/Haugesund University College, Norway, 2009. 11
- [70] K.B. McGrattan, A. Hamins, and D. Stroup. Sprinkler, Smoke & Heat Vent, Draft Curtain Interaction — Large Scale Experiments and Model Development. NISTIR 6196-1, National Institute of Standards and Technology, Gaithersburg, Maryland, September 1998. 11
- [71] A. Hamins and K.B. McGrattan. Reduced-Scale Experiments to Characterize the Suppression of Rack Storage Commodity Fires. NISTIR 6439, National Institute of Standards and Technology, Gaithersburg, Maryland, 1999. 12
- [72] A. Hamins and K.B. McGrattan. Reduced-Scale Experiments on the Water Suppression of a Rack-Storage Commodity Fire for Calibration of a CFD Fire Model. In *Fire Safety Science – Proceedings of the Seventh International Symposium*, pages 457–468. International Association for Fire Safety Science, 2002. 12
- [73] S. Olenick, M. Klassen, and R.J. Roby. Validation Study for FDS for a High Rack Storage Fire Involving Pool Chemicals. In *Proceedings of the 3rd Technical Symposium on Computer Applications in Fire Protection Engineering*. Society of Fire Protection Engineers, Bethesda, Maryland, September 2001. 12
- [74] S.C. Kim and H.S. Ryou. An Experimental and Numerical Study on Fire Suppression using a Water Mist in an Enclosure. *Building and Environment*, 38:1309–1316, 2003. 12
- [75] S.C. Kim and H.S. Ryou. The Effects of Water Mist on the Compartment Fire. *International Journal of Air-Conditioning and Refrigeration*, 12(1):30–36, 2004. 12
- [76] B.P. Hume. Water Mist Suppression in Conjunction with Displacement Ventilation. Master's thesis, University of Canterbury, Christchurch, New Zealand, February 2003. Fire Engineering Research Report 03/4. 12
- [77] S. Hostikka and K.B. McGrattan. Numerical modeling of radiative heat transfer in water sprays. *Fire Safety Journal*, 41:76–86, 2006. 12
- [78] N. O'Grady and V. Novozhilov. Large Eddy Simulation of Sprinkler Interaction with a Fire Ceiling Jet. *Combustion Science and Technology*, 181(7):984–1006, 2009. 12
- [79] H. Ingason and S. Olsson. Interaction between Sprinklers and Fire Vents. Technical report, Swedish National Testing and Research Institute (SP), 1992. SP Report 1992:11. 12
- [80] P. Friday and F. W. Mowrer. Comparison of FDS Model Predictions with FM/SNL Fire Test Data. NIST GCR 01-810, National Institute of Standards and Technology, Gaithersburg, Maryland, April 2001. 12
- [81] W. Zhang, A. Hamer, M. Klassen, D. Carpenter, and R. Roby. Turbulence Statistics in a Fire Room Model by Large Eddy Simulation. *Fire Safety Journal*, 37:721–752, 2002. 12
- [82] S. Cochard. Validation of Fire Dynamics Simulator (Version 2.0) Freeware. *Tunnel Management International Journal*, 6(4), December 2003. 13

- [83] K. B. McGrattan and A. Hamins. Numerical Simulation of the Howard Street Tunnel Fire, Baltimore, Maryland, July 2001. NISTIR 6902, National Institute of Standards and Technology, Gaithersburg, Maryland, January 2003. Joint Publication of NIST and the US Nuclear Regulatory Commission (NUREG/CR-6793). [13](#)
- [84] A. Piergiorgio, D. Giuseppe, F. Dino, G. Zappellini, and A. Ferrari. CFD Simulations of a Truck Fire in the Underground Gran Sasso National Laboratory. In *Proceedings of the 5th Italian Conference on Chemical and Process Engineering*, volume 5 of *AIDIC Conference Series*. Associazione Italiana Di Ingegneria Chimica (AIDIC), Elsevier, May 2002. Papers presented at ICeAP-5, Florence, Italy, May 20-23, 2001. [13](#)
- [85] J.C. Edwards, R.A. Franks, G.F. Friel, and L. Yuan. Experimental and Modeling Investigation of the Effect of Ventilation on Smoke Rollback in a Mine Entry. In *Proceedings of the SME Annual Meeting*, pages 1–6. Society for Mining, Metallurgy and Exploration, 2005. [13](#)
- [86] C.C. Hwang and J.C. Edwards. The critical ventilation velocity in tunnel fires – a computer simulation. *Fire Safety Journal*, 40:213–244, 2005. [13](#)
- [87] J.C. Edwards and C.C. Hwang. CFD Modeling of Fire Spread Along Combustibles in a Mine Entry. In *Proceedings of the SME Annual Meeting*, pages 1–5. Society for Mining, Metallurgy and Exploration, 2006. [13](#)
- [88] M. Bilson, A. Purchase, and C. Stacey. Deluge System Operating Effectiveness in Road Tunnels and Impacts on Operating Policy. In *Proceedings 13th Australian Tunnelling Conference, Melbourne, Victoria, Australia*, May 2008. The Australasian Institute of Mining and Metallurgy. [13](#)
- [89] K.J. Harris. Water Application Rates for Fixed Fire Fighting Systems in Road Tunnels. In *Proceedings of the Fourth International Symposium on Tunnel Safety and Security*, pages 351–362, 2010. [13](#)
- [90] M. Arvidson. Large-Scale Water Spray and Water Mist Fire Suppression System Tests. In *Proceedings of the Fourth International Symposium on Tunnel Safety and Security*, pages 283–296, 2010. [13](#)
- [91] V. D’Souza, J.A. Sutula, S.M. Olenick, W. Zhang, and R.J. Roby. Use of Fire Dynamics Simulator to Predict Smoke Detector Activation. In *Proceedings of the 2001 Fall Technical Meeting, Eastern States Section*, pages 175–178. Combustion Institute, Pittsburgh, Pennsylvania, December 2001. [13](#)
- [92] R.J. Roby, S.J. Olenick, W. Zhang, D.J. Carpenter, M.S. Klassen, and J.L. Torero. A Smoke Detector Algorithm for Large Eddy Simulation Modeling. NIST GCR 07-911, National Institute of Standards and Technology, Gaithersburg, Maryland, 2007. [13](#)
- [93] W. Zhang, S.M. Olenick, M.S. Klassen, D.J. Carpenter, R.J. Roby, and J.L. Torero. A smoke detector activation algorithm for large eddy simulation fire modeling. *Fire Safety Journal*, 43:96–107, 2008. [13](#)
- [94] D.R. Brammer. A Comparison between Predicted and Actual Behaviour of Domestic Smoke Detectors in a Realistic House Fire. Master’s thesis, University of Canterbury, Christchurch, New Zealand, 2002. [13](#)
- [95] T. Cleary, M. Donnelly, G. Mulholland, and B. Farouk. Fire Detector Performance Predictions in a Simulated Multi-Room Configuration. In *Proceedings of the 12th International Conference on*

Automatic Fire Detection (AUBE '01). National Institute of Standards and Technology, Gaithersburg, Maryland, March 2001. NIST SP 965. [14](#)

- [96] A. Mukhopadhyay and I.K. Puri. An Assessment of Stretch Effects on Flame Tip Using the Thin Flame and Thick Formulations. *Combustion and Flame*, 133:499–502, 2003. [14](#)
- [97] A. Hamins, M. Bundy, I.K. Puri, K.B. McGrattan, and W.C. Park. Suppression of Low Strain Rate Non-Premixed Flames by an Agent. In *Proceedings of the 6th International Microgravity Combustion Workshop, NASA/CP-2001-210826*, pages 101–104. National Aeronautics and Space Administration, Lewis Research Center, Cleveland, Ohio, May 2001. [14](#)
- [98] S. Dillon and A. Hamins. Ignition Propensity and Heat Flux Profiles of Candle Flames for Fire Investigation. In Vytenis Babrauskas, editor, *Fire Science Applications to Fire Investigations*, pages 363–376. Interscience Communications, London, 2003. [14](#)
- [99] A. Hamins, M. Bundy, and S.E. Dillon. Characterization of Candle Flames. *Journal of Fire Protection Engineering*, 15(4):265–285, 2005. [14](#)
- [100] J.E. Floyd, C. Wieczorek, and U. Vandsburger. Simulations of the Virginia Tech Fire Research Laboratory Using Large Eddy Simulation with Mixture Fraction Chemistry and Finite Volume Radiative Heat Transfer. In *Proceedings of the Ninth International Interflam Conference*. Interscience Communications, London, 2001. [14](#)
- [101] Y. Xin and J.P. Gore. Measurements and Calculations of Spectral Radiation Intensities in Buoyant Turbulent Flames. In *Proceedings of the Third Joint Meeting of the U.S. Sections of the Combustion Institute*. Combustion Institute, Pittsburgh, Pennsylvania, 2003. [14](#)
- [102] W. Zhang, N. Ryder, R.J. Roby, and D. Carpenter. Modeling of the Combustion in Compartment Fires Using Large Eddy Simulation Approach. In *Proceedings of the 2001 Fall Technical Meeting, Eastern States Section*. Combustion Institute, Pittsburgh, Pennsylvania, December 2001. [14](#)
- [103] W.L. Grosshandler, N. Bryner, D. Madrzykowski, and K. Kuntz. Report of the Technical Investigation of The Station Nightclub Fire. NIST NCSTAR 2, National Institute of Standards and Technology, Gaithersburg, Maryland, July 2005. [15](#)
- [104] D. Madrzykowski and R.L. Vettori. Simulation of the Dynamics of the Fire at 3146 Cherry Road NE Washington D.C., May 30, 1999. NISTIR 6510, National Institute of Standards and Technology, Gaithersburg, Maryland, April 2000. [15](#)
- [105] R.L. Vettori, D. Madrzykowski, and W.D. Walton. Simulation of the Dynamics of a Fire in a One-Story Restaurant – Texas, February 14, 2000. NISTIR 6923, National Institute of Standards and Technology, Gaithersburg, Maryland, October 2002. [15](#)
- [106] D. Madrzykowski, G.P. Forney, and W.D. Walton. Simulation of the Dynamics of a Fire in a Two-Story Duplex – Iowa, December 22, 1999. NISTIR 6854, National Institute of Standards and Technology, Gaithersburg, Maryland, January 2002. [15](#)
- [107] D. Madrzykowski and W.D. Walton. Cook County Administration Building Fire, 69 West Washington, Chicago, Illinois, October 17, 2003: Heat Release Rate Experiments and FDS Simulations. NIST Special Publication SP-1021, National Institute of Standards and Technology, Gaithersburg, Maryland, July 2004. [15](#)

- [108] P. Camp and N. Townsend. Computer Modelling vs Reality – Can We Predict the Behaviour of Fires? In *Proceedings of the Ninth International Interflam Conference*, pages 195–202. Interscience Communications, London, 2001. [15](#)
- [109] G. Rein, A. Bar-Ilan, N. Alvares, and A.C. Fernandez-Pello. Estimating the Performance of Enclosure Fire Models by Correlating Forensic Evidence of Accidental Fires. In *Proceedings of the Tenth International Interflam Conference*, pages 1183–1194. Interscience Communications, London, 2004. [15](#)
- [110] M. Spearpoint, F.W. Mowrer, and K. McGrattan. Simulation of a Compartment Flashover Fire Using Hand Calculations, Zone Models and a Field Model. In *Proceedings of the Third International Conference on Fire Research and Engineering (ICFRE3)*, pages 3–14. Society of Fire Protection Engineers, Bethesda, Maryland, 1999. [16](#)
- [111] D.J. Carpenter and C.B. Wood, editors. *Proceedings of the 3rd Technical Symposium on Computer Applications in Fire Protection Engineering*. Society for Fire Protection Engineers, Bethesda, Maryland, September 2001. [16](#)
- [112] A.M. Christensen and D.J. Icove. The Application of NIST's Fire Dynamics Simulator to the Investigation of Carbon Monoxide Exposure in the Deaths of Three Pittsburgh Fire Fighters. *Journal of Forensic Sciences*, 49(1):1–4, 2004. [16](#)
- [113] S. Hostikka, M. Kokkala, and J. Vaari. Experimental Study of the Localized Room Fires. VTT Research Notes 2104, VTT Technical Research Centre of Finland, Espoo, Finland, 2001. [17](#)
- [114] A. Tewarson. *SFPE Handbook of Fire Protection Engineering*, chapter Generation of Heat and Gaseous, Liquid, and Solid Products in Fires. National Fire Protection Association, Quincy, Massachusetts, fourth edition, 2008. [18](#)
- [115] D.T. Sheppard and D.R. Steppan. Sprinkler, Heat & Smoke Vent, Draft Curtain Project – Phase 1 Scoping Tests. Technical report, Underwriters Laboratories, Northbrook, Illinois, May 1997. [20](#), [118](#)
- [116] A. Hamins, A. Maranghides, R. Johnsson, M. Donnelly, G. Yang, G. Mulholland, and R.L. Anleitner. Report of Experimental Results for the International Fire Model Benchmarking and Validation Exercise 3. NIST Special Publication 1013-1, National Institute of Standards and Technology, Gaithersburg, Maryland, May 2006. Joint Publication of NIST and the US Nuclear Regulatory Commission (NUREG/CR-6905). [23](#)
- [117] S.P. Nowlen. Enclosure Environment Characterization Testing for the Baseline Validation of Computer Fire Simulation Codes. NUREG/CR-4681 (SAND86-1296), Sandia National Laboratory, Albuquerque, New Mexico, March 1987. Work performed under contract to the US Nuclear Regulatory Agency, Washington DC. [27](#)
- [118] J.M. Chavez and S.P. Nowlen. An Experimental Investigation of Internally Ignited Fires in Nuclear Power Plant Control Cabinets, Part II: Room Effects Tests. NUREG/CR-4527 (SAND86-0336), Sandia National Laboratory, Albuquerque, New Mexico, November 1988. Work performed under contract to the US Nuclear Regulatory Agency, Washington DC. [27](#)
- [119] R.D. Peacock, S. Davis, and W.T. Lee. An Experimental Data Set for the Accuracy Assessment of Room Fire Models. NBSIR 88-3752, National Bureau of Standards (now NIST), Gaithersburg, Maryland, April 1988. [29](#)

- [120] K.D. Steckler, J.G. Quintiere, and W.J. Rinkinen. Flow Induced By Fire in A Compartment. NBSIR 82-2520, National Bureau of Standards (now NIST), Gaithersburg, Maryland, September 1982. [31](#), [78](#), [143](#)
- [121] R.A. Bryant. A comparison of gas velocity measurements in a full-scale enclosure fire. *Fire Safety Journal*, 44:793–800, 2009. [33](#), [152](#)
- [122] U. Wickström, R. Jansson, and H. Tuovinen. Verification fire tests on using the adiabatic surface temperature for predicting heat transfer. Technical Report 2009:19, SP Technical Research Institute of Sweden, Börsas, Sweden, 2009. [33](#), [202](#)
- [123] D.T. Sheppard and B.W. Klein. Burn Tests in Two Story Structure with Hallways. Technical report, ATF Laboratories, Ammendale, Maryland, 2009. [33](#)
- [124] B.J. McCaffrey. Purely Buoyant Diffusion Flames: Some Experimental Results. NBSIR 79-1910, National Bureau of Standards (now NIST), Gaithersburg, Maryland, October 1979. [36](#)
- [125] T. J. O’Hern, E. J. Weckman, A. L. Gerhart, S. R. Tieszen, and R. W. Schefer. Experimental study of a turbulent buoyant helium plume. *J. Fluid Mech.*, 544:143–171, 2005. [36](#), [95](#)
- [126] T. K. Blanchat. Characterization of the air source and plume source at FLAME. Technical Report SAND01-2227, Sandia National Laboratory, Albuquerque, New Mexico, 2001. [36](#), [95](#)
- [127] P. E. DesJardin, T. J. O’Hern, and S. R. Tieszen. Large eddy simulation and experimental measurements of the near-field of a large turbulent helium plume. *Phys. Fluids*, 16(6):1866–1883, 2004. [36](#), [95](#)
- [128] S. R. Tieszen, T. J. O’Hern, E. J. Weckman, and R. W. Schefer. Experimental study of the effect of fuel mass flux on a 1-m-diameter methane fire and comparison with a hydrogen fire. *Combustion and Flame*, 139:126–141, 2004. [36](#), [98](#), [103](#)
- [129] S. R. Tieszen, T. J. O’Hern, R. W. Schefer, E. J. Weckman, and T. K. Blanchat. Experimental study of the flow field in and around a one meter diameter methane fire. *Combustion and Flame*, 129:378–391, 2002. [36](#), [98](#), [102](#)
- [130] T.S. Norton, K.C. Smyth, J.H. Miller, and M.D. Smooke. Comparison of Experimental and Computed Species Concentration and Temperature Profiles in Laminar, Two-Dimensional Methane/Air Diffusion Flames. *Combustion Science and Technology*, 90:1–34, 1993. [36](#)
- [131] K.C. Smyth. NO Production and Destruction in a Methane/Air Diffusion Flame. *Combustion Science and Technology*, 115:151–176, 1996. [36](#)
- [132] C. Belyer. Major Species Production by Diffusion Flames in a Two-Layer Compartment Fire Environment. *Fire Safety Journal*, 10:47–56, 1986. [36](#)
- [133] N. Bryner, E. Johnsson, and W. Pitts. Carbon Monoxide Production in Compartment Fires - Reduced-Scale Test Facility. NISTIR 5568, National Institute of Standards and Technology, Gaithersburg, MD, 1994. [36](#), [179](#)
- [134] A. Restivo. Turbulent Flow in Ventilated Rooms. Technical report, University of London, Department of Mechanical Engineering, 1979. [37](#)

- [135] G. Back, C. Beyler, P. DiNenno, and P. Tatem. Wall Incident Heat Flux Distributions Resulting from an Adjacent Fire. In *Fire Safety Science – Proceedings of the Fourth International Symposium*, pages 241–252. International Association of Fire Safety Science, 1994. [37](#)
- [136] J.P. Zhang, M. Delichatsios, M. Colobert, J. Hereid, M. Hagen, and D. Bakirtzis. Experimental and Numerical Investigations of Heat Impact and Flame Heights from Fires in SBI Tests. In *Proceedings of the Ninth Symposium on Fire Safety Science*, September 2008. Karlsruhe, Germany. [37](#)
- [137] P.A. Beaulieu. Parallel Panel Experiments of FRP Composites. Technical Report 0003024286, FM Global, Norwood, Massachusetts, December 2007. [37](#)
- [138] I. Oleszkiewicz. Heat Transfer from a Window Fire Plume to a Building Facade. In *HTD – Collected Papers in Heat Transfer*, volume 123, pages 163–170. American Society of Mechanical Engineers, 1989. Book No. H00526. [38](#)
- [139] I. Oleszkiewicz. Fire Exposure to Exterior Walls and Flame Spread on Combustible Cladding. *Fire Technology*, 26(4):357–375, 1990. [38](#)
- [140] S.P. Nowlen, F.J. Wyant, and K.B. McGrattan. Cable Response to Live Fire (CAROLFIRE). NUREG/CR 6931, United States Nuclear Regulatory Commission, Washington, DC, April 2008. [38, 223](#)
- [141] P. Andersson and P. Van Hees. Performance of Cables Subjected to Elevated Temperatures. In *Fire Safety Science – Proceedings of the Eighth International Symposium*, pages 1121–1132. International Association of Fire Safety Science, 2005. [38](#)
- [142] J.V. Murrel, D. Crowhurst, and P. Rock. Experimental Study of The Thermal Radiation Attenuation of Sprays from Selected Hydraulic Nozzles. In *Proceedings of Halon Options Technical Working Conference 1995*, pages 369–378. The University of New Mexico, Albuquerque, 1995. [40](#)
- [143] K.A. Notarianni and G.W. Parry. *SFPE Handbook of Fire Protection Engineering*, chapter Uncertainty. National Fire Protection Association, Quincy, Massachusetts, 4th edition, 2008. [45](#)
- [144] N.O. Siu and G.E. Apostolakis. Probabilistic Models for Cable Tray Fires. *Reliability Engineering*, 3:213–227, 1982. [45](#)
- [145] W.D. Walton and P.H. Thomas. *SFPE Handbook of Fire Protection Engineering*, chapter Estimating Temperatures in Compartment Fires. National Fire Protection Association, Quincy, Massachusetts, 4th edition, 2008. [48](#)
- [146] R.D. Peacock, P.A. Reneke, W.D. Davis, and W.W. Jones. Quantifying fire model evaluation using functional analysis. *Fire Safety Journal*, 33:167–184, 1999. [51](#)
- [147] G. Oehlert. A Note on the Delta Method. *The American Statistician*, 46(1):27–29, 1992. [51](#)
- [148] A. Gelman, J.B. Carlin, H.S. Stein, and D.B. Rubin. *Bayesian Data Analysis*. Chapman and Hall/CRC Press, Boca Raton, Florida, 2nd edition, 2004. [52](#)
- [149] M.L. Janssens and H.C. Tran. Data Reduction of Room Tests for Zone Model Validation. *Journal of Fire Science*, 10:528–555, 1992. [59](#)
- [150] Y.P. He, A. Fernando, and M.C. Luo. Determination of interface height from measured parameter profile in enclosure fire experiment. *Fire Safety Journal*, 31:19–38, 1998. [60](#)

- [151] U. Wickström, D. Duthinh, and K.B. McGrattan. Adiabatic Surface Temperature for Calculating Heat Transfer to Fire Exposed Structures. In *Proceedings of the Eleventh International Interflam Conference*. Interscience Communications, London, 2007. [202](#)